Diagenetic controls on the reservoir quality of a Lower Carboniferous Tight Gas Sandstone: The Breagh Field.

NWACHUKWU, CHIMAOBI,MAUREEN

Diagenetic controls on the reservoir quality of a Lower Carboniferous Tight Gas Sandstone: The Breagh Field.

Nwachukwu, Chimaobi Maureen

ABSTRACT

The Breagh Field is the first and presently the only field developed within the Lower Carboniferous clastic reservoir sequence in the UK SNS. Breagh is estimated to contain 909 bcf (P50) in tight (low permeability) sandstones with an expected recovery factor of 50%. The reservoir quality has been strongly influenced by diagenetic processes which significantly reduced porosity and permeability, and increased reservoir heterogeneity. This study integrates quantitative petrographic data, cathodoluminescence study, stable isotope analyses and 3D-XCT to investigate the impact of diagenesis and depositional facies variation on reservoir quality of the Breagh Sandstone by investigating the clay-poor sandstones within the reservoir.

Based on examination of core log and petrographic analyses, eleven facies associations were identified. The primary reservoirs are the stacked braided fluvial channel deposits although numerous thinner and finer-grained sandstone bodies exist within the delta front sands and abandoned channel facies. The connectivity of these thinner, secondary reservoirs will be critical for adding pay at Breagh and the other potential gas fields identified to the SSW, NE, and West of the Breagh Field.

The Breagh Sandstone consists of very fine- to coarse-grained, moderately well sorted to very well sorted, arenite to sublitharenite sands. The reservoir properties of the sandstone are relatively poor and with permeabilities between 0.1-100mD and porosities in the range of 9.5–19.6%. COPL and CEPL analysis show that mechanical compaction is the dominant process for the destruction of pore spaces, leading to a porosity reduction of 22.6% to 27.68% but, cementation still accounts for further reduction of porosity to the current range of 14.8% to 17.4%.

Features observed during early diagenesis include alteration of iron bearing silicates, clay coats, early carbonate cements, early quartz overgrowth, precipitation of sulphates and dissolution of feldspars. Mid-stage diagenetic events include dissolution of earlier formed sulphates, formation of kaolinite and illitization of mica. Late diagenetic features include late carbonate cementation, clay mineral cementation (illite and late-stage kaolinite), precipitation of further iron oxides, dissolution of illite and carbonate cements. Barite and anhydrite are minor late diagenetic cement phases.

Further investigation using SEM 2D images and 3D-XCT show that permeability is primarily controlled by the distribution of pore types, pore throat radius and pore connectivity. Whilst inter-grain pores (larger than 22µm) have the most potential for reservoir flow, the large number of smaller pore-throats do have negligible contribution to reservoir flow potential, albeit more significant for the reservoir storage capability.

The diagenetic control on the studied sandstone as well as the extracted pore network here will be a good input in predicting multi-phase flow properties of the studied reservoir and other potential gas fields. In particular, understanding the pore network and distribution of the thinner, secondary reservoirs will be critical for increasing producibility at the Breagh Field itself.

DIAGENETIC CONTROLS ON THE RESERVOIR QUALITY OF A LOWER CARBONIFEROUS TIGHT GAS SANDSTONE: THE BREAGH FIELD.

Nwachukwu, Chimaobi Maureen.

A thesis submitted for the degree of Doctor of Philosophy.

Department of Earth Sciences

Durham University

2023

Table of Contents

List of Tables

List of Figures

List of Abbreviations.

2D = Two-dimensional
3D = Three-dimensional
BSE = Back-Scatter Electron
CL = Cathodoluminescence
EDX = Energy Dispersive X-ray spectroscopy
EISB = Southern North Sea
EqD = Equivalent Diameter
Ft = Feet
mD = Millidarcy
m = meter
PPL = Plane Polarised Light
SE = Secondary Electron
SEM = Scanning Electron Microscopy
XCT = X-ray Computed Tomography
XPL = Cross Polarised Light
PPL = Plane polarized light
XRD = X-Ray Diffraction
BCF = Billion Cubic Feet
BCM = Billion cubic meters
SCF = Standard Cubic Feet
FA = Facies association
TCF = Trillion cubic feet
FWL = Free water level
GIIP = Gas initially in place
SST = Surface Sea Temperature
IGV = Intergranular Volume
CEM = Total Cement Volume
BBL = Barrel of crude oil
MMSCF = Million standard cubic feet
TVDSS = True vertical depth below sea level
COPL = Porosity loss by Compaction
CEPL = Porosity loss by cementation
OP = Original porosity
K = Permeability
Φ = Porosity

Declaration

I declare that no portion of the work referred to in the thesis has been submitted in support of an application for another degree or qualification, of this, or any other university or other institutes of learning.

Chapter 3 however has been published as part of the United Kingdom Oil and Gas Fields: 50th Anniversary Commemorative Volume. Geological Society, London, Memoirs. Volume 52. Pages 109 – 118. https://doi.org/10.1144/M52-2019-15

Nwachukwu, Chimaobi Maureen.

Statement of copyright

Acknowledgement.

I give thanks to the Almighty Triune God who has been my provider, strength, and refuge throughout my PhD Journey.

Words cannot express my profound gratitude to my Supervisor Prof. Jon Gluyas for his generosity, invaluable patience, and feedback. I also want to thank Prof. Andy Aplin and Dr. Stuart Jones for their supervision and feedback. I could not have undertaken this journey without my reviewers Prof. Chris Greenwell and Dr. Martin Smith who generously provided knowledge and expertise. I thank my mentor Prof. Mark Allen for his professional guidance and Prof. Stefan Neilson for helping me to learn programming. Additionally, this endeavor would not have been possible without the financial assistance from Durham University, Petroleum Technology Development Funds (PTDF), Ebonyi State Government Scholarship (ESGS), Dr Amos Abu, Hoper Dixon Trust, Funds for Women Graduates (FfWG), and the Sydney Perry Foundation.

I want to also thank Prof Jon Gluyas and Zoe Barnett for all their contributions in the Breagh field paper in chapter 3.

I am also grateful to everyone in Earth sciences, especially my bay 2 mates (Open plan area), for their editing help, late-night feedback sessions, and moral support. Thanks should also go to the University Librarians, research assistants, and the helpful study group organized by Naema Alnofeli.

Furthermore, I would like to thank the British Geological Survey for providing data and helpful discussions; Mr Wang for his insights on facies analysis, Shanzi for providing helpful skills in pore analysis on MATLAB; Mr Ian Chaplin and his team for the preparation of hundreds of thin sections; Mr Leon Bowen for his support and time at the scanning electron microscope; Joanne Peterkin for her assistance in preparing isotopic samples and James Dyson for all the technical and administrative support. Thanks are also given to Earth Science and Science Faculty Post Graduate administrative staff most especially Louise Bowron for all their support.

Lastly, I would be remiss in not mentioning my family, especially my parents who though passed on during this PhD journey continued to strengthen me with their love and faith in me. I thank my Sister Florence Obison so very much for all her emotional support. And to my darling husband, words alone cannot express my profound gratitude for who you are and everything you did for me.

Dedication

I dedicate this work to God Almighty, the Blessed Virgin Mary, all the Angels and saints and to my parents who though not being physically with me here, continue to love me from above.

Blank Page

Chapter 1

Introduction

Contents

Chapter 1: Introduction

1.1: Introduction

The UK's gas production peaked in 1999 at 3.5tcf/day. Since then, it has steadily fallen to 2.5tcf/day in 2010, then to 1.1tcf/day in 2020 and will continue to fall according to all forecasts.

Today the United Kingdom (UK) only produces 50% of its gas needs with the balance being supplied from Norway, Qatar, and the US. 55% of its imported gas come from pipelines, primarily from Norway. The other 41% of gas imports come as LNG, mainly via ships from Qatar and the USA. However, 4% of LNG imports were from Russia in 2021 (making Russia the UK's third largest supplier). The UK government has committed to phasing out Russian LNG as soon as possible in 2023 and is also competing with Asia for LNG.

Russia's invasion of Ukraine in 2022, and subsequent western sanctions, heaped new pressures on oil and gas supplies already strained from the rapid economic rebound from the pandemic (Khudaykulova *et al*., 2022; Mbah and Wasum, 2022; Pisani-Ferry, 2022). The gas supply is vulnerable.

In addition to the gas supply issues faced by the UK, the nation also has minimal gas storage due in part to the decision to shut down the 'Rough storage facility' in 2017 by the operator because seasonal gas storage was unprofitable. The North Sea Gas Fields themselves therefore serve as both storage and back up. The UK now has 12 days of storage compared with 89 days for Germany and 103days for France. Gas supply in the UK has already reached crisis point during the cold winter of 2010 after there were technical supply problems from Norway and 5.5M households in the UK were estimated to be energy poor. It is in this context that the current and previous governments have been pre-emptive about the shale-gas potential of the onshore UK.

However, it is unlikely that the speculative shale-gas resource in the UK will ever be exploited but much gas could still be produced from undeveloped discoveries in the North Sea. Some such discoveries were made over 40 years ago at a time when well completion, well geometries and reservoir stimulation were much less well developed than they are today (Cameron, 2005). Much of this gas can be classified as occurring in tight gas sandstones that did not flow at economic rates at the time of discovery but evidence that many of these old tight gas discoveries could today deliver gas at economic rates already exists (McPhee, 2009; Symonds, 2015). Breagh is an example of one of such gas fields and demonstrates that the Dinantian reservoirs have potential and provides encouragement for Lower Carboniferous clastic (Rodriguez *et al*., 2014) prospectivity. The Breagh success story has reignited exploration interest in the northern margin of the Southern North Sea by both government and industry with the acquisition of a new regional 2D survey and applications in the 32nd UK offshore Licensing Round (Brackenridge *et al*., 2020; Grant *et al*., 2020).

Due to reopening possibilities for previously unconventional gas, tight gas has now become an important component of the wide hydrocarbon inventory as one of the major unconventional resources contributing significantly to the global hydrocarbon reserve (Greene *et al*., 2006; Economides and Wood, 2009; Taylor *et al*., 2010; Stroker *et al*., 2013; Pang *et al*., 2015; Grasso, 2019).

A tight-gas is a reservoir with matrix porosity less than or equal to 10% and permeability exclusive of fracture permeability is less than or equal to of 1mD (Newman, 1999; Holditch, 2006; Higgs *et al*., 2007; Zou *et al*., 2012), pore throat diameter less than 1 μm, gas saturation less than 60% and pore sizes range between 0.3 μm and 2 μm (Netto, 1993; Nelson, 2009). This characteristic micro porosity makes possible a high irreducible water saturation and as such an increased rate of chemical reactions/transformations around/on the framework grains. Thus, producing diagenetic clay minerals which clog pore space, increase tortuosity of pore throats and promote even further diagenetic reactions. Since it is pore space geometry and pore throat connectivity that governs permeability, characterizing various types of porosity and clay minerals is vital to forecasting reservoir quality distribution in tight gas reservoirs.

The poor reservoir quality in sandstone reservoirs (including tight sandstones) is often triggered from early on with the deposition of fine-grained sediments and dispersed clays. This is followed by extensive diagenesis (Primmer *et al*., 1997; Burley and Worden, 2003; Schmid *et al*., 2004; Higgs *et al*., 2007; Taylor *et al*., 2010) which destroys the primary porosity and permeability by creating secondary porosity and/or micro porosity. Hence modifying the original pore structure and pore throat diameter by creating varying distribution of isolated and disconnected pores (Higgs *et al*., 2007; Rushing *et al*., 2008; Golab *et al*., 2010; Xi *et al*., 2016)- (See details in Chapter 6).

Consequently, a key factor in identifying net pay zones in tight sandstones is the ability to understand the controls and distribution of diagenetic process and linking them to depositional facies as a function of temperature (Burley and Worden, 2003), burial and formation fluid histories. Thus provide a powerful tool in predicting the distribution of reservoir quality and heterogeneity in these reservoirs (Morad *et al*., 2010; Fic and Pedersen, 2013; Stroker *et al*., 2013; Xi *et al*., 2015).

Studies on sandstone diagenesis have however been mostly associated with high permeability examples since they are better reservoirs (Hayes, 1979; Bjørlykke, 1983; Schmoker and Gautier, 1988; Bjorkum, 1996; Primmer *et al*., 1997; Burley and Worden, 2003; Ajdukiewicz and Lander, 2010; Ali *et al*., 2010; Bjorlykke and Jahren, 2012; Lai *et al*., 2015, 2017; Oluwadebi *et al*., 2018). More, studies on diagenetic alteration in low permeability sandstones (tight sandstone) are valuable as they may identify net pay zones in previously abandoned gas discoveries. Isolated examples from Chinese and US basins (Stroker and Harris, 2009; Stroker *et al*., 2013; Xi *et al*., 2016; Li *et al*., 2017; Zhang *et al*., 2017; Lai *et al*., 2018) and more recently East Irish Sea Basin (Oluwadebi *et al*., 2018) provide plenty of insight into potential geological controls on tight sandstone reservoir quality but more examples are needed in order to gain sufficiently broad knowledge on the diagenetic controls of tight gas reservoir quality. More so, adequate research on diagenesis in low permeability reservoirs will be helpful - partly to the development of substantial gas reserves in tight sandstones (Stroker *et al*., 2013) but also to boost gas security and supply in the light of the on-going gas crises.

Within the study area itself -Southern North Sea (SNS), studies on diagenesis and reservoir quality have previously focused on the well understood, high permeability Permian Rotliegend reservoirs, Triassic Bunter Sandstone and Late Carboniferous Sandstones (Nagtegal, 1979; Seemann, 1982; Burley, 1984; Collinson *et al*., 1988; Cowan, 1989a, 1989b; Glennie and Provan, 1990; Ketter, 1991, 1991; Stuart and Cowan, 1991; Knox and Holloway, 1992; Besly *et al*., 1993, 1993; Leveille *et al*., 1997; Fisher *et al*., 1999; Rodriguez *et al*., 2014, 2014; Heidsiek *et al*., 2020; Monsees *et al*., 2021; Wasielka, 2021; Blackbourn and Collinson, 2022). This thesis is focused on the diagenetic studies in the Breagh Sandstone and thus serve as a good example of the diagenetic evolution of a tight gas sandstone reservoir within the SNS and the UK more widely.

The Breagh field reservoir is an important gas reservoir in the UK SNS. It is a gas field with multiple reservoir intervals within sandstones of the cyclic paralic Early Carboniferous (Mississippian) Yoredale Formation. On this stratigraphic location (Fig 1.1), Breagh has become a very significant field to the UK gas supply being the first field to be developed within this stratigraphic age in the offshore UK. The discovery well 42/13-2 encountered a 121m of gas column within the Early Carboniferous Visean aged Yoredale Formation sandstones, and subsequent wells have indicated that the field contains a P50 reserve of 552Bcf (15.6Bcm) (Nwachukwu *et al*., 2020), with 2 MMbbl (0.32 $MMSm^3$) recoverable condensate, making it the 60th largest gas field in the UK, in terms of ultimate recoverable reserves (Grant *et al*., 2020).

However, due to an average permeability of less than 1 mD and porosity below 10% in most of the zones (Zone 2-4)- (See chapter 2 &3 for more details on the zonation), it is considered to be a tight sandstone reservoir (Newman, 1999; Smythe, 2014; Oluwadebi *et al*., 2018).

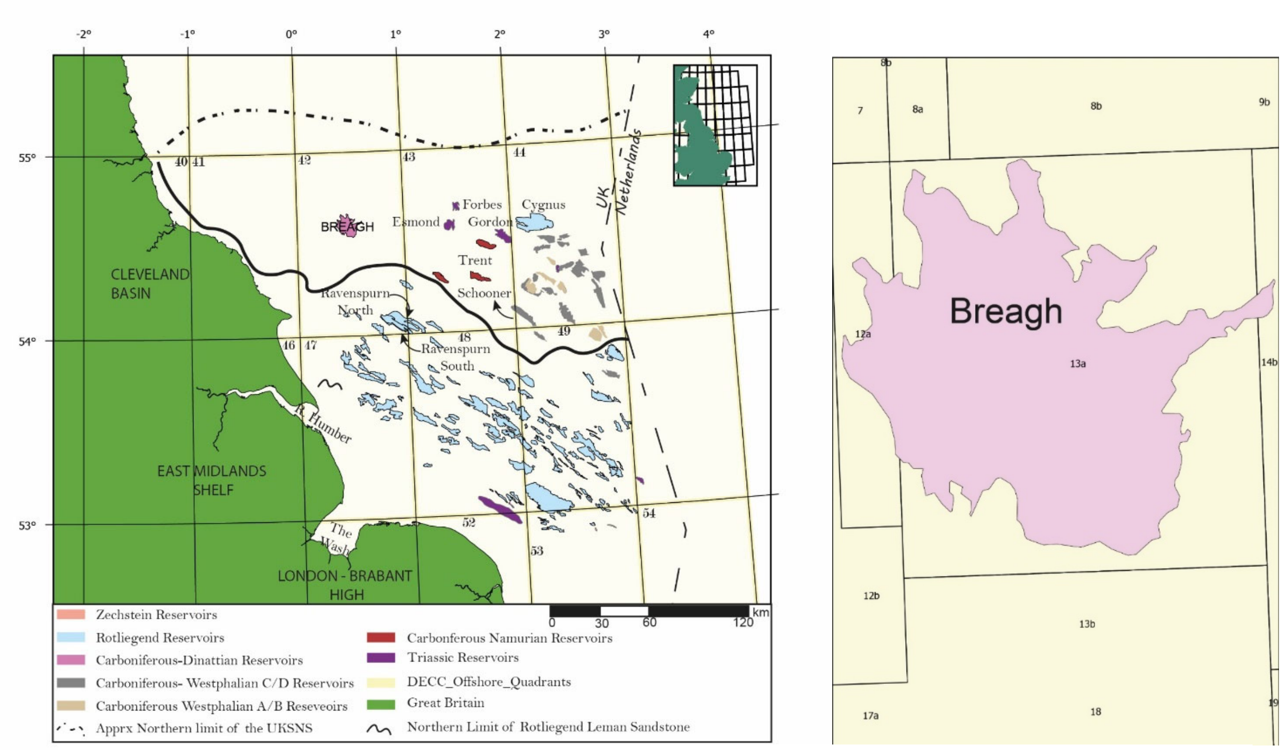

Figure 1.1: Left- Location map for the Breagh; Right- Expanded map of the Breagh (not to scale)

Although, the topmost zone (zone 1) which contains the best reservoirs (channel sands) has an average porosity of 11.6% and permeability between 1- 10mD, in this case and in all cases, post-depositional burial has reduced reservoir quality through compaction and diagenesis, resulting in tight sandstones with gas production reliant on hydraulic fracturing (Booth *et al*., 2020).

In addition to the characteristic low permeability of tight sandstones, paralic reservoirs like the Breagh constitute other challenges to exploration because they reflect a range of clastic depositional environments developed along or near coastlines, including deltas, shoreline–shelf systems and estuaries. Strata that host these reservoirs are shaped by a wide variety of depositional processes and controls which reflect the upstream supply of sediment and water, the characteristics of the receiving basin, relative sea level, tectonic setting, and the internal dynamics of depositional systems. Therefore, they exhibit much variability in their stratigraphic architecture and sedimentological heterogeneity, which translates into complex patterns of reservoir distribution and reservoir performances that are challenging to predict, optimize and manage (Reynolds, 1999; Symonds *et al*., 2015).

The focus of the current thesis is to characterize the diagenetic controls on the reservoir quality of Breagh Field reservoirs. The aim of this research is to understand porosity and permeability evolution as well as the architecture of tight gas sandstones using the Breagh as a test bed. Such an understanding will enable better development and ranking and so underpin the forecast of reservoir quality distribution ahead of drilling.

1.2 Objectives

A few works have been published on regional geology, stratigraphy, tectonic setting, and hydrocarbon potential (Booth *et al*., 2020; Brackenridge *et al*., 2020; Grant *et al*., 2020) of the study area. However, little has been published on petrography, lithofacies, diagenesis and reservoir quality of the gas-bearing Breagh Sandstone. In respect to this, there still exists a gap between the understanding of the reservoir quality of the Breagh gas field and the factors controlling it. Therefore, the overall aim of this research is to bridge the gap, by considering detail diagenetic analysis on the Breagh Sandstone reservoir rock and develop its diagenetic sequence model, from which to obtain quantitative information on the diagenetic effect on the reservoir quality. The sub-objectives of the study include:

1. Document history of exploration, appraisal, and development as well as the production history and reserves of the Breagh field to gain insight into the prospectivity of the

Lower Carboniferous reservoirs of the SNS- a stratigraphic interval which had been underexplored.

2. Investigate the possibility for further reservoir potential within Lower Carboniferous Visean clastic reservoirs away from the Breagh area into other areas of the Southern North Sea (SNS).
3. Describe the facies associations, vertical and lateral facies architecture and the gross depositional environment using cores cut in wells drilled into the Breagh Field (42/13-2, 42/13-4, and 42/13a-6).
4. Assess the petrographic and mineralogical composition of the studied sandstone towards the reconstruction of diagenetic sequence and understand the control on reservoir quality.
5. Link porosity measurement, pore structure and permeability to initial mineralogy and depositional facies.
6. Investigate the clay minerals clogging the pore spaces of the study samples as a function of burial and formation fluid histories to be able to predict areas that may contain formation damaging clay minerals.
7. Describe the pore geometry and permeability evolution in terms of the burial, thermal and formation fluid histories.
8. Characterize pore throat dimensions and connectivity to understand the spatial and temporal distribution of permeability in the study areas.
9. Characterize pore structure at a variety of scales with reference to the depositional fabric and diagenesis of the sandstones on the μm and cm scales. Check if the reservoir quality is equally spread through the reservoir or if there are depositional facies with particularly good reservoir quality. And if so, why?
10. Link measurements of permeabilities, pore structures and diagenetic minerals to understand and predict how differences in diagenesis control flow properties in the studied sandstones.

The petrographic, sedimentological, and tomographic results obtained from these objectives will assist in better understanding of the diagenetic processes and their influence on the reservoir quality of the studied sandstone. The outcome data will also provide useful insight to further exploration activity, appraisal and recovery of the studied reservoir and similar tight-gas sandstone reservoirs.

1.3 Data sets

Table 1.1: Research data set

Item	Quantity
Field (Breagh)	1
Wells with Breagh cores (Fig 1.2)	3
Composite well logging curves (Secondary data)	25
Seismic section (secondary data- Fig 1.3)	3
Thin sections	36
SEM rock chips	18
XRD Samples (Secondary)	23
Cathodoluminescence samples	8
Carbonate samples for isotopic analysis	23
X-ray Tomography sample	1

The datasets in (Table 1.1) were employed in achieving the above-listed objectives include:

1. Three subsurface wells (42/13-2. 42/13-4 and 42/13a-6) from the east and west of the Breagh Field were provided by British Geological Survey, Nottingham. Laboratory. Porosity and permeability data of these wells were supplied by IHS energy Limited.
2. XRD data of wells 42/13-2 and 42/13-4 were supplied by IHS Energy. See Chapter 5 Table 5.4
3. Seismic datasets for the study area with surrounding lines and wells (a subset of the PGS MegaSurvey 2015 and the INEOS Lochran 3D surveys). The orientation and locations of the well correlation and seismic sections A–A′ (Chapter 4: Figs 4.7a) and C–C′ (Chapter 4: Figs 4.7b) were supplied from Grant *et al*, 2020.

Figure 1.2: Core from well 42/13-6.

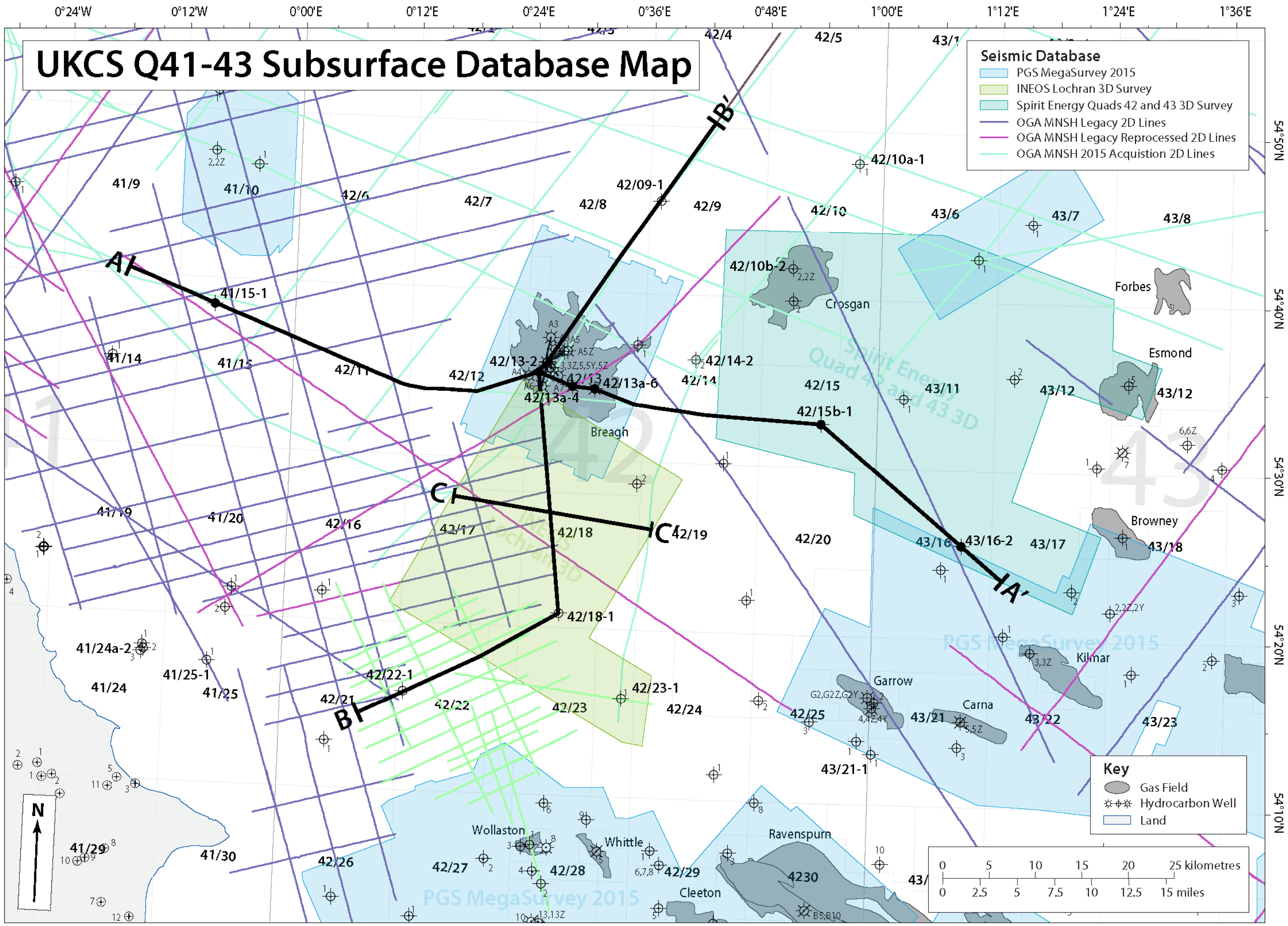

Figure 1.3: Database map of the Breagh study area in Quadrants 41–43 showing the extent of the 3D seismic datasets (a subset of the PGS MegaSurvey 2015 and the INEOS Lochran 3D surveys), regional 2D lines, well control and the location of gas fields, including the Breagh Field. The orientation and locations of the well correlation and seismic sections A–A' (see Figs 4.7a) and C–C' (Figs 4.7b) are indicated after Grant et al, 2020.

1.4 Research Methodology.

The research methods used in this study links a multi-level approach of traditional core sampling and logging, optical and electron microscopy, analysis of XRD data, X-ray tomography data acquisition and imaging techniques (Fig 1.4).

Petrographic studies of core samples were used to characterize sedimentological, and diagenetic processes, as well as reservoir quality variability within each sample of the sandstone formation. X-ray computed tomography was utilised for 3D imaging and pore characterisation. The study was carried out in three stages: large-scale architecture (Chapters 2-4), microfacies description (Chapter 5) and 3D pore structure characterisation (Chapter 6).

The first stage of analysis unraveled the large-scale architecture of the studied sandstones. This is crucial for understanding the sedimentary facies distribution as well as the depositional environment settings. Core samples were taken systematically at approximately 0.5 m interval within the sandstone facies from wells 42/13-2 and 42/13-4, and sedimentary logs were drawn from the three studied wells. The analysis was based on grain size description, lithology, fabrics, thickness, and sedimentary structures. Sedimentological analysis of the Breagh sandstone was performed by defining different lithofacies which were later classified into facies associations and depositional environments were interpreted. A total of 37 thin sections were prepared from the core samples, which were used for petrographic analysis, and thereby discussed in the second stage of analysis.

This second stage of the analysis made use of various methods to identify and characterize mineralogical contents and diagenetic processes in sandstones. This includes optical microscopy, scanning electron microscopy (SEM), X-ray diffraction (XRD), cathodoluminescence (CL), and stable isotopes analysis. The methods are described in detail below and they altogether reveal the diagenetic minerals and reservoir properties of the studied sandstones.

The last stage used X-ray computed tomography (XCT) for 3D imaging for pore throat characterisation and connectivity in order to characterize the spatial and temporal distribution of permeability in the study areas. Additional 2D images from SEM were also used to link pore systems through to reservoir production.

The tools and techniques used are discussed in more details below:

1.4.1 Optical Microscopy

Thin section petrography was used to measure optical porosity, textural relationships between detrital grains and authigenic minerals, and, also to find the fraction of authigenic mineral. As a result, petrographic observation of the thin sections gives insight into the diagenetic processes and visual evaluation of the reservoir properties (Burley, 1984; Nedkvitne and Bjorlykke, 1992; Besly *et al*., 1993; Qureshi *et al*., 2023).

All thin sections were impregnated with blue dye to enhance the visible porosity. All samples were analysed using a standard petrographic microscope (Leica DM2500P and DM750P) attached to an automated PETROG counting stage (PETROG – Conwy Valley Systems Limited).

300 counts per thin section were used for general mineral identification. Different magnifications were used under plane polarised light (PPL) as well as crossed polarised light (XPL) to improve mineral visibility (fig 1.5). Grain size distribution was measured and analysed by using the Leica QWin (V. 3.5.0) software on the produced thin section micrographs and the fraction of the authigenic grains were measured as well.

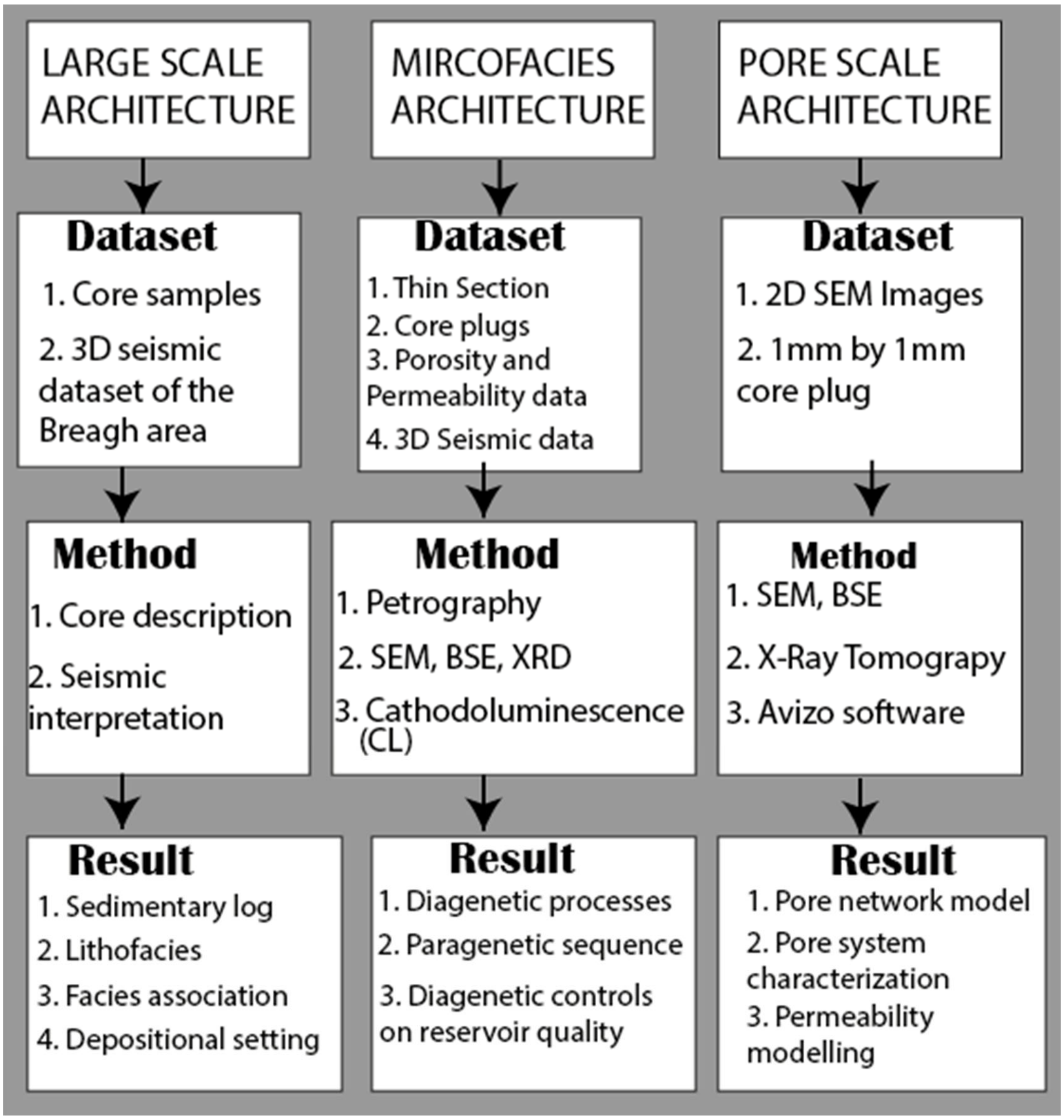

Fig 1.4: Summary of Research methodology and output results.

The resulting data (i.e., grain size, sorting, roundness, Quartz-Feldspar-Rock fragment (QFR) composition, visible porosity, grain contact relationships, cement types, fraction of coated grains and non-coated grains) were used to select samples for additional petrographic analysis, including intergranular volume (IGV) (Paxton *et al*., 2002), total cement volume (C), porosity-loss by mechanical compaction (COPL) and porosity-loss by cementation (CEPL) (Lundegard, 1992).

The helium porosity and permeability data used in this study was provided by IHS Markit Limited.

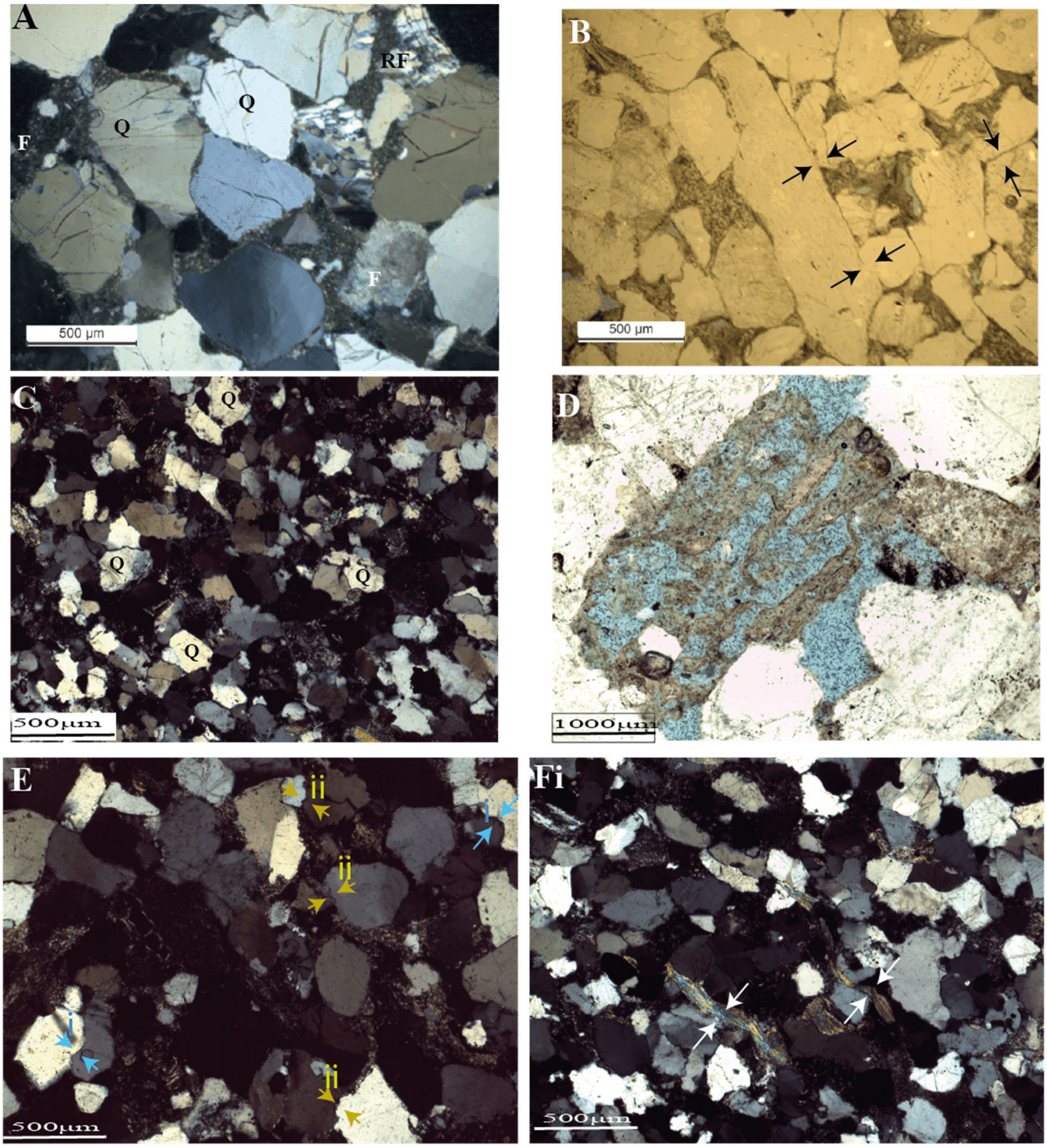

Figure 1.5: A: Photomicrograph of coarse grained, poorly sorted sandstone showing quartz, rock fragments and feldspar grains (7535ft); B: Photomicrograph of coarse grained poorly sorted sandstone angular to subrounded sandstone quartz to quartz point and long grain contact (PPL-7546ft); C:Photomicrograph of fine to medium grained moderately sorted sandstone showing predominantly quartz grains (7404ft); D:Photomicrgraph of medium grained well sorted sandstone with relics of partially dissolved of feldspar (7491ft); E: Photomicrgraph of medium grained well sorted sandstone indicating concavo-convex contact (arrow i) and the onset of sutured contact (arrow ii) (PPL-7491.9ft); Fi: Photomicrograph a slide with bended muscovite (XPL-7497.5ft).

1.4.2 Scanning electron microscope (SEM) and Energy-dispersive X-ray spectroscopy (SEM-EDS).

Scanning electron microscope (SEM) compliments optical microscopy although it offers an advantage as observation of microstructure and petrological characteristics below the limit of resolution of optical microscopic analysis is made possible with SEM.

The SEM can provide high magnitude enlargement for clay morphology and pore space geometry. In this study, SEM-EDX was used for rapid identification of chemical species (i.e., K ratio in I/S mixed minerals). Whilst the BSE detectors on the other hand is used for mineral identification. Observations were mostly performed with back-scattered electron (BSE) for petrological and mineralogical identifications.

Selected polished thin sections and tiny rock chips (approx. 1 cm * 1 cm * 0.5 cm) were coated by 30 nm carbon and 35 nm gold prior to analysis by a Hitachi SU-70 scanning electron microscope (SEM) equipped with an energy-dispersive X-ray detector (EDX). Samples were to minimize possible charging problems during observation and were performed under vacuum.

The acquired SEM data were used for petrographic observation, to characterise morphology and distribution of fine-grained minerals (detrital and authigenic) and for pore identification. Energy Dispersive X-ray (EDX) combined with SEM provides qualitative information about the chemical composition of the identified minerals- a combination which offers an added advantage in mineral identification since clay minerals of the same structural group could exhibit varying texture and morphology (Wilson and Pittman, 1977; Johnson-Henry *et al*., 2007; Tantra *et al*., 2010; Chew *et al*., 2018).

In the current study, SEM analysis on the thin sections and bulk rock chips were conducted at 5 kV to 20 kV acceleration voltages with beam currents of 1.0 nA and 0.6 nA, respectively. Within the software, both point analysis and line scan elemental analysis were used too. Whilst point analyses takes an average duration of 2 minutes for spot mineral identification, line scan measures length based the concentration of the different minerals of interest. (See chapter 5.5.2).

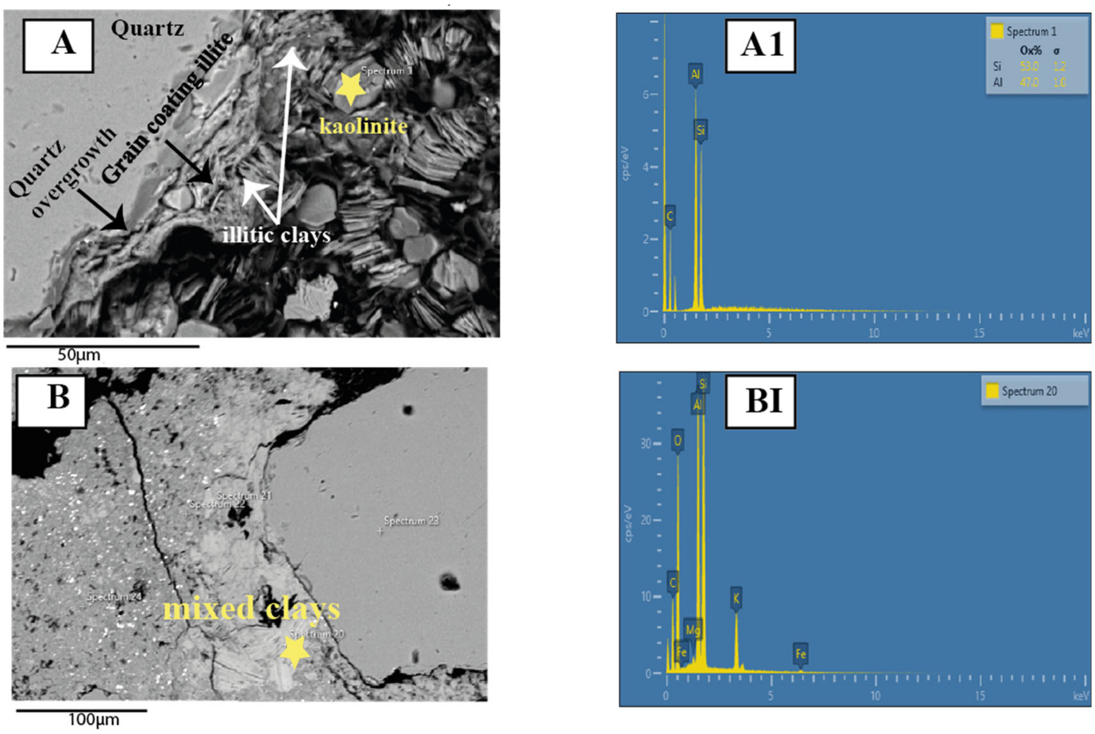

Fig 1.6: SEM photomicrograph of samples from study area showing mixed layer clays (A and B); A^1 and B^1 - Spectrum analysis of kaolinite and mixed layer clays respectively.

1.4.3 Cathodoluminescence.

Cathodoluminescence technique is useful in examining and interpreting the composition and fabrics of minerals as well as variation within an individual grain (Ziegler *et al*., 2006).

Application of cold cathodoluminescence microscopy in this study was useful in identifying different carbonate phases and quartz overgrowth. Cathodoluminescence petrography has been a useful tool in the study of sandstone cements particularly silica and carbonates (Hayes, 1979; Matter and Ramseyer, 1985; Machel, 2000).

Within the current study, the cathodoluminescence (CL) analysis was carried out on selected thin section with visible macro-quartz overgrowths by using Gata MonoCL system with a panchromatic imaging mode operated at 8 kV. The purpose being to distinguish whether the quartz overgrowth was formed by a single precipitation or multiple generations since CL can show varying degree of authigenic quartz content. The CL studies were also used to map the zonation within the carbonate mineral based on changing mineral composition.

1.4.4 One dimensional basin modelling (1-D Model)- Petromod.

One-dimensional basin modelling provides an insight into the burial history of a reservoir and especially the temperature and pore fluid pressure evolution of the reservoir. Schlumberger's burial history simulation software PetroMod (V. 2012.2) was used in this study to model the burial history and to provide a framework for understanding the evolution of the main diagenetic reaction relative to burial history of the Breagh field.

Data for building the 1-D thermal model include well tops, age, general lithology, Paleo thickness, eroded thickness, paleo water depth and heat flow data.

The stratigraphic well tops, age and lithology have all been extracted from composite logs and well description provided by IHS Markit Limited. Of the 3 study wells in this work, well 42/13-3 was used as the input well for the 1-D model (see chapter 5-Figure 5.4.1) because the other 2 wells show a repeat stratigraphy and might introduce error to the model. Paleo and eroded thickness have been estimated from Southern Permian Basin Atlas (SPBA) and finally, paleo water depths and heat flow data were taken from literature. The lithological unit types used in the model are PetroMod default lithology types or mixed default lithology types, chosen on the basis of well log descriptions and core analysis reports.

Several heat flow histories from the Southern North Sea and more specifically, the UK Quandrant 42 (Vincent, 2015; Monaghan *et al*., 2017) have been suggested from in literature. Out of the different heat flow scenerio presented, the authors (Vincent, 2015; Monaghan *et al*., 2017) assumed the best possible scenerio to be a high heat flow of 65-70MWm^{-2} during the Visean to Late Permian and also a high heat flow of 62-68 MWm^{-2} during the late Cretaceous to recent times.

Palaeotemperatures and burial curves for wells 42/13-6 (Besly, 2019), 42/10-01 (Collinson and Jones, 1995) and from comparable nearby wells- 41/20-10, 41/14-01 and the Crosgan Field well 42/10b-2 (Vincent, 2015; Monaghan *et al*., 2017; Besly, 2019; Grant *et al*., 2020) were used to help calibrate the model.

1.4.5 Stable Isotope.

In this study, the Thermo Fisher Scientific MAT 253 gas source mass spectrometer has been used to determine the carbon and oxygen isotope composition of the carbonate cements of 23 individual samples from three wells (42/13-2, 42/13-4, and 42/13-6 – chapter 5-Table 5.1) in the Breagh Sandstone at the Durham University isotope laboratory.

Carbon ($\delta^{13}C$) and oxygen ($\delta^{18}O$) isotope ratios were measured in the carbonate (CO_3) component of dolomite, calcite, and siderite cements of the samples. Each sample was then weighed out based on carbonate content. Product CO_2 was recovered cryogenically, and mass ratios were measured against a comparison CO_2 ('reference' gas) using a dual-inlet VG SIRA 12 mass spectrometer and transferred into individual exetainer vials.

Vials were then flushed with helium and CO_2 was liberated by reaction with 99% ortho-phosphoric acid for 2 hours at 70°C. The resultant gas mix of helium and CO_2 was transferred through a Thermo Fisher Scientific Gasbench II in which a gas chromatographic column separated the CO_2 from the helium and then passed into a Thermo Fisher Scientific MAT 253 gas source mass spectrometer for isotopic analysis.

The following international reference materials were analysed within each batch of samples: NBS 18 (calcite, n=3), IAEA-CO-1 (marble, n=3) and LSVEC (lithium carbonate, n=3). In addition, an internal standard, DCS01 (calcium carbonate, n=7) was also analysed. Repeated analysis of both international and internal standards yielded an analytical precision better than 2σ for $\delta^{13}C$ and 2 s.d. for $\delta^{18}O$. Duplicate analyses of the samples themselves yielded precision with a mean difference of 2.2σ for $\delta^{13}C$ and 2σ for $\delta^{18}O$. Normalisations and corrections were made using IAEA-CO-1 and LSVEC, with all $\delta^{13}C$ and $\delta^{18}O$ values reported relative to the Vienna PeeDee Belemnite (VPDB) standard. $\delta^{18}O$ was additionally reported relative to the Vienna Standard Mean Ocean Water (vsmow) standard for comparison purposes.

1.4.6 X-ray Computed Tomography (XCT).

X-ray computed tomography scanning provides high-resolution images in applications ranging from medical to material sciences and failure analysis(Siddiqui and Sarker, 2010; Elkhoury *et al.*, 2019). X-ray Computed Tomography technique is used to study the pore system of the sandstone in this research to enhance the understanding of reservoir properties at the micron level. XCT imaging works on the principle that the X-rays intensity is attenuated differently when passing through different materials and the detector measures the attenuation degree by generating a 2D slices in grey scale (Fig 1.7). The attenuation therefore depends on both the sample material and source energy and can be used to quantify the density of the sample being imaged.

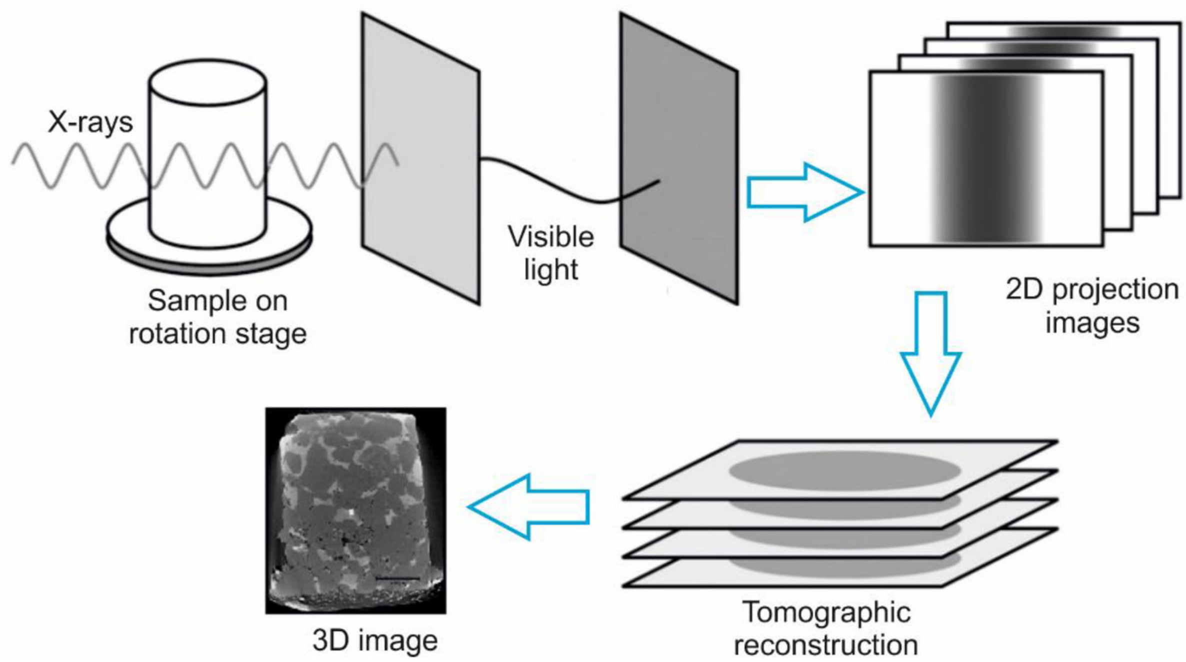

Figure 1.7: Schematic illustration of X-ray computed tomographic images acquisition and reconstruction, after (Landis and Keane, 2010; Schoeman et al., 2016)

Within the current study, one core sample was scanned using the XCT microscope. The sample size used is 5mm by 1mm core held in 1ml plastic tubing placed on the XCT system rotation stage (Figure 1.7).

The specimen stands on the X-ray beam, rotating at 360oaround a vertical axis; while images are collected at regular intervals by recording a series of 2D radiographic image which are then reconstructed to produce a 3D image (Cnudde *et al*., 2006; Landis and Keane, 2010; Cnudde and Boone, 2013; Schoeman *et al*., 2016; Elkhoury *et al*., 2019; Behrooz *et al*., 2020).
There is specific x-ray absorption for each mineral phase; therefore, the mineral assemblage along the beam path varies as the sample rotates, leading to variation in total X-ray flux bombarding each pixel on the detector.

To obtain an optimum X-ray transmission of 20-30% through the region of interest with a good signal to noise ratio, an accelerating voltage of 80kv, 7Watts and 5s per exposure for each projection were applied and voxel resolution is 1.03 microns.
MicroXCT is a non-destructive technique (Doost *et al*., 2020) significant for visualising and quantifying the internal structure of an object in three-dimensional (3D) way (Behrooz *et al*., 2020).

1.5 Thesis layout

This thesis is made up of seven chapters.

1.5.1 Chapter 1: Introduction

The chapter- current chapter, gives a general background for the research based on previous studies. It contains the introduction of the thesis, as well as the rationale behind the project. It emphasizes the main ideas, including the research aim and objectives and how each will be addressed. The techniques used and database involved in this project are also briefly introduced.

1.5.2 Chapter 2: Geological evolution of the Breagh Field Area.

This chapter presents a summary of the of the Geology of the Southern North Sea and the southern flank of the Mid North Sea High. Although concerned mainly with the Carboniferous Succession of the Southern North Sea basin, occasional forays are made into the comparative land areas of the Northumberland coast, based on published references.

1.5.3 Chapter 3: The Breagh Field, Blocks 1 42/12a, 42/13a and 42/8a, UK North Sea.

This chapter introduces the Breagh field and its contribution to the UK energy mix. It also lays out the history of exploration and appraisal, the field's development, production history and reserves development. It contains a summary of the regional context as well as the petroleum system elements. This chapter has been submitted as part of the United Kingdom Oil and Gas Fields: 50th Anniversary Commemorative Volume. Geological Society, London, Memoirs.

1.5.4 Chapter 4: Lithofacies and depositional Environment of the Breagh field area.

Chapter 4 provides a detailed description of the sedimentary architecture of the study sandstone and various interpretations on the depositional environments. It concludes by combining seismic data, core data and proxy well data to predict reservoir quality in areas away from the studied wells.

1.5.5 Chapter 5: Diagenetic Controls on the reservoir quality of the Breagh Sandstones.

This chapter describes, quantifies, and characterizes the detrital and diagenetic mineralogy of the Breagh sandstones. It also characterizes the impact of diagenesis on the studied sandstones.

1.5.6 Chapter 6: 2D and 3D Characterisation of the pore structure in the Breagh Sandstone reservoir.

This chapter focuses on the quantitative description of pore bodies and pore throats of the Breagh field reservoirs on 2D and 3D. It characterises and quantifies the 3D porosity and interconnectivity of the Breagh sandstone.

1.5.7 Chapter 7: Synthesis, conclusion, and recommendation for future work.

Chapter seven integrates the key findings on the control of diagenesis on the reservoir quality in Breagh sandstones and provides recommendation for future studies.

1.6 References.

Ajdukiewicz, J. M., and R. H. Lander, 2010, Sandstone reservoir quality prediction: The state of the art: AAPG Bulletin, v. 94, no. 8, p. 1083–1091, doi:10.1306/intro060110.

Ali, S. A., W. J. Clark, W. R. Moore, and J. R. Dribus, 2010, Diagenesis and reservoir quality: Oilfield Review, v. 22, no. 2, p. 14–27.

Behrooz, A., J.-C. Tseng, and J. Meganck, 2020, Image Resolution in MicroCT: Principles and Characterization of the Quantum FX and Quantum GX Systems: p. 5.

Besly, B., 2019, Exploration and development in the Carboniferous of the Southern North Sea: a 30-year retrospective: Geological Society, London, Special Publications, v. 471, no. 1, p. 17–64, doi:10.1144/SP471.10.

Besly, B. M., S. D. Burley, and P. Turner, 1993, The late Carboniferous ‘Barren Red Bed’ play of the Silver Pit area, Southern North Sea: Geological Society, London, Petroleum Geology Conference series, v. 4, no. 1, p. 727–740, doi:10.1144/0040727.

Bjorkum, P. A., 1996, How important is pressure in causing dissolution of quartz in sandstones? Journal of Sedimentary Research, v. 66, no. 1, p. 147–154.

Bjørlykke, K., 1983, Diagenetic reactions in sandstones: Sediment diagenesis, p. 169–213.

Bjorlykke, K., and J. Jahren, 2012, Open or closed geochemical systems during diagenesis in sedimentary basins: Constraints on mass transfer during diagenesis and the prediction of porosity in sandstone and carbonate reservoirs: AAPG bulletin, v. 96, no. 12, p. 2193–2214.

Blackbourn, G. A., and J. D. Collinson, 2022, Quartzitic Sandstones in the Namurian and Lower Westphalian Succession of the Southern North Sea: A New High-Permeability Carboniferous Reservoir Type: Journal of Petroleum Geology, v. 45, no. 4, p. 363–393, doi:10.1111/jpg.12824.

Booth, M. G., J. R. Underhill, A. Gardiner, and D. McLean, 2020, Sedimentary and tectonic controls on Lower Carboniferous (Visean) mixed carbonate–siliciclastic deposition in NE England and the Southern North Sea: implications for reservoir architecture: Petroleum Geoscience, v. 26, no. 2, p. 204–231.

Brackenridge, R. E., J. R. Underhill, R. Jamieson, and A. Bell, 2020, Structural and stratigraphic evolution of the Mid North Sea High region of the UK Continental Shelf: Petroleum Geoscience, v. 26, no. 2, p. 154–173.

Burley, S. D., 1984, Patterns of diagenesis in the Sherwood Sandstone Group (Triassic), United Kingdom: Clay Minerals, v. 19, no. 3, p. 403–440.

Burley, S. D., and R. H. Worden (eds.), 2003, Sandstone Diagenesis: The Evolution of Sand to Stone, *in* Sandstone Diagenesis: Oxford, UK, Blackwell Publishing Ltd., p. 1–44, doi:10.1002/9781444304459.ch.

Chew, M., G. Tompkins, A. Tawse-Smith, J. N. Waddell, S. Ma, and S. Ma, 2018, Reusing Titanium Healing Abutments: Comparison of Two Decontamination Methods.: International Journal of Prosthodontics, v. 31, no. 6.

Cnudde, V., and M. N. Boone, 2013, High-resolution X-ray computed tomography in geosciences: A review of the current technology and applications: Earth-Science Reviews, v. 123, p. 1–17, doi:10.1016/j.earscirev.2013.04.003.

Cnudde, V., B. Masschaele, M. Dierick, J. Vlassenbroeck, L. Van Hoorebeke, and P. Jacobs, 2006, Recent progress in X-ray CT as a geosciences tool: Applied geochemistry, v. 21, no. 5, p. 826–832.

Collinson, J. D., B. M. Besly, and G. Kelling, 1988, Controls on Namurian sedimentation in the Central Province basins of northern England: Sedimentation in a synorogenic basin complex: the Upper Carboniferous of Northwest Europe. Blackie, Glasgow, v. 85, p. 101.

Collinson, J., and C. Jones, 1995, Source rock potential of the sub-Westphalian Carboniferous of the Southern North Sea: Report and Appendix.

Cowan, G., 1989a, Diagenesis of upper carboniferous sandstones: southern North Sea Basin: Geological Society, London, Special Publications, v. 41, no. 1, p. 57–73.

Cowan, G., 1989b, Diagenesis of Upper Carboniferous sandstones: southern North Sea Basin: Geological Society, London, Special Publications, v. 41, no. 1, p. 57–73.

Doost, A., A. Rangel, Q. Nguyen, G. Morahan, and L. Arnolda, 2020, Micro-CT scan with virtual dissection of left ventricle is a non-destructive, reproducible alternative to dissection and weighing for left ventricular size: Scientific Reports, v. 10, no. 1, p. 13853.

Economides, M. J., and D. A. Wood, 2009, The state of natural gas: Journal of Natural Gas Science and Engineering, v. 1, no. 1–2, p. 1–13.

Elkhoury, J. E., R. Shankar, and T. S. Ramakrishnan, 2019, Resolution and limitations of X-ray micro-CT with applications to sandstones and limestones: Transport in Porous Media, v. 129, no. 1, p. 413–425.

Fic, J., and P. K. Pedersen, 2013, Reservoir characterization of a “tight” oil reservoir, the middle Jurassic Upper Shaunavon Member in the Whitemud and Eastbrook pools, SW Saskatchewan: Marine and Petroleum Geology, v. 44, p. 41–59.

Fisher, Q. J., M. Casey, M. B. Clennell, and R. J. Knipe, 1999, Mechanical compaction of deeply buried sandstones of the North Sea: Marine and Petroleum Geology, v. 16, no. 7, p. 605–618.

Glennie, K. W., and D. M. J. Provan, 1990, Lower Permian Rotliegend reservoir of the Southern North Sea gas province: Geological Society, London, Special Publications, v. 50, no. 1, p. 399–416, doi:10.1144/GSL.SP.1990.050.01.25.

Golab, A. N., M. A. Knackstedt, H. Averdunk, T. Senden, A. R. Butcher, and P. Jaime, 2010, 3D porosity and mineralogy characterization in tight gas sandstones: The Leading Edge, v. 29, no. 12, p. 1476–1483.

Grant, R. J., M. G. Booth, J. R. Underhill, and A. Bell, 2020, Structural evolution of the Breagh area: implications for carboniferous prospectivity of the Mid North Sea High, Southern North Sea: Petroleum Geoscience, v. 26, no. 2, p. 174–203.

Grasso, M., 2019, Oily politics: A critical assessment of the oil and gas industry’s contribution to climate change: Energy Research & Social Science, v. 50, p. 106–115.

Greene, D. L., J. L. Hopson, and J. Li, 2006, Have we run out of oil yet? Oil peaking analysis from an optimist’s perspective: Energy policy, v. 34, no. 5, p. 515–531.

Hayes, J. B., 1979, Sandstone diagenesis—the hole truth.

Heidsiek, M., C. Butscher, P. Blum, and C. Fischer, 2020, Small-scale diagenetic facies heterogeneity controls porosity and permeability pattern in reservoir sandstones: Environmental Earth Sciences, v. 79, p. 1–14.

Higgs, K. E., H. Zwingmann, A. G. Reyes, and R. H. Funnell, 2007, Diagenesis, Porosity Evolution, and Petroleum Emplacement in Tight Gas Reservoirs, Taranaki Basin, New Zealand: Journal of Sedimentary Research, v. 77, no. 12, p. 1003–1025, doi:10.2110/jsr.2007.095.

Holditch, S. A., 2006, Tight Gas Sands: Journal of Petroleum Technology, v. 58, no. 06, p. 86–93, doi:10.2118/103356-JPT.

Johnson-Henry, K. C., K. E. Hagen, M. Gordonpour, T. A. Tompkins, and P. M. Sherman, 2007, Surface-layer protein extracts from Lactobacillus helveticus inhibit enterohaemorrhagic

Escherichia coli O157: H7 adhesion to epithelial cells: Cellular microbiology, v. 9, no. 2, p. 356–367.

Ketter, F. J., 1991, The Esmond, Forbes and Gordon Fields, Blocks 43/8a, 43/13a, 43/15a, 43/20a, UK North Sea: Geological Society, London, Memoirs, v. 14, no. 1, p. 425–432, doi:10.1144/GSL.MEM.1991.014.01.53.

Khudaykulova, M., H. Yuanqiong, and A. Khudaykulov, 2022, Economic consequences and implications of the Ukraine-russia war: International Journal of Management Science and Business Administration, v. 8, no. 4, p. 44–52.

Knox, R., and S. Holloway, 1992, Lithostratigraphic nomenclature of the UK North Sea.

Lai, J., G. Wang, Y. Chai, Y. Xin, Q. Wu, X. Zhang, and Y. Sun, 2017, Deep burial diagenesis and reservoir quality evolution of high-temperature, high-pressure sandstones: Examples from Lower Cretaceous Bashijiqike Formation in Keshen area, Kuqa depression, Tarim basin of China: AAPG Bulletin, v. 101, no. 6, p. 829–862.

Lai, J., G. Wang, Y. Ran, and Z. Zhou, 2015, Predictive distribution of high-quality reservoirs of tight gas sandstones by linking diagenesis to depositional facies: Evidence from Xu-2 sandstones in the Penglai area of the central Sichuan basin, China: Journal of Natural Gas Science and Engineering, v. 23, p. 97–111, doi:10.1016/j.jngse.2015.01.026.

Lai, J., G. Wang, Z. Wang, J. Chen, X. Pang, S. Wang, Z. Zhou, Z. He, Z. Qin, and X. Fan, 2018, A review on pore structure characterization in tight sandstones: Earth-Science Reviews, v. 177, p. 436–457.

Landis, E. N., and D. T. Keane, 2010, X-ray microtomography: Materials characterization, v. 61, no. 12, p. 1305–1316.

Leveille, G. P., T. J. Primmer, G. Dudley, D. Ellis, and G. J. Allinson, 1997, Diagenetic controls on reservoir quality in Permian Rotliegendes sandstones, Jupiter Fields area, southern North Sea: Geological Society, London, Special Publications, v. 123, no. 1, p. 105–122.

Li, P., M. Zheng, H. Bi, S. Wu, and X. Wang, 2017, Pore throat structure and fractal characteristics of tight oil sandstone: a case study in the Ordos Basin, China: Journal of Petroleum Science and Engineering, v. 149, p. 665–674.

Lundegard, P. D., 1992, Sandstone porosity loss; a" big picture" view of the importance of compaction: Journal of Sedimentary Research, v. 62, no. 2, p. 250–260.

Machel, H. G., 2000, Application of cathodoluminescence to carbonate diagenesis, *in* Cathodoluminescence in Geosciences: Springer, p. 271–301.

Matter, A., and K. Ramseyer, 1985, Cathodoluminescence Microscopy as a Tool for Provenance Studies of Sandstones, *in* G. G. Zuffa, ed., Provenance of Arenites: Dordrecht, Springer Netherlands, NATO ASI Series, p. 191–211, doi:10.1007/978-94-017-2809-6_9.

Mbah, R. E., and D. F. Wasum, 2022, Russian-Ukraine 2022 War: A review of the economic impact of Russian-Ukraine crisis on the USA, UK, Canada, and Europe: Advances in Social Sciences Research Journal, v. 9, no. 3, p. 144–153.

Monaghan, A. A. *et al*., 2017, Carboniferous petroleum systems around the Mid North Sea High, UK: Marine and Petroleum Geology, v. 88, p. 282–302, doi:10.1016/j.marpetgeo.2017.08.019.

Monsees, A. C., B. Busch, and C. Hilgers, 2021, Compaction control on diagenesis and reservoir quality development in red bed sandstones: a case study of Permian Rotliegend sandstones: International Journal of Earth Sciences, v. 110, no. 5, p. 1683–1711.

Morad, S., K. Al-Ramadan, J. M. Ketzer, and L. De Ros, 2010, The impact of diagenesis on the heterogeneity of sandstone reservoirs: A review of the role of depositional facies and sequence stratigraphy: AAPG bulletin, v. 94, no. 8, p. 1267–1309.

Nagtegal, P. J. C., 1979, Relationship of facies and reservoir quality in Rotliegendes desert sandstones, southern North Sea region: Journal of Petroleum Geology, v. 2, no. 2, p. 145–158.

Nedkvitne, T., and K. Bjorlykke, 1992, Secondary porosity in the Brent Group (Middle Jurassic), Huldra Field, North Sea: implication for predicting lateral continuity of sandstones? Journal of Sedimentary Research, v. 62, no. 1.

Nelson, P. H., 2009, Pore-throat sizes in sandstones, tight sandstones, and shales: AAPG Bulletin, v. 93, no. 3, p. 329–340, doi:10.1306/10240808059.

Netto, A., 1993, Pore-Size Distribution in Sandstones: GEOLOGIC NOTE: Aapg Bulletin, v. 77, no. 6, p. 1101–1104.

Newman, P. J., 1999, The geology and hydrocarbon potential of the Peel and Solway Basins, East Irish Sea: Journal of Petroleum Geology, v. 22, no. 3, p. 305–324.

Nwachukwu, C. M., Z. Barnett, and J. G. Gluyas, 2020, The Breagh Field, Blocks 42/12a, 42/13a and 42/8a, UK North Sea: Geological Society, London, Memoirs, v. 52, no. 1, p. 109–118.

Oluwadebi, A. G., K. G. Taylor, and P. J. Dowey, 2018, Diagenetic controls on the reservoir quality of the tight gas Collyhurst sandstone formation, Lower Permian, East Irish Sea Basin, United Kingdom: Sedimentary geology, v. 371, p. 55–74.

Pang, X.-Q., C.-Z. Jia, and W.-Y. Wang, 2015, Petroleum geology features and research developments of hydrocarbon accumulation in deep petroliferous basins: Petroleum Science, v. 12, p. 1–53.

Paxton, S. T., J. O. Szabo, J. M. Ajdukiewicz, and R. E. Klimentidis, 2002, Construction of an intergranular volume compaction curve for evaluating and predicting compaction and porosity loss in rigid-grain sandstone reservoirs: AAPG bulletin, v. 86, no. 12, p. 2047–2067.

Pisani-Ferry, J., 2022, The economic policy consequences of the war.: Bruegel-Blogs, p. NA-NA.

Primmer, T. J., C. A. Cade, J. Evans, J. G. Gluyas, M. S. Hopkins, N. H. Oxtoby, P. C. Smalley, E. A. Warren, and R. H. Worden, 1997, Global Patterns in Sandstone Diagenesis: Their Application to Reservoir Quality Prediction for Petroleum Exploration: p. 61–77.

Qureshi, K. A., M. Arif, A. Basit, S. Ahmad, H. T. Janjuhah, and G. Kontakiotis, 2023, Sedimentological Controls on the Reservoir Characteristics of the Mid-Triassic Tredian Formation in the Salt and Trans-Indus Surghar Ranges, Pakistan: Integration of Outcrop, Petrographic, and SEM Analyses: Journal of Marine Science and Engineering, v. 11, no. 5, p. 1019.

Reynolds, A. D., 1999, Dimensions of paralic sandstone bodies: AAPG bulletin, v. 83, no. 2, p. 211–229.

Rodriguez, K., R. Wrigley, N. Hodgson, and H. Nicholls, 2014, Southern North Sea: unexplored multi-level exploration potential revealed: First Break, v. 32, no. 6, p. 107–113.

Rushing, J. A., K. E. Newsham, and T. A. Blasingame, 2008, Rock Typing: Keys to Understanding Productivity in Tight Gas Sands: Society of Petroleum Engineers, doi:10.2118/114164-MS.

Schmid, S., R. H. Worden, and Q. J. Fisher, 2004, Diagenesis and reservoir quality of the Sherwood Sandstone (Triassic), Corrib field, Slyne basin, west of Ireland: Marine and Petroleum Geology, v. 21, no. 3, p. 299–315.

Schmoker, J. W., and D. L. Gautier, 1988, Sandstone porosity as a function of thermal maturity: Geology, v. 16, no. 11, p. 1007–1010.

Schoeman, L., P. Williams, A. Du Plessis, and M. Manley, 2016, X-ray micro-computed tomography (μCT) for non-destructive characterisation of food microstructure: Trends in Food Science & Technology, v. 47, p. 10–24.

Seemann, U., 1982, Depositional facies, diagenetic clay minerals and reservoir quality of Rotliegend sediments in the Southern Permian Basin (North Sea): a review: Clay Minerals, v. 17, no. 1, p. 55–67.

Siddiqui, S., and M. R. H. Sarker, 2010, Trends in CT-Scanning of Reservoir Rocks: Medical CT to Micro CT: Advances in Computed Tomography for Geomaterials: GeoX 2010, p. 189–196.

Smythe, D. K., 2014, Planning application no. LCC/2014/0101 by Cuadrilla Bowland Limited to drill at Roseacre Wood, Lancashire: Objection on grounds of geology and hydrogeology.

Stroker, T., and N. Harris, 2009, AV K-Ar Dating of Authigenic Illites: Integrating Diagenetic History of the Mesaverde Group, Piceance Basin, NW Colorado.

Stroker, T. M., N. B. Harris, W. C. Elliott, and J. M. Wampler, 2013, Diagenesis of a tight gas sand reservoir: upper Cretaceous Mesaverde Group, Piceance Basin, Colorado: Marine and Petroleum Geology, v. 40, p. 48–68.

Stuart, I. A., and G. Cowan, 1991, The South Morecambe Field, Blocks 110/2a, 110/3a, 110/8a, UK East Irish Sea: Geological Society, London, Memoirs, v. 14, no. 1, p. 527–541.

Symonds, R., R. Lippmann, B. Mueller, and A. Kohok, 2015, Yoredale sandstone Architecture in Breagh Field (UK SNS). Presentation for Sedimentology of Paralic Reservoirs: Recent advances and their applications.: p. 24.

Tantra, R., J. Tompkins, and P. Quincey, 2010, Characterisation of the de-agglomeration effects of bovine serum albumin on nanoparticles in aqueous suspension: Colloids and Surfaces B: Biointerfaces, v. 75, no. 1, p. 275–281.

Taylor, T. R., M. R. Giles, L. A. Hathon, T. N. Diggs, N. R. Braunsdorf, G. V. Birbiglia, M. G. Kittridge, C. I. Macaulay, and I. S. Espejo, 2010, Sandstone diagenesis and reservoir quality prediction: Models, myths, and reality: AAPG Bulletin, v. 94, no. 8, p. 1093–1132, doi:10.1306/04211009123.

Vincent, C. J., 2015, Maturity modelling of selected wels in the Central North sea, Energy and Marine Geoscience Programme Commissioned Report CR/15/122: British Geological Survery, Nottingham.

Wasielka, N., 2021, Controls of reservoir quality in Carboniferous tight gas sandstone, PhD Thesis: Durham University.

Wilson, M. D., and E. D. Pittman, 1977, Authigenic clays in sandstones; recognition and influence on reservoir properties and paleoenvironmental analysis: Journal of Sedimentary Research, v. 47, no. 1, p. 3–31.

Xi, K., Y. Cao, B. G. Haile, R. Zhu, J. Jahren, K. Bjørlykke, X. Zhang, and H. Hellevang, 2016, How does the pore-throat size control the reservoir quality and oiliness of tight sandstones? The case of the Lower Cretaceous Quantou Formation in the southern Songliao Basin, China: Marine and Petroleum Geology, v. 76, p. 1–15, doi:10.1016/j.marpetgeo.2016.05.001.

Xi, K., Y. Cao, J. Jahren, R. Zhu, K. Bjørlykke, B. G. Haile, L. Zheng, and H. Hellevang, 2015, Diagenesis and reservoir quality of the Lower Cretaceous Quantou Formation tight sandstones in the southern Songliao Basin, China: Sedimentary Geology, v. 330, p. 90–107.

Zhang, L., S. Lu, D. Xiao, and B. Li, 2017, Pore structure characteristics of tight sandstones in the northern Songliao Basin, China: Marine and Petroleum Geology, v. 88, p. 170–180, doi:10.1016/j.marpetgeo.2017.08.005.

Ziegler, P. A., M. E. Schumacher, P. Dèzes, J.-D. Van Wees, and S. Cloetingh, 2006, Post-Variscan evolution of the lithosphere in the area of the European Cenozoic Rift System: Geological Society, London, Memoirs, v. 32, no. 1, p. 97–112.

Zou, C., R. Zhu, K. Liu, L. Su, B. Bai, X. Zhang, X. Yuan, and J. Wang, 2012, Tight gas sandstone reservoirs in China: characteristics and recognition criteria: Journal of Petroleum Science and Engineering, v. 88–89, p. 82–91, doi:10.1016/j.petrol.2012.02.001.

Blank Page

Chapter 2

Geological evolution of the Breagh Field Area.

Contents

Chapter 2: Geological evolution of area of the Breagh Field area.

2.1 Introduction

The Breagh Field (Fig. 2.1, 2.2) lies approximately 40 miles west of the decommissioned Esmond Field (Block 43/13a), 32 miles north-west of the Garrow Field (Block 42/25a and 43/21a), 38 miles north-east of Flamborough Head on the Yorkshire coast and 53 miles west-north-west of the INEOS Oil and Gas UK operated Cavendish Field (Block 43/19a). It lies within Quadrant 42 of the UK Southern North Sea (SNS), immediately to the north of the inverted Sole Pit Basin and the Dowsing Fault Zone. It is very close to the southern edge of the Mid North Sea High (MNSH) (Glennie, 1986).

Gravity data place the Breagh area along the NW–SE-striking boundary between the lower-gravity anomaly (denser) crust of the Silverpit Basin and higher-anomaly (less dense) crust in the offshore Cleveland Basin (Grant *et al.*, 2020). At this position, it forms part of the southern flank of the MNSH and is the most westerly of the fields with Carboniferous age reservoir in the SNS and northeast of the pinchout of the Lower Permian Rotliegend Group sandstones (Fig. 2.2).

Many workers have detailed the geological evolution of the SNS (Glennie, 1986, 2005; Fraser and Gawthorpe, 1990; Leeder and Hardman, 1990; Collinson *et al.*, 1993; McLean, 1993; Glennie and Underhill, 1998; Maynard and Dunay, 1999; Cameron *et al.*, 2005; John David Collinson *et al.*, 2005; Milton-Worssell *et al.*, 2010; Nesbit and Overshott, 2010; Pharaoh *et al.*, 2010; Rodriguez *et al.*, 2014; Monaghan *et al.*, 2017). The Breagh area together with the other surrounding flanks of the MNSH have remained largely under-explored and historically viewed as unprospective probably due to absence of the Upper Carboniferous coals (Monaghan *et al.*, 2015, 2017; Besly, 2019) or due to lack well penetrations of the prolific Permian reservoirs and Mesozoic source-rock intervals of the North Sea (Grant *et al.*, 2020).

The area instead includes a number of Devonian and Carboniferous basins (Vincent, 2015; Arsenikos *et al.*, 2019; Grant *et al.*, 2020) formed during the Variscan plate cycle. Devonian and Carboniferous rocks (Fig 2.3) within the SNS occur in a large ESE-plunging anticline termed the Southern North Sea Carboniferous Basin (SNSCB) (Leeder and Hardman, 1990; Glennie, 2005).

Upper Devonian and Lower Carboniferous age sedimentary rocks unconformably overlie the Caledonian Unconformity, the deposition of which largely occurred in a series of NE–SW-striking extensional half-graben developed on the northern margin to the Rheic Ocean during the Early Carboniferous (Booth *et al*., 2020). The SNS inherited the strong NW-SE structural trends from Palaeozoic Caledonian Orogeny (Pharaoh *et al*., 1987), which strongly influenced the pattern of sediment deposition during the Carboniferous.

The SNSCB, along with the onshore East Midlands area of England, Tweed basin, Northumberland Trough, Soloway basin, Craven basin and the Netherland Basins (Gibbs, 1986; Booth *et al*., 2020), form a single post-Palaeozoic syn-rift megasequence termed the Variscan Cycle (Underhill, 2003). They were superimposed or inherited from structures created during the Caledonian Orogeny (Booth *et al*., 2020) and are characterized by major strike zone such as the Sole Pit and Market-Weighton axis in the UK (Fig.2.4).

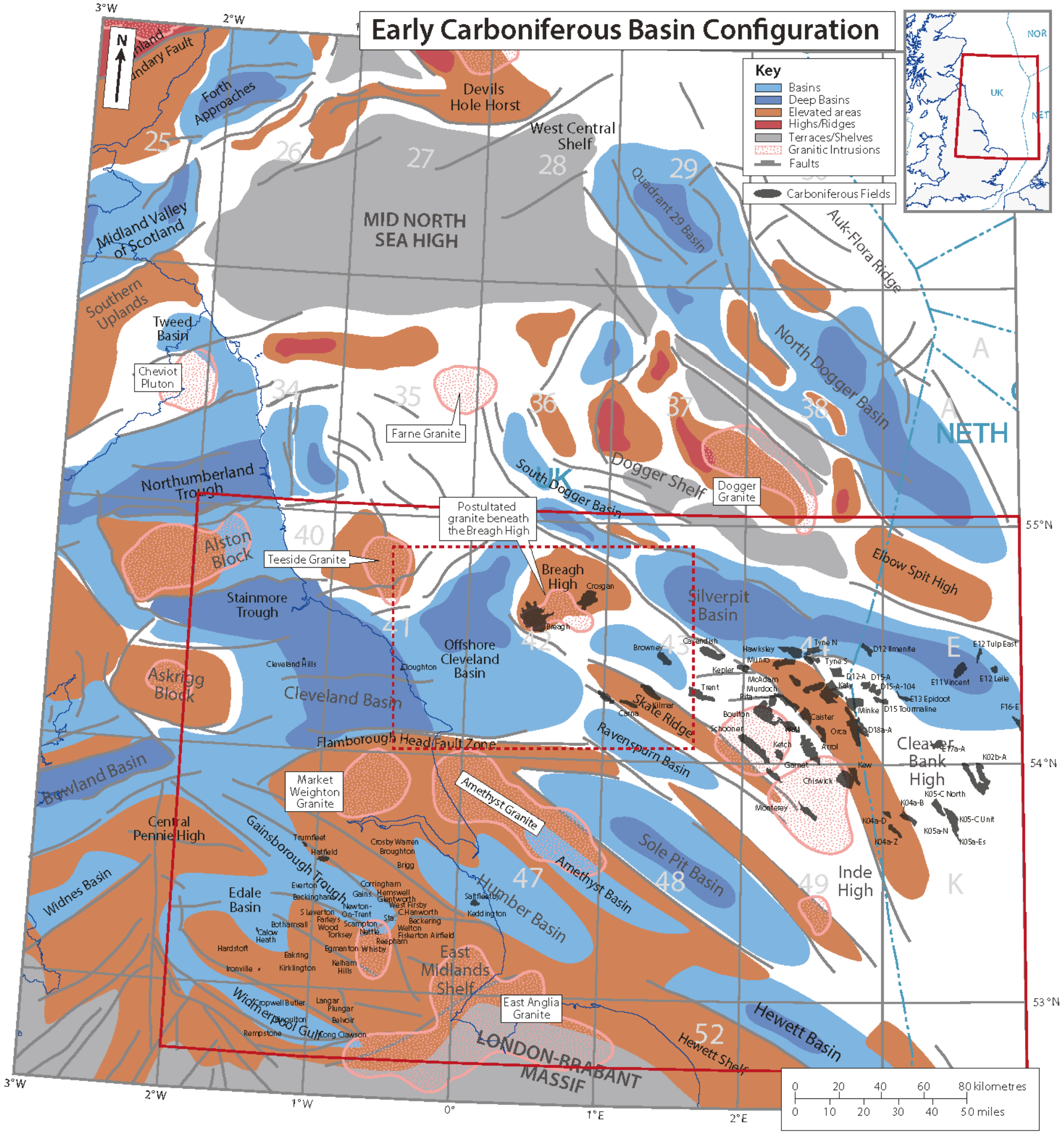

Figure 2.1: Structural map of the Southern North Sea showing the Early Carboniferous Configuration of basins in the Southern North Sea but also those in the and Central North Sea, Mid North Sea High, and onshore eastern England. From (Grant et al., 2020).

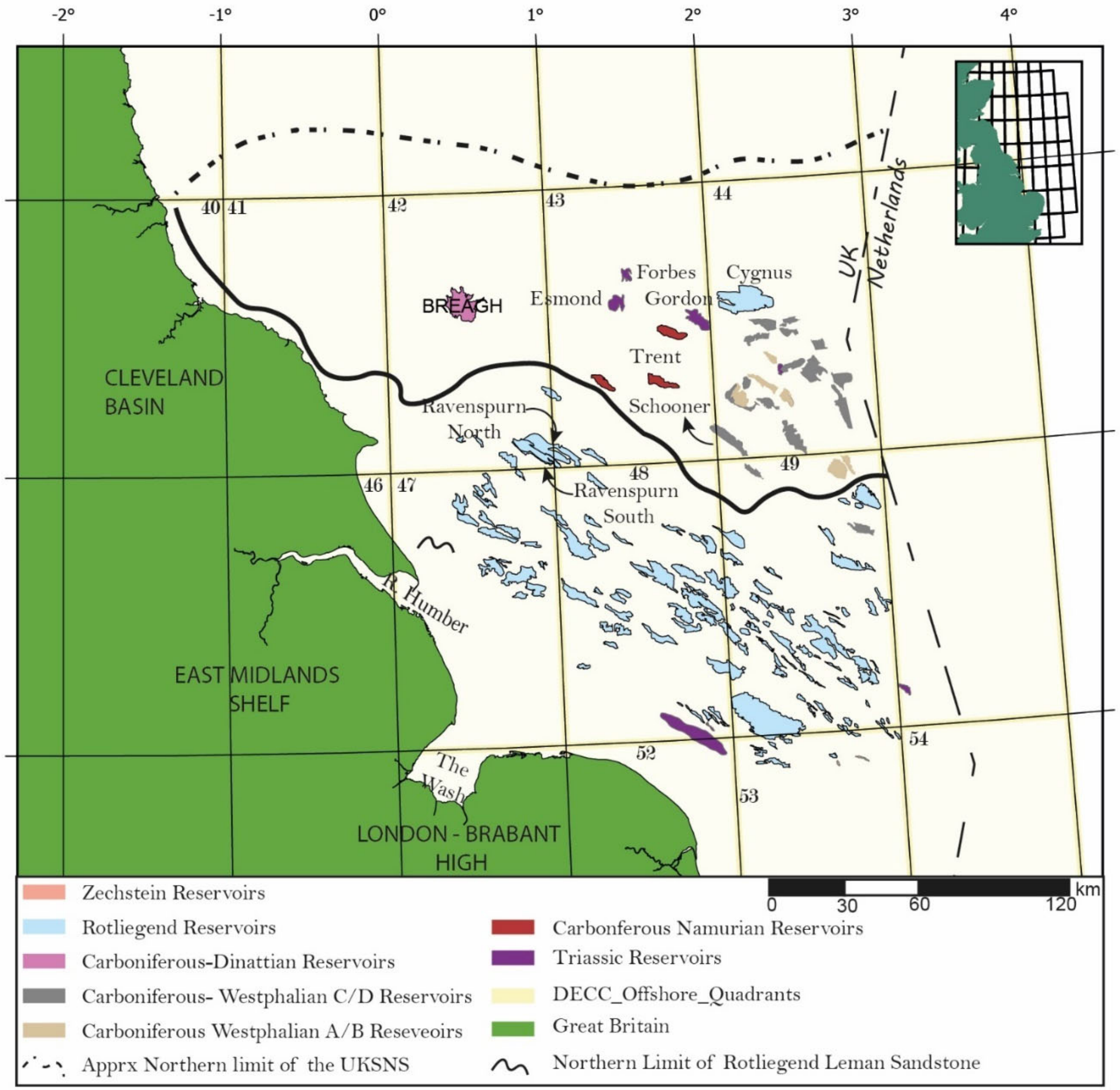

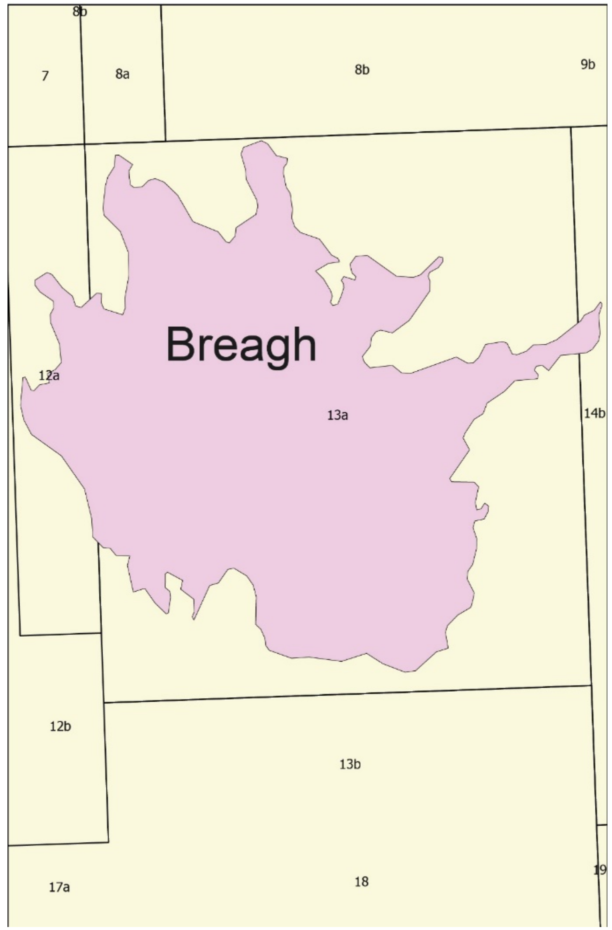

Fig 2.2: Left-Location Map for the Breagh Field and neighbouring areas (from Nwachukwu et al., 2020); Right- Expanded view (not to scale) of the Breagh Field.

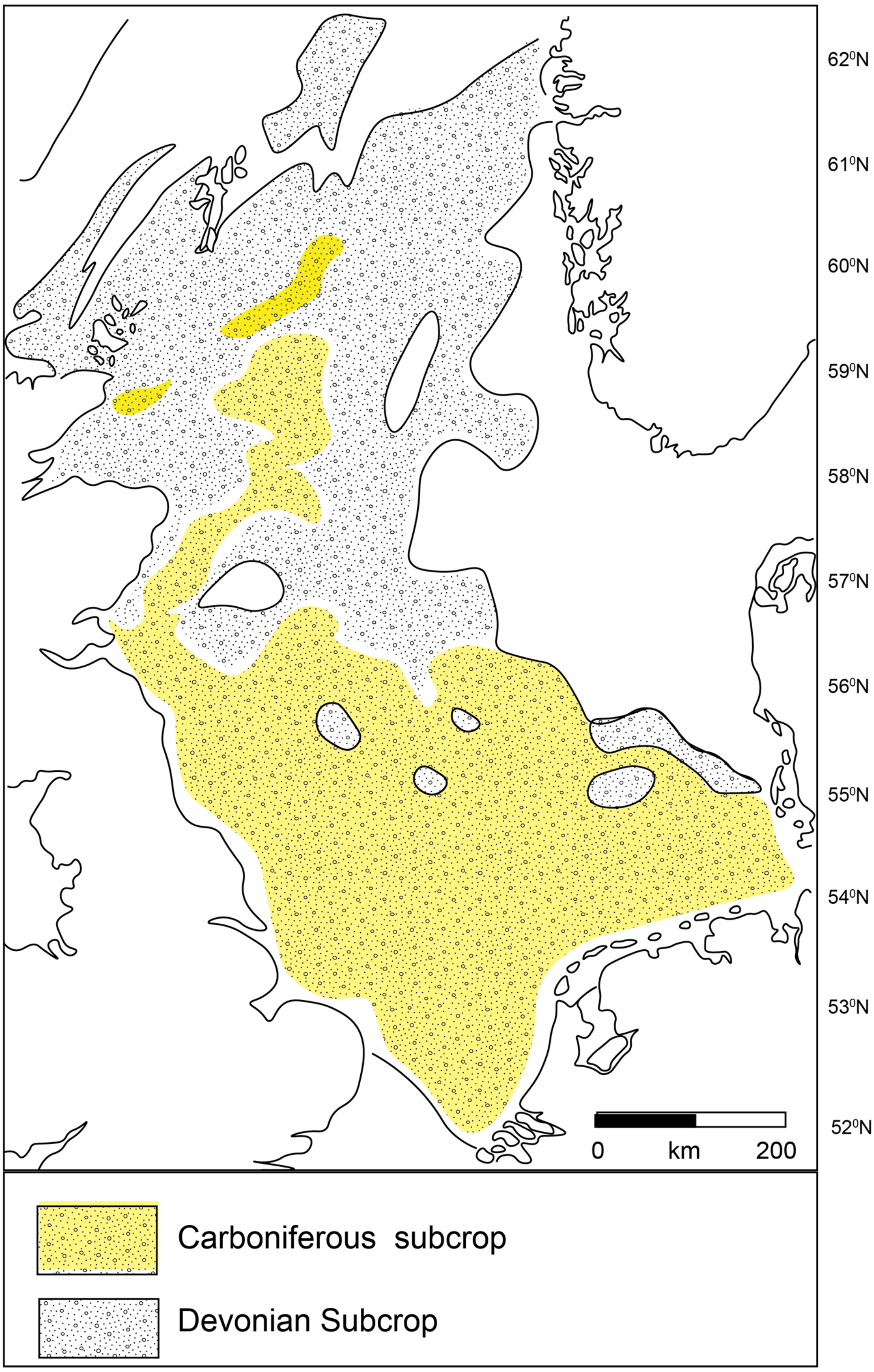

Figure 2.3: Outline map of the North Sea with Devonian and Carboniferous subcrop below the Base Permian and Base Mesozoic unconformities. Modified from (Besley., 2019). The Northern limit of the Southern North Sea is at 55^0N.

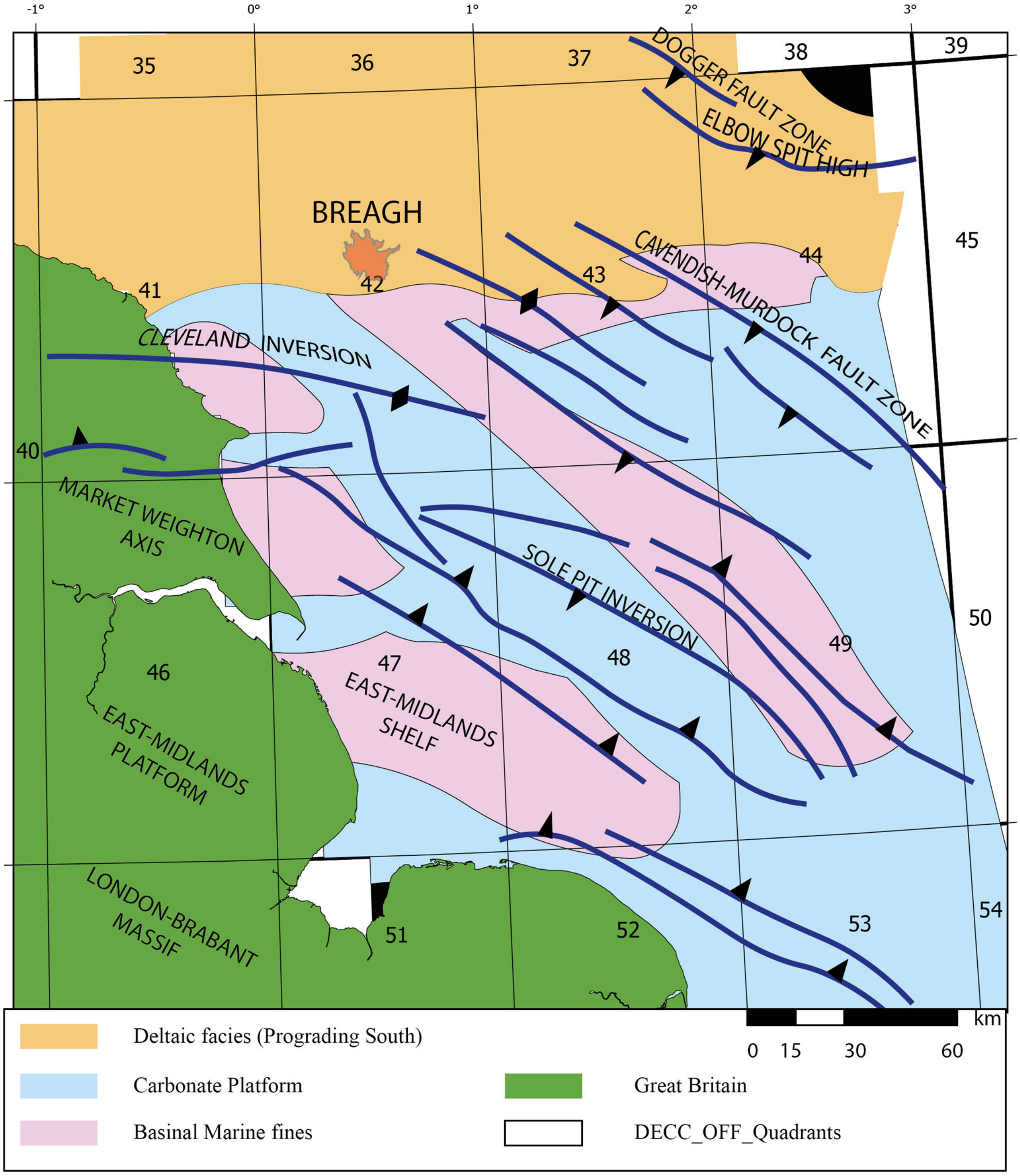

Figure 2.4: Major strike slip zones of the Southern North Sea with Breagh field outline. The map was compiled from various sources including Glennie, 1986 for the NW Southern Permian Gas basin and Grant et al., 2020 (see Fig 1) and authors therein. Coastline outline is from Underhill, 2003.

2.2 Caledonian orogeny

The SNSCB and the rest of the British Isles occupied widely separated continental fragments which lay on the different parts of the WNW-ESE trending Tornquist ocean and the SW-NE the trending Iapatus Ocean so are in this regards products of deposition around these ancient oceans (Glennie *et al*., 2005). The SNS areas together with the northeast US Nova Scotia, southeast Newfoundland, southern Ireland, England and southern Denmark lay on East Avalonia crust just south of Tornquist Sea, whereas the Scottish highlands and Northwest Ireland lay on Laurentia (Glennie, 2005).

Palaeomagnetic data and outline history of the Iapatus Ocean have been used to deduce the detailed history of the Iapetus Ocean and events leading up to its final closure, although this chapter is mainly concerned with the resulting structural framework from the Late Silurian and Devonian closure of the Iapatus Ocean which was a major control on the pattern of Carboniferous deposition in SNS (Glennie, 1986, 2005).

Long before the closure of the Iapatus Ocean, the Tornquist Sea between eastern Avalonia and Baltica closed following a dextral movement (Frost *et al*., 1981; Pharaoh, 1999; Pharaoh *et al*., 2006) in the late Ordovician and resulted in Trans European Suture Zone (TESZ). The TESZ is a line of structural weakness extending from southern Denmark (Thor suture) through the Sorgenfrei-Tornquist Zone (Sweden) to the Teisseyre-Tornquist Zone in the Polish Trough (Glennie, 2005); Cocks & Fortey, 1982; Tait *et al*., 1997; Cocks & Torsvik, 2005) along the southern edge of the Ringkøbing Highs to the Mid North Sea High.

This suture zone is noted for its role in the reservoir geology of the SNS fields by creating a zone between the North and South Permian Basins which had withstood the crustal stretching and subsidence from the Variscan Orogeny and as such enabled a configuration that received the influx of the successive Zechstein cycles from Tethys Ocean (Glennie, 1986). In addition, the TESZ also served as a focus for Carboniferous to Mesozoic strike slip displacement and Alpine inversion (Pegrum, 1984; Pharaoh *et al*., 2006).

Long after the closure of the Tornquist sea, Laurentia, and Baltica collided, closing off the northern Iapetus by the end Silurian times, to create the Scottish-Scandinavian Caledonian Mountain system with its high-grade metamorphic rocks.

2.3 Post Caledonian history.

2.3.1 Devonian

By the end of the Caledonian Orogeny, the northern (Laurentia) and southern (Baltica and Avalonia) lithospheric plates had welded together to form the large Devonian (Old Red Sandstone) continent. Erosion of the long SW-NE trending Caledonian mountain ranges resulted in fluvial transport of large volumes of sediments southwards across the adjacent plains (Besly, 2009) towards the margins of the Proto-Tethys Ocean (Rheic Ocean). Erosion was in an almost vegetation-free, arid, continental climate (Barrell, 1916) that experienced low seasonal rainfall and resulted in the deposition of widespread red, clastic sediments dominated by alluvial, fluvial and aeolian sequences (Allen and Marshall, 1981) with only minor marine incursions (Marshall *et al*. 1996).

Not much is known about the Devonian sedimentation in the SNS in contrast to the Lower and Upper Devonian sequences containing dune sands and sabkhas in SW Ireland (Richmond and Williams, 2000) and in the NE Scotland and Orkney Isles (Marshall and Hewett, 2003; Marshall *et al*., 2007; Mendum, 2012) where deposition took place in a series of post-orogenic basins created through extensional collapse of the fold and thrust belt.

Through the early Devonian, both Laurussia and Gondwana were moving northwards until they collided later on in the early Carboniferous resulting in the closure of the Proto-Tethys (Rheic) Ocean (Ziegler, 1987) to create the roughly W-E trending Hercynian-Variscan orogenic belt that sutured Laurussia and Gondwana into the unstable supercontinent Pangea.

2.4 The Carboniferous

2.4.1 Variscan Orogeny

The Carboniferous period records one of the most important time in the evolution of the SNS and indeed European Geology (McCann *et al*., 2008) as it bears the climax of the Variscan Orogeny and marks the final amalgamation of the Pangea (Cameron *et al*., 1992; McCann *et* *al*., 2008) The final phase of Variscan activity was also a period of terrane mobility and tectonic instability with sinistral wrench faulting causing widespread rifting (Pegrum, 1984; Ziegler, 1990; McCann *et al*., 2008).

By the end of the Variscan Orogeny, oblique convergence of Gondwana and Laurussia created the Variscan mountain belt (Leveridge and Hartley, 2006) a curvilinear feature extending across Europe from Russia through Western Europe and into North America (McCann *et al*., 2008) which in the SNS serves as the effective southern limit to the Devonian and Carboniferous play fairway (Fig 2.5). By this time, the area of the SNSCB had now formed in broad back arc region along the southern margin of Laurussia (Cameron *et al*., 1992; Hollywood and Whorlow, 1993).

The Collision of Gondwana with Laurussia also resulted in additional structuration parallel to those of the underlying Caledonian basement. Structures to the east of the Midland Platform (Fig 2.5) were aligned NW-SE subparallel to the Tornquist Sea, whereas those to the west inherited the NE-SW Caledonian structural trend (Glennie *et al*., 2005). The patterns of sedimentation were strongly influenced by syn-sedimentary tectonics and inherited many of the strong NW- SE and NE –SW structural trends from Caledonian orogeny. These faults trends were consistently reactivated throughout the Carboniferous in an extensional sense and beyond in a compressional sense (Fraser and Gawthorpe, 1990; Underhill, 2003).

It seems that the Breagh area and with the areas in the southern flanks of the MNSH has neither of the obvious NW-SE or NE-SW trend of the SNS gas fields (Fig 2.1 & 2.2) may have been hinged by their proximity to the rather stable Mid North Sea high. It is possible that TESZ running up to the Mid North Sea high may have given the added rigidity needed to prevent the area from shearing, stretching and deforming to the same extent as the basins farther away from it (Glennie, 1986). It is also likely that the relative stability of the Breagh area is because it may have been situated on a small granite pluton, resulting in a subtle palaeotopographical high (Collinson *et al*., 2005; Kimbell and Williamson, 2015; Monaghan *et al*., 2017; Arsenikos *et al*., 2019; Booth *et al*., 2020; Grant *et al*., 2020; Donato and Megson, 1990; Pharaoh *et al*., 1995, 2006; Kimbell and Williamson, 2015).

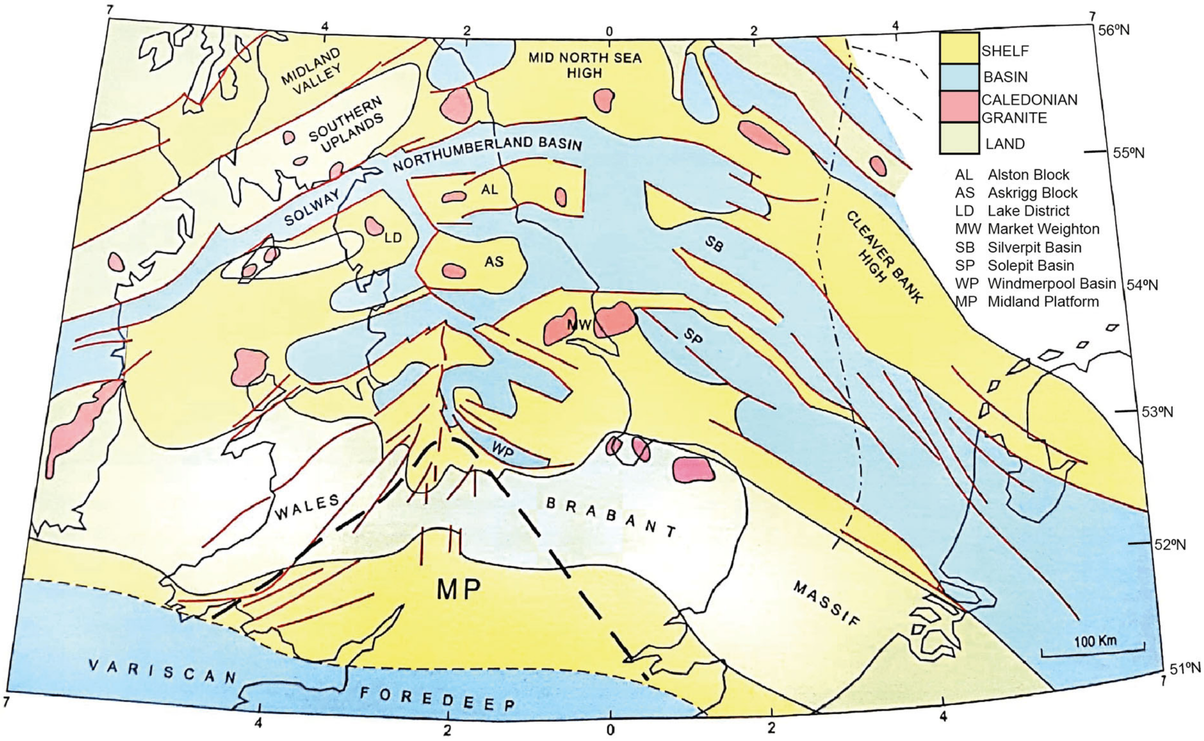

Figure 2.5: Early Carboniferous structural pattern across SNS draping around the Midland Platform see also the Variscan deformation front to the bottom left marking the southern limit Carboniferous play fairway in the SNS (Glennie; 2005).

2.4.2 Tectonic and stratigraphic control on Dinantian reservoir development.

The structural framework of the SNSCB together with central and northern England during the Early Carboniferous times was dominated by tectonic instability and faulting causing widespread rifting (Leeder, 1988; Leeder and Hardman, 1990; McCann *et al*., 2008) and the formation of numerous extensional basins (eg the Northumberland, Stainmore and Gainsborough Troughs, the Bowland Basin and the Widmerpool Gulf). (Fig 2.6)

Fault bounded graben (basins) were separated by platforms and tilt-block highs (Leeder and Hardman, 1990; Cameron *et al*., 1992; Waters and Davies, 2006; Besly, 2009) and were responsible for the initial position of carbonate and clastic sedimentation (Fraser and Gawthorpe, 1990; Chadwick and Holliday, 1991; Hollywood and Whorlow, 1993) and the resulting facies variation in Northern England and SNSCB during the Early Carboniferous.
Two important palaeogeographical changes occurred progressively during the Visean. Firstly, clastic, mainly deltaic sediments became dominant in the northern British basins and over much of the North Sea. Secondly, as lower Carboniferous crustal extension proceeded,

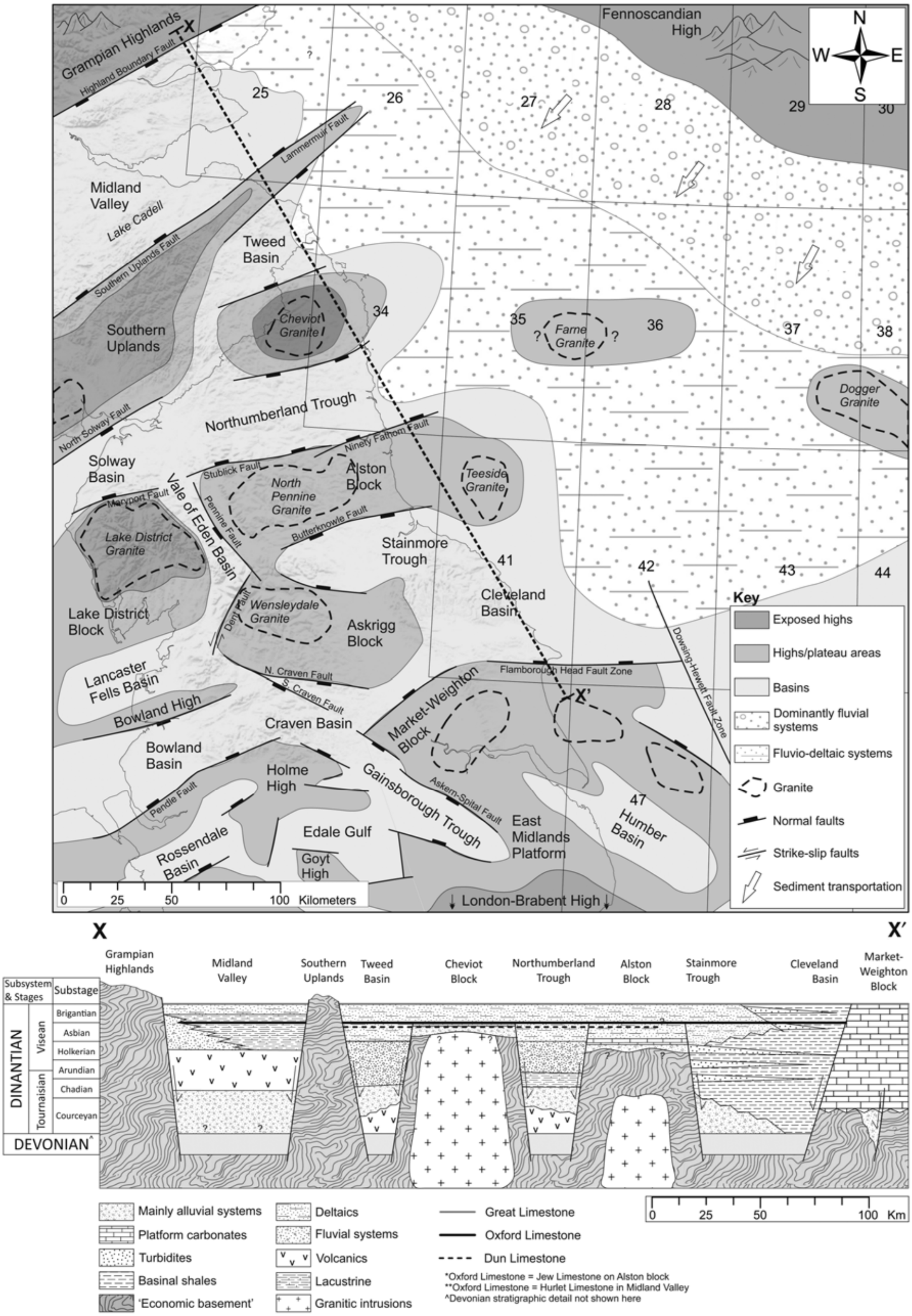

Figure 2.6: Palaeotectonic map of the early Carboniferous times showing the highs and intermittently exposed areas ('blocks') and intervening elongate basins. (From Booth et al., 2020).

topographic differentiation between highs (horst, tilt blocks) and corresponding area of more rapid subsidence became pronounced. Where deposition was taking place in areas of low relief, sea level rises would have flooded large areas of land, producing events that can be correlated over great distances (Stephenson *et al*., 2008). This Early Carboniferous eustatic sea level fluctuations combined with the basin-scale tectonic has been used to explain cyclicity in the Early Carboniferous successions and discussed more in chapter 4.

The input of clastic sediments into the basins developed during the Early Carboniferous were derived from several sources. Alluvial fans were sourced from footwalls of the Late Devonian and early Carboniferous rift (Fraser and Gawthorpe, 1990; Besly, 2019), and fairly small deltas were sources from the remaining Caledonian upland area in Scotland (Leeder and Hardman, 1990).

Erosion of the Caledonian highlands fed a Yoredale type delta (Jones and Kirkby, 1886; Fraser and Gawthorpe, 1990; Leeder and Hardman, 1990; Glennie *et al*., 2005) into the Northumberland Trough and the rest of Northern England (Hollywood and Whorlow, 1993) at various intervals through the Dinantian (Johnson, 1984; Waters and Davies, 2006). A typical Yoredale cycle is an interplay of two environments- an epicontinental sea and a deltaic system (Moore, 1959; Elliott, 1975). It begins with a marine limestone overlain by a coarsening- and cleaning-upward siliciclastic succession, capped by rooted palaeosols including coals (Moore, 1959; Retallack, 1988, 2014; Tucker *et al*., 2003).

About 4000m of alternating limestones, sandstones and marine shales were deposited during this time in the Northumberland Trough whereas only about 500m of sediments were deposited on the horst like the Alston Block (Fig 2.6). The same deltaic depositional system continued into the SNS where mid-Dinantian age sediments are locally more than 3000m thick. Examination of cores suggest that facies and general depositional styles in offshore area are like those at onshore Britain especially the section seen at the Northumberland trough. In the Breagh area, The Yoredale Formation is represented by four zones (Fig 2.7) each zone comprises a series of channel sandstones and sheet sandstones that are divided by mudstones, heterolithics and local coal beds. These zones are separated by different marine limestone members typical of a Yoredale cyclotherm (Symonds *et al*., 2015).

In the more southerly areas however, south of latitude 54^0N, clastic turbidites were deposited in basinal areas and carbonate reefs were formed along basin margins and as progradational wedges on depositional slopes (Fraser and Gawthorpe, 1990; Underhill, 2003). Basinal marine shales of Tournaisian and Visean age are believed to be the candidate source rocks for the oils of the East Midlands Province (Raji *et al*., 2013). Although carbonate deposition in the East Midlands soon came to a halt as Early Carboniferous rifting passed into thermal subsidence during early Namurian when the basinal areas became progressively filled with clastic material from rejuvenated northern sediment source manifest in eastern England and the SNS as a sequence of major delta advances.

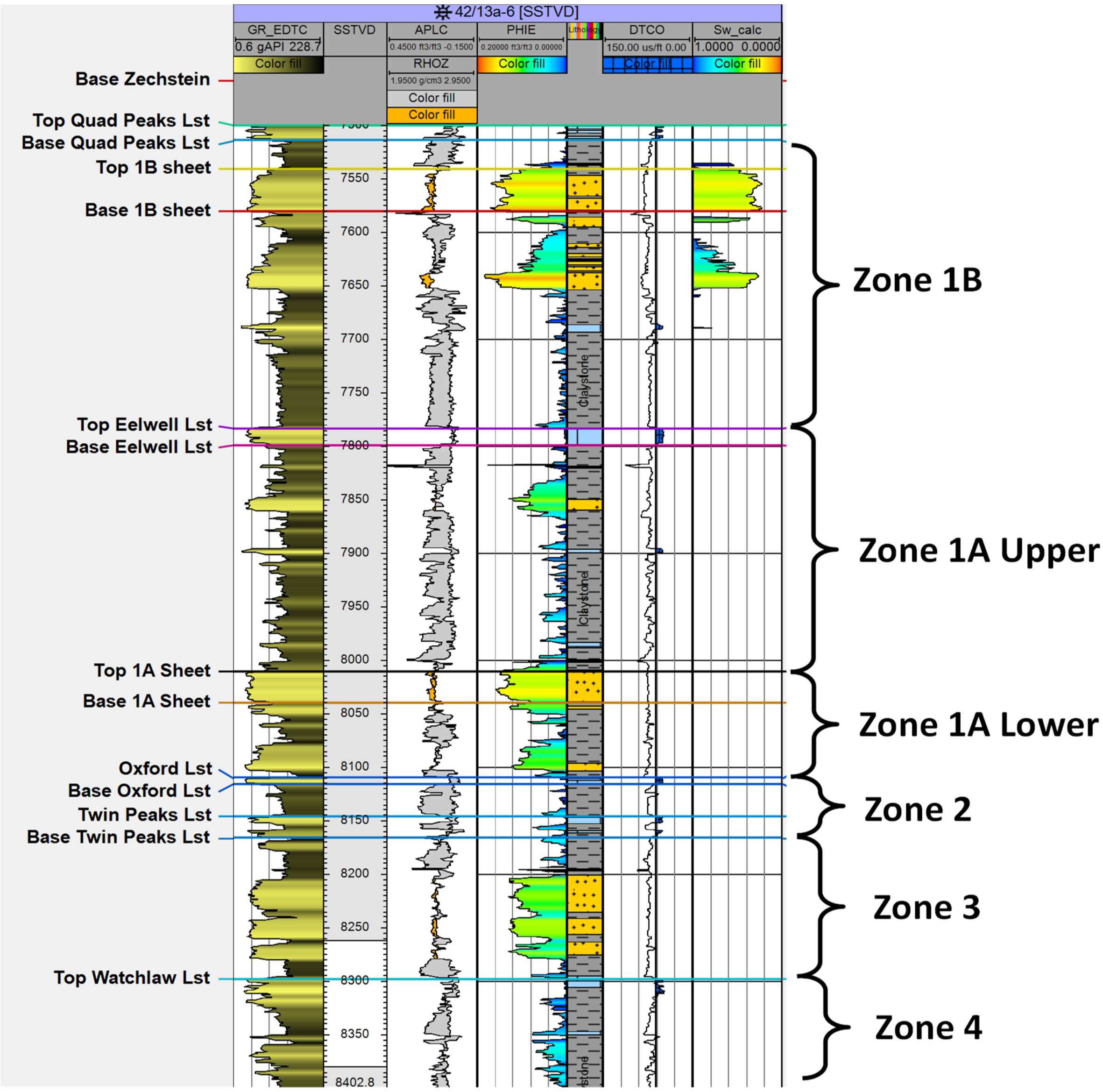

Figure 2.7: Appraisal well 42/13a-6 log responses and reservoir zonation.

2.4.3 Namurian to Stephanian structural development

2.4.3.1 Inversion tectonics

By Late Namurian times, shallow water deltaic conditions had become dominant and prevailed over much of what is now the UK onshore and offshore and similar conditions continued through the Westphalian A and into the late Westphalian B with the development of lower and upper delta plain sequences respectively (Hollywood and Whorlow, 1993). Back arc extension was no longer the dominant tectonic process and thermal subsidence is interpreted to have produced a more uniform distribution of sediment thickness throughout the Namurian and Westphalian (Collinson *et al*., 1988; Guion and Fielding, 1988; Steele, 1988; Corfield *et al*., 1996; Besly, 2009).

This inversion signalled the onset of compression related to the approaching Variscan deformation from the south (Corfield *et al*., 1996; Underhill, 2003) More widespread delta advances during the Namurian then extended fluvial deltaic deposition of the Millstone Grit Formation southwards across the remainder of eastern England and the SNS.
The influence of block faulting diminished by the end of the Namurian and the Coal Measures of Westphalian age were deposited in more extensive downwarps and exhibiting a remarkable lateral continuity over very large areas. Although older extensional faults were locally active through the Westphalian B, movement along these faults had largely ceased by Early Namurian times. By mid Westphalian B times, the tectonic regime had changed from passive thermal subsidence to compression.

The regional uplift associated with the Variscan compression, caused a switch in sedimentary facies from predominantly coal bearing delta plain to alluvial environment with associated red beds during the Westphalian C times (Besly, 2009). By the late Westphalian D, red beds were being deposited locally on the flanks of London-Brabant Massif (Davies *et al*., 1999; Hallsworth and Chisholm, 2000) with improved drainage and increased aridity, these extended across the remainder of the SNS. Stephanian age sediments have not been proven in the UK sector.

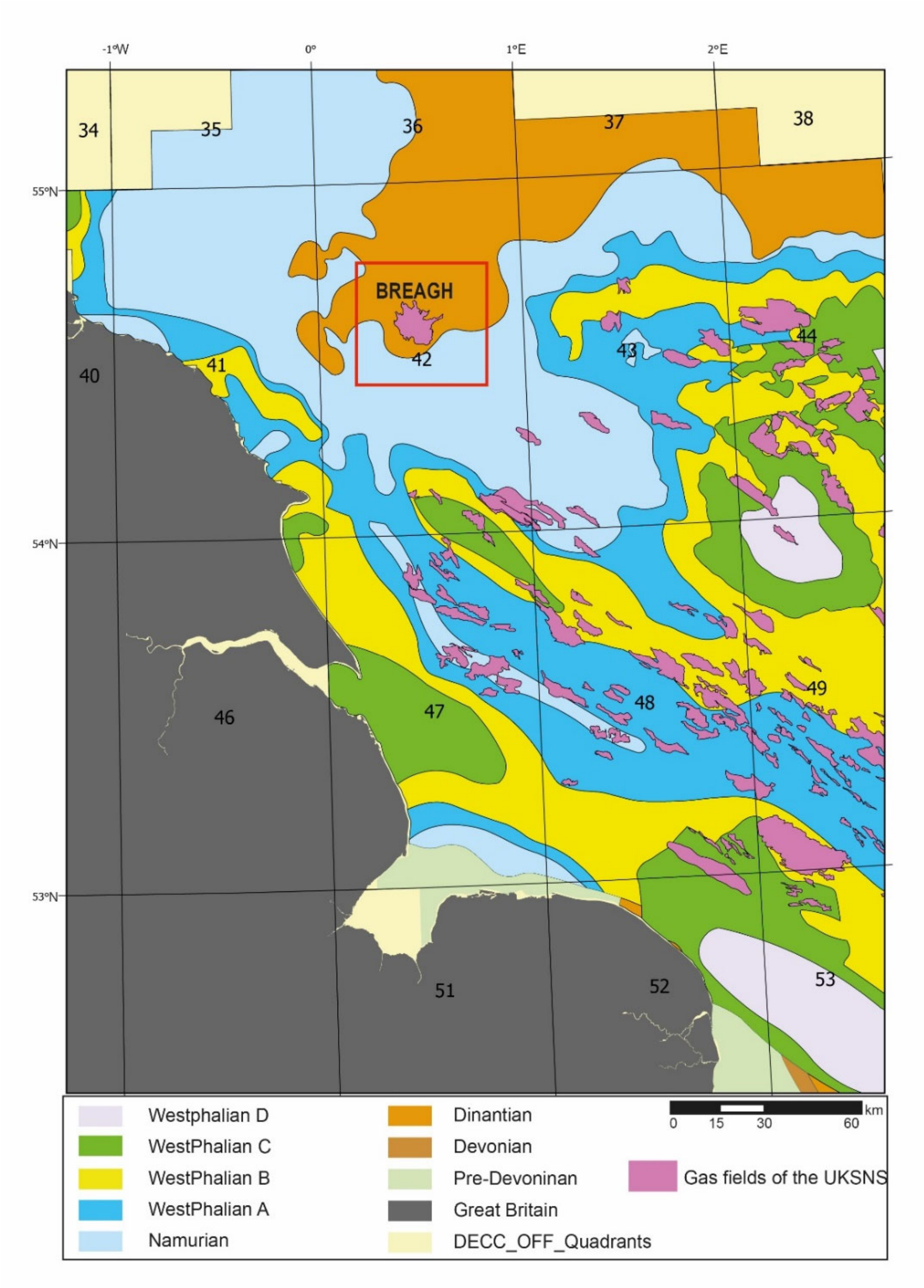

Figure 2.8: Distribution pattern of the Base Permian subcrop facies on the UKSNS areas. Breagh (in the red box) lies in the area of Dinantian subcrop. (From Nwachukwu et al., 2020). For field names see Fig 2.2.

2.4.4 Effect of Carboniferous tectonics and paleo environment on reservoir potential of the Breagh area

The Carboniferous was a time of major changes in the Earth's paleogeography, climate and carbon cycle. Both sedimentary facies and palaeomagnetic data (Glennie, 2005) demonstrate that the slow drift of the Laurussian continent during the Carboniferous period carried what is now the SNS from the southern, subtropical, arid climes through humid, equatorial latitudes of Coal Measure Group deposition.

Combined with the evolution of land plants and the Variscan orogeny, the Carboniferous was the time of formation of the world's largest coal deposits. The evolution of terrestrial plants and widespread coal formation created a new organic carbon reservoir and changed the global carbon cycle (Buggisch *et al*., 2003).

Within the SNS sedimentary sequence changed progressively from mixed marine and paralic sedimentation with limestones, sandstones and shales deposited in the Early Carboniferous (Yoredale Fm.), to pro-delta and delta front sedimentation in the earliest Late Carboniferous (Besly, 1998). These sedimentary rocks are in turn overlain by coal bearing delta top sediments during the Westphalian (A and B) and ultimately continental fluvial and alluvial deposits (Westphalian C and D) (Besly *et al*., 1993).

Continued syn-and post-depositional compression across the newly formed Variscan foreland basin through the Late Carboniferous resulted in folding - the partial or complete structural inversion of many former extensional faults. Regional uplift accompanied by deep erosion caused a variety of Dinantian, Namurian and Westphalian rocks to subcrop beneath the regional unconformity at the base of the Permian in the SNS (Fig 2.8) (Underhill, 2003).

This orogenic movement became responsible for creating the small oil and gas traps of Carboniferous age by creating inversion anticlines in the hanging walls of the major graben boundary faults (Fraser and Gawthorpe, 1990). Successful drilling and appraisal of the inversion structures has led to production from numerous fields in the East Midlands. Drilling of preserved footwall highs formed during the earlier extensional episode has also led to local production of Carboniferous sourced oil from Dinantian carbonates (Craig *et al*., 2013). The Breagh field itself lies within a large-scale inversion structure and comprises tilted fault blocks with fault closure to the southwest and 3-way dip closure in other directions (Fig 2.9). Although later Mesozoic and Cenezoic tectonic events associated with rifting in Atlantic and Tethyan provinces have also modified the trapping geometries (Fraser and Gawthorpe, 1990; Cameron *et al*., 1992; Besly *et al*., 1993) in the Breagh structure.

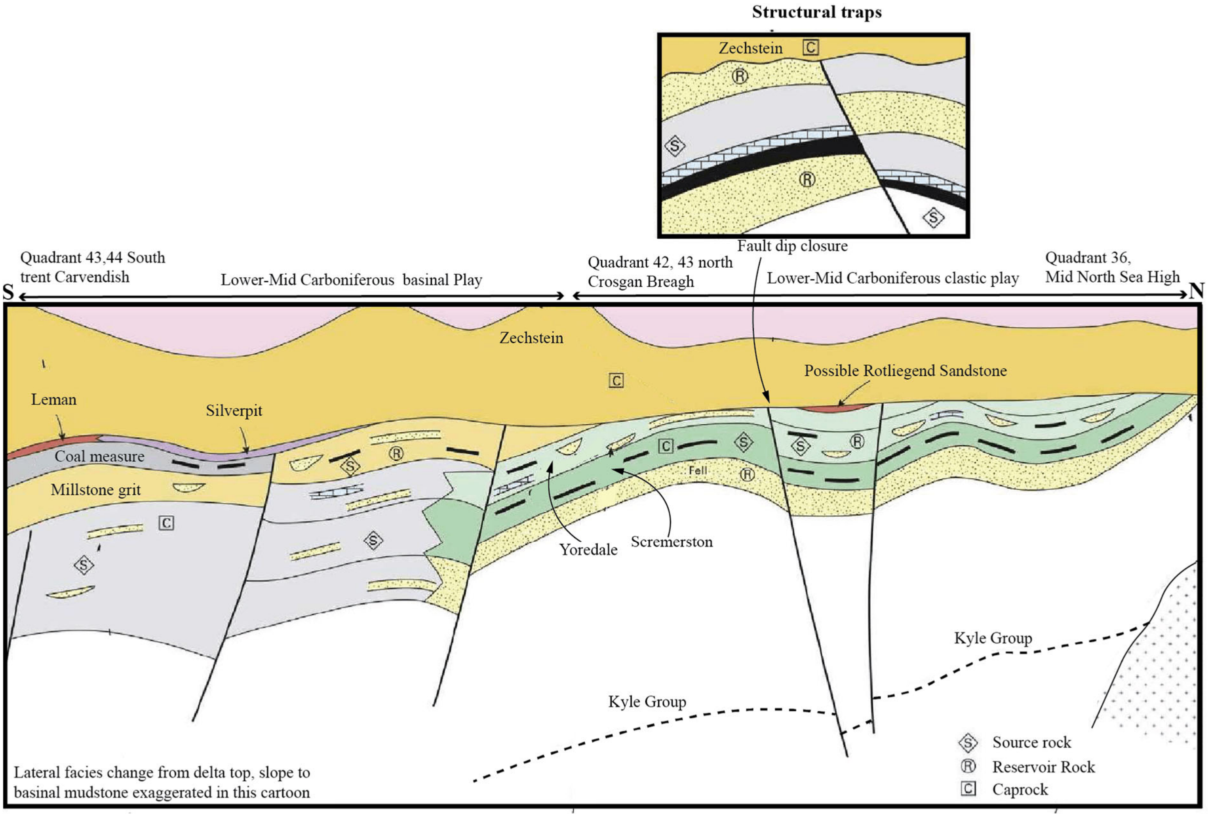

Figure 2.9: Trapping Configuration of Carboniferous age reservoirs. Top extract– Cartoon of the Breagh inversion structure with a tilted fault block (modified from Monaghan et al., 2017).

An additional consequence of the inversion in the Breagh area is that the source of gas is not entirely certain since regional uplift and subsequent erosion of Westphalian Coal Measures means that the Upper Permian (Zechstein) strata unconformably overlie the Dinantian Yoredale Formation (Monaghan *et al*., 2017). Elsewhere in the SNS, coals within the Westphalian Coal Measures are considered to be the source of gas (Barnard and Cooper, 1983; Ritchie and Pratsides, 1993). At Breagh, since Permian Zechstein strata lie direct upon Early Carboniferous strata, the gas that now fills Breagh could have arrived via long distance migration from stratigraphically younger Upper Carboniferous coals (Fig 2.10). Alternatively, it could also be the basinal Namurian mudstones containing disseminated organic material to the east or there may be as yet an unidentified source in the Early Carboniferous such as the Mid-Dinantian Scremerston Formation (Chadwick *et al*., 1993; Milton-Worssell *et al*., 2010; Booth *et al*., 2017).

The presence and geometry of the overlying Zechstein (Late Permian) sequence has also posed additional structural complexity in imaging the trap consequently there is uncertainty in calculating the resulting depth and the perceived gas in place volume is therefore not well constrained.

2.5 Permian

2.5.1 Early Permian

Early Permian deposits are absent from the deeply eroded Breagh area (Booth *et al*., 2017) (Fig 2.10 & 2.11). In Breagh area, the Early Permian deposits are overstepped in the Late Permian by Zechstein carbonates and evaporites deposited after the Southern Permian Basin connected to the Tethyan Ocean. A Complete Permian age sedimentation can be observed in the eastern half of the South Permian Basin where the Rotliegend is divided into two distinct layers, the Upper and the Lower Rotliegend Group which are separated by the important Salian unconformity. Where encountered in the SNS, Permian age sedimentation began with Rotliegend Group continental sandstones and their basinal temporal equivalent lacustrine mudstones (aeolian, fluvial and sabkha) belonging to the Leman Sandstone Fm. and Silverpit Formation respectively.

These sequences were deposited in a climate that alternated from humid equatorial position under which the Carboniferous Coal Measures were deposited to the semiarid arid climate in which the Upper Rotliegend sandstones were deposited. (Fraser and Gawthorpe, 1990) estimated that erosion may have removed about 3000m of strata in parts of northern England during this period.

During the Early Carboniferous, Gondwana moved northward and collided with Laurussia, then continued rotating clockwise and suturing with it through the rest of the Carboniferous. This movement subjected the newly formed Variscan foreland basins to right lateral wrench movements and the development of a complex pattern of conjugate faults. This led to the rapid collapse of the Variscan fold belt during the late stages of the orogeny and by the Early Permian times development of several important E-W trending, intermontane basins including the Northern and Southern Permian Basins (Glennie, 1986; Van Wees and Beekman, 2000; Underhill, 2003; Ziegler *et al*., 2004).

Throughout this time, sediments of the SNS were deposited in a gradually subsiding South Permian Basin (SPB) (Ziegler, 1982, 1990; Glennie, 1998; Van Wees and Beekman, 2000) that extended continuously from eastern England across northern Germany into Poland (Ziegler, 1982).

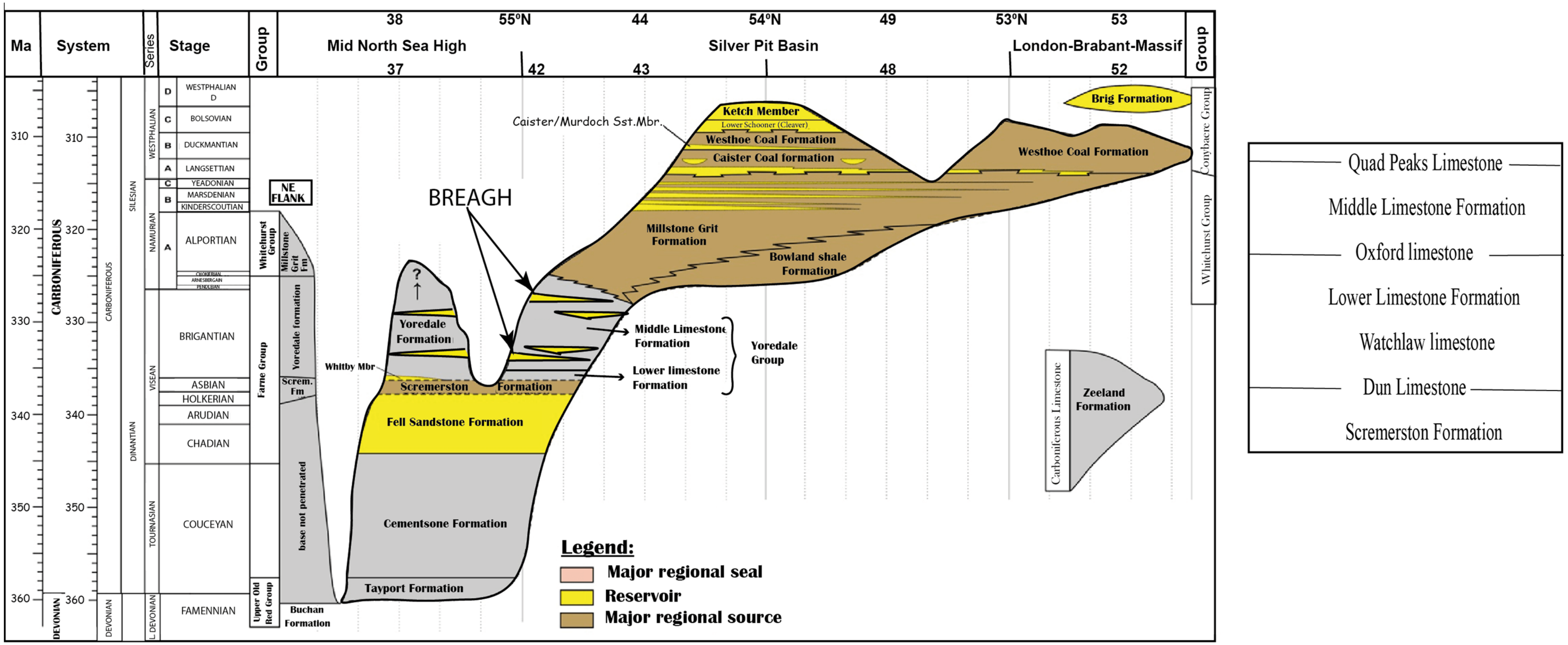

Figure 2.10: Lower Carboniferous stratigraphy with Breagh zonation and onshore stratigraphic terminology of the Yoredale Group, as utilized in the Breagh Field area, including the key limestone markers (from Nwachukwu et al., 2020).

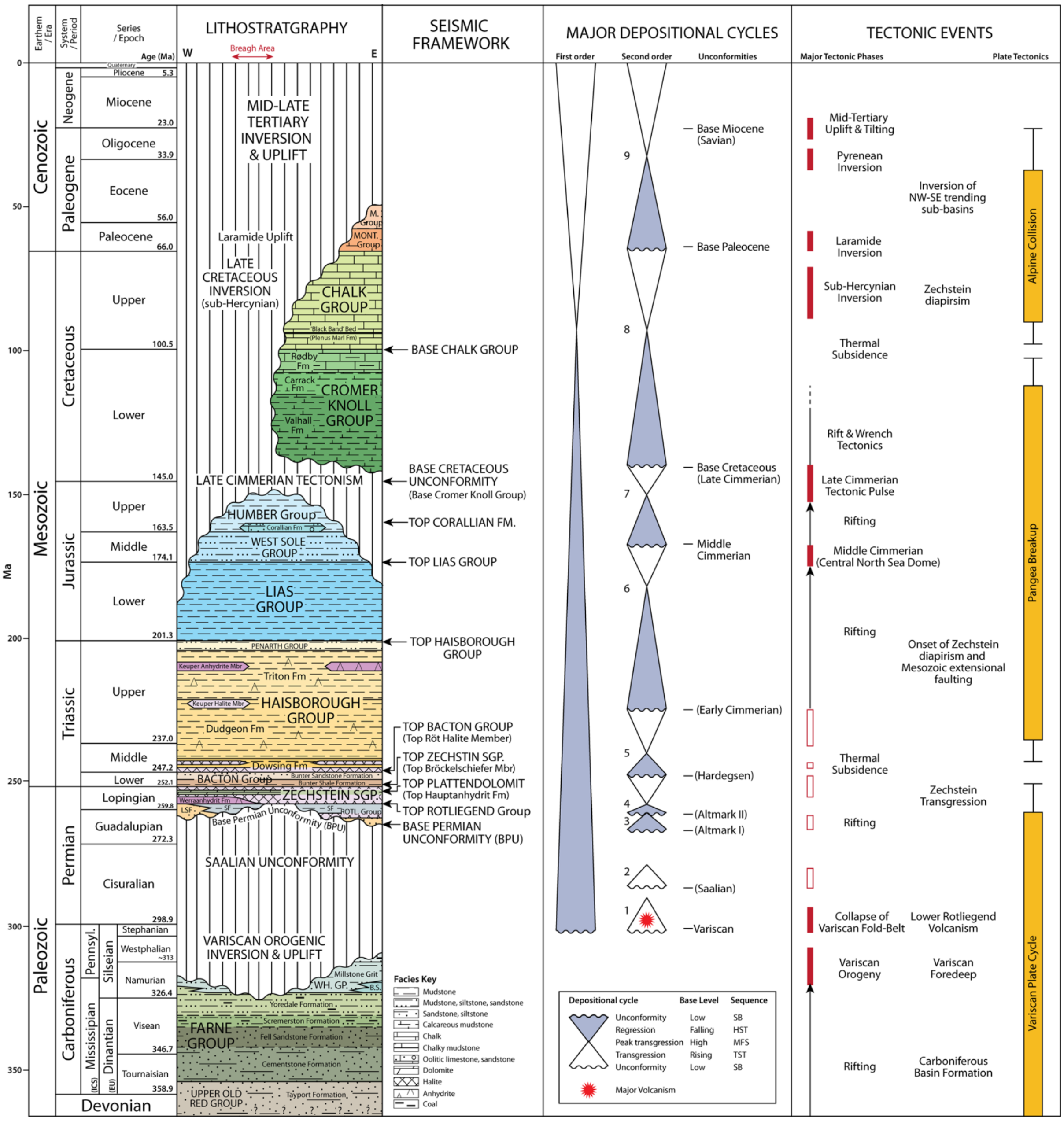

Figure 2.11: Tectonostratigraphic chart for the Breagh study area. (From (Grant et al., 2020).

2.5.2 South Permian Basin: Accommodation for Zechstein supergroup

The differential subsidence in the SPB in the Early Permian, allowed for topographic differences across the SNS and the British Isles with the resulting development principal topographic features in the area (Taylor and Colter, 1975; Cameron *et al*., 1992). The Pennine High became elevated for the first time, it separated the SNS from the Irish Sea Basin.

The London-Brabant Massif and the Mid-North Sea High formed the southern and northern boundary of the SNS respectively and continued to stay so as positive structural features throughout much of the Permian to early Mesozoic and only subsided sufficiently to receive significant thicknesses of sediment during Cretaceous and Tertiary times (Barnard and Cooper, 1983). The Cleaverbank High and the northern part of the East Midland Shelf formed as intrabasinal highs and remained so until the Late Permian. The Solepit Trough also began to subside, it became an important depocenter from Permian to the Triassic times.

By late Permian both the SPB and NPB had subsided by as much as 250-300m below global sea level (Smith, 1989; Ziegler, 1990; Glennie, 1998; Heeremans and Faleide, 2004). This made room for the wide spread marine transgression (Ziegler, 1981; Smith, 1989; Clark *et al*., 1998) from the rising arctic sea (Smith, 1989; Ziegler, 1990) between Greenland and Norway that deposited complex Zechstein Supergroup (Cameron *et al*., 1992; Underhill and Hunter, 2008).

2.5.3 Zechstein transgression.

The Zechstein Group consist of six sedimentary cycles which reflect deposition in response to marine recharge and its subsequent regression and evaporation in the Northern and Southern Permian Basin (Cameron *et al*., 1992; Underhill, 2003; Besly, 2009). Each cycle begins with a pronounced marine incursion and with each successive depositional cycle, limestone was progressively succeeded by evaporates. These evaporates generally show an upward transition from anhydrite to halite and then to magnesium or potassium salts to form a very effective seals for the gas generated from Carboniferous shales and coals in the SNS.

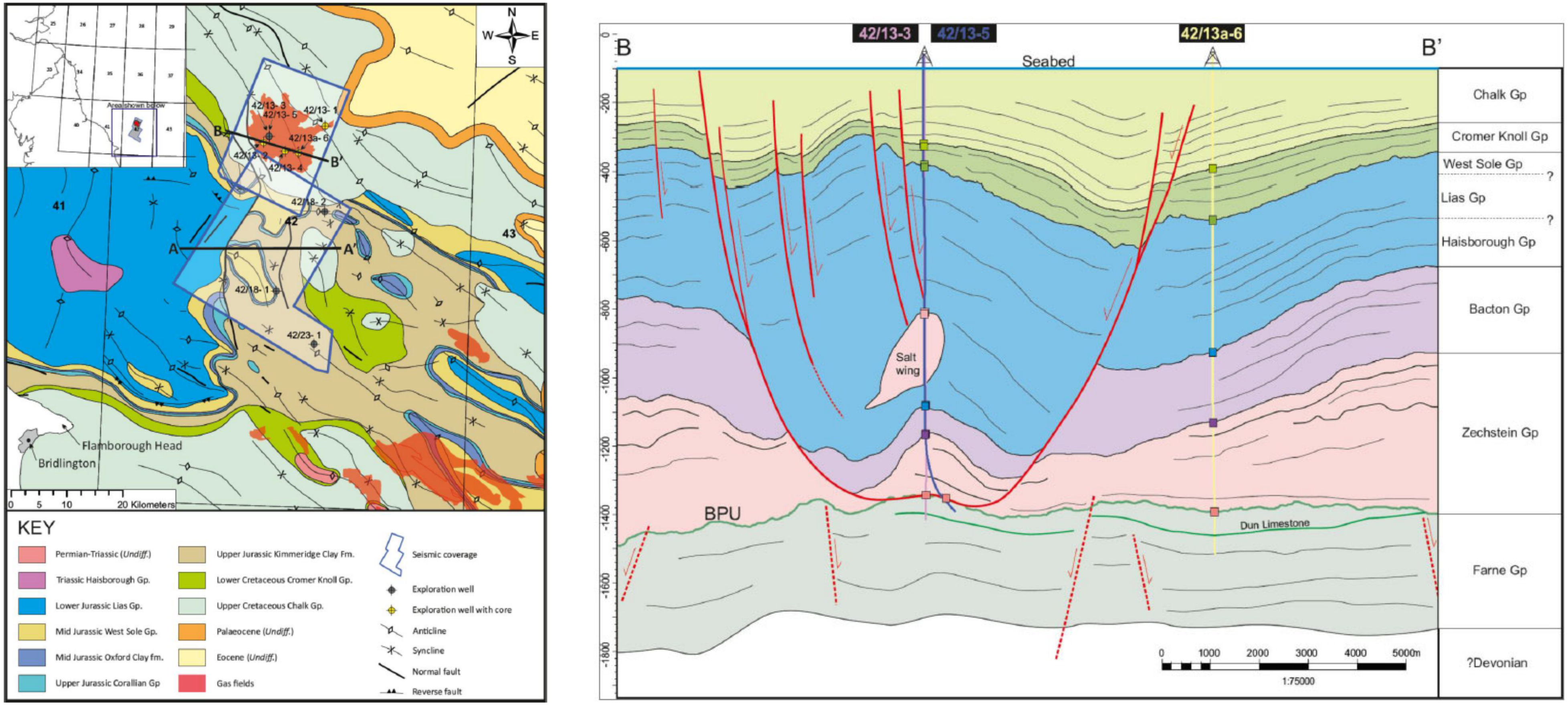

Figure 2.12: Left - Map showing the offshore geology at seabed to the northeast of Flamborough Head for the seismic interpretation to the right (from Booth et al., 2017); Right- Geo-seismic section oriented NWN-ESE through the Breagh Field.

About 300m of carbonate and anhydrite were deposited around the margins of the Permian basins during the first Zechstein cycles, allowing most of the basin to remain well below wave base throughout the second Zechstein transgression (Taylor and Colter, 1975; Cameron *et al*., 1992). It was the precipitation of thick second-cycle evaporates in the centre of the basin that brought most of the area close to sea level through the remainder of the Permian, although subsidence continued throughout the offshore area.

In all, more than 1000m of Upper Permian Zechstein group sediment accumulated in the centre of the SNS. Many of the evaporites were remobilized to form diapirs and salt pillows and pierced through the Triassic section into Jurassic and Cretaceous rocks (Fig 12 also see Fig 10); because of this, the thickness of the Upper Permian section varies across the SNS from less than 50m in the zones of extreme salt withdrawal to more than 2500m in some of the major salt diapirs.

2.6 Mesozoic-Cenozoic: Inversion and modification of trapping geometry

2.6.1 Triassic-Jurassic:

The close of the Permian saw the end of widespread marine sedimentation and a return to dominantly non-marine condition. With the withdrawal of the Zechstein seas from the SNS, the already established continental and paralic environments were extended from the periphery of the basin into the centre of the basin.

Meanwhile, the crustal thinning and rifting along the axis of Atlantic and the westward extension of the Tethys associated with early attempts to break up the Pangea throughout the Permian and Triassic established a new structural framework across North-West Europe. This would control deposition throughout the Mesozoic. It generated an E-W extension on a series of N-S trending faults (Fraser and Gawthorpe, 1990), the effect being modification of the Palaeozoic fault zones, several episodes uplift and subsidence; and a switch in principal depocenters (Brennand, 1975; Fisher and Mudge, 2009).

Throughout the Triassic, renewed movement along the Palaeozoic faults resulted in local areas of uplift and erosion, and in the development half graben in and around the British Isles that on three occasions became the sites of halite deposition (Röt, Mulschelkak and Keuper Halite).

During this time period, the Sole Pit Trough became the principal depocenter in the SNS whereas the Cleaver Bank High began to develop as a complementary area though with reduced subsidence (Arthur, 1993; Oudmayer and De Jager, 1993; Stewart and Coward, 1995).

In terms of Configuration, the Triassic of the SNS maintained the same Configuration already established for the SPB during the Permian (Fisher and Mudge, 2009) but for the last Zechstein marine incursion which had drowned the MNSH leaving it as a relatively low topographic feature. Although regional regression accompanied by faulting and uplift rejuvenated this physiographic profile in the SNS but did not significantly modify the basin geometry.

The Triassic was also a time of global sea level rise and combined with extensive halokinesis of the Zechstein evaporates resulting in thin to absent Zechstein deposit within the graben areas (Ormaasen *et al*., 1980; Haq *et al*., 1987; Fisher and Mudge, 2009). The halokinesis and listric extension led to the formation of turtle back structures, salt diapirs and salt wings in some inter-graben areas, the full appreciation which govern depth conversion and accurate mapping at the reservoir level. Examples of these features are shown in the geoseismic sections in Fig. 12.

Another global rise in sea level during the late Triassic to early Jurassic resulted in a widespread marine transgression, the connection of the Arctic seas and Tethyan Ocean over the SPB and the deposition of Liassic age source rocks over the SPB. Mid-Jurassic tectonism led to the uplift of the MNSH and the Central Graben; these broke the connection between the SPB and the Tethyan Ocean. It was soon followed by another major global rise in sea level that deposited the Kimmeridge Clay Formation source rock during the Late Jurassic. In the Central and Viking Graben, this source rock draped over older reservoir sequences that had subsided and rotated and provided seal and source for many oil fields. Throughout this time, the some of the sub-basins in the SNS underwent considerable subsidence; Sole Pit, Broad Fourteens and resulted in the generation of considerable volume of gas from underlying coal measures (Glennie, 1986).

The Mesozoic stratigraphy of Breagh and the surrounding area is comparable to that of the nearby Esmond, Forbes and Gordon fields with a thick Triassic section overlain by attenuated Jurassic and Cretaceous sections (Ketter, 1991).

In the Breagh area, Lower Triassic reddish brown mudstones, anhydrites and sandstones of the Bacton Group conformably overlie the Permian section. There is a complete absence of marine fossils within the Bacton Group which coupled with the lithofacies identified in core indicate that deposition of sediments occurred in a major desert with ephemeral lake deposits.

The desert extended from eastern England to Poland where there was a possible connection with Tethys. The climate was arid, as the SNS area was then within a trade-wind zone in low northern latitudes(Clemmensen, 1985; Clemmensen and Thomsen, 2005). Precipitation was principally in cloudburst which initiated sheet floods that at first drained into large playa lakes (Fisher 1986) The Triassic period had undoubtedly brought about a return to terrestrial system after Permian marine incursion. Up to 700m thick of the Bacton sediments were deposited in the Playa Lake, flood plain and fluvial environment during the early Triassic times.

Shales of the Haisborough Group were deposited during the late Triassic with thin shale and interbedded anhydrite belonging to the Röt Halite Formation at the base. The Triassic formation of the northern England and SNS have only minor thickness and lateral facies variations and record deposition in a pre-rift phase of sedimentation, those changes that do occur are related to local faults movement along the Variscan basement faults which probably triggered the start of diapirism in areas where both salt and over burden were relatively thick.

The conformable Lower Jurassic sediment In the Breagh area, comprise of Lias Group and Middle Jurassic mixed sandstone and shale deposits belonging to the West Sole Group. The Jurassic sediment vary in thickness in the wells and often display prominent wedge-shaped geometries thickening into faults zones indicative of syn-sedimentary extension and which are characterized by slow velocities in the seismic data (Booth *et al*., 2017).

The Jurassic sediments preserved in the offshore area are locally significantly thicker than their equivalents in eastern England. The maximum proven thickness of some 950m compares with 600m in East midlands, 700m in Cleveland basin, more than 2000m in West Netherlands Basin, over 1400m in Central Graben and 3000m in the Viking Graben (Cameron *et al*., 1992).

2.6.2 Jurassic-Cretaceous boundary.

The Jurassic-Cretaceous boundary is quite ambiguous especially in the SNS because most offshore hydrocarbon wells have been drilled on structural highs where Cretaceous sequences are incomplete. This time boundary coincided with a worldwide regression although transgression continued in areas of active subsidence. In the SNS, it was a period of major uplift and erosion in basin flanks- erosion penetrated deeply into the Cleaver bank high and more than 2000m Jurassic and Triassic sediments may have been removed.

Although folding was not involved, the intervals of uplift and erosion were sufficient to result in complex series of unconformities in the basal part of the Cretaceous interval. These are commonly and collectively referred to as the Late-Cimmerian unconformity.

Towards the south of Breagh in wells 42/18-1, 42/18-2, and 42/23-1 sediments belonging to the Upper Jurassic Humber Group are encountered at the sea bed. (Booth *et al*., 2017) postulated that these sediments were likely deposited over the Breagh area but have subsequently been eroded. Jurassic West Sole Group are unconformably overlain by interbedded sandstones and shales followed by clays belonging to the Cromer Knoll Group.

The Cretaceous was a period of continuous global rise in sea level – A decrease in the supply of terrigenous material from shrinking landmasses allowed the deposition of chalk to be established widely on the continental shelf. The Cretaceous Chalk Group occurs gradationally above the Cromer Knoll Group (mudstones). The chalks drapes over older Mesozoic faults indicating a post-rift phase of deposition. No strata younger than the Cretaceous Chalk are encountered in the Breagh area.

2.7 Post Cretaceous tectonism- Inversion.

Rifting associated with opening of the Atlantic Ocean in early Cenozoic caused large scale volcanic activity in the UK. The stretching of the crust as the Atlantic Ocean opened between Scotland and North America causing weaknesses in the surface of the rocks at right angles to the direction of the tension and brought about reorganisation of the stress field in Northwest Europe. The South Permian Basin which had been associated with deposition in local sub-basins under the influence of E-W tension since the Early Triassic, and of erosion from the effects of E-W compression returned to N-S compression and reactivation of the right-lateral movement across the dominant NW-SE faults. This resulted in the inversion of former basinal areas, uplift of Sole Pit (Glennie, 1981; Cooper *et al*., 1989) and Broad Fourteens, West Netherlands Basins (Oele *et al*., 1981) in during the late Cretaceous and earliest Tertiary.

Regional uplift of the onshore UK accompanying the rifting between induced a 1-2^0 easterly tilt on eastern England (Fraser and Gawthorpe, 1990). It also brought an end to carbonate deposition, and gave rise to the outbuilding of clastic, fan deposits eastwards into the Viking and Central grabens to the north of the SNS although the SNS continued to subside during this period (Cameron *et al*., 1992).

Slow closure of the Tethys (Keppie, 2015) which resulted in Alpine Orogeny later on in the in the Palaeogene and Neogene periods (Fig 2.11). Widespread inversion and uplift, in response to Alpine–Atlantic plate-margin events, affected the NW European and SNS–MNSH area in the Early Cenozoic(Van Hoorn, 1987; Ziegler, 1990; Underhill, 2003; Pharaoh *et al*., 2010; Grant *et al*., 2020) and led to partial reactivation of older fault systems and further complexity of structural fabrics and styles. Inversion also probably led to re-migration of gas (Hawkes *et al*., 1998) from the older simple tilted fault blocks into the younger structures with Late Cretaceous to Tertiary structural orientations. The Tertiary inversion folds are an important feature the Breagh and of several existing gas fields such as Amethyst, Pickerill, Waveney and indeed many other fields in the SNS(Kent, 1980; Leeder and Hardman, 1990; Offer, 2020; de Jonge-Anderson and Underhill, 2022). The early phases of inversion were aligned due to generally N-S compression and subsequent pulses were more NNW-SSE in orientation. The pervasive NW–SE structural grain in the SNS and the thick Zechstein evaporites continued to affect structural styles during the inversion, serving to decouple sub- and supra-Zechstein fault systems (Van Hoorn, 1987; de Jager, 2003; Grant *et al*., 2020).

The movement of salt diapirs originating from underlying Permian evaporates probably affected Tertiary sedimentation in the UK sector(Booth *et al*., 2017), where basal contours on the top of the Chalk show a strongly modified topography. This halokinesis is believed to have been most active during the Oligocene, contemporaneous with the main phase of Alpine orogeny (Van Hoorn, 1987).

Regional uplift and easterly tilting also affected Britain during the Paleogene and Neogene, and resulted in a variable Cenozoic–Mesozoic present-day subcrop to the seabed across the

SNS (Gabrielsen *et al*., 2002; Rasmussen *et al*., 2005; Guariguata-Rojas and Underhill, 2017; Brackenridge *et al*., 2020; Grant *et al*., 2020).

2.8 References.

Allen, P. A., and J. E. A. Marshall, 1981, Depositional Environments and Palynology of the Devonian South-east Shetland Basin: Scottish Journal of Geology, v. 17, no. 4, p. 257–273, doi:10.1144/sjg17040257.

Arsenikos, S., M. Quinn, G. Kimbell, P. Williamson, T. Pharaoh, G. Leslie, and A. Monaghan, 2019, Structural development of the Devono-Carboniferous plays of the UK North Sea: Geological Society, London, Special Publications, v. 471, no. 1, p. 65–90.

Arthur, T. J., 1993, Mesozoic structural evolution of the UK Southern North Sea: insights from analysis of fault systems, *in* Geological Society, London, Petroleum Geology Conference Series: The Geological Society of London, p. 1269–1279.

Barnard, P. C., and B. S. Cooper, 1983, A Review of Geochemical Data Related to the Northwest European Gas Province: Geological Society, London, Special Publications, v. 12, no. 1, p. 19–33, doi:10.1144/GSL.SP.1983.012.01.04.

Barrell, J., 1916, Influence of Silurian-Devonian climates on the rise of air-breathing vertebrates: Bulletin of the Geological Society of America, v. 27, no. 1, p. 387–436.

Besly, B. M., 2009, Carboniferous, *in* Petroleum Geology of the North Sea: Wiley-Blackwell, p. 104–136, doi:10.1002/9781444313413.ch4.

Besly, B. M., 1998, Carboniferous: Petroleum geology of the North Sea: basic concepts and recent advances, p. 104–136.

Besly, B., 2019, Exploration and development in the Carboniferous of the Southern North Sea: a 30-year retrospective: Geological Society, London, Special Publications, v. 471, no. 1, p. 17–64, doi:10.1144/SP471.10.

Besly, B. M., S. D. Burley, and P. Turner, 1993, The late Carboniferous 'Barren Red Bed' play of the Silver Pit area, Southern North Sea: Geological Society, London, Petroleum Geology Conference series, v. 4, no. 1, p. 727–740, doi:10.1144/0040727.

Booth, M. G., J. R. Underhill, A. Gardiner, and D. McLean, 2020, Sedimentary and tectonic controls on Lower Carboniferous (Visean) mixed carbonate–siliciclastic deposition in NE England and the Southern North Sea: implications for reservoir architecture: Petroleum Geoscience, v. 26, no. 2, p. 204–231.

Booth, M., J. R. Underhill, R. J. Jamieson, and R. Brackenridge, 2017, Controls on Lower Carboniferous (Dinantian) Prospectivity in the Mid North Sea High Region: AAPG/SEG International Conference and Exhibition, London, p. 8.

Brackenridge, R. E., J. R. Underhill, R. Jamieson, and A. Bell, 2020, Structural and stratigraphic evolution of the Mid North Sea High region of the UK Continental Shelf: Petroleum Geoscience, v. 26, no. 2, p. 154–173.

Brennand, T. P., 1975, THE TRIASSIC OF THE NORTH SEA.

Buggisch, W., A. S. Alekseev, V. I. Davydov, and M. M. Joachimski, 2003, Stable oxygen and carbon isotopes-the problem od late Carboniferous and early Permian data, *in* EGS-AGU-EUG Joint Assembly.

Cameron, T. D. J., A. Crosby, P. S. Balson, H. J. Jeffery, G. K. Lott, J. Bulat, and D. Harrison J., 1992, Geology of the Southern North Sea Basin, British Geological Survey: London, ASCE, United Kingdom Offshore Official report, 14–26 p.

Cameron, D., J. Munns, and S. J. Stoker, 2005, Remaining hydrocarbon exploration potential of the Carboniferous fairway, UK southern North Sea, *in* J. D. Collinson, D. J. Evans, D. W. Holliday, and N. S. Jones, eds., Carboniferous hydrocarbon geology : the southern North Sea and surrounding onshore areas: Yorkshire Geological Society, p. 209–224.

Chadwick, R. A., and D. W. Holliday, 1991, Deep crustal structure and Carboniferous basin development within the Iapetus convergence zone, northern England: Journal of the Geological Society, v. 148, no. 1, p. 41–53.

Chadwick, R. A., D. W. Holliday, S. T. Holloway, and A. G. Hulbert, 1993, The evolution and hydrocarbon potential of the Northumberland–Solway Basin, *in* Geological Society, London, Petroleum Geology Conference series: Geological Society of London, p. 717–726.

Clark, J. A., S. A. Stewart, and J. A. Cartwright, 1998, Evolution of the NW margin of the North Permian Basin, UK North Sea: Journal of the Geological Society, v. 155, no. 4, p. 663–676, doi:10.1144/gsjgs.155.4.0663.

Clemmensen, L. B., 1985, Desert sand plain and sabkha deposits from the Bunter Sandstone Formation (L. Triassic) at the northern margin of the German Basin: Geologische Rundschau, v. 74, no. 3, p. 519–536.

Clemmensen, A., and E. Thomsen, 2005, Palaeoenvironmental changes across the Danian–Selandian boundary in the North Sea Basin: Palaeogeography, palaeoclimatology, palaeoecology, v. 219, no. 3–4, p. 351–394.

Collinson, J. D., B. M. Besly, and G. Kelling, 1988, Controls on Namurian sedimentation in the Central Province basins of northern England: Sedimentation in a synorogenic basin complex: the Upper Carboniferous of Northwest Europe. Blackie, Glasgow, v. 85, p. 101.

Collinson, John David, D. J. Evans, D. W. Holliday, and N. S. Jones, 2005, Carboniferous hydrocarbon geology: the southern North Sea and surrounding onshore areas.

Collinson, John D., D. J. Evans, D. W. Holliday, and N. S. Jones, 2005, Dinantian and Namurian depositional systems in the southern North Sea: Yorkshire Geological Society Occasional Publication, v. 7, p. 35–56.

Collinson, J., C. Jones, G. Blackbourn, B. Besly, G. Archard, and A. McMahon, 1993, Carboniferous depositional systems of the southern North Sea: Geological Society of London, p. 677–687.

Cooper, M. A., G. D. Williams, P. C. De Graciansky, R. W. Murphy, T. Needham, D. De Paor, R. Stoneley, S. P. Todd, J. P. Turner, and P. A. Ziegler, 1989, Inversion tectonics—a discussion: Geological Society, London, Special Publications, v. 44, no. 1, p. 335–347.

Corfield, S. M., R. L. Gawthorpe, M. Gage, A. J. Fraser, and B. M. Besly, 1996, Inversion tectonics of the Variscan foreland of the British Isles: Journal of the Geological Society, v. 153, no. 1, p. 17–32, doi:10.1144/gsjgs.153.1.0017.

Craig, J., J. Gluyas, C. Laing, and P. Schofield, 2013, Hardstoft–Britain's first oil field.

Davies, S., G. Hampson, S. Flint, and T. Elliott, 1999, Continental-scale sequence stratigraphy of the Namurian, Upper Carboniferous and its applications to reservoir prediction, *in* Geological Society, London, Petroleum Geology Conference series: Geological Society of London, p. 757–770.

Elliott, T., 1975, The sedimentary history of a delta lobe from a Yoredale (Carboniferous) cyclothem: Geological Society of London, p. 505–536.

Fisher, M. J., and D. C. Mudge, 2009, Triassic, *in* Petroleum Geology of the North Sea- Basic concept and recent advances: doi:10.1002/9781444313413.ch7.

Fraser, A. J., and R. L. Gawthorpe, 1990, Tectono-stratigraphic development and hydrocarbon habitat of the Carboniferous in northern England: Geological Society, London, Special Publications, v. 55, no. 1, p. 49–86.

Frost, R. T. C., F. RTC, F. FJ, and M. JA, 1981, The age and nature of the crystalline basement of the North Sea Basin.

Gabrielsen, R., H. Jordt, and S. Fanavoll, 2002, Tectonic impact on sedimentary processes during Cenozoic evolution of the northern North Sea and surrounding areas: Exhumation of the North Atlantic Margin: Timing, mechanisms and implications for petroleum exploration, no. 196, p. 235.

Gibbs, A. D., 1986, Strike-slip basins and inversion: a possible model for the southern North Sea gas areas: Geological Society, London, Special Publications, v. 23, no. 1, p. 23–35.

Glennie, K. W., 1986, Development of NW Europe's Southern Permian gas basin: Geological Society, London, Special Publications, v. 23, no. 1, p. 3–22.

Glennie, K. W., 1998, Lower Permian- Rotliegend, *in* Petroleum Geology of the North Sea- Basic concept and recent advances: p. 137–211.

Glennie, K., 2005, Regional tectonics in relation to Permo-Carboniferous hydrocarbon potential, Southern North Sea Basin: Carboniferous hydrocarbon resources: the southern North Sea and surrounding areas. Occasional Special Publication of the Yorkshire Geological Society, v. 7, p. 1–12.

Glennie, K. W., 1981, Sole Pit inversion tectonics: Petroleum geology of the continental shelf of northwest Europe, p. 110–120.

Glennie, K. W., J. D. Collinson, D. J. Evans, D. W. Holliday, and N. S. Jones, 2005, Regional tectonics in relation to Permo-Carboniferous hydrocarbon potential, Southern North Sea Basin: Carboniferous Hydrocarbon Geology: The Southern North Sea and Surrounding Onshore Areas. Yorkshire Geological Society, Occasional Publications, v. 7, p. 1–12.

Glennie, K. W., and J. R. Underhill, 1998, Origin, development and evolution of structural styles: Petroleum geology of the North Sea: Basic concepts and recent advances, p. 42–84.

Grant, R. J., M. G. Booth, J. R. Underhill, and A. Bell, 2020, Structural evolution of the Breagh area: implications for carboniferous prospectivity of the Mid North Sea High, Southern North Sea: Petroleum Geoscience, v. 26, no. 2, p. 174–203.

Guariguata-Rojas, G. J., and J. R. Underhill, 2017, Implications of Early Cenozoic uplift and fault reactivation for carbon storage in the Moray Firth Basin: Interpretation, v. 5, no. 4, p. SS1–SS21.

Guion, P. D., and C. R. Fielding, 1988, Westphalian A and B sedimentation in the Pennine Basin, UK. 153-177 in Sedimentation in a synorogenic basin complex: the Upper Carboniferous of north-west Europe: BESLY, BM, and KE1l. lN (l, G (editors).(Glasgow and London: Blackie.).

Hallsworth, C. R., and J. I. Chisholm, 2000, Stratigraphic evolution of provenance characteristics in Westphalian sandstones of the Yorkshire Coalfield: Proceedings of the Yorkshire Geological Society, v. 53, no. 1, p. 43–72.

Haq, B. U., J. A. N. Hardenbol, and P. R. Vail, 1987, Chronology of fluctuating sea levels since the Triassic: Science, v. 235, no. 4793, p. 1156–1167.

Hawkes, P. W., A. J. Fraser, and C. C. G. Einchcomb, 1998, The tectono-stratigraphic development and exploration history of the Weald and Wessex basins, Southern England, UK: Geological Society, London, Special Publications, v. 133, no. 1, p. 39–65.

Heeremans, M., and J. I. Faleide, 2004, Late Carboniferous-Permian tectonics and magmatic activity in the Skagerrak, Kattegat and the North Sea: Geological Society, London, Special Publications, v. 223, no. 1, p. 157–176, doi:10.1144/GSL.SP.2004.223.01.07.

Hollywood, J. M., and C. V. Whorlow, 1993, Structural development and hydrocarbon occurrence of the Carboniferous in the UK Southern North Sea Basin: Geological Society, London, Petroleum Geology Conference series, v. 4, no. 1, p. 689–696, doi:10.1144/0040689.

de Jager, J., 2003, Inverted basins in the Netherlands, similarities and differences: Netherlands Journal of Geosciences - Geologie en Mijnbouw, v. 82, no. 4, p. 339–349, doi:10.1017/S0016774600020175.

Johnson, G. A. L., 1984, Subsidence and sedimentation in the Northumberland Trough: Proceedings of the Yorkshire Geological Society, v. 45, no. 1–2, p. 71–83.

Jones, T. R., and J. W. Kirkby, 1886, Notes on the distribution of the Ostracoda of the Carboniferous formations of the British Isles: Quarterly Journal of the Geological Society, v. 42, no. 1–4, p. 496–514.

de Jonge-Anderson, I., and J. R. Underhill, 2022, Use of Subsurface Geology in Assessing the Optimal Co-Location of CO2 Storage and Wind Energy Sites: Earth Science, Systems and Society, v. 2, p. 10055.

Kent, P. E., 1980, Subsidence and uplift in East Yorkshire and Lincolnshire: a double inversion: Proceedings of the Yorkshire Geological Society, v. 42, no. 4, p. 505–524.

Keppie, D. F., 2015, How the closure of paleo-Tethys and Tethys oceans controlled the early breakup of Pangaea: Geology, v. 43, no. 4, p. 335–338, doi:10.1130/G36268.1.

Ketter, F. J., 1991, The Esmond, Forbes and Gordon Fields, Blocks 43/8a, 43/13a, 43/15a, 43/20a, UK North Sea: Geological Society, London, Memoirs, v. 14, no. 1, p. 425–432, doi:10.1144/GSL.MEM.1991.014.01.53.

Kimbell, G. S., and J. P. Williamson, 2015, A gravity interpretation of the Central North Sea.

Leeder, M. R., 1988, Recent developments in Carboniferous geology: a critical review with implications for the British Isles and NW Europe: Proceedings of the Geologists' Association, v. 99, no. 2, p. 73–100.

Leeder, M. R., and M. Hardman, 1990, Carboniferous geology of the Southern North Sea Basin and controls on hydrocarbon prospectivity: Geological Society, London, Special Publications, v. 55, no. 1, p. 87–105.

Leveridge, B. E., and A. J. Hartley, 2006, The Variscan Orogeny: the development and deformation of Devonian/ Carboniferous basins in SW England and South Wales, *in* P. J. Brenchley, and P. F. Rawson, eds., The Geology of England and Wales: The Geological Society of London, p. 225–255, doi:10.1144/GOEWP.10.

Marshall, J. E. A., T. R. Astin, J. F. Brown, E. Mark-Kurik, and J. Lazauskiene, 2007, Recognizing the Kačák Event in the Devonian terrestrial environment and its implications for understanding land–sea interactions: Geological Society, London, Special Publications, v. 278, no. 1, p. 133–155, doi:10.1144/SP278.6.

Marshall, J. E. A., and A. J. Hewett, 2003, Devonian: Geological Society of London.

Maynard, J. R., and R. E. Dunay, 1999, Reservoirs of the Dinantian (Lower Carboniferous) play of the southern North Sea, *in* Geological Society, London, Petroleum Geology Conference series: Geological Society of London, p. 729–745.

McCann, T. *et al.*, 2008, Carboniferous, *in* The Geology of Central Europe: Precambrain and Palaeozoic: p. 411–530.

McLean, D., 1993, A palynostratigraphic classification of the Westphalian of the Southern North Sea Carboniferous Basin, PhD: University of Sheffield, 303 p.

Mendum, J. R., 2012, Late Caledonian (Scandian) and Proto-Variscan (Acadian) orogenic events in Scotland: Journal of the Open University Geological Society, v. 33, no. 1, p. 37–51.

Milton-Worssell, R., K. Smith, A. Mcgrandle, J. Watson, and D. Cameron, 2010, The search for a Carboniferous petroleum system beneath the Central North Sea, *in* Petroleum Geology: From Mature Basins to New Frontiers—Proceedings of the 7th Petroleum Geology Conference: Geological Society of London, p. 57–75, doi:10.1144/0070057.

Monaghan, A. A. *et al*., 2017, Carboniferous petroleum systems around the Mid North Sea High, UK: Marine and Petroleum Geology, v. 88, p. 282–302, doi:10.1016/j.marpetgeo.2017.08.019.

Monaghan, A. A., S. Arsenikos, E. Callaghan, R. Ellen, C. Gent, S. Hannis, A. Henderson, G. Leslie, K. Johnson, and M. Kassyk, 2015, Palaeozoic Petroleum Systems of the Central North Sea/Mid North Sea High.

Moore, D., 1959, Role of Deltas in the Formation of Some British Lower Carboniferous Cyclothems: The Journal of Geology, v. 67, no. 5, p. 522–539.

Nesbit, R., and K. Overshott, 2010, Overcoming multiple uncertainties in a challenging gas development: Chiswick Field UK SNS, *in* Geological Society, London, Petroleum Geology Conference series: Geological Society of London, p. 315–323.

Oele, J. A., H. Acpj, and J. Tiemens, 1981, Some Rotliegend gas Feilds of the K and L Blocks, Netherlands offshore (1968-1978) A case history.

Offer, D. J., 2020, The Juliet Field, Block 47/14b, UK North Sea: Geological Society, London, Memoirs, v. 52, no. 1, p. 217–225.

Ormaasen, O. E., G. P. Hamar, K. H. Jakobsson, and O. Skarpnes, 1980, Permo-Triassic correlations in the North Sea area north of the Central Highs: The sedimentation of the North Sea. Norsk Petroleums Forening, p. 1–15.

Oudmayer, B. C., and J. De Jager, 1993, Fault reactivation and oblique-slip in the Southern North Sea, *in* Geological Society, London, Petroleum Geology Conference Series: The Geological Society of London, p. 1281–1290.

Pegrum, R. M., 1984, The extension of the Tornquist Zone in the Norwegian North Sea: Geologiska Föreningen i Stockholm Förhandlingar, v. 106, no. 4, p. 394–395, doi:10.1080/11035898509454679.

Pharaoh, T. C., 1999, Palaeozoic terranes and their lithospheric boundaries within the Trans-European Suture Zone (TESZ): a review: Tectonophysics, v. 314, no. 1–3, p. 17–41.

Pharaoh, T. C., M. Dusar, M. Geluk, F. Kockel, C. M. Krawczyk, P. Krzywiec, M. Scheck-Wenderoth, H. Thybo, O. Vejbaek, and J.-D. Van Wees, 2010, Tectonic evolution, *in* Petroleum geological atlas of the Southern Permian Basin area: EAGE, p. 25–57.

Pharaoh, T. C., R. J. Merriman, P. C. Webb, and R. D. Beckinsale, 1987, The concealed Caledonides of eastern England: preliminary results of a multidisciplinary study: Proceedings of the Yorkshire Geological Society, v. 46, no. 4, p. 355–369, doi:10.1144/pygs.46.4.355.

Pharaoh, T. C., J. A. Winchester, J. Verniers, A. Lassen, and A. Seghedi, 2006, The western accretionary margin of the East European Craton: an overview: MEMOIRS-GEOLOGICAL SOCIETY OF LONDON, v. 32, p. 291.

Raji, M., C. Cornford, A. Pather, and D. Satterfield, 2013, Unconventional Oil and Gas Potential of the Widmerpool Gulf in the East Midlands Province of England, *in* Unconventional Resources Technology Conference, Denver, Colorado, 12-14 August 2013: Society of Exploration Geophysicists, American Association of Petroleum Geologists, Society of Petroleum Engineers, SEG Global Meeting Abstracts, p. 949–961, doi:10.1190/urtec2013-097.

Rasmussen, E. S., O. V. Vejbæk, T. Bidstrup, S. Piasecki, and K. Dybkjær, 2005, Late Cenozoic depositional history of the Danish North Sea Basin: implications for the petroleum systems in the Kraka, Halfdan, Siri and Nini fields, *in* Geological Society, London, Petroleum Geology Conference Series: The Geological Society of London, p. 1347–1358.

Retallack, G. J., 1988, Field recognition of paleosols: Geological Society of America Special Paper, v. 216, p. 1–20.

Retallack, G. J., 2014, Paleosols☆, *in* Reference Module in Earth Systems and Environmental Sciences: Elsevier, doi:10.1016/B978-0-12-409548-9.09099-0.

Richmond, L. K., and B. P. Williams, 2000, A new terrane in the Old Red Sandstone of the Dingle Peninsula, SW Ireland: Geological Society, London, Special Publications, v. 180, no. 1, p. 147–183.

Ritchie, J. S., and P. Pratsides, 1993, The Caister Fields, Block 44/23a, UK North Sea: Geological Society, London, Petroleum Geology Conference series, v. 4, no. 1, p. 759–769, doi:10.1144/0040759.

Rodriguez, K., R. Wrigley, N. Hodgson, and H. Nicholls, 2014, Southern North Sea: unexplored multi-level exploration potential revealed: First Break, v. 32, no. 6, p. 107–113.

Smith, D. B., 1989, The late Permian palaeogeography of north-east England: Proceedings of the Yorkshire Geological Society, v. 47, no. 4, p. 285–312, doi:10.1144/pygs.47.4.285.

Steele, R. P., 1988, The Namurian sedimentary history of the Gainsborough Trough: Sedimentation in a synorogenic basin complex: the Upper Carboniferous of Northwest Europe. Blackie, Glasgow & London, v. 102, p. 113.

Stephenson, M. H., D. Millward, M. J. Leng, and C. H. Vane, 2008, Palaeoecological and possible evolutionary effects of early Namurian (Serpukhovian, Carboniferous) glacioeustatic cyclicity: Journal of the Geological Society, v. 165, no. 6, p. 993–1005, doi:10.1144/0016-76492007-153.

Stewart, S. A., and M. P. Coward, 1995, Synthesis of salt tectonics in the southern North Sea, UK: Marine and Petroleum Geology, v. 12, no. 5, p. 457–475.

Symonds, R., R. Lippmann, B. Mueller, and A. Kohok, 2015, Yoredale sandstone Architecture in Breagh Field (UK SNS). Presentation for Sedimentology of Paralic Reservoirs: Recent advances and their applications.: p. 24.

Taylor, J. C. M., and V. S. Colter, 1975, Zechstein of the English sector of the southern North Sea Basin: Petroleum and the continental shelf of north-west Europe, v. 1, p. 249–263.

Tucker, M., J. Gallagher, K. Lemon, and M. Leng, 2003, The Yoredale cycles of Northumbria: High-frequency clastic-carbonate sequences of the Mid-Carboniferous icehouse world: Northumbria Rocks, v. 18, no. 26, p. 5–10.

Underhill, J. R., 2003, The tectonic and stratigraphic framework of the United Kingdom's oil and gas fields: Geological Society, London, Memoirs, v. 20, no. 1, p. 17–59, doi:10.1144/GSL.MEM.2003.020.01.04.

Underhill, J. R., and K. L. Hunter, 2008, Effect of Zechstein Supergroup (Z1 cycle) Werrahalit pods on prospectivity in the southern North Sea: AAPG Bulletin, v. 92, no. 7, p. 827–851, doi:10.1306/02270807064.

Van Hoorn, B., 1987, Structural evolution, timing and tectonic style of the Sole Pit inversion: Tectonophysics, v. 137, no. 1, p. 239–284, doi:10.1016/0040-1951(87)90322-2.

Van Wees, J. D., and F. Beekman, 2000, Lithosphere rheology during intraplate basin extension and inversion: Inferences from automated modeling of four basins in western Europe: Tectonophysics, v. 320, no. 3, p. 219–242, doi:10.1016/S0040-1951(00)00039-1.

Vincent, C. J., 2015, Maturity modelling of selected wels in the Central North sea, Energy and Marine Geoscience Programme Commissioned Report CR/15/122: British Geological Survery, Nottingham.

Waters, C. N., and S. J. Davies, 2006, Carboniferous: extensional basins, advancing deltas and coal swamps: In: The geology of England and Wales/edited by PJ Brenchley and PF Rawson. London: Geological Society of London, v. 2006, p. 173–223.

Ziegler, P. A., 1981, Evolution of sedimentary basins in North-West Europe: Petroleum geology of the continental shelf of north-west Europe, v. 2, p. 3–39.

Ziegler, P. A., 1990, Geological Atlas of Western and Central Europe. 2nd and completely revised edition: Shell Internationale Petroleum Maatschappij BV, Den Haag.

Ziegler, P. A., 1982, Geological Atlas of Western and Central Europe■ Elsevier: Amsterdam.

Ziegler, P. A., 1987, Late Cretaceous and Cenozoic intra-plate compressional deformations in the Alpine foreland—a geodynamic model: Tectonophysics, v. 137, no. 1, p. 389–420, doi:10.1016/0040-1951(87)90330-1.

Ziegler, P. A., M. E. Schumacher, P. Dèzes, J.-D. V. Wees, and S. Cloetingh, 2004, Post-Variscan evolution of the lithosphere in the Rhine Graben area: constraints from subsidence modelling: Geological Society, London, Special Publications, v. 223, no. 1, p. 289–317, doi:10.1144/GSL.SP.2004.223.01.13.

Blank Page

Chapter 3

The Breagh Field, Blocks 42/12a, 42/13a and 42/8a, UK North Sea.

Table of Contents

Chapter 3: The Breagh Field, Blocks 42/12a, 42/13a and 42/8a, UK North Sea.

This chapter has been published as part of the United Kingdom Oil and Gas Fields: 50th Anniversary Commemorative Volume. Geological Society, London, Memoirs. Volume 52. Pages 109 – 118. https://doi.org/10.1144/M52-2019-15

3.1 Introduction.

Historically, exploration for petroleum in Early Carboniferous reservoirs had been very limited in the UK offshore. In contrast, hundreds of wells have targeted Permian Rotliegend Group sandstones, Triassic Bunter sandstones and Late Carboniferous sandstones (Glennie and Provan, 1990; Ketter, 1991; Besly *et al*., 1993; Rodriguez *et al*., 2014) (Fig. 3.1). However, in the past couple of decades discoveries in Carboniferous age reservoirs, such as Pegasus in 43/13b, Crosgan in 42/ 10b and 42/15a in addition to the large fields, Breagh and Cygnus, have now upgraded the potential of the Quadrant 42/43 area.

The Breagh Field (Fig. 3. 2) contains a low permeability sandstone reservoir. The field lies approximately 40 miles (64 km) west of the decommissioned Esmond Field (Block 43/13a), 32 miles (51 km) NW of the Garrow Field (Block 42/25a and 43/21a), 38 miles (61 km) NE of Flamborough Head on the Yorkshire coast and 53 miles (85 km) WNW of the INEOS Oil and Gas UK-operated Cavendish Field (Block 43/19a). It lies within Quadrant 42 of the UK Southern North Sea (SNS), immediately to the north of the Sole Pit Basin. It is very close to the southern edge of the Mid North Sea High (Glennie, 1986). It is the also most westerly of the fields with Carboniferous age reservoir in the SNS and NE of the pinchout of the Lower Permian Rotliegend Group sandstones (Fig. 3. 1).

The field has an area of 94 km^2 below a four-way dip closure at the Base Permian Unconformity (BPU) (Fig. 3.3). The field has gas initially in place (GIIP) of approximately 1 tcf in the Early Carboniferous (Mississippian) Yoredale Formation, also known as the Middle Limestone Formation of the Yoredale Group onshore UK (Mclean, 2011).

3.2 History of exploration and appraisal.

The first well on the Block, 42/13-1, was drilled in 1968 by a BP/Phillips/Amax joint venture on the eastern edge of the then BP concession (Fig. 3.2). The well penetrated an elevated structure identified on a two-way-time map at the BPU. The objective was to drill to the

Carboniferous interval as well as to evaluate the Triassic Bunter Sandstone Formation and Permian Rotliegend Group sandstone reservoirs.

However, Bunter and Rotliegend strata were absent and the Namurian (lowermost Upper Carboniferous) section was largely shale (thickness of 330 ft). Consequently, the well was terminated in Lower Carboniferous Limestone at 8243 ft TVDSS (true vertical depth subsea). It was plugged and abandoned as a dry hole on 30 August 1968 and the block was then relinquished.

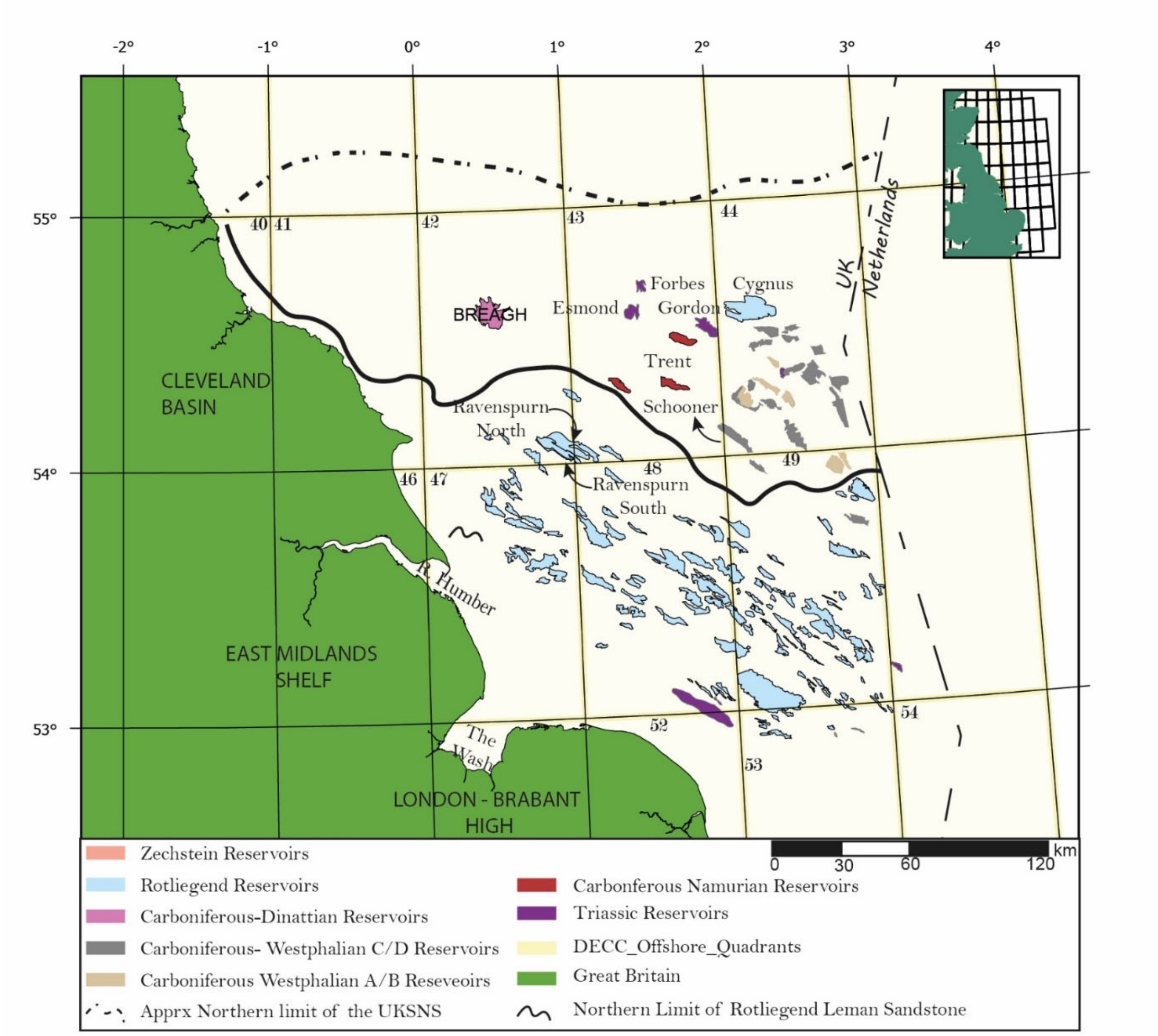

Figure 3.1: Location map for the Breagh

Some 29 years later in 1994, Mobil acquired 3D seismic data over Block 42/13a and subsequently drilled and cored well 42/13-2 in 1997; a gas discovery that was eventually to become the Breagh Field (named in 2007). The prospect drilled by well 42/13-2 was a large base Zechstein closure and part of a deliberate test of the Yoredale Formation as a potential reservoir interval (Maynard *et al*., 1997; Maynard and Dunay, 1999). It proved a gas column of at least 400 ft containing approximately 66 ft of net pay (McPhee *et al*. 2008). The well found five gas-bearing sandstones in the Yoredale Formation (Middle Limestone Formation) between 7410 and 7800 ft TVDSS, but all tested at low rates of 3–4 MMscfgd. The discovery was not thought to be commercial and again the block was relinquished (21 August 1997). Sterling Resources (UK) ('Sterling') was the next company to operate the block. The company acquired a Promote Licence in 2005 based upon the work of the late Frank Barker who had re-evaluated the Carboniferous gas-bearing interval in 43/13-2, and the likely reservoir continuity based upon reservoir analogues exposed on the Northumberland coast (Jones, 2007). Sterling Resources (operator, 45%) in turn farmed out equity to joint venture partners (Encore, 15%; Regenesys, 15%; Stratic, 10%; and Petroventures, 5%) in the second year period of the Promote Licence.

Following the evaluation of well 42/13-2, the new operator considered that the low-rate well-test had been caused by reservoir damage prior to testing, but the field contained considerable upside potential (McPhee *et al*., 2008). An integrated study of the subsurface data followed, and the new operator decided to drill well 42/13-3 using oil-based mud to prevent water-related formation damage. Well 42/13-3 is of critical importance as it was a license obligation well with a primary objective to prove the commercial viability of the Breagh discovery by drilling and testing the Early Carboniferous section.

Well 42/13-3 was spudded in September 2007, 1 mile NE of the 42/13-2 discovery well. It successfully tested two gasbearing sandstone intervals in the lower part of the Carboniferous section, establishing a combined flow rate of 17.6MMscfgd. Such a rate was considered sufficient for a commercially viable development of the field. The well also proved the presence and continuity of sandstones between 42/13-2 and 42/13-3 and so gave rise to a potential framework for a broader correlation of the Carboniferous strata over the Breagh area. Following this success, a vertical appraisal well, 42/13-4, was spudded 2.5 miles (4 km) SE in 2008. It successfully tested gas-bearing sandstone within the same Early Carboniferous reservoir interval at 7531 ft TVDSS, a similar depth to the earlier two wells and flowed gas at

1.6 (lower interval only) and 10.2 MMscfgd (upper and lower interval). The well was drilled to a terminal depth within the Scremerston Formation at 8140 ft TVDSS.

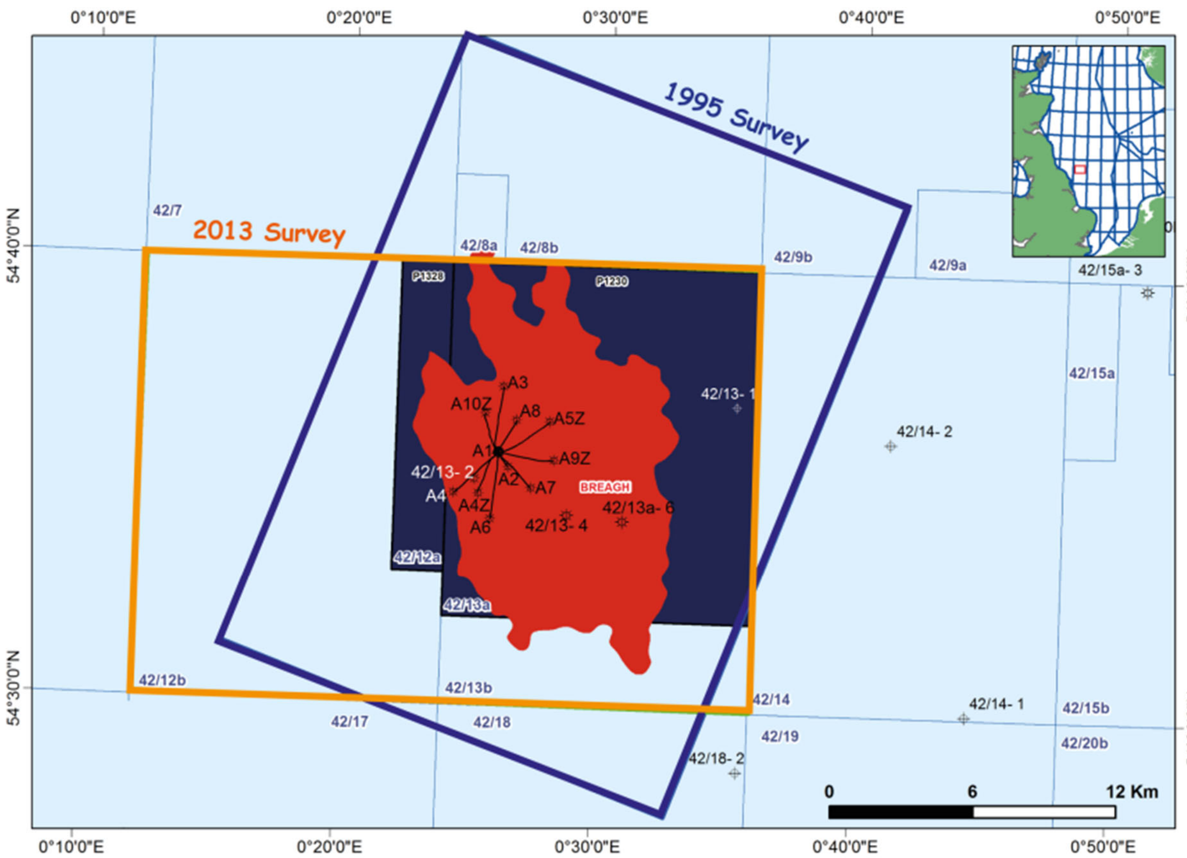

Figure 3.2: Map of the Breagh Field (solid red) and licence area (solid dark blue) indicating the extent of the Geco-Prakla 1995 seismic survey (blue) and the 2013 Polarcus seismic.

Appraisal well 42/13-5 was drilled ahead of field development. The well had a 68.9° inclination and was drilled from the same surface location as 42/13-3 as a pilot hole for a horizontal side-track well 42/13-5Z. It penetrated the same Lower Carboniferous gas-bearing sandstones tested previously. Well 42/13-5Z was completed with a 2500 ft reservoir section and tested gas at rates of up to 26 MMscfgd. Despite the difficulty of maintaining the wellbore in the reservoir, due to the occurrence of small faults along the well track, the flow rate achieved gave confidence that development of Breagh would be commercially viable. Sterling thus drew up a development plan involving an unmanned platform and tieback to Teesside and then marketed the field. RWE Dea acquired a 70% interest from Sterling and the other non-operating partners and took operatorship in 2009. Sterling was the remaining partner with 30%. The field development plan (FDP) was submitted in 2010. By 2011, a downdip appraisal well 42/13a–6 was drilled and cored to appraise the eastern side of the field. It found two gas-bearing sandstones appearing similar in thickness to those seen in the western part of the field. This well terminated at a depth of 8622 ft TVDSS.

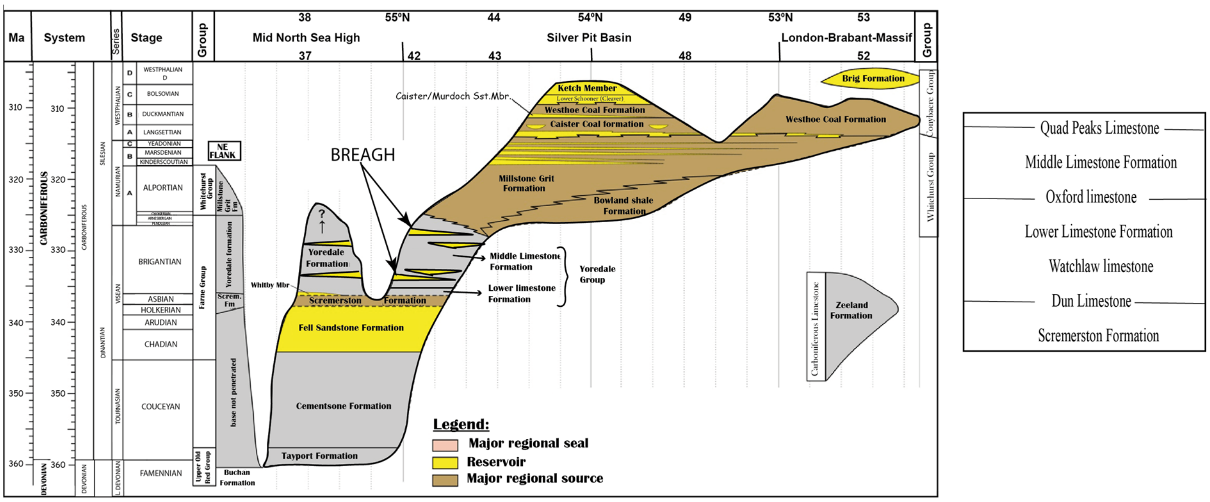

Figure 3.3: Lower Carboniferous stratigraphy with Breagh zonation (modified from (Cameron 1993) and onshore stratigraphic terminology of the Yoredale Group, as utilized in the Breagh Field area, including the key limestone markers.

3.3 Development.

Following the discovery of the field in 1997 it was thought that developing the field was not economically or commercially viable and the licence was subsequently relinquished. The entry of Sterling in 2005 and further studies led to the drilling of the four appraisal wells discussed above and a decision to develop the field in 2010/11. A phased development was chosen for the Breagh Field as uncertainties presented themselves due to the complex overburden and its effect on the depth conversion. These, in turn, had implications for the way in which the structure was mapped as well as the identification of field closure and subcrop patterns. The FDP specified two phases, an initial phase of ten wells (Fig. 3.2) followed by a provision for a possible second phase of development.

In spring 2012 development wells A1 and A2 were drilled at an inclination of 45° as side-tracks of appraisal well 42/13-3 (42/13-3z and 42/13-5y, respectively). Subsequently, in the summers of 2012–14 wells A3, A4, A5z and A6 were drilled at an inclination of 65° and conventionally completed, all of which produced at a combined rate of approximately 100 MMscfgd for the first year. The decision to drill at this angle was in part to increase the flow rates compared to the vertical appraisal wells, as the greater along-hole section through the sandstones was anticipated to increase productivity. The sandstones were, however, of lower permeability than originally expected. From operator experience and success on the Clipper South Field, it was thought that hydraulically fracturing the wells would increase flow rates in the lower permeability sandstones. Fracture stimulation was implemented after drilling A7 as the rig had a period of maintenance allowing the operator to plan for fracturing wells A7 and A8 (drilled in 2013–14).

The stimulation programme was as follows: (1) diagnostic fracture injection test to assess the formation properties; (2) breakdown and stepdown test to analyse formation strength and what pressures and injection rates would be required; (3) 'minifrac' to test the hydraulic fracture design; and (4) main fracture. However, hydraulically fractured wells were not planned when the Breagh Alpha platform (minimum facilities normally unattended installation) was installed so no solids production could be handled. Therefore, following clean-up where special precautions were taken to protect the hydraulic fractures, ceramic sand screens were installed downhole. Although the stimulation programme posed challenges, the fractured wells performed strongly, contributing approximately 45% of the average daily production. At this point, the use of hydraulic stimulation was considered a viable option for developing the field (Jones *et al*. 2015).

In 2017–18, following the acquisition and interpretation of the new 2013 3D seismic data, wells A9z, A10z and A4z were drilled and hydraulically fractured. The wells were drilled as 'S-shaped' wells penetrating the reservoir at near vertical to maximize the efficiency for hydraulic stimulation.

3.4 Regional context.

(Underhill, 2003) documented how changes in Caledonian and Variscan orogenic regimes, climate, eustasy and sediment supply combined to influence the tectonic structure and reservoir sedimentology of the sandstones that now hostthe gas fields in the SNS and the rest of the UK Continental Shelf (UKCS). In addition, several other authors have also described the complex geological evolution of the SNS area(Glennie, 1986, 2005; Fraser and Gawthorpe, 1990; Leeder and Hardman, 1990; Collinson *et al*., 1993; McLean, 1993; Underhill, 2003; Nesbit and

Overshott, 2010). This section will only focus on key events specific to the Breagh Field within the framework of the SNS.

Devonian and Early Carboniferous rocks within the SNS occur in a large ESE-plunging anticline termed the Southern North Sea Carboniferous Basin (SNSCB) (Leeder and Hardman, 1990; Glennie, 2005). The SNSCB, along with the onshore East Midlands area of England and the Netherland basins, forms a single post-Paleozoic syn-rift megasequence termed the Variscan Cycle (Underhill, 2003) and characterized by major strike-slip zones such as the Sole Pit and Market-Weighton axis in the UK (Fraser and Gawthorpe, 1990; Underhill, 2003). The SNS inherited the strong NW–SE structural trends from the Paleozoic Caledonian Orogeny (Pharaoh *et al*., 1987), which strongly influenced the pattern of sediment deposition during the Carboniferous.

Carboniferous sedimentation within the SNS changed progressively from mixed marine and paralic sedimentation with limestones, sandstones and shales deposited in the Early Carboniferous (Yoredale Formation), to pro-delta and delta front sedimentation in the earliest Late Carboniferous (Besly, 1998). These sedimentary rocks are, in turn, overlain by delta top sediments during the Westphalian (A and B) and ultimately continental fluvial and alluvial deposits of the Westphalian (C and D); (Besly *et al*., 1993) (Fig. 3.3).

The Carboniferous period closed with the Variscan Orogeny, caused by the formation of Pangaea(Cameron *et al*., 1992; McCann *et al*., 2008). Subsequent Permian-age sedimentation in the SNS began with Rotliegend Group continental sandstones (aeolian, fluvial and sabkha) and their basinal temporal-equivalent lacustrine mudstones belonging to the Leman Sandstone Formation and Silverpit Formation, respectively.

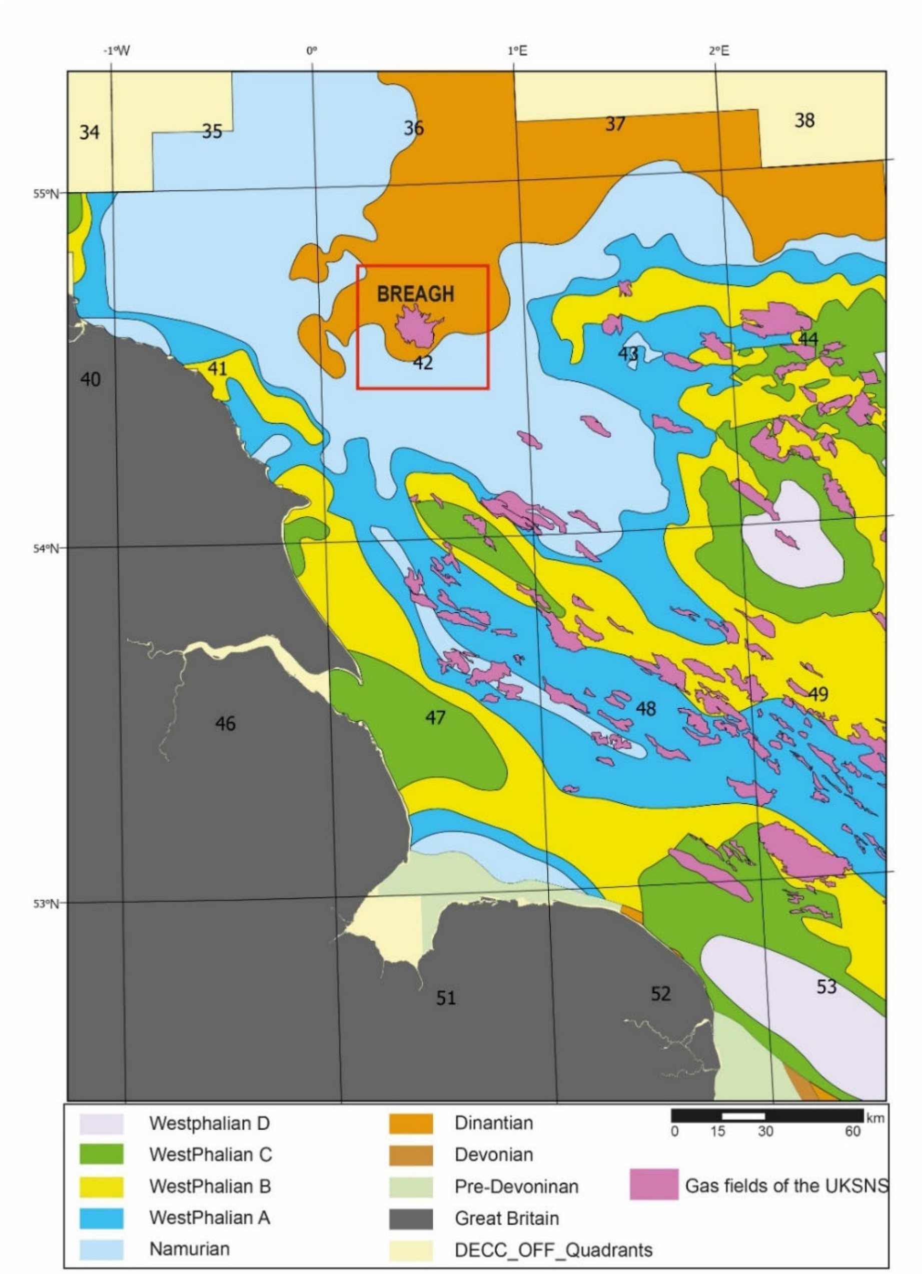

Figure 3.4. Distribution pattern of the Base Permian subcrop facies on the UK SNS areas. Breagh (in the red box) lies in the area of Dinantian subcrop (modified from Underhill 2003).

These Early Permian deposits are absent from the heavily eroded Breagh area (Booth *et al*., 2017) (Figs 3.3, 3.4 & 3.5), which was only overstepped in the Late Permian by Zechstein carbonates and evaporites deposited after the Southern Permian Basin connected to the Tethyan Ocean. The Mesozoic stratigraphy of Breagh and the surrounding area is comparable to that of the nearby Esmond, Forbes and Gordon fields with a thick Triassic section overlain by attenuated Jurassic and Cretaceous sections (Ketter, 1991).

The source of gas in the Breagh area is not entirely certain. Elsewhere in the SNS, coals within the paralic sequences of the lowermost Late Carboniferous are considered to be the source of gas (Barnard and Cooper, 1983; Ritchie and Pratsides, 1993). However, at Breagh, Permian Zechstein strata lie directly upon Early Carboniferous strata. The gas that now fills Breagh could have arrived via long distance migration from structurally deeper Late Carboniferous coals. The source could also be the Namurian mudstones containing disseminated organic material to the east or there may be and, as yet, uncharacterized source in the Early Carboniferous such as the Mid-Dinantian Scremerston Formation (Chadwick *et al*., 1993; Milton-Worssell *et al*., 2010; Booth *et al*., 2017).

Nonetheless, gas generation probably occurred in the Late Cretaceous–Early Tertiary (Cameron *et al*., 2005), but since the SNSCB was tilted into its present configuration in the Late Tertiary, adequate understanding of Mesozoic burial and inversion postdating trap-forming events in SNSB is critical for the exploration success of its hydrocarbon province (Fraser and Gawthorpe, 1990).

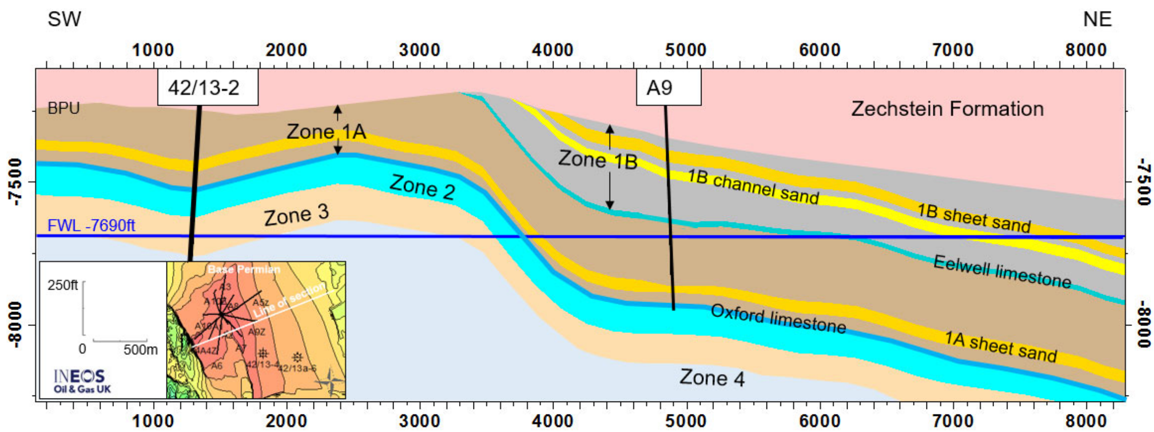

Figure 3.5. An illustrative geo-seismic section SW–NE through the Breagh Field showing the structure and erosion of the Zone 1B reservoir.

3.5 Database.

The Breagh Field database includes six exploration/appraisal wells and 11 production wells. While drilling these wells a series of measurement while drilling, logging while drilling and wireline logs were obtained. These included the caliper, gamma ray, sonic, density, neutron and resistivity logs in addition to the acquisition of formation pressures and well test data. These data were used to establish lithologies, shale volume, total and effective porosity and permeability, formation water resistivity and water saturation, pressure gradients, fluid contacts and saturation height functions. Furthermore, core and core plugs were acquired in 42/13-2, 42/13-4, 42/13a-6, 42/13a-A4 and 42/13a-A5z and routine core analysis and special core analysis have been carried out. Data from these studies include overburden-corrected porosity and permeability, petrographic analysis and relative permeability.

There are two main seismic surveys that have been acquired over the Breagh area: the 2013 Polarcus seismic survey, which covers an area of 480 km^2 (data owned by TGS), and the older, 1995 Geco-Prakla seismic volume covering 387 km^2 (Fig. 3.2). The 2013 3D survey was acquired using a 6 km cable with a nominal fold of 80 and a record length of 6.2s. Post acquisition, the 2013 Polarcus survey was infilled at the platform site with the vintage 1995 data to give a final dual azimuth seismic volume. This new seismic cube provided better data quality than the vintage 1995 data and, with the well data, gave an improved image of the overburden, the BPU and intra-Carboniferous reflectors.

The seismic interpretation of the intra-Carboniferous section is based on correlatable biostratigraphic and chemostratigraphic limestone markers named according to the onshore stratigraphic terminology (Fig. 3.3). A palynological study was carried out on the 42/13a-6, Crosgan 42/10b-2 and Macanta 42/14-2 wells and was used to correlate all the Breagh wells in the block. Based on limestone markers the reservoir has been further divided and correlated into four zones. However, on a reservoir scale, there are remaining issues with achieving reliable regional correlation of the sandstone bodies because with an average thickness of 30 ft they are too thin to resolve on seismic data. Moreover, correlation was made more ambiguous in places by variable erosional levels beneath the BPU (Symonds *et al.*, 2015).

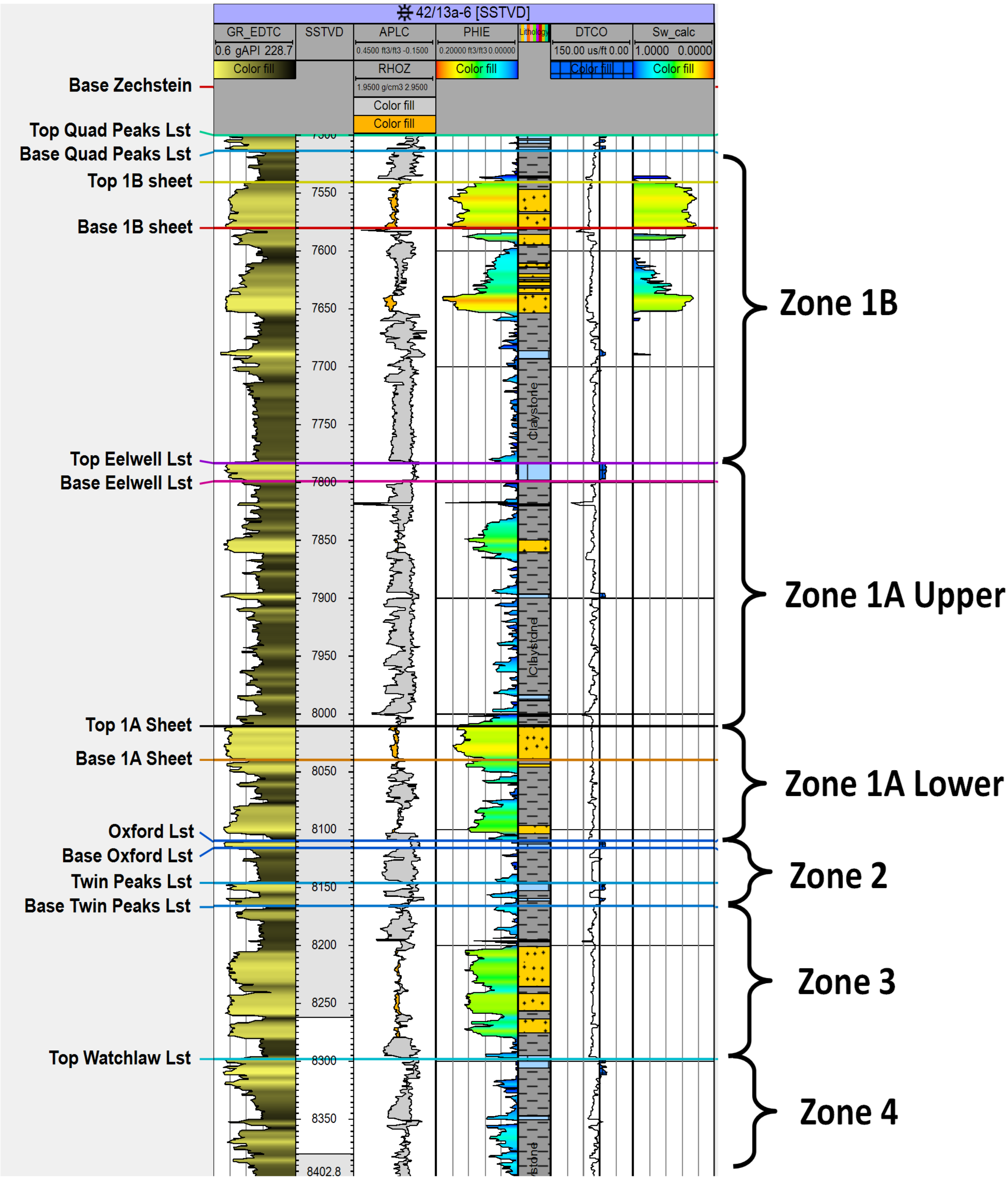

Figure 3.6. Appraisal well 42/13a-6 log responses and reservoir zonation.

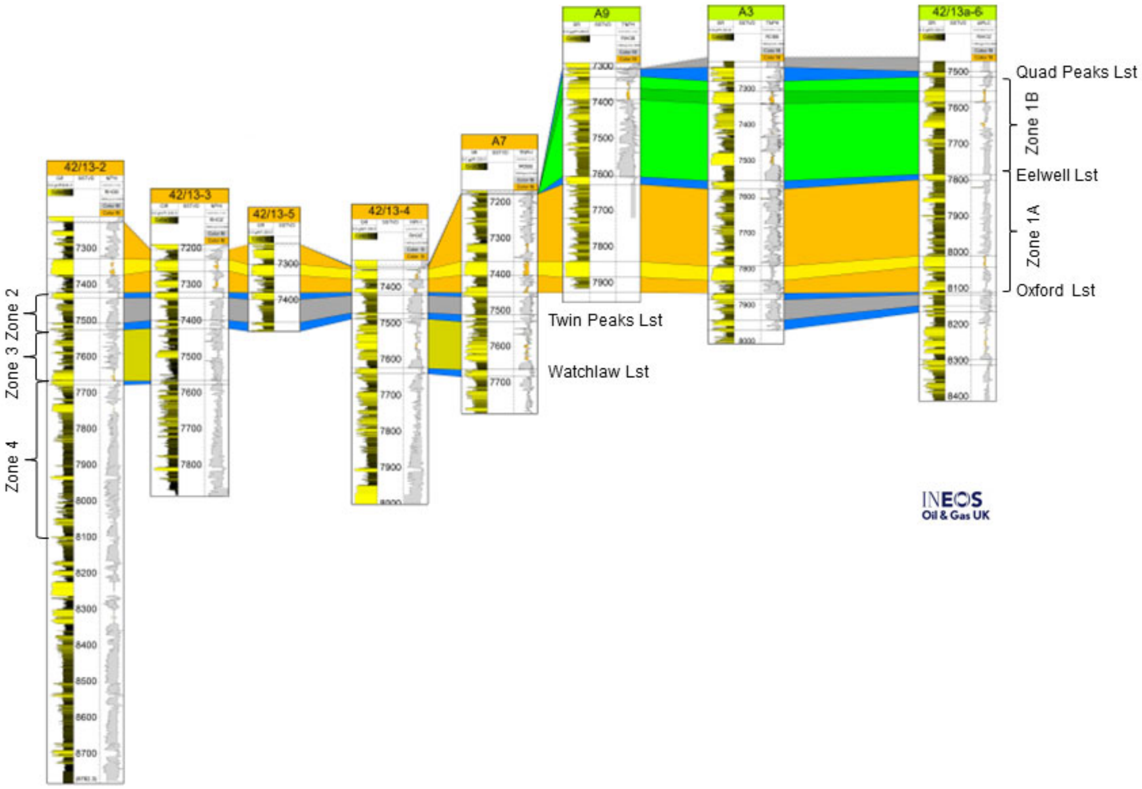

Figure 3.7 A well correlation panel across the Breagh Field. The orange wells are Zone 1A wells and the green wells are Zone 1B wells. Each zone is subdivided by limestone bands.

3.6 Trap.

The main trap-forming event in the Breagh area was the Late Carboniferous–Early Permian Variscan Orogeny, which created inversion anticlines in the hanging walls of the major graben boundary faults (Fraser and Gawthorpe, 1990).

Later Mesozoic and Cenozoic tectonic events associated with rifting in Atlantic and Tethyan provinces have modified the trapping geometries(Fraser and Gawthorpe, 1990; Cameron *et al*., 1992; Besly *et al*., 1993) in the Breagh structure. These created a closure of erosionally truncated and highly faulted reservoirs at BPU level, which are then sealed by Upper Permian (Zechstein Group) evaporites.

The field itself lies within a large-scale inversion structure and comprises tilted fault blocks with fault closure to the SW and three-way dip closure in other directions. The trap is polygonal and has an area of 94 km^2.

In addition to the structural complexity, there were significant challenges in imaging the trap because of the presence and geometry of the overlying Zechstein Group (Late Permian) sequence. The resulting depth uncertainty has caused difficulty in mapping the reservoir structure, consequently the perceived gas in place volume is not well constrained.

3.7 Reservoir and petrophysics.

The primary reservoirs are fluvio-deltaic sandstone units in the Middle Limestone (Yoredale) Formation of the Carboniferous (Visean stage) (Booth *et al.*, 2017; Monaghan *et al.*, 2017). The onshore stratigraphic terminology is here adopted to subdivide the reservoir package. The Middle Limestone Formation itself comprises of a series of 'Yoredale'-type cycles, with each cycle typically c. 120 ft thick. Each cycle consists of thin marine limestones with coral fragments and brachiopods, succeeded by fine-grained shales and siltstones, coarsening up into fine- to medium-grained sandstones. In many cases the coarsening-up intervals are capped by a fining-upwards sequence of thin shales and coals before the next cycle, marked by a limestone band. These cycles have been interpreted as the product of marine transgression into the intermontane basin, forming the limestones, followed by a prograding paralic system of pro-delta shales, silts and fine sandstones(Maynard and Dunay, 1999; Jones *et al.*, 2015; Booth *et al.*, 2017).

The reservoir is subdivided into four zones (based on chronostratigraphic and biostratigraphic studies) with the primary reservoir being the topmost zone – Zone 1 (Fig. 3.5). Well 42/13a-6 contains all four zones (Fig. 3.6) and has been used as a type section for reservoir correlation (Jones *et al.*, 2015).

The Zone 1 reservoir is a series of channel sandstones and sheet sandstones that are separated by mudstones, heterolithics and local coal beds. The sandstones in most cases form isolated simple channels or may be superimposed on top of one another to form complex, stacked multi-storey channels or composite channels. Individual sets range in thickness from approximately 1–2 ft to a maximum of approximately 30 ft and display sharp and locally scoured bases (Fig. 3.7).

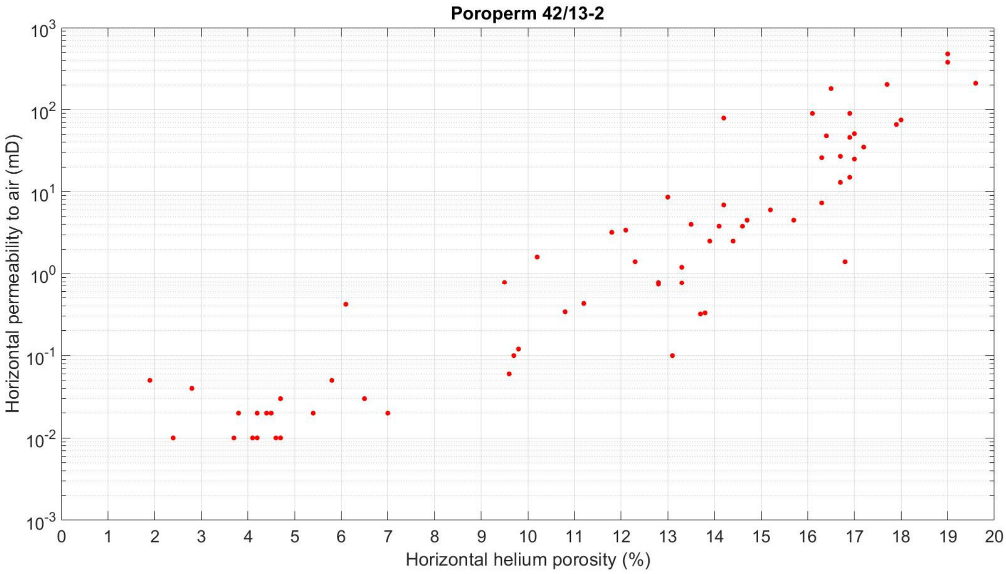

Figure 3.8a. Porosity–permeability cross-plots from the Breagh Field @ well 42/13-2 in the west of the field.

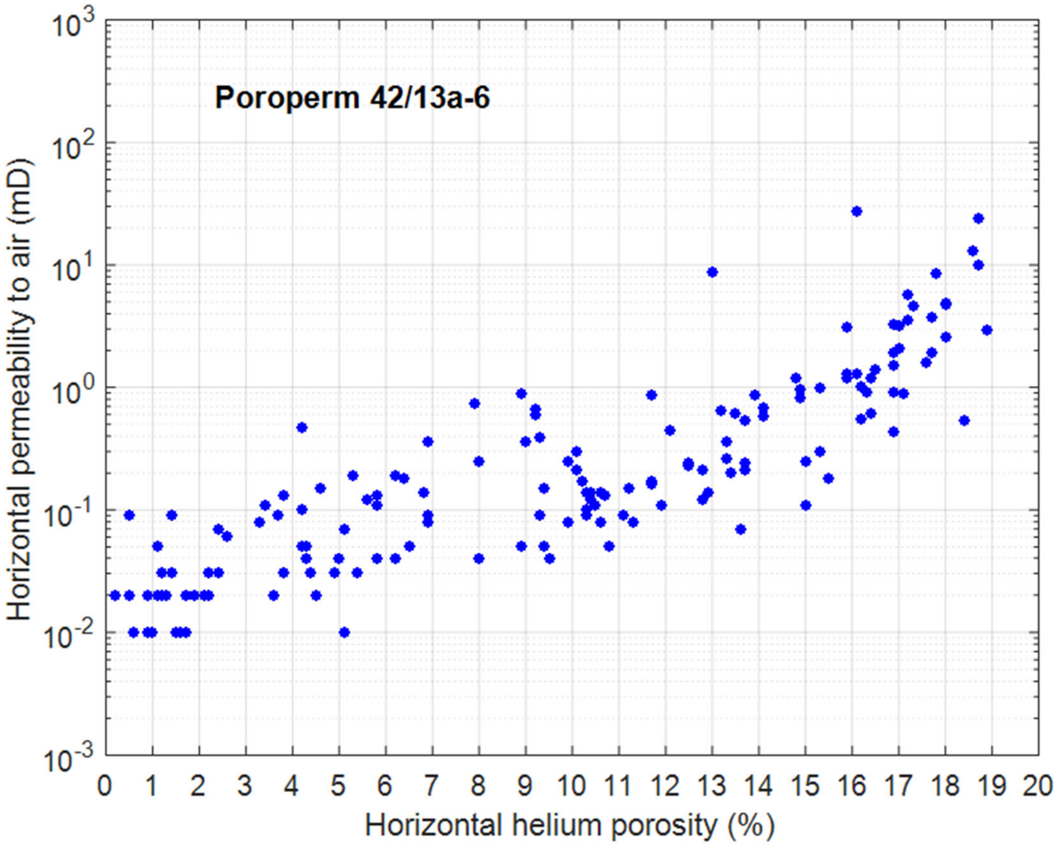

Figure 3.8b. Porosity–permeability cross-plots from the Breagh Field: @ well 42/13a-6 in the east of the field.

Reservoir quality is primarily controlled by depositional facies, which controls grain size, sorting and volume of diagenetic clay (Jones *et al*., 2015) (Fig. 3.8a &b). The best reservoir intervals have permeabilities in the range 0.1–100 mD (average 1–10 mD in Zone 1) and porosities in the range of 9.5–19.6% (average 11.6%). Net-to-gross ratio varies across the zones, averaging 56% in Zone 1, 34% in Zone 3 and 14% in Zone 4. Despite these variations, petrophysical results across the field are comparable for the same reservoir units. A 'mini' drill stem test was conducted in three zones on well 42/13a-6, which found formation permeability in 42/13a-6 in the eastern part of the field to be in line with permeabilities in 42/13-2 and 42/13-4 at the western part of the field.

For the Field Development Plan a free water level (FWL) of 7750 ft TVDSS was used to derive a saturation height function based on the exploration/appraisal wells 42/13-2, 42/13-3 and 42/13-4. This, however, was later superseded by a contact that was established in the 42/13a-6 well (post-FDP), which showed a well-defined gas gradient and water gradient, with FWL at 7690 ft TVDSS (Fig. 3.9a). Based on this FWL, P90, P50 and P10 GIIP were computed as 751, 909, 1040 bcf respectively.

The Breagh Field reservoir is normally pressured and has a reservoir temperature of 185°F (85°C) at 7200 ft TVDSS. The field has a gas column of 510 ft based on the deeper FWL described above.

The Breagh Field gas is rich in CO2 (c. 2–3%) relative to its neighbouring Permian (Rotliegend Group) reservoirs – Ravenspurn South and North fields (Corbin *et al*., 2005). The gas is sweet as it does not contain any H2S and has a methane content of around 91% and N2 content of 2.53%. The condensate content is approximately 3 bbl/MMscf of gas.

3.8 Production history and reserves.

The Breagh Field received its FDP approval in July 2011 after commercial viability was confirmed from the appraisal wells. The FDP specified a two-phase development: the first phase began in 2011 with seven wells drilled from the Breagh Alpha platform with quoted P50 reserves of 552 bcf.

The Alpha platform has a dedicated 20-inch diameter 100 km long export pipeline to transport gas and liquids from the Breagh Field to landfall at Coatham Sands near Teesside. From there the natural gas is transported through a 10 km pipeline to the Teesside Gas Processing Plant (TGPP) at Seal Sands in Middlesbrough before entering the National Transmission System following dilution with lower inert gas to meet system entry specifications. The plant, consisting of two gas-processing trains, has a total capacity to process 675 MMscfgd.

First gas from the field was achieved in October 2013 with an initial total flow rate of 99 MMscfgd. By November 2014, the field production had increased to 156 MMscfgd but due to natural decline of the field, production fell to 135 MMscfgd by January 2015. By the second quarter of 2015, production rates were at 111 MMscfgd of sales gas and condensate at 3.6 bbl/MMscf. Production remained high into the third quarter of the same year with daily sales rates at 109 MMscfgd net, which was higher than forecasted in the reserve evaluation. By the first quarter of 2016, production from the field had fallen to 84 MMscfgd gross and continued to drop to an average of 72 MMscfgd for the remainder of 2016, again due to natural decline. An average annual production volume of 86 MMscfgd between January 2014 and December 2017 has been reported (Fig. 3.10), and INEOS Oil and Gas UK expects Breagh to remain in production until 2040. Currently, an onshore compression project is ongoing to enhance the production of the field to end of field life.

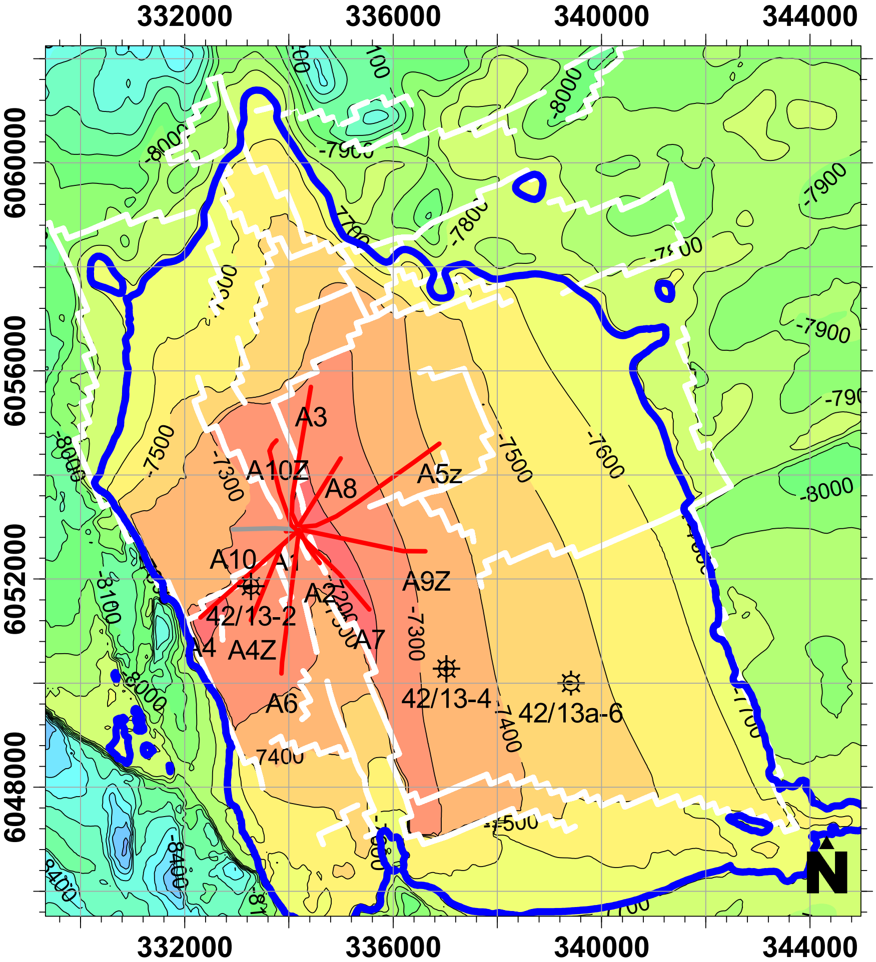

Figure 3.9a. Base Zechstein Group maps illustrating the contact at 7690 ft TVDSS in dark blue and fault pattern (the stair-stepped fault traces are the output from the Petrel model, with location and geometries from seismic interpretation). Appraisal wells are vertical marked by a black circle; development wells are all deviated marked in red/grey.

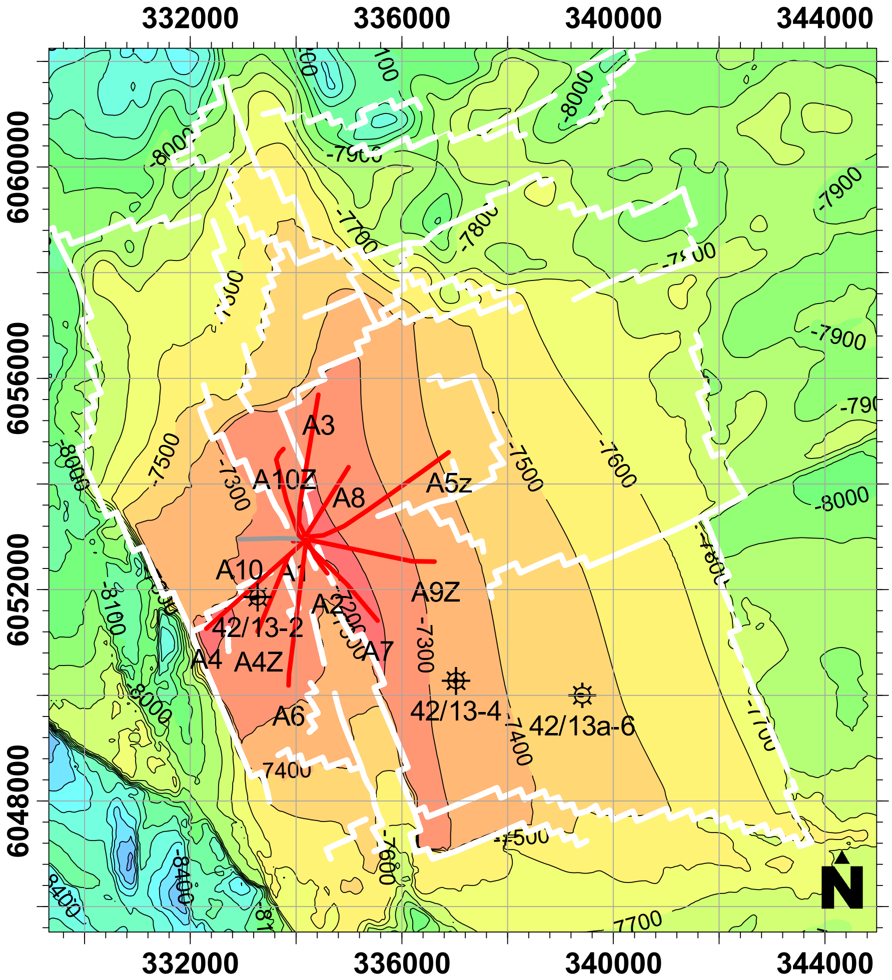

Figure 3.9b. Base Zechstein Group maps without free water level. Fault pattern (the stair-stepped fault traces are the output from the Petrel model, with location and geometries from seismic interpretation). Appraisal wells are vertical marked by a black circle; development wells are all deviated marked in red/grey.

Fig. 3. 10: Breagh Field production history.

TABLE: 3.1: BREAGH SUMMARY TABLE- See also appendix 1		
Breagh Field	*(Data and suggested Units)*	*(Author's explanatory comments)*
Trap		
Type	Combination of tilted fault block with dip closure	
Depth to crest	8400 (ft MD) 7200 ft TVDSS	
Hydrocarbon contacts	Free Water Level at 7690 (ft TVDSS)	From 42/13a-6 Gas-Down-To (GDT) levels are established as follows 42/13-2: 7668ft TVDSS 42/13-3: 7503ft TVDSS 42/13-4: 7599ft TVDSS 42/13-5: 7347ft TVDSS
Maximum oil column thickness	NA	
Maximum gas column thickness	510 ft	
Main Pay Zone		
Formation	Middle and Lower Limestone	
Age	Visean, Early Carboniferous	
Depositional setting	Fluvial-deltaic setting	Distributary channels and sheet sands
Gross/net thickness	66 ft	
Average porosity	11.60% Zone 1B: 14% Zone 1A: 13%	Interbedded sandstones and claystones
Average net:gross ratio	Zone 1B: 0.35 Zone 1A: 0.30	:
Cutoff for net reservoir estimation	Phie 0.075 Vclay 0.4	
Permeability range Average permeability	0.1-100 mD Zone 1: 1-10 mD	
Average hydrocarbon saturation	Zone 1B: 0.65 Zone 1A: 0.7	
Productivity index range	NA	
Hydrocarbons		
Fluid type	Dry Gas	
Gas specific gravity	0.618	
Bubble point (oil) Dew point (condensate)	NA	At reservoir depth (185˚F) no condensate will appear over the field life
Condensate /gas ratio Water/gas ratio	3 bbl/MMscf 2 bbl/MMscf	
Formation Volume Factor (oil)	NA	
Gas Expansion Factor	0.00444	
Formation Water		
Salinity	~188,500 ppm NaCl equivalent	
Resistivity	0.056 ohm.m @ 60˚F	
Water gradient	0.49 psi/ft	From 42/13a-6
Reservoir Conditions		
Temperature @ Top reservoir	185˚F at 7200 ft TVDSS	
Pressure @ Top reservoir	3,744psia at 7200 ft TVDSS	
Gas gradient	0.088 psi/ft	From 42/13a-6
Field Size		
Area	94 km²	
Gross Rock Volume	1220 Mm³	
GIIP	P90: 751 bcf P50: 909 bcf P10: 1040 bcf	
Drive mechanism (primary, secondary)	Depletion	
Recovery to date - oil	NA	
Recovery to date - gas	125 bcf	
Expected ultimate recovery factor/volume - oil	NA	
Expected ultimate recovery factor/volume - gas	50% (2040)	
Production		
Start-up date	Oct-13	
Number of Exploration/Appraisal Wells	6	
Number of Production Wells	10	
Number of Injection Wells	NA	
Development scheme	Phased development	
Highest rate - gas	158 MMscf/d (November 2014)	
Planned abandonment	*Undeveloped*	

3.9 References.

Barnard, P. C., and B. S. Cooper, 1983, A Review of Geochemical Data Related to the Northwest European Gas Province: Geological Society, London, Special Publications, v. 12, no. 1, p. 19–33, doi:10.1144/GSL.SP.1983.012.01.04.

Besly, B. M., 1998, Carboniferous: Petroleum geology of the North Sea: basic concepts and recent advances, p. 104–136.

Besly, B. M., S. D. Burley, and P. Turner, 1993, The late Carboniferous 'Barren Red Bed' play of the Silver Pit area, Southern North Sea: Geological Society, London, Petroleum Geology Conference series, v. 4, no. 1, p. 727–740, doi:10.1144/0040727.

Booth, M., J. R. Underhill, R. J. Jamieson, and R. Brackenridge, 2017, Controls on Lower Carboniferous (Dinantian) Prospectivity in the Mid North Sea High Region: AAPG/SEG International Conference and Exhibition, London, p. 8.

Cameron, T. D. J., A. Crosby, P. S. Balson, H. J. Jeffery, G. K. Lott, J. Bulat, and D. Harrison J., 1992, Geology of the Southern North Sea Basin, British Geological Survey: London, ASCE, United Kingdom Offshore Official report, 14–26 p.

Cameron, D., J. Munns, and S. J. Stoker, 2005, Remaining hydrocarbon exploration potential of the Carboniferous fairway, UK southern North Sea, *in* J. D. Collinson, D. J. Evans, D. W. Holliday, and N. S. Jones, eds., Carboniferous hydrocarbon geology : the southern North Sea and surrounding onshore areas: Yorkshire Geological Society, p. 209–224.

Chadwick, R. A., D. W. Holliday, S. T. Holloway, and A. G. Hulbert, 1993, The evolution and hydrocarbon potential of the Northumberland–Solway Basin, *in* Geological Society, London, Petroleum Geology Conference series: Geological Society of London, p. 717–726.

Collinson, J. D., C. M. Jones, G. A. Blackbourn, B. M. Besly, G. M. Archard, and A. H. McMAHON, 1993, Carboniferous depositional systems of the Southern North Sea: Geological Society, London, Petroleum Geology Conference series, v. 4, no. 1, p. 677–687, doi:10.1144/0040677.

Corbin, S., S. Gorringe, and D. Torr, 2005, Challenges of developing Carboniferous gas fields in the UK Southern North Sea: Geological Society, London, Petroleum Geology Conference series, v. 6, no. 1, p. 587–594, doi:10.1144/0060587.

Fraser, A. J., and R. L. Gawthorpe, 1990, Tectono-stratigraphic development and hydrocarbon habitat of the Carboniferous in northern England: Geological Society, London, Special Publications, v. 55, no. 1, p. 49–86, doi:10.1144/GSL.SP.1990.055.01.03.

Glennie, K. W., 1986, Development of NW Europe's Southern Permian gas basin: Geological Society, London, Special Publications, v. 23, no. 1, p. 3–22.

Glennie, K., 2005, Regional tectonics in relation to Permo-Carboniferous hydrocarbon potential, Southern North Sea Basin: Carboniferous hydrocarbon resources: the southern North Sea and surrounding areas. Occasional Special Publication of the Yorkshire Geological Society, v. 7, p. 1–12.

Glennie, K. W., and D. M. J. Provan, 1990, Lower Permian Rotliegend reservoir of the Southern North Sea gas province: Geological Society, London, Special Publications, v. 50, no. 1, p. 399–416, doi:10.1144/GSL.SP.1990.050.01.25.

Jones, N. S., 2007, The Scremerston Formation: results of a sedimentological study of onshore outcrop sections and offshore Well 42/13-2., British Geological Survey Commisioned Report CR/07/101: 122 p.

Jones, P., R. Symonds, D. Talbot, P. Jeffs, A. Kohok, J. Shaoul, and W. Spitzer, 2015, Successful Hydraulic Fracture Stimulation of Yoredale Carboniferous Sands in the UKCS: Society of Petroleum Engineers, doi:10.2118/174171-MS.

Ketter, F. J., 1991, The Esmond, Forbes and Gordon Fields, Blocks 43/8a, 43/13a, 43/15a, 43/20a, UK North Sea: Geological Society, London, Memoirs, v. 14, no. 1, p. 425–432, doi:10.1144/GSL.MEM.1991.014.01.53.

Leeder, M. R., and M. Hardman, 1990, Carboniferous geology of the Southern North Sea Basin and controls on hydrocarbon prospectivity: Geological Society, London, Special Publications, v. 55, no. 1, p. 87–105.

Maynard, J. R., and R. E. Dunay, 1999, Reservoirs of the Dinantian (Lower Carboniferous) play of the southern North Sea, *in* Geological Society, London, Petroleum Geology Conference series: Geological Society of London, p. 729–745.

Maynard, J. R., W. Hofmann, R. E. Dunay, P. N. Benthan, K. P. Dean, and I. Watson, 1997, The Carboniferous of Western Europe; the development of a petroleum system: Petroleum Geoscience, v. 3, no. 2, p. 97–115.

McCann, T. *et al*., 2008, Carboniferous, *in* The Geology of Central Europe: Precambrain and Palaeozoic: p. 411–530.

McLean, D., 1993, A palynostratigraphic classification of the Westphalian of the Southern North Sea Carboniferous Basin, PhD: University of Sheffield, 303 p.

Mclean, D., 2011, Biostratigraphy of the Carboniferous interval in Breagh East well 42/13a-6, Southern North Sea, 68: MB Stratigraphy Ltd.

McPhee, C. A., M. R. Judt, D. McRae, and J. M. Rapach, 2008, Maximising Gas Well Potential In The Breagh Field By Mitigating Formation Damage: Society of Petroleum Engineers, doi:10.2118/115690-MS.

Milton-Worssell, R., K. Smith, A. Mcgrandle, J. Watson, and D. Cameron, 2010, The search for a Carboniferous petroleum system beneath the Central North Sea, *in* Petroleum Geology: From Mature Basins to New Frontiers—Proceedings of the 7th Petroleum Geology Conference: Geological Society of London, p. 57–75, doi:10.1144/0070057.

Monaghan, A. A. *et al*., 2017, Carboniferous petroleum systems around the Mid North Sea High, UK: Marine and Petroleum Geology, v. 88, p. 282–302, doi:10.1016/j.marpetgeo.2017.08.019.

Nesbit, R., and K. Overshott, 2010, Overcoming multiple uncertainties in a challenging gas development: Chiswick Field UK SNS, *in* Geological Society, London, Petroleum Geology Conference series: Geological Society of London, p. 315–323.

Pharaoh, T. C., R. J. Merriman, P. C. Webb, and R. D. Beckinsale, 1987, The concealed Caledonides of eastern England: preliminary results of a multidisciplinary study: Proceedings of the Yorkshire Geological Society, v. 46, no. 4, p. 355–369, doi:10.1144/pygs.46.4.355.

Ritchie, J. S., and P. Pratsides, 1993, The Caister Fields, Block 44/23a, UK North Sea: Geological Society, London, Petroleum Geology Conference series, v. 4, no. 1, p. 759–769, doi:10.1144/0040759.

Rodriguez, K., R. Wrigley, N. Hodgson, and H. Nicholls, 2014, Southern North Sea: unexplored multi-level exploration potential revealed: First Break, v. 32, no. 6, p. 107–113.

Symonds, R., R. Lippmann, B. Mueller, and A. Kohok, 2015, Yoredale sandstone Architecture in Breagh Field (UK SNS). Presentation for Sedimentology of Paralic Reservoirs: Recent advances and their applications.: p. 24.

Underhill, J. R., 2003, The tectonic and stratigraphic framework of the United Kingdom's oil and gas fields: Geological Society, London, Memoirs, v. 20, no. 1, p. 17–59, doi:10.1144/GSL.MEM.2003.020.01.04.

Chapter 4

Lithofacies and Depositional Environment of the Breagh Field area.

Contents

Chapter 4: Lithofacies and Depositional Environment of the Breagh Field Area.

4.1 Introduction.

The geological and depositional setting of the Breagh Field area and associated lithologies have been discussed in chapter 2. The aim of this chapter is to describe the facies associations, vertical and lateral facies architecture and the gross depositional environment using cores cut in wells (42/13-2, 42/13-4, and 42/13a-6) drilled into the Breagh Field (See- Fig 4.2 & 4.3). In addition to the studied cores, better understanding of the lateral facies architecture as well as the possibility for further reservoir potential within Lower Carboniferous Visean reservoirs away from the Breagh Field into other areas of the Southern North Sea (SNS) has been developed from existing well reports and previous work done in the SNS (Maynard and Dunay, 1999; Underhill, 2003; Besly, 2019; Booth *et al.*, 2020; Brackenridge *et al.*, 2020; Grant *et al.*, 2020).

4.2: Facies analysis.

Eleven facies associations namely Limestone (FA1), prodelta (FA2), distributary mouthbar (FA3), proximal delta front sands (FA4), distal delta front sands (FA5), interdistributary bay (FA7), distributary channel (FA8), braided fluvial channel (FA9), abandoned channel (FA10), crevasse splay (FA11) and swamp (FA12) have been identified from the studied cores. They have been grouped into marine, prodelta, delta front, and delta plain gross depositional environments as tabularized in Table 4.1/ Appendix 2.

The facies associations are interpreted as deposited in a mixed carbonate and siliciclastic fluvio-deltaic environment and are arranged into coarsening- and cleaning-upward cycles (parasequences) bounded by flooding surfaces which is at either the base of a limestone (FA1) or a marine deposit that lies directly on top of a more proximal deposit. The facies associations record the vertical and lateral changes in delta morphology due to the effects of autocyclic and allocyclic processes within an evolving rift setting. The depositional processes that formed each cycle have important implications for the eventual reservoir quality and reservoir prediction away from the Breagh area into other areas of the SNS.

Discovery of the Breagh gas field in the SNS demonstrates that the Dinantian (Visean, 346.7–330.9 Ma) reservoirs have potential to contribute to the UK's future energy mix (Booth *et al*., 2020) and provides encouragement for Lower Carboniferous clastic prospectivity in the southern North Sea (Rodriguez *et al*., 2014; Brackenridge *et al*., 2020; Grant *et al*., 2020).

Table 4.1: Summary of interpreted facies associations, depositional paleoenvironments, and study wells where facies are present. Key defining criteria- bioturbation index adapted from Taylor et al. 2003. Table format is modified after Booth et al 2020.- See also appendix 2

ENVIRONMENT	SUBENVIRONMENT	FACIES ASSOCIATION	DESCRIPTION
Delta Plain	Swamp	FA12	Mudstones, siltstones and current-rippled and/or climbing current-rippled fine sandstones that are typically overlain by coal. Rooted horizons are observed. Weakly to highly bioturbated (0-4)
	Crevasse Splay	FA11	Erosive-based, fine to medium grained sandstone. Often upward-fining. The sandstone is moderately- to well-sorted and display cross-stratification at the base with current-ripple lamination dominating upwards. Abundant carbonaceous plant material throughout. Very weakly bioturbated (0-1)
	Abandoned Channel	FA10	Heterolithic very-fine- to fine-grained sandstones and siltstones with current ripples, occasional thin trough cross- bedding. It has deformed/slumped horizons and rooted bed tops. Includes bioturbated horizons (0-2)
	Braided fluvial channel	FA9	Erosive-based, medium to coarse grained sandstones with planar cross beds or trough cross-beds. The bases are very coarse and occasionally pebbly. The bottom horizons also contain occasional rip up clast and plant material. Bioturbation is not visible (0-1)
	Distributary Channel	FA8	Erosive-based, well-sorted, fine- to medium-grained sandstone. It consists of occasional coal clasts and plant debris.
	Interdistributary Bay	FA7	Very-fine- to fine-grained sandstones with lenticular or flaser bedding, parallel lamination, wave, and current ripples. Also consist of heterolithic mudstones and siltstones. slump and water escape structures are visible. Weakly to highly bioturbated (3-5)
Delta front	Distal Delta Front sand	FA5	Alternating between muddy siltstone and silty sandstones with decemeter sized climbing ripples, wave formed ripples, horizontal planar lamination, Parallel- to ripple-laminated siltstones, and very-fine-grained sandstone. Abundant plant material is common along bedding planes. Siderite concretions are also visible. Sparsely to highly bioturbated (1-4)
	Proximal Delta Fronts Sand	FA4	Muddy, very-fine- to fine-grained sandstone with coarsening upward vertical profiles. Silt drapes are found within the sandstones. Silty mudstone and the mudstones display climbing ripples whilst the siltstones have planar parallel lamination. Abundant plant material and common coal clasts are preserved. Sparsely to weakly bioturbated (1-3)
	Distributary mouth bar	FA3	Well-sorted, medium to coarse -grained sandstones displaying trough crossbedding. Occasionally pebbly with coarse- to very- coarse-grained erosive bed bases, with rip up and coal clasts. Sparsely to moderately bioturbated (1-3)

Pro-delta	Prodelta	FA2	Dark grey massive mudstones. Sometimes laminated, with crinoid and brachiopod debris near the base. Siderite nodules are common. This FA contains rare soft-sediment deformation including convolute lamination and slump structures. Bioturbation is not common (0-1)
Carbonate Platform	Limestone	FA1	Highly bioturbated (5-6) fossiliferous limestone (corals and rugose corals), crinoid ossicles, brachiopods, bryozoa. Also, as part of this FA is muddy limestones and some mudstone partings.

4.2.1 Facies association FA1: Carbonate Platform.

Description: This FA consist of light grey to medium dark grey limestones (typically packstones or wackestones. This FA contains an abundance of fossils, mostly small crinoid ossicles, brachiopods, shells, and fossil debris (42/13-4: 7602.3 ft – 7604.3 ft, 42/13a-6: 7903ft) are seen (Fig 4.1a). The fossils within the limestone beds are typically broken and disseminated throughout the bed(s) and are often associated with wavy lamination. This facies association are heavily bioturbated with some horizontal and vertical burrows that are difficult to identify except for the Helminthopsis burrows and Zoophycos.

Interpretation: The limestone beds represent deposition in shallow, calm, warm open-marine, platform setting and likely to have developed during times of low clastic supply.

They mostly overlie prodelta (FA2) but can also be found to be overlying swamp (FA12) and delta front sands (FA4 and FA5) -The shift from a subaerial deposition to a carbonate platform setting represent a rise in relative sea level and the top of it represents a maximum flooding surface. The abundance of crinoid and shell debris material represent deposition in a fully marine setting (Fig 4.1a). In Well 42/13-4 (Fig 4.2-left), five maximum flooding surfaces have been picked, three of which are at the top of limestone (7606.5 ft, 7602.3 ft, 7568.3 ft).

The crinoid ossicles are small suggesting that these are stunted forms possibly due to the periodic influx of terrigenous material or stressful bottom conditions as seen in core from 42/13a-6 between 7919 - 7903ft, and 7811.3 – 7806.5ft. The broken nature of the fossil material in some beds, and the association with wavy lamination suggests reworking by wave and tidal actions (Booth *et al*., 2020).

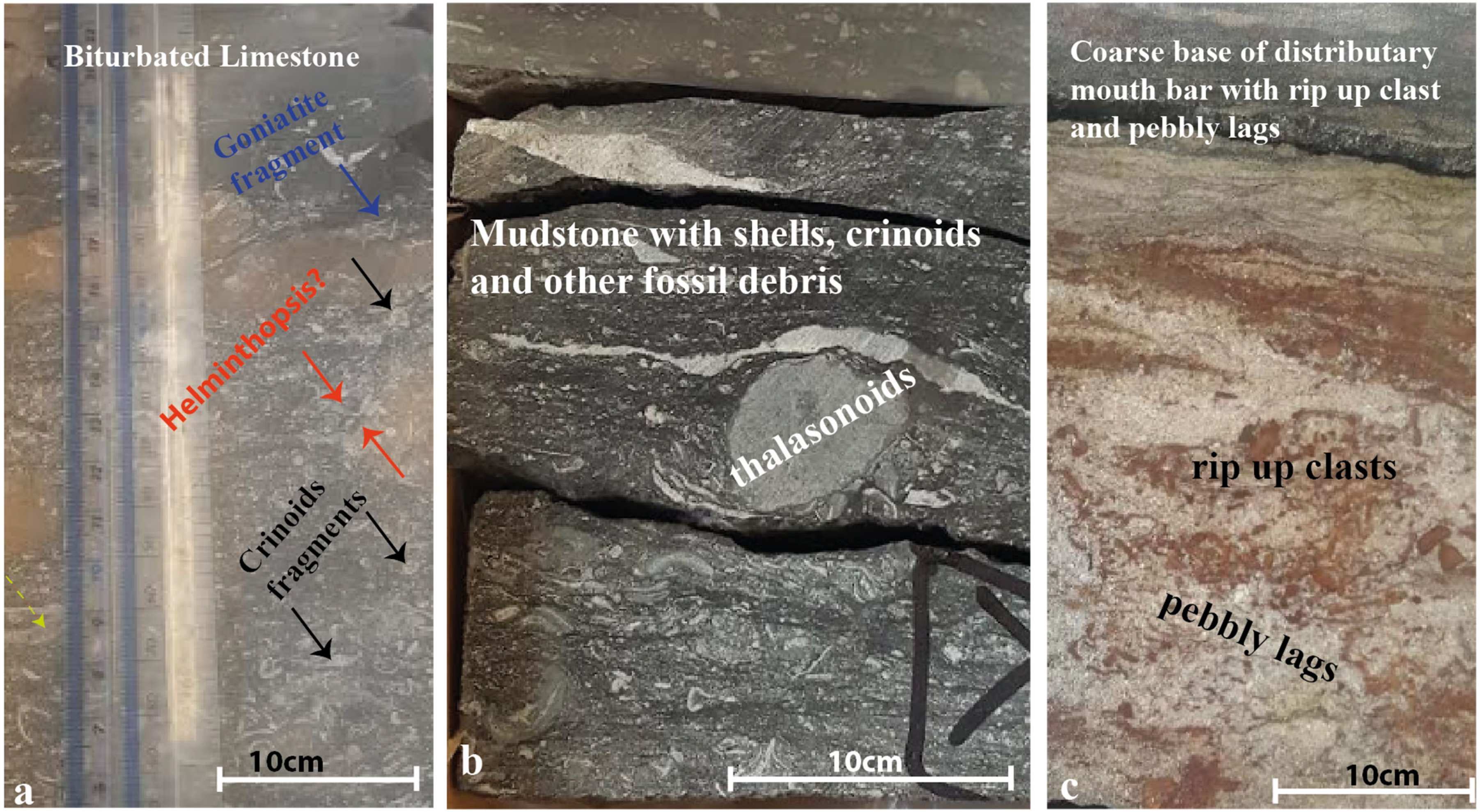

Fig 4.1- a) *Argillaceous limestone that includes crinoids' fragment (black arrow) and possible goniatite fragment (blue arrow). The sediments have been bioturbated and traces include helminthopsis (red arrow) and zoophycos (yellow arrow) @7903.5ft;* ***b)*** *A mudstone that includes thin shells, crinoids, and other fossil debris. Includes thalasonoids (th). Dark patches could be @7719ft;* ***c)*** *Coarse grain base of distributary mouth bar (FA3) with rip up clast and pebbly lags @7773.5ft. All photos taken from well 42/13a-6.*

4.2.2 Facies association FA2: Prodelta.

Description: This FA consists of dark grey, laminated mudstones. They range in thickness from less than 1m to about 10m (3-32ft). This FA sometimes have intervals of shell and crinoid material that appear to be bioturbated (see well 42/13-4 @ 7609.1ft). They have also been extensively bioturbated with the dominant traces being Helminthopsis and Zoophycos (Fig 4.1b). Some of the fossil debris could have passively infilled large burrows (see 7605.6 ft). Other intervals for instance at (well 42/13-4: 7609.3 ft – 7612.4 ft) includes very little in the way of fossil material and trace fossils but display common siderite nodules and rare soft sediment deformation suggesting that the deposition could have been within anoxic bottom waters as such are interpreted as prodelta. These units typically directly overlie swamp deposits (FA12) and interdistributary bay (FA7); limestones (FA1) but rarely delta front sands (FA4 and FA5).

Interpretation: Based on the overall fine-grained nature of this FA, parallel lamination, and similarity to prodelta deposits described (Hutsky *et al*., 2012; S. Liu *et al*., 2022), this FA can be interpreted as prodelta. Prodelta mudstones, record low-energy deposits in areas far away from turbulent sources of sediment supply. Less commonly as seen in 42/13-4: 7576.5 ft, are thin interbeds of siltstone become increasingly common within this FA as muds accumulate commonly by suspension.

The crinoid ossicles are small suggesting that they are the stunted forms possibly due to the periodic influx of terrigenous material. The broken nature of the fossil material may suggest reworking by current.

The depth change from limestone to mudstone deposition suggests an increase in the rate of influx of terrigenous mud into the basin.

The observed small scale sediment deformation may have formed due to localized slumping of sediment, sediment loading from the delta front to pro-delta (Mtelela *et al*., 2016) Siderite nodules could be related to methonogenesis (Sengupta *et al*., 2021; Wang *et al*., 2022; Z. Liu *et al*., 2022) by bacteria activities that promote the saturation of methane in bottom sediments immediately after burial under saline condition (Antoshkina *et al*., 2017, 2020, 2020; Booth *et al*., 2020).

4.2.3 Facies association FA3: Distributary mouth bar.

Description: Erosive based medium to coarse grained sandstone with no significant internal facies variability. They show continuous fining-upward grain-size profile. Current generated structures notably trough crossbedding like that found in FA8 and FA9 below are the dominant structure type in these facies. Planar crossbedding with smaller-scale cross-stratification is also encountered. The lowermost beds are highly erosive, poorly sorted, have outsized, pebble lags, coal clast and mud rip up clast (Fig 4.1c). Occasional thin laminations of plant debris are also encountered at the base.

Interpretation: Rapid deposition of sediment, coupled with active processes within the zone of the distributary mouth bar, results in a distinctive sequence composed almost entirely of sand. Thin, abundant, multidirectional trough cross-laminations are a product of wave and current processes constantly acting on the sediment. As the distributary channel builds seaward, the bar advances over organic-rich bay, carving out mud and clay rip up clast that gets embedded within its sequence. Similar features have been found in bar deposits of other areas of the Mississippi Delta (Morisawa, 2020; Roberts *et al*., 2020; Zhang *et al*., 2020; Xu *et al*., 2022), indicating their common nature. Cross-laminations, wave and current ripples, and rare occurrences of parallel laminations characterize this environment. The bar deposits are subjected to reworking and winnowing by wave action.

4.2.4 Facies association FA4: Proximal Delta Front Sand.

Description: These facies consist of a repeated pattern of muddy planar to ripple cross-laminated siltstones occasional hummocky cross stratification and fine-grained well sorted sandstones with current-ripple cross lamination with occasional tabular and trough cross bedding. The beds are predominantly arranged in coarsening upward sequences.

FA4 is fossiliferous with abundant well preserved carbonaceous plant debris that is aligned with the laminae of the siltstone beds. Flame structures, slump structures and convolute lamination, are seen in some of the sandstone lenses. The strata are sparsely to highly bioturbated, with some Cruziana ichnofacies.

Interpretation: Based on the overall alternating stacking pattern from muddy siltstones to sandstones, this FA can be interpreted to represent delta-front deposits of a river-dominated delta (Elliott, 1975) as they reflect relative variations in flow velocity associated with proximal to distal sub-environments of a delta-front system (Smith *et al*., 2019; Yan *et al*., 2020; Jin *et al*., 2021; Liu *et al*., 2021).

The alternation of planar to ripple cross lamination with stacked unidimensional cross lamination suggests a fluctuating flow of energy related to long lived fluvial discharge in a delta-mouth environment in which hyperpycnal flows are typical (Plink-Björklund, 2020; Zavala, 2020).

The abundance of plant material suggests that they were sourced directly from delta front distributary channels during seasonal flood events (Bhattacharya *et al*., 2020, 2020; Plink-Björklund, 2020). The presence of hummocky cross-stratification (HCS) also suggests that storm events redistributed sediments in this setting. In these sands most of the disruption appears to have been caused by water escape in the form of dewatering pillars. Like FA5 below, siderite nodules are likely to have formed during diagenesis and soon after deposition from the reduction of organic material under saline conditions (Antoshkina *et al*., 2017). Siderite nodules is concentrated in the current-rippled siltstones and sandstone stringers due to the increased porosity and permeability of those layers.

Tabular crossbedding represents the migration of subaqueous 2D dunes. The trough crossbedding represents the migration of 3D dunes from higher-energy flows. HCS records the interaction of storms (Booth *et al*., 2020).

4.2.5 Facies association FA5: Distal Delta Front Sand.

Description: This facies is similar with the FA4 above. It consists of alternating layer of planar laminated mudstones, and planar to ripple cross-laminated siltstones arranged into overall coarsening upward sequence. They sometimes grade into very fine-grained sandstones with current ripples. The sandstone where seen as well as the siltstone show preference for hosting siderite nodules. Unlike the FA4 facies however, the FA5 does not contain abundant plant material and bioturbation is scares with a Cruziana ichnofacies dominated by Planolites, and Chondrites. Soft-sediment deformation, including convolute lamination and slump structures, is recorded in some of the sandstone lenses. Typically, they gradationally overlie prodelta (FA1) facies and underlie FA5 facies.

Interpretation: The upward coarsening vertical profile is suggestive of a delta front facies as delta front always prograde basinward. The presence of laminated mudstones and siltstones suggest that deposition of this facies occurred at the distal part of the delta front from suspension fallout from hypopycnal flows (Booth *et al*., 2020). Whilst the repeated alternation between fine grained thinly laminated intervals and the coarser interval reflects episodic waxing and waning of subaqueous flow and sediment fallout.

The upward-coarsening grain size and the presence of very-fine-grained, cross-laminated sandstone lenses suggest tractional currents that may have originated from low concentration. The sedimentation in the delta front is usually sourced from plumes (hypopycnal and hyperpycnal) and sediment rich water from river mouth. Unidirectional, current-ripple cross lamination in the fine sandstones could have occurred during the rapid deposition of fine-grained material from hyperpycnal plume in the river mouth or as flow during high discharge events (Gani and Bhattacharya, 2007; Bhattacharya *et al*., 2020; Zavala, 2020). These sediments were deposited within the reach of storm waves suggesting a distal delta front sand setting.

4.2.6 Facies association FA7: Interdistributary bay.

Description: This FA is dominated by high percentage of mudstone with occasional thin beds of wave ripple laminated sandstone. Heterolithic laminations consisting of alternations of argillaceous siltstone to very fine and fine sandstone are very common. The sandstones are very fine where interbedded with argillaceous siltstones.

The argillaceous siltstone displays diffuse horizontal laminae with few noticeable coarser laminae. As the proportion of the coarser lamina increases, the sedimentary structure changes from flatter lamination to wave ripple cross lamination. The most common structure in these

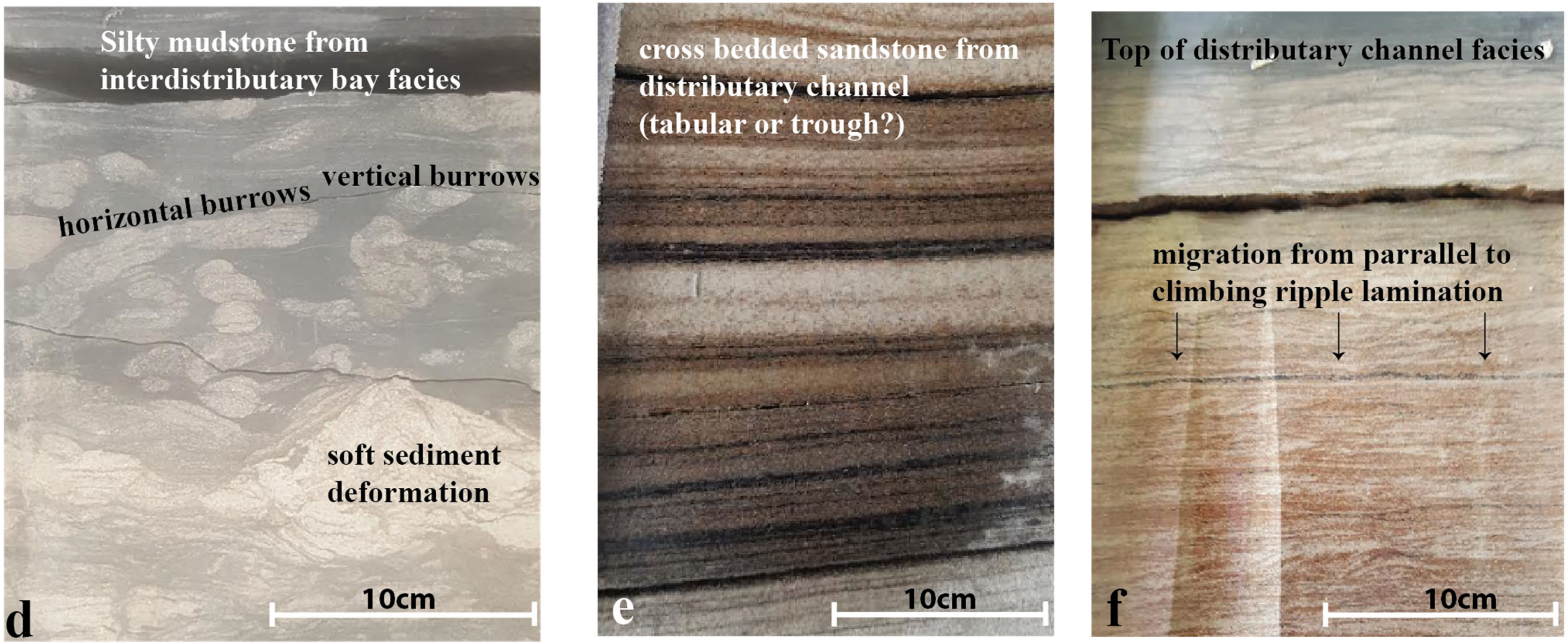

Fig 4.1 - d) *A silty mudstone from the interdistributary bay facies (FA7) that has been disrupted by vertical and horizontal escape burrows and soft sediment deformation @7950.5ft;* ***e)*** *Cross bedded sandstone from distributary channel facies (FA8). Crossbedding could be tabular or trough but difficult to differentiate at this scale @7749ft;* ***f)*** *Top of distributary channel facies representing wanning stage flow and showing migration from parallel lamination to climbing ripple lamination @7694ft. All photos taken from well 42/13a-6.*

siltstones is lenticular lamination. Sometimes flaser bedding (Fig 4.1i) with some flat lamination, current-ripple and wave-ripple cross-lamination are also observed.

Scour and fill structures are observed at bases, and fluid escape structures is also observed. Synaeresis cracks, siderite nodules and rootlets are also seen. Bioturbation intensity varies from moderate to intense. Burrows are common (Fig 4.1d). The trace fossil assemblage of Zoophycos, Planolites and Helminthopsis is consistent with deposition in an interdistributary bay. Inclusions consisting of shells and shell fragments, plant debris, seed, and rootlets are also observed.

Interpretation: Within the studied core, this FA is typically interlaced with the crevasse splay facies but also occurs in close association with the channel facies and the non-marine facies (FA12- Flood plain). This is to be expected as overbank flooding, crevassing and avulsion are the three major processes by which sediment-laden flood waters can be transferred to the bay. These processes combine to produce a family of sedimentary sequences, the majority of which are small-scale coarsening upwards sequences representing infilling of the bay(Coleman *et al*., 1964; Elliott, 1975; Li *et al*., 2019; Qin *et al*., 2021).

Current ripple marks and scour and fill structures are present in some intervals and indicate that currents were occasionally active during deposition. These structures were formed by tidal currents that overflow during floods.

The flat laminations indicate subaqueous deposition under quiet water conditions. The extensive reworking of the sediments by burrowing worms and mud-inhabiting molluscs emphasizes the relatively slow rate of deposition in this environment in contrast to facies associated with channel facies.

4.2.7 Facies association FA8: Distributary channel.

Description: Fluvial channels commonly depict an upward-fining grain size profile combined with progressively smaller bedforms (i.e., from trough and planar crossbedding in the medium grained sandstones through to current ripple laminated horizons in the fine-grained sandstones) demonstrating an upward decrease in depositional energy as the channel abandoned and infilled with sediments (Ashraf *et al*., 2019; Okobiebi and Okobiebi, 2021; Okeugo *et al*., 2022; Shehata *et al*., 2023).

Within the studies sandstones, this FA comprises erosive based well sorted and sometimes micaceous sandstone. Bed bases are commonly coarser grained, with rip up clast, coal clasts and pebbles, and large plant debris. The beds are clean to slightly silty, typically medium-grained, fining-upward sequences. Within the finer grained horizons, some sub-mm scale rhythmic lamination can be observed between the mud rich very fine-grained sands and mud rich micaceous silts. In some instances, like in 42/13-2 these facies consist medium grained sandstones that do not typically fine upward, although the top of the sequence still consists of smaller bedforms.

The uppermost parts of the succession are often rooted and overlain by flood plain (FA12). This facies association erosively overlies delta front and interdistributary bay dep (FA4-5 & FA7: and is often overlain by lower or upper delta plain facies (FA8, FA9 and FA11–FA12).This is similar to the pattern seen in (Wang *et al*., 2019; Kashif *et al*., 2020; Muhammad *et al*., 2020).

Erosional truncation, scour and fill, and clay inclusions are seen although less frequently. Distorted laminations, flaser or lenticular bedding and load casts are also visible along the tops (Fig 4.1f) of mud- sand contacts. The upper contact of the mud layers typically displays scour features.

Interpretation: Distributary channels are a common feature of river deltas. They are the downstream distributive element of a fluvial system which are usually formed as a stream nears the lake or the ocean. Due to the erosive-based profile, finning upward sequence, trough crossbedding (Fig 4.1e) to current-ripple lamination as the grain size decreases, as well as its close association with delta plain facies, FA8 is interpreted as distributary channel facies deposited on lower (subaqueous) delta plain.

Trough and planar cross-stratification as described by (Mckee and Weir,1953; in (Cseh and Andrews, 2019) are common in channel sands and is interpreted to have been deposited by traction currents. Whereas the siltstone intervals could have developed as rapid and gradual suspension fallout from low-energy, during waning-flow regimes (Fig 4.1f). The muddy layers are deposited during low river stage but may be eroded during subsequent floods. The observed alternation of sandstone and siltstone indicates waxing and waning of traction currents associated with flash floods.

Also, the predominance of coarse material interbedded with mud layers of various thicknesses is characteristic of channel fill deposits. In the upper reaches of the distributary channel, where stream velocity varies greatly between flood and low stage, thick sand deposits accumulate. Erosional truncation, scour and fill, and clay inclusions occur less frequently, but are nevertheless significant components of the structural assemblage. Distorted laminations, believed to be the product of gravity slumping of the steep channel walls, are common. Distortion may also be caused by silt-laden currents flowing along the channel bottom.

4.2.8 Facies association FA9: Braided fluvial channel.

Description: This FA consist of fine – medium grained moderately sorted sandstones with coarse grained bases that are highly erosive. The bottom beds are poorly sorted and contain oversized pebbles, with abundant rip-up and coal clast. The bottom beds display trough crossbedding which gives way to less-erosive tabular cross-bedded sandstones then to current ripple cross-lamination within the upper, thinner and finer-grained parts of the successions.

The uppermost parts of the bed are often silty and are associated with horizontal lamination. Muddy partings are seen separating cross-bed sets. Occasionally, lithified plant remains are seen throughout the beds.

This facies association erosively overlies floodplain (FA12) facies associations (Fig 4.1g) and is normally overlain by delta top channel abandonment (FA10) and or distributary channel facies (FA8) facies associations.

Interpretation: The record of ancient braided-stream deposits shows that channel deposits rest on scour surfaces and commonly contain a coarse-grained base with gravel lags (Miall, 1977; Jones *et al*., 2001; Babikir *et al*., 2021; Selim, 2021). Braided rivers typically consist of a series of broad, shallow channels and bars, with elevated areas active only during floods, (Herbert *et al*., 2020; Oyanyan *et al*., 2021; Shanmugam, 2022) and as such, braided-river deposits comprise of several different facies ranging from gravel facies to sand facies and to fine-grained facies. As a result, both large and smaller bed form sedimentary structures can be visible.

Within this FA, the presence of erosive-based, coarse-grained sandstone beds with trough cross-stratification suggest large, channelized deposits formed from high-energy currents and subaqueous migration of 3D dunes. Whereas the tabular cross-stratification probably indicates bedload transport from subaqueous, downstream-migration of 2D dunes (Miall, 1977; Allen and Marshall, 1981; Glennie and Provan, 1990). Together, the bedforms and the vertically consistent grain-size profiles are consistent with deposition in low-sinuosity, braided, sandy river systems (Miall, 1977, 1985, 2016; Schumm, 1985).

Current ripple cross-lamination within the upper, thinner and finer-grained parts may represent shallow-water deposition at the edges of bar forms, or quiescent periods with lower-energy currents.

The lithified plant remains (Fig 4.1m) and bioturbated horizons could have resulted from channel abandonment or avulsion. The thick deformed and dewatered horizons are interpreted as seismities, implying active local tectonism (Fig 4.1L) (Wizevich *et al*., 2016; Booth *et al*., 2020; Shanmugam, 2022). Also, the basal coal, mudstone lags and plant debris might have been added to the bedload by erosion of channel banks.

4.2.9 Facies association FA10: Abandoned Channel.

Description: This FA consist of, micaceous, fine to medium- grained slightly silty massive sandstones. This FA may also be interbedded with argillaceous siltstones containing laminae of coarser siltstones and sandstones and occasional mudstone drapes.

Sandstone of this FA are typically well sorted with low-angle crossbedding often associated current-ripple cross-lamination and occasional thin trough cross bedding. These sandstones may display internal flaser or lenticular bedding with deformed/slumped horizons ((Fig 4.1h) and rooted bed tops. FA10 is also characterized by disseminated and fragmented carbonized plant material and has bioturbated horizons (4.1n).

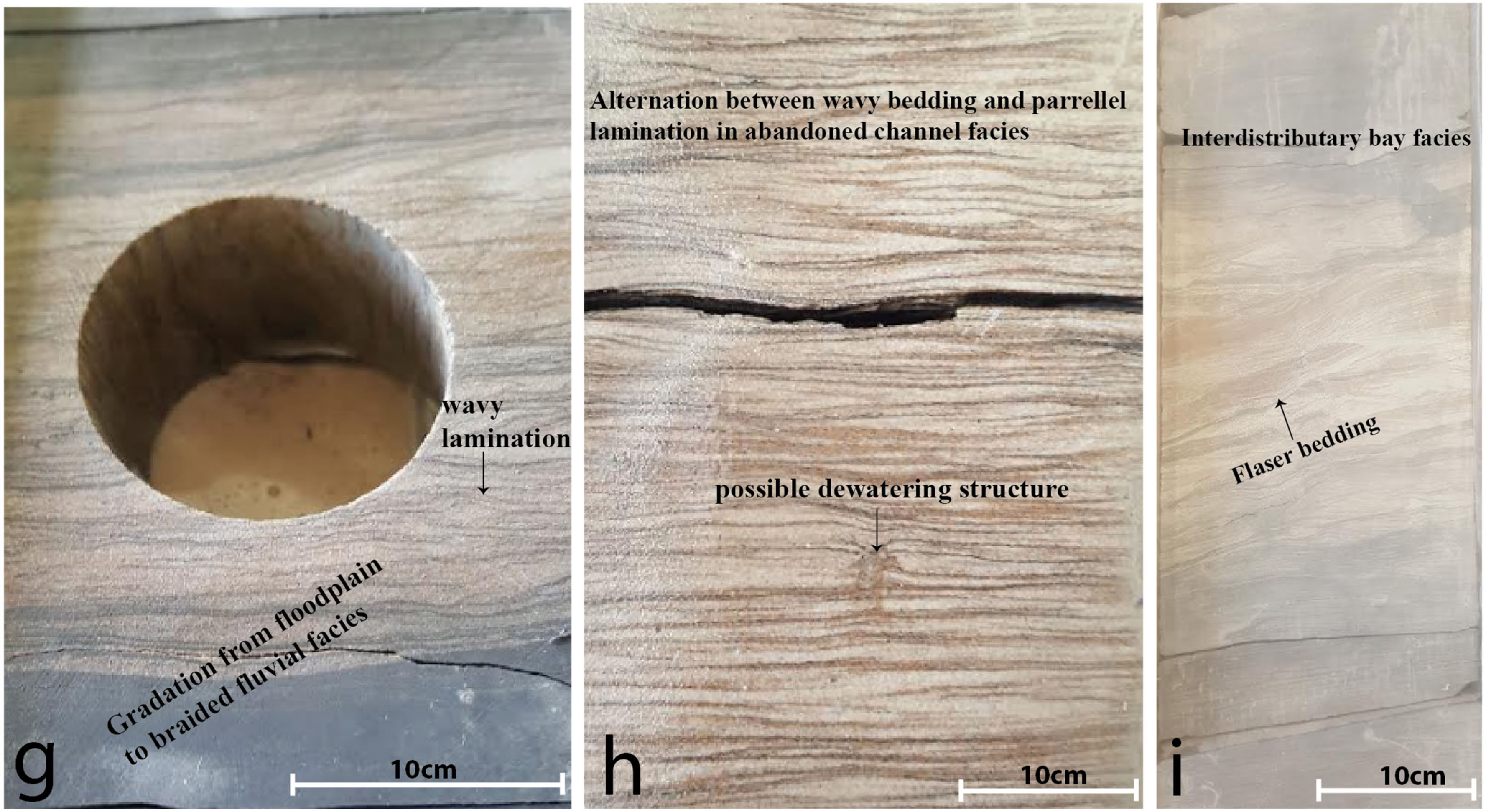

Fig 4.1 - g) *Gradational boundary from floodplain facies (FA12) to braided fluvial channel facies (FA9). Wavy ripple lamination is seen @7702.5ft;* ***h)*** *Alternation between wavy bedding and parallel lamination in the abandoned channel facies (FA10). Dewatering structure and vertical escape burrows are also seen @7737.5ft;* ***i)*** *Flaser bedding with very fine gained sandstone and small drapes of mud in the interdistributary bay (FA7) facies @7951.5ft; All photos taken from well 42/13a-6.*

This facies association is present is typically above fluvial channel facies associations (FA8 and FA9), with sharp or gradational boundaries. They can also be found sandwiched between interdistributary bay facies (FA7). They are sometimes overlain by floodplain FA12 (FA12), in which case vertical burrows penetrate down from the overlying bay fill facies.

Interpretation: FA10 represents the gradual abandonment of parts of the channel system. Abandoned channel is formed because of channel migration. As the channels migrate, parts of it may become abandoned and left behind as "Oxbow" lakes (Toonen *et al*., 2012). These lakes have a characteristic horseshoe shape that mimics a river bend which become sites for deposition of fine-grained lake sediment and these mud-plugs may form vertical/lateral permeability barriers (Leila and Moscariello, 2019; Stow *et al*., 2020; Gugliotta *et al*., 2022).

The fine grain size, thin laminations, small-scale sedimentary structure, and upward finning character indicate lower flow velocities and gradual sediment accumulation mainly by suspension fallout (Mtelela *et al*., 2016) with the mudstone (occasionally organic) and siltstone beds deposited during quiescent phases. The colonization by plants and coal development also indicates channel abandonment (Booth *et al*., 2020).

4.2.10 Facies association FA11: Crevasse splay.

Description: The close association of this facies with interdistributary bay (FA7) or floodplain facies associations (F12) is characteristic of crevasse splay deposits. They comprise fine to medium-grained, often fining-upward, moderately- to well-sorted sandstones. This FA is characterised by erosive based sandstones that are sandwiched between interdistributary bay deposits and/ or floodplain deposits or concordantly overlies floodplain deposit. In the reworked part of the splay, the cross-laminated unit is common at the base and may be overlain by a thin bed of ripple cross laminated or wavy or parallel-laminated sand (Fig 4.1j). Carbonaceous plant material is abundant throughout. Bioturbation is sparse to intense (1-5 Taylor and Goldring, 1993), and burrows, traces are widespread, consisting of both vertical and horizontal pipe burrows common.

Interpretation: A crevasse splay is a sedimentary fluvial deposit which forms when a stream breaks its natural or artificial levees and deposits sediment on a floodplain (Taylor *et al*., 2003; Bomer *et al*., 2019; Zhou *et al*., 2019; Rahman *et al*., 2022). The process that forms the splay is like the process that forms fluvial channel deposit making this facies association superficially very similar to the distributary channel facies association (FA9).

Therefore erosive-based contacts and structureless nature some of the beds in addition to the presence of climbing ripple cross lamination signifies rapid deposition from unconfined flow, and indicate high rates of sediment fallout and tractional deposition that is attributed to rapid expansion and deposition from moderate to low concentration of unconfined flows (Allen, 1973) from a nearby fluvial channel during a flooding event (Hubert and Hyde, 1982; Nichols and Fisher, 2007).

However, as water spreads onto the flood plain sediments will start to fall out of suspension as the water loses energy. The resulting deposition can create a graded deposit like the Bouma sequences. Hence the upwards development of cross stratification grading into ripple cross lamination and then parallel lamination indicates deposition by tractional bedload in a progressively lower concentration (and velocity) flow (O'Brien and Wells, 1986).

4.2.11 Facies association FA12: Floodplain and palaeosol.

Description: This facies association is dominated by friable homogenous and structureless mudstones sometimes exhibiting mud cracks and root traces. They also contain coal, crudely stratified siltstones, and very fine-grained sandstone. The mudstones are light to dark grey, green to red and occasional pink to brown and with occasional brown patches. They are typically rich in organic matter. Locally, these deposits contain abundant rootlets, burrows, and isolated calcareous nodules, siderite nodules and ferric rhizocretions. They also contain some carbonaceous debris with occasional and other indeterminate burrow traces.

In vertical session, the mudstones could be interrupted by the very fine sandstone, thin coal horizons as seen in 42/13-4 @ 7524ft and occasional carbonaceous horizons. The interrupting sandstone portions of this FA are observed to be well sorted with non- parallel and current-ripple cross-lamination which are sometimes affected by padogenesis.

Interpretation. This FA includes mixture of overbank deposits, marsh, floodplain, gravity fall out fines and mire deposits, coupled with the abundance of features interpreted as pedogenic

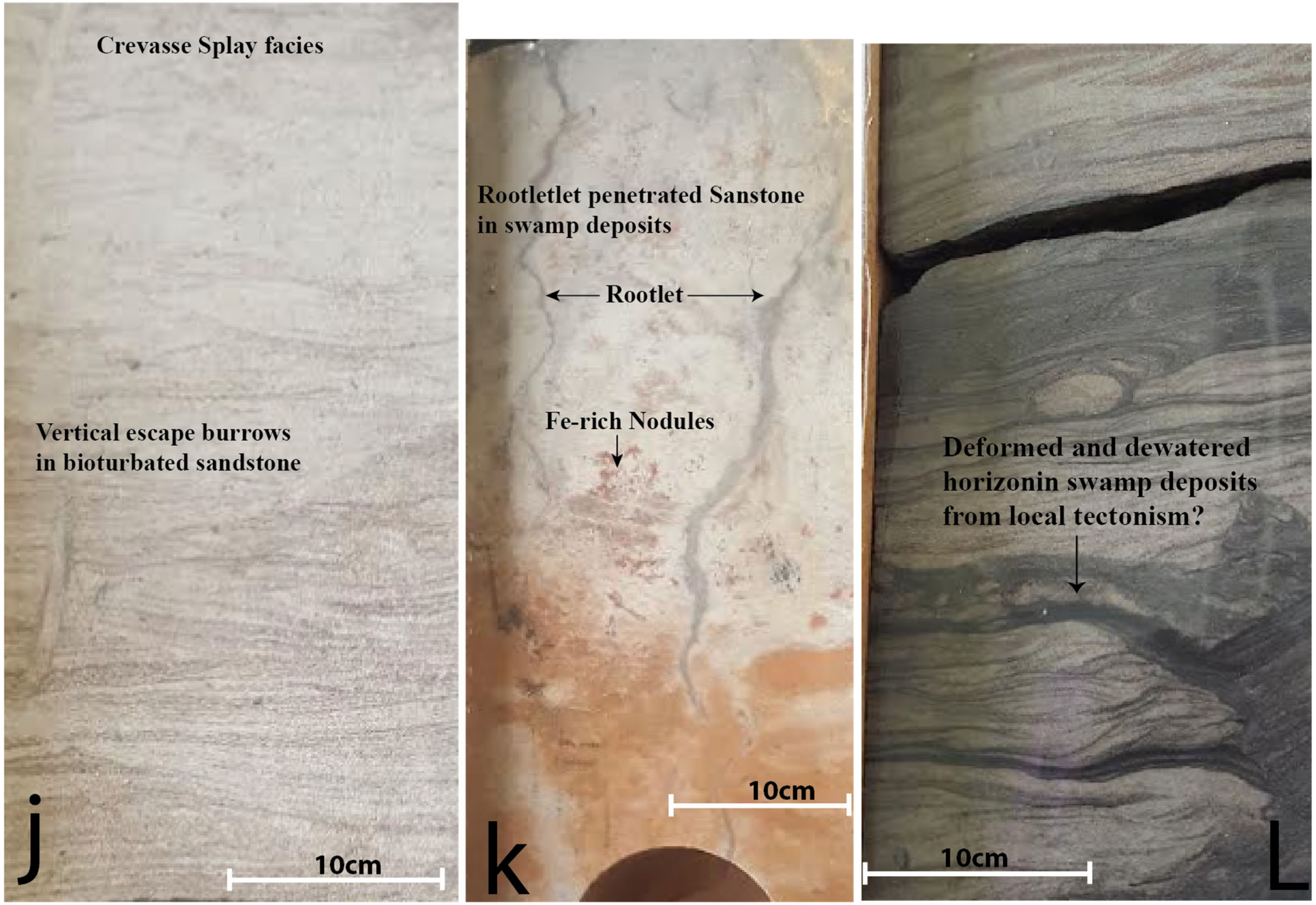

Fig 4.1- j) *Wavy bedding progressing into extensively bioturbated fine sandstone with possible vertical escape structures in (FA11) facies @7822.5ft;* ***k)*** *A rootlet penetrated sandstone that includes nodular carbonates seen in (FA12) facies @7784ft;* ***l)*** *The thick deformed and dewatered horizons probably indicating seismities, implying active local tectonism seen in (FA12) facies @7704ft. All photos taken from 42/13a-6.*

(rootlets, calcareous and siderite nodules), suggest a floodplain environment in which low-energy suspension fallout and sediment-gravity-flow deposits is developed in an upper-delta-plain environment (Mtelela *et al*., 2016). This facies association is interpreted to represent low energy sediment accumulation into small, ponded depressions, marshes in wetlands, or waterlogged floodplains. The interpretation is based on the fine-grained, lenticular nature of the sediment infill, high organic content, and the presence of abundant plant debris (Bridge, 1984; Miall, 1987; Kraus and Gwinn, 1997; Thayer and Ashmore, 2016; Yeste *et al*., 2020).

Palaeosols (Fig 4.1k) were also recognised based on fossil root traces and soil horizons (Retallack, 1988). Paleosols are ancient soils, formed on landscapes of the past (Ahmad, 1983; Reinhardt and Sigleo, 1988; Mack *et al*., 1993; Kraus, 1999; Basilici *et al*., 2009; Retallack, 2014). Since palaeosol have been buried in the sedimentary record, they are able to give clues of ancient environment. In this case it's likely that the observed fossil root formed over the long period of subaerial exposure from fluvial abandonment.

Since most coals are formed from plants that grew in and adjacent to swamps in warm, humid regions. Material derived from the plants accumulated in low-lying areas that remained wet most of the time and was converted to peat through the activity of microorganisms. Eventually, heat and pressure transformed these organic remains into coal. The presence of coal in this FA thus reflect progressive subsidence and burial of an abandoned delta lobe (Elliott, 1975; Booth *et al*., 2020).

The nodular carbonates are calcretes formed by mineral precipitation from groundwaters moving through the subsurface (Wright and Tucker, 2009; Alonso-Zarza and Wright, 2010) .

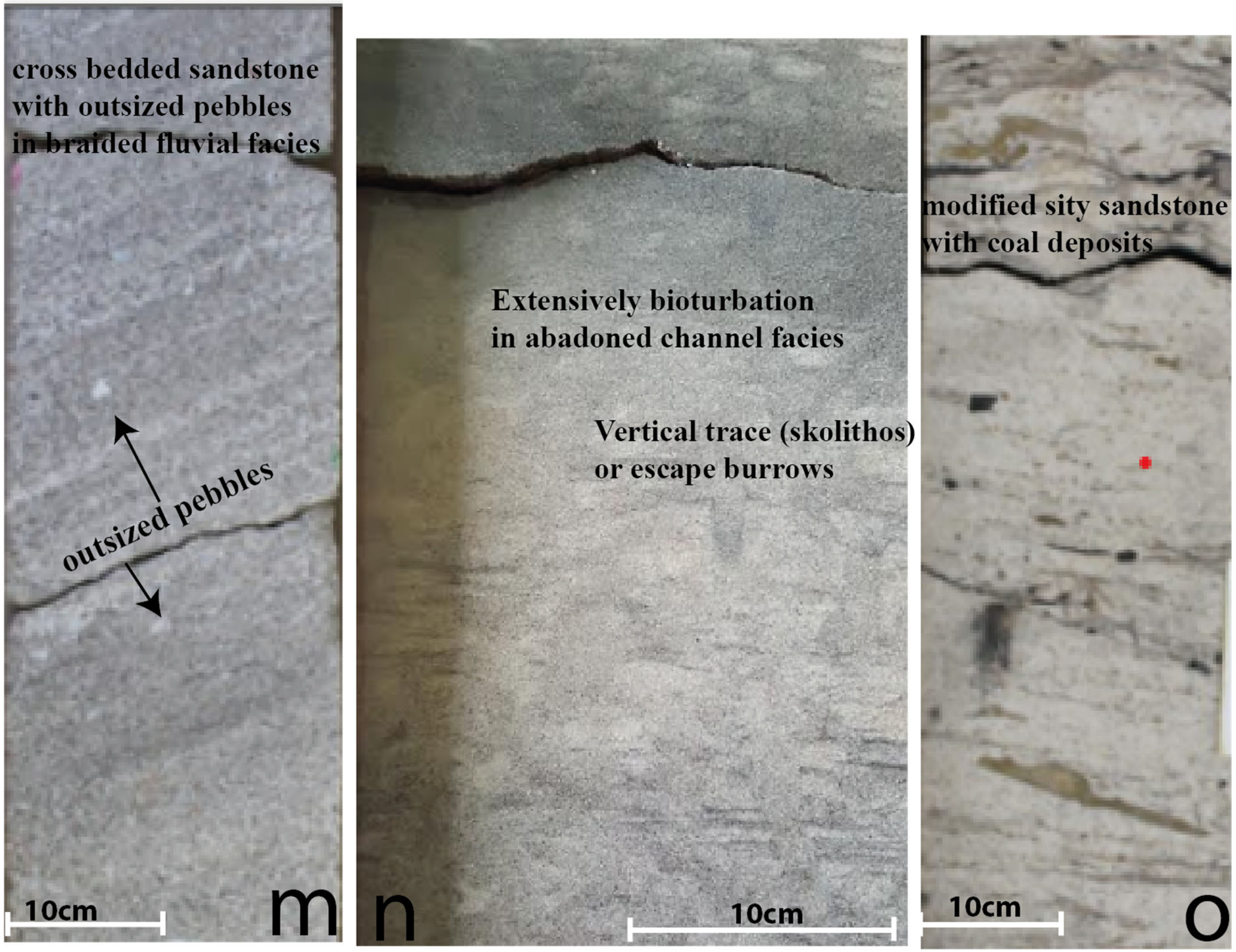

Fig 4.1- m) *cross bedded sandstones with outsized pebbles seen in (FA9) facies @ 7685ft;* ***n)*** *Extensively bioturbated micaceous very fine sandstone seen in (FA10) facies @7667.5ft , there is also a prominent vertical trace which could skolithos, diplocretarion or an escape burrow;* ***O)*** *pedogenically modified silty sandstones with coal deposits.*

4.3 Facies architecture.

The lithofacies study in this work shows that the Breagh Field is composed of mixed carbonate–siliciclastic deposits characterized by progradational clastic successions bounded between marine flooding surfaces.

By using wireline log data, core log with core plugs, seismic surveys, as well as the knowledge of geometry and architecture from analogue outcrop study in other works (Underhill, 2003; Besly, 2019; Booth *et al*., 2020; Brackenridge *et al*., 2020; Grant *et al*., 2020; Nwachukwu *et al*., 2020) it has been possible to study the Breagh Field facies architecture in both vertical and lateral directions.

4.4 Vertical architecture

In the core logs, facies associations FA1 to FA12 represent a migration from deposition in a marine to terrestrial setting, with FA1-FA5 being entirely marine and FA7 to FA12 being entirely terrestrial. During progradation, elements of each facies association (FA1 to FA12) should stack on top of each other to form a continuous depositional succession (or 'cycle'), locally known as 'Yoredale cycles'(Elliott, 1975; Johnson, 1984; Leeder, 1988; Leeder and Hardman, 1990; Chadwick *et al*., 1993; Collinson *et al*., 1993; Booth *et al*., 2020; Nwachukwu *et al*., 2020).

Each cycle consists of a thin marine limestone with coral fragments and brachiopods, succeeded by fine-grained shales and siltstones, coarsening up into fine to medium grained sandstones. In some cases, the coarsening-up intervals are capped by finning upward sequence of thin shales and coals before the next cycle. Each cycle is marked by the base of a flooding surface which is at either the base of a limestone (FA1) or a marine deposit that lies directly on top of a more proximal deposit.

Within the studied cores, the cycles typically begin with either a marine limestone (FA1) or prodelta mudstone (FA2) at the base. When it begins with marine limestone, it is followed by an upward-coarsening succession of prodelta mudstone (FA1) that grades vertically into heterolithic, planar to current-ripple cross-laminated distal delta front sands (FA5). This limestone typically includes crinoid and shell debris deposited within a fully marine setting and the top of it represents a maximum flooding surface (Fig 4.2). Sometimes, the mudstones have very little in the way of fossil material and trace fossils but includes nodules of pyrite and dolomite suggesting that deposition could have been within anoxic bottom waters (Fig 4.2-right @ 7609.3 ft – 7612.4 ft) but at other times the mudstones are highly fossiliferous and include fragments of crinoids and other fossil debris (Fig 4.1b) which are calcite cemented.

The mudstones and limestones could also be found to occur in alternation in which case, the degree of cementation increases upwards with the mudstones grading into a bioturbated micritic limestone (well 42/13-4 @ 7605.3 ft – 7608.1 ft) with trace fossils including helminthopsis and Zoophycos.

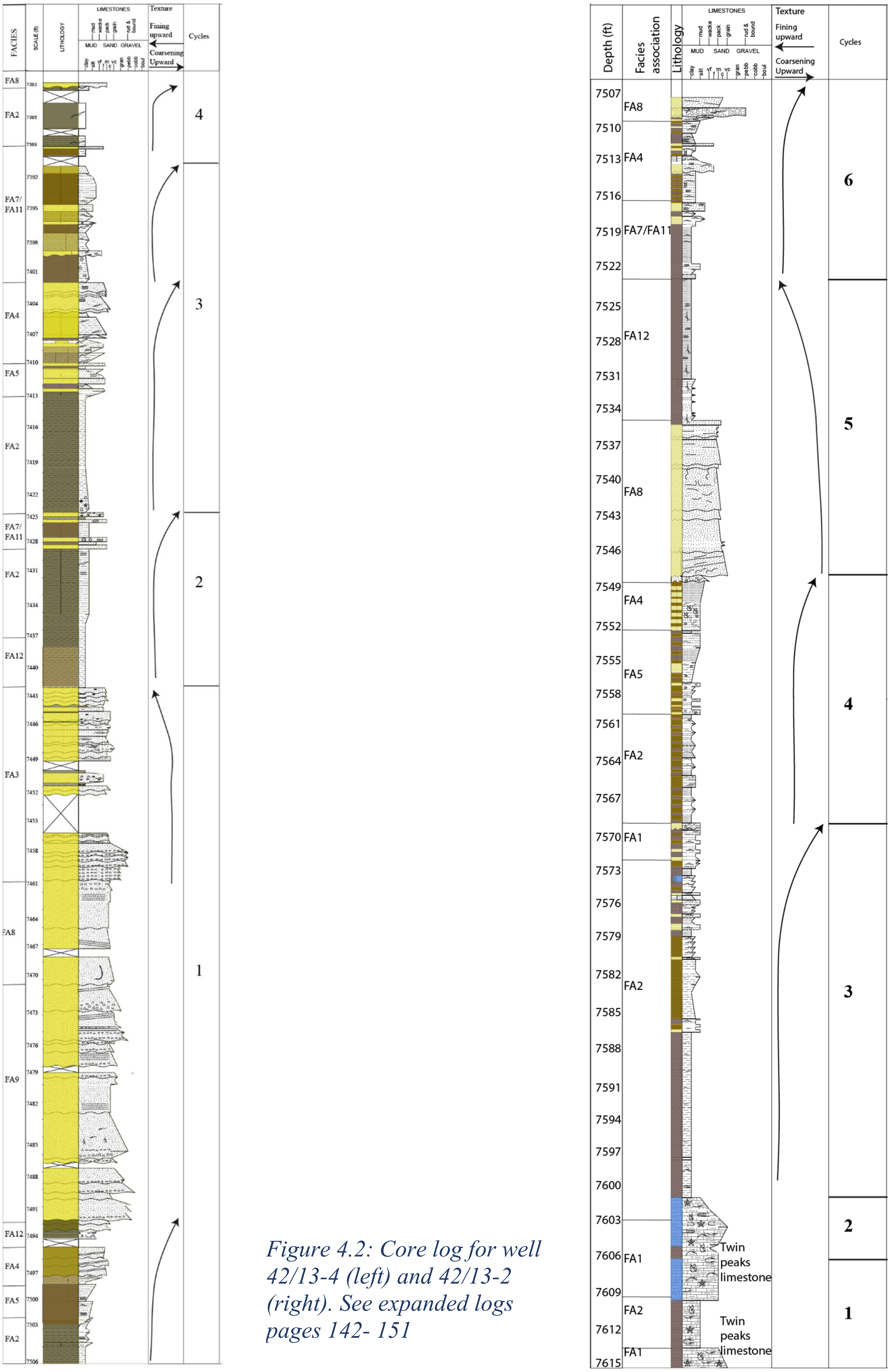

Figure 4.2: Core log for well 42/13-4 (left) and 42/13-2 (right). See expanded logs pages 142- 151

LEGEND

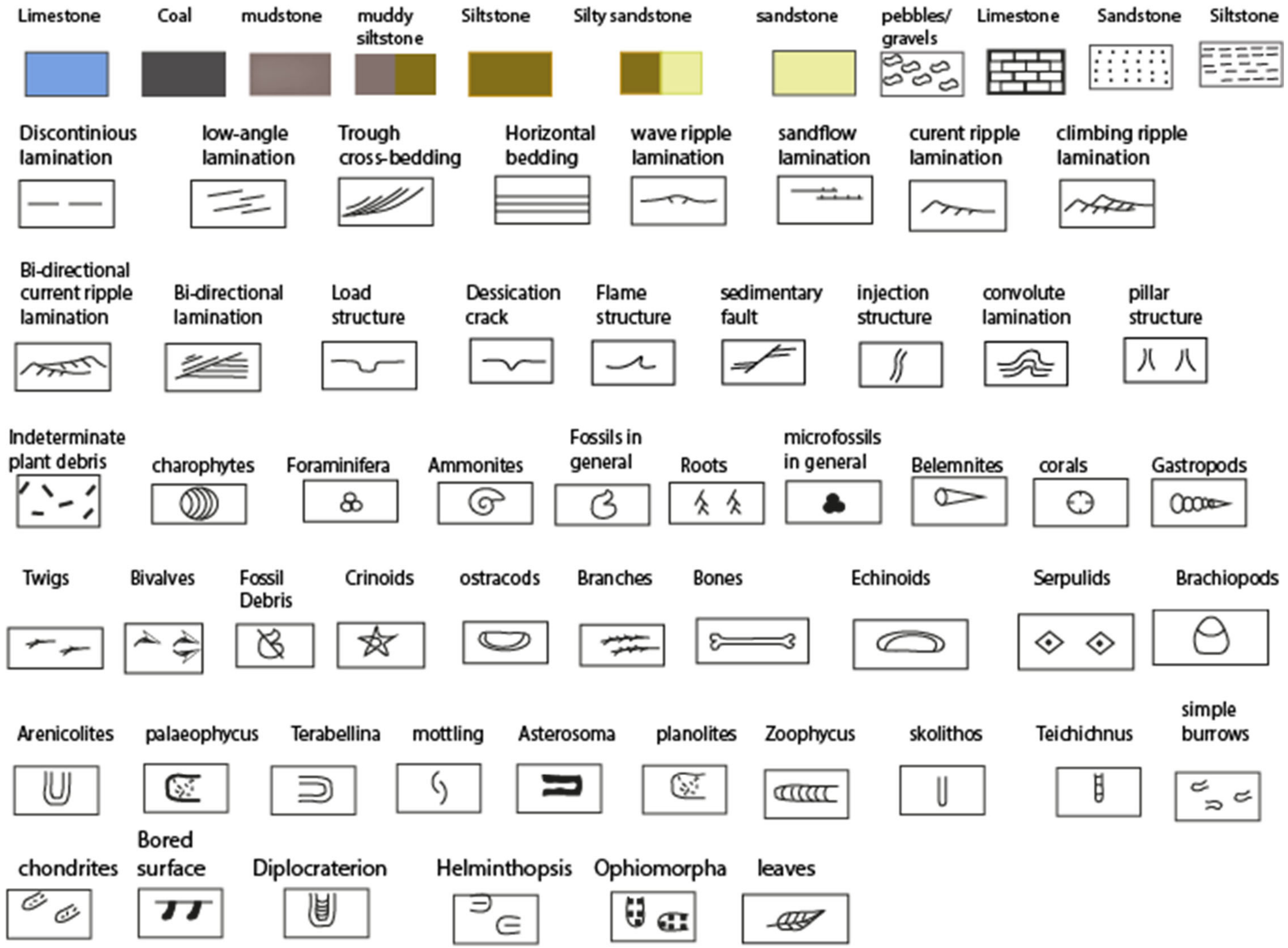

Limestone
Coal
mudstone
muddy siltstone
Siltstone
Silty sandstone
sandstone
pebbles/ gravels
Limestone
Sandstone
Siltstone
Discontinious lamination
low-angle lamination
Trough cross-bedding
Horizontal bedding
wave ripple lamination
sandflow lamination
curent ripple lamination
climbing ripple lamination
Bi-directional current ripple lamination
Bi-directional lamination
Load structure
Dessication crack
Flame structure
sedimentary fault
injection structure
convolute lamination
pillar structure
Indeterminate plant debris
charophytes
Foraminifera
Ammonites
Fossils in general
Roots
microfossils in general
Belemnites
corals
Gastropods
Twigs
Bivalves
Fossil Debris
Crinoids
ostracods
Branches
Bones
Echinoids
Serpulids
Brachiopods
Arenicolites
palaeophycus
Terabellina
mottling
Asterosoma
planolites
Zoophycus
skolithos
Teichichnus
simple burrows
chondrites
Bored surface
Diplocraterion
Helminthopsis
Ophiomorpha
leaves

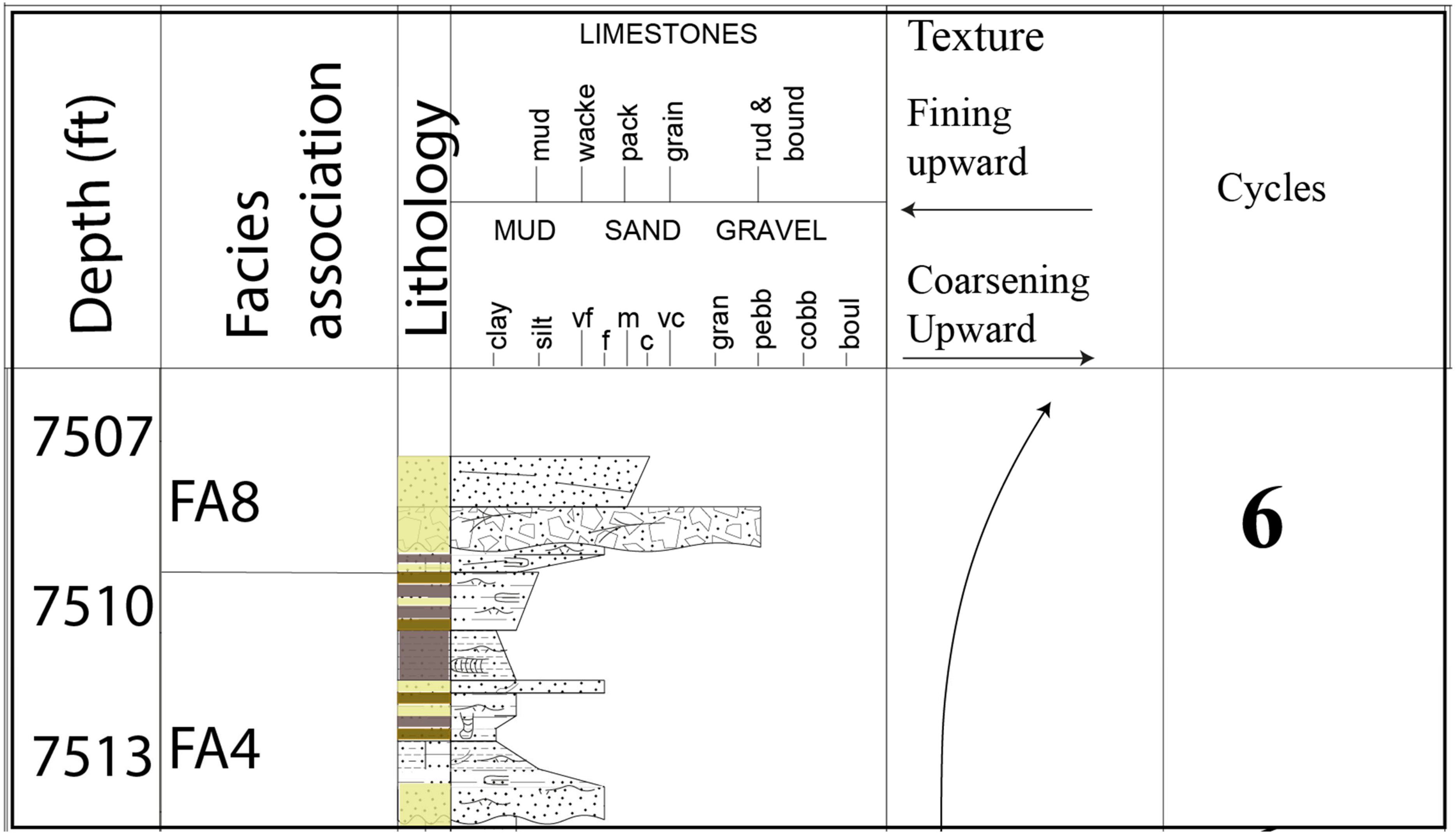
Depth (ft)
Facies association
Lithology
LIMESTONES
mud
wacke
pack
grain
rud & bound
MUD
SAND
GRAVEL
clay
silt
vf
f
m
c
vc
gran
pebb
cobb
boul
Texture
Fining upward
Coarsening Upward
Cycles
7507
7510
7513
FA8
FA4
6

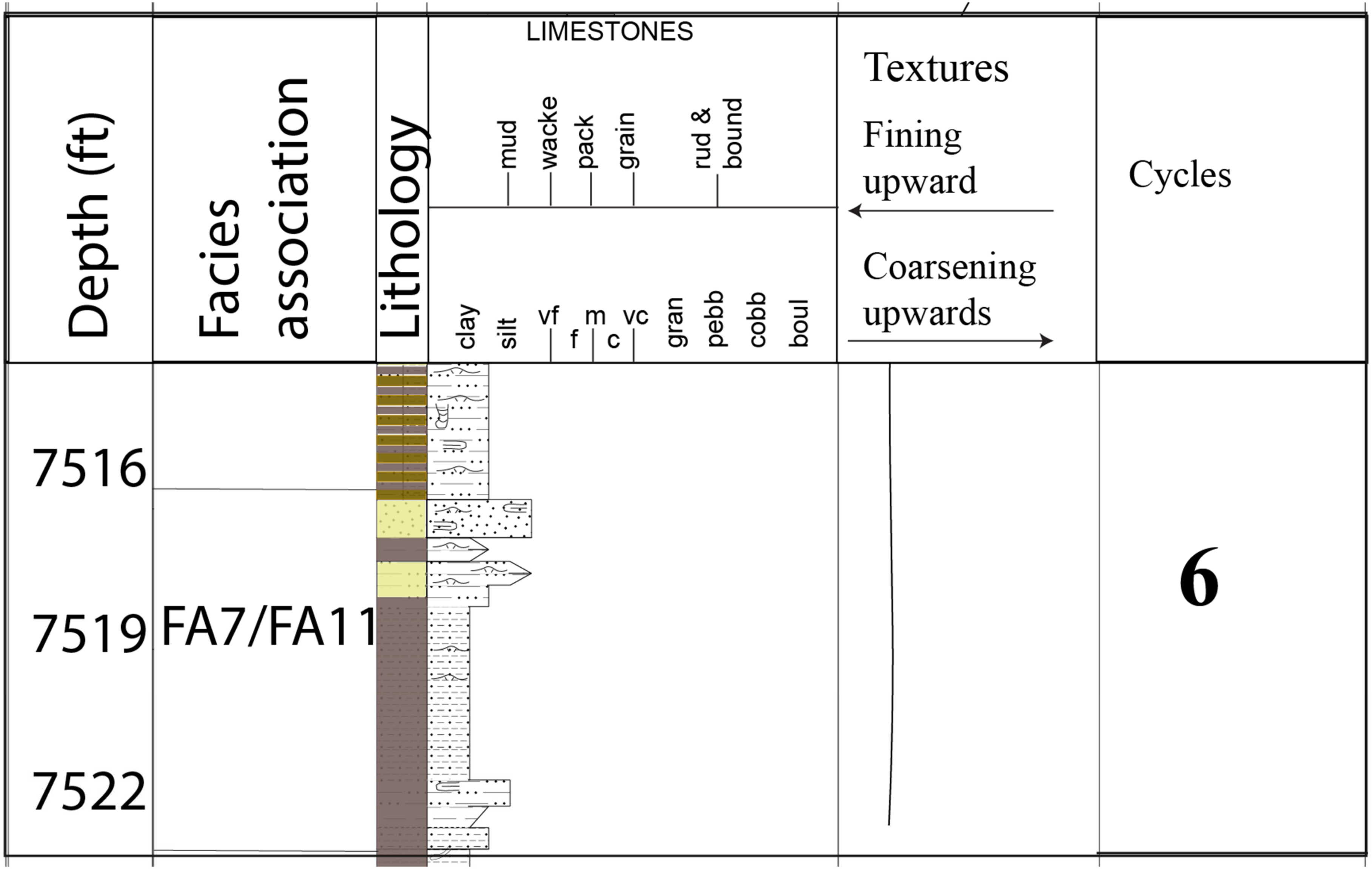
Depth (ft)
Facies association
Lithology
LIMESTONES
mud
wacke
pack
grain
rud & bound
clay
silt
vf
f
m
c
vc
gran
pebb
cobb
boul
Textures
Fining upward
Coarsening upwards
Cycles
7516
7519
7522
FA7/FA11
6

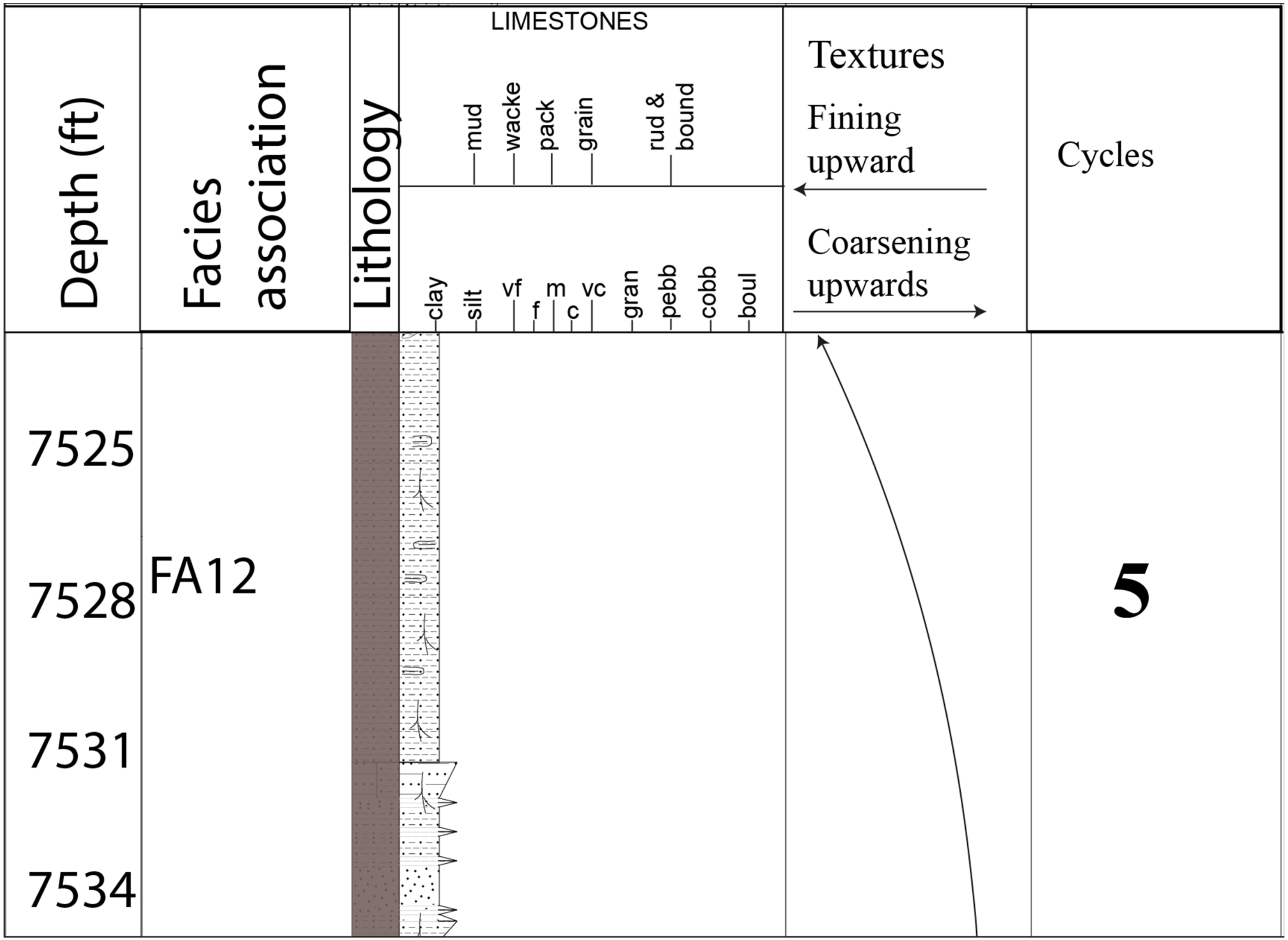

Depth (ft)
Facies association
Lithology
LIMESTONES
mud
wacke
pack
grain
rud & bound
clay
silt
vf
f
m
c
vc
gran
pebb
cobb
boul
Textures
Fining upward
Coarsening upwards
Cycles
7525
7528
7531
7534
FA12
5

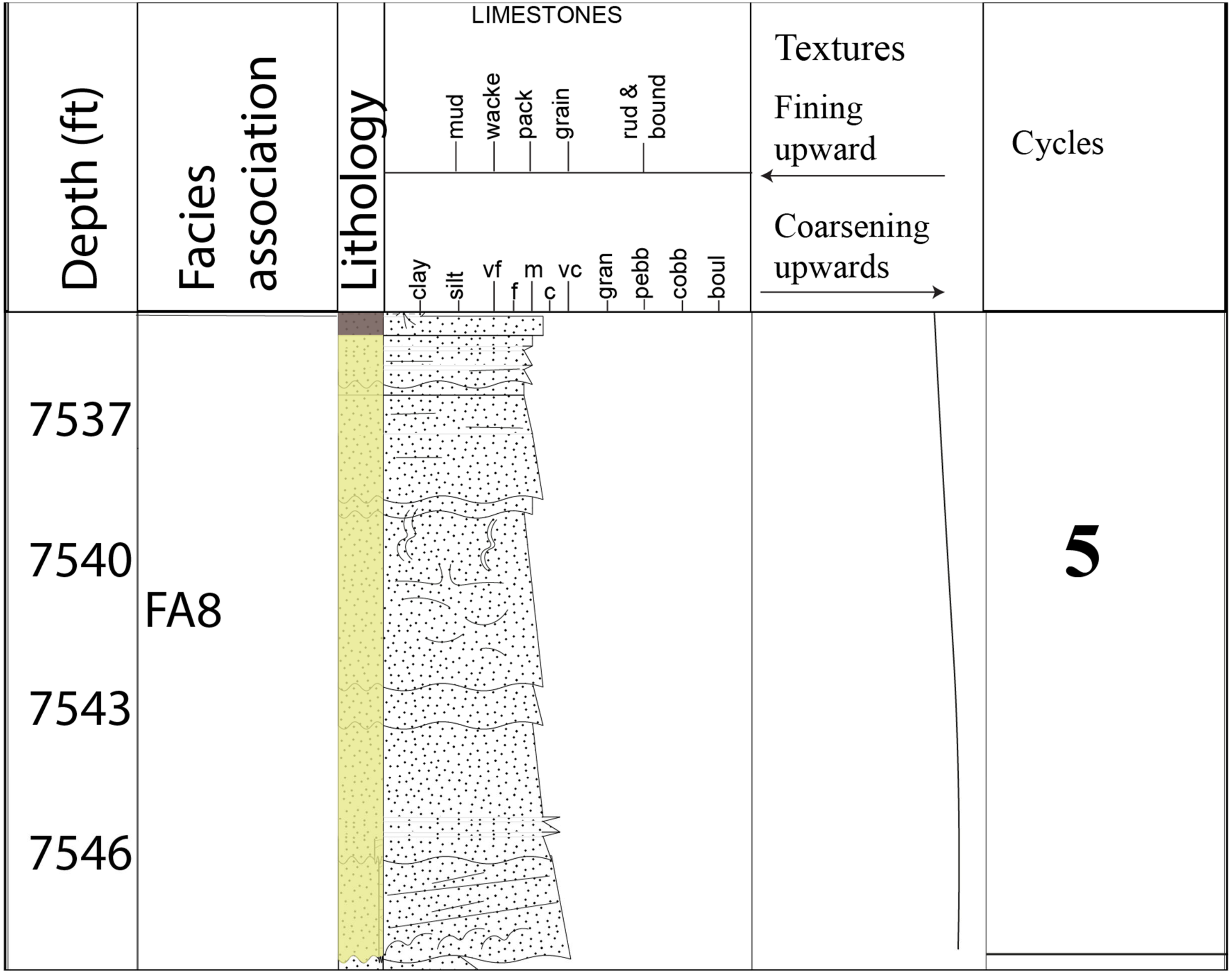
Depth (ft)
Facies association
Lithology
LIMESTONES
mud
wacke
pack
grain
rud & bound
clay
silt
vf
f
m
c
vc
gran
pebb
cobb
boul
Textures
Fining upward
Coarsening upwards
Cycles
7537
7540
7543
7546
FA8
5

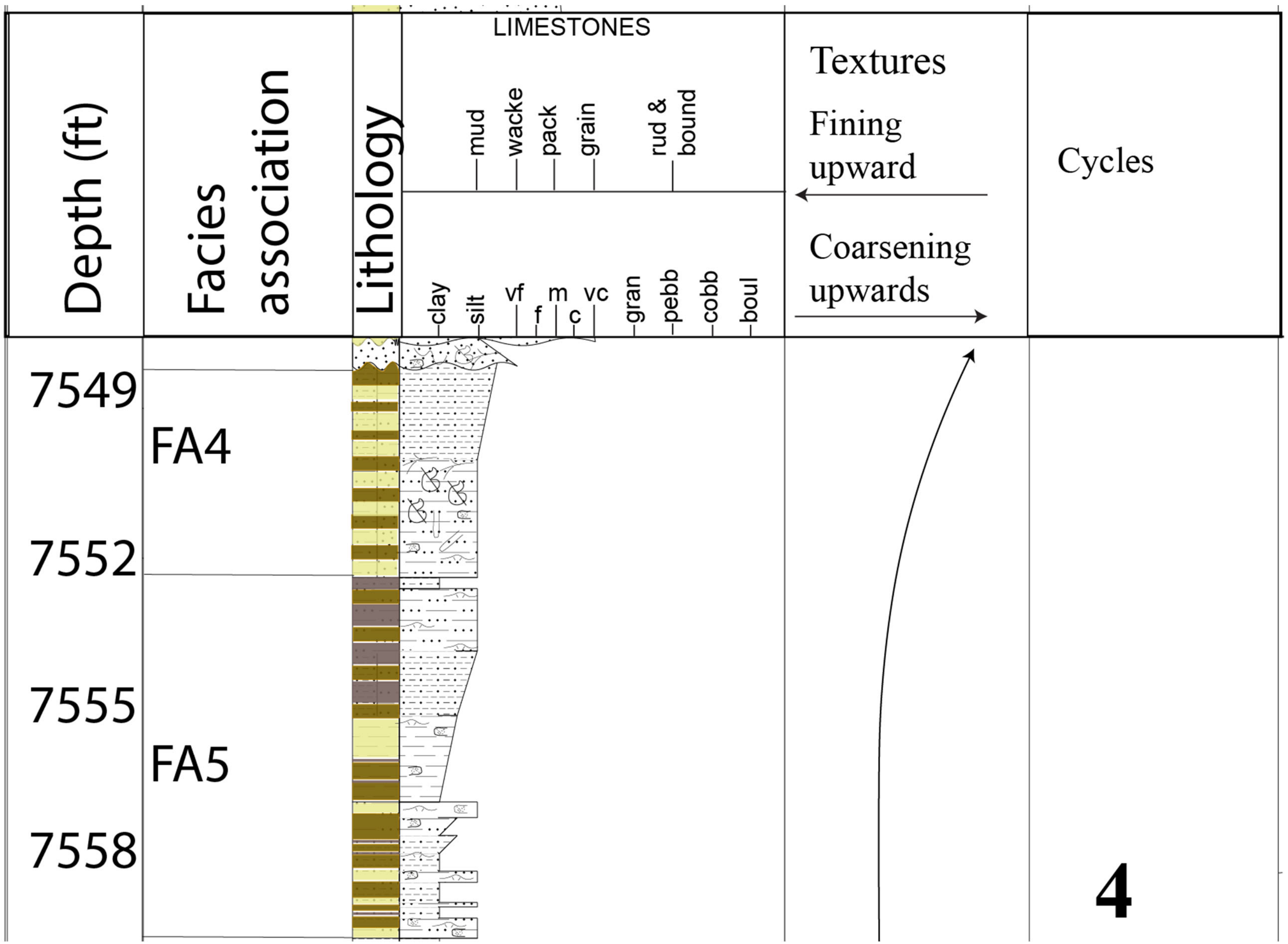

Depth (ft)
Facies association
Lithology
LIMESTONES
mud
wacke
pack
grain
rud & bound
clay
silt
vf
f
m
c
vc
gran
pebb
cobb
boul
Textures
Fining upward
Coarsening upwards
Cycles
7549
7552
7555
7558
FA4
FA5
4

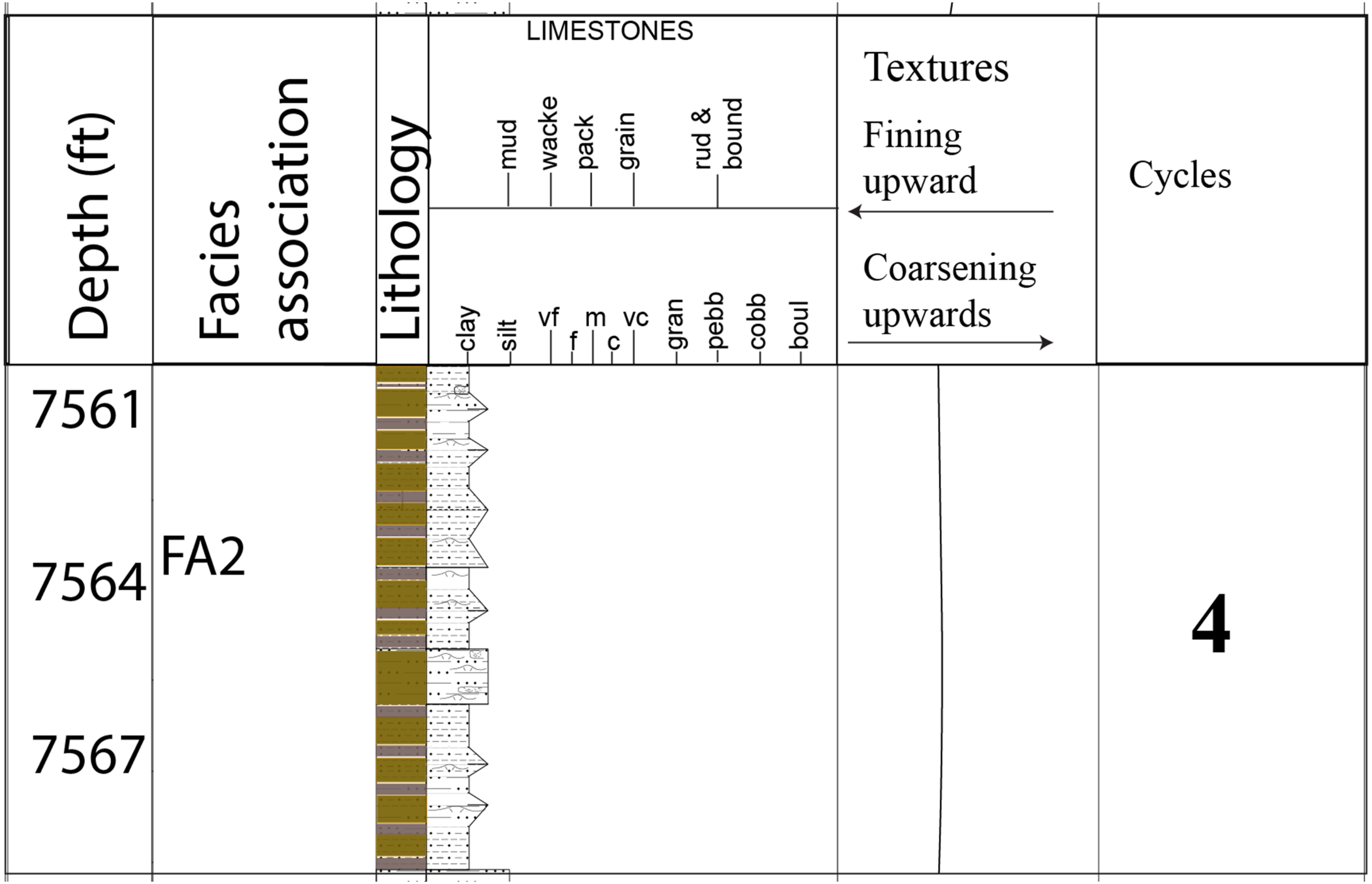
Depth (ft)
Facies association
Lithology
LIMESTONES
mud
wacke
pack
grain
rud & bound
clay
silt
vf
f
m
c
vc
gran
pebb
cobb
boul
Textures
Fining upward
Coarsening upwards
Cycles
7561
7564
7567
FA2
4

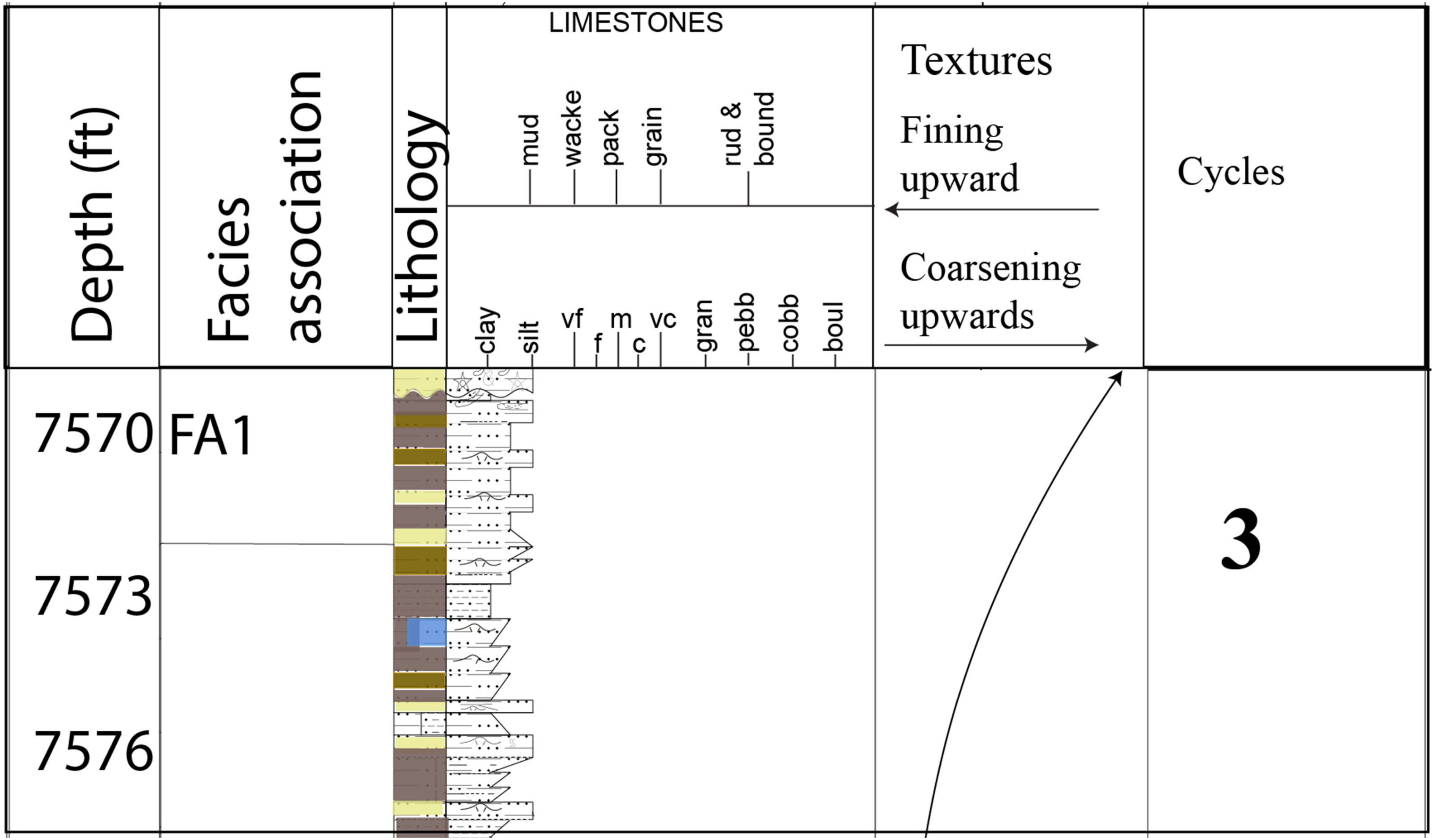
Depth (ft)
Facies association
Lithology
LIMESTONES
mud
wacke
pack
grain
rud & bound
clay
silt
vf
f
m
c
vc
gran
pebb
cobb
boul
Textures
Fining upward
Coarsening upwards
Cycles
7570
FA1
7573
7576
3

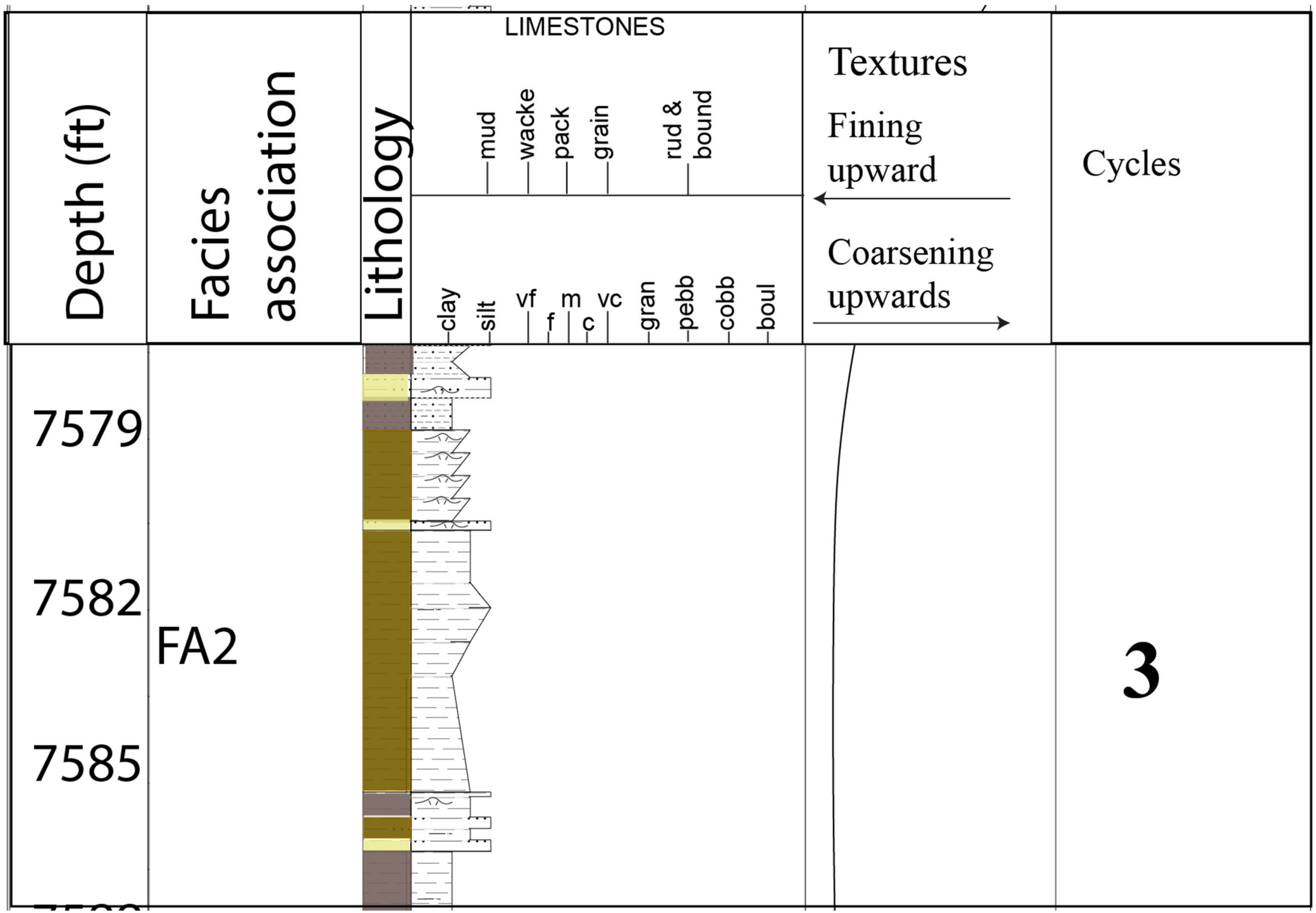
Depth (ft)
Facies association
Lithology
LIMESTONES
mud
wacke
pack
grain
rud & bound
clay
silt
vf
f
m
c
vc
gran
pebb
cobb
boul
Textures
Fining upward
Coarsening upwards
Cycles
7579
7582
7585
FA2
3

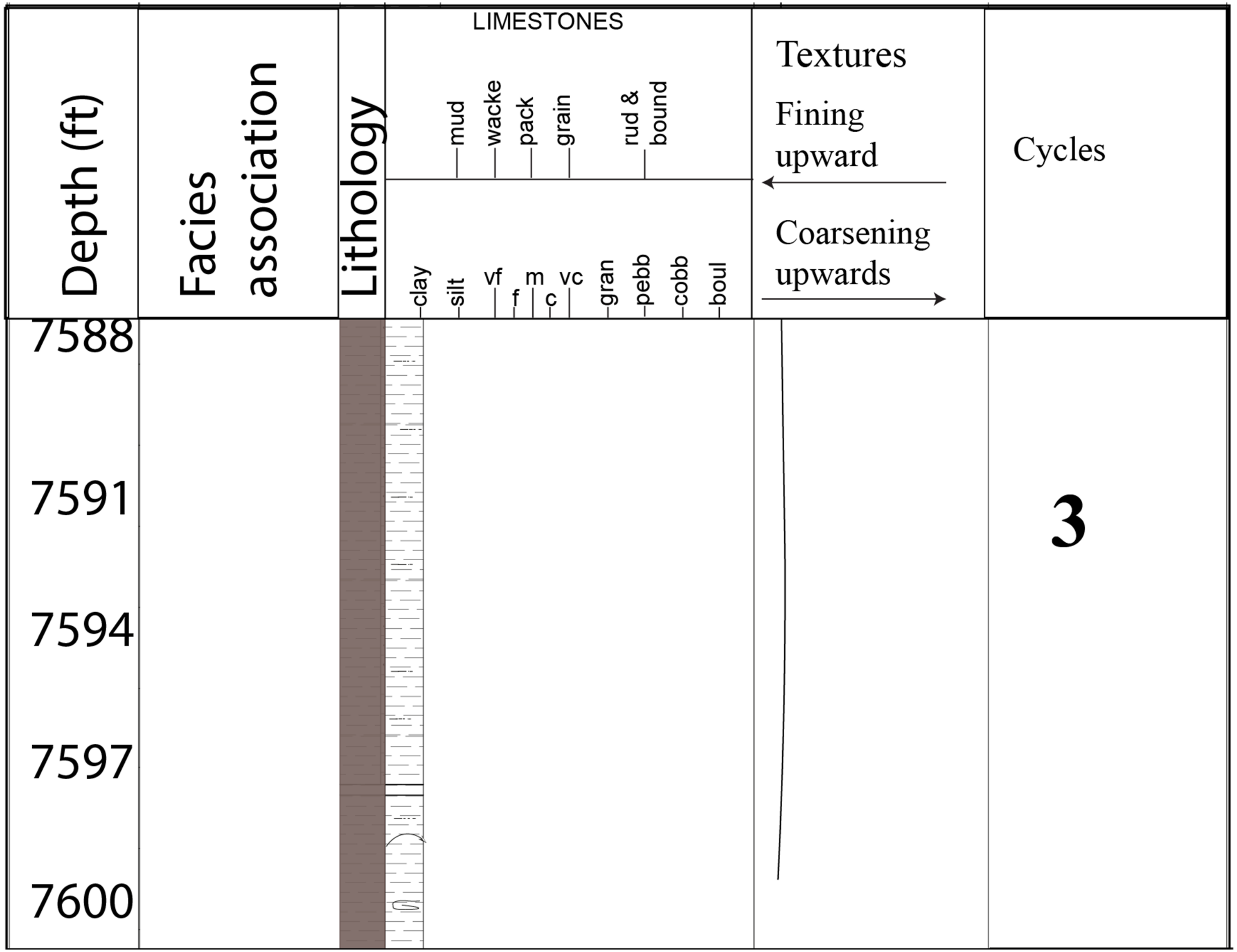
Depth (ft)
Facies association
Lithology
LIMESTONES
mud
wacke
pack
grain
rud & bound
clay
silt
vf
f
m
c
vc
gran
pebb
cobb
boul
Textures
Fining upward
Coarsening upwards
Cycles
7588
7591
7594
7597
7600
3

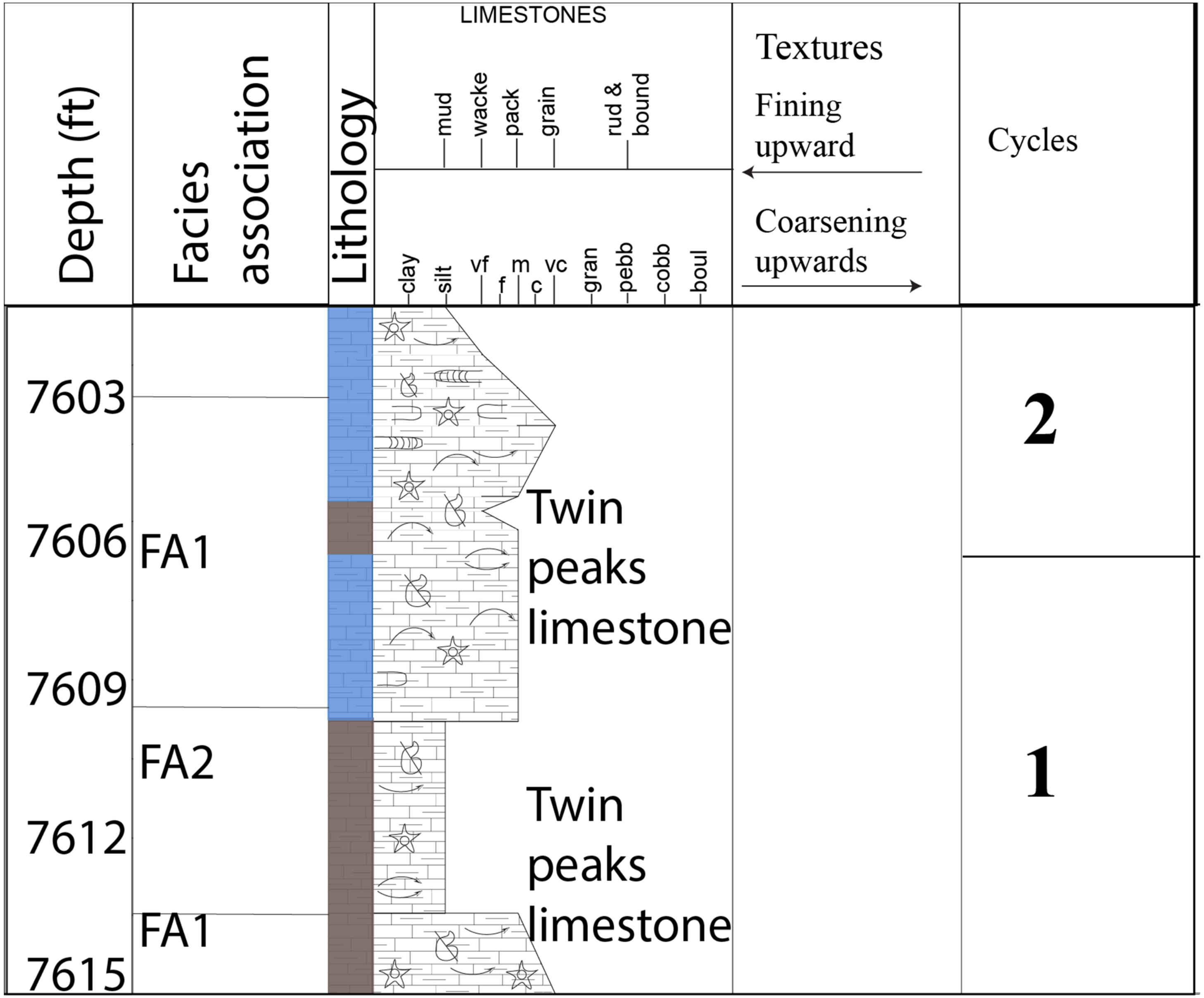

Depth (ft)
Facies association
Lithology
LIMESTONES
mud
wacke
pack
grain
rud & bound
clay
silt
vf
f
m
c
vc
gran
pebb
cobb
boul
Textures
Fining upward
Coarsening upwards
Cycles
7603
7606
7609
7612
7615
FA1
FA2
FA1
Twin peaks limestone
Twin peaks limestone
2
1

As the prodelta mudstones continue into the distal delta front sands, see 7561.5 ft in (Fig 4.2 left), thin interbeds of siltstone become increasingly common and many of them show evidence for reworking by storm generated currents. The interbedded sequence of sandstones, siltstones, and mudstones between well 7561.8 ft – 7549.5 ft in well 42/13-4 include numerous waves generated structures including hummocky and swaley cross-stratification. These sediments are essentially undisturbed by bioturbation except for some rare helminthopsis traces.

The FA4 facies are gradationally overlain by planar to current-ripple cross-laminated and cross-bedded sandstones representing proximal Delta front sands (FA5). At well 42/13-2 7551.8 ft there is a slight increase in grain size and the sandstones are extensively bioturbated with macaronichnus style fabrics and the vertical Skolithos style burrows become increasingly common towards the top of the interval (Fig 4.1n).

The delta front sands are often erosively overlain by coarser-grained distributary channel deposits (FA8). In well 42/13-4 for instance, FA8 sequence as in between 7534.8 ft – 7547.4 ft is the main reservoir sand within the cored interval and comprises medium sandstones that include pebbles and granules within some of the bed bases. Distributary channels (FA8) range in thickness from 1 to 9 m (3-29ft), with grain sizes typically ranging from fine to medium.

FA8 is also closely linked with floodplain deposit (FA12). In 7535ft (Fig 4.2 left- Well 42/13-4) the top of the sand passes abruptly into a sequence of floodplain mudstones (Fig 4.2f). FA8 facies can also be observed to be sandwiched between other channel facies before passing into the flood plain. This is seen in well 42/13-2 (Fig 4.2 right), and 42/13-6 (Fig 4.3). FA8 facies are observed to be underlain by braided fluvial channel facies (FA9) and gradually pass into distributary mouth bar facies (FA3) and or abandoned channel facies (FA10) before passing into the flood plain facies (FA12).

Other associated facies are the interdistributary bay facies (FA7) and the crevasse splay facies (FA11). Where seen they occur in close association with the flood plain facies. FA7 and FA11 can also be seen to occur in close association with distributary channel as seen in well 42/13-4 (Fig. 4.3: 7822.5ft) where interdistributary bay deposits underlie distributary channel deposits or can be seen overlying delta front sands or prodelta. The prodelta and the delta front sandstone deposits are typically rich in terrestrial plant material and coaly debris, which is a diagnostic indicator of river-influence and river-derived hyperpycnal deposits(Yan *et al*., 2020; Zavala, 2020; Jin *et al*., 2021).

The above vertical architecture shows a lack of well-organized vertical trend. This probably suggests that the river which deposited the sandstone may have been braided. Thick successions (c. 20 m/65ft) of medium- to coarse-grained sandstones with erosive bases are deposited within braided fluvial channels (FA9). The thickness is symbolic as braided river channels are known to the highest width/ thickness ratios, ranging from 50 to 1000 (Dou *et al*., 2022; Jiang *et al*., 2022).

Three regional limestone beds were recorded within the studied cores (Fig. 4.2 and 4.3). The well 42/13a-6 core contains the twin peak limestone, the Oxford Limestone and Eelwell Limestone beds. There is no recorded limestone bed in 42/13-2 but the 42/13-4 contains only the twin peak limestone bed. The base of these limestones has been marked to represent the base of the flooding surfaces where they occur.

In summary, the above facies associations and facies relationships are interpreted as river-dominated deltas (Elliott, 1975; Collinson *et al*., 1993; Gani and Bhattacharya, 2007; Bhattacharya *et al*., 2020; Booth *et al*., 2020) with minor tide- or wave-influenced components.

The multistorey nature of the sandbody, the coarseness of the bases of the sandstone and the lack of well organised vertical trends which suggest that the river which deposited the sandstone may have been braided.

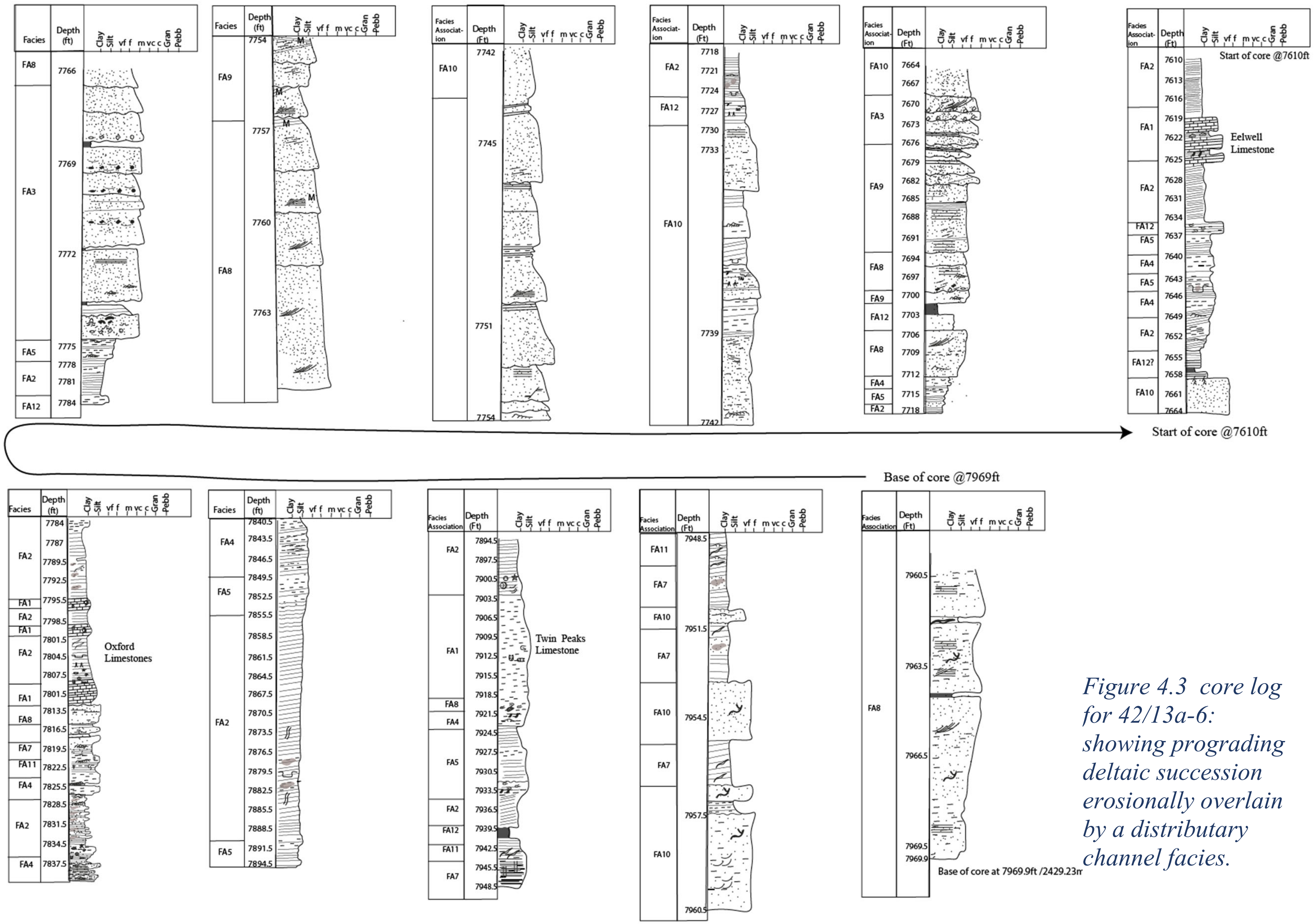

Figure 4.3 core log for 42/13a-6: showing prograding deltaic succession erosionally overlain by a distributary channel facies.

Figure 4.4: prograding deltaic succession erosionally overlain by a distributary channel in 42/13-6. See pages 157-166 for expanded cores

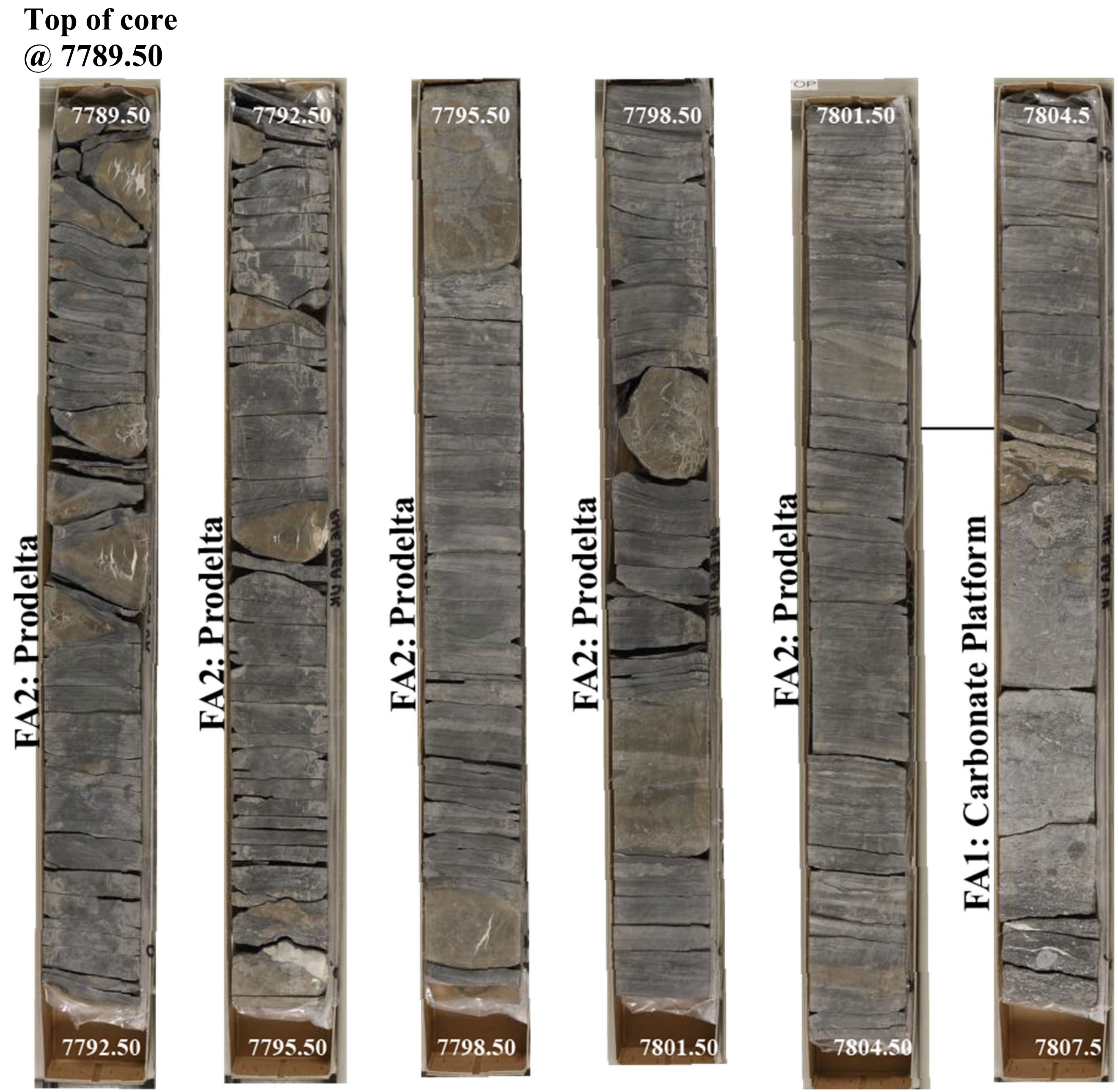
Top of core
@ 7789.50
7789.50
7792.50
7795.50
7798.50
7801.50
7804.5
FA2: Prodelta
FA2: Prodelta
FA2: Prodelta
FA2: Prodelta
FA2: Prodelta
FA1: Carbonate Platform
7792.50
7795.50
7798.50
7801.50
7804.50
7807.5


7807.5
7810.5
FA1: Carbonate Platform
7810.5
7813.5
FA1: Carbonate Platform
FA10: Abandoned Channel
7807.50
7810.5
FA1: Carbonate Platform
7810.5
7813.50
FA1: Carbonate Platform
FA10: Abandoned Channel
7813.50
7816.50
FA8: Distributary Channel
FA4
FA8

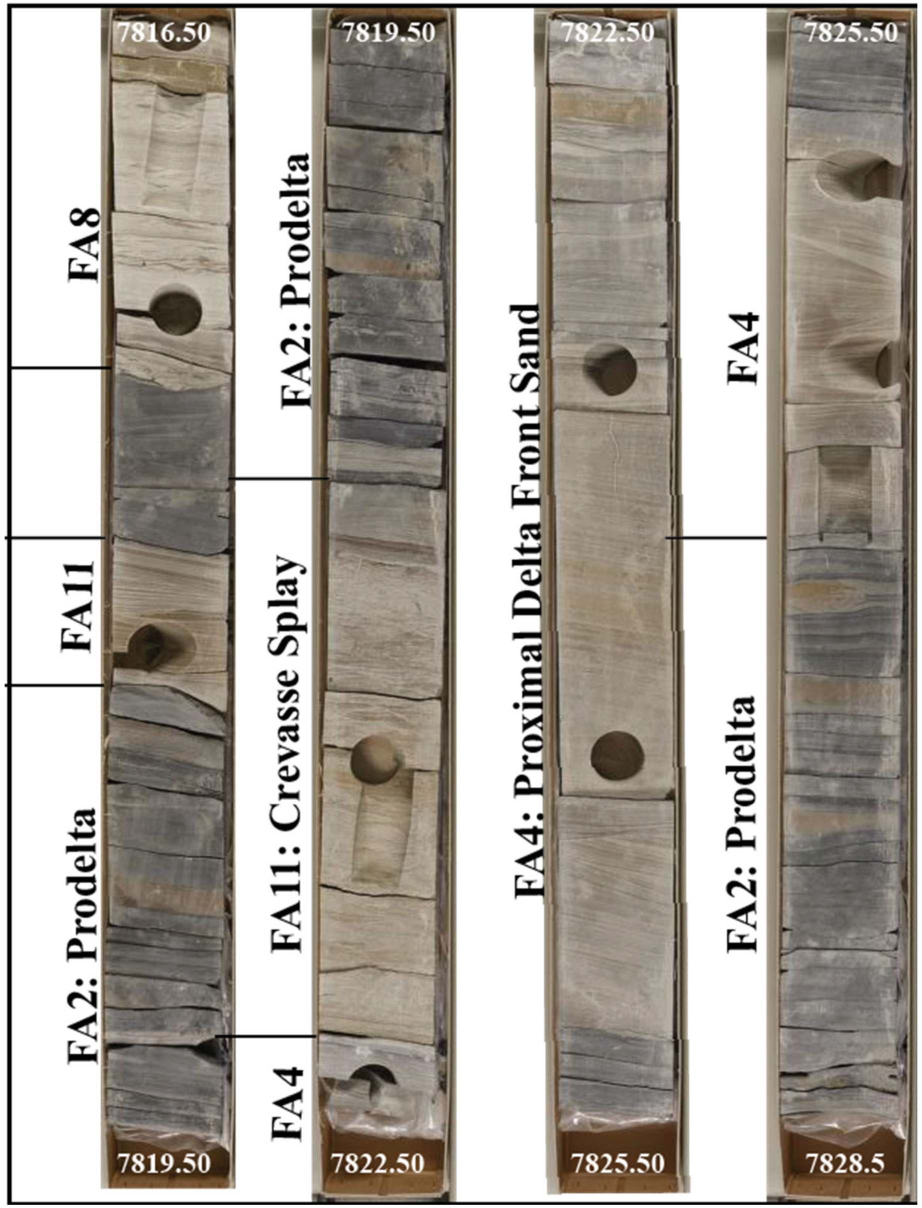
7816.50
7819.50
7822.50
7825.50
FA8
FA11
FA2: Prodelta
FA2: Prodelta
FA11: Crevasse Splay
FA4
FA4: Proximal Delta Front Sand
FA4
FA2: Prodelta
7819.50
7822.50
7825.50
7828.5

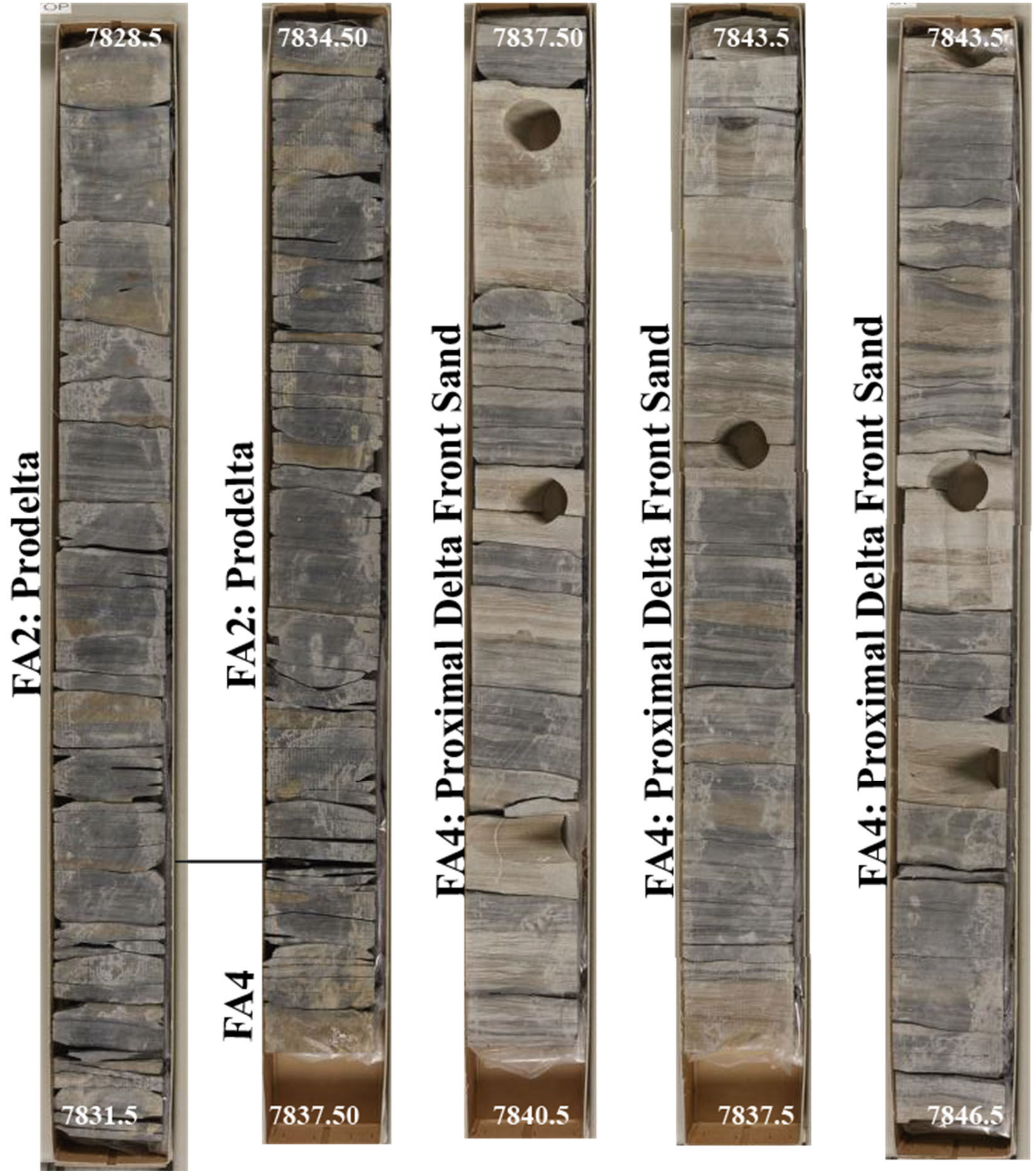
7828.5
7831.5
FA2: Prodelta
7834.50
7837.50
FA2: Prodelta
FA4
7837.50
7840.5
FA4: Proximal Delta Front Sand
7843.5
7837.5
FA4: Proximal Delta Front Sand
7843.5
7846.5
FA4: Proximal Delta Front Sand


7864.50
7867.50
FA2: Prodelta
7861.50
7864.50
FA2: Prodelta
7858.50
7861.50
FA2: Prodelta
7855.50
7858.50
FA2: Prodelta
7852.50
7855.50
FA5: Distal Delta Front Sand
7849.50
7852.50
FA5: Distal Delta Front Sand
7846.50
7849.50
FA4: Proximal Delta Front Sand


7882.50
7879.5
7876.50
7873.5
7870.50
7867.50
7864.50
FA2: Prodelta
FA2: Prodelta
FA2: Prodelta
FA2: Prodelta
FA2: Prodelta
FA2: Prodelta
FA2: Prodelta
7885.50
7882.50
7879.50
7876.5
7873.50
7870.50
7867.50

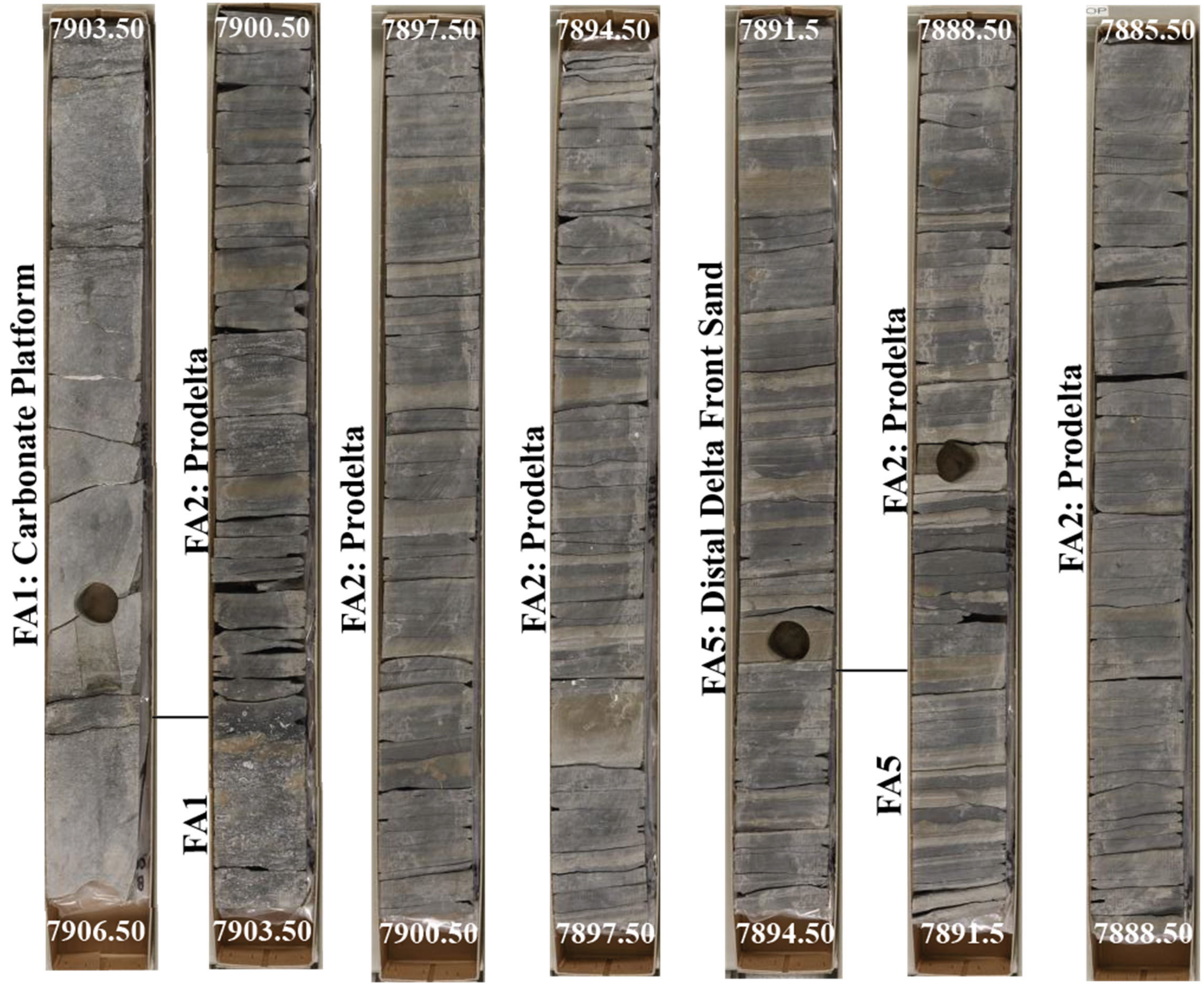
7903.50
7906.50
FA1: Carbonate Platform
7900.50
7903.50
FA2: Prodelta
FA1
7897.50
7900.50
FA2: Prodelta
7894.50
7897.50
FA2: Prodelta
7891.5
7894.50
FA5: Distal Delta Front Sand
7888.50
7891.5
FA2: Prodelta
FA5
7885.50
7888.50
FA2: Prodelta

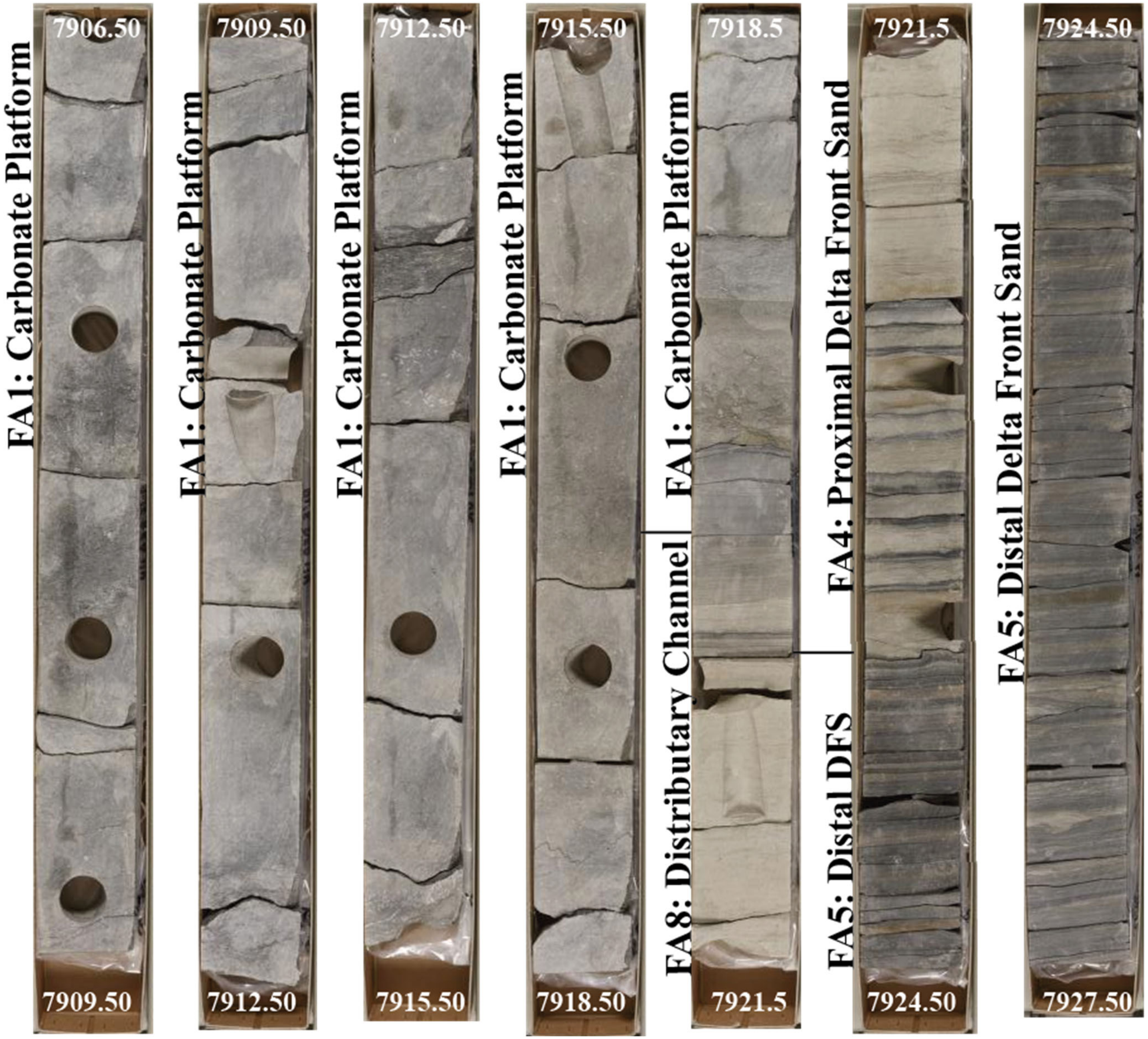
7906.50
7909.50
FA1: Carbonate Platform
7909.50
7912.50
FA1: Carbonate Platform
7912.50
7915.50
FA1: Carbonate Platform
7915.50
7918.50
FA1: Carbonate Platform
7918.5
7921.5
FA1: Carbonate Platform
FA8: Distributary Channel
7921.5
7924.50
FA4: Proximal Delta Front Sand
FA5: Distal DFS
7924.50
7927.50
FA5: Distal Delta Front Sand


7927.50
FA5: Distal Delta Front Sand
7930.50
7930.50
FA5: Distal Delta Front Sand
7933.50
7933.50
FA2: Prodelta
7936.50
7936.50
FA2: Prodelta
7939.50
7939.50
FA12: Flood plain
7942.5
7942.50
FA7: Interdistributary bay
7945.50
7945.50
FA7: Interdistributary bay
7948.50

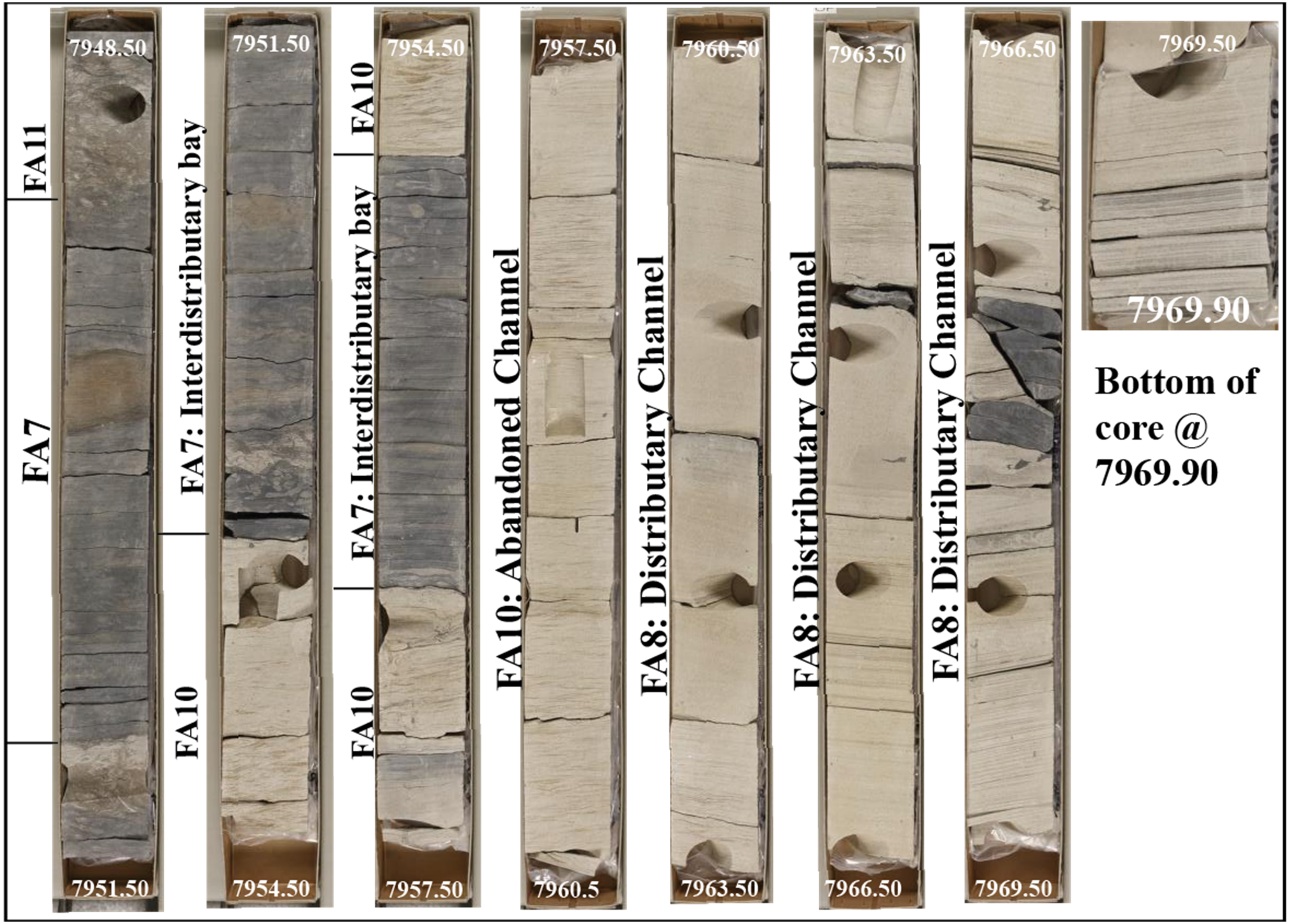
FA11
FA7
FA7: Interdistributary bay
FA10
FA10
FA7: Interdistributary bay
FA10
FA10: Abandoned Channel
FA8: Distributary Channel
FA8: Distributary Channel
FA8: Distributary Channel
7948.50
7951.50
7951.50
7954.50
7954.50
7957.50
7957.50
7960.5
7960.50
7963.50
7963.50
7966.50
7966.50
7969.50
7969.50
7969.90
Bottom of core @ 7969.90

4.5: Depositional environment.

The facies associations described and interpreted above indicate deposition in a reoccurring deltaic system (Fig 4.2, 4.3 and 4.4). Eleven facies association representing four distinct depositional environments (open marine, delta front, lower delta plain and upper delta plain) have been identified from the cores of the Breagh Field.

These deposits are composed of coarsening-upward clastic ‘cycles’, each characterized by a prograding siliciclastic succession between marine flooding events normally defined by a limestone bed or mudstone. The sedimentary sequences commence with either prodelta mudstones or marine limestone and coarsen-upward to channels sands through delta front siltstones and very fine sandstones, although some sequences only reach a lower shoreface setting before being flooded.

The upward-coarsening sequences indicate repeated filling of interdistributary bays, with the swamps and coals marking periods of emergence. The presence of marine trace fossils and body fossils indicates that these bays were connected to the sea, but the relatively small scale of the sequences suggests that the bays were relatively shallow perhaps only a few feet deep.

The presence of very fine sandstones and siltstones that are generally wave ripple laminated and occasional hummocky cross-stratified within the delta front facies and margins of the distributary channel facies demonstrate that the depositional setting was subjected to storm waves.

The thick interval of cross-bedded channel sandstone like that in (well 42/13-4 from 7451.3' and 7492.9' and 42/13-2 from 7549-7535ft) represents a major stacked fluvial channel sandbody. As earlier noted, the multistorey nature of the sandbody, the coarseness of the bases of the sandstone and the lack of well-organized vertical trends suggests that the river which deposited the sandstone may have been braided. The scale of the sandstone and its possible braided nature indicate a proximal position in the fluvio-deltaic environment (Fig 4.5) (Zhu *et al*., 2016; Booth *et al*., 2020).

Detail analysis of the studied cores as well as the sedimentary architecture and recent biostratigraphy from onshore sequences (Collinson *et al*., 2005; Grant *et al*., 2020; Nwachukwu *et al*., 2020) suggest that the depositional process in Breagh field area is controlled by both autocyclic and allocyclic process. Historically, 'cyclicity' in deltaic sediments was attributed mainly to autocyclic processes (Morozova, 2022), that is those, such as avulsion (Elliott, 1975) and delta switching (Roberts, 1997; Coleman *et al*., 1998; Goodbred and Kuehl, 2000; Roberts *et al*., 2020) which are the result of natural fluvio-deltaic processes but studies show that delta progradation can also be controlled by a combination of autocyclic and allocyclic processes (Kim and Lee, 1998; Cecil, 2003, 2013).

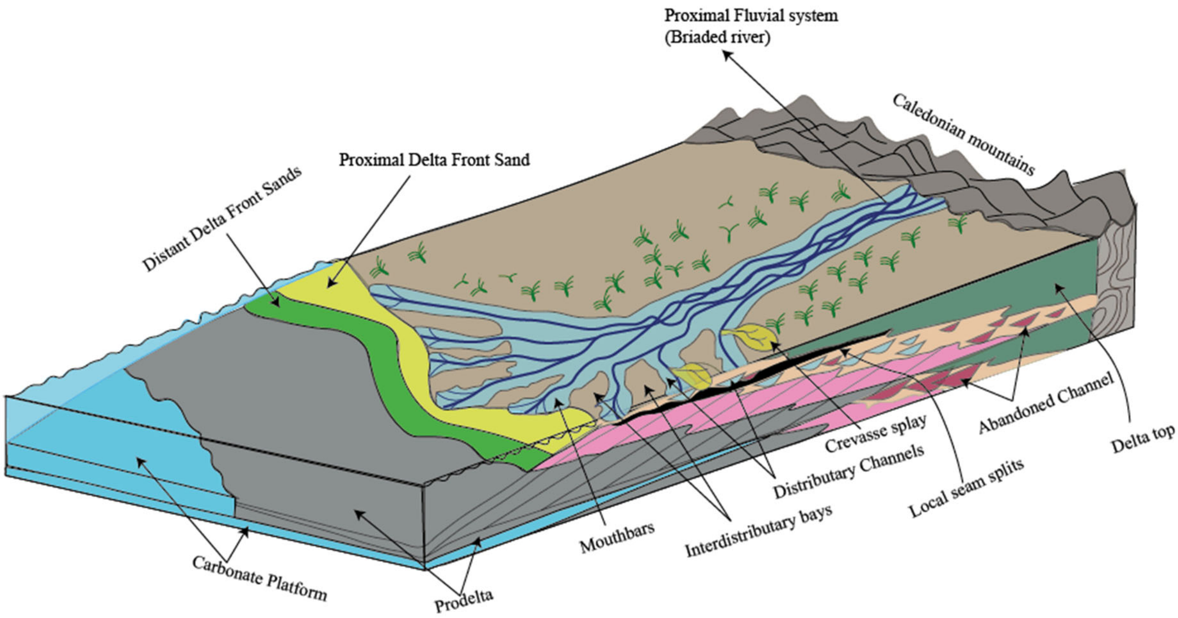

Figure 4.5: Conceptual model of the Breagh field depositional environment depicting maximum progradation.

Stratigraphic correlations of thicker limestone beds from Nothumberland coast to the offshore area, show that the Oxford limestone can be correlated laterally from Nothumberland coast to the Breagh gas field area. The Eelwell limestone can be correlated laterally from the Breagh gas field area to the Cheviot and Alston block. It is most likely that these laterally extensive limestone would record eustatic sea level rises as opposed to autocyclic process thus candidate maximum flooding surfaces (Fig 4.8).

In addition, several marine horizons have been identified, both based on marine trace fossils and body fossils. The trace fossils include *Teichichnus, Rhizocorallium,* and probable *Thallasinoides, Chondrites, Planolites* and *Skolithos* and generally occur near the base of FA2 or in FA1 and include brachiopods, and bivalves and crinoids. These marine horizons, which commonly overlie rootletted intervals or thin coals, clearly represent marine incursions over previously emergent sub-environments which have been attributed to glacioeustatic rises in sea level (proprietary well data: British Geological Survey, 1997a, 1997b).

It is most likely that these limestones and mudstones which mark the maximum flooding surfaces were deposited during a period of considerable fluctuations in sea level(Stephenson *et al*., 2008), probably glacioeustatic in origin with sea level fluctuating by tens of metres. Where deposition was taking place in areas of low relief, sea level rises would have flooded large areas of land, producing events that can be correlated over great distances. As the coastal areas were flooded, the shoreline retreated towards the sediment source and the basinal waters became fully marine. When the high stand was reached the rivers started building deltas into the basin and the shoreline slowly prograded.

Taking well 42/13-4 for instance the most obvious changes in facies in the cored interval occur at the base and top of the major stacked channel sandstone. These clearly represent, respectively, a major seaward and landward shift in facies. The seaward shift in facies at the base of the channel sandstone at 7492.9’ represents a marked progradation of relatively proximal fluvial facies over the lower delta plain. It is not clear whether this progradation represented merely the gradual seaward advance of the fluvio-deltaic system or may have been a 'forced regression' produced by a fall in relative sea level. The bioturbated interval of FA12, which overlies the channel sandstone at 7441.3' (driller’s depth), represents a major transgression, and the slow deposition rate which accompanied this transgressive event is mirrored in the siderite cementation of this interval.

This major shifts in facies, which occur at 7492.9' and 7451.3' (driller’s depth), at the base and top of the major stacked fluvial channel sandstone thus represent a major progradation (possibly a 'forced regression') followed by a major transgression.

Such transgressive events could also be produced by autocyclic processes such as through compaction following abandonment of minor delta lobes. In the pre- modern and modern Mississippi Delta, as many as fifteen discreet major delta lobes have formed, then been abandoned and either reworked or drowned, in the last 6000 years (Frazier, 1967; Penland *et al*., 1988; Stephenson *et al*., 2008; Blum and Roberts, 2012). In the case of the Mississippi, abandonment is felt to be due to autocyclic processes (e.g., channel switching).

4.6 Lateral correlation and further reservoir prospectivity.

Lateral correlation of channel belts within the Breagh Field has been made possible by chemostratigrpahic and biostratigraphic markers (see discussed in reservoir above) however, lateral correlation and reservoir prediction away from Breagh area remains a challenge due to factors such as structural complexity posed by Mesozoic and Cenozoic tectonic activities coupled with halokenesis (discussed earlier in chapter 2 and trap above) which makes subsidence and uplift histories difficult to reconcile.

Other challenges revolve around the variable erosional level beneath the BPU. As discussed earlier, the primary reservoir in the Breagh Field is the thick (20-50 ft) massive, stacked fluvial channel sands contained in two discrete intervals below the BPU at Zone 1 and Zone 3 very similar to the stacked, braided fluvial channel deposits exposed onshore (Besly, 2019; Booth *et al*., 2020; Grant *et al*., 2020; Nwachukwu *et al*., 2020). Although the channel sands probably form channel belts that could be several kilometres wide and thick enough to be resolvable with modern 3D seismic (Nwachukwu *et al*., 2020) however, where well separations are more than c. 2–7 km in the Breagh area, the channel belt may not directly correlate. For instance, while the Oxford Limestone which overlies the primary reservoir interval in the Breagh (Fig 4.8) is correlatable from the Breagh to the Northumberland coast, the Eelwell Limestone which overlies the reservoir sequences within the onshore sequences has been mostly removed by the BPU in the offshore sequences and therefore absent in Breagh area. As such, it is unlikely that the Northumberland fluvial channels form part of the same channel belt as those interpreted in the Breagh.

The implication for the absence of the Eewell limestone in the Breagh highlights the important role that incision by the BPU has in eroding and truncating the reservoir bearing Visean sequence in Breagh, which could imply that perspectivity of the Visean in other areas of the SNS is likely to be in part reliant upon the level of BPU erosion. Within the SNS area itself, chances for better correlation seem to improve, although other challenges become prominent.

Interpretation of a subset of the PGS MegaSurvey 2015 and the INEOS Lochran 3D surveys (Grant *et al*., 2020) - see Fig 4.6 and 4.7a & b for more knowledge of the area.

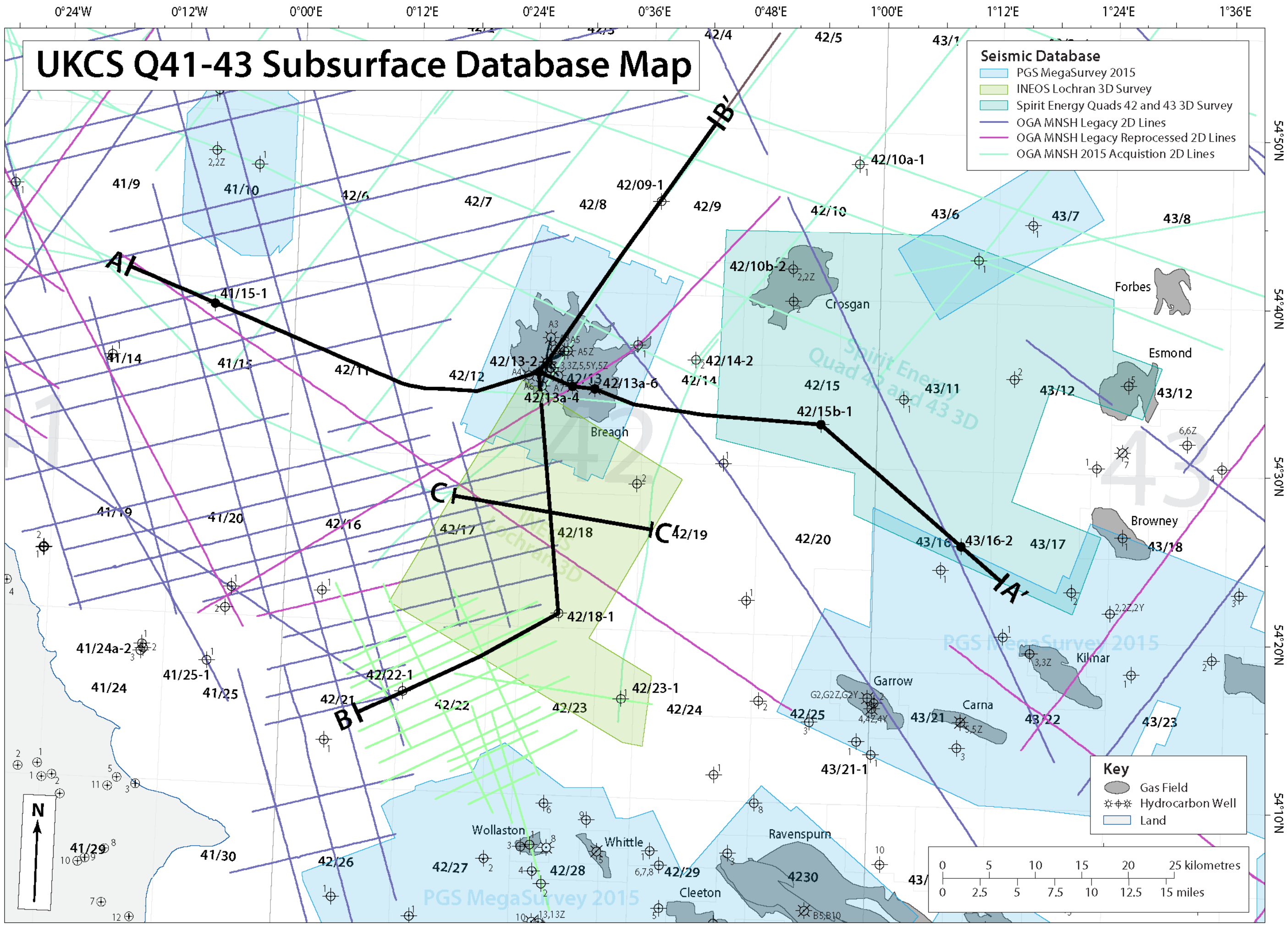

Figure 4.6: Database map of the Breagh study area in Quadrants 41–43 showing the extent of the 3D seismic datasets (a subset of the PGS MegaSurvey 2015 and the INEOS Lochran 3D surveys), regional 2D lines, well control and the location of gas fields, including the Breagh Field. The orientation and locations of the well correlation and seismic sections A–A' (Figs 4.7a) and C–C' (Figs 4.7b) are indicated after Grant et al, 2020.

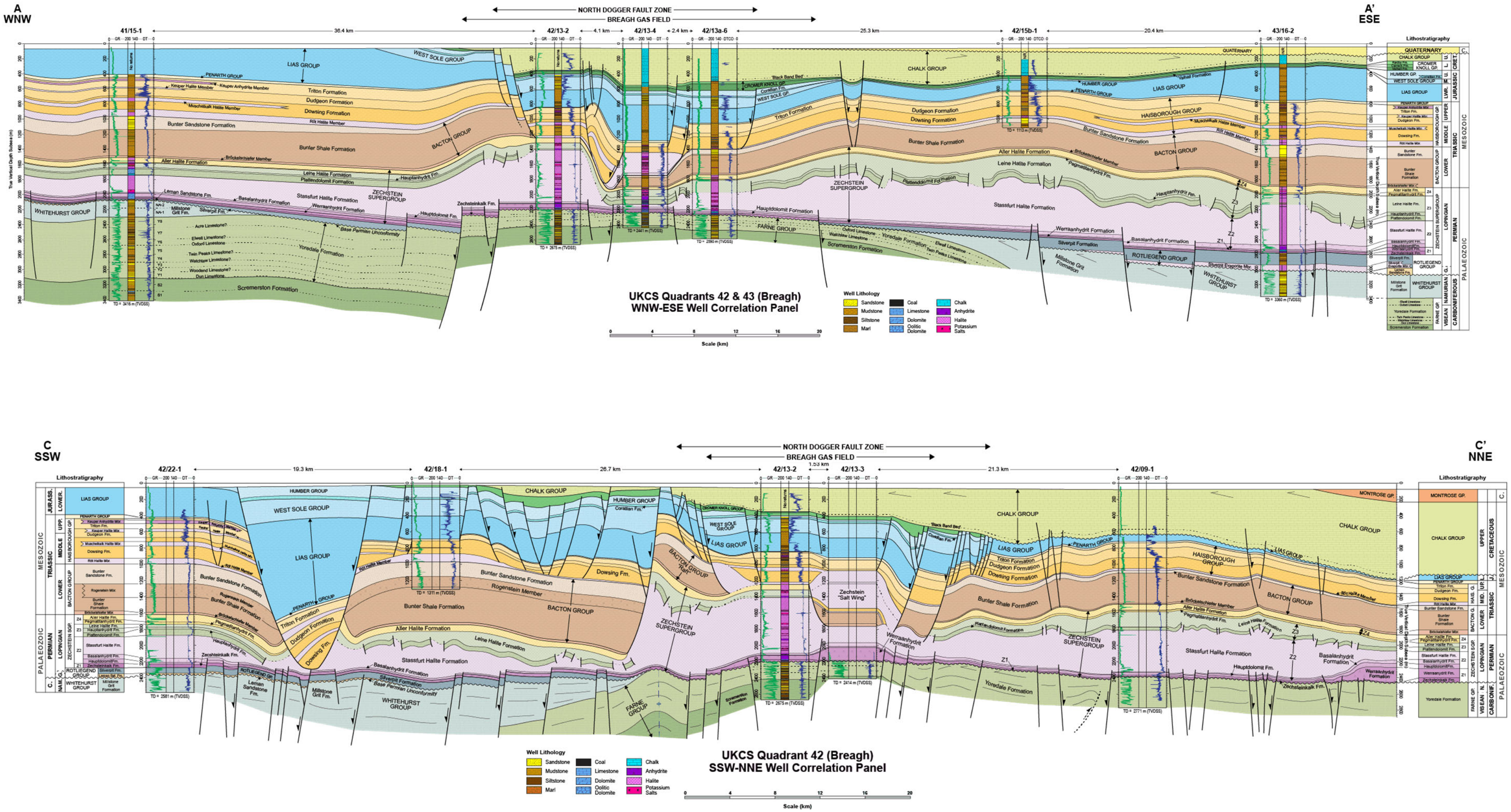

Figure 4.7: Well correlation. (a-top) WNW–ESE (A–A') and (b) SSW–NNE (C–C'), true vertical depth subsea (TVDSS) well correlation panels across the Breagh area in Quadrants 41–43. The line of section (a) intersects wells 41/15-1, 42/13-2 (Breagh), 42/13-4 (Breagh), 42/13a-6 (Breagh), 42/15b-1 and 43/16-2. The line of section (b) intersects wells 42/22-1, 42/15-1, 43/13-2 (Breagh), 43/13-3 (Breagh) and 42/09-1. The locations of sections are shown in Figure 4.6. Well spacing is proportional and the section is displayed with an approximate vertical exaggeration of ×7. Well tracks show lithology, gamma-ray (GR) and sonic (DT) logs where available. (Taken from Grant et al 2020).

The Yoredale Formation is seen to subcrop beneath the BPU for up to 21.1km NNE of the Breagh toward well 42/09-1 (Fig 4.7b). The difficulty in predicting reservoir quality here however is the complex fault pattern within the area which may compartmentalize the reservoir by either baffling fluid flow or by altering the juxtaposition of sandstone bodies from their original depositional configuration.

There is a further possibility for a Lower Carboniferous extension 10 km SSW of Breagh towards well 42/18-1 given the presence of anticlinal structure within a fault-controlled closure just like the Breagh structure see also (Fig 4.7b). Additional possibility for this prospect have been discussed in (Grant *et al*., 2020). Considering the difficulties in mapping the BPU and predicting Lower Carboniferous thicknesses (Collinson *et al*., 2005; Glennie, 2005; Besly, 2019), considerable risk should be accounted for when exploring for such targets, and structural closures at base Zechstein would present less uncertainty. This contrast to the direction WNW of the Breagh towards well 41/15-1 where structural closures will pose the maximum risk.

Correlation between the limestone markers to the west of Breagh towards the Cleveland Basin, suggests an expansion of over three times the thickness of the lower part of the Yoredale Formation between the Oxford and Dun limestones (e.g. 446 m in 41/15-1 and 130 m in 42/13-2) to the west (Fig 4.7a). The lowermost Dun Limestone Member marks the boundary between the Yoredale Formation with the underlying Scremerston Formation. Like earlier, successful reservoir correlation away from the Breagh towards the SW will rely on better understanding of the complex fault pattern.

Despite these complexities, the discovery in the Crosgan field (Fig 4.6), 25 km to the NE of Breagh in Blocks 42/10 and 42/15a, gives evidence that more discovery could still be possible within the Lower Carboniferous Visean stratigraphy of the SNS. Crosgan was discovered by well 42/15a-2 in 1990 by Industrial Scotland Energy plc and contains an estimated 2.8 Bcm-Billion cubic meters (100 Bcf- Billion cubic feet) of P50 contingent recoverable resource.

Both Breagh and Crosgan were marked as ‘outliers’, and unsuccessful but their discoveries have challenged long held views concerning the prospectivity of the Lower Carboniferous in the region. The success of Crosgan could be attributed to the fact that it probably shares similar origin with the Breagh (Besly, 2019; Brackenridge *et al*., 2020; Grant *et al*., 2020).

Previous study of gravity and magnetic data indicate that both the Breagh and the Crosgan Fields may have been situated on a small granite pluton, resulting in a subtle palaeotopographical high (Collinson *et al*., 2005; Kimbell and Williamson, 2015; Monaghan *et al*., 2017; Arsenikos *et al*., 2019; Booth *et al*., 2020; Grant *et al*., 2020). There is evidence from gravity to suggest the presence of a buoyant basement granite (Donato and Megson, 1990; Pharaoh *et al*., 1995, 2006; Kimbell and Williamson, 2015) in other Similar areas of the SNS like the Market Weighton–Amethyst High in Quadrant 47 or the Dogger High in Quadrants 37 and 38.

Therefore, harnessing further prospectively from the area or in other comparable basins may best come from the search for similar paleotopographical highs (Booth *et al*., 2020; Grant *et al*., 2020), which would provide a more robust structural setting to the multiple phases of deformation that have affected the area. Investigating other gravity anomalies may be a good place to start.

Within the Breagh field itself, numerous thinner and finer-grained sandstone bodies exist within delta front sands (FA4, FA5) and abandoned channel facies (FA10). The connectivity of these thinner, secondary reservoirs will be critical for adding pay at Breagh and other potential gas fields. In this and in the case of the primary reservoir (see reservoir section above) post-depositional burial reduced reservoir quality through compaction and diagenesis (Chapter 4 & 5), resulting in tight sandstones, and as a consequence gas production is reliant on hydraulic fracturing (Jones *et al*., 2001; Underhill, 2003; Symonds *et al*., 2015).

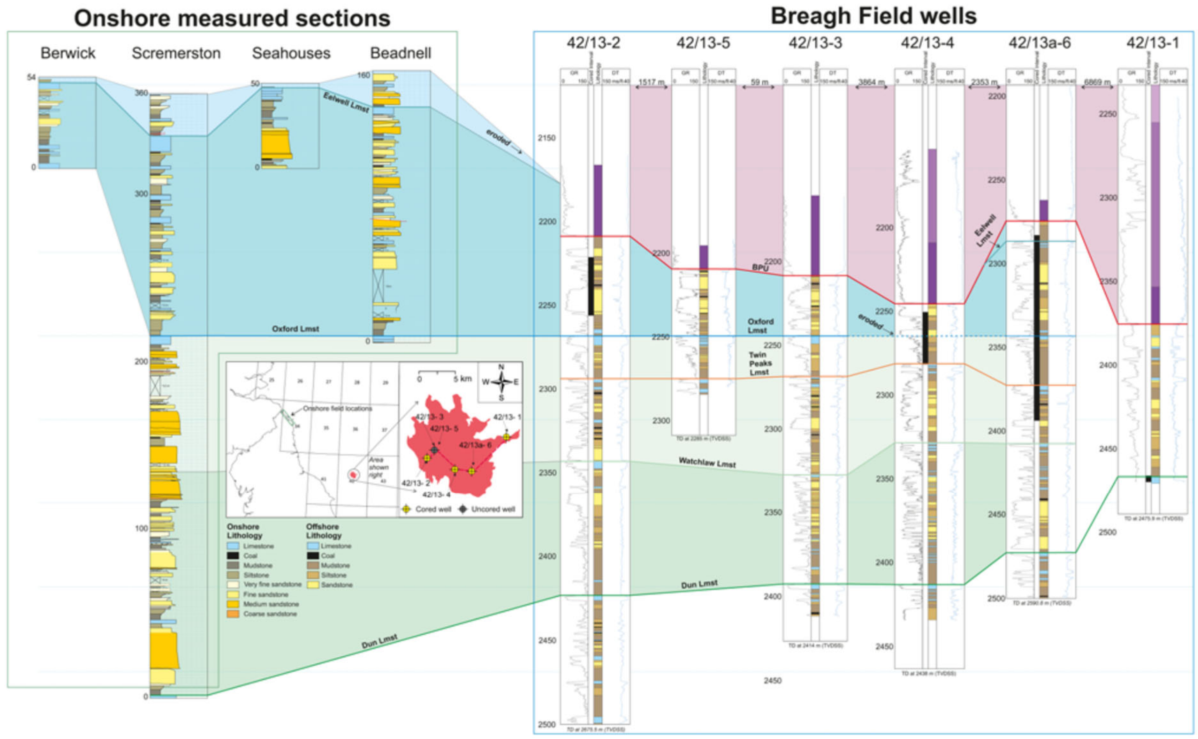

Figure 4.8: Breagh gas field and select onshore wells correlation panel. correlations are based on limestones and palynology data provided from adjacent mudstones and taken from Booth et al, 2010.

4.7: Conclusion.

Eleven facies association were observed representing four distinct depositional environments (open marine, delta front, lower delta plain and upper delta plain) have been identified in the breagh field cores. The detailed interpretations of the studied cores reveal that these fluvio-deltaic deposits are composed of multiple depositional deltaic 'cycles', each characterized by a prograding siliciclastic succession and bounded by flooding surfaces.

The detailed analysis of the sedimentary architecture demonstrates that the studied facies association are dominated by river influenced delta with minor tide- or wave-influenced components. The multistorey nature of the sandbody, the coarseness of the bases of the sandstone and the lack of well organised vertical trends suggest that the river which deposited the sandstone may have been braided.

Prior to the discovery of the Breagh, the prospectivity of the Lower Carboniferous in the Southern North Sea has largely been ignored, mainly because of its depth of burial and a perceived lack of charge implicit from an absence of the Westphalian Coal Measures Group source rock (discussed both in the current chapter and in chapter 2). However, the discovery and development of Visean reservoirs in the Breagh Field and its cousin field Crosgan demonstrate that there is potential at this stratigraphic level.

The results of integrated evaluation of the 3D seismic data volumes with well and core data from the greater Breagh area of the Mid North Sea High emphasize the link between understanding the structure, trapping geometry and burial history, and the exploration and production success away from the Breagh area into other areas of the Southern North Sea. The data suggest that reservoir success may yet be possible in the Lower Carboniferous of the SNS by harnessing further prospectivity from the area or by searching in other comparable basins. The search for similar long-lived antecedent highs as the Breagh and Crosgan fields, which would provide a more robust structural setting given multiple phases of deformation that have affected the area.

The studied cores also show that numerous thinner and finer-grained sandstone bodies exist within delta front sands (FA4, FA5) and abandoned channel facies (FA10) within the Breagh field itself. The connectivity of these thinner, secondary reservoirs will be critical for adding pay at Breagh and other potential gas fields.

4.8 References

Ahmad, N., 1983, Vertisols, *in* Developments in Soil Science: Elsevier, p. 91–123.

Allen, P. A., and J. E. A. Marshall, 1981, Depositional Environments and Palynology of the Devonian South-east Shetland Basin: Scottish Journal of Geology, v. 17, no. 4, p. 257–273, doi:10.1144/sjg17040257.

Alonso-Zarza, A. M., and V. P. Wright, 2010, Calcretes: Developments in Sedimentology, v. 61, p. 225–267.

Antoshkina, A. I., N. N. Ryabinkina, and O. V. Valyaeva, 2017, Genesis of siderite nodules from the lower carboniferous terrigenous sequence in the Subpolar Urals: Lithology and Mineral Resources, v. 52, no. 2, p. 111–124.

Antoshkina, A. I., E. A. Zhegallo, and S. I. Isaenko, 2020, Microbially mediated organomineralization in Paleozoic carbonate ooids: Paleontological Journal, v. 54, no. 8, p. 825–834.

Arsenikos, S., M. Quinn, G. Kimbell, P. Williamson, T. Pharaoh, G. Leslie, and A. Monaghan, 2019, Structural development of the Devono-Carboniferous plays of the UK North Sea: Geological Society, London, Special Publications, v. 471, no. 1, p. 65–90.

Ashraf, U., P. Zhu, Q. Yasin, A. Anees, M. Imraz, H. N. Mangi, and S. Shakeel, 2019, Classification of reservoir facies using well log and 3D seismic attributes for prospect evaluation and field development: A case study of Sawan gas field, Pakistan: Journal of Petroleum Science and Engineering, v. 175, p. 338–351.

Babikir, I. A., E. Nagm, A. O. Bamousa, and N. Barazi, 2021, Facies analysis of the Quaternary fluvial system of Khor Eit, Red Sea coast, Sudan: Journal of African Earth Sciences, v. 184, p. 104370.

Basilici, G., P. F. F. Dal Bó, and F. S. B. Ladeira, 2009, Climate-induced sediment-palaeosol cycles in a Late Cretaceous dry aeolian sand sheet: Marília Formation (North-West Bauru Basin, Brazil): Sedimentology, v. 56, no. 6, p. 1876–1904, doi:10.1111/j.1365-3091.2009.01061.x.

Besly, B., 2019, Exploration and development in the Carboniferous of the Southern North Sea: a 30-year retrospective: Geological Society, London, Special Publications, v. 471, no. 1, p. 17–64, doi:10.1144/SP471.10.

Bhattacharya, J. P., C. D. Howell, J. A. MacEachern, and J. P. Walsh, 2020, Bioturbation, sedimentation rates, and preservation of flood events in deltas: Palaeogeography, Palaeoclimatology, Palaeoecology, v. 560, p. 110049.

Blum, M. D., and H. H. Roberts, 2012, The Mississippi Delta Region: Past, Present, and Future: Annual Review of Earth and Planetary Sciences, v. 40, no. 1, p. 655–683, doi:10.1146/annurev-earth-042711-105248.

Bomer, E. J., S. J. Bentley, J. E. Hughes, C. A. Wilson, F. Crawford, and K. Xu, 2019, Deltaic morphodynamics and stratigraphic evolution of Middle Barataria Bay and Middle Breton Sound regions, Louisiana, USA: Implications for river-sediment diversions: Estuarine, Coastal and Shelf Science, v. 224, p. 20–33.

Booth, M. G., J. R. Underhill, A. Gardiner, and D. McLean, 2020, Sedimentary and tectonic controls on Lower Carboniferous (Visean) mixed carbonate–siliciclastic deposition in NE England and the Southern North Sea: implications for reservoir architecture: Petroleum Geoscience, v. 26, no. 2, p. 204–231.

Brackenridge, R. E., J. R. Underhill, R. Jamieson, and A. Bell, 2020, Structural and stratigraphic evolution of the Mid North Sea High region of the UK Continental Shelf: Petroleum Geoscience, v. 26, no. 2, p. 154–173.

Bridge, J. S., 1984, Large-scale facies sequences in alluvial overbank environments: Journal of Sedimentary Research, v. 54, no. 2, p. 583–588.

Cecil, C. B., 2013, An overview and interpretation of autocyclic and allocyclic processes and the accumulation of strata during the Pennsylvanian–Permian transition in the central Appalachian Basin, USA: International Journal of Coal Geology, v. 119, p. 21–31, doi:10.1016/j.coal.2013.07.012.

Cecil, C. B., 2003, The Concept of Autocyclic and Allocyclic Controls on Sedimentation and Stratigraphy, Emphasizing the Climatic Variable.

Chadwick, R. A., D. W. Holliday, S. T. Holloway, and A. G. Hulbert, 1993, The evolution and hydrocarbon potential of the Northumberland–Solway Basin, *in* Geological Society, London, Petroleum Geology Conference series: Geological Society of London, p. 717–726.

Coleman, J. M., S. M. Gagliano, and J. E. Webb, 1964, Minor sedimentary structures in a prograding distributary: Marine Geology, v. 1, no. 3, p. 240–258.

Coleman, J. M., H. H. Roberts, and G. W. Stone, 1998, Mississippi River Delta: An Overview: Journal of Coastal Research, v. 14, no. 3, p. 699–716.

Collinson, J. D., D. J. Evans, D. W. Holliday, and N. S. Jones, 2005, Dinantian and Namurian depositional systems in the southern North Sea: Yorkshire Geological Society Occasional Publication, v. 7, p. 35–56.

Collinson, J. D., C. M. Jones, G. A. Blackbourn, B. M. Besly, G. M. Archard, and A. H. McMAHON, 1993, Carboniferous depositional systems of the Southern North Sea: Geological Society, London, Petroleum Geology Conference series, v. 4, no. 1, p. 677–687, doi:10.1144/0040677.

Cseh, C., and J. Andrews, 2019, Significance of Swaley cross-stratification in the Carstone Formation, Hunstanton, Norfolk: Bulletin of the Geological Society of Norfolk, v. 69, p. 3–34.

Donato, J. A., and J. B. Megson, 1990, A buried granite batholith beneath the East Midland Shelf of the Southern North Sea Basin: Journal of the Geological Society, v. 147, no. 1, p. 133–140, doi:10.1144/gsjgs.147.1.0133.

Dou, M., S. Li, T. Lei, G. Ren, X. Li, Y. Guo, and W. Feng, 2022, Reservoir Modeling of Braided River Reservoirs Based on Geological Knowledge Database: A Case Study of P1x Formation of the Daniudi Gas Field, Ordos Basin, China: Lithosphere, v. 2022, no. Special 13, p. 6913641, doi:10.2113/2022/6913641.

Elliott, T., 1975, The sedimentary history of a delta lobe from a Yoredale (Carboniferous) cyclothem: Geological Society of London, p. 505–536.

Frazier, D. E., 1967, Recent Deltaic Deposits of the Mississippi River: Their Development and Chronology: v. 17.

Gani, M. R., and J. P. Bhattacharya, 2007, Basic Building Blocks and Process Variability of a Cretaceous Delta: Internal Facies Architecture Reveals a More Dynamic Interaction of River, Wave, and Tidal Processes Than Is Indicated by External Shape: Journal of Sedimentary Research, v. 77, no. 4, p. 284–302, doi:10.2110/jsr.2007.023.

Glennie, K., 2005, Regional tectonics in relation to Permo-Carboniferous hydrocarbon potential, Southern North Sea Basin: Carboniferous hydrocarbon resources: the southern North Sea and surrounding areas. Occasional Special Publication of the Yorkshire Geological Society, v. 7, p. 1–12.

Glennie, K. W., and D. M. J. Provan, 1990, Lower Permian Rotliegend reservoir of the Southern North Sea gas province: Geological Society, London, Special Publications, v. 50, no. 1, p. 399–416, doi:10.1144/GSL.SP.1990.050.01.25.

Goodbred, S. L., and S. A. Kuehl, 2000, The significance of large sediment supply, active tectonism, and eustasy on margin sequence development: Late Quaternary stratigraphy and evolution of the Ganges–Brahmaputra delta: Sedimentary Geology, v. 133, no. 3, p. 227–248, doi:10.1016/S0037-0738(00)00041-5.

Grant, R. J., M. G. Booth, J. R. Underhill, and A. Bell, 2020, Structural evolution of the Breagh area: implications for carboniferous prospectivity of the Mid North Sea High, Southern North Sea: Petroleum Geoscience, v. 26, no. 2, p. 174–203.

Gugliotta, M., Y. Saito, T. K. O. Ta, V. L. Nguyen, A. D. La Croix, Z. Wang, T. Tamura, R. Nakashima, and K. P. Lieu, 2022, Late Holocene stratigraphic evolution and sedimentary facies of an active to abandoned tide-dominated distributary channel and its mouth bar: Sedimentology, v. 69, no. 3, p. 1151–1178, doi:10.1111/sed.12940.

Herbert, C. M., J. Alexander, K. J. Amos, and C. R. Fielding, 2020, Unit bar architecture in a highly-variable fluvial discharge regime: Examples from the Burdekin River, Australia: Sedimentology, v. 67, no. 1, p. 576–605.

Hubert, J. F., and M. G. Hyde, 1982, Sheet-flow deposits of graded beds and mudstones on an alluvial sandflat-playa system: Upper Triassic Blomidon redbeds, St Mary's Bay, Nova Scotia: Sedimentology, v. 29, no. 4, p. 457–474, doi:10.1111/j.1365-3091.1982.tb01730.x.

Hutsky, A. J., C. R. Fielding, T. J. Hurd, and C. K. Clark, 2012, Sedimentology and stratigraphy of the Upper Cretaceous (Cenomanian) Frontier Formation, northeast Bighorn Basin, Wyoming, USA.

Jiang, L., S. Li, D. Duan, F. Ding, and S. Yu, 2022, A New Modeling Method for the Sandbody Architecture of Braided River Reservoirs: A Case Study from HG Formation, N Gas Field: Lithosphere, v. 2022, no. Special 12, p. 9366688, doi:10.2113/2022/9366688.

Jin, L., X. Shan, X. Shi, M. Fonnesu, S. Qiao, S. Kandasamy, H. Wang, S. Liu, X. Fang, and X. Zou, 2021, Hybrid event beds generated by erosional bulking of modern hyperpycnal flows on the Choshui River delta front, Taiwan Strait: Sedimentology, v. 68, no. 6, p. 2500–2522.

Johnson, G. A. L., 1984, Subsidence and sedimentation in the Northumberland Trough: Proceedings of the Yorkshire Geological Society, v. 45, no. 1–2, p. 71–83.

Jones, S. J., L. E. Frostick, and T. R. Astin, 2001, Braided stream and flood plain architecture: the Rio Vero Formation, Spanish Pyrenees: Sedimentary Geology, v. 139, no. 3, p. 229–260.

Kashif, M., Y. Cao, G. Yuan, M. Asif, F. Rehman, K. Shehzad, M. F. Ullah, and G. Mustafa, 2020, Sedimentology of Shahejie Formation, Bohai Bay Basin: a case study of Es1 member in Nanpu Sag: Carbonates and Evaporites, v. 35, no. 2, p. 1–18.

Kim, J. C., and Y. I. Lee, 1998, Cyclostratigraphy of the Lower Ordovician Dumugol Formation, Korea: meter-scale cyclicity and sequence-stratigraphic interpretation: Geosciences Journal, v. 2, no. 3, p. 134–147, doi:10.1007/BF02910257.

Kimbell, G. S., and J. P. Williamson, 2015, A gravity interpretation of the Central North Sea.

Kraus, M. J., 1999, Paleosols in clastic sedimentary rocks: their geologic applications: Earth-Science Reviews, v. 47, no. 1, p. 41–70, doi:10.1016/S0012-8252(99)00026-4.

Kraus, M. J., and B. Gwinn, 1997, Facies and facies architecture of Paleogene floodplain deposits, Willwood Formation, Bighorn basin, Wyoming, USA: Sedimentary Geology, v. 114, no. 1–4, p. 33–54.

Kusuma, W. H. D., I. S. Julian, E. L. H. Johan, D. Rus, and S. S. Eka, n.d., Paleofluvial Cross Stratification Structure as the Paleocurrent Analysis on Western Part of Tarakan Sub-Basin, Tarakan, North Kalimantan.

Leeder, M. R., 1988, Recent developments in Carboniferous geology: a critical review with implications for the British Isles and NW Europe: Proceedings of the Geologists' Association, v. 99, no. 2, p. 73–100.

Leeder, M. R., and M. Hardman, 1990, Carboniferous geology of the Southern North Sea Basin and controls on hydrocarbon prospectivity: Geological Society, London, Special Publications, v. 55, no. 1, p. 87–105.

Leila, M., and A. Moscariello, 2019, Seismic stratigraphy and sedimentary facies analysis of the pre-and syn-Messinain salinity crisis sequences, onshore Nile Delta, Egypt: implications for reservoir quality prediction: Marine and Petroleum Geology, v. 101, p. 303–321.

Li, A., F. T.-C. Tsai, K. Xu, J. Wang, C. M. White, S. J. Bentley, and Q. J. Chen, 2019, Modeling sediment texture of river-deltaic wetlands in the Lower Barataria Bay and Lower Breton Sound, Louisiana, USA: Geo-Marine Letters, v. 39, no. 2, p. 161–173.

Liu, S., A. Feng, S. Gao, Y. P. Wang, J. Jia, J. Du, G. Xu, P. Li, W. Hu, and W. Feng, 2022, Evidence for a second deflected prodelta of the Yellow River: Insights into a complex pattern of delta asymmetry: Marine and Petroleum Geology, v. 143, p. 105815.

Liu, Z., Y. Liu, X. Du, D. Lyu, H. Wu, and H. Wang, 2022, Early Diagenesis in the Lacustrine Ostracods from the Songliao Basin 91.35 Million Years Ago and Its Geological Implications: Minerals, v. 13, no. 1, p. 5.

Liu, J., R. Zhu, C. Zhang, G. Hou, M. He, and L. Huang, 2021, Hyperpycnal flow depositional characteristics and model in an ancient continental basin: a record from the Oligocene Lower Huagang Formation in the Xihu Sag, East China Sea Shelf Basin: Canadian Journal of Earth Sciences, v. 58, no. 2, p. 122–133.

Mack, G. H., W. C. James, and H. C. Monger, 1993, Classification of paleosols: Geological Society of America Bulletin, v. 105, no. 2, p. 129–136.

Maynard, J. R., and R. E. Dunay, 1999, Reservoirs of the Dinantian (Lower Carboniferous) play of the southern North Sea, *in* Geological Society, London, Petroleum Geology Conference series: Geological Society of London, p. 729–745.

Miall, A. D., 1977, A review of the braided-river depositional environment: Earth-Science Reviews, v. 13, no. 1, p. 1–62, doi:10.1016/0012-8252(77)90055-1.

Miall, A. D., 1985, Architectural-element analysis: A new method of facies analysis applied to fluvial deposits: Earth-Science Reviews, v. 22, no. 4, p. 261–308, doi:10.1016/0012-8252(85)90001-7.

Miall, A. D., 1987, Recent developments in the study of fluvial facies models.

Miall, A. D., 2016, Stratigraphy: A modern synthesis: Berlin:Springer-Verlag.

Monaghan, A. A. *et al.*, 2017, Carboniferous petroleum systems around the Mid North Sea High, UK: Marine and Petroleum Geology, v. 88, p. 282–302, doi:10.1016/j.marpetgeo.2017.08.019.

Morisawa, M., 2020, Topologic properties of delta distributary networks, *in* Models in Geomorphology: Routledge, p. 239–268.

Morozova, G. S., 2022, Autocyclic (avulsion-induced) base-level change, its upstream and downstream controls, and effects on floodbasin sedimentation: The 1870s avulsion of the Saskatchewan River, Cumberland Marshes, Canada: Earth Surface Processes and Landforms, v. 47, no. 1, p. 308–327, doi:10.1002/esp.5249.

Mtelela, C., E. M. Roberts, R. Downie, and M. S. Hendrix, 2016, Interplay of structural, climatic, and volcanic controls on late quaternary lacustrine–deltaic sedimentation patterns in the Western Branch of the East African Rift System, Rukwa Rift Basin, Tanzania: Journal of sedimentary research, v. 86, no. 10, p. 1179–1207.

Muhammad, K., C. Yingchang, Y. Guanghui, A. Muhammad, R. Faisal, S. Kamran, M. F. Ullah, and M. Ghulam, 2020, Sedimentology of Shahejie Formation, Bohai Bay Basin: a case study of Es 1 member in Nanpu Sag: Carbonates and Evaporites, v. 35, no. 2.

Nichols, G. J., and J. A. Fisher, 2007, Processes, facies and architecture of fluvial distributary system deposits: Sedimentary Geology, v. 195, no. 1, p. 75–90, doi:10.1016/j.sedgeo.2006.07.004.

Nwachukwu, C. M., Z. Barnett, and J. G. Gluyas, 2020, The Breagh Field, Blocks 42/12a, 42/13a and 42/8a, UK North Sea: Geological Society, London, Memoirs, v. 52, no. 1, p. 109–118.

O'Brien, P. E., and A. T. Wells, 1986, A small, alluvial crevasse splay: Journal of Sedimentary Research, v. 56, no. 6, p. 876–879, doi:10.1306/212F8A71-2B24-11D7-8648000102C1865D.

Okeugo, C. G., K. M. Onuoha, C. I. P. Dim, and O. C. Ekwenye, 2022, Early Oligocene HX-sands depositional fairways and distribution across faulted blocks, onshore–shelf, Niger Delta Basin, Nigeria: Journal of African Earth Sciences, p. 104654.

Okobiebi, O., and B. Okobiebi, 2021, Delineating Depositional Environment through Lithostratigraphy and 2D Sequence Stratigraphy of a Typical Ramp Succession: In the Obom Field Niger Delta, *in* SPE Nigeria Annual International Conference and Exhibition: OnePetro.

Oyanyan, R. O., M. C. Ohaegbulem, C. C. Agbo, and N. S. Iloanya, 2021, Sedimentary Architectural Elements and Sandy Braided Fluvial Successions in Ajali Sandstone Ridges, Western Afikpo Basin, Uturu, Nigeria: Earth Sciences Malaysia, v. 5, no. 1, p. 49–57.

Penland, S., R. Boyd, and J. R. Suter, 1988, Transgressive depositional systems of the Mississippi Delta plain; a model for barrier shoreline and shelf sand development: Journal of Sedimentary Research, v. 58, no. 6, p. 932–949, doi:10.1306/212F8EC2-2B24-11D7-8648000102C1865D.

Pharaoh, T., R. England, and M. Lee, 1995, The concealed Caledonide basement of eastern England and the southern North Sea—a review: Studia geophysica et geodaetica, v. 39, no. 3, p. 330–346.

Pharaoh, T. C., J. A. Winchester, J. Verniers, A. Lassen, and A. Seghedi, 2006, The western accretionary margin of the East European Craton: an overview: MEMOIRS-GEOLOGICAL SOCIETY OF LONDON, v. 32, p. 291.

Plink-Björklund, P., 2020, Shallow-water deltaic clinoforms and process regime: Basin Research, v. 32, no. Clinoforms and Clinothems: Fundamental Elements of Basin Infill, p. 251–262.

Qin, Y., X. Zhu, S. Zhu, and B. McElroy, 2021, Impact of deep-time palaeoclimate on the sedimentary records and morphology of lacustrine shoal-water deltas, Upper Eocene Dongying Depression, Bohai Bay Basin, China: Sedimentology, v. 68, no. 7, p. 3253–3278.

Rahman, M. M., J. A. Howell, and D. I. MacDonald, 2022, Quantitative analysis of crevasse-splay systems from modern fluvial settings: Journal of Sedimentary Research, v. 92, no. 9, p. 751–774.

Reinhardt, J., and W. R. Sigleo, 1988, Paleosols and weathering through geologic time: principles and applications: Geological Society of America.

Retallack, G. J., 1988, Field recognition of paleosols: Geological Society of America Special Paper, v. 216, p. 1–20.

Retallack, G. J., 2014, Paleosols☆, *in* Reference Module in Earth Systems and Environmental Sciences: Elsevier, doi:10.1016/B978-0-12-409548-9.09099-0.

Roberts, H. H., 1997, Dynamic Changes of the Holocene Mississippi River Delta Plain: The Delta Cycle: Journal of Coastal Research, v. 13, no. 3, p. 605–627.

Roberts, H. H., J. N. Suhayda, and J. M. Coleman, 2020, Sediment deformation and transport on low-angle slopes: Mississippi River delta, *in* Thresholds in geomorphology: Routledge, p. 131–167.

Rodriguez, K., R. Wrigley, N. Hodgson, and H. Nicholls, 2014, Southern North Sea: unexplored multi-level exploration potential revealed: First Break, v. 32, no. 6, p. 107–113.

Schumm, S. A., 1985, Patterns of Alluvial Rivers. Ann. Rev. Earth Planet. Sci. 1985. 13: 5-27: Earth Planet. Sci., no. 13, p. 5–27.

Selim, S. S., 2021, Evolution of a gradually abandoned Oligocene fluvial palaeovalley fill: Abu-Roash area, north Western Desert, Egypt: Sedimentology, v. 68, no. 7, p. 3405–3446.

Sengupta, R., S. A. Robinson, and N. J. Tosca, 2021, Sphaerosiderites as sensitive recorders of non-marine depositional and diagenetic history: Insights from the Lower Cretaceous Wealden Supergroup: The Depositional Record, v. 7, no. 3, p. 520–540.

Shanmugam, G., 2022, Comment on “Ichnological analysis: A tool to characterize deep-marine processes and sediments” by Francisco J. Rodriguez-Tovar [Earth-Science Reviews, 228 (2022), 104014]: Earth-Science Reviews, p. 104047.

Shehata, A. A., M. A. Sarhan, M. I. Abdel-Fattah, and E. M. Assal, 2023, Sequence stratigraphic controls on the gas-reservoirs distribution and characterization along the Messinian Abu Madi incision, Nile Delta Basin: Marine and Petroleum Geology, v. 147, p. 105988.

Smith, E., M. S. Daniller-Varghese, P. M. Myrow, and D. Mohrig, 2019, Experimental Investigations of Combined Flow Sediment Transport: Journal of Sedimentary Research, v. 89, no. 8, p. 808–814.

Stephenson, M. H., D. Millward, M. J. Leng, and C. H. Vane, 2008, Palaeoecological and possible evolutionary effects of early Namurian (Serpukhovian, Carboniferous) glacioeustatic cyclicity: Journal of the Geological Society, v. 165, no. 6, p. 993–1005, doi:10.1144/0016-76492007-153.

Stow, D., U. Nicholson, S. Kearsey, D. Tatum, A. Gardiner, A. Ghabra, and M. Jaweesh, 2020, The Pliocene-Recent Euphrates river system: Sediment facies and architecture as an analogue for subsurface reservoirs: Energy Geoscience, v. 1, no. 3, p. 174–193, doi:10.1016/j.engeos.2020.07.005.

Symonds, R., R. Lippmann, B. Mueller, and A. Kohok, 2015, Yoredale sandstone Architecture in Breagh Field (UK SNS). Presentation for Sedimentology of Paralic Reservoirs: Recent advances and their applications.: p. 24.

Taylor, A., R. Goldring, and S. Gowland, 2003, Analysis and application of ichnofabrics: Earth-Science Reviews, v. 60, no. 3–4, p. 227–259.

Thayer, J. B., and P. Ashmore, 2016, Floodplain morphology, sedimentology, and development processes of a partially alluvial channel: Geomorphology, v. 269, p. 160–174.

Toonen, W. H., M. G. Kleinhans, and K. M. Cohen, 2012, Sedimentary architecture of abandoned channel fills: Earth surface processes and landforms, v. 37, no. 4, p. 459–472.

Underhill, J. R., 2003, The tectonic and stratigraphic framework of the United Kingdom's oil and gas fields: Geological Society, London, Memoirs, v. 20, no. 1, p. 17–59, doi:10.1144/GSL.MEM.2003.020.01.04.

Wang, J., A. D. La Croix, S. Gonzalez, J. He, and J. Underschultz, 2019, Sequence stratigraphic analysis of the Lower Jurassic Precipice Sandstone and Evergreen Formation in the Surat Basin, Australia: Implications for the architecture of reservoirs and seals for CO2 storage: Marine and Petroleum Geology, v. 102, p. 829–843.

Wang, D., Q. Mao, K. Liu, D. Lyu, H. Liu, Y. Yin, and H. Hu, 2022, Genetic mechanism of Carboniferous-Permian coal measures siderite nodules in an epicontinental sea basin—An example from the Zibo area in North China: Ore Geology Reviews, p. 105254.

Wizevich, M. C., E. L. Simpson, H. L. Hilbert-Wolf, and S. E. Tindall, 2016, Development of large-scale seismites in Upper Cretaceous fluvial sandstones in a fault-proximal setting: Sedimentology, v. 63, no. 6, p. 1719–1738, doi:10.1111/sed.12283.

Wright, V. P., and M. E. Tucker, 2009, Calcretes: John Wiley & Sons, 1–22 p.

Xu, Z., P. Plink-Björklund, S. Wu, Z. Liu, W. Feng, K. Zhang, Z. Yang, and Y. Zhong, 2022, Sinuous bar fingers of digitate shallow-water deltas: Insights into their formative processes and deposits from integrating morphological and sedimentological studies with mathematical modelling: Sedimentology, v. 69, no. 2, p. 724–749.

Yan, D., H. Xu, Z. Xu, Z. Lei, M. Tian, L. Cheng, Y. Ma, Z. Wang, and M. Ostadhassan, 2020, Sedimentary architecture of hyperpycnal flow deposits: Cretaceous Sangyuan outcrop, from the Luanping Basin, North East China: Marine and Petroleum Geology, v. 121, p. 104593.

Yeste, L. M., A. N. Varela, C. Viseras, N. D. Mcdougall, and F. García-García, 2020, Reservoir architecture and heterogeneity distribution in floodplain sandstones: key features in outcrop, core and wireline logs: Sedimentology, v. 67, no. 7, p. 3355–3388.

Zavala, C., 2020, Hyperpycnal (over density) flows and deposits: Journal of Palaeogeography, v. 9, no. 1, p. 1–21.

Zhang, X., D. Fan, Z. Yang, S. Xu, W. Chi, and H. Wang, 2020, Sustained growth of river-mouth bars in the vulnerable Changjiang Delta: Journal of Hydrology, v. 590, p. 125450.

Zhou, X., Z. Jiang, J. A. Quaye, Y. Duan, C. Hu, C. Liu, and C. Han, 2019, Ichnology and sedimentology of the trace fossil-bearing fluvial red beds from the lowermost member of the Paleocene Funing Formation in the Jinhu Depression, Subei Basin, East China: Marine and Petroleum Geology, v. 99, p. 393–415, doi:10.1016/j.marpetgeo.2018.10.032.

Zhu, X., D. Zhong, X. Yuan, H. Zhang, S. Zhu, H. Sun, Z. Gao, and B. Xian, 2016, Development of sedimentary geology of petroliferous basins in China: Petroleum Exploration and Development, v. 43, no. 5, p. 890–901, doi:10.1016/S1876-3804(16)30107-0.

Blank Page

Chapter 5

Diagenetic controls on the reservoir quality of the Breagh Sandstones.

Table of Contents

Chapter Five: Diagenetic Controls on the reservoir quality of the Breagh Sandstones.

5.1 Introduction.

The Breagh field reservoir is an important gas reservoir in the UK Southern North Sea. The discovery well 42/13-2 encountered a 121m of gas column within the Early Carboniferous Visean aged Yoredale Formation sandstones, and subsequent wells have indicated that the field contains a P50 reserve of 552Bcf (15.6Bcm) (Nwachukwu *et al*., 2020), with 2 MMbbl (0.32MMSm^3) recoverable condensate, making it the 60th largest gas field in the UK, in terms of ultimate recoverable reserves (Grant *et al*., 2020).

However, due to an average permeability of less than 1 mD and porosity below 10% in most of the zones (Zone 2-4)- (See chapter 2 &3 for more details on the zonation), it is considered to be a tight sandstone reservoir (Newman, 1999; Smythe, 2014; Oluwadebi *et al*., 2018). The primary reservoir is the topmost zone (zone 1 – channel sandstones contain the best reservoir) has an average porosity of 11.6% and permeability between 1- 10mD. In all cases, post-depositional burial has reduced reservoir quality through compaction and diagenesis resulting in tight sandstones with gas production reliant on hydraulic fracturing (Booth *et al*., 2020).

Studies on sandstone diagenesis have been mostly associated with high permeability examples since they are better reservoirs (Okunuwadje *et al*., 2020; Blackbourn and Collinson, 2022; Khan *et al*., 2023). More, studies on diagenetic alteration in low permeability sandstones (tight sandstone) are valuable as they may identify net pay zones in previously abandoned gas discoveries. Isolated examples from Chinese and US basins (Stroker and Harris, 2009; Stroker *et al*., 2013; Xi *et al*., 2016; Li *et al*., 2017; Zhang *et al*., 2017; Lai *et al*., 2018) and more recently East Irish Sea Basin (Oluwadebi *et al*., 2018) provide plenty of insight into potential geological controls on tight sandstone reservoir quality but more examples are needed in order to gain sufficiently broad knowledge on the diagenetic controls of tight gas reservoir quality.

Within the Southern North Sea (SNS) itself, studies on diagenesis and reservoir quality have also previously focused on the well understood, high permeability Triassic Bunter Sandstone and late Carboniferous Sandstones (Nagtegal, 1979; Burley, 1984; Collinson *et al*., 1988;

Cowan, 1989; Glennie and Provan, 1990; Ketter, 1991; Besly *et al*., 1993; Leveille *et al*., 1997; Rodriguez *et al*., 2014; Wasielka, 2021; Blackbourn and Collinson, 2022). The diagenetic studies in the Breagh Sandstone will thus serve as a good example of the diagenetic evolution of a tight gas sandstone reservoir within the SNS and the UK more widely.

Diagenesis exerts a strong control on the quality and heterogeneity of sandstone reservoirs (including tight sandstones) (Hayes, 1979; Bjørlykke, 1983; Kupecz *et al*., 1997; Primmer *et al*., 1997; Thyne, 2001; Burley and Worden, 2003; Schmid *et al*., 2004; Taylor *et al*., 2010; Bjorlykke and Jahren, 2012; Yuan *et al*., 2015). Since differences in diagenetic alterations usually accentuate the variation in depositional porosity and permeability, it is crucial to understand and predict diagenetic processes and their impact on reservoir quality (Bloch and Helmold, 1995; Salem *et al*., 2000; Schmid *et al*., 2004; Ali *et al*., 2010; Zou *et al*., 2012).

Petrographic observations and plot of intergranular volume against cement (IGV) (see Fig 5.3 & 5.4) does show that the degree of compaction in the studied sandstone is higher than cementation. Mechanical compaction has played an important part in reducing depositional porosities to their present values (see section 5.3), with chemical compaction probably sourcing some silica for precipitation as quartz overgrowth cements. These cements (also sourced by reactions with feldspar grains- see section 5.6.2.4) have occluded some IGV, resulting in further porosity loss. Whilst compaction of detrital grains, quartz cementation and precipitation of kaolinite have reduced pore volumes, the presence of common, widespread authigenic illite has severely restricted permeability. Petrographic studies also show that the presence of carbonate cement have contributed to the near absence of permeability in particularly the non-fluvial sands.

The diagenetic regimes used in this study is adopted after (Cowan, 1989; Worden and Morad, 2003; Higgs *et al*., 2007; Morad *et al*., 2010). The broad regimes are eodiagenesis and mesodiagianesis. Eodiagenesis commonly occurs between 0- 2 km and burial depth greater than 70^0C during which pore-water chemistry is controlled by depositional and/or meteoric waters. In this work, Eodiagenesis is divided into early diagenesis, and early burial diagenesis/uplift diagenesis. Mesodiagenesis commonly occurs at greater than 2 km and above 70^0C and mediated by evolved formation waters. This stage has been divided into burial diagenesis and late burial diagenesis.

Although it is difficult to obtain the precise timing and duration for the individual diagenetic processes within both stages, an overall paragenetic sequence can be constructed based on petrographic textural relationships, fluid inclusion, burial history curves (Mansurbeg *et al*., 2008; Lai *et al*., 2015, 2018) and oxygen and carbon isotope study (Lee *et al*., 1989; Purvis, 1992; Karim and Veizer, 2000; El-Ghali *et al*., 2006; Karim *et al*., 2011). This integrated approach enables elucidation of the diagenetic and fluid-flow histories and may have implications for both exploration and reservoir management of tight gas reservoirs.

At least 10 diagenetic events were observed in the studied sandstones. They include, (i) precipitation of early sulphate cements (ii) development of early quartz overgrowth (iii) initial mechanical compaction (iv) alteration and dissolution of framework grains and early diagenetic cements (v) significant secondary porosity created by cement and framework-grain dissolution (vi) precipitation of kaolinite (vii) precipitation of zoned and mottled textured iron- rich carbonate cements, (viii) at least two generations of authigenic illite, (ix) precipitation of anhydrite, halite and baryte cements and, (x) subsequent though minor dissolution of the late diagenetic illite and carbonate cement.

In addition to the diagenetic cements, other factors such as depositional environment (discussed in chapters 2-4), grain size, sorting, clay content, mechanical compaction, pore chemistry, also play a critical role (Worden and Morad, 2003) in reservoir quality modification. Depositional environment is a master control on early diagenetic processes because it controls the type and amount of water present in sediment, water influx versus evaporation rate, temperature, exposure to atmospheric oxygen, plant-derived CO_2 and organic matter content (Burley and Worden, 2003; Worden and Morad, 2003).

To predict and quantify the diagenetic control on the Breagh field wells, the current chapter will begin with characterizing the detrital mineral assemblage followed by the effect of compaction and diagenesis on the current day reservoir quality.

5.2 Detrital Mineralogy.

Table 5.1: Modal Point count Summary 1: [P: Point contact, L: Line contact; C: Concavo Contact, S; Sutured contact; A: Angular, SA: Subangular, SR: Subrounded]

			% for QFL			% of 300 counts per sample										
FA	Depth (m)	Depth (ft)	Quartz	Rock fragments	Feldspars	Detrit al grain %	Mica %	Total diagenetic mineral %	Total porosity %	% Matrix	Minus cement porosity (IGV) %	Initial porosity (OP)	CEPL	COPL	Grain contact	Grain shape
42/13-2 FA4	2276.8	7469.9	92.9	6.6	0.5	63.5	1.3	22.0	5.0	3.3	30.3	45.0	17.37	21.05	P, L	SA-SR
42/13-2 FA4	2283.5	7491.9	70.2	29.3	0.5	58.7	1.0	25.7	6.0	0.0	31.7	45.0	20.66	19.51	L, S, C,	SA-SR
42/13-2 FA4	2280.5	7481.9	92.9	7.1	0.0	71.7	1.3	17.7	5.7	0.0	23.3	45.0	12.67	28.26	P, L, C	SA-SR
42/13-2 FA3	2256.7	7404.0	91.3	8.7	0.0	72.7	4.7	19.3	2.3	0.0	21.7	45.0	13.57	29.79	L, C	A-SR
42/13-2 FA3	2274.2	7461.3	95.4	4.6	0.0	69.7	0.7	19.0	7.0	0.0	26.0	45.0	14.12	25.68	P, L	SA-SR
42/13-2 FA3	2271.1	7451.0	93.5	6.0	0.5	63.0	1.7	28.0	9.0	0.0	37.0	45.0	24.44	12.70	P, L, C	SA-SR
42/13-2 FA3	2270.0	7447.5	94.2	5.8	0.0	74.7	3.7	23.0	0.0	0.3	23.3	45.0	16.50	28.26	P, L	A-SR
42/13-2 FA9	2282.6	7489.0	88.1	11.9	0.0	71.3	0.0	11.0	13.7	0.0	24.7	45.0	8.03	26.99	L	SA-SR
42/13-2 FA8	2257.5	7406.4	92.6	7.4	0.0	68.0	3.3	23.0	2.7	0.0	25.7	45.0	17.02	26.01	L, C	SA-SR
42/13-2 FA8	2268.4	7442.1	83.0	17.0	0.0	71.0	8.7	30.7	0.0	0.0	30.7	45.0	24.33	20.67	P, L	SA-SR
42/13-2 FA9	2285.2	7497.5	83.2	16.8	0.0	62.0	1.7	34.0	1.3	0.0	35.3	45.0	28.92	14.95	L, S	SA-SR
42/13-2 FA9	2275.0	7463.9	89.7	9.8	0.5	72.3	0.3	16.3	10.0	0.0	26.3	45.0	12.19	25.34	L, C	A-SR
42/13-2 FA9	2282.5	7488.5	66.9	33.1	0.0	60.0	0.3	15.0	25.3	0.0	40.3	45.0	13.83	7.82	P, L	SA-SR
42/13-2 FA9	2257.3	7405.8	72.5	27.5	0.0	67.1	11.0	19.7	0.7	0.0	20.3	45.0	13.58	30.96	P, L	SA-SR
42/13-2 FA4	2263.1	7425.0	76.7	22.3	1.0	67.7	6.7	29.7	0.7	0.0	30.3	45.0	23.42	21.05	P, L, C	SA-SR
42/13-4 FA8	2288.2	7507.1	97.0	3.0	0.0	76.6	0.3	23.3	4.0	2.7	27.3	45.0	17.63	24.35	P	SA-SR
42/13-4 FA8	2288.4	7507.8	99.6	0.4	0.0	75.3	0	24.7	5.0	1.7	29.7	45.0	19.32	21.76	P	SA-SR
42/13-4 FA4	2288.5	7508.3	99.1	0.9	0.0	78.0	1	20.1	0.3	0.0	20.4	45.0	13.89	30.90	P, L	SA-SR
42/13-4 FA12	2293.7	7525.4	100.0	0.0	0.0	25.0	1	0.7	0.0	0.0	0.7	45.0	0.39	44.61	M, L	SA-SR
42/13-4 FA8	2296.6	7534.9	100.0	0.0	0.0	78.7	0	21.3	4.6	0.0	25.9	45.0	15.81	25.78	P	SA-SR
42/13-4 FA8	2297.0	7536.0	100.0	0.0	0.0	82.6	0.3	17.3	6.0	0.0	23.3	45.0	12.41	28.29	P	SA-SR
42/13-4 FA8	2297.3	7537.0	99.6	0.4	0.0	76.6	0.3	23.0	4.6	0.0	27.6	45.0	17.47	24.03	P	SA-SR
42/13-4 FA8	2297.6	7538.1	100.0	0.0	0.0	77.0	0.3	23.0	3.0	0.0	26.0	45.0	16.64	27.63	P	SA-SR
42/13-4 FA8	2297.9	7539.0	99.6	0.4	0.0	76.9	0.3	23.1	2.7	0.0	25.8	45.0	17.12	25.88	P	SA-SR
42/13-4 FA8	2298.3	7540.5	100.0	0.0	0.0	79.3	1	20.7	5.7	0.0	26.4	45.0	15.47	25.27	P	SA-SR
42/13-4 FA8	2298.8	7542.1	98.7	1.3	0.0	79.3	0.3	20.7	5.0	0.0	25.7	45.0	15.32	25.98	P	SA-SR
42/13-4 FA8	2299.1	7542.9	100.0	0.0	0.0	77.7	0	21.9	5.0	0.0	26.9	45.0	16.48	24.76	P	SA-SR
42/13-4 FA8	2299.3	7543.5	99.6	0.4	0.0	78.3	1	21.7	3.3	0.0	25.0	45.0	15.91	26.67	P	SA-SR
42/13-4 FA8	2299.7	7545.0	100.0	0.0	0.0	80.0	0	20.0	3.3	0.0	23.3	45.0	14.34	28.29	P	SA-SR
42/13-4 FA8	2300.0	7545.9	99.6	0.4	0.0	74.0	0	26.0	3.7	0.0	29.7	45.0	20.34	21.76	P	SA-SR
42/13-4 FA4	2300.6	7548.0	99.6	0.4	0.0	82.3	4.7	12.6	0.3	0.0	12.9	45.0	7.96	36.85	P, L	SA-SR

Table 5.2: Grain size measurements

Grain size and other measured parameters for the wells 42/13-2 and 42/13-4 in the Breagh field, United Kingdom Quad 42

Well	Depth (ft)	Depth (m)	No. of Grains Counted	Facies association	Modal size class	Mean (mm)	Median (mm)	Standard Deviation (mm)	Sorting (Trask-Trask)	Sorting (Trask-Tucker)	Sorting (Trask-SqrtPhi)	Sorting (Trask)	Sorting (F&W)	Sorting (F&W)	Skewness (mm)	Kurtosis (F&W))
42/13-2	7469.9	2276.8	300	FA4	Coarse sand	0.5274	0.6088	0.1363	1.181	1.407	1.304	moderately well sorted	0.373	well sorted	0.6	0.614
42/13-2	7491.9	2283.5	300	FA4	Medium sand	0.5085	0.5684	0.1341	1.217	1.393	1.266	well sorted	0.368	well sorted	0.971	0.652
42/13-2	7481.9	2280.5	300	FA4	Coarse sand	0.5361	0.605	0.1228	1.168	1.374	1.284	well sorted	0.34	very well sorted	0.512	0.661
42/13-2	7404	2256.7	300	FA3	Fine sand	0.1892	0.1872	0.0764	1.235	1.758	1.179	moderately sorted	0.635	moderately well sorted	0.64	0.651
42/13-2	7461.3	2274.2	300	FA3	Medium sand	0.3501	0.3337	0.1172	1.195	1.564	1.236	moderately well sorted	0.544	moderately well sorted	0.287	0.671
42/13-2	7451.11	2271.1	300	FA3	Medium sand	0.3403	0.2785	0.1075	1.262	1.451	1.181	moderately well sorted	0.414	well sorted	1.575	0.683
42/13-2	7447.5	2270.0	300	FA3	Fine sand	0.2159	0.1605	0.0582	1.2	1.414	1.119	moderately well sorted	0.389	well sorted	0.687	0.652
42/13-2	7489	2282.6	300	FA9	Coarse sand	0.6436	0.5874	0.2032	1.263	1.519	1.575	moderately well sorted	0.457	well sorted	0.912	0.652
42/13-2	7406.4	2257.5	300	FA8	Fine sand	0.1941	0.2027	0.0655	1.222	1.562	1.142	moderately well sorted	0.506	moderately well sorted	0.39	0.704
42/13-2	7442.1	2268.4	48	FA8	Coarse sand	0.7653	1.3816	0.3947	1.507	1.85	2.486	moderately sorted	0.647	moderately well sorted	1.473	0.812
42/13-2	7497.5	2285.2	300	FA9	Fine sand	0.2475	0.1706	0.0517	1.149	1.352	1.112	well sorted	0.312	very well sorted	0.455	0.646
42/13-2	7463.9	2275.0	300	FA9	Medium sand	0.4098	0.3543	0.0979	1.185	1.355	1.18	well sorted	0.349	very well sorted	0.687	0.739
42/13-2	7488.5	2282.5	300	FA9	Coarse sand	0.6628	0.4032	0.2617	1.299	1.618	1.737	moderately sorted	0.506	moderately well sorted	1.872	0.682
42/13-2	7405.8	2257.3	300	FA9	Fine sand	0.1898	0.1286	0.1052	1.537	1.752	1.172	moderately sorted	0.666	moderately well sorted	2.135	0.807
42/13-2	7442.12	2268.4	300	FA4	Fine sand	0.1962	0.1323	0.0524	1.182	1.417	1.11	moderately well sorted	0.368	well sorted	1.21	0.664
42/13-4	7507.5	2288.3	300	FA8	Medium sand	0.3469	0.3303	0.0879	1.172	1.398	1.169	well sorted	0.368	well sorted	0.246	0.707
42/13-4	7508.5	2288.6	300	FA4	Medium sand	0.5243	0.4868	0.3127	1.382	1.701	1.41	moderately sorted	0.705	moderately well sorted	2.302	0.677
42/13-4	7512.9	2289.9	300	FA4	Very fine sand	0.1114	0.091	0.049	1.391	1.713	1.125	moderately sorted	0.573	moderately well sorted	1.68	0.66
42/13-4	7513.4	2290.1	300	FA4	Fine sand	0.1508	0.0962	0.0596	1.332	1.609	1.129	moderately sorted	0.551	moderately well sorted	1.256	0.653
42/13-4	7535.1	2296.7	300	FA8	Coarse sand	0.5413	0.5348	0.1416	1.182	1.419	1.322	moderately well sorted	0.399	well sorted	0.484	0.668
42/13-4	7535.11	2296.7	300	FA8	Coarse sand	0.5529	0.6556	0.1266	1.155	1.35	1.282	well sorted	0.344	very well sorted	0.279	0.683
42/13-4	7539	2297.9	300	FA8	Coarse sand	0.5525	0.5012	0.1479	1.185	1.432	1.346	moderately well sorted	0.388	well sorted	0.521	0.66
42/13-4	7540	2298.2	300	FA8	Medium sand	0.4463	0.4459	0.1001	1.157	1.403	1.23	moderately well sorted	0.325	very well sorted	0.313	0.596
42/13-4	7542	2298.8	300	FA8	Medium sand	0.4909	0.4924	0.1256	1.22	1.345	1.222	well sorted	0.354	well sorted	0.994	0.7
42/13-4	7542.8	2299.0	300	FA8	Medium sand	0.4728	0.7022	0.1179	1.183	1.392	1.239	well sorted	0.377	well sorted	0.48	0.652
42/13-4	7543.3	2299.2	300	FA8	Medium sand	0.4579	0.3166	0.1109	1.156	1.391	1.237	well sorted	0.392	well sorted	0.149	0.592
42/13-4	7544.8	2299.7	300	FA8	Medium sand	0.5254	0.2586	0.1611	1.296	1.411	1.29	moderately well sorted	0.383	well sorted	1.8	0.749
42/13-4	7545.6	2299.9	300	FA8	Coarse sand	0.9201	0.999	0.2823	1.25	1.406	-99	moderately well sorted	0.426	well sorted	1.146	0.747
42/13-4	7546	2300.0	300	FA8	Coarse sand	0.529	0.4442	0.1718	1.286	1.494	1.354	moderately well sorted	0.434	well sorted	1.562	0.677
42/13-4	7547.8	2300.6	300	FA4	Fine sand	0.1616	0.1581	0.0467	1.213	1.371	1.088	well sorted	0.358	well sorted	2.469	0.656
42/13-4	7549.2	2301.0	300	FA4	Very fine sand	0.0898	0.1225	0.0283	1.194	1.446	1.078	moderately well sorted	0.428	well sorted	1.352	0.673
42/13-4	7550.7	2301.5	300	FA4	Very fine sand	0.0853	0.1388	0.024	1.208	1.424	1.073	moderately well sorted	0.419	well sorted	0.687	0.659
42/13-4	7551.5	2301.7	300	FA4	Very fine sand	0.086	0.0959	0.0218	1.181	1.397	1.07	well sorted	0.384	well sorted	0.495	0.655
42/13-4	7539.19	2297.9	300	FA8	Medium sand	0.4857	0.4095	0.1455	1.244	1.502	1.311	moderately well sorted	0.401	well sorted	1.204	0.622
42/13-4	7548.5	2300.8	300	FA4	Very fine sand	0.099	0.1225	0.0286	1.202	1.484	1.088	moderately well sorted	0.41	well sorted	0.755	0.674

FA3-Distributary mouth bar facies; FA4-Distal delta front sand; FA8-Distributary channel facies; FA9-Briaded fluvial channel facies

Mineralogical description and quantification of the Breagh Sandstones made use of samples from wells 42/13-2 and 42/13-4. Based on the classification scheme of (Pettijohn, 1957), the Quartz, Feldspars and Lithic fragments (QFL) composition for the sandstone range from quartz arenite to sublitharenite. Majority of samples from both wells falls within the quartzarenite group and fewer samples are sublitharenite (Table 5.; Figure 5.).

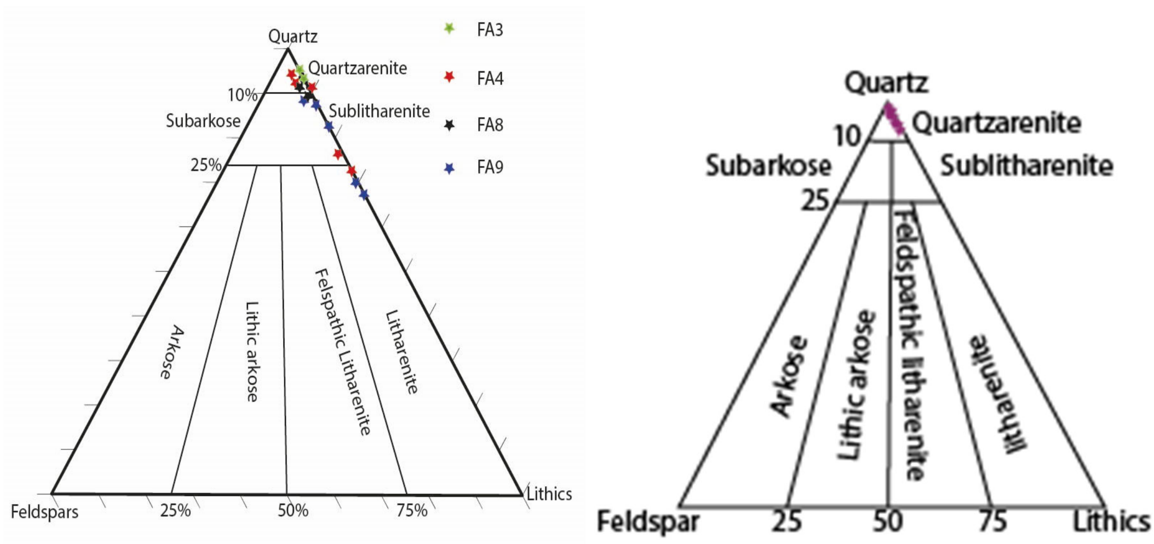

Figure 5.1: QFL diagram for Well 42 13-2 after Pettijohn, 1957. Left is QFL for 42/13-2 and Right is QFL is 42/13-4.

Petrographic analysis of the samples indicates that the detrital grains of the Breagh Sandstone consist of very fine grained to coarse grained sands (with granule particles at intervals) although the medium grain ranges predominate (Table 5.2, Figure A- E). The grains are mostly subangular to subrounded with locally angular grains (Table 5., Figure A- E).

Compositionally, quartz is the dominant detrital mineral (25-82.3% - av. 65%) (Table 5.1 and Fig 5.1) and it is dominated by monocrystalline grains, with subordinate polycrystalline and microcrystalline grains. XRD analysis from well report corroborates the data that quartz is abundant in all samples (18-85 wt%)). Feldspars are generally absent and where present is very scant (1-2counts/ per 300grains); as noted under XRD, Feldspars only make up: 0-1 wt% are composed of both potassium and plagioclase feldspar. Significant dissolution of Feldspars occurs in all samples where feldspars are seen (Figure 5.2D).

Rock fragments are dominated by mud clast but also comprise of granite, mica schist grains, quartz-schist, and volcanics. They make up (trace to 2.3%, - av. 0.3%) of the grains (Table 5.1). The quartz schist grains are stable and show little deformation or alteration, whereas the mica schist and phyllite grains show varying degrees of deformation, alteration (mainly to kaolinite and illite) and in some cases dissolution.

Detrital micas (Trace-13.7%, av. 3%) are present in all samples in trace to minor abundances with high percentages occurring in mudrock rich sections. They also have higher abundances in the mudstones samples which are not analyzed for this study. The mica minerals are predominantly muscovite with some local biotite observed under SEM. Although they appear commonly well preserved at the scale of thin section, SEM analysis reveals that they are locally deformed (Figure 5.2Fi-ii). Splitting and fanning of the mica grains also occurs as observed in (Fig 5.2Fi-ii, & 5.16 k, l).

Oil streaks are present within primary porosity and seen lining the rims of secondary porosity (details residual hydrocarbon is discussed section 5.6.2.2 below).

Packing is typically moderate to high, with point/tangential grain contact (Table 5., Figure a-e) dominating throughout. Some quartz-to-quartz long/straight grain contacts can be seen in the more tightly packed samples (Fig 5.2b). Concavo-convex and sutured contacts are also observed in mostly the delta front sands (FA3 and FA4) (Fig 5.2e), indicating significant mechanical compaction. The COPL-CEPL results, shown in (Fig 5.6e below), indicate that mechanical compaction is the driver of porosity loss in both cored sections, leading to minimal primary porosity (Fig 3x) and reduced intergranular volume (IGV) (Table 5.; Fig. 4x).

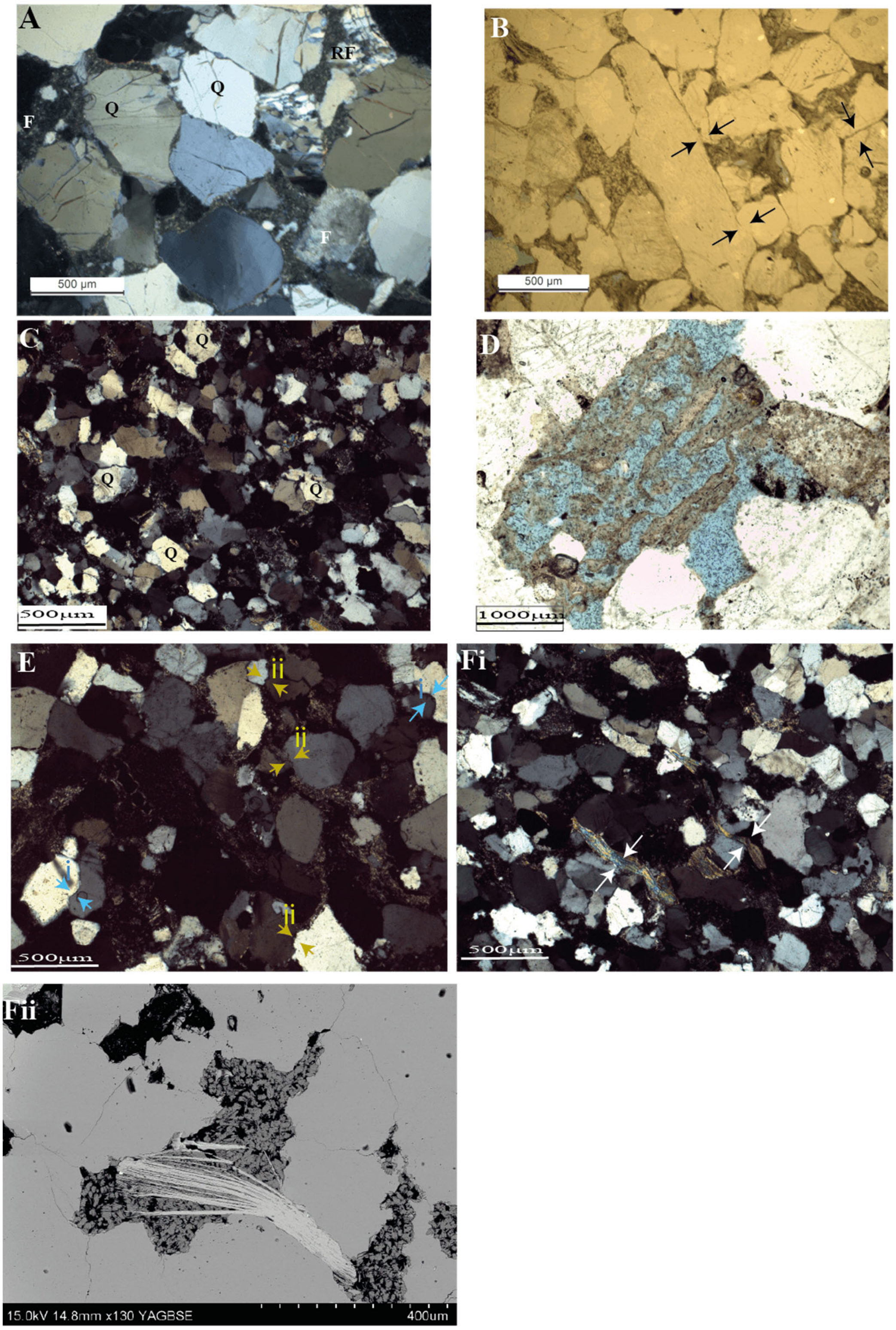

Figure 5.2: A: Photomicrograph of coarse grained, poorly sorted sandstone showing quartz, rock fragments and feldspar grains (7535ft); B: Photomicrograph of coarse grained poorly sorted sandstone angular to subrounded sandstone quartz to quartz point and long grain contact (PPL-7546ft); C:Photomicrograph of fine to medium grained moderately sorted sandstone showing predominantly quartz grains (7404ft); D:Photomicrgraph of medium grained well sorted sandstone with relics of partially dissolved of feldspar (7491ft); E: Photomicrograph of medium grained well sorted sandstone indicating concavo-convex contact (arrow i) and the onset of sutured contact (arrow ii) (PPL-7491.9ft); Fi: Photomicrograph a slide with bended muscovite (XPL-7497.5ft) and Fii: Bended muscovite under SEM probably indicating moderately high compaction (7542ft): [PPL= Plane polarized, XPL= Plane polarized Q = quartz, F = feldspar, RF= rock fragments].

5.3 Intergranular volume, Cementation and Mechanical compaction.

The samples used for the Intergranular volume (IGV) and total cement (CEM) measurements were selected based on the criteria set forth by (Ajdukiewicz *et al*., 1991; Szabo and Paxton, 1991; Paxton *et al*., 2002). The authors defined suite of petrographic criteria necessary for ensuring that burial compaction pathways, as monitored by porosity and permeability are defined by sands and sandstones with comparable grain composition, size, sorting, and volume of depositional matrix. These criteria are set because variations in sorting can significantly lower the initial intergranular volume prior to the onset of compaction. Also rates of intergranular pressure solution and quartz cementation have been shown to be sensitive to grain size (Houseknecht, 1987, 1989; Lander and Walderhaug, 1999).

In terms of sorting, only moderately well sorted to very well sorted sample (see table 5.2) were used. For grain size, samples were restricted to grain sizes greater than or equal to 0.08mm (80μm). The sandstones samples range from sub angular to subrounded with a couple of angular to subrounded samples (Table 5.1).

The sample type used to calculate the intergranular volume and total cement measurements are thin sections from the cores of two wells in the Breagh Field (well 42/13-2 and 42/13-4; (Table 1 & Table 2; see also Chapter 4 for well logs). The 36 sample points used for the petrographic and textural analysis were collected from core depth (7385ft-7506ft for 42/13-2) and (7507ft -7615ft for 42/13-4) to cover the main reservoir facies for Breagh Sandstone which are FA3-distributary mouth bar facies; FA4-distal delta front sand facies; FA8-distributary channel facies; FA9-briaded fluvial channel facies).

All thin sections were highly polished to 30 μm and impregnated with blue epoxy to help with identification of visible porosity. Sections were counted with 300 points per thin section. The sections were coated with carbon prior to analysis using a Hitachi SU-70 field emission gun scanning electron microscope (SEM) and equipped with an energy-dispersive detector (EDS). Scanning electron microscope analyses of thin section and bulk rock samples were conducted at 5 to 20 kV acceleration voltage with beam currents of 1.0 and 0.6 nA, respectively. Point analyses had an average duration of 2 minutes, whereas line analyses were dependent on length. SEM–EDS was used for rapid identification of chemical species and orientation on the sample. Samples were analyzed using transmitted-light microscopy on impregnated thin sections and modal analysis was undertaken on all samples to ascertain mineralogy (300 counts per section).

The resulting data were used to calculate intergranular volume (IGV) (Paxton *et al*., 2002), porosity loss through mechanical compaction (COPL) and porosity loss by cementation (CEPL) (Lundegard, 1992). Optical porosity, grain size, cements fraction and depositional matrix were measured for this study. Grain size distribution was analyzed by using the Leica QWin (V. 3.5.0) software on thin section micrographs and the fraction of cements, depositional matrix and optical porosity were measured by point counting with 300 counts per thin section. In all sections, care was taken to use only intergranular porosity. Also distinguished were grain replacements from intergranular cements and only intergranular cements were counted to avoid exaggerating the intergranular volume (Paxton *et al*., 2002). Likewise, care was taken to ensure that secondary leached-grain (intragranular) porosity was not classified as intergranular porosity.

The measured total cement volume (*CEM*) and Intergranular Volume (IGV) were then used to calculate the porosity losses caused bycompaction (*COPL*) and cementation (*CEPL*) using the following equations (Ehrenberg, 1989; Lundegard, 1992).

$$\mathrm{COPL} = OP - \frac{(100 * IGV) - OP * IGV)}{(100 - IGV)} \ldots\ Equation\ 1$$

$$\mathrm{CEPL} = (OP - COPL) * \frac{CEM}{IGV} \ldots \ldots \ldots \ldots \ldots Equation\ 2$$

Where IGV is the sum of intergranular pore space, intergranular cement, and depositional matrix (Paxton *et al*., 2002) and total cement volume represents the volume of all pore-filling diagenetic cements, including quartz, carbonate minerals, pyrite, sulfate minerals, kaolinite, illite and other clay cements. OP represents an original porosity estimate of 45% based on the experimental data of on wet sands and the measured grain size and modal analysis from thin sections (Beard and Weyl, 1973; Nguyen *et al*., 2013). The results of the IGV measurements show very small variation between the sample sets from wells 42/13-2 and

42/13-4. The 42/13-2 intergranular volumes vary from 20.3% to 40.3% with a mean value of 28.5%. The 42/13-4 IGV plots in between 12.9% and 36.9% and has a mean of 24.2% (Fig 5.3). The total cement (CEM) volume varies for the 42/13-2 samples from 11.0% up to 34.0%, with an average of 22.3%. The 42/13-4 field samples show total cement volumes from 7.9% to 26%, with a slightly lower average of 20.4% (Table 5.2 Fig 5.3).

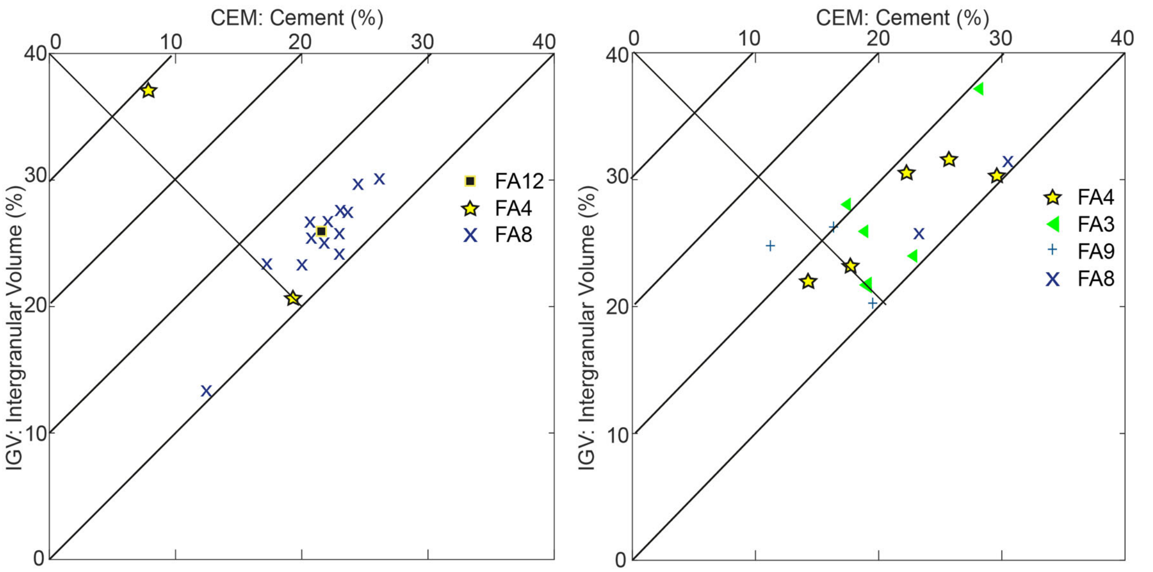

Fig 5.3: Plot of total Cement (CEM) vs intergranular volume (IGV). Left- 42/13_4 and Right: 42/13_2 (FA3-Distributary mouth bar facies; FA4-Distal delta front sand facies; FA8-Distributary channel facies; FA9-Braided fluvial channel facies); diagonal lines measure lines intergranular volume.

The resulting plots of intergranular volume (IGV) against cement volume for well 42/13-2 and 42-13-4 is shown in (Fig 5.3) respectively. Both plots are similar and indicates that 90% of the samples from 42-13-2 and all except one of the samples 42/13-4 well falls between the 0% and 10% intergranular porosity lines. Based on lithofacies, all the samples from lithofacies FA3 to FA12 fall within 0 to 10% intergranular porosity line for both wells indicating higher compaction than cementation. The samples outside of these lines are the 3 samples points (from the chaotic and pebbly zones) of the FA9 lithofacies in 42/13-4 and one sample point from (fine grained silty sandstone) zone from the FA4 facies in 42/13-4.

Further illustration of the relative impact of compaction and cementation on porosity loss is shown by the plot of COPL vs CEPL (Fig 5.4). It should be noted however that the calculated COPL and CEPL from equations 1 and 2 are only accurate if three conditions are met. First, the assumed initial porosity (OP) must be correct. Second, the amount of cement derived by local grain dissolution must be negligible or known. And third, the amount of framework mass exported by grain dissolution must be negligible or known (Lundegard, 1992). Because the Breagh sandstones have undergone minimal pressure dissolution, it is possible to calculate COPL and CEPL, respectively (Ehrenberg 1989) using the Equation 1 and 2.

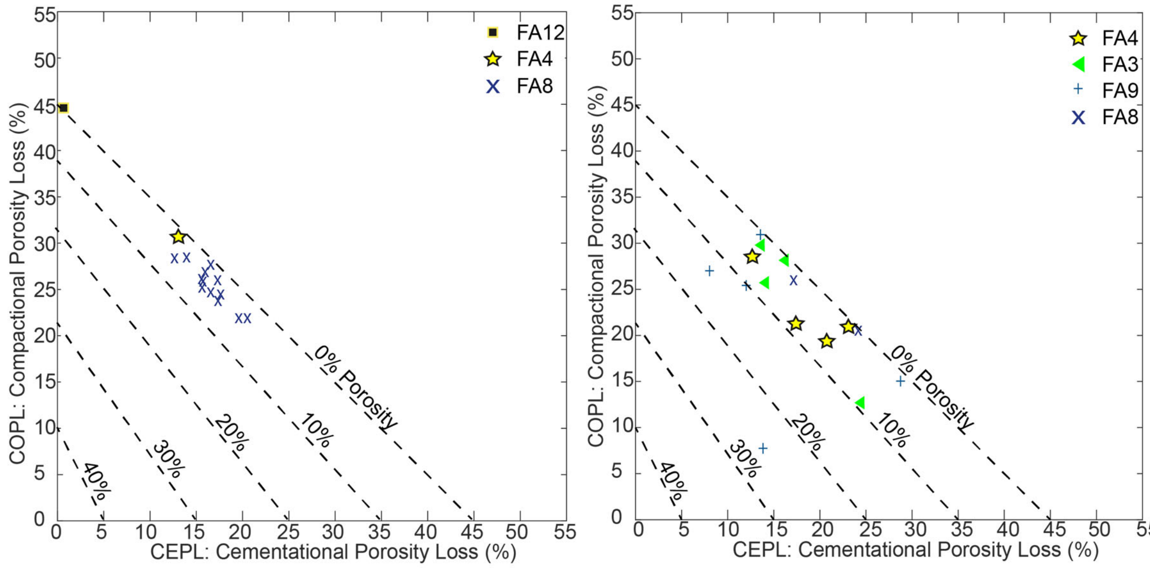

Fig 5.4: Plot of Original Porosity loss by compaction (COPL) vs Original Porosity loss by cementation (CEPL). Left- 42/13_4 and Right: 42/13_2 (FA3-Distributary mouth bar facies; FA4-Distal delta front sand facies; FA8-Distributary channel facies; FA9-Briaded fluvial channel facies.

The COPL-CEPL results show porosity loss for both sample sets were predominantly by mechanical compaction (Fig 5.4), with averages of 22.6% and 27.68% for the 42/13-2 and 42/13-4 sample sets, respectively. Furthermore, the results show lower values for porosity loss by cementation with an average of 17.4% and 14.8% for the 42/13-2 for the 42/13-4 sample sets respectively.

5.4 Porosity and Permeability.

The Breagh sandstones have a wide range of porosity and permeability (ϕ = 0.1% - 19% and K= 0.1 mD – 379 mD) (Fig 5.5). Porosity and permeability follow the same trend in most samples. Hence factors which affect porosity would mostly affect permeability.

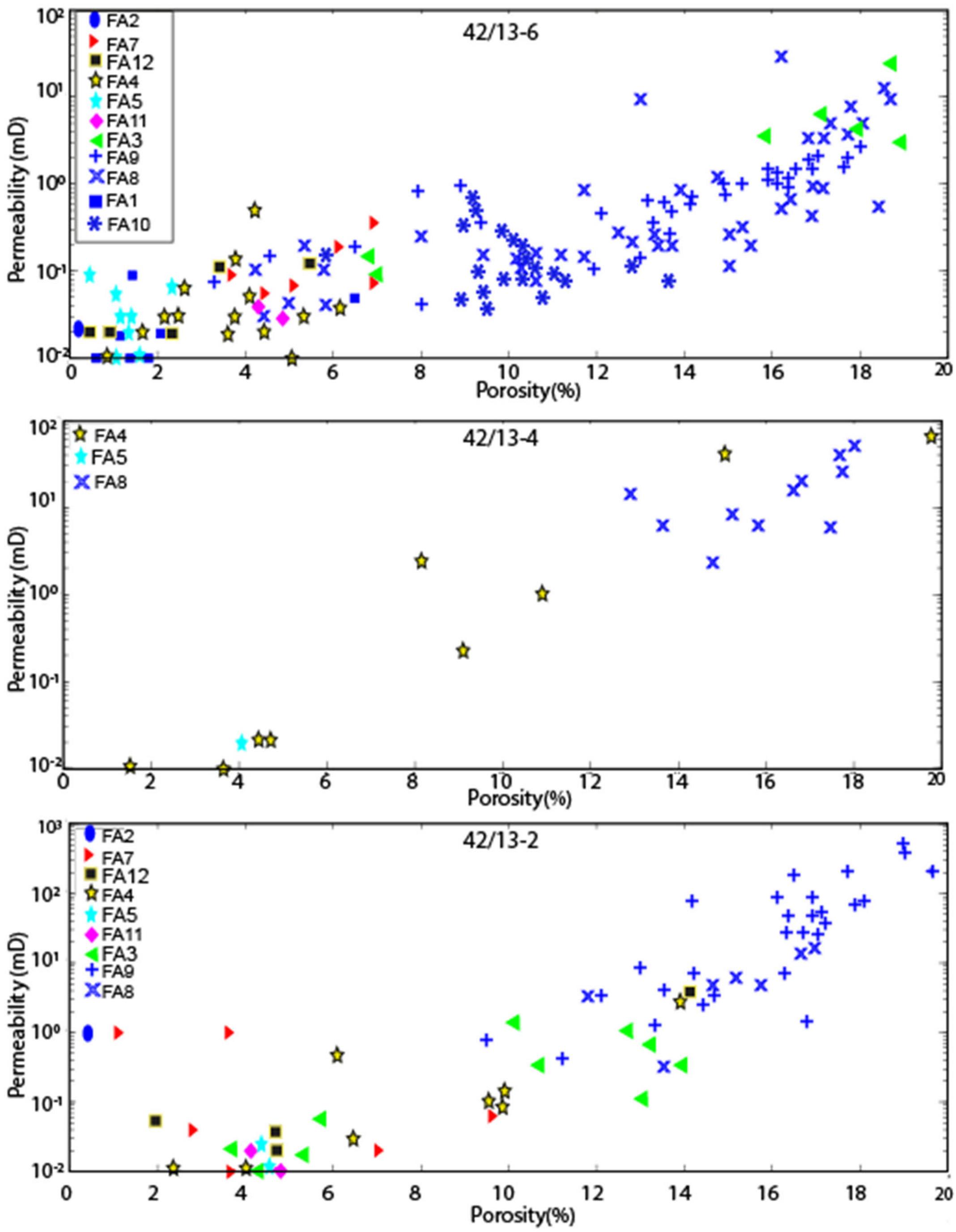

Fig 5.5: Porosity and permeability cross plots for the Breagh field wells

Reservoirs sandstones in the Breagh comprises a mixture of sand sheets and channels. The reservoir properties of the sandstone are relatively poor although the best reservoir intervals found in the channel sands (FA3, FA8, FA9, and FA10) have permeability in the range 0.1 to 100 mD. Most permeabilities range from 1-10mD and porosities in the range of 9.5–19.6% (average 11.6%). The non-channel sands (FA1, FA2, FA4, FA5, FA6, FA7 and FA11) all have porosities less than 10% and permeabilities ranges 0.1mD and 1mD. (Fig 5.5). In all cases, post-depositional burial has reduced reservoir quality through compaction and diagenesis, resulting in tight sandstones.

5.5 Diagenetic minerals.

The main diagenetic processes identified in the studied samples include cementation by carbonate, clay minerals and quartz cements (Fig 5.6 & 5.7). The vertical distribution of major cements in 42/13-4 and 42/13-2 well is shown in (Fig. 5.7). Clay mineral (kaolinite and illite rich clays) and carbonate (mainly dolomite and calcite) cements are the most common pore-filling cements, followed by authigenic quartz cement and bituminous hydrocarbon. Hematite, pyrite, anhydrite and barite, are minor cements.

5.5.1 Clay mineral cements.

Authigenic clays are present in all samples and are the dominant diagenetic phase (Fig 5.6 & 5.7). Point count data (Table 5.3) identifies 5 to 23% (average of 15.3%) total clay mineral cement concentration in both studied wells.

From point count analysis, authigenic clays are predominantly kaolinite (Fig 5.8a), with subordinate undifferentiated clays. XRD (Table 5.4) shows that the undifferentiated clays are illitic and regularly ordered mixed layer illite/smectite.

Under the SEM however other authigenic clays that were unresolvable at the scale of thin section become more visible. Based on SEM morphological characteristics, illite (including illite/mica and illite/smectite), mixed layer clays were identified (Fig 5.8a b,c,d,e,f,g,h,i). XRD data (Table 5.4) supports the finding from the SEM based analysis and confirms the presence of chlorite in trace (trace -1% av. Of 0.2%) amounts.

Each clay mineral has varying textures and concentrations. kaolinite is present as a common to abundant primarily pore-filling/lining phase and appears as aggregates of books and verms with individual crystals up to (~10-20μm) A stacked aggregate of vermicular kaolinite is observed to fill intergranular pore. Rounded aggregates, as observed under SEM, are suspected as being potentially grain/clast-replacive. Locally, larger forms may indicate dickite. This is supported by XRD analysis which indicates that dickite is present in all samples. Exact quantification of the value for dickite, is however difficult but is listed as minor.

Detailed SEM analysis on chips and thin-section reveal that the illitic clays are typically wispy to locally morphologically indeterminate, locally forming tangential grain-coatings, locally forming ridges on grain surfaces, and bridging pore throats. Continuous growth of illite cement is observed as the fibrous morphology of interlocking meshwork, bridging, and filling intergranular pores (Fig 5.8g). Under the SEM, illite fibre can be as long as 30-50 μm.

Undifferentiated/mixed layer clays are observed as both pore-lining and grain-coating. Energy dispersive X-ray (EDX) indicates the presence of mixed illite-smectite, and illite-mica composition preserved in the coated grains, which complement XRD result (Table 5.3). These clays show a platy–sheetlike morphology (Fig 5.8 b,c) and are commonly seen to be intergrown with kaolinite (Fig 5.8b,e).

In terms of relative abundance, SEM analysis of the samples show that kaolinite ranges from 0.5% to 15.5% av. 13.56%. Kaolinite is more abundant in samples from 42/13-4 well and observed to postdate quartz overgrowth. Kaolinite cement is also observed to replace detrital feldspar and mica grains and thus predates the development of illite rich cements.

Undifferentiated mixed layer clay is more widespread and range in volume between 15.8% to 20.1%. As earlier noted, the illitic phase was hard to differentiate however after careful observation of the samples, SEM result reveal an illite/smectite peak at 7491ft and 7447.5ft and an illite/mica peak in 7497.5ft and 7451.1ft. From XRD data, illite/mica range from (0 to 39% av. 8.5%), and (illite/smectite 0-31% av. 9.25%).

The high content of illite within the illite/smectite, (Table 5.3) coupled with the almost total absence of potassium feldspar (Table 5.4) may be a possible indicator of widespread illitization. The presence of dickite and the high amount of illite/illite-rich, illite/smectite (R3) seems to indicate a high level of mineralogical maturity (further details on dickite in section 5.6.1.7 below).

In both studied wells, point counting, and SEM data do not reveal any definite order of increment or decrease with depth of the clay mineral volume. However, the XRD values of 42-13/4, shows that the highest volume of clay minerals is present at depth. From the same data set, illite/smectite content increases with depth while illite/mica appears to decrease with depth. Kaolinite abundance decreases with depth (Table 5.4).

Table 5.3: Point counting values normalized to 100% for the diagenetic minerals of the Breagh Sandstones (42/13-4 and 42/13-2).																			
Well No	Facies	Dept (m)	Depth (Ft)	Quartz Overgrowth	Hydrocarbon (bitumen?)	Resin & Amber	Liptinite/ Extinite	Amorphous organic mater	Ankerite (Pore filling)	Dolomite – (Pore filling)	Siderite	Mixed clays (Illite-Smectite?)	Kaolinite	Grin coating clays	Non resolvable opaques & Haematite	Pyrite (pore filling)	Limonite	Anhydrite (Pore filling)	Barite
42/13-2	FA4	2276.8	7469.9	0.0	1.0	1.3	0.0	1.3	0.0	3.0	0.0	11.2	6.0	0.5	0.0	0.0	0.7	0.7	0.0
42/13-2	FA4	2283.5	7491.9	2.7	2.7	0.0	0.0	0.0	0.0	0.0	0.0	10.3	8.0	2.0	1.7	0.3	0.7	0.0	0.0
42/13-2	FA4	2280.5	7481.9	0.0	1.0	0.3	0.0	0.0	0.0	0.0	0.0	8.4	2.3	1.6	3.3	1.0	0.3	0.7	0.0
42/13-2	FA3	2256.7	7404.0	0.0	5.0	0.0	0.3	0.0	0.0	0.0	0.0	4.3	8.0	1.1	3.0	2.3	0.7	0.0	0.0
42/13-2	FA3	2274.2	7461.3	0.0	5.3	0.0	0.0	0.0	0.0	3.7	0.0	8.0	2.3	0.0	0.0	0.0	0.7	4.3	0.0
42/13-2	FA3	2271.1	7451.0	0.0	1.0	0.0	0.0	0.0	1.3	1.7	0.0	11.2	5.0	2.8	0.3	1.3	3.3	1.0	0.0
42/13-2	FA3	2270.0	7447.5	0.3	0.7	0.0	0.0	0.0	0.0	0.0	0.0	18.0	3.7	0.0	0.0	0.0	1.0	0.0	0.0
42/13-2	FA9	2282.6	7489.0	0.0	0.3	0.0	0.0	0.0	0.0	0.0	0.0	4.9	1.3	1.1	1.3	0.7	0.3	1.3	0.0
42/13-2	FA8	2257.5	7406.4	0.0	6.0	0.0	0.0	0.0	0.0	1.0	0.0	3.5	9.7	0.5	2.3	3.7	2.0	0.3	0.0
42/13-2	FA8	2268.4	7442.1	0.0	1.7	0.7	0.0	0.0	2.7	0.7	0.0	15.8	0.7	3.9	1.3	0.3	0.3	5.0	0.0
42/13-2	FA9	2285.2	7497.5	5.0	1.7	0.0	0.0	0.0	0.0	0.0	0.0	8.1	13.3	1.5	1.3	2.3	0.7	1.7	0.0
42/13-2	FA9	2275.0	7463.9	0.0	0.3	0.3	0.0	0.0	1.0	0.7	0.0	3.1	1.3	0.5	5.0	0.3	3.0	1.3	0.0
42/13-2	FA9	2282.5	7488.5	0.0	0.3	0.0	0.0	0.0	2.0	0.7	0.0	6.1	0.0	1.5	1.7	0.3	1.3	1.3	0.0
42/13-2	FA9	2257.3	7405.8	0.0	10.0	0.3	0.3	0.0	0.0	0.0	0.0	8.1	5.0	1.9	0.3	3.3	1.0	0.0	0.0
42/13-2	FA4	2263.1	7425.0	2.0	3.3	0.0	0.0	0.0	1.7	0.7	0.0	7.9	7.3	1.5	3.7	1.7	0.3	3.0	0.0
42/13-4	FA8	2288.2	7507.1	4.3	2.7	0.0	0.0	0.0	0.0	0.0	0.0	0.0	13.0	2.0	1.3	0.0	0.0	0.0	0.0
42/13-4	FA8	2288.4	7507.8	6.0	1.7	0.0	0.0	0.0	0.0	2.7	0.0	0.0	12.0	2.3	1.0	0.0	0.0	0.0	0.0
42/13-4	FA4	2288.5	7508.3	1.7	0.0	0.0	0.0	0.0	0.0	0.3	0.0	0.0	15.7	1.7	0.7	0.0	0.0	0.0	0.0
42/13-4	FA12	2293.7	7525.4	0.0	0.0	0.0	0.0	0.0	0.0	0.0	0.0	0.0	0.0	0.0	0.7	0.0	0.0	0.0	0.0
42/13-4	FA8	2296.6	7534.9	3.0	0.0	0.0	0.0	0.0	0.0	0.0	0.0	0.0	14.3	3.3	0.0	0.0	0.0	0.0	0.7
42/13-4	FA8	2297.0	7536.0	1.0	0.0	0.0	0.0	0.0	0.0	0.0	0.0	0.0	15.3	1.0	0.0	0.0	0.0	0.0	0.0
42/13-4	FA8	2297.3	7537.0	0.7	0.0	0.0	0.0	0.0	0.0	5.7	0.0	0.0	14.3	2.3	0.0	0.0	0.0	0.0	0.0
42/13-4	FA8	2297.6	7538.1	1.0	0.0	0.0	0.0	0.0	0.0	1.3	0.0	2.0	13.3	4.7	0.7	0.0	0.0	0.0	0.0
42/13-4	FA8	2297.9	7539.0	1.7	0.0	0.0	0.0	0.0	0.0	0.7	0.0	0.0	18.0	2.7	0.0	0.0	0.0	0.0	0.0
42/13-4	FA8	2298.3	7540.5	0.3	0.0	0.0	0.0	0.0	0.0	2.7	0.0	0.0	13.3	3.7	0.0	0.0	0.0	0.0	0.7
42/13-4	FA8	2298.8	7542.1	0.3	0.0	0.0	0.0	0.0	0.0	2.7	0.0	0.0	14.0	3.7	0.0	0.0	0.0	0.0	0.0
42/13-4	FA8	2299.1	7542.9	4.3	0.0	0.0	0.0	0.0	0.0	2.3	0.0	0.0	13.3	2.0	0.0	0.0	0.0	0.0	0.0
42/13-4	FA8	2299.3	7543.5	1.0	0.0	0.0	0.0	0.0	0.0	1.3	0.0	0.0	16.0	2.7	0.0	0.0	0.0	0.0	0.0
42/13-4	FA8	2299.7	7545.0	2.7	0.0	0.0	0.0	0.0	0.0	0.3	0.0	0.0	14.0	3.0	0.0	0.0	0.0	0.0	0.0
42/13-4	FA8	2300.0	7545.9	2.7	0.0	0.0	0.0	0.0	0.0	1.3	0.0	0.0	12.7	9.3	0.0	0.0	0.0	0.0	0.0
42/13-4	FA4	2300.6	7548.0	0.3	0.0	0.0	0.0	0.0	0.0	3.3	0.0	0.05.7	0		0.3	3.0	0.0	0.0	0.0

Table 5.4: Whole-Rock & Clay Mineralogy of selected Breagh sandstones samples (42/13-4) as determined Via X-Ray Diffraction (adapted from sterling resources).

BULK CLAY AND XRD FRACTION																							
	Calculated whole rock composition (Weight %)																		Relative clay abundance- Normlised to 100%				
Depth (ft)	Quartz	Anhydrite	K-Feldspar	Plagioclase	Hematite	Calcite	Dolomite	Halite	Siderite	Natrite ?$Na_2(C0_3)$	Pyrite	Illite/Smectite	Illite+ mica	Kaolinite	Chlorite	Total	Total clay	Other cement	Illite + Mica	Kaolinite	Chlorite	Mixed layer Illite/ Smectite	% Smectite in Illite/ Smectite
7507.1	79	0	0.1	0.1	0	0.1	0	0.1	0	0	0	0	7	13	1	21.2	21	0.2	33	64	4	0	0
7507.75	85	0	0	0	0	Tr	0	Tr	0	0	0	0	5	10	Tr	15	15	0	32	66	2	0	0
7508.25	70	0	0	0	0	0.1	0.1	0.1	0.1	0	0	0	13	17	0.1	30.5	30.1	0.4	42	57	1	0	0
7511.1	18	0	0	0	41	0	6	1	6	2	0	0	17	9	0	82	26	56	67	33	0	0	0
7513.2	58	0.1	0	0	1	0	0	0.1	8	0.1	0	0	10	22	1	42.2	33	9.2	29	69	2	0	0
7518.4	28	0	0.1	0	0.1	0.1	0.1	0	2	0.1	0	0	34	35	1	72.4	70	2.4	48	51	1	0	0
7519.3	27	0	1	0	0	0.1	0.1	0.1	3	0.1	2	0	39	27	1	72.4	67	5.4	57	41	2	0	0
7520.3	23	0	1	1	0	0	0.1	1	0.1	0.1	0	31	0	43	0	75.3	74	1.3	0	58	0	42	5-10%
7525.4	27	0	1	0.1	0	0.1	0.1	0.1	0	0	0	27	0	45	0	72.3	72	0.3	0	63	0	37	5-10%
7534.9	76	0.1	0	0	0	0	0	0	0	0	0	16	0	8	0.1	24.1	24.1	0	0	35	1	64	5-10%
7536	78	0.1	0	0	0	0	1	0.1	0.1	0	0	14	0	7	0.1	22.3	21.1	1.2	0	34	2	64	5-10%
7537	81	0.1	0	0.1	0	0	2	0	0	0	0	12	0	5	0	19	17	2	0	30	0	70	5-10%
7538.1	78	0.1	0.1	0	0	0	2	0.1	0	0	0	19	0	1	0.1	22.2	20.1	2.1	0	7	0	92	5-10%
7539	78	0.1	0	0	0	0	1	0	0	0	0	17	0	4	0.1	22.1	21.1	1	0	17	1	82	5-10%
7540.5	77	0.1	0.1	0	0	0	2	0.1	0	0	0	18	0	3	0	23.1	21	2.1	0	15	0	85	5-10%
7542.1	78	0.1	0	0	0	0	3	0.1	0	0	0.1	0	13	6	0	22.2	19	3.2	68	32	0	0	0
7542.9	82	0.1	0	0	0	0	2	0.1	0	0	0	0	9	7	0	18.1	16	2.1	56	44	0	0	0
7543.5	78	0.1	0	0.1	0.1	0	3	0.1	0	0	0	14	0	5	0	22.2	19	3.2	0	25	0	75	5-10%
7545	74	0.1	0	0	0	0	0.1	0.1	0	0	0	0	23	3	0.1	26.3	26.1	0.2	87	12	0	0	0
7545.9	79	0.1	0	0	0	0.1	1	0.1	0	0	0	17	0	3	0.1	21.3	20.1	1.2	0	15	0	85	5-10%

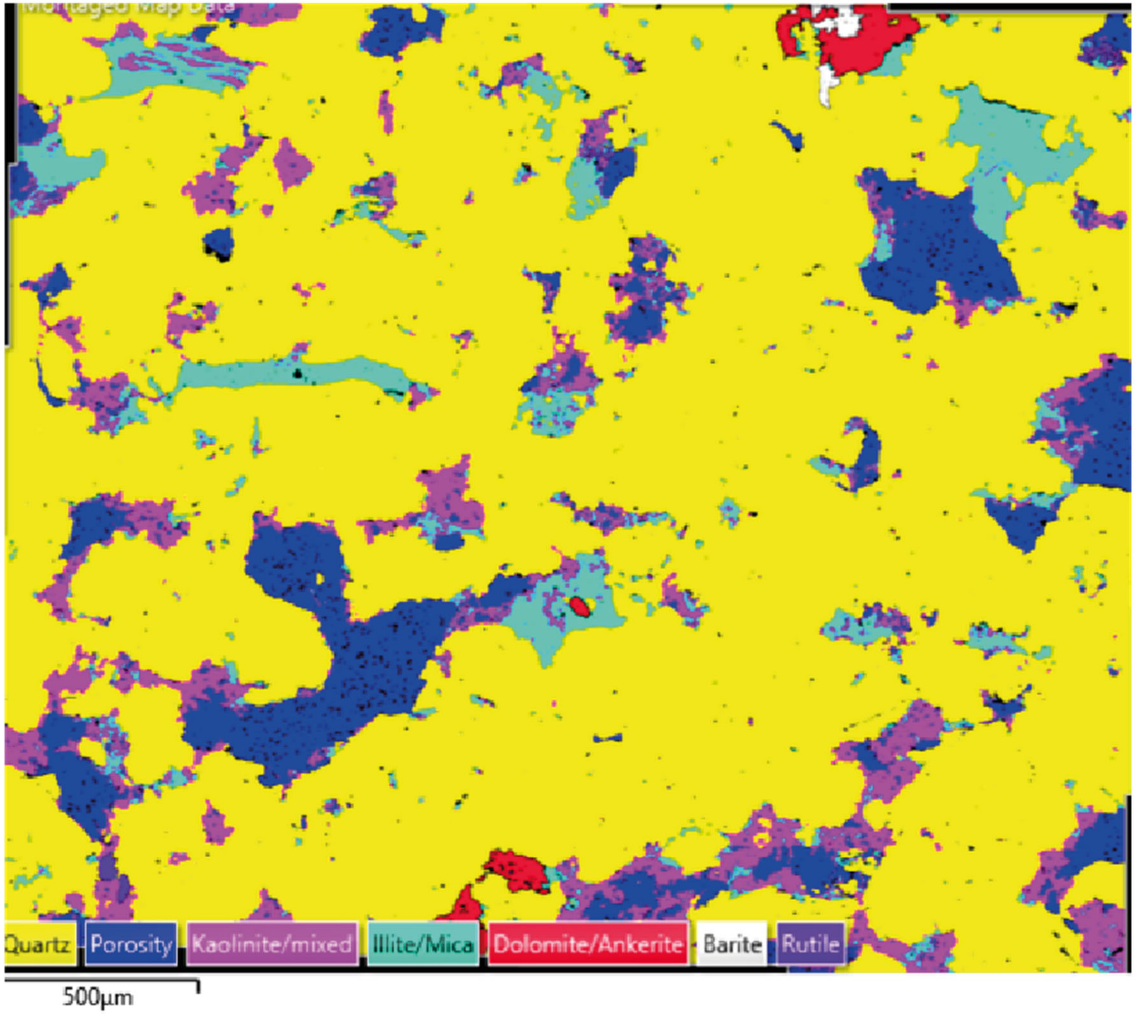

Phase	Fraction (%)	Pixel Count
Quartz	76.2	1914332
Porosity	7.8	195638
Kaolinite/mixed clays	7.5	189576
Illite/Mica	5.1	128483
Dolomite/Ankerite	0.8	19500
Barite	0.1	3344
Rutile	0.2	4027
Unassigned pixels	7.2	182129

Figure 5.6: SEM photo image showing the distribution of common diagenetic minerals in the Breagh Sandstones @7497.5ft from well 42/13-2. See pages 210 - 212 for distribution of the extracted respective minerals.

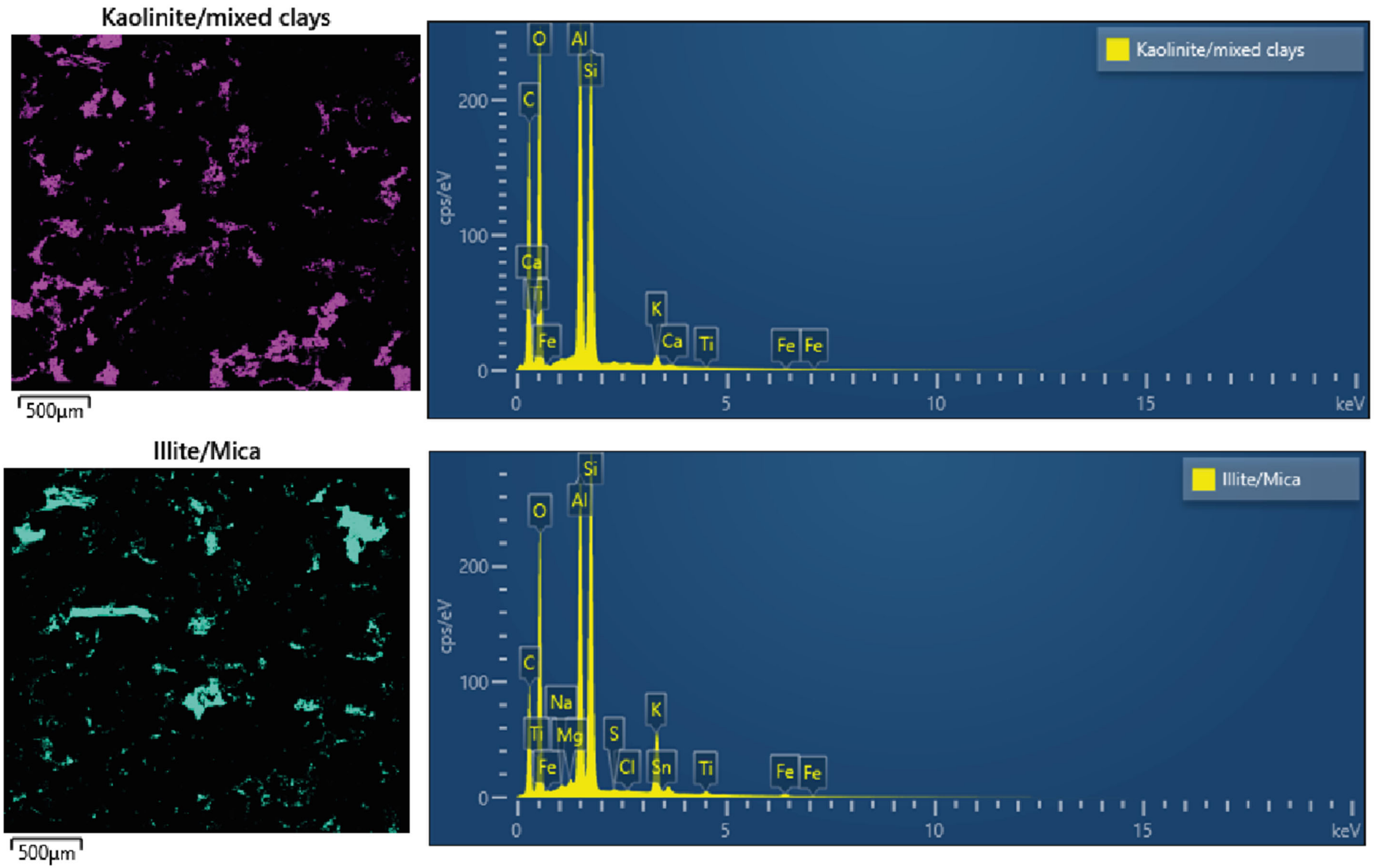

Kaolinite/mixed clays
500µm
Kaolinite/mixed clays
cps/eV
200
100
0
O
Al
Si
C
Ca
Ti
Fe
K
Ca
Ti
Fe
Fe
0
5
10
15
keV
Illite/Mica
500µm
Illite/Mica
cps/eV
200
100
0
Si
Al
O
C
Na
Ti
Mg
Fe
S
Cl
K
Sn
Ti
Fe
Fe
0
5
10
15
keV

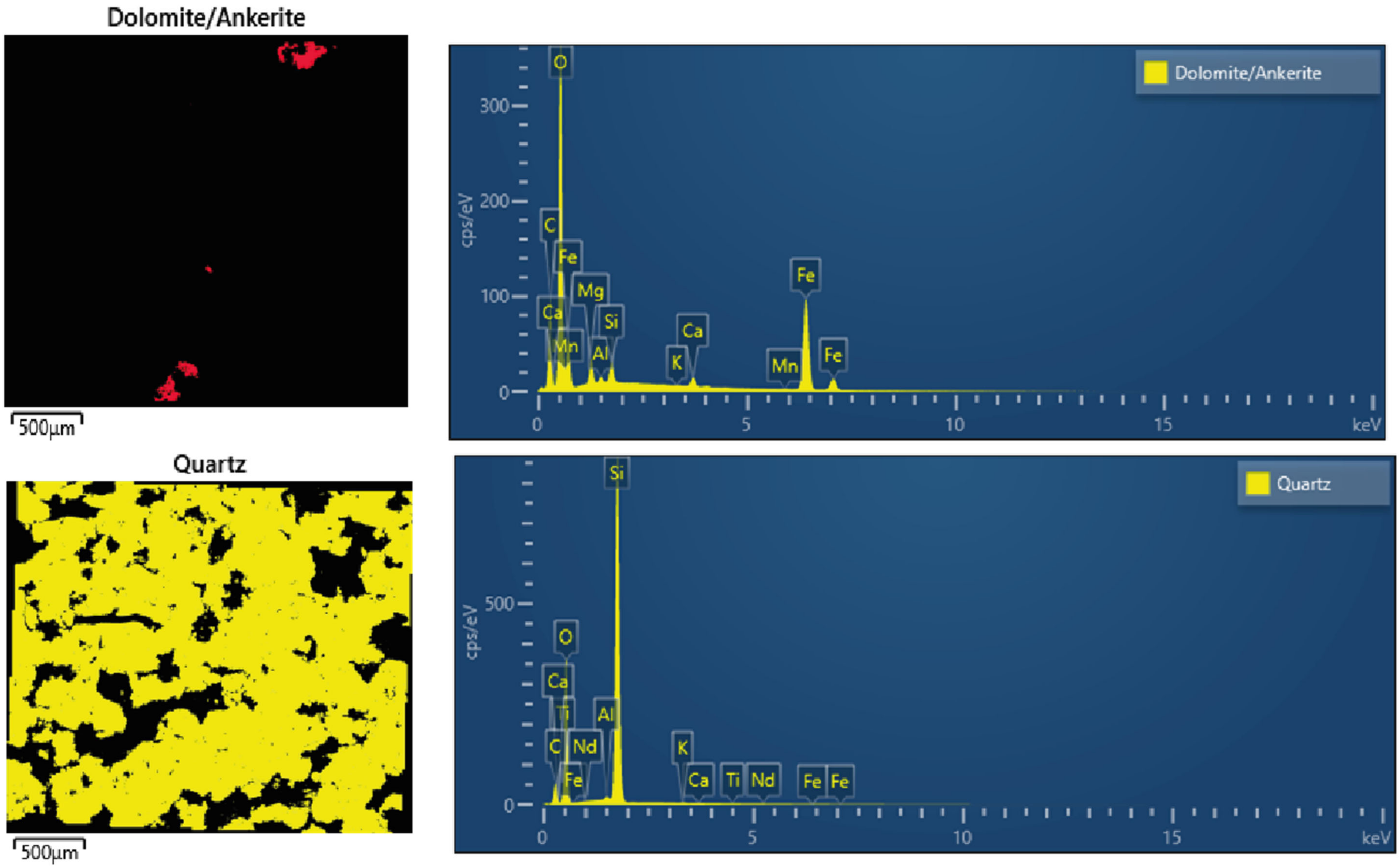

Dolomite/Ankerite
500µm
Dolomite/Ankerite
cps/eV
300
200
100
0
O
C
Fe
Mg
Ca
Si
Mn
Al
K
Ca
Fe
Mn
Fe
0
5
10
15
keV
Quartz
500µm
Quartz
cps/eV
500
0
Si
O
Ca
Ti
Al
C
Nd
Fe
K
Ca
Ti
Nd
Fe
Fe
0
5
10
15
keV

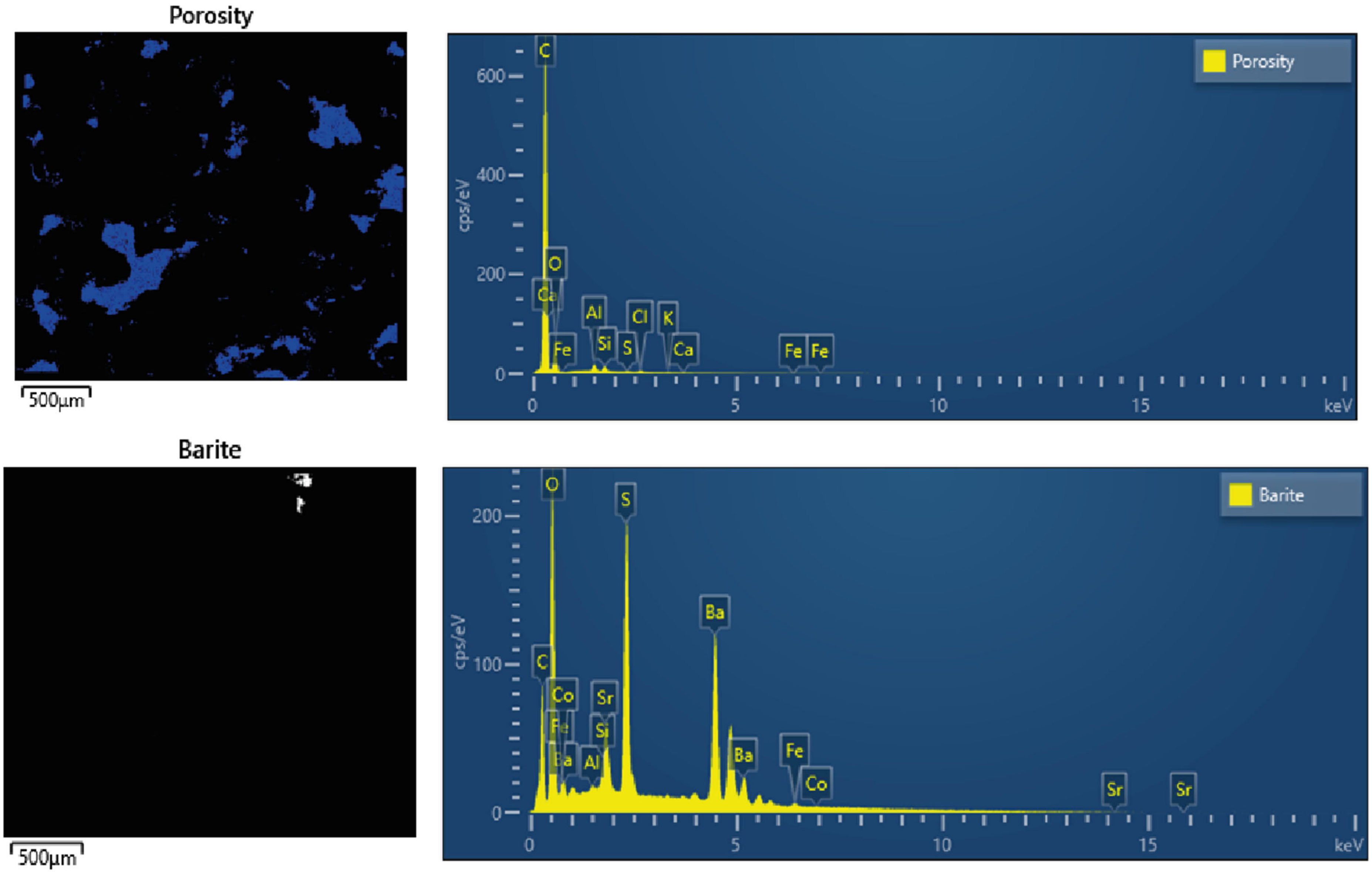
Porosity
500µm
Porosity
cps/eV
600
400
200
0
C
O
Ca
Fe
Al
Si
S
Cl
K
Ca
Fe
Fe
0
5
10
15
keV
Barite
500µm
Barite
cps/eV
200
100
0
O
S
Ba
C
Co
Sr
Fe
Si
Ba
Al
Ba
Fe
Co
Sr
Sr
0
5
10
15
keV

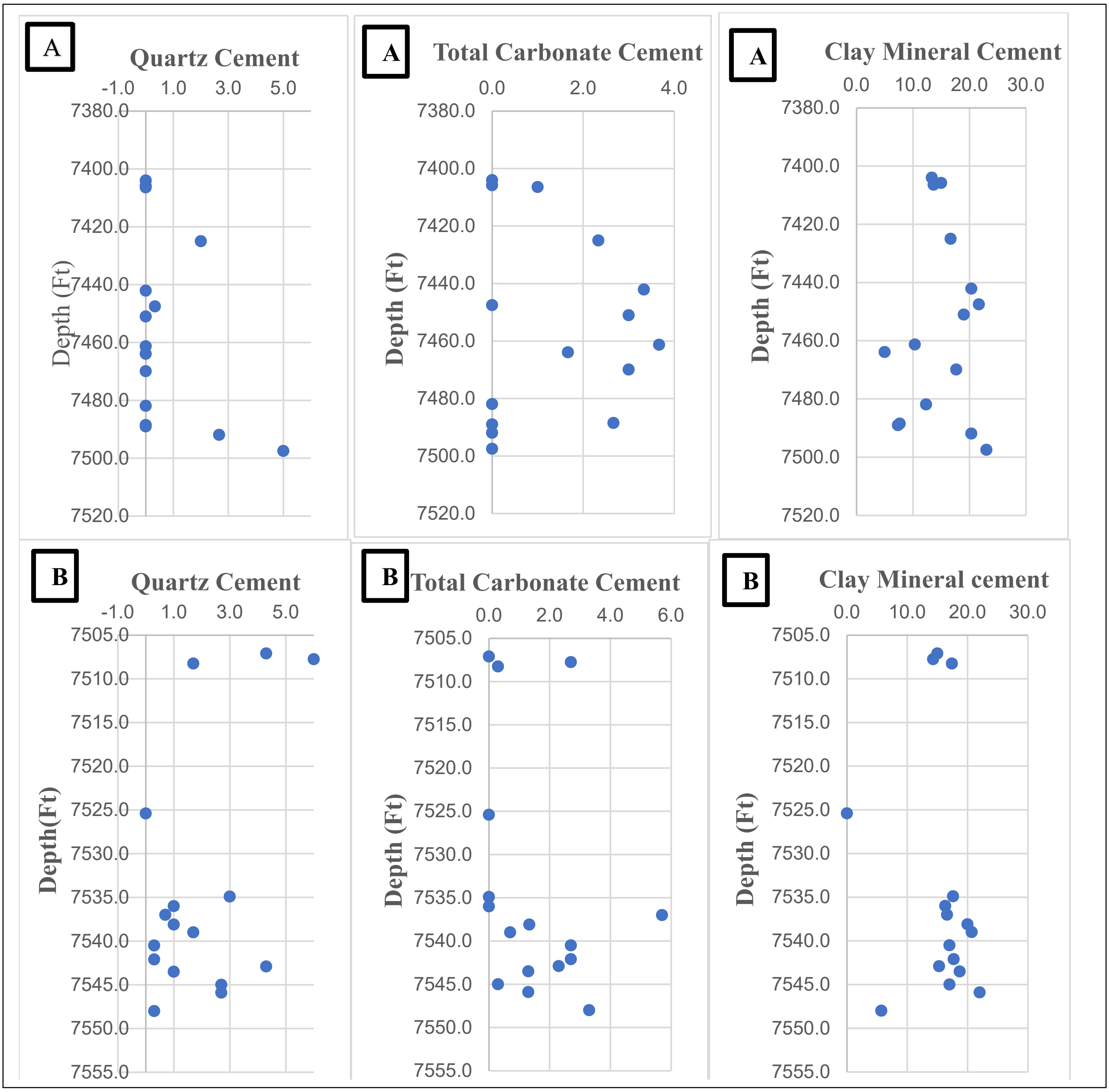

Figure 5.7: Major diagenetic mineral distribution with depth for Breagh Sandstones. Top chats with the As- 42/13-2 well, Bottom chats with the Bs- 42/13-4.

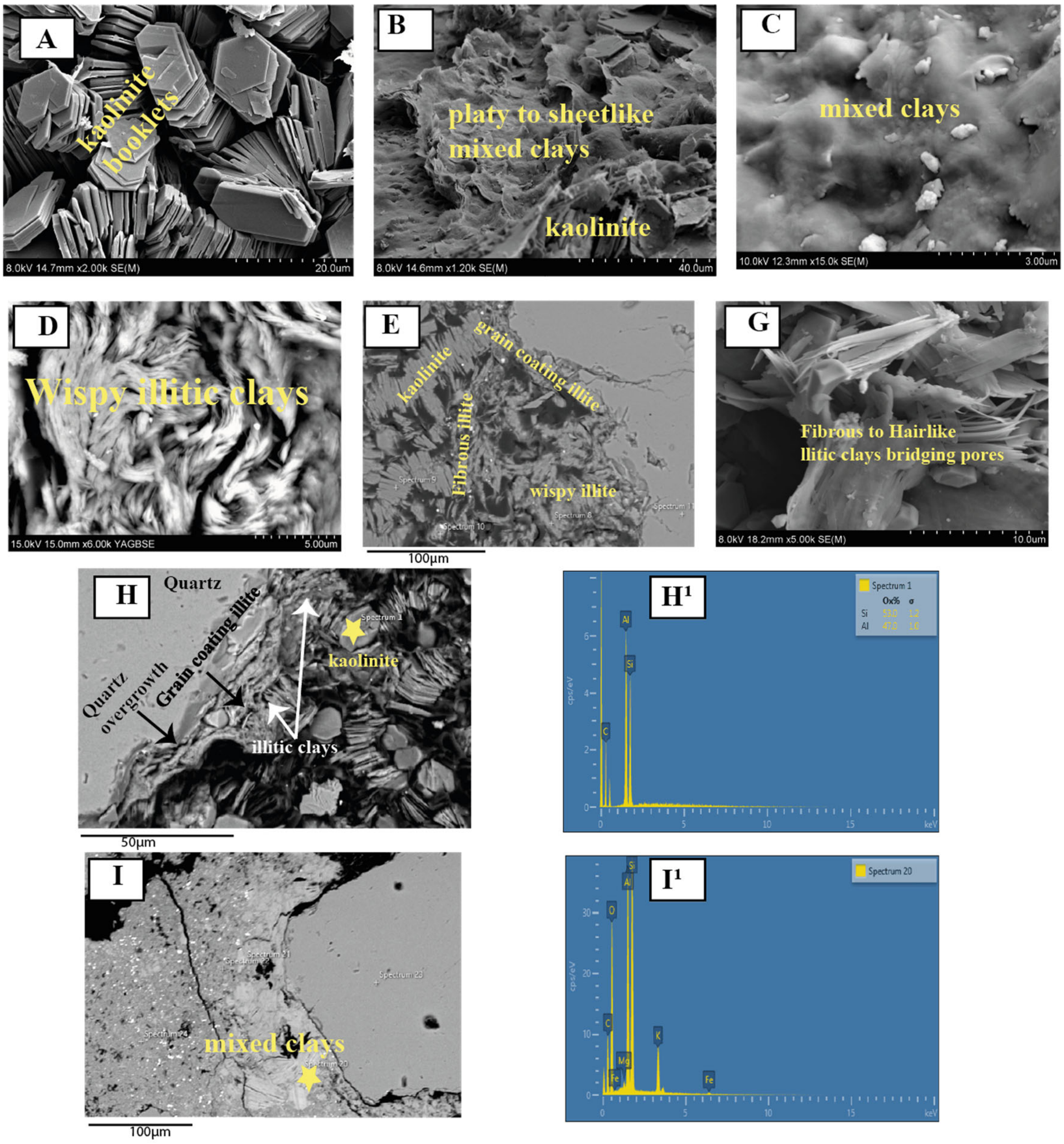

Figure 5.8: Clay cements. (A) SEM image of kaolinite aggregates filling intergranular pore (B)SEM photomicrograph of Platy to sheet-like undifferentiated clay intergrown with kaolinite; (C) SEM photomicrograph of grain coating mixed clays; (D)BSE photomicrograph of wispy illitic clays (E) BSE image of the different clays: Kaolinite intergrow with illitic clays; (G) SEM micrograph showing pore bridging fibrous hairlike illite; (H[1] and I[1]) Spectrum analysis of kaolinite and mixed layer clays respectively.

5.5.2 Carbonate cements.

Carbonate cement in the analyzed sample sets exists in various forms and has compositions that have probably evolved with time, temperature, and pore fluid chemistry in the study area. Carbonate cements in the studied sandstones occur as dolomite and rarely as calcite and siderite (Fig. 5.9). Based on quantitative petrographic analysis data, dolomite is the dominant carbonate cement and where present ranges from trace to 3.7% although increases to 12% within the mudstone dominated samples. XRD analysis records Trace-3 wt%.

Dolomite is most commonly present as developed rhombs and is noted to be finely to moderately crystalline filing intergranular pores and destroying macro-porosity across large area (Fig 5.9).

The dominant crystal habit are as those observed by (Stewart, 1986) – as coalesced aggregates (Fig 5.9a), as well as isolated rhombohedral crystals (10-200 µm) (Fig 5.9 b,e) unevenly distributed throughout the studied sandstones. They also occur locally as poikilotopic dolomite within available pore spaces as intergranular pore-occluding cement. They are also observed as mottled-textured cements (Fig 5.9g). They are also observed locally in samples where they are associated with moldic porosities that are likely a product of carbonate grain dissolution (Fig 5.8e). The isolated form may form floating grain textures (Fig 5.9d), and can be recognized easily on both petrographic microscope on stained slides and SEM.

Cathodoluminescence (CL) studies indicate that most of the dolomite crystals occur as zoned 'species' and become increasingly Fe-rich outwards (dolomite core surrounded by ferroan dolomite and Ankerite) (Fig. 5.9 a, b, d, e, h). Line scan elemental analysis of Fe and other elements concentrations in analyzed samples (Fig. 5.10) validates this CL result. Non-ferroan dolomite cements at the core have low Fe contents whereas, ferroan dolomite with higher iron contents increases outwards. Both ferroan and non-ferroan dolomite cements are observed in the two studied wells, but they are more common in the 42/13-4 well. In some instances, as in (Fig 5.9e), the carbonates have a calcite rich mottled-textured core with patches of high magnesium and traces of iron and manganese (Fig. 5.10) depicting subtle compositional variations (Yan *et al*., 2000).

Visual inspection of the line scan data (Fig 5.10) shows that the iron content of the pore-filling carbonates tends to rise and fall spasmodically across the length of the samples. Changes in CL intensity show an increase in iron concentration with lighter CL colours and a decrease with the darker colour (indicating zonation from dolomite to ferroan-dolomite followed by ankerite and then repeat away from the core). It was not possible within the scope of this study to quantitatively compare the iron content of ferroan dolomite with the ankerite using microprobe or similar analysis however visual inspection of the samples show that an increase in iron goes along with a decrease in magnesium, whereas the calcium content does not change significantly although there is a noticeable fall at the point of maximum iron intensity.

Away from the core on all studied samples, CL photo images (Fig 5.9 & 5.10) shows that a seven-stage zonation of carbonate cements is most common, but, owing to distinctive luminescence, up to nine zones can be picked out, with up to five being recorded in any one zoned sample. The zonation can be caused by either variation in rate of growth or pore fluid chemistry or by discrete phases of authigenesis separated by periods of non-growth (Cowan, 1989; Lee *et al*., 2005).

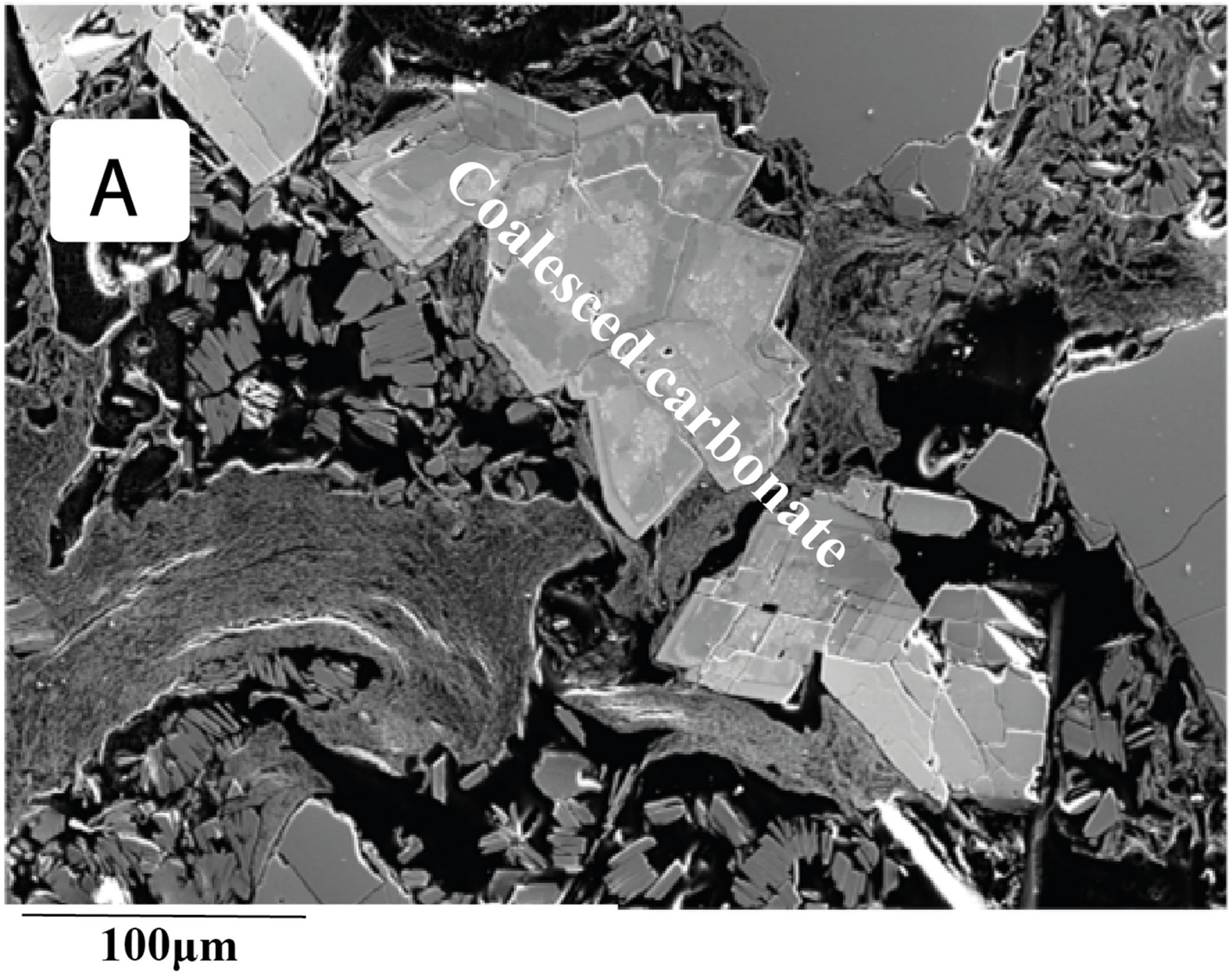

Fig 5.9; (A) BSE photo image of coalesced carbonate filling intergranular pore (see E for zonation of individual cement)

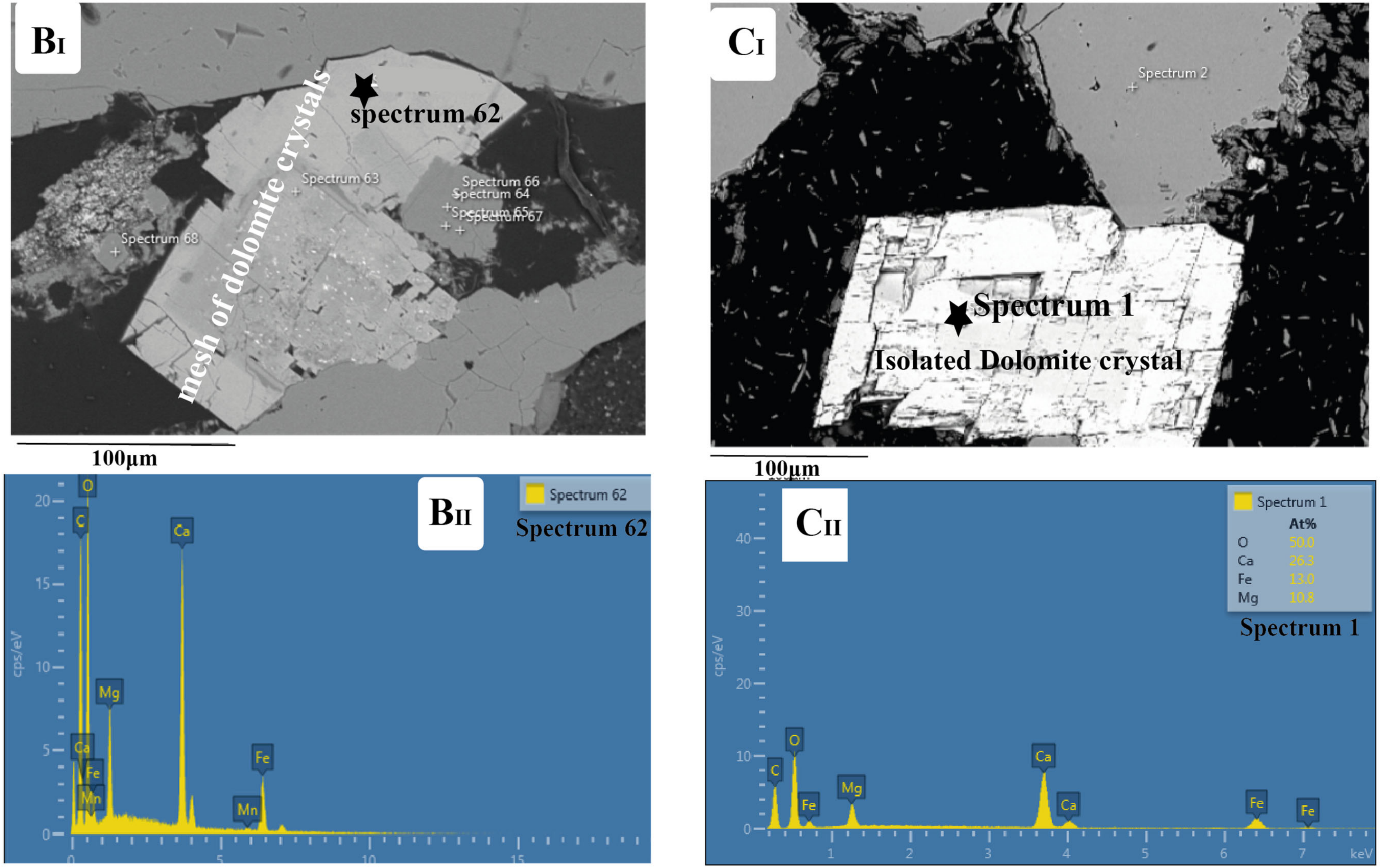

Fig 5.9- (B1, and C1): SEM photomicrograph of isolated dolomite crystals; (Bii & Cii)- SEM point analysis (black star) of the Bi &Ci.

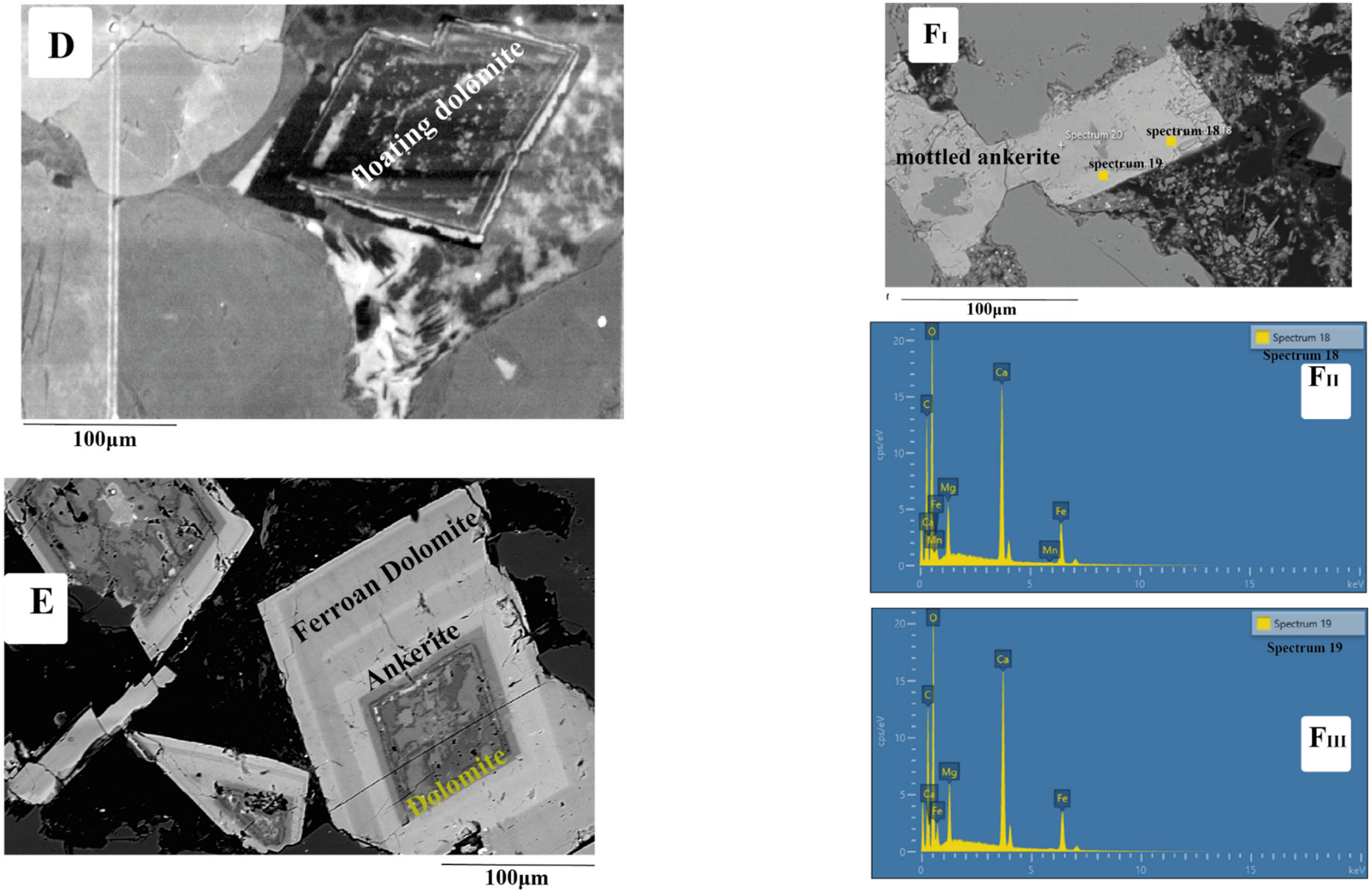

Fig 5.9- (D) BSE photomicrograph of floating dolomite crystal - zonation are labelled in E; (E)SEM photomicrograph of zoned carbonate showing Dolomite-ferroan Dolomite-Ankerite zonation; (F)SEM photo image of single mottled ankerite as seen in G. Spectra analysis of two points at Fii & Fiii

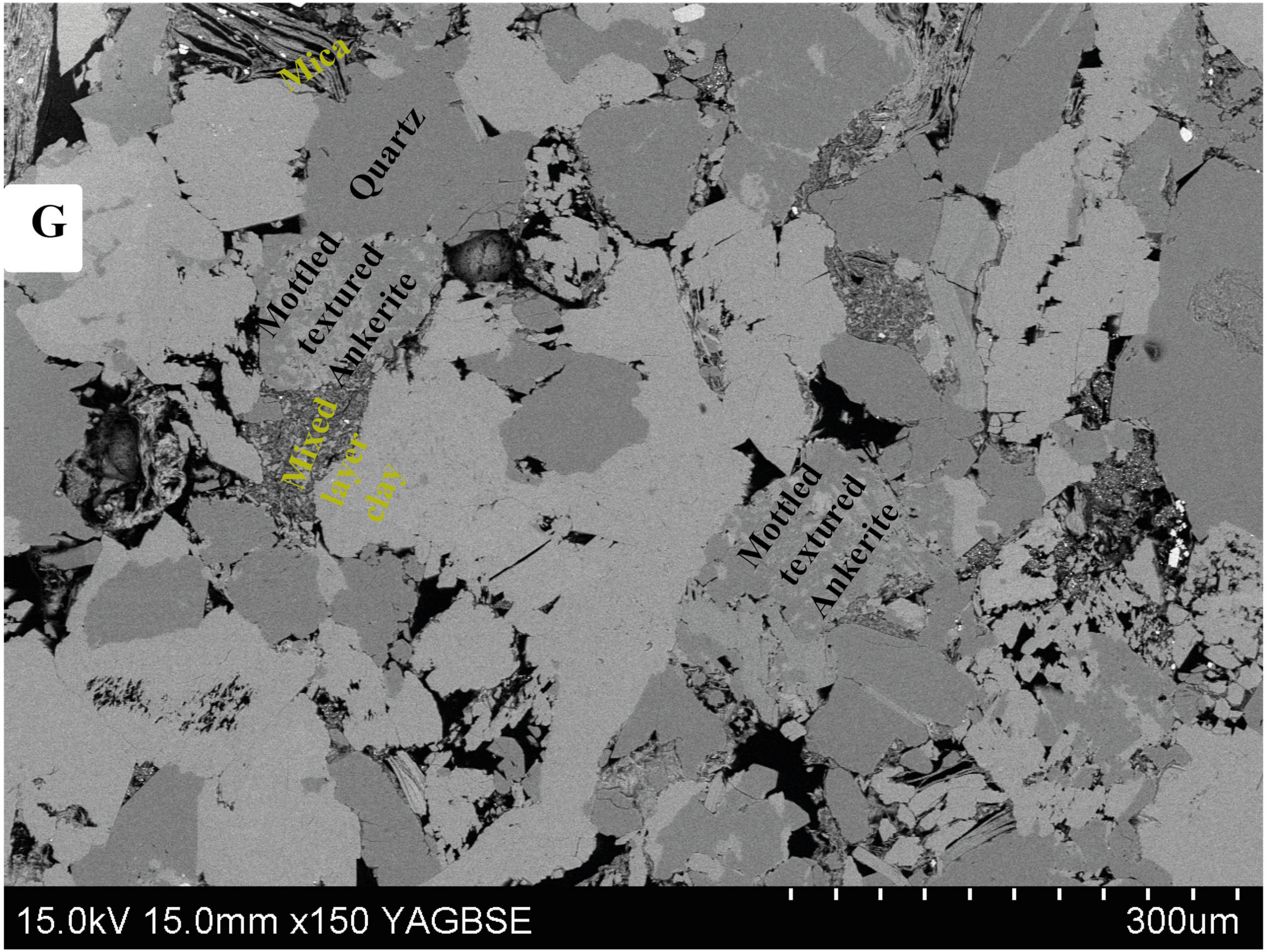

Fig 5.9- (G) BSE images of mottled textured ankerite

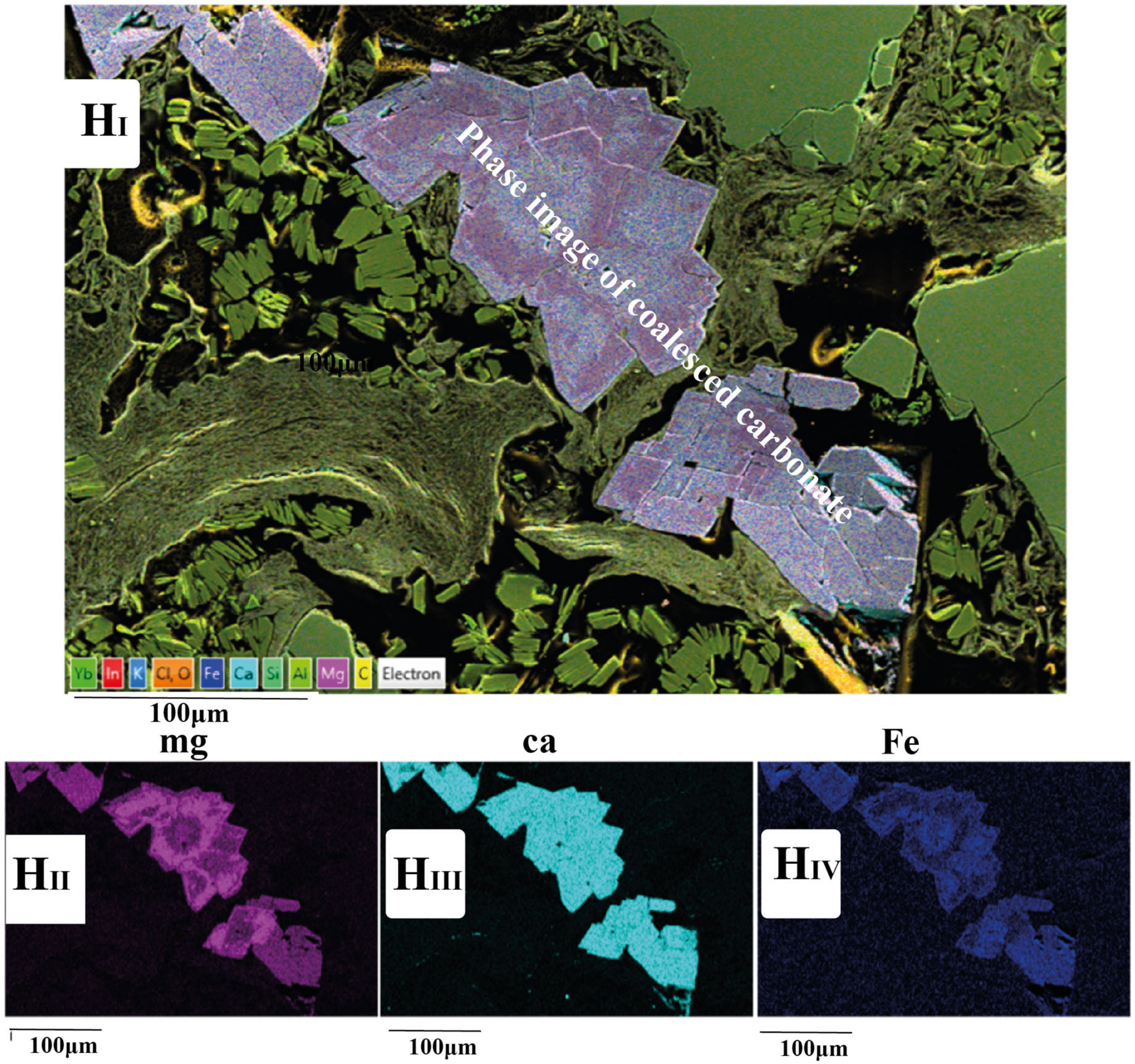

Fig 5.9- (Hi) SEM coloured montaged of carbonate cements in A; (Hii -Hiv)- separated images of Hi showing different elemental composition (mg, ca, Fe) of the carbonate cement.

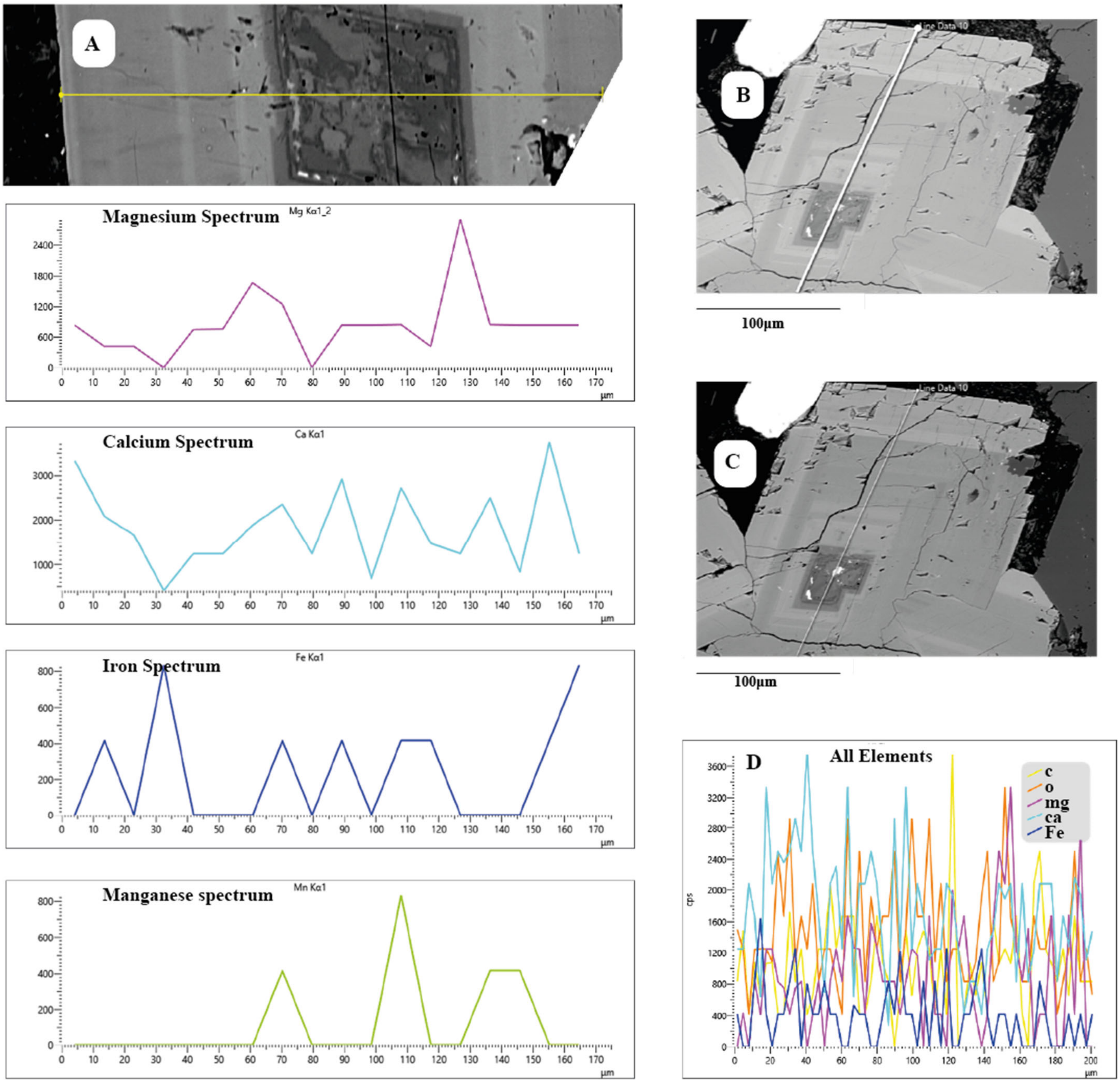

Figure 5.10: Line scan analysis of carbonate cements. A (left): Line scan analysis of major element intensity in a Fe-Mg-Mn- zoned Ankerite crystal; (B-right) - SEM (Top) and BSE (middle): Line scan analysis of major element distribution in a Fe-zoned dolomite crystal.

Apart from dolomite and ferroan dolomite, two series of ankerite cements, (Fe-series) and (Fe+Mn-series), were observed in the samples. In this study, the Fe-series is distinguished from ferroan dolomite based on their Fe/Mg ratios; (Fig 5.10) akin to those carried out in other fields (Hendry *et al*., 2000).

Calcite cement is mostly recognized from XRD. On XRD, it makes up only 0.0 to 0.1%. It is quite obscure in petrographical analysis and perhaps due to contamination is not readily picked up by SEM. Where seen, it is only detected by presence of the remnant background pinkish microcrystalline cement in the site previously occupied by sulphate cements and engulfs quartz overgrowths, indicating that it may post-dates early quart cementation.

Siderite is present in several samples in common proportions and is seen as a grain replacive/pore-filling phase. Apparent replacive material is likely to be replacing original clay-rich lithic fragments. Siderite is noted under SEM as being intermixed with kaolinite and other pore-filling phases. XRD analysis records Trace-8 wt% siderite, where present.

5.5.3 Quartz cement.

Quartz cementation is a very important diagenetic cement in the analysed sandstones in the Breagh fields. Authigenic quartz occurs in varying degrees in all the samples studied (where present: 0.3- 4.3% and average of 1.9%). Quartz overgrowth is unevenly distributed in both studied wells although more common in samples from 42/13-4 than 42/13-2 well.

Standard petrography and the SEM were used to quantitatively analyse the volume of quartz cement in all sample sets. The quartz cements recognised in this study were precipitated as macroquartz overgrowth. Macroquartz overgrowths (interchanged with quartz overgrowth for the purpose of this study) are syntaxial, blocky overgrowth larger than 20 μm and in optical continuity with their detrital host grain.

It was difficult discriminating some of the detrital grains and their overgrowths by standard petrography because (1) some mineral grains in the sample set were coated with bitumen and (2) the clay rims at the boundaries between some detrital quartz and their overgrowths could not be easily resolved. Where dust rims/clay layers are preserved, quartz overgrowths are observed to be angular and discontinuous projections on grain surface at the scale of thin section.

Under SEM and CL quartz overgrowths are noted to range between ~10-30/50µm – 100 µm in thickness and are seen enclosing the margins of clay aggregates (Fig 5.11 a^1- d^1, i, j). They are also seen to interlock forming a pore-occluding phase as well as have interlocking relationships with carbonates and kaolinite (Fig 5.11 i, j, k).

Macro-quartz is also seen to fill fractures within the quartz grains (Fig. 5.11 e^1, f^1, g^1, h^1) where it displays similar fluorescence to the overgrowths, which is suggestive of equivalence. Minute diagenetic micro-quartz is also present as rims on detrital quartz grains and as overgrowths.

CL work allowed discrimination of the detrital quartz from the quartz overgrowths and reveal zonation within some of the overgrowths (Fig 5.11 a^1 and c^1). A three-stage zonation of quartz overgrowths is most common, but, owing to distinctive luminescence, up to six zones can be picked out, with up to five being recorded in any one sample. The zonation can be caused by either variation in rate of growth or pore fluid chemistry or by discrete phases of authigenesis separated by periods of non-growth (Cowan, 1989).

Cathodoluminescence (CL) photomicrographs show varying degree of authigenic quartz content and evidence of multiple projection development (Fig 5.11 a^1– d^1). Visual estimation of the CL photomicrographs shows that authigenic quartz content makes up to 65% of the fluvial channel facies and about 20% on the distributary mouth bar facies.

Clearly the cement has had a long history in the samples studied. They occur as one of the earlier recorded cements and as a late-stage cement. Quartz precipitation could probably be considered as an essentially continuous process from early diagenesis to deepest burial, only interrupted by the precipitation of other cements.(Cowan, 1989).

Quartz overgrowths are best developed in the medium to coarse-grained fluvial channel sands (FA8). They are least well developed in fine grained parts of the distributary bar facies and the argillaceous crevasse sands, where the compaction of detrital clays might have inhibited the formation of quartz overgrowths, and in rare cases where haematite or clay rims have inhibited overgrowths.

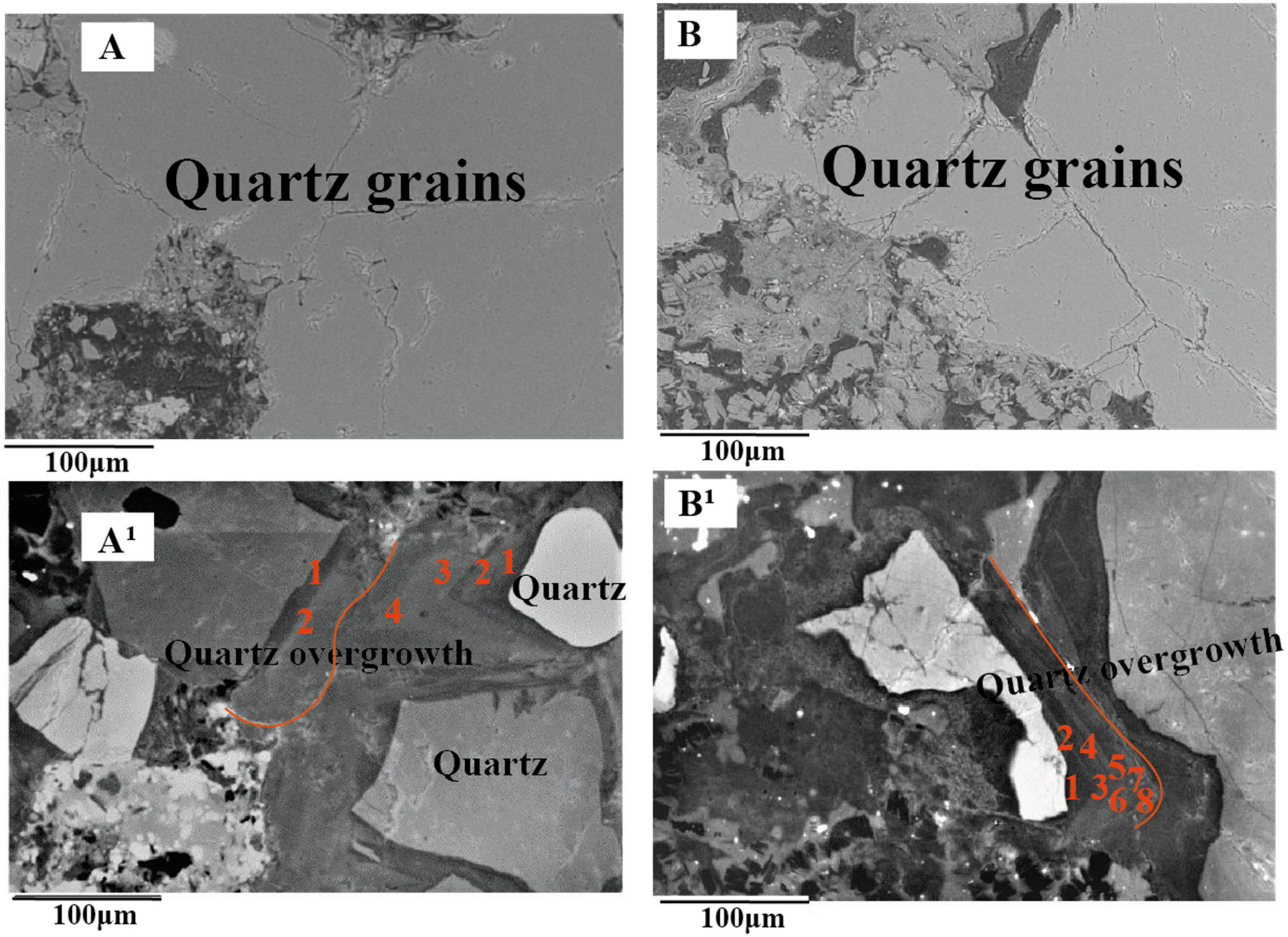

Fig 5.11- (A, B): *SEM photomicrograph of quartz grains; A1 to B1: SEM micrograph of their corresponding overgrowth pair. A1: interlocking quartz overgrowth; B1: Interlocking quartz overgrowth only interrupted by clay mineral cement. Red numbers represent generations of quartz overgrowth.*

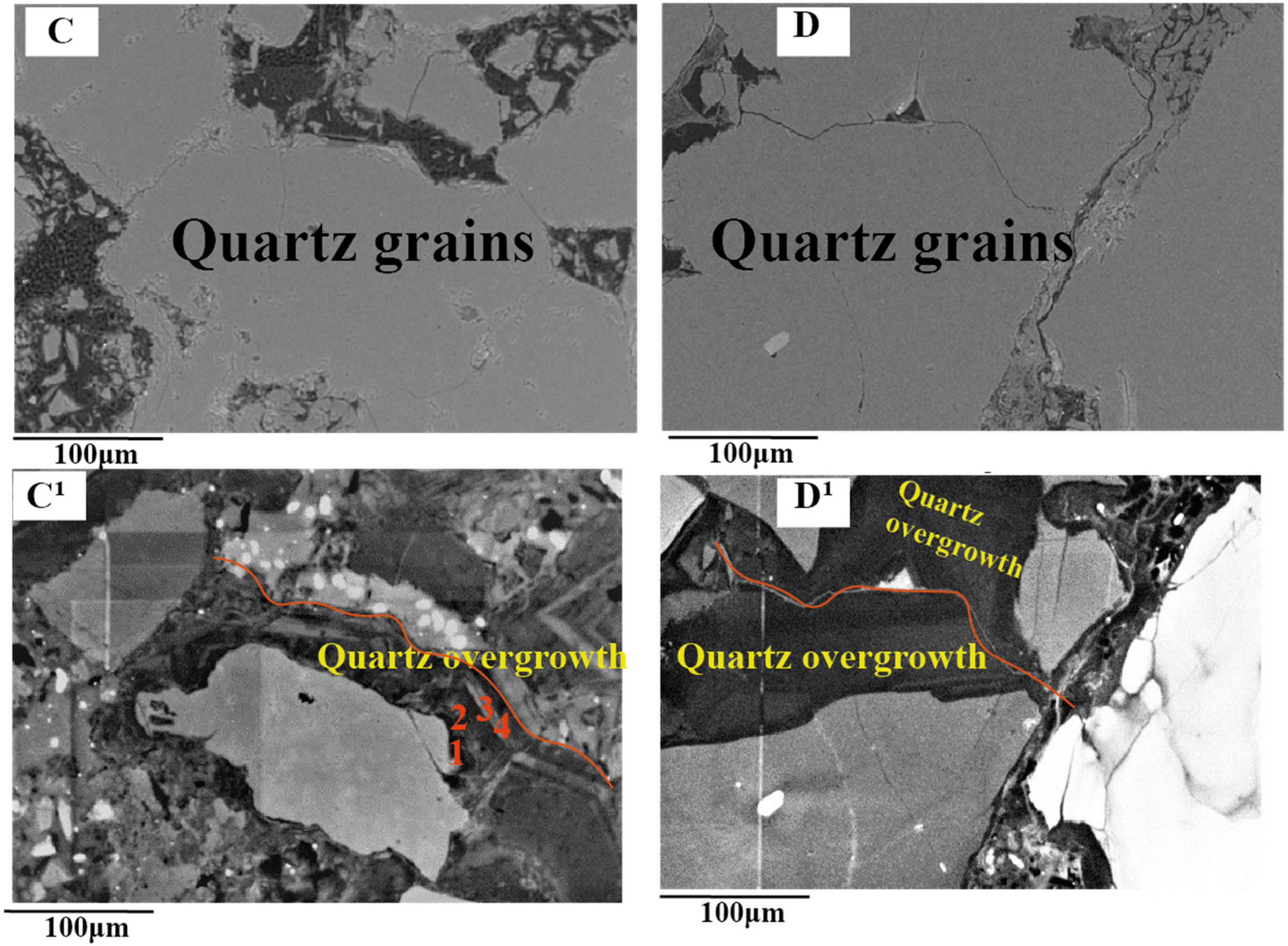

Fig 5:11 (C,D): SEM photomicrographs of quartz cements; C1: SEM photomicrograph showing multiple generations of quartz overgrowth from C; D1: BSE photomicrograph showing large uninterrupted quartz overgrowth partially occluding pores from D. Red numbers represents generations of quartz overgrowth

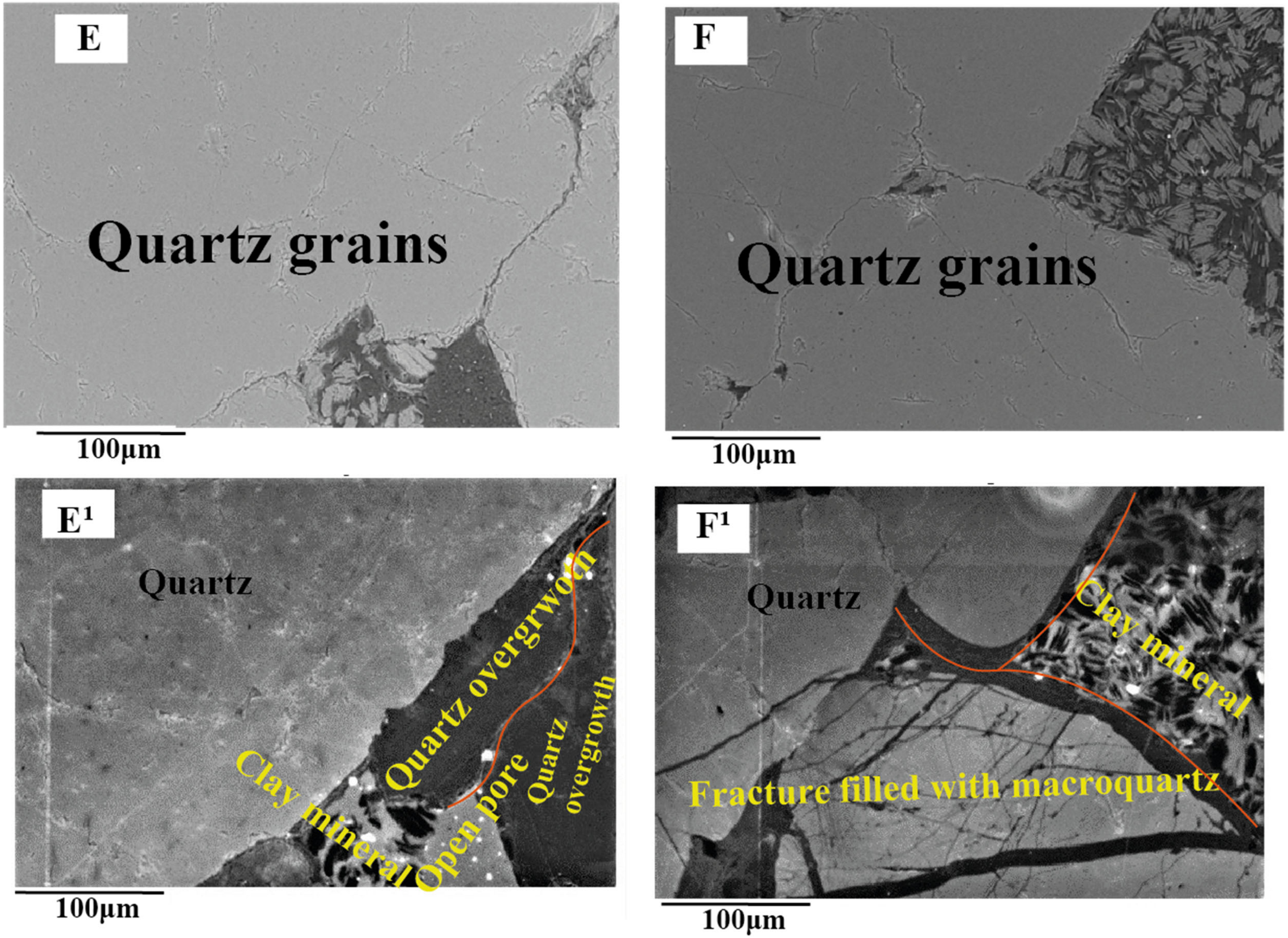

Fig 5.11- E_1: BSE photomicrograph showing large uninterrupted quartz overgrowth partially occluding pores from E; F_1: SEM photomicrograph showing macro quartz filling fractures from F

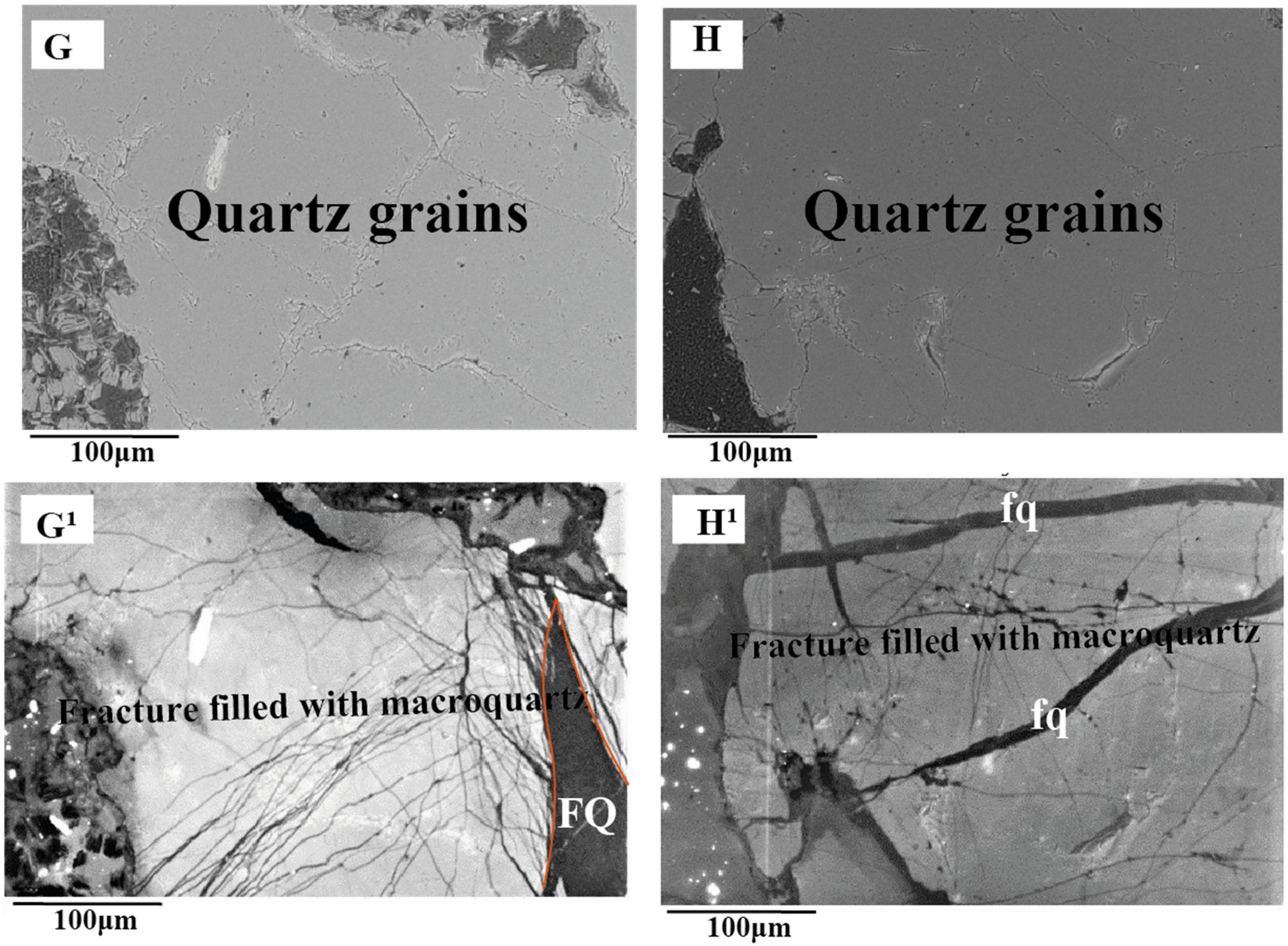

Fig 5.11- G_1 and H_1: SEM photomicrograph showing macro quartz filling fractures from G and H respectively.

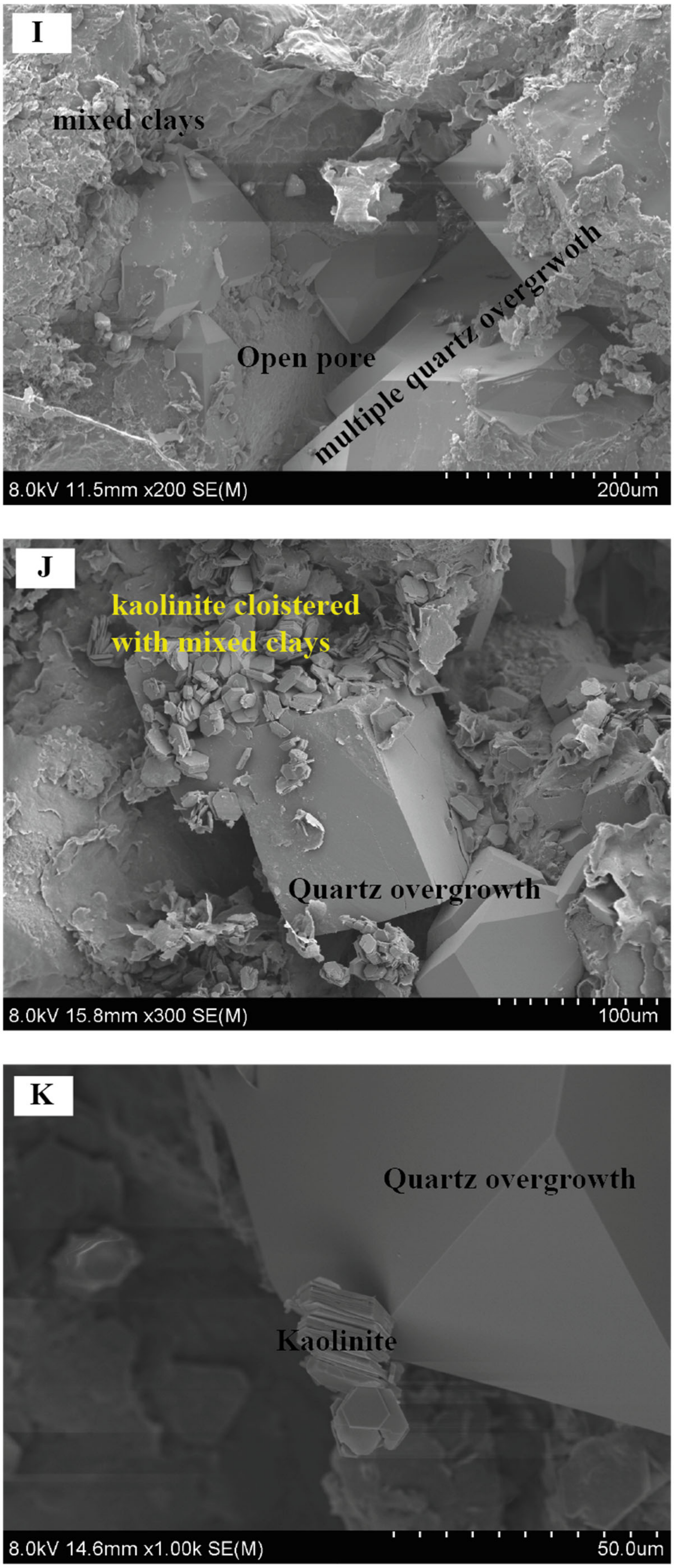

Fig 5.11- I to K: Multiple quartz overgrowth interlocking with clay minerals and partially occluding pores.

5.5.4 Anhydrite, Barite and Halite.

Anhydrite and Barite are minor sulphate cements in both studied wells. Anhydrite cement is common in 42/13-2 well. Anhydrite occurs as poikilotopic cement filling large intergranular pores (60µm across) (Fig 5.12 a, b, c, d). It engulfs quartz overgrowths but replaced by dolomite and calcite suggesting that it postdates earlier formed quartz overgrowth and predates carbonate cements.

Petrographic analysis of the samples indicate that sulphate cement makes up 0.7 to 5% of the bulk rock volume. Since the visual estimates of porosities formed from dissolution of sulphate comprise more than 55% of the total intergranular porosities in the sample sets, the presence of sulphate cement within the sample set is therefore a very important cement for reservoir quality development in the Breagh Sandstones.

Examination of thin section show that pervasive sulphate cement in the form of anhydrite form sheets that formally occluded large pores in the sample sets. Some of the anhydrite cements have either totally or partially dissolved and left relics of their formal shape which are now infilled by clay and carbonate cements (Fig 5.12e). Some of these infilling diagenetic minerals which subsequently become completely dissolved or partially dissolved leave behind large secondary pores that significantly enhance permeability (more details on this in chapter 5).

The extent to which these anomalously large pores influence reservoir quality in the study samples is not a straightforward one because, the characteristic microporosity of the infilling clay mineral (Fig 5.12e) increases tortuosity of the pore throat and therefore reduces permeability to the extent to which it fills the available pore space (more details on this in chapter 6).

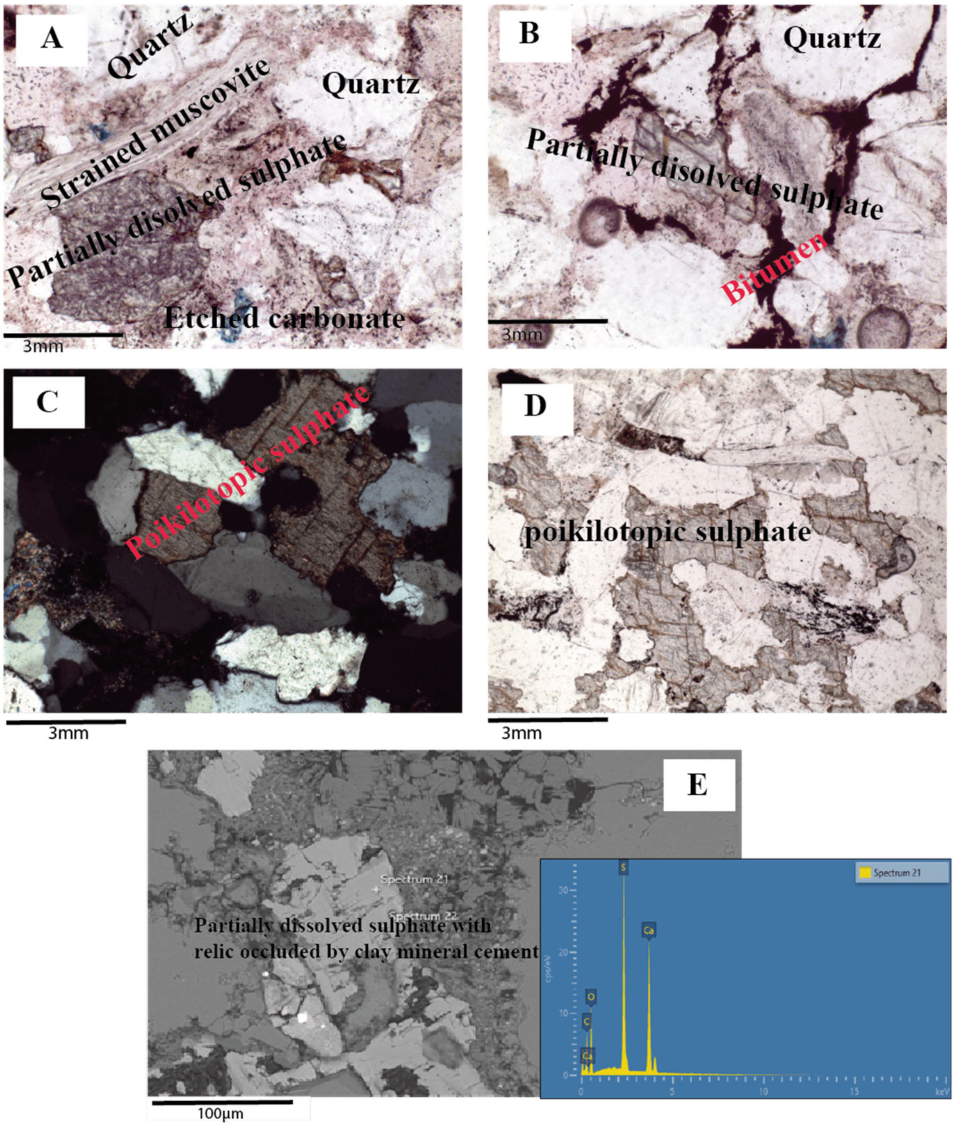

Figure 5.12: Sulphate Cements: A: Partially dissolved sulphate cement with relics filled carbonates and clay minerals, B; Photomicrographs of partially dissolved sulphates with relics filled by bitumen C-D: Photomicrographs of poikilotopic sulphates at different points of dissolution E: (Left): BSE image of dissolving anhydrite and relic of original shape now filled with clay minerals; (right): point identification for anhydrite cement.

5.5.4 Barite

Barite is noted in XRD and thin section and is seen as a trace to rare pore-filling phase. Barite was observed in only two samples in 42/13-4 and occur as poikilotopic, pore-filling cement (ranges from 50 µm to 600 µm). It engulfs quartz overgrowths (Fig. 4.5). Observation of barite in some samples revealed that it developed after clay mineral cements (kaolinite and illite) and Fe-dolomite. Suggesting it precipitated after late carbonate cements.

5.5.5 Unresolvable opaques and hematite.

Minor authigenic opaques are present as unresolvable opaques (0.3-5% av. of 0.9%) locally pervasive. They occur as anhedral crystals within the samples. They are present in both wells although mostly common within the sandstones of 42/13-2 well. Opaques are mostly associated with altered detrital clays which show as reddish-brown colour on grain rims under reflected light indicating haematite. Authigenic grain coating illite are sometimes associated with haematite cement. XRD analysis of 42/13-4 well show hematite values to be as high as 41%.

5.5.6 Residual hydrocarbon.

Moderate pore lining residual hydrocarbon is observed as enclosing quartz overgrowth and lining pores (more details in section 5.6.2 below) and its generally seen to postdate diagenetic quartz development. Residual hydrocarbons (where present: 1.7-2.7%) are noted as a grain-coating phase and are evident as a brown stain/film that postdates quartz overgrowth development.

5.6 Paragenetic sequence.

As discussed in section 5.5 above, the main diagenetic minerals identified are carbonates, authigenic clay minerals and quartz cements. The relative timing of the diagenetic reactions has been interpreted from paragenetic relationships (see fig 5.13) observed in thin section, cathodoluminescence, burial history curves and isotope data. Proxy data provided from fluid inclusion (Cowan and Shaw, 1991; McNeil *et al*., 1995) and 1-D thermal model from other fields (Vincent, 2015; Monaghan *et al*., 2017; Arsenikos *et al*., 2019; Grant *et al*., 2020) in the SNS have also been used to corroborate findings.

Analysis of the data shows that most diagenetic reactions that affected reservoir quality of the Breagh Field reservoir probably occurred within the last 330ma (during and after the Variscan orogeny). They are typically associated with moderate to deep burial, occur at temperatures more than 80^0C, and post gas generation in the Late Cretaceous. Apart from quartz cements, the diagenetic cements precipitating below 80^0C are relatively minor.

Although it is difficult to obtain the precise timing and duration of the individual diagenetic processes, data from fluid inclusion, burial history curves and oxygen and carbon isotope study implies that all of stage 1 (eodiagenetic events) are likely to have formed before or during the uplift associated with Variscan orogeny while stage 2 (mesodiagenetic events) during and after the Variscan orogeny.

5.6.1 Eodiagenesis.

Eodiagenesis refers to processes that affect sediments after deposition due to their proximity to the surface (Choquette and Pray, 1970), it is often a regime with depth range of 1-2 km and temperature range of 30°C to 70 °C (Surdam *et al*., 1991; Worden and Morad, 2003; Burley and Worden, 2009). During eodiagenesis, the detrital mineral assemblage may be inherently unstable since they still contain minerals that were formed under a wide range of conditions (temperature, pressure, oxidation state, water composition) and thus will tend to react with the ambient water.

The eodiagenetic process in the current study will be divided into two stages: (1) early diagenesis (2) early burial diagenesis.

5.6.1.1 Early diagenesis.

The earliest events observed in the study area are the (i) infiltration of clay to form clay coats, (ii) precipitation of non-ferroan calcite, (iii) precipitation of sulphates and (iv) the development of quartz overgrowth. All events are dominant in all the lithofacies present apart from the early sulphate cements which is more dominant in the fluvial facies (Fig 5.12) where they are observed to initially plug pore spaces and on later dissolution create large, oversized pores that have shown to have a marked increase in reservoir permeability within the samples where they occur (more details in chapter 6).

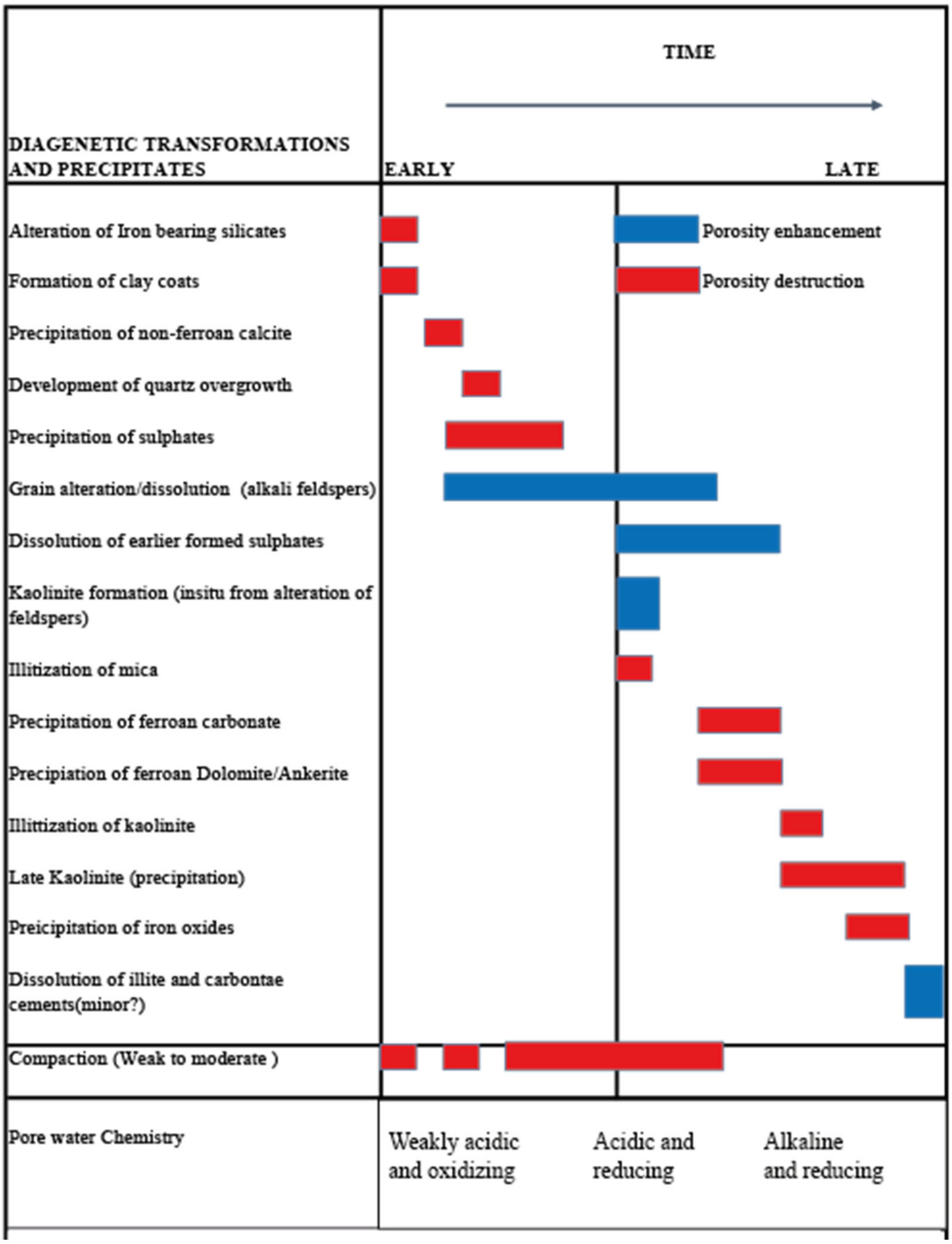

Figure 5.13: Paragenetic sequence of diagenetic events in the Breagh field wells (42/13-2 42/13-4 and 42/13a-6).

5.6.1.2 Clay coats and quartz overgrowth.

Observed data shows that early clay coats and quartz overgrowth (Fig 5.15) were the earliest cements to precipitate in the study area. They were probably produced by action of initial (syndepositional) pore fluids on framework grains (Burley, 1984; Bjørlykke and Egeberg, 1993; Walderhaug, 1996; Bjørkum *et al.*, 1998; Fisher *et al.*, 1999; Porten *et al.*, 2019; Qiao *et al.*, 2020).

$$2KAlSi_3O_8 + 2CO_2 + 11H_20 \Rightarrow 2Al_2Si_2O_5(OH)_4 + 2K^+ + 4H_4SiO_4 + 2HCO_3^- \text{…………} \quad \textbf{(3)}$$

k-feldspar + carbon dioxide+water = kaolinite+ potassium+ silica+bicarbonate

$$2NaAlSi_3O_8 + 2CO_2 + 11H_20 \Rightarrow 2Al_2Si_2O_5(OH)_4 + 2Na^+ + 4H_4SiO_4 + 2HCO_3^- \text{……..} \quad \textbf{(4)}$$

Na-feldspar + carbon dioxide+water = kaolinite+ sodium+ silica+ bicarbonate

$$CaAlSi_3O_8 + 2CO_2 + 3H_20 \Rightarrow 2Al_2Si_2O_5(OH)_4 + 2Ca^{+2} + 2HCO_3^- \text{…………………….} \textbf{(5)}$$

Plagioclase + carbondioxide+water = kaolinite+ Calcium + bicarbonate

Precipitation of early clay coats can be interpreted to be the result of ferrous iron oxidation released during the dissolution of ferromagnesian minerals (Glennie *et al.*, 1978; Hubert and Reed, 1978; Walker *et al.*, 1978; Al-Juboury *et al.*, 2020) occurring shortly after deposition.

As the sandstones in the study area were laid down by fluvial activity in a warm, humid tropical environment prevailing during the Early Carboniferous times, the paleoclimate would have exerted a profound control on the position and chemistry of ground water, keeping the initial syndepositional pore fluid both slightly oxidizing and weakly acidic and dominated by Na^+, Ca^+, Mg^{2+} and HCO_3^-. The quartz overgrowths were also probably produced by the action of these pore waters on unstable detrital grains (as shown in equation 3-5) (Worden and Morad, 2003; Morad *et al.*, 2010). Silica from equations (3) and (4) can precipitate quartz overgrowth as seen in equation 6 (Land, 1984; Higgs *et al.*, 2007), while bicarbonate from equations 3, 4, and 5 can react with available calcium and other ions to form carbonate cements (equation 7).

Petrographic evidence revealed concave-convex, long grain suture and stylolite contacts (Table 5.1, Figs.5.2 in section 5.3 above & Fig 5.16 in section 5.6 below) of detrital grains, indicating that chemical compaction possibly accounts for a small part of the quartz cementation.

$$H_4SiO_4 \Rightarrow SiO_2 + 2H_2O$$
$$silica \Rightarrow quartz + water \quad \ldots\ldots\ldots\ldots\ldots\ldots\ldots\ldots\ldots\ldots \textbf{(6)}$$

$$Ca^{+2} + HCO_3^{-} \Rightarrow CaCO_3 + H^{+}$$
$$Calcium + bicarbonate \Rightarrow calcite + hydrogen \quad \ldots\ldots\ldots\ldots\ldots\ldots\ldots\ldots\ldots\ldots \textbf{(7)}$$

5.6.1.3 Early calcite cement.

XRD data shows that early calcite cement occurs in trace to minute amount in the study area. Very little evidence of this early cement now remains, but the background pink discoloration within pore spaces, high intergranular porosities, over-sized intergranular pores which the later early sulphate cement filled up provide evidence of their former existence. Small patches of etching are seen on the later zoned dolomite cement and might be relics of this early cement.

Petrographic evidence indicates that they probably developed prior to precipitation of quartz cement, as there is no indication that the cement has engulfed quartz overgrowth, but mostly has direct contact with quartz grains. This suggests that their temperature of formation is lower than the typical lower temperatures (~60°C) required for quartz cement precipitation (Walderhaug, 1994, 1996). Early calcite cements although difficult to discriminate in the studied sandstones are common diagenetic features in many sandstone examples (Cowan, 1989; Oluwadebi *et al*., 2018).

5.6.1.4 Early diagenetic sulphate cement.

The source of early diagenetic sulphate (anhydrite) is not very clear. Textural relationship indicates that it precipitated following early quartz and calcite but since availability of sulphate (SO_4^{2-}) is low in fluvially derived pore waters which tend to be dominated by Na^{+}, Ca^{+}, Mg^{2+} and HCO_3^{-} (Eugster and Hardie, 1975; Bjorlykke, 1984; Worden and Morad, 2003). The early sulphates cement then were probably sourced from the Early Carboniferous epicontinental sea that deposited the marine shales and limestone of the Yoredale cycles.

5.6.1.5 Uplift diagenesis and Early burial diagenesis.

5.6.1.6 Effects of Variscan orogeny of diagenesis.

The effect of the deformation and uplift associated with variscan orogeny (Cameron *et al*. 1992; McCann *et al*. 2008) is seen to exert some control on the diagenesis of the study area. Deformation probably drove mechanical compaction while uplift may have caused re-exposure of the basin to meteorically driven oxidizing fluid.

The development of the early diagenetic cements (quartz overgrowth, calcite, and sulphates) most likely predates the effect of mechanical compaction that has bent and fractured mica between framework grains and the relic left by the early cements (Fig 5.2 Fi, Fii). It seems likely that the quartz cementation was essentially a continuous process throughout diagenesis and the zones indicated by differing CL response (refer to 5.5.3 above) represents variations in trace-element chemistry or pressure and temperature conditions rather than discrete phases of overgrowth. This is because CL photomicrographs show that there has been remarkably little mechanical compaction of the framework grains even though with plane polarized light, the junction between the overgrowth and the detrital cores are visible, and so gives the impression of a highly compacted rock with interpenetrating grain contacts. With CL however, this is only an effect of different zonation.

The burial curves show that the Breagh Field area was consistently at shallow burial depth (<1 km) until the Variscan orogeny in the Late Carboniferous (Fig 5.14, see also chapter 4 for more details on burial history). Following the Variscan orogeny, it seems that these quartz overgrowths have halted the compaction of the sediments after only minor compaction of the micas and soft lithics. The amount of quartz cementation is difficult to estimate because of the lack of visible dust rims around the detrital cores, but where visible and possible to estimate it, up to 20-65% of the rock volume can be accounted for by quartz cementation.

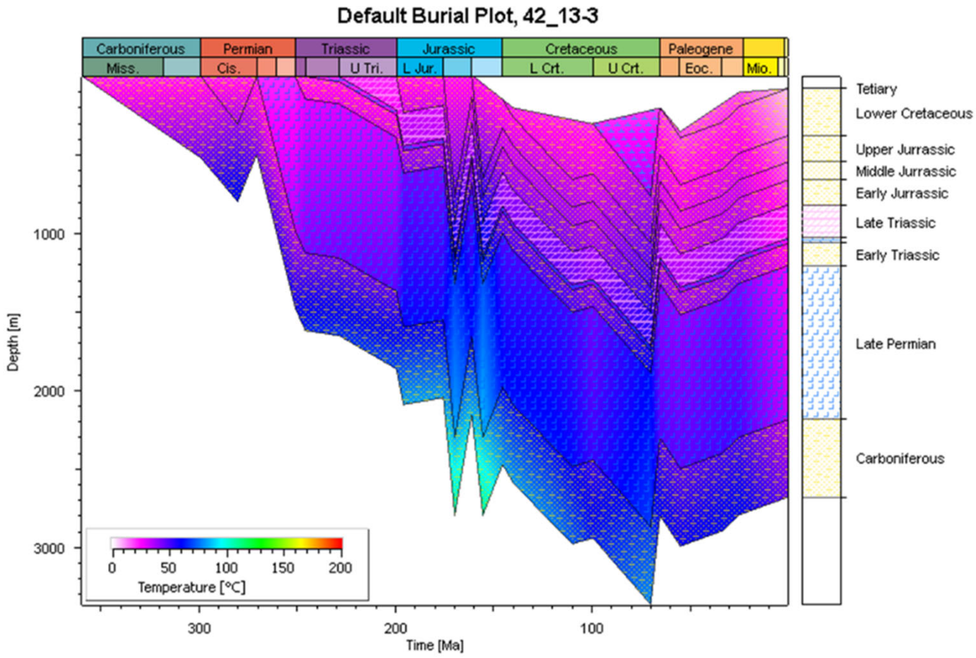

Figure 5.14a: Burial thermal plot for the Breagh field using wells 42/13-3.

The re-exposure of the Breagh area would have allowed percolation of post-inversion acidic ground waters resulting in the *in-situ* breakdown of feldspar (Bjørlykke, 1984; Surdam *et al*., 1991; Mansurbeg *et al*., 2008; Oluwadebi *et al*., 2018) to produce abundant authigenic kaolinite, widespread dissolution of carbonate cements and removal of early-formed sulphates and iron oxide cements, as well as the formation of secondary porosity.

5.6.1.7 Precipitation of kaolinite.

The warm humid environment prevailing during the Westphalian A and B times could have made possible the prolific precipitation of kaolinite in the study area since kaolinite is known to proliferate under warm humid conditions (Basham, 1974; Robert and Chamley, 1991; Robert and Kennett, 1992, 1994; Bolle and Adatte, 2001; Chen *et al*., 2016). This is followed by the continental fluvial and alluvial deposits of Westphalian C and D (Besly *et al*., 1993) which probably enhanced further clay coating of hematite and iron hydroxide observed around framework grains. Elsewhere in the SNS, the uppermost Carboniferous rocks were exposed to meteorically derived oxidizing fluids which caused the visible reddening of the top Carboniferous. (Holliday and Cutbill, 1972; Cowan, 1989; Jones and Holliday, 2006). This event oxidized the organic matter in the sediments and altered the early iron bearing silicates to haematite. (Hubert and Reed, 1978; Ixer *et al*., 1979; Walker *et al*., 1981; Besly *et al*., 1993;

Burley and Worden, 2009; Chen *et al*., 2016; He *et al*., 2022; Mbongonya *et al*., 2022). But since the uppermost Carboniferous strata are absent in the heavily eroded Breagh area, (Booth *et al*., 2017; Nwachukwu *et al*., 2020) (refer to chapter 3 & 4, for more details), the same event would have been responsible for promoting precipitation of the iron hydroxides seen around grains in the studied samples (Fig 5.15a, b & 5.16g, h). Formation of iron hydroxides is typical in arid environment with low organic matter content, deep water tables and fully oxidized sediments - iron tends to be fully oxidized (ferric) and often coats minerals as a hydroxide or sesquioxide (Curtis, 1985; Worden and Morad, 2003).

Given that the silicate dissolution in the presence of the action of organic acids, occurs at 80^0C and above, it is possible to fix the boundary between the early diagenetic precipitation and early burial diagenetic dissolution at the 80^0C isotherm (Carothers and Kharaka, 1980; Cowan, 1989; Dixon *et al*., 1989; Surdam *et al*., 1989). The burial curve (Fig 5.14) indicates that the 80^0C isotherm was crossed by the Lowermost Carboniferous strata at a depth of less than 1300m during the Late Permian – Mid/Late Triassic. It is therefore suggested that much of the diagenetic dissolution in the study area happened between c. 230 Ma and 290 Ma.

Petrographic observations show the presence of vermicular kaolinite and blocky kaolinite/dickite within the studied samples (Fig 5.15a, d, e). Vermicular kaolinite is however the common occurring pore-occluding and pore-filling clay cement. The presence of dickite may indicate a higher influence of organic acids since it precipitates upon deeper burial and higher temperature (Berger *et al*., 1997; Van Keer *et al*., 1998; Rossi *et al*., 2001, 2002; Lanson *et al*., 2002; Paganoni *et al*., 2016). The temperature range estimated for organic-rich fluid expulsion is ~100°C (Platt, 1993; Morad *et al*., 2010), which is compatible with temperature for the precipitation of blocky kaolinite/dickite (high temperature kaolinite).

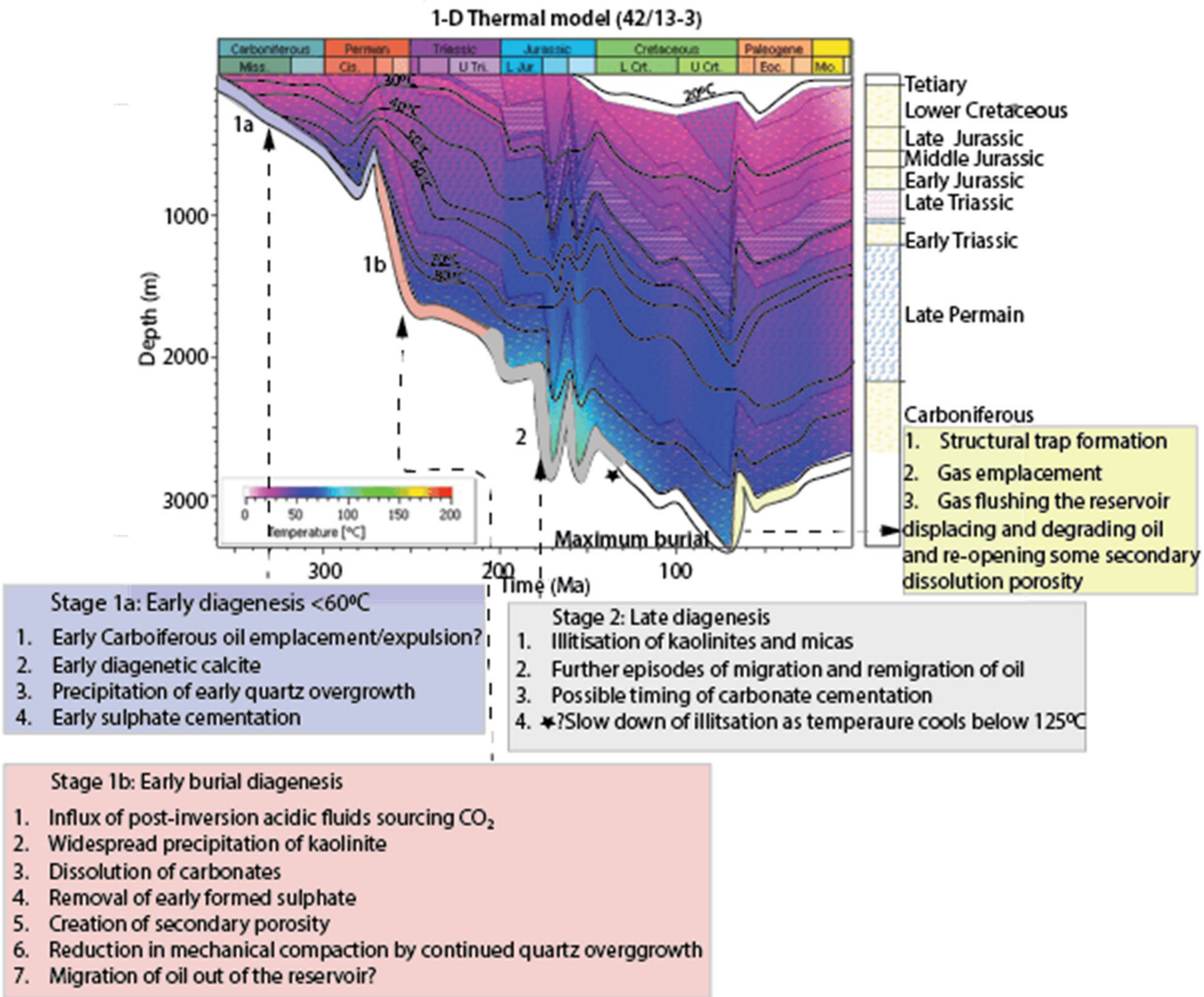

Figure 5.14b: Interpreted 1D burial thermal plot for the Breagh field using wells 42/13-3.

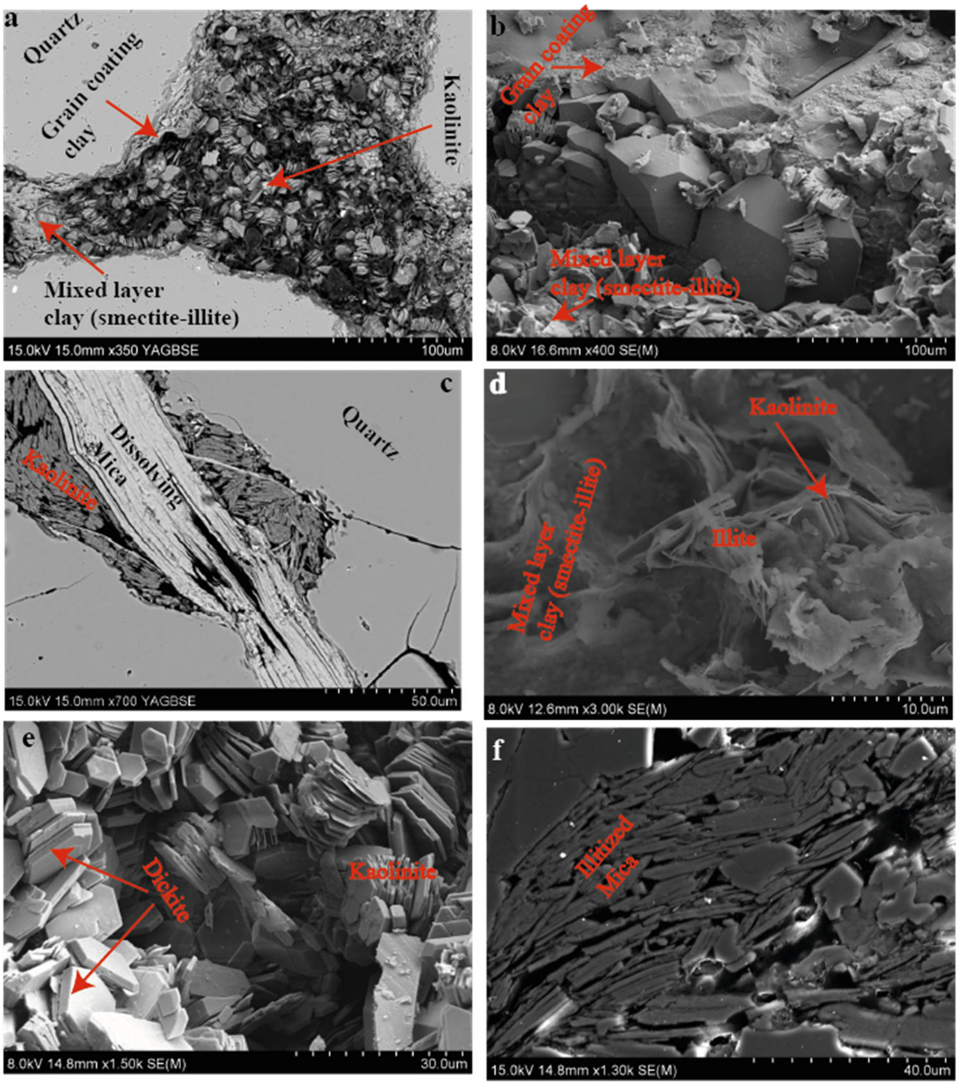

Figure 5.15 - a) BSE photo-image of large pore showing kaolinite filling pore, with mixed layer clay toward rim. Also shows grain coating clay around quartz grain. b) SEM photo image of rock chip showing the grain coating clay and mixed layer clay morphology c) BSE photo-image mica sheet lying across pore space, mica sheet probably once occupied the space between two feldspar grains prior to transformation to illite (see section 5.6.2.4). d) Rock-chip SEM photo image of pore space showing the interrelationship between the diagenetic clay minerals (Kaolinite, illite and mixed layer clays). e) SEM photo image of diagenetic clay showing blocky kaolinite(dickite) alongside vermicular kaolinite. f) SEM Photo image showing illitised mica within pore space. All images are from 7488.5ft@ 42/13-2.

5.6.1.8 The source of acidity for dissolution.

The most obvious source of acidity required to drive feldspar dissolution during burial diagenesis is through the generation of CO_2 because of the thermal degradation of kerogen during maturation (Schmidt and McDonald, 1979; Surdam *et al*., 1984; Curtis *et al*., 1986; Yuan *et al*., 2015; Akintola *et al*., 2021). When acidic fluids carrying alumina in solution react with soluble minerals (carbonates or feldspars) in the sandstones, the pH may be increased sufficiently to cause the alumina to precipitate, forming kaolinite and dickite (see equation 3-5 above). The Yoredale Formation in the SNS contain locally significant coaly source rocks, and these locally thick, organic-rich, compacting and thermally maturing coaly sequences could have provided important sources of acidic fluids. A similar process has been documented as affecting different regions in the SNS basin at different times (Ingrams *et al.*, 2020; Słowakiewicz *et al.*, 2020; Waters *et al.*, 2020; Wasielka, 2021; Blackbourn and Collinson, 2022).

In addition to organic acid source, "meteoric-water flushing" probably contributes to the precipitation of kaolinite within the studied sandstones. "Meteoric-water flushing" is a process, by which kaolinite precipitates at shallow depth by meteoric fluid like the process that prevailed during early diagenesis (see section 5.6.1.2 above). (Irwin and Hurst, 1983; Lanson *et al.*, 2002; C. Xia *et al.*, 2020; Yang *et al.*, 2020; Zhong *et al.*, 2020; Birkle *et al.*, 2021; Gordon *et al.*, 2022). Meteoric fluids have been proposed as causing the dissolution of feldspar and ferromagnesian grains (see again equations 3,4,5), while sourcing quartz and kaolinite (Bjørlykke and Brendsdal, 1986; Oluwadebi *et al.*, 2018; Lorentzen *et al.*, 2019; Yang *et al.*, 2020; Gao *et al.*, 2022; Mu, 2022, 2023). Additional studies show that vermicular kaolinite morphology typically indicate a meteoric water origin (Lanson *et al.*, 2002; Worden and Morad, 2003; Schmid *et al.*, 2004; Oluwadebi *et al.*, 2018). The occurrence of vermicular kaolinite in the study area will therefore probably indicate some influence from meteoric-water flushing in addition to the organic acids.

5.6.2 Mesodiagenesis (Late Diagenesis).

Superimposed on the early diagenetic fabric are a series of mesodiagenetic minerals precipitating in the Breagh Sandstone. Mesodiagenesis refers to late diagenetic processes following eodiagenesis. Mesodiagenetic processes are isolated from surface related processes (Schmid *et al.*, 2004), with burial depth from 1 to 2 km and temperature up to 200–250 °C (Worden and Morad, 2003). Temperature and the integrated thermal history are master controls at this stage. The mesodiagenetic events in this study include development of illite, late pore-filling carbonate (dolomite, ferroan dolomite, ankerite and siderite), quartz overgrowth, late formed sulphates (barite and anhydrite), and pyrites (see Fig 5.6 above).

5.6.2.1 Diagenetic Illites.

Late formed illites are noted to be most favorable where nucleation sites are available (e.g., pores with authigenic kaolin or other clays). However, some large and isolated macropores (with little internal evidence of illitization) where kaolinite or other clays had not precipitated are still preserved. Petrographic examination shows that the isolated macropores are lined by bituminous hydrocarbon (Fig 5.16 b, e, f). Bituminous stains are also observed to be caught between mica flakes and kaolinite sheets (Fig 5.16 j, k, l) giving an indication that oil saturated pore fluids migrated through the Breagh Field at some point prior to the development of illite but possibly during or after the development of kaolinite. Going by this, it can be suggested then that oil emplacement mostly occurred during or after eodiagenesis but before mesodiagenesis.

It is therefore possible to fix the likely time for illite development in the Late Triassic to Mid-Cretaceous in between pulses of oil emplacement. The transformation of kaolinite into illite is prevalent at temperatures greater than about 70°C (Oluwadebi *et al*., 2018) - 80^0C (Platt, 1993) but becomes pervasive at temperatures greater than about 125°C (Morad *et al*., 2000, 2010) with a low precipitation rate (Bjørlykke *et al*., 1995; Oye *et al*., 2023). Burial curve (Fig 5.14a,b) indicates that this 80^0C isotherm was crossed by the Lowermost Carboniferous strata again in Late Triassic at a depth of greater than 1900m. Fig 5.14b shows that illitization could have become pervasive in the Late Jurassic – Early Cretaceous as the temperature rose to 125^0C.

This could explain the occurrence of the large, clay-free secondary pores, despite the typically pervasive nature of illitic clays elsewhere in the studied samples. It could also suggest that migration could be a possible factor in the preservation of porosity and enhancement of permeability within the studied samples and that gas in the reservoir may have displaced an earlier oil phase. Thus provides a new exploration play with the possibility for redistribution of oil into an adjacent up-dip trap. Visual observation of the studied samples shows that the large isolated macropores make up 1-8% of the studied samples, hence it may yet be possible to flow more gas from the isolated macropores.

5.6.2.2 Timing of hydrocarbon migration and illite.

It is documented that the deeper parts of the Carboniferous basin fill first entered the hydrocarbon generation window during the Carboniferous burial (Corfield *et al*., 1996; Besly, 2019; Doornenbal *et al*., 2022; Petersen *et al*., 2022) (see also chapter 2.3.6). Any oil and gas that already migrated during this burial phase is likely to have escaped during the major phase of fluid expulsion that accompanied the end-Carboniferous Variscan deformation episode (Hollis and Walkden, 2012; Besly, 2019). Inversion episodes of Mesozoic in the Late Jurassic and Late Cretaceous are interpreted to have led to multiple episodes of migration and remigration of hydrocarbon. This process, although not well studied in Early Carboniferous succession has been documented for Rotliegend reservoirs (Roos and Smits, 1983; Parnell, 2002; Verweij *et al*., 2003; Browning-Stamp *et al*., 2023).

Integration of petrographic evidence and the interpreted 1D- Thermal model (Fig 5.14b) in this study may however support the case for multiple episodes of migration and remigration in the study area. The Bituminous stains between mica flakes and kaolinite sheets (more details in 5.6.2.4 below) could mean that an episode of oil emplacement could have occurred at the same time as kaolinization – during and following the Variscan orogeny, and the oil stain on the illitized mica sheet could mean that another phase of migration took place at the beginnings of illitization (Late Triassic - Early Jurassic). Any oil that migrated into the reservoir at that point, probably escaped during the Late Jurassic and Late Cretaceous tectonism but the presence of large isolated illite free pores despite the pervasive nature of illite could indicate that subsequent episodes of oil migration may have happened throughout illitization which continued until Mid-Cretaceous.

The oil remained in the reservoir until gas generation which would have flushed the reservoir displacing and degrading the oil. The exact timing of gas migration is uncertain although Cenozoic generation has been suggested to be likely critical for the trapping of oil and gas accumulations for areas in the SNS nearest to the southern margin of the Mid-North Sea High (MNSH) (more details in chapter 2.6).

In the Breagh area, the coals within the Scremerston Formation have reached maturities low in the gas window. One-dimensional basin modelling of the 42/13a-06 well in the Breagh Field suggests that the bulk of charge occurred before the BPU (Grant *et al*., 2020). It would be however unlikely that gases expelled locally from the Scremerston Formation prior to the BPU would be retained until the present day due to the inversion and trap modification that occurred later. Therefore, the charge into the structure is likely to have occurred later in geological history (Grant *et al*., 2020). A comparable burial graph and 1D basin model of wells of 41/20-10, 41/14-01 and the Crosgan Field well 42/10b-2 shows that there is a later charge episode than that in the Breagh area, with some expulsion occurring in the Late Cretaceous and Paleocene (Vincent, 2015; Besly, 2019; Grant *et al*., 2020). Results of 3D maturity and migration modelling, integrating a 5 km resolution seismic depth grids validates this suggestion because Cenezoic generation and expulsion is in agreement with observed shows and discoveries in the southern margin of the MNSH. (Collinson and Jones, 1995; Andrews, 2013; Monaghan *et al*., 2015, 2017; Whitelaw *et al*., 2017; Arsenikos *et al*., 2019).

The large illite-free pores in the studied sandstones may have been preserved by oil. The gas generated in the Cenezoic must have flushed the reservoir displacing and degrading oil and reopening more secondary dissolution porosity. Therefore, provides a new exploration play with the possibility for redistribution of oil into an adjacent up-dip trap.

Within the studied sandstones, illite is the next dominant cement after kaolinite. It occupies 8.5-9.5% of the pore spaces (see 5.5.1 above). They appear mostly as multiple sets within the dissolution pores. This texture seems to be related to the stacking sequence of the layers in mica or kaolinite in the core of the illite fibers (Fig 5.8 b, d, e & 5.15f) which suggests that illite probably formed via the alteration of kaolinite and micas (Ehrenberg and Nadeau, 1989; Nedkvitne and Bjorlykke, 1992; Bjorkum, 1996; Lanson *et al*., 2002; Bauluz *et al*., 2008; Ehlmann *et al*., 2009).

Petrographic observation indicates that more illite nucleates around kaolinite than they do around the micas thereby supporting a higher prevalence from the kaolinite precursor than mica. In addition, observation of the samples with SEM data shows the presence of smectite in the pores (Fig 5.15b, d). However, the observed sheet-like morphology has been reported to be more common with illite formed from kaolinite source as opposed to a predominate flaky morphology (Pollastro, 1990; Permana *et al*., 2019) usually associated with smectite mixed layer precursor (Pollastro, 1990; Storvoll *et al*., 2002). Regardless of the precursor however, the formation of illite would usually require a source of potassium.

5.6.2.3 Source of potassium for illitization.

Thermodynamic calculation shows that the precipitation of illite relies on the dissolving aluminosilicate minerals like smectite and kaolinite due to the extremely low solubility of aluminium (<1ppm @130^{0}C) even in the presence of organic acids (Bjørlykke, 1984). In addition, potassium could come from further dissolution of K-feldspar grains with or without kaolinite or influx of potassium from external sources.

According to equilibrium thermodynamic models, feldspar and kaolinite can coexist together (Bjørlykke *et al*., 1995; Birkle *et al*., 2019, 2021) at lower diagenetic temperatures < 125^{0}C (Yuan *et al*., 2015). Their coexistence at this lower diagenetic temperature is unstable and they often react very slowly (Bjorkum and Gjelsvik, 1988; Bjørlykke *et al*., 1995; Ramm and Ryseth, 1996; Bjørkum and Nadeau, 1998; Thyne *et al*., 2001; Wang *et al*., 2019; Weibel *et al*., 2020; Birkle *et al*., 2021) in a pH-neutral, isochemical process. However, with increasing temperature (>125°C [257°F]) and high potassium/hydrogen activity ratio aK^{+}/aH^{+}, illites become more stable. The illitization of minerals can thus be represented by the following equation from (Bjørlykke, 1998; Lanson *et al*., 2002; Franks and Zwingmann, 2010).

$$\underset{\text{Kaolinite}}{Al_2Si_2O_5(OH)_4} + \underset{\text{K-Feldspars}}{KALSi_3O_8} \Rightarrow \underset{\text{illite}}{KAl_3Si_3O_{10}(OH)_2} + \underset{\text{quartz}}{SiO_2} + 3H_20$$

The quartz by-product from the reaction is thought to provide further overgrowths on earlier generations of quartz overgrowths.

2. In the absence of kaolinite, K-feldspar can also proceed directly to illite (Surdam *et al*., 1989; McAulay *et al*., 1993; Platt, 1993; Lanson *et al*., 2002; Wang *et al*., 2019) if there is a source of acidity as seen in the equation below by (Lanson *et al*., 2002; Bauluz *et al*., 2008; Bjorlykke and Jahren, 2012). Since feldspar is largely absent in the study area, even the relics of previously present feldspar constitute less than 0.1% of the point count data, this route may only contribute a very small amount to the overall illite content. As earlier mentioned, the acidic fluids used in this reaction might have been sourced from the locally occurring Yoredale coaly source rocks. As organic CO_2 from migrating gas phase partitions formation water, it dissociates to produce low pH water (Barclay and Worden, 2000; Lei *et al*., 2019; Li *et al*.,

2019). With a mud/sand ratio of 2:1 to 4:1 (visual estimate from core log – see chapter 4), the organic CO_2 and organic acids are probably not enough for generation of the feldspar within the pores of the Breagh sandstones (Lundegard *et al*., 1984; Giles and Marshall, 1986; Ehrenberg, 1991; Surdam *et al*., 1993; Ma *et al*., 2022; Wang *et al*., 2023). Because a large volume of meteoric water can provide inorganic CO_2, illitization of minerals in these sandstones could have occurred in the presence of both acids from meteoric water and from organic matter. More studies are still needed to confirm the vitrinite reflectance (R_0) and thermal evolution of organic matter within the mudstones and shales of the Breagh Field. However, because the Breagh sandstone reservoirs are generally interfingered with or directly packaged in the thick source rock beds, the acidic fluids can be expelled into sandstones from source rocks by compaction and overpressure related to hydrocarbon generation and clay dehydration (Guo *et al*., 2010; Wang *et al*., 2019).

$$\underset{K\text{-}feldspar}{3KALSi_3O_8} + H_2O + 2H^+ + \Rightarrow \underset{illte}{KAL_3Si_3O_{10}(OH)_2} + \underset{Quartz}{6SiO_2} + 2K^+$$

3. In addition to the two routes above, the most probable route for the illitization of kaolinite within the studied samples is through a flux of K^+ from external sources, including the dissolution of adjacent evaporite deposits (Underhill, 2003; Booth *et al*., 2017, 2020; Brackenridge *et al*., 2020; Grant *et al*., 2020; Nwachukwu *et al*., 2020) and the overlying Permian evaporates within the study area. Equation for the transformation is represented as below (Bjørlykke, 1998; Lanson *et al*., 2002; Franks and Zwingmann, 2010).

$$\underset{Kaolinite}{3Al_2Si_2O_5(OH)_4} + 2K^+ \Rightarrow \underset{illite}{2KAl_3Si_3O_{10}(OH)_2} + 2H^+ + 3H_20$$

5.6.2.4 Illitization of micas.

Textural relationships within the studies sandstones shows that illitised micas are synchronized with illitised kaolinite (Fig. 9F), suggesting that both illite from kaolinite and micas probably precipitated at a similar time. For the non-channel sandstones (Fig 5.16 j, k,l) however, illitisation of micas probably started much earlier during eogenetic processes because the high amount of minerals released in the immediate vicinity of micas would have elevated the pH of the alteration sites and drove much earlier illitisation in comparison with the channel facies (Fig 5.16; a-f).

Mica alteration to illitic clays and other minerals have been described for several sandstone sequences from different parts of the North Sea and other basins of the worlds (Boles, 1978; Burley, 1984; Hugget, 1984; Warren, 1987; Morad, 1990; Rafiei *et al*., 2020; Khanam *et al*., 2021; Bello *et al*., 2022). Since many minerals result from alteration of micas, illtisation of micas have been described as the most important factor controlling the porosity and permeability in sandstone reservoirs (Bjørlykke, 1984; Bjørlykke and Brendsdal, 1986; Hurst and Archer, 1986).

The alteration of micas provides ions that typically raise the pH in the vicinity of the mica flakes and migrate with the pore fluids to precipitate visibly on thin section scale (Boles, 1978; Boles and Franks, 1979; Bjørlykke and Brendsdal, 1986; Morad *et al*., 2000; Kim *et al*., 2007).

Variable amounts of potassium, K-feldspars, siderite, dolomite, Titanium oxides, and pyrite were seen from the SEM data between the cleavage planes of the illitised micas in the studied sandstones (Fig 5.17). Similar effects to this have been noted in other rocks (Boles, 1984; Boles and Johnson, 1984; Dasgupta *et al*., 1990; Morad, 1990; Bjorkum, 1996; Bjorkum and Nadeau, 1998; Weibel *et al*., 2020; Gao *et al*., 2022; Sun *et al*., 2022). Further, the release of water from the alteration reactions would dilute the pore fluids and enhance even further diagenetic reactions, particularly in deep-burial environments where porosity and permeability are low and pore-fluid flow is limited, this probably explains the higher amount of illitised micas in lower porosity horizons (see table 5.1 & Fig 5.16; k l).

Within the studied sandstones, illitised mica are observed to develop as pore-lining and pore-filling cement in both studied wells. SEM and BSE revealed a gradual transition in chemical composition between the original mica and the replacive illite (Fig 5.17). This type of chemical trend is not uncommon. It has been analyzed by electron beam in Jurassic reservoir sandstones from the Haltenbanken area, offshore Norway where (Morad, 1990) had suggested it to be due to the changing proportions of mica and clay minerals from the core of the mica sheets outwards.

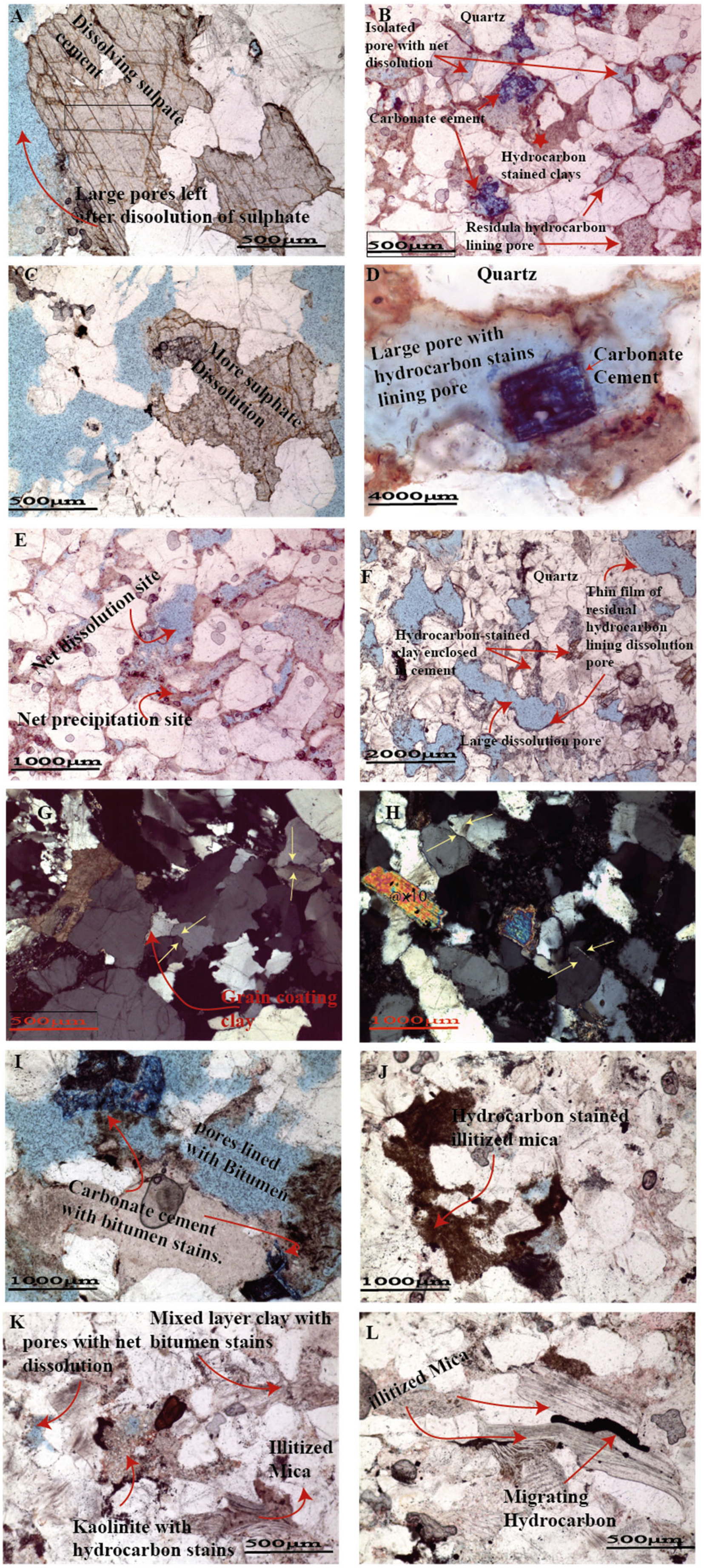

Figure 5.16 a) Photo image showing oversized pores left after dissolution of sulphate cements and remnant of dissolving sulphate cement @ 7488.5ft b)Photo image of sample at 7549.0ft showing the distribution of cements in pores and pores lined by hydrocarbon stains c) Photo image showing more sulphate dissolution revealing larger pore space@7488.5ft d)Photo image showing grain coating clay and pores of net dissolution lined with residual bitumen @7540.5ft (e) Photo image sowing secondary pores dissolution in non-channel facies @7497.5ft g) Photo image of sample at 7488.5ft showing the beginnings of stylolitic contact (yellow arrows) at quartz to quartz boundary and grain coating clay h)Grain coating clay (yellow arrow) @7497ft i)Photo image showing pores lined with bitumen and carbonate stained with residual hydrocarbon @7488.5ft h) Photo image of sample @7497.5ft showing j)hydrocarbon stained illitized mica k)Photo image @7497.5 showing different cements stained with hydrocarbon and pores with net dissolution lined with hydrocarbon. L) Photo image showing illitized Mica and migration hydrocarbon caught between mica flakes.

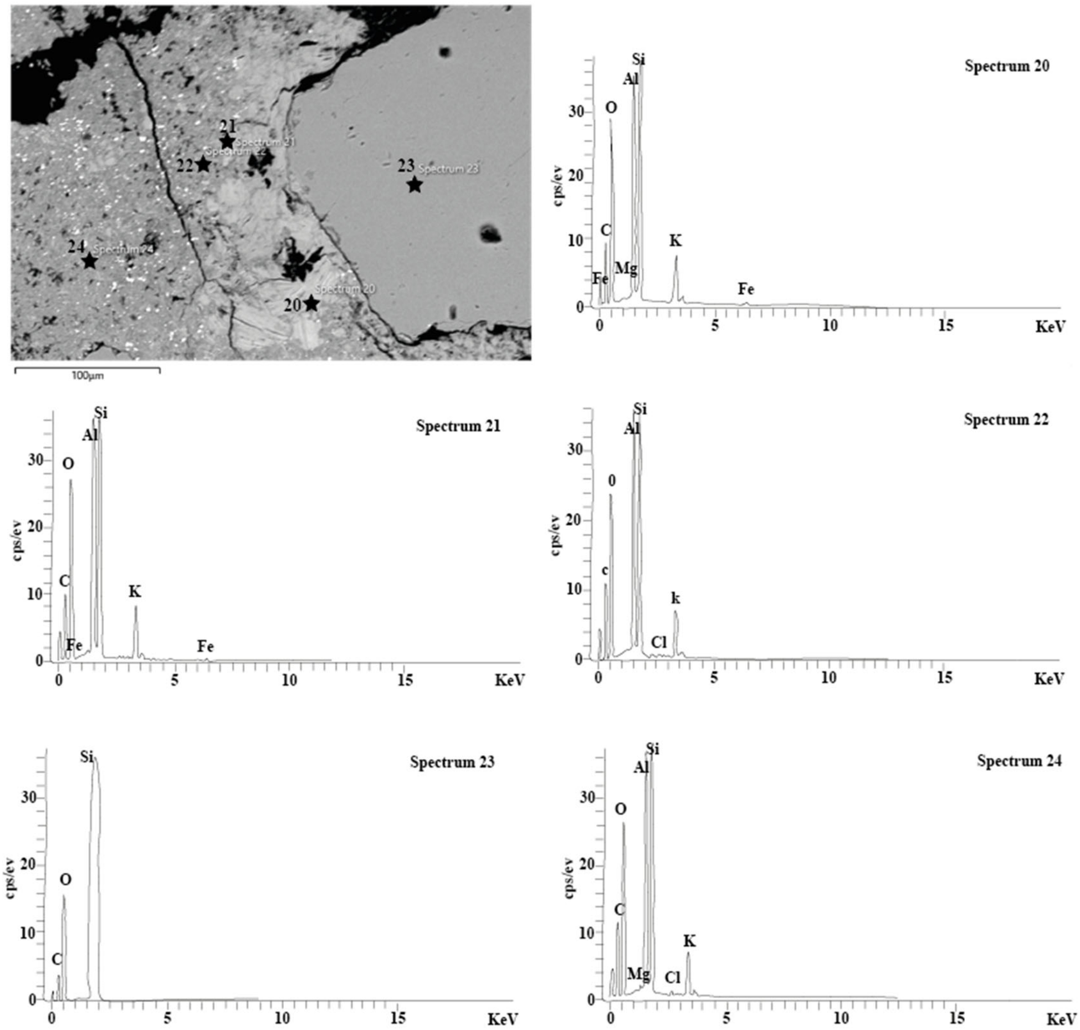

Figure 5.17: SEM phot-image showing the gradual transition in chemical composition between the original mica and the replacive illite across spectra @ 42/13-2 7488.5ft.

5.6.2.5 Late Carbonate cementation.

It is difficult to precisely determine the timing of carbonate cements given that they are highly reactive (Moore, 1989; Marshall and Pirrie, 2013; Scott *et al.*, 2021). However, based on thin section observation, carbonates in the studied samples most likely post-dates but could have also precipitated concomitantly with illite thereby supporting a late diagenetic event. The precipitation of carbonates as a late diagenetic cement indicates that the pH must have become neutral to alkaline in contrast to the acidic conditions prevalent during the intermediate burial stage (Cowan, 1989). The late-stage diagenesis hypothesis can also be supported with the fact that the ions which formed the carbonate cements were probably released into the pore waters during later stages of diagenesis either from the alteration of micas or the reaction of the bicarbonate produced as by product from the transformation of feldspars into illite.

In all the samples, the carbonate cements- both ferroan and non-ferroan can be seen as fresh rhombs in secondary dissolution pores (Fig 5.9 see also section 5.5.2) although there is preferential occurrence of the cements within the secondary pores of the coarser-grained horizons which may be due to the easier movement of fluids through these horizons compared to finer-grained horizons (McNeil *et al*., 1995, 1998).

Much of the carbonate cement is zoned. Different styles of zonation are present, often within the same pore. Equant concentrically zoned rhombs present the simplest case (Fig 5.9). Each zone probably represents a significant variation in carbonate composition (Fig 5.10) which may be the result of episodic precipitation from intervening periods of dissolution and replacement, as the pore-fluids became enriched in Fe or depleted in Mg (Dickson, 1966; Meyers, 1991; Roberts *et al*., 2020). In most of the studied samples Fe-dolomite/Ankerite precipitation appears to post-date the formation of non-ferroan dolomite cements (Fig 5.9)- since they grow as outer zone on the non-Fe-dolomite.

As, increasing Fe^{2+} content in diagenetic sequences has been described by several works as proxy for burial cementation (Machent *et al*., 2007; Taylor and Machent, 2010; Sliwinski *et al*., 2016; Liu *et al*., 2019; Sun *et al*., 2022), Fe-dolomite/ankerite in the Breagh sandstone would therefore indicate late carbonate phase. The explanation for this could be bacterial mediated cementation through microbial methanogenesis (Gluyas, 1984; Coleman *et al*., 1997; Morad, 1998; Wei *et al*., 2022). This happens as the Fe contents in porewaters increases during sandstone burial, because of increased supply of Fe (II) to pore waters through the reduction of Fe (III) residing in iron oxides and iron silicates. Therefore, with increasing burial and temperature, oxygen, Ca^{2+}, Mn and Mg^{2+} level becomes depleted, as Fe^{2+} is released into the pore water, resulting in precipitation of ferroan dolomite/ankerite.

Proxy data from neighboring field show that the temperature necessary for bacterial mediated carbonate cementation to be greater than 110^0C (Schmid *et al*., 2004). Data from specific fields also corroborate this temperature range. For example, fluid inclusion for carbonate cement in Rotliegend Sandstones in the V-Fields of the SNS just SW of Breagh showed that the Th values for the dolomite is between 100-125°C. In addition, the Upper Carboniferous Namurian interval Trumpfleet Field-South Yorkshire SW of the Breagh identified precipitation of ankerite at a temperature range of 120 °C and 160°C (Cowan and Shaw, 1991). At this temperature, the late Fe-dolomite/Ankerite cements in the study area must have precipitated during deep burial, at depths of 2,500-2,800m during the Late Jurassic -Early Cretaceous (Fig 5.14a, b).

5.6.2.6 Origin of Carbonate cement.

The origin of carbonate cements can be established based on carbon isotopic compositions of the cements (Irwin *et al*., 1977; Stewart, 1995; Ma *et al*., 2017; Mao *et al*., 2019). The $\delta\ ^{13}C$ values for the carbonate cements in the studied sandstones (Table 5.) range from 1.1‰ to -2.4 ‰ (V-PDB) whilst the oxygen isotope has a $\delta\ ^{18}O$ has a wider range from +0.26 to -9‰ (V-PDB).

From the work of (Taylor *et al*., 2000; Moore, 2001), this range suggest that the carbon is sourced from mixed meteoric input (Fig 5.18). Early meteoric flushing based on carbonate isotope evidence has been suggested for other fields (Clayton *et al*., 1966; Kharaka *et al*., 1973; Bjørlykke, 1988, 1994, 1998; Watson *et al*., 1995; Macaulay *et al*., 1998; Baker, 2003; Cao *et al*., 2022; Gao *et al*., 2022) where meteoric water flushed the reservoir during early burial, carrying with it excess oxygen and microbes which later biodegraded the migrated oil.

Table 5.5: Showing $\delta^{13}C_{V\text{-}PDB}$, $\delta^{18}O_{V\text{-}PDB}$ and $\delta^{18}O_{V\text{-}SMOW}$ of the dolomite cements in the studied wells in the Breagh field. All depths are measured in TVDSS.

Facies	Well	Depth (Ft)	$\delta^{13}C_{V\text{-}PDB}$	$\delta^{18}O_{V\text{-}PDB}$	$\delta^{18}O_{V\text{-}SMOW}$
		Run 1			
FA4	42-13-2	7425.2	**-0.39**	**-7.04**	**23.65**
FA9	42-13-2	7463.9	**-2.04**	**-2.23**	**28.61**
FA3	42-13-2	7451.11	**-0.65**	**-6.44**	**24.27**
FA8	42-13-2	7461.3	**-2.32**	**-0.10**	**30.80**
FA4	42-13-4	7550.7	**0.49**	**-8.45**	**22.19**
FA4	42-13-4	7549.2	**0.13**	**-7.20**	**23.48**
FA8	42-13-4	7537.7	**0.21**	**-6.83**	**23.86**
FA8	42-13-4	7539.1	**0.42**	**-7.32**	**23.36**
FA8	42-13-4	7547.8	**-0.38**	**-5.94**	**24.79**
FA4	42-13-4	7551.5	**0.65**	**-8.44**	**22.21**
FA4	42-13a-6	7826.1	**0.99**	**-9.42**	**21.20**
FA10	42-13a-6	7956	**-1.17**	**-8.28**	**22.37**
FA9	42-13a-6	7701.4	**0.11**	**-7.77**	**22.90**
FA10	42-13a-6	7956 (duplicate)	**-1.17**	**-8.60**	**22.05**
		Run 2			
FA3	42-13-2	7404.0	**-1.14**	**-7.01**	**23.68**
FA4	42-13-2	7406.4	**-0.32**	**-6.26**	**24.46**
FA11/12	42-13-2	7425.2	**-0.34**	**-6.69**	**24.02**
FA12	42-13-2	7442.10	**-0.99**	**-6.68**	**24.02**
FA3	42-13-2	7451.11	**-0.69**	**-6.91**	**23.79**
FA8	42-13-2	7461.3	**-2.35**	**-0.45**	**30.44**
FA8	42-13-2	7463.9	**-1.91**	**-2.12**	**28.72**
FA8	42-13-2	7469.9	**-2.31**	**-1.09**	**29.78**
FA9	42-13-2	7488.5	**-0.33**	**-7.74**	**22.93**
FA8	42-13-4	7537.7	**0.08**	**-6.82**	**23.88**
FA8	42-13-4	7539.1	**0.20**	**-7.53**	**23.15**
FA8	42-13-4	7539.1	**0.49**	**-7.34**	**23.35**
FA8	42-13-4	7543.3	**0.37**	**-6.09**	**24.63**
FA8	42-13-4	7547.8	**-0.40**	**-5.75**	**24.98**
FA4	42-13-4	7549.2	**0.12**	**-6.90**	**23.79**
FA4	42-13-4	7550.7	**0.58**	**-8.33**	**22.32**
FA4	42-13-4	7551.5	**0.72**	**-8.24**	**22.42**
FA10	42-13a-6	7956	**-1.11**	**-8.29**	**22.36**
FA4	42-13a-6	7826.1	**1.11**	**-9.11**	**21.52**
FA9	42-13a-6	7701.4	**-1.43**	**-8.87**	**21.77**
FA8	42-13a-6	7963.5	**-1.13**	**-8.48**	**22.17**
FA8	42-13-2	7469.9 (duplicate)	**-2.08**	**-1.12**	**29.76**
FA4	42-13-4	7551.5 (duplicate)	**0.67**	**-8.51**	**22.13**

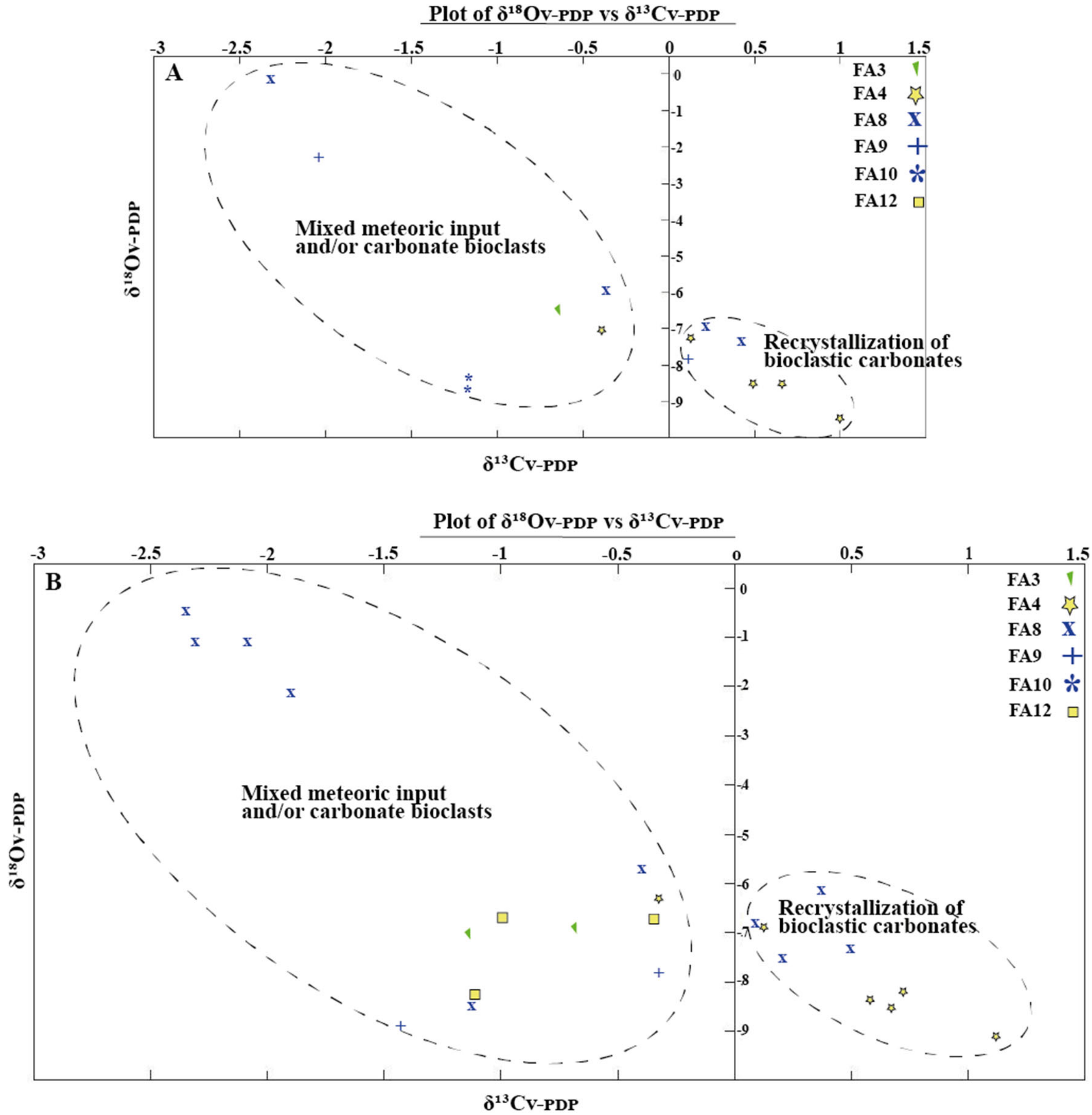

Figure 5.18: Plot of δ^{18}Ov-PDP vs δ^{18}Cv-PDP of the dolomite cements in the Breagh field. Two runs A and B show similar results.

Meteoric water composition for the study area has not been properly documented. Also, because no fluid inclusion data were obtained for the carbonate cements in the study area and there are currently no published data on the detailed isotopic composition of the carbonate cements in the area, the conditions for carbonate precipitation are poorly constrained hence will rely on proxy data. Previous authors have estimated δ^{18}O of -3.2 to –6‰ (VSMOW) in the Early Carboniferous meteoric water (Bruckschen *et al.*, 1999). Since this is a wide range to work off the precipitation temperature from, the current study will assume mid value of -4.5‰. With respect to an estimated δ^{18}O water composition of -4.5‰SMOW, a precipitation temperature of 23 °C to 58 °C is calculated for the carbonate cements in the Breagh sandstone

(Fig 5.19). Given, that earlier works from (Bruckschen *et al*., 1999; Mii *et al*., 1999) proposed 25-35^{0}C as the tropical sea surface temperature (SST) for the Visean (Early Carboniferous) of the European Carboniferous, the calculated precipitated temperature of 23 °C to 58 °C is within reason. As described earlier however (see section 5.6.1.2), the early calcite cement in the study area have been dissolved away and, its former existence only known by the background pink discolouration and the trace amount picked up by XRD. But the early calcite cements though minor may have interfered with the values for the precipitation temperature and therefore accounting for the lower temperature range between 23^{0}C-35^{0}C. If this assumption is true, the precipitation temperature for the late carbonate cement in Breagh is probably between 35^{0}C to 58^{0}C. Further work is needed to verify this, but that will be outside the scope of this thesis.

Similar value for late dolomite precipitation temperature have been calculated by Permo-Triassic sandstones in North Sea (Oluwadebi *et al*., 2018) utilizing the same equation and figure at (Fig 5.19) used in this study. The calculated value of δ18OSMOW is derived from: δ^{18}OSMOW = 1.03091× δ^{18}OPDB + 30.91 (Coplen *et al*., 1983), and the temperature is calculated by using fractionation equation between carbonate and water: 1000× ln α dolomite-water = 3.06 × 106/T2 - 3.24 (Matthews and Katz, 1977).

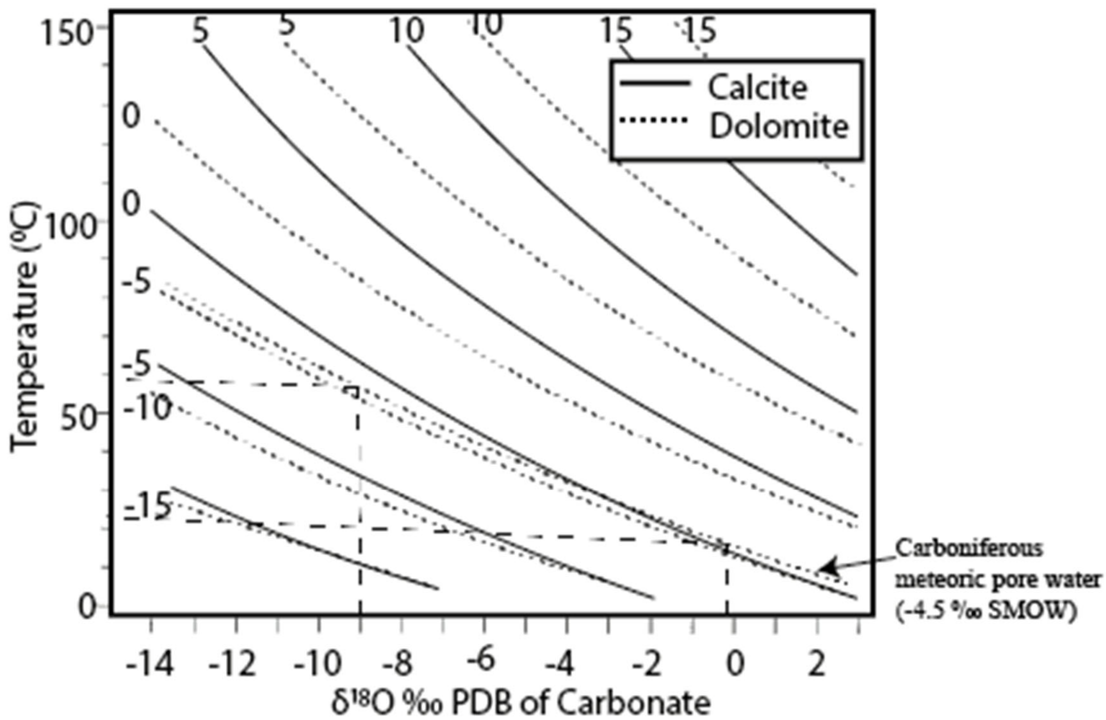

Figure 5.19: Temperature versus δ 18O for dolomite cement after (Ehrenberg et al., 2002). Dotted curve represents SMOW value for Carboniferous meteoric pore water (−4.5‰.) Drawn from fractionation equation of (Matthews and Katz,

5.6.2.7 Pyrite.

XRD and SEM analysis of the samples from the studied wells indicates that pyrite cement occurs trace to minor amount. The low abundance of pyrite cement from the studied wells indicates a depletion or low sulphate concentration in the deeper sequence of the sediments an event which according to (Curtis *et al*., 1975, 1986; Curtis, 1980, 1987; Curtis and Coleman, 1986; Coleman *et al*., 1997), is dominated by microbial methanogenesis which possibly contributed to the late ferroan carbonate.

5.6.2.8 Sulphate.

Both sulphate cements (anhydrite and barite) are late cements. Microscopic observation indicates that anhydrite developed earlier than the growth of barite cement. Dissolution or re-precipitation of early gypsum cement can generate late anhydrite precipitation due to its high solubility (Taylor and Colter, 1975; Colter, 1997; Greenwood and Habesch, 1997; Meadows *et al*., 1997; Thompson and Meadows, 1997; Schmid *et al*., 2004; Marsh *et al*., 2022) suggested that fluid for anhydrite precipitation can be supplied from evaporates within, above or beneath a sequence (Gluyas *et al*., 1997). The Breagh Sandstone Formation is overlain by Permian Zechstein; therefore, Zechstein evaporites could probably supply the fluids needed for sulphate precipitation.

5.7 Diagenetic controls on reservoir quality.

Poor reservoir quality has been reported from the Breagh Field sandstones. Petrographic observations and plot of intergranular volume against cement (Fig 5.3) is evidence that the degree of compaction in the studied sandstone is higher cementation. The plot revealed that over 90% of the samples from 42/13-2 and all except one of the samples from 42/13-4 well fall between 0-10% intergranular porosity line suggesting that compaction processes control the present-day porosity values. Because porosity and permeability are highly correlated (Fig 5.5), the factor controlling porosity will also to a large extent control permeability.

Direct observation from thin sections in this study also supports the effect of higher compaction. Common straight and concave-convex grain contacts between detrital framework grains (Table 5.2 & Fig 5.2E-) indicate high compaction although highly influenced by lithofacies variation. Infrequent zones of stylolites observed in some samples indicate the onset of extensive compaction.

The average values for the data from well 42/13-2 are 28.5% intergranular volume and 22.3% of cement. This indicates that 22.6% of original porosity has been destroyed by compaction whereas 17.4% has been destroyed by cementation assuming the original porosity was 45%. For 42/13-4 well, average data revealed intergranular volume of 24.2% and cement of 20.4%. This indicates that 27.68% of original porosity has been destroyed by compaction, whereas only 14.8% has been destroyed by cementation.

Mechanical and chemical compaction has therefore played an important part in reducing depositional porosities to their present values, with chemical compaction probably sourcing some silica for precipitation as quartz overgrowth cements. These cements (also sourced by reactions with feldspar grains) have occluded some IGV, resulting in further porosity loss. Whilst compaction and quartz cementation have reduced pore volumes, the precipitation of authigenic illite is interpreted as a major control on permeability.

Petrographic observations identify mica grain bending (Fig.5.2Fii &5.16 k, l) and the fracturing of quartz grains. Compaction thus contributed to permeability loss within the reservoir, by the deformation and bending of lithic grains, ductile grains get crushed and extruding between rigid sands grains, block pore throats and reduce the pore connectivity (Morad, 1990; Chi *et al*., 2003; Aagaard and Jahren, 2010).

Further, petrographic results suggest that the Breagh field reservoir has undergone advanced diagenetic alteration. Precipitation kaolinite and precipitation of quartz cement are observed to have reduced porosity whist the illitic clays and carbonate cements are observed to be more detrimental to permeability (details on this in chapter 6). Earlier eogenetic grain dissolution (see section 5.6.1) on the other hand seems to create macro pores that first increase porosity but later in the diagenetic sequence get filled with authigenic cements.

More than 50% of the visual porosity in the studied sandstones are noted to be secondary in origin after dissolution of sulphate cements but also to a lesser degree, dissolution of carbonate cements and unstable grains. Such secondary pore spaces have also made possible sites for significant precipitation of authigenic clay minerals, authigenic quartz, and associated intragranular and inter-crystalline microporosity that further damaged reservoir quality- For example, the kaolinite aggregates within the macropores (Fig 5.8a, b,e,h & 5.15a,b,d,e) are rich in inter-crystalline microporosity. Kaolinite have been observed in other studies to generally exhibits 25%–50% microporosity in the total volume (Nadeau and Hurst, 1991; Hayes and Boles, 1992; Macaulay *et al*., 1993; Hurst and Nadeau, 1995; Li *et al*., 2019; H. Xia *et al*., 2020; Giannetta *et al*., 2021).

Examination of the studied thin section show that pervasive sulphate cement in the form of anhydrite form sheets that formally occluded large pores in the sample sets. Some of the anhydrite cements have either totally or partially dissolved and left relics of their formal shape which are now infilled by clay. Whereas other relics that have not been occupied by clay minerals have been completely dissolved thereby leaving behind large secondary pores that significantly enhance permeability (see more in Chapter 6).

Petrographc analysis of samples from 42/13-2 indicate that visible sulphate cement makes up 0.7 to 5% of the bulk rock volume. Quantitative intergranular porosities make up 0.7 to 25.3% (av of 6.0%). There was no differentiation between primary and secondary porosity for the 42/13-2 sample set but visible secondary porosities from sample set of 42/13-4 make up 5-42% (av of 15%) of the total visible porosity.

Visual estimates of porosity formed from dissolution of sulphate covers more than 55% of the total intergranular porosity in the sample sets where seen thereby making the presence of sulphate cement a very important cement for reservoir quality development in the Breagh Sandstones.

The extent to which these anomalously large dissolution pores influence reservoir quality in the study samples is not a straight forward one because, in places these large pores are partially or completed occluded by clay mineral cements whose characteristic microporosity increases tortuosity of the pores throat and therefore damaging to permeability whilst in other areas, where these large macropores are preserved (where other cements have not precipitated) permeability is noted to increase by several orders of magnitude. For example, Fig 5.20 are two channel-fill sandstones (FA8) samples – where the presence of pores with radius (50-100µm) in the sample from 7469ft (top sample) significantly increases permeability to 35mD in comparison to the sample below from 7442.1ft (bottom sample) without the (50-100μm) pore radius and so a permeability of 0.02mD.

Macropores within the sample sets form approximately 5–42% of the total measured porosity. In most cases, macroporosity has formed by secondary dissolution, and occurs either as isolated grain-dissolution pores or the grain-dissolution component of hybrid pores (Fig. 5.20-top).

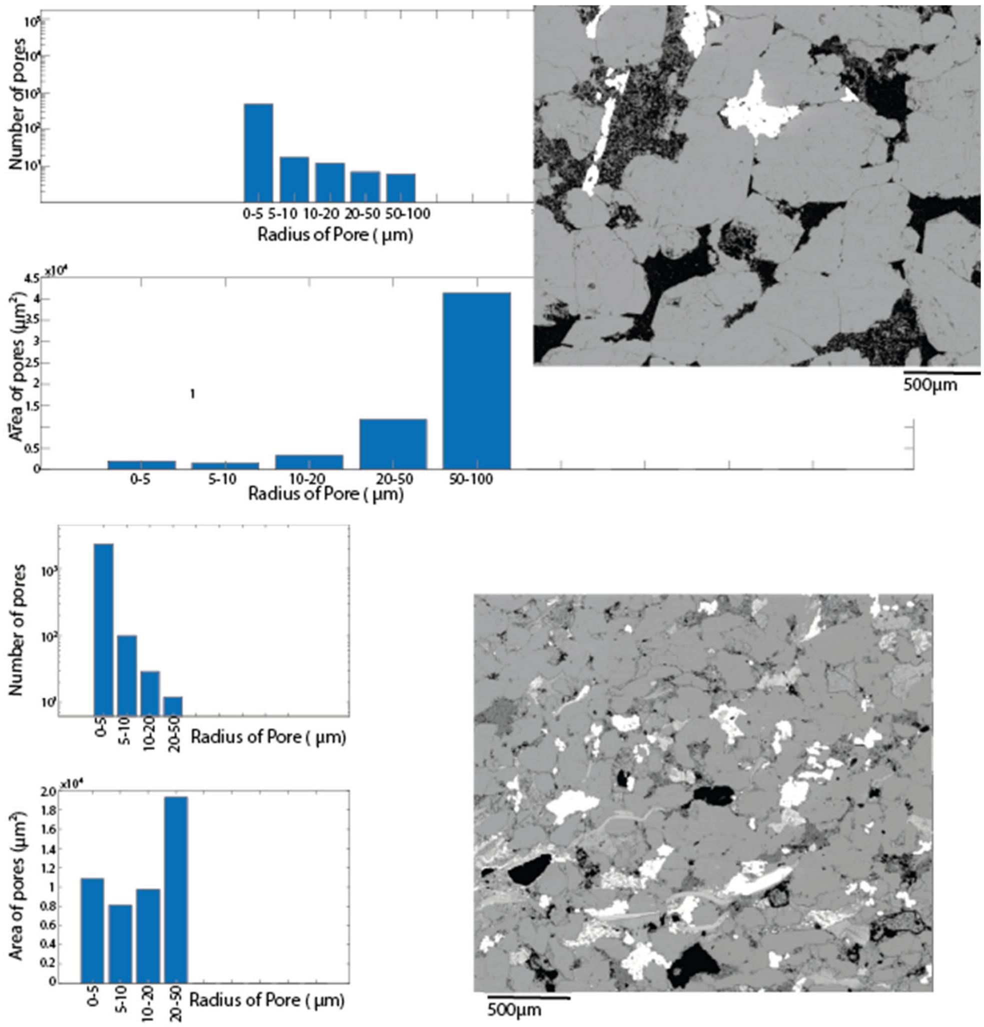

Figure 5.20: macroporosity and infilling authigeneic clays; Top - FA8 Sample at 7469ft; bottom FA8 Sample at 7442.1ft.

Visual estimates of average macropore size ranges from 50 μm to 400μm, whilst the mean hybrid pore size ranges from 16μm to 500 μm, locally reaching a maximum size of 1000μm (more details of measurement in Chapter 6). These large macropores are likely to be connected by a highly tortuous system of microporosity associated with the abundant clay minerals and carbonate cements (more detail on pore system network in chapter 6).

Authigenic clay mineral precipitation can significantly influence sandstone reservoir properties. The relative abundance of illitic clays and kaolinite within the sample sets contribute greatly to the reduction of reservoir quality of the studied sandstone.

A stacked aggregate of vermicular kaolinite is observed to occlude and fill intergranular pore, thus reducing the sandstone permeability. Kaolinite accounts for approximately 60% of the of the observed cement in the study area thereby making kaolinite the most significant diagenetic cement in the study area. Kaolinite is more abundant in the fluvial channel (FA8) samples where they reduce porosity to less than 10% (Fig 5.21a).

The amount and distribution pattern of kaolinite is influenced by the amount of unstable detrital silicates, hydraulic conductivity and rate of fluid flow in the sand body so therefore eogenetic grain dissolution are known to be most prevalent in permeable sediments, such as channel sand deposits (Worden and Morad, 2003). The presence of kaolinite has little effect in reducing the permeability of the channel sandstones as they still retain the highest permeability (>20mD) within the studied samples (Fig 5.21b).

Illitic clays are the second most abundant diagenetic minerals in the Breagh field samples. They account for approx. 40% of the diagenetic cements and are observed to have the most damaging

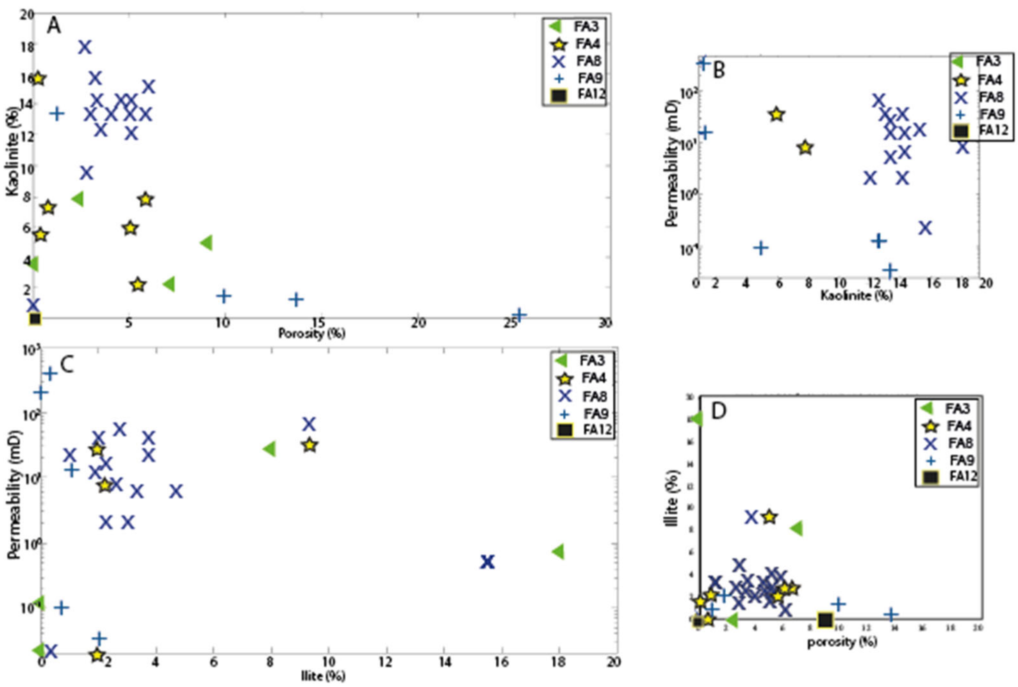

Figure 5.21: Plots of diagenetic cement against permeability and porosity. A- Kaolinite/porosity; B- Permeability/Kaolinite; C: Permeability/illite; D: Illite/porosity.

effect on the permeability of the sample sets within this study. Authigenic illite usually reduces permeability in sandstone reservoir (e.g., Kantorowicz, 1990; Gaupp *et al*., 1993; Leveille *et al*., 1997). Wispy illite is observed to locally form tangential grain coat, it forms ridges on grain surfaces and also bridge pores throats but the fibrous illite is observed to form interlocking meshwork bridging and filling intergranular pores (Fig 5.8a, d,e,g,h & 5.15a,b,d,e)

Illitic clays are observed in all facies although where present. They are generally seen to reduce the permeability in the non-fluvial sands (FA3, FA4 and FA12) more than they do in the fluvial sands (FA8 and FA9). Permeability range in the FA3, FA4, and FA12 between (0.02 – 1mD) whereas it is between 20 to 375mD in the Channel sands (FA8) and braided fluvial sands (FA8) sample sets. However specific evidence from a few outliers in (Fig 5.21c and 5.21d) show that samples with the very low illitic clays have the highest permeability and vice versa.

Quartz cementation has been recognised as one of the main causes of porosity loss in many sandstone reservoirs (e.g., Blatt, 1979; McBride, 1989; Ehrenberg, 1990; Swarbrick, 1999). Quartz cementation is a very important diagenetic cement in the analysed sandstones. Authigenic quartz occurs in varying degrees in all the samples studied (where present: 0.3-4.3% and average of 1.9%), although it makes up approx. 10% the total diagenetic cement in this study. It plays a role in reducing the reservoir quality but not as much as the dominating clay minerals. It is important to note that due to the difficulty of discriminating detrital quartz grain from overgrowth with standard petrography, it is most likely that the detrimental effect of quartz overgrowth on porosity is diminished from the plot (Fig 5.22b). However, the highest porosity ranges (samples with porosity 9%-25%) are in samples with no discernible quartz cement.

Carbonate cement accounts for almost 10% of the total observed cements, indicating that carbonate cement has a significant impact on reservoir quality of the studied formation. Dolomite is most commonly present as developed rhombs and is observed to be finely to moderately crystalline filing intergranular pores, blocking pore throats and destroying macro-porosity across large area (see 5.5.2). and thereby reducing reservoir quality. Sample set with 0% carbonate cement are noted to have the highest permeability ranges from 41.46 to 378mD.

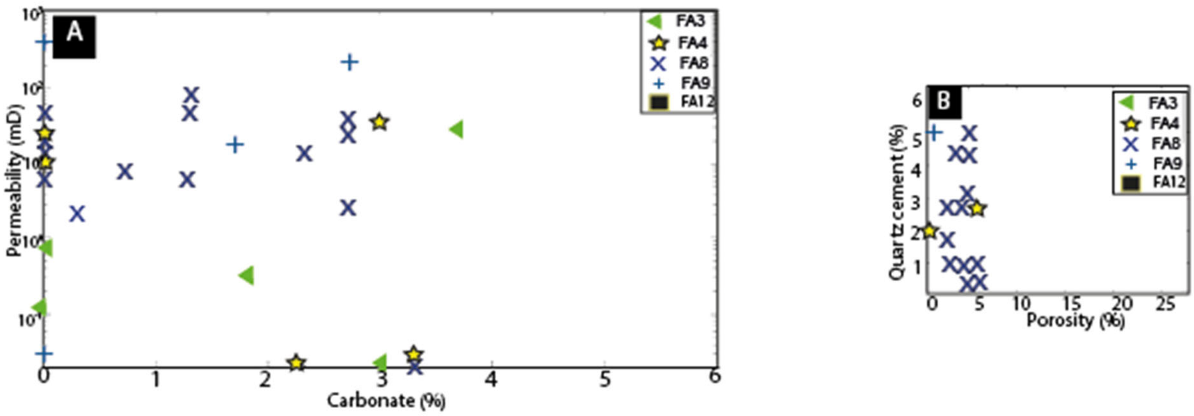

Figure 5.22: Plots of diagenetic cement against porosity and permeability. A-Permeability/Carbonate, B- Quartz cement/ Porosity.

Whereas permeability is observed to decrease with increase in carbonate cement count. The samples with the highest amount of carbonate count of 2.3 to 3.5% have zero permeability. In general, there is no discernible difference on the effect of carbonate cements on the reservoir quality of the fluvial sands whereas it significantly reduces permeability in the non-fluvial sands (Fig 5.2).

Sulphate cement (barite and anhydrite) and albite occur as minor cement (<1%), so may have a negligible effect on the reservoir quality.

5.8 Conclusion.

The creation and destruction of secondary porosity is the result of changes in porewater chemistry during burial and subsequent uplift. The pattern and sequence of the diagenetic features observed in studied samples reveal that three pore-fluid regimes can be identified: (1) weakly acidic oxidizing pore waters during shallow to intermediate burial; (2) acid, reducing condition intermediate to deep burial; (3) alkaline, reducing conditions during deep burial and uplift.

Precipitation of quartz, calcite, dolomite, anhydrite, kaolinite, smectite, and illite as authigenic cements is mainly controlled by fluid flow, pore fluid chemistry and the temperature, which have all acted to reduce the reservoir quality in the studied samples. However, early precipitation of small amounts of mineral cements, e.g., quartz, calcite, anhydrite, can also preserve porosity by strengthening the grain framework and preventing late-stage compaction. In the studied sandstones, feldspars and lithic framework grains appear to have experienced *in situ* alteration to kaolinite at shallow to intermediate burial depths. Much of the kaolinite has subsequently been altered to illite and quartz. The resulting diagenetic illites, have a detrimental effect on reservoir quality.

The feldspar reaction is thought to have been driven by circulation of CO_2-rich fluids generated by thermogenic maturation of the Yoredale coaly source rocks. Kaolinization of the feldspars probably occurred when the sandstones were invaded by acid CO_2-rich waters expelled by compaction of shales in the underlying Carboniferous Coal Measures or local Yoredale coaly layers. A similar process has been invoked to explain feldspar dissolution and kaolinization in many other sandstones.

Invasion of the study area by acid shale waters probably also resulted in the almost complete dissolution of early diagenetic carbonate and sulphate cements. Very little evidence of these early cements (particularly the carbonates) remains, but the high intergranular porosities, over-sized intergranular pores and limited pressure solution seen in some samples provide evidence of their former existence.

Development of secondary porosity is in the Breagh Sandstone. The products of grain dissolution are reprecipitated as authigenic minerals close to the site of dissolution; as a result, only microporosity is created whilst the products of dissolution are not precipitated within the immediate vicinity and substantial macro-porosity is created; this may, however, be filled by authigenic minerals later.

Poor reservoir quality in the Breagh sandstone is due to a combination of mechanical compactional effects, quartz cementation, kaolinization and illitization. Despite being a tight gas reservoir, the presence of a gas column and 1–8% observed large (more details in chapter 6), illite-free secondary pores appear to be key reasons why the Breagh field is a now a gas play.

The large and illite-free pores in the studied sandstones pores may have been preserved by oil. The results from this study suggest that gas in the reservoir may have displaced an earlier oil phase. This provides a new exploration play with the possibility for redistribution of oil into an adjacent up-dip trap.

Given the currently buoyant gas market, together with advances in modern production techniques (e.g., hydraulic fracturing), it may now be possible to flow more gas from the locally large, but isolated, pores identified in the Breagh reservoir. In addition, the potential for redistributed petroleum into up-dip traps represents a new exploration play.

5.8 References

Aagaard, P., and J. Jahren, 2010, Diagenetic controls on evolution of porosity and permeability in lower Tertiary Wilcox sandstones from shallow to ultradeep (200—6700 m) burial, Gulf of Mexico Basin, USA [Marine and Petroleum Geology 27 (2010), 69—81]: Marine and petroleum geology, v. 27, no. 8.

Ajdukiewicz, J. M., S. T. Paxton, and J. O. Szabvo, 1991, Deep porosity preservation in the Norphlet Formation, Mobil Bay, Alabama: AAPG Bulletin (American Association of Petroleum Geologists);(United States), v. 75, no. CONF-910403-.

Akintola, G. O., F. Amponsah-Dacosta, S. Rupprecht, N. Palaniyandy, S. E. Mhlongo, W. M. Gitari, and J. N. Edokpayi, 2021, Methanogenesis Potentials: Insights from Mineralogical Diagenesis, SEM and FTIR Features of the Permian Mikambeni Shale of the Tuli Basin, Limpopo Province of South Africa, 6: Minerals, v. 11, no. 6, p. 651, doi:10.3390/min11060651.

Ali, S. A., W. J. Clark, W. R. Moore, and J. R. Dribus, 2010, Diagenesis and reservoir quality: Oilfield Review, v. 22, no. 2, p. 14–27.

Al-Juboury, A. I., S. H. Hussain, T. McCann, and T. A. Aghwan, 2020, Clay mineral diagenesis and red bed colouration: A SEM study of the Gercus Formation (Middle Eocene), northern Iraq: Geological Journal, v. 55, no. 12, p. 7977–7997.

Andrews, I. J., 2013, The Carboniferous Bowland Shale gas study: geology and resource estimation.

Arsenikos, S., M. Quinn, G. Kimbell, P. Williamson, T. Pharaoh, G. Leslie, and A. Monaghan, 2019, Structural development of the Devono-Carboniferous plays of the UK North Sea: Geological Society, London, Special Publications, v. 471, no. 1, p. 65–90.

Baker, J. C., 2003, Diagenesis and reservoir quality of the Aldebaran Sandstone, Denison Trough, east-central Queensland, Australia: Sandstone Diagenesis: Recent and Ancient, p. 561–582.

Barclay, S. A., and R. H. Worden, 2000, Effects of reservoir wettability on quartz cementation in oil fields: Quartz cementation in sandstones, p. 103–117.

Basham, I. R., 1974, Mineralogical changes associated with deep weathering of gabbro in Aberdeenshire: Clay Minerals, v. 10, no. 3, p. 189–202.

Bauluz, B., M. J. Mayayo, A. Yuste, and J. M. González López, 2008, Genesis of kaolinite from Albian sedimentary deposits of the Iberian Range (NE Spain): analysis by XRD, SEM and TEM: Clay Minerals, v. 43, no. 3, p. 459–475.

Beard, D. C., and P. K. Weyl, 1973, Influence of texture on porosity and permeability of unconsolidated sand: AAPG bulletin, v. 57, no. 2, p. 349–369.

Bello, A. M., M. B. Usman, U. Abubakar, K. Al-Ramadan, L. O. Babalola, A. O. Amao, B. M. S. Yandoka, A. Kachalla, I. A. Kwami, and M. A. Ismail, 2022, Role of diagenetic alterations on porosity evolution in the cretaceous (Albian-Aptian) Bima Sandstone, a case study from the Northern Benue Trough, NE Nigeria: Marine and Petroleum Geology, v. 145, p. 105851.

Berger, G., J.-C. Lacharpagne, B. Velde, D. Beaufort, and B. Lanson, 1997, Kinetic constraints on illitization reactions and the effects of organic diagenesis in sandstone/shale sequences: Applied Geochemistry, v. 12, no. 1, p. 23–35.

Besly, B., 2019, Exploration and development in the Carboniferous of the Southern North Sea: a 30-year retrospective: Geological Society, London, Special Publications, v. 471, no. 1, p. 17–64, doi:10.1144/SP471.10.

Besly, B. M., S. D. Burley, and P. Turner, 1993, The late Carboniferous 'Barren Red Bed' play of the Silver Pit area, Southern North Sea: Geological Society, London, Petroleum Geology Conference series, v. 4, no. 1, p. 727–740, doi:10.1144/0040727.

Birkle, P., C. Van Dijk, K. Dasgupta, M. J. Murphy, Y. K. Kharaka, J. J. Thordsen, and J. L. Bischoff, 2019, Controls On Illite Cementation In Unayzah Sandstones, Saudi Arabia: Mineralogy, K-Ar Dating, Numerical Modeling, and Hydrothermal Experiments: Journal of Sedimentary Research, v. 89, no. 2, p. 89–109, doi:10.2110/jsr.2018.71.

Birkle, P., C. Van Dijk, M. M. Murphy, and Y. K. Kharaka, 2021, Hydrothermal Fluid-Rock Experiments and Geochemical Modeling of Illite Forming Processes in a Paleozoic Sandstone, Middle East, *in* 82nd EAGE Annual Conference & Exhibition: EAGE Publications BV, p. 1–5.

Bjorkum, P. A., 1996, How important is pressure in causing dissolution of quartz in sandstones? Journal of Sedimentary Research, v. 66, no. 1.

Bjorkum, P. A., and N. Gjelsvik, 1988, An isochemical model for formation of authigenic kaolinite, K-feldspar and illite in sediments: Journal of Sedimentary Research, v. 58, no. 3, p. 506–511.

Bjorkum, P. A., and P. H. Nadeau, 1998, Temperature controlled porosity/permeability reduction, fluid migration, and petroleum exploration in sedimentary basins: The APPEA Journal, v. 38, no. 1, p. 453–465.

Bjørkum, P. A., E. H. Oelkers, P. H. Nadeau, O. Walderhaug, and W. M. Murphy, 1998, Porosity prediction in quartzose sandstones as a function of time, temperature, depth, stylolite frequency, and hydrocarbon saturation: AAPG bulletin, v. 82, no. 4, p. 637–648.

Bjørlykke, K., 1998, Clay mineral diagenesis in sedimentary basins—a key to the prediction of rock properties. Examples from the North Sea Basin: Clay minerals, v. 33, no. 1, p. 15–34.

Bjørlykke, K., 1983, Diagenetic reactions in sandstones, *in* Sediment diagenesis: Springer, p. 169–213.

Bjørlykke, K., 1994, Fluid-flow processes and diagenesis in sedimentary basins: Geological Society, London, Special Publications, v. 78, no. 1, p. 127–140.

Bjorlykke, K., 1984, Formation of secondary porosity: How important is it?: Part 2. Aspects of porosity modification.

Bjørlykke, K., 1988, Sandstone diagenesis in relation to preservation, destruction and creation of porosity, *in* Developments in sedimentology: Elsevier, p. 555–588.

Bjørlykke, K., P. Aagaard, P. K. Egeberg, and S. P. Simmons, 1995, Geochemical constraints from formation water analyses from the North Sea and the Gulf Coast Basins on quartz, feldspar and illite precipitation in reservoir rocks: Geological Society, London, Special Publications, v. 86, no. 1, p. 33–50, doi:10.1144/GSL.SP.1995.086.01.03.

Bjørlykke, K., and A. Brendsdal, 1986, Diagenesis of the Brent Sandstone in the Statfjord Field, North Sea.

Bjørlykke, K., and P. K. Egeberg, 1993, Quartz cementation in sedimentary basins: AAPG bulletin, v. 77, no. 9, p. 1538–1548.

Bjorlykke, K., and J. Jahren, 2012, Open or closed geochemical systems during diagenesis in sedimentary basins: Constraints on mass transfer during diagenesis and the prediction of porosity in sandstone and carbonate reservoirs: AAPG bulletin, v. 96, no. 12, p. 2193–2214.

Blackbourn, G. A., and J. D. Collinson, 2022, Quartzitic Sandstones in the Namurian and Lower Westphalian Succession of the Souther North Sea: A new high-permeability Carboniferous reservoir type: Journal of Petroleum Geology, v. 45, no. 4, p. 363–393.

Bloch, S., and K. P. Helmold, 1995, Approaches to predicting reservoir quality in sandstones: AAPG bulletin, v. 79, no. 1, p. 97–114.

Boles, J. R., 1978, Active ankerite cementation in the subsurface Eocene of southwest Texas: Contributions to Mineralogy and Petrology, v. 68, no. 1, p. 13–22.

Boles, J. R., 1984, Secondary porosity reactions in the stevens sandstone, san joaquin valley, california: Part 2. aspects of porosity modification.

Boles, J. R., and S. G. Franks, 1979, Clay diagenesis in Wilcox sandstones of southwest Texas: implications of smectite diagenesis on sandstone cementation: Journal of Sedimentary Research, v. 49, no. 1.

Boles, J. R., and K. S. Johnson, 1984, Influence of mica surfaces on pore-water pH: Chemical Geology, v. 43, no. 3–4, p. 303–317.

Bolle, M.-P., and T. Adatte, 2001, Palaeocene-early Eocene climatic evolution in the Tethyan realm: clay mineral evidence: Clay minerals, v. 36, no. 2, p. 249–261.

Booth, M. G., J. R. Underhill, A. Gardiner, and D. McLean, 2020, Sedimentary and tectonic controls on Lower Carboniferous (Visean) mixed carbonate–siliciclastic deposition in NE England and the Southern North Sea: implications for reservoir architecture: Petroleum Geoscience, v. 26, no. 2, p. 204–231.

Booth, M., J. R. Underhill, R. J. Jamieson, and R. Brackenridge, 2017, Controls on Lower Carboniferous (Dinantian) Prospectivity in the Mid North Sea High Region: AAPG/SEG International Conference and Exhibition, London, p. 8.

Brackenridge, R. E., J. R. Underhill, R. Jamieson, and A. Bell, 2020, Structural and stratigraphic evolution of the Mid North Sea High region of the UK Continental Shelf: Petroleum Geoscience, v. 26, no. 2, p. 154–173.

Browning-Stamp, P., C. Caldarelli, G. Heard, J. Ryan, and J. Hendry, 2023, The Zechstein z2 Hauptdolomit Platform in the Southern UK Mid North Sea High and its Associated Petroleum Plays, Potential and Prospectivity: Journal of Petroleum Geology, v. 46, no. 3, p. 295–328.

Bruckschen, P., S. Oesmann, and J. Veizer, 1999, Isotope stratigraphy of the European Carboniferous: proxy signals for ocean chemistry, climate and tectonics: Chemical Geology, v. 161, no. 1, p. 127–163, doi:10.1016/S0009-2541(99)00084-4.

Burley, S. D., 1984, Patterns of diagenesis in the Sherwood Sandstone Group (Triassic), United Kingdom: Clay Minerals, v. 19, no. 3, p. 403–440.

Burley, S., and R. Worden, 2009, Sandstone diagenesis: recent and ancient: John Wiley & Sons.

Burley, S. D., and R. H. Worden (eds.), 2003, Sandstone Diagenesis: The Evolution of Sand to Stone, *in* Sandstone Diagenesis: Oxford, UK, Blackwell Publishing Ltd., p. 1–44, doi:10.1002/9781444304459.ch.

Cao, B., X. Luo, X. Wang, L. Zhang, and H. Shi, 2022, Calcite-cemented concretions in non-marine sandstones: An integrated study of outcrop sedimentology, petrography and clumped isotopes: Sedimentology.

Carothers, W. W., and Y. K. Kharaka, 1980, Stable carbon isotopes of HCO3- in oil-field waters—implications for the origin of CO2: Geochimica et Cosmochimica Acta, v. 44, no. 2, p. 323–332.

Chen, Z., Z. Ding, S. Yang, C. Zhang, and X. Wang, 2016, Increased precipitation and weathering across the Paleocene-Eocene Thermal Maximum in central China: Geochemistry, Geophysics, Geosystems, v. 17, no. 6, p. 2286–2297.

Chi, G., P. S. Giles, M. A. Williamson, D. Lavoie, and R. Bertrand, 2003, Diagenetic history and porosity evolution of Upper Carboniferous sandstones from the Spring Valley #1 well, Maritimes Basin, Canada–implications for reservoir development: Journal of Geochemical Exploration, v. 80, no. 2, p. 171–191, doi:10.1016/S0375-6742(03)00190-0.

Choquette, P. W., and L. C. Pray, 1970, Geologic nomenclature and classification of porosity in sedimentary carbonates: AAPG bulletin, v. 54, no. 2, p. 207–250.

Clayton, R. N., I. Friedman, D. L. Graf, T. K. Mayeda, W. F. Meents, and N. F. Shimp, 1966, The origin of saline formation waters: 1. Isotopic composition: Journal of Geophysical Research, v. 71, no. 16, p. 3869–3882.

Coleman, M. L. *et al*., 1997, Microbial mineralization of organic matter: mechanisms of self-organization and inferred rates of precipitation of diagenetic minerals: Philosophical Transactions of the Royal Society of London. Series A: Physical and Engineering Sciences, v. 344, no. 1670, p. 69–87, doi:10.1098/rsta.1993.0076.

Collinson, J. D., B. M. Besly, and G. Kelling, 1988, Controls on Namurian sedimentation in the Central Province basins of northern England: Sedimentation in a synorogenic basin complex: the Upper Carboniferous of Northwest Europe. Blackie, Glasgow, v. 85, p. 101.

Collinson, J., and C. Jones, 1995, Source rock potential of the sub-Westphalian Carboniferous of the Southern North Sea: Report and Appendix.

Colter, V. S., 1997, The East Irish Sea Basin—from caterpillar to butterfly, a thirty-year metamorphosis: Geological Society, London, Special Publications, v. 124, no. 1, p. 1–9.

Coplen, T. B., C. Kendall, and J. Hopple, 1983, Comparison of stable isotope reference samples: Nature, v. 302, p. 236–238.

Corfield, S. M., R. L. Gawthorpe, M. Gage, A. J. Fraser, and B. M. Besly, 1996, Inversion tectonics of the Variscan foreland of the British Isles: Journal of the Geological Society, v. 153, no. 1, p. 17–32, doi:10.1144/gsjgs.153.1.0017.

Cowan, G., 1989, Diagenesis of upper carboniferous sandstones: southern North Sea Basin: Geological Society, London, Special Publications, v. 41, no. 1, p. 57–73.

Cowan, G., and H. Shaw, 1991, Diagenesis of Namurian fluvio-deltaic sandstones from the Trumfleet Field, South Yorkshire: Marine and petroleum geology, v. 8, no. 2, p. 212–224.

Curtis, C. D., 1985, Clay mineral precipitation and transformation during burial diagenesis: Philosophical Transactions of the Royal Society of London. Series A, Mathematical and Physical Sciences, v. 315, no. 1531, p. 91–105.

Curtis, C. D., 1980, Diagenetic alteration in black shales: Journal of the Geological Society, v. 137, no. 2, p. 189–194.

Curtis, C., 1987, Mineralogical consequences of organic matter degradation in sediments: inorganic/organic diagenesis: Marine Clastic Sedimentology: Concepts and Case Studies, p. 108–123.

Curtis, C. D., and M. L. Coleman, 1986, Controls on the Precipitation of Early Diagenetic Calcite, Dolomite and Siderite Concretions in Complex Depositional Sequences.

Curtis, C. D., M. L. Coleman, and L. G. Love, 1986, Pore water evolution during sediment burial from isotopic and mineral chemistry of calcite, dolomite and siderite concretions: Geochimica et Cosmochimica Acta, v. 50, no. 10, p. 2321–2334, doi:10.1016/0016-7037(86)90085-2.

Curtis, C. D., M. J. Pearson, and V. A. Somogyi, 1975, Mineralogy, chemistry and origin of a concretionary siderite sheet (clay-ironstone band) in the Westphalian of Yorkshire: Mineralogical Magazine, v. 40, no. 312, p. 385–393.

Dasgupta, S., A. K. Chaudhuri, and M. Fukuoka, 1990, Compositional characteristics of glauconitic alterations of K-feldspar from India and their implications: Journal of Sedimentary Research, v. 60, no. 2, p. 277–281.

Dickson, J. A. D., 1966, Carbonate identification and genesis as revealed by staining: Journal of Sedimentary Research, v. 36, no. 2, p. 491–505.

Dixon, S. A., D. M. Summers, and R. C. Surdam, 1989, Diagenesis and preservation of porosity in Norphlet Formation (Upper Jurassic), southern Alabama: AAPG bulletin, v. 73, no. 6, p. 707–728.

Doornenbal, J. C., H. Kombrink, R. Bouroullec, R. A. F. Dalman, G. De Bruin, C. R. Geel, A. J. P. Houben, B. Jaarsma, J. Juez-Larré, and M. Kortekaas, 2022, New insights on subsurface energy resources in the Southern North Sea Basin area.

Ehlmann, B. L., J. F. Mustard, G. A. Swayze, R. N. Clark, J. L. Bishop, F. Poulet, D. J. Des Marais, L. H. Roach, R. E. Milliken, and J. J. Wray, 2009, Identification of hydrated silicate minerals on Mars using MRO-CRISM: Geologic context near Nili Fossae and implications for aqueous alteration: Journal of Geophysical Research: Planets, v. 114, no. E2.

Ehrenberg, S. N., 1989, Assessing the relative importance of compaction processes and cementation to reduction of porosity in sandstones: discussion; compaction and porosity evolution of Pliocene sandstones, Ventura Basin, California: discussion: AAPG Bulletin, v. 73, no. 10, p. 1274–1276.

Ehrenberg, S. N., 1991, Kaolinized, potassium-leached zones at the contacts of the Garn Formation, Haltenbanken, mid-Norwegian continental shelf: Marine and Petroleum Geology, v. 8, no. 3, p. 250–269.

Ehrenberg, S. N., and P. H. Nadeau, 1989, Formation of diagenetic illite in sandstones of the Garn Formation, Haltenbanken area, Mid-Norwegian continental shelf: Clay Minerals, v. 24, no. 2, p. 233–253.

El-Ghali, M. A. K., K. G. Tajori, H. Mansurbeg, N. Ogle, and R. M. Kalin, 2006, Origin and timing of siderite cementation in Upper Ordovician glaciogenic sandstones from the Murzuq basin, SW Libya: Marine and Petroleum Geology, v. 23, no. 4, p. 459–471.

Eugster, H. P., and L. A. Hardie, 1975, Sedimentation in an ancient playa-lake complex: the Wilkins Peak Member of the Green River Formation of Wyoming: Geological Society of America Bulletin, v. 86, no. 3, p. 319–334.

Fisher, Q. J., M. Casey, M. B. Clennell, and R. J. Knipe, 1999, Mechanical compaction of deeply buried sandstones of the North Sea: Marine and Petroleum Geology, v. 16, no. 7, p. 605–618.

Franks, S. G., and H. Zwingmann, 2010, Origin and timing of late diagenetic illite in the Permian–Carboniferous Unayzah sandstone reservoirs of Saudi Arabia: AAPG bulletin, v. 94, no. 8, p. 1133–1159.

Gao, J., B. Ma, Y. Lu, W. Zhang, and Q. Cao, 2022, Origin of authigenic kaolinite with implications for Permian tight gas sandstone reservoirs in the northern Ordos Basin, central China: Journal of Natural Gas Science and Engineering, v. 99, p. 104429, doi:10.1016/j.jngse.2022.104429.

Giannetta, L. G., N. D. Webb, S. K. Butler, and N. P. Grigsby, 2021, Using clay microporosity to improve formation evaluation in potential residual oil zones: Cypress Sandstone, Illinois Basin: AAPG Bulletin, v. 105, no. 8, p. 1595–1625.

Giles, M. R., and J. D. Marshall, 1986, Constraints on the development of secondary porosity in the subsurface: re-evaluation of processes: Marine and petroleum Geology, v. 3, no. 3, p. 243–255.

Glennie, K. W., G. C. Mudd, and P. J. C. Nagtegaal, 1978, Depositional environment and diagenesis of Permian Rotliegendes sandstones in Leman Bank and Sole Pit areas of the UK southern North Sea: Journal of the Geological Society, v. 135, no. 1, p. 25–34.

Glennie, K. W., and D. M. J. Provan, 1990, Lower Permian Rotliegend reservoir of the Southern North Sea gas province: Geological Society, London, Special Publications, v. 50, no. 1, p. 399–416, doi:10.1144/GSL.SP.1990.050.01.25.

Gluyas, J. G., 1984, Early carbonate diagenesis within Phanerozoic shales and sandstones of the NW European shelf: Clay Minerals, v. 19, no. 3, p. 309–321.

Gluyas, J., L. Jolley, and T. Primmer, 1997, Element mobility during diagenesis: sulphate cementation of Rotliegend sandstones, Southern North Sea: Marine and Petroleum Geology, v. 14, no. 7, p. 1001–1011, doi:10.1016/S0264-8172(97)00038-X.

Gordon, J. B., H. Sanei, and P. K. Pedersen, 2022, Secondary porosity development in incised valley sandstones from two wells from the Flemish Pass area, offshore Newfoundland: Marine and Petroleum Geology, v. 140, p. 105644.

Grant, R. J., M. G. Booth, J. R. Underhill, and A. Bell, 2020, Structural evolution of the Breagh area: implications for carboniferous prospectivity of the Mid North Sea High, Southern North Sea: Petroleum Geoscience, v. 26, no. 2, p. 174–203.

Greenwood, P. J., and S. M. Habesch, 1997, Diagenesis of the Sherwood Sandstone Group in the southern East Irish Sea Basin (Blocks 110/13, 110/14 and 110/15): constraints from preliminary isotopic and fluid inclusion studies: Geological Society, London, Special Publications, v. 124, no. 1, p. 353–371.

Guo, X., S. He, K. Liu, G. Song, X. Wang, and Z. Shi, 2010, Oil generation as the dominant overpressure mechanism in the Cenozoic Dongying depression, Bohai Bay Basin, China: AAPG bulletin, v. 94, no. 12, p. 1859–1881.

Hayes, J. B., 1979, Sandstone diagenesis—the hole truth.

Hayes, M. J., and J. R. Boles, 1992, Volumetric relations between dissolved plagioclase and kaolinite in sandstones: Implications for aluminum mass transfer in the San Joaquin Basin, California.

He, W., Z. Yang, H. Du, J. Hu, K. Zhang, W. Hou, and H. Li, 2022, Micro-Mechanisms and Implications of Continental Red Beds: Minerals, v. 12, no. 8, p. 934.

Higgs, K. E., H. Zwingmann, A. G. Reyes, and R. H. Funnell, 2007, Diagenesis, Porosity Evolution, and Petroleum Emplacement in Tight Gas Reservoirs, Taranaki Basin, New Zealand: Journal of Sedimentary Research, v. 77, no. 12, p. 1003–1025, doi:10.2110/jsr.2007.095.

Holliday, D. W., and J. L. Cutbill, 1972, The Ebbadalen Formation (Carboniferous), Spitsbergen: Proceedings of the Yorkshire Geological Society, v. 39, no. 1, p. 1–32.

Hollis, C., and G. Walkden, 2012, Burial diagenetic evolution of the Lower Carboniferous (Dinantian) of the southern margin of the Askrigg Platform and a comparison with the Derbyshire Platform: Petroleum Geoscience, v. 18, no. 1, p. 83–95.

Houseknecht, D. W., 1987, Assessing the Relative Importance of Compaction Processes and Cementation to Reduction of Porosity in Sandstones: AAPG Bulletin, v. 71, no. 6, p. 633–642.

Houseknecht, D. W., 1989, Assessing the relative importance of compaction processes and cementation to reduction of porosity in sandstones: reply: AAPG Bulletin, v. 73, no. 10, p. 1277–1279.

Hubert, J. F., and A. A. Reed, 1978, Red-bed diagenesis in the east Berlin Formation, Newark group, Connecticut Valley: Journal of Sedimentary Research, v. 48, no. 1, p. 175–184.

Hugget, J. M., 1984, Controls on mineral authigenesis in Coal Measures sandstones of the East Midlands, UK: Clay Minerals, v. 19, no. 3, p. 343–357.

Hurst, A., and J. S. Archer, 1986, Sandstone reservoir description: An overview of the role of geology and mineralogy: Clay minerals, v. 21, no. 4, p. 791–809.

Hurst, A., and P. H. Nadeau, 1995, Clay microporosity in reservoir sandstones: an application of quantitative electron microscopy in petrophysical evaluation: AAPG bulletin, v. 79, no. 4, p. 563–573.

Ingrams, S., D. McLean, M. Booth, and D. J. Bodman, 2020, Biostratigraphy and paleoecology of Asbian–Brigantian (Mississippian) miospores from Berwick-upon-Tweed, Northumberland, UK: Preliminary results: Review of Palaeobotany and Palynology, v. 276, p. 104206, doi:10.1016/j.revpalbo.2020.104206.

Irwin, H., C. Curtis, and M. Coleman, 1977, Isotopic evidence for source of diagenetic carbonates formed during burial of organic-rich sediments: Nature, v. 269, no. 5625, p. 209–213, doi:10.1038/269209a0.

Irwin, H., and A. Hurst, 1983, Applications of Geochemistry to Sandstone Reservoir Studies: Geological Society, London, Special Publications, v. 12, no. 1, p. 127–146, doi:10.1144/GSL.SP.1983.012.01.13.

Ixer, R. A., P. Turner, and B. Waugh, 1979, Authigenic iron and titanium oxides in Triassic red beds:(St. Bees Sandstone), Cumbria, northern England: Geological Journal, v. 14, no. 2, p. 179–192.

Jones, N. S., and D. W. Holliday, 2006, The stratigraphy and sedimentology of Upper Carboniferous Warwickshire Group red-bed facies in the Canonbie area of SW Scotland.

Karim, A., K. Dubois, and J. Veizer, 2011, Carbon and oxygen dynamics in the Laurentian Great Lakes: Implications for the CO2 flux from terrestrial aquatic systems to the atmosphere: Chemical Geology, v. 281, no. 1–2, p. 133–141.

Karim, A., and J. Veizer, 2000, Weathering processes in the Indus River Basin: implications from riverine carbon, sulfur, oxygen, and strontium isotopes: Chemical Geology, v. 170, no. 1–4, p. 153–177.

Ketter, F. J., 1991, The Esmond, Forbes and Gordon Fields, Blocks 43/8a, 43/13a, 43/15a, 43/20a, UK North Sea: Geological Society, London, Memoirs, v. 14, no. 1, p. 425–432, doi:10.1144/GSL.MEM.1991.014.01.53.

Khan, M. A., T. Khan, A. Ali, A. M. Bello, and A. E. Radwan, 2023, Role of depositional and diagenetic controls on reservoir quality of complex heterogenous tidal sandstone reservoirs: An example from the Lower Goru formation, Middle Indus Basin, Southwest Pakistan: Marine and Petroleum Geology, v. 154, p. 106337.

Khanam, S., M. A. Quasim, and A. H. M. Ahmad, 2021, Diagenetic control on the distribution of porosity within the depositional facies of Proterozoic Rajgarh Formation, Alwar sub-basin, Northeastern Rajasthan: Journal of the Geological Society of India, v. 97, p. 697–710.

Kharaka, Y. K., F. A. Berry, and I. Friedman, 1973, Isotopic composition of oil-field brines from Kettleman North Dome, California, and their geologic implications: Geochimica et Cosmochimica Acta, v. 37, no. 8, p. 1899–1908.

Kim, J. C., Y. I. Lee, and K. Hisada, 2007, Depositional and compositional controls on sandstone diagenesis, the Tetori Group (Middle Jurassic–Early Cretaceous), central Japan: Sedimentary Geology, v. 195, no. 3–4, p. 183–202.

Kupecz, J. A., J. Gluyas, and S. Bloch, 1997, Reservoir quality prediction in sandstones and carbonates: An overview: AAPG Memoir, v. 69.

Lai, J., G. Wang, Y. Chai, Y. Ran, and X. Zhang, 2015, Depositional and Diagenetic Controls on Pore Structure of Tight Gas Sandstone Reservoirs: Evidence from Lower Cretaceous Bashijiqike Formation in Kelasu Thrust Belts, Kuqa Depression in Tarim Basin of West China: Resource Geology, v. 65, no. 2, p. 55–75, doi:10.1111/rge.12061.

Lai, J., G. Wang, Z. Wang, J. Chen, X. Pang, S. Wang, Z. Zhou, Z. He, Z. Qin, and X. Fan, 2018, A review on pore structure characterization in tight sandstones: Earth-Science Reviews, v. 177, p. 436–457.

Land, L. S., 1984, Frio Sandstone Diagenesis, Texas Gulf Coast: A Regional Isotopic Study: Part 1. Concepts and Principles.

Lander, R. H., and O. Walderhaug, 1999, Predicting porosity through simulating sandstone compaction and quartz cementation: AAPG bulletin, v. 83, no. 3, p. 433–449.

Lanson, B., D. Beaufort, G. Berger, A. Bauer, A. Cassagnabere, and A. Meunier, 2002, Authigenic kaolin and illitic minerals during burial diagenesis of sandstones: a review: Clay minerals, v. 37, no. 1, p. 1–22.

Lee, M., J. L. Aronson, and S. M. Savin, 1989, Timing and Conditions of Permian Rotliegende Sandstone Diagenesis, Southern North Sea: K/Ar and Oxygen Isotopic Data1: AAPG bulletin, v. 73, no. 2, p. 195–215.

Lee, M. R., R. W. Martin, C. Trager-Cowan, and P. R. Edwards, 2005, Imaging of cathodoluminescence zoning in calcite by scanning electron microscopy and hyperspectral mapping: Journal of Sedimentary Research, v. 75, no. 2, p. 313–322.

Lei, Z., H. Xu, Q. Liu, W. Li, D. Yan, S. Li, P. Lei, M. Yan, and J. Li, 2019, The influence of multiple-stage oil emplacement on deeply buried marine sandstone diagenesis: A case study on the Devonian Donghe sandstones, Tabei Uplift, Tarim Basin, NW China: Marine and Petroleum Geology, v. 110, p. 299–316.

Leveille, G. P., T. J. Primmer, G. Dudley, D. Ellis, and G. J. Allinson, 1997, Diagenetic controls on reservoir quality in Permian Rotliegendes sandstones, Jupiter Fields area, southern North Sea: Geological Society, London, Special Publications, v. 123, no. 1, p. 105–122.

Li, P., M. Zheng, H. Bi, S. Wu, and X. Wang, 2017, Pore throat structure and fractal characteristics of tight oil sandstone: a case study in the Ordos Basin, China: Journal of Petroleum Science and Engineering, v. 149, p. 665–674.

Li, M., R. Zhu, Z. Lou, W. Yin, Z. Hu, H. Zhu, and A. Jin, 2019, Diagenesis and its impact on the reservoir quality of the fourth member of Xujiahe Formation, Western Sichuan Depression, China: Marine and Petroleum Geology, v. 103, p. 485–498.

Liu, Y., W. Hu, J. Cao, X. Wang, F. Zhu, Q. Tang, and W. Gao, 2019, Fluid–rock interaction and its effects on the Upper Triassic tight sandstones in the Sichuan Basin, China: insights from petrographic and geochemical study of carbonate cements: Sedimentary Geology, v. 383, p. 121–135.

Lorentzen, S., C. Augustsson, J. Jahren, J. P. Nystuen, and N. H. Schovsbo, 2019, Tectonic, sedimentary and diagenetic controls on sediment maturity of lower Cambrian quartz arenite from southwestern Baltica: Basin Research, v. 31, no. 6, p. 1098–1120.

Lundegard, P. D., 1992, Sandstone porosity loss; a" big picture" view of the importance of compaction: Journal of Sedimentary Research, v. 62, no. 2, p. 250–260.

Lundegard, P. D., L. S. Land, and W. E. Galloway, 1984, Problem of secondary porosity: Frio Formation (Oligocene), Texas Gulf Coast: Geology, v. 12, no. 7, p. 399–402.

Ma, B., Y. Cao, K. A. Eriksson, Y. Jia, and B. C. Gill, 2017, Depositional and diagenetic controls on deeply-buried Eocene sublacustrine fan reservoirs in the Dongying Depression, Bohai Bay Basin, China: Marine and Petroleum Geology, v. 82, p. 297–317, doi:10.1016/j.marpetgeo.2017.02.014.

Ma, Z., J. Tan, L. Zheng, C. Ni, R. Hu, and J. Ma, 2022, Simulation experiment of fluid-feldspar sandstone interactions and their implications for tight oil and gas exploration of the Yanchang Formation, Ordos Basin, China: Marine and Petroleum Geology, v. 142, p. 105737.

Macaulay, C. I., A. E. Fallick, and R. S. Haszeldine, 1993, Textural and isotopic variations in diagenetic kaolinite from the Magnus oilfield sandstones: Clay Minerals, v. 28, no. 4, p. 625–639.

Macaulay, C. I., A. E. Fallick, O. M. McLaughlin, R. S. Haszeldine, and M. J. Pearson, 1998, The significance of δ13C of carbonate cements in reservoir sandstones: a regional perspective from the Jurassic of the northern North Sea: Carbonate Cementation in Sandstones: Distribution Patterns and Geochemical Evolution, p. 395–408.

Machent, P. G., K. G. Taylor, J. H. Macquaker, and J. D. Marshall, 2007, Patterns of early post-depositional and burial cementation in distal shallow-marine sandstones: Upper Cretaceous Kenilworth Member, Book Cliffs, Utah, USA: Sedimentary Geology, v. 198, no. 1–2, p. 125–145.

Mansurbeg, H., S. Morad, A. Salem, R. Marfil, M. A. K. El-Ghali, J. P. Nystuen, M. A. Caja, A. Amorosi, D. Garcia, and A. La Iglesia, 2008, Diagenesis and reservoir quality evolution of palaeocene deep-water, marine sandstones, the Shetland-Faroes Basin, British continental shelf: Marine and Petroleum Geology, v. 25, no. 6, p. 514–543.

Mao, S. W., Z. D. Bao, X. X. Wang, Y. S. Gao, J. Song, Z. C. Wang, W. Liu, L. Zhang, M. Y. Wei, and Y. F. Bao, 2019, Origin of carbonate cements and reservoir evolution of tight sandstone in the Upper Triassic Yanchang Formation, Ordos Basin, China: Australian Journal of Earth Sciences, v. 66, no. 8, p. 1175–1194, doi:10.1080/08120099.2019.1596981.

Marsh, J. R., S. J. Jones, N. S. Meadows, and J. G. Gluyas, 2022, Petrographic and diagenetic investigation of the distal Triassic 'Budleighensis' fluvial system in the Solway and Carlisle Basins for potential CO2 storage: Petroleum Geoscience, v. 28, no. 3.

Marshall, J. D., and D. Pirrie, 2013, Carbonate concretions—explained: Geology Today, v. 29, no. 2, p. 53–62.

Matthews, A., and A. Katz, 1977, Oxygen isotope fractionation during the dolomitization of calcium carbonate: Geochimica et Cosmochimica Acta, v. 41, no. 10, p. 1431–1438.

Mbongonya, M. A., K. Liu, and C. Baiyegunhi, 2022, Effects of weathering on the mineralogical composition of banded iron-formation (BIF): a case study of the Kuruman Formation (Transvaal Supergroup) in the Prieska area, Northern Cape Province, South Africa: Arabian Journal of Geosciences, v. 15, no. 22, p. 1688.

McAulay, G. E., S. D. Burley, and L. H. Johnes, 1993, Silicate mineral authigenesis in the Hutton and NW Hutton fields: implications for sub-surface porosity development, *in* Geological Society, London, Petroleum Geology Conference Series: The Geological Society of London, p. 1377–1394.

McNeil, B., H. F. Shaw, and A. H. Rankin, 1995, Diagenesis of the Rotliegend Sandstones in the V-Fields, southern North sea: a fluid inclusion study: Geological Society, London, Special Publications, v. 86, no. 1, p. 125–139.

McNeil, B., H. F. Shaw, and A. H. Rankin, 1998, The timing of cementation in the Rotliegend sandstones of the Southern North Sea: A petrological and fluid inclusion study of cements: Journal of Petroleum Geology, v. 21, no. 3, p. 311–327.

Meadows, N. S., M. Hardman, and G. Cowan, 1997, Petroleum geology of the Irish Sea and adjacent areas: Geological Society of London.

Meyers, W. J., 1991, Calcite Cement Stratigraphy: An Overview.

Mii, H., E. L. Grossman, and T. E. Yancey, 1999, Carboniferous isotope stratigraphies of North America: Implications for Carboniferous paleoceanography and Mississippian glaciation: GSA Bulletin, v. 111, no. 7, p. 960–973, doi:10.1130/0016-7606(1999)111<0960:CISONA>2.3.CO;2.

Monaghan, A. A., S. Arsenikos, E. Callaghan, R. Ellen, C. Gent, S. Hannis, A. Henderson, G. Leslie, K. Johnson, and M. Kassyk, 2015, Palaeozoic Petroleum Systems of the Central North Sea/Mid North Sea High.

Monaghan, A. A., S. Arsenikos, M. F. Quinn, K. R. Johnson, C. J. Vincent, C. H. Vane, A. W. Kim, C. N. Uguna, S. D. Hannis, and C. M. A. Gent, 2017, Carboniferous petroleum systems around the Mid North Sea High, UK: Marine and Petroleum Geology, v. 88, p. 282–302.

Moore, C. H., 1989, Carbonate diagenesis and porosity: Elsevier.

Morad, S., 1998, Carbonate Cementation in Sandstones: Distribution Patterns and Geochemical Evolution, *in* Carbonate Cementation in Sandstones: John Wiley & Sons, Ltd, p. 1–26, doi:10.1002/9781444304893.ch1.

Morad, S., 1990, Mica alteration reactions in Jurassic reservoir sandstones from the Haltenbanken area, offshore Norway: Clays and clay minerals, v. 38, no. 6, p. 584–590.

Morad, S., K. Al-Ramadan, J. M. Ketzer, and L. De Ros, 2010, The impact of diagenesis on the heterogeneity of sandstone reservoirs: A review of the role of depositional facies and sequence stratigraphy: AAPG bulletin, v. 94, no. 8, p. 1267–1309.

Morad, S., J. M. Ketzer, and L. F. De Ros, 2000, Spatial and temporal distribution of diagenetic alterations in siliciclastic rocks: implications for mass transfer in sedimentary basins: Sedimentology, v. 47, no. s1, p. 95–120, doi:10.1046/j.1365-3091.2000.00007.x.

Mu, N., 2023, Impact of meteoric water flushing on diagenesis of deep-marine turbidite sandstones: A case study from the Tertiary sandstones of Frigg and Grane fields, northern North sea: Marine and Petroleum Geology, v. 150, p. 106116, doi:10.1016/j.marpetgeo.2023.106116.

Mu, N., 2022, The Impact of Meteoric Water Flushing on Diagenesis of Tertiary Deep-Marine Turbidite Sandstones in the Northern North Sea?-Case Study: Frigg vs. Grane Field: Case Study: Frigg vs. Grane Field.

Nadeau, P. H., and A. Hurst, 1991, Application of back-scattered electron microscopy to the quantification of clay mineral microporosity in sandstones: Journal of Sedimentary Research, v. 61, no. 6, p. 921–925.

Nagtegal, P. J. C., 1979, Relationship of facies and reservoir quality in Rotliegendes desert sandstones, southern North Sea region: Journal of Petroleum Geology, v. 2, no. 2, p. 145–158.

Nedkvitne, T., and K. Bjorlykke, 1992, Secondary porosity in the Brent Group (Middle Jurassic), Huldra Field, North Sea: implication for predicting lateral continuity of sandstones? Journal of Sedimentary Research, v. 62, no. 1.

Newman, P. J., 1999, The geology and hydrocarbon potential of the Peel and Solway Basins, East Irish Sea: Journal of Petroleum Geology, v. 22, no. 3, p. 305–324.

Nguyen, B. T., S. J. Jones, N. R. Goulty, A. J. Middleton, N. Grant, A. Ferguson, and L. Bowen, 2013, The role of fluid pressure and diagenetic cements for porosity preservation in Triassic fluvial reservoirs of the Central Graben, North SeaPorosity Preservation in Triassic Fluvial Reservoirs: AAPG Bulletin, v. 97, no. 8, p. 1273–1302, doi:10.1306/01151311163.

Nwachukwu, C. M., Z. Barnett, and J. G. Gluyas, 2020, The Breagh Field, Blocks 42/12a, 42/13a and 42/8a, UK North Sea: Geological Society, London, Memoirs, v. 52, no. 1, p. 109–118.

Okunuwadje, S. E., S. A. Bowden, and D. I. Macdonald, 2020, Diagenesis and reservoir quality in high-resolution sandstone sequences: An example from the Middle Jurassic Ravenscar sandstones, Yorkshire CoastUK: Marine and Petroleum Geology, v. 118, p. 104426.

Oluwadebi, A. G., K. G. Taylor, and P. J. Dowey, 2018, Diagenetic controls on the reservoir quality of the tight gas Collyhurst sandstone formation, Lower Permian, East Irish Sea Basin, United Kingdom: Sedimentary geology, v. 371, p. 55–74.

Oye, O. J., A. C. Aplin, I. J. Orland, and J. W. Valley, 2023, Low volumes of quartz cement in deeply buried Fulmar Formation sandstones explained by a low effective stress burial history: Geoenergy Science and Engineering, v. 221, p. 211383, doi:10.1016/j.geoen.2022.211383.

Paganoni, M., A. Al Harthi, D. Morad, S. Morad, A. Ceriani, H. Mansurbeg, A. Al Suwaidi, I. S. Al-Aasm, S. N. Ehrenberg, and M. Sirat, 2016, Impact of stylolitization on diagenesis of a Lower Cretaceous carbonate reservoir from a giant oilfield, Abu Dhabi, United Arab Emirates: Sedimentary Geology, v. 335, p. 70–92.

Parnell, J., 2002, Diagenesis and fluid flow in response to uplift and exhumation: Geological Society, London, Special Publications, v. 196, no. 1, p. 433–446.

Paxton, S. T., J. O. Szabo, J. M. Ajdukiewicz, and R. E. Klimentidis, 2002, Construction of an intergranular volume compaction curve for evaluating and predicting compaction and porosity loss in rigid-grain sandstone reservoirs: AAPG bulletin, v. 86, no. 12, p. 2047–2067.

Permana, B. R., Y. Darmadi, M. Firdaus, and I. Y. Syukri, 2019, Unique Gamma Ray Log Signature - Genesis and Implication to Reservoir Characterization: Case Study in Corridor Block, South Sumatra Basin.

Petersen, H. I., B. Holland, and M. Olivarius, 2022, Source rock evaluation and fluid inclusion reconnaissance study of Carboniferous and Zechstein rocks in the northern margin of the Southern Permian Basin, onshore Denmark: International Journal of Coal Geology, v. 255, p. 103985.

Pettijohn, F., 1957, Sedimentary Rocks: Harpers, New York, NY, p. 718.

Platt, J. D., 1993, Controls on Clay Mineral Distribution and Chemistry in the Early Permian Rotliegend of Germany: Clay Minerals, v. 28, no. 3, p. 393–416, doi:10.1180/claymin.1993.028.3.05.

Pollastro, R. M., 1990, The Illite/Smectite Geothermometer—Concepts, Methodology, and Application to Basin History and Hydrocarbon Generation: p. 1–18.

Porten, K. W., M. J. Warcho\l, and I. A. Kane, 2019, Formation of detrital clay grain coats by dewatering of deep-water sands and significance for reservoir quality: Journal of Sedimentary Research, v. 89, no. 12, p. 1231–1249.

Primmer, T. J., C. A. Cade, J. Evans, J. G. Gluyas, M. S. Hopkins, N. H. Oxtoby, P. C. Smalley, E. A. Warren, and R. H. Worden, 1997, Global Patterns in Sandstone Diagenesis: Their Application to Reservoir Quality Prediction for Petroleum Exploration: p. 61–77.

Purvis, K., 1992, Lower Permian Rotliegend sandstones, southern North Sea: a case study of sandstone diagenesis in evaporite-associated sequences: Sedimentary Geology, v. 77, no. 3–4, p. 155–171.

Qiao, J., J. Zeng, S. Jiang, Y. Zhang, S. Feng, X. Feng, and H. Hu, 2020, Insights into the pore structure and implications for fluid flow capacity of tight gas sandstone: A case study in the upper paleozoic of the Ordos Basin: Marine and Petroleum Geology, v. 118, p. 104439.

Rafiei, M., S. Löhr, A. Baldermann, R. Webster, and C. Kong, 2020, Quantitative petrographic differentiation of detrital vs diagenetic clay minerals in marine sedimentary sequences: Implications for the rise of biotic soils: Precambrian Research, v. 350, p. 105948.

Ramm, M., and A. E. Ryseth, 1996, Reservoir quality and burial diagenesis in the Statfjord Formation, North Sea: Petroleum Geoscience, v. 2, no. 4, p. 313–324.

Robert, C., and H. Chamley, 1991, Development of early Eocene warm climates, as inferred from clay mineral variations in oceanic sediments: Palaeogeography, Palaeoclimatology, Palaeoecology, v. 89, no. 4, p. 315–331.

Robert, C., and J. P. Kennett, 1994, Antarctic subtropical humid episode at the Paleocene-Eocene boundary: Clay-mineral evidence: Geology, v. 22, no. 3, p. 211–214.

Robert, C., and J. P. Kennett, 1992, Paleocene and Eocene kaolinite distribution in the South Atlantic and Southern Ocean: Antarctic climatic and paleoceanographic implications: Marine Geology, v. 103, no. 1–3, p. 99–110.

Roberts, N. M., K. Drost, M. S. Horstwood, D. J. Condon, D. Chew, H. Drake, A. E. Milodowski, N. M. McLean, A. J. Smye, and R. J. Walker, 2020, Laser ablation inductively coupled plasma mass spectrometry (LA-ICP-MS) U–Pb carbonate geochronology: strategies, progress, and limitations: Geochronology, v. 2, no. 1, p. 33–61.

Rodriguez, K., R. Wrigley, N. Hodgson, and H. Nicholls, 2014, Southern North Sea: unexplored multi-level exploration potential revealed: First Break, v. 32, no. 6, p. 107–113.

Roos, B. M., and B. J. Smits, 1983, Rotliegend and Main Buntsandstein gas fields in Block K/13—a case history, *in* Petroleum Geology of the Southeastern North Sea and the Adjacent Onshore Areas: (The Hague, 1982): Springer, p. 75–82.

Rossi, C., O. Kälin, J. Arribas, and A. Tortosa, 2002, Diagenesis, provenance and reservoir quality of Triassic TAGI sandstones from Ourhoud field, Berkine (Ghadames) Basin, Algeria: Marine and Petroleum Geology, v. 19, no. 2, p. 117–142, doi:10.1016/S0264-8172(02)00004-1.

Rossi, C., R. Marfil, K. Ramseyer, and A. Permanyer, 2001, Facies-Related Diagenesis and Multiphase Siderite Cementation and Dissolution in the Reservoir Sandstones of the Khatatba Formation, Egypt's Western Desert: Journal of Sedimentary Research, v. 71, no. 3, p. 459–472, doi:10.1306/2DC40955-0E47-11D7-8643000102C1865D.

Salem, A. M., S. Morad, L. F. Mato, and I. Al-Aasm, 2000, Diagenesis and reservoir-quality evolution of fluvial sandstones during progressive burial and uplift: Evidence from the Upper Jurassic Boipeba Member, Reconcavo Basin, Northeastern Brazil: AAPG bulletin, v. 84, no. 7, p. 1015–1040.

Schmid, S., R. Worden, and Q. Fisher, 2004, Diagenesis and reservoir quality of the Sherwood Sandstone (Triassic), Corrib Field, Slyne Basin, west of Ireland: Marine and Petroleum Geology, v. 21, no. 3, p. 299–315.

Schmidt, V., and D. A. McDonald, 1979, The role of secondary porosity in the course of sandstone diagenesis.

Scott, A., C. Oze, V. Shah, N. Yang, B. Shanks, C. Cheeseman, A. Marshall, and M. Watson, 2021, Transformation of abundant magnesium silicate minerals for enhanced CO2 sequestration: Communications Earth & Environment, v. 2, no. 1, p. 25.

Sliwinski, M. G., R. Kozdon, K. Kitajima, A. Denny, and J. W. Valley, 2016, Microanalysis of carbonate cement δ18O in a CO2-storage system seal: Insights into the diagenetic history of the Eau Claire Formation (Upper Cambrian), Illinois Basin: AAPG Bulletin, v. 100, no. 06.

Słowakiewicz, M., J. Gluyas, A. Kowalski, T. Edwards, S. Słama, M. Mawson, M. E. Tucker, P. Scovell, and I. Polonio, 2020, A new and working petroleum source rock on the UK Continental Shelf (Upper Permian, offshore Yorkshire): Marine and Petroleum Geology, v. 121, p. 104605, doi:10.1016/j.marpetgeo.2020.104605.

Smythe, D. K., 2014, Planning application no. LCC/2014/0101 by Cuadrilla Bowland Limited to drill at Roseacre Wood, Lancashire: Objection on grounds of geology and hydrogeology.

Stewart, D. J., 1986, Diagenesis of the shallow marine Fulmar Formation in the central North.

Stewart, R. N. T., 1995, Regional diagenetic porosity change in palaeocene oilfield sandstones, U.K. North Sea: University of Glasgow, 24–150 p.

Storvoll, V., K. Bjørlykke, D. Karlsen, and G. Saigal, 2002, Porosity preservation in reservoir sandstones due to grain-coating illite: a study of the Jurassic Garn Formation from the Kristin and Lavrans fields, offshore Mid-Norway: Marine and Petroleum Geology, v. 19, no. 6, p. 767–781, doi:10.1016/S0264-8172(02)00035-1.

Stroker, T., and N. Harris, 2009, AV K-Ar Dating of Authigenic Illites: Integrating Diagenetic History of the Mesaverde Group, Piceance Basin, NW Colorado.

Stroker, T. M., N. B. Harris, W. C. Elliott, and J. M. Wampler, 2013, Diagenesis of a tight gas sand reservoir: upper Cretaceous Mesaverde Group, Piceance Basin, Colorado: Marine and Petroleum Geology, v. 40, p. 48–68.

Sun, N., J. Zhong, Y. Ge, and A. T. van Loon, 2022, Reservoir quality of the Middle-Late Triassic Yanchang Formation (Ordos Basin) as controlled by sedimentology and diagenesis, *in* The Ordos Basin: Elsevier, p. 421–460.

Surdam, R. C., S. W. Boese, and L. J. Crossey, 1984, The Chemistry of Secondary Porosity: Part 2. Aspects of Porosity Modification: v. 59, p. 127–149.

Surdam, R. C., L. J. Crossey, E. S. Hagen, and H. P. Heasler, 1989, Organic-Inorganic Interactions and Sandstone Diagenesis: AAPG Bulletin, v. 73, no. 1, p. 1–23.

Surdam, R. C., Z. S. Jiao, and D. B. MacGowan, 1993, Redox reactions involving hydrocarbons and mineral oxidants: A mechanism for significant porosity enhancement in sandstones: AAPG bulletin, v. 77, no. 9, p. 1509–1518.

Surdam, R. C., D. B. MacGowan, and T. L. Dunn, 1991, Predictive models for sandstone diagenesis: Organic Geochemistry, v. 17, no. 2, p. 243–253.

Szabo, J. O., and S. T. Paxton, 1991, Intergranular volume (IGV) decline curves for evaluating and predicting compaction and porosity loss in sandstones: AAPG Bulletin (American Association of Petroleum Geologists);(United States), v. 75, no. CONF-910403-.

Taylor, J. C. M., and V. S. Colter, 1975, Zechstein of the English sector of the southern North Sea Basin: Petroleum and the continental shelf of north-west Europe, v. 1, p. 249–263.

Taylor, T. R., M. R. Giles, L. A. Hathon, T. N. Diggs, N. R. Braunsdorf, G. V. Birbiglia, M. G. Kittridge, C. I. Macaulay, and I. S. Espejo, 2010, Sandstone diagenesis and reservoir quality prediction: Models, myths, and reality: AAPG Bulletin, v. 94, no. 8, p. 1093–1132, doi:10.1306/04211009123.

Taylor, K. G., and P. G. Machent, 2010, Systematic sequence-scale controls on carbonate cementation in a siliciclastic sedimentary basin: Examples from Upper Cretaceous shallow marine deposits of Utah and Coloradao, USA: Marine and Petroleum Geology, v. 27, no. 7, p. 1297–1310.

Thompson, J., and N. S. Meadows, 1997, Clastic sabkhas and diachroneity at the top of the Sherwood Sandstone Group: East Irish Sea Basin: Geological Society, London, Special Publications, v. 124, no. 1, p. 237–251.

Thyne, G., 2001, A model for diagenetic mass transfer between adjacent sandstone and shale: Marine and Petroleum Geology, v. 18, no. 6, p. 743–755.

Thyne, G., B. P. Boudreau, M. Ramm, and R. E. Midtbø, 2001, Simulation of potassium feldspar dissolution and illitization in the Statfjord Formation, North Sea: AAPG bulletin, v. 85, no. 4, p. 621–635.

Underhill, J. R., 2003, The tectonic and stratigraphic framework of the United Kingdom's oil and gas fields: Geological Society, London, Memoirs, v. 20, no. 1, p. 17–59, doi:10.1144/GSL.MEM.2003.020.01.04.

Van Keer, I., P. H. Muchez, and W. Viaene, 1998, Clay mineralogical variations and evolutions in sandstone sequences near a coal seam and shales in the Westphalian of the Campine Basin (NE Belgium): Clay Minerals, v. 33, no. 1, p. 159–169.

Verweij, J. M., H. J. Simmelink, R. T. Van Balen, and P. David, 2003, History of petroleum systems in the southern part of the Broad Fourteens Basin: Netherlands Journal of Geosciences, v. 82, no. 1, p. 71–90.

Vincent, C. J., 2015, Maturity modelling of selected wels in the Central North sea, Energy and Marine Geoscience Programme Commissioned Report CR/15/122: British Geological Survery, Nottingham.

Walderhaug, O., 1996, Kinetic modeling of quartz cementation and porosity loss in deeply buried sandstone reservoirs: AAPG bulletin, v. 80, no. 5, p. 731–745.

Walderhaug, O., 1994, Precipitation rates for quartz cement in sandstones determined by fluid-inclusion microthermometry and temperature-history modeling: Journal of Sedimentary Research, v. 64, no. 2a, p. 324–333.

Walker, T. R., E. E. Larson, and R. P. Hoblitt, 1981, Nature and origin of hematite in the Moenkopi Formation (Triassic), Colorado Plateau: A contribution to the origin of magnetism in red beds: Journal of Geophysical Research: Solid Earth, v. 86, no. B1, p. 317–333.

Walker, T. R., B. Waugh, and A. J. Grone, 1978, Diagenesis in first-cycle desert alluvium of Cenozoic age, southwestern United States and northwestern Mexico: Geological Society of America Bulletin, v. 89, no. 1, p. 19–32.

Wang, J., F. Jiang, Q. Hu, C. Zhang, X. Yang, W. Mo, X. Wang, and Z. Qi, 2023, A quantitative model and controlling factors of secondary pore development for tight sandstone reservoirs in the carboniferous Benxi Formation, Ordos Basin, China: Marine and Petroleum Geology, v. 148, p. 106034.

Wang, A., D. Zhong, H. Zhu, L. Guo, Y. Jiang, X. Yang, and R. Xie, 2019, Diagentic features of illite in Upper Triassic Chang-7 tight oil sandstones, Ordos Basin: Geosciences Journal, v. 23, p. 281–298.

Warren, E. A., 1987, The application of a solution-mineral equilibrium model to the diagenesis of Carboniferous sandstones, Bothamsall oilfield, East Midlands, England: Geological Society, London, Special Publications, v. 36, no. 1, p. 55–69.

Wasielka, N., 2021, Controls of reservoir quality in Carboniferous tight gas sandstone, PhD Thesis: Durham University.

Waters, C. N., D. W. Holliday, and J. I. Chisholm, 2020, The contribution of publications of the Yorkshire Geological Society to the understanding of the geological development of the Carboniferous Pennine Basin, northern England: Proceedings of the Yorkshire Geological Society, v. 63, no. 1, p. 1–32, doi:10.1144/pygs2018-019.

Watson, R. S., N. H. Trewin, and A. E. Fallick, 1995, The formation of carbonate cements in the Forth and Balmoral Fields, northern North Sea: a case for biodegradation, carbonate cementation and oil leakage during early burial: Geological Society, London, Special Publications, v. 94, no. 1, p. 177–200.

Wei, W., K. Azmy, and X. Zhu, 2022, Impact of diagenesis on reservoir quality of the lacustrine mixed carbonate-siliciclastic-volcaniclastic rocks in China: Journal of Asian Earth Sciences, v. 233, p. 105265.

Weibel, R., M. T. Nielsen, J. Therkelsen, F. C. Jakobsen, M. Bjerager, F. Mørk, A. Mathiesen, J. Hovikoski, S. S. Pedersen, and P. N. Johannessen, 2020, Illite distribution and morphology explaining basinal variations in reservoir properties of Upper Jurassic sandstones, Danish North Sea: Marine and Petroleum Geology, v. 116, p. 104290.

Whitelaw, P., C. Uguna, L. Stevens, W. Meredith, C. E. Snape, C. Vane, V. Moss-Hayes, and A. D. Carr, 2017, An Evaluation of Shale Gas Potential in the Bowland Shale, UK using Sequential High Water Pressure Pyrolysis and Methane Adsorption.

Worden, R., and S. Morad, 2003, Clay minerals in sandstones: controls on formation, distribution and evolution: Wiley Online Library.

Xi, K., Y. Cao, B. G. Haile, R. Zhu, J. Jahren, K. Bjørlykke, X. Zhang, and H. Hellevang, 2016, How does the pore-throat size control the reservoir quality and oiliness of tight sandstones? The case of the Lower Cretaceous Quantou Formation in the southern Songliao Basin, China: Marine and Petroleum Geology, v. 76, p. 1–15, doi:10.1016/j.marpetgeo.2016.05.001.

Xia, H., E. H. Perez, and T. L. Dunn, 2020, The impact of grain-coating chlorite on the effective porosity of sandstones: Marine and Petroleum Geology, v. 115, p. 104237.

Xia, C., M. Wilkinson, and S. Haszeldine, 2020, Petroleum emplacement inhibits quartz cementation and feldspar dissolution in a deeply buried sandstone: Marine and Petroleum Geology, v. 118, p. 104449.

Yan, X.-P., R. Kerrich, and M. J. Hendry, 2000, Trace element geochemistry of a thick till and clay-rich aquitard sequence, Saskatchewan, Canada: Chemical Geology, v. 164, no. 1–2, p. 93–120.

Yang, S., Ya Wang, S. Zhang, Yongchao Wang, Y. Zhang, and Y. Zhao, 2020, Controls on Reservoirs Quality of the Upper Jurassic Mengyin Formation Sandstones in Dongying Depression, Bohai Bay Basin, Eastern China: Energies, v. 13, no. 3, p. 646.

Yuan, G., Y. Cao, J. Gluyas, X. Li, K. Xi, Y. Wang, Z. Jia, P. Sun, and N. H. Oxtoby, 2015, Feldspar dissolution, authigenic clays, and quartz cements in open and closed sandstone geochemical systems during diagenesis: Typical examples from two sags in Bohai Bay Basin, East China: AAPG Bulletin, v. 99, no. 11, p. 2121–2154.

Yuan, G.-H., Y.-C. Cao, J. Gluyas, Y.-Z. Wang, K.-Y. Liu, K.-L. Xi, T. Yang, and J. Wang, 2019, How important is carbonate dissolution in buried sandstones: evidences from petrography, porosity, experiments, and geochemical calculations: Petroleum Science, v. 16, no. 4, p. 729–751, doi:10.1007/s12182-019-0344-4.

Zhang, L., S. Lu, D. Xiao, and B. Li, 2017, Pore structure characteristics of tight sandstones in the northern Songliao Basin, China: Marine and Petroleum Geology, v. 88, p. 170–180, doi:10.1016/j.marpetgeo.2017.08.005.

Zhong, Y.-J., K.-K. Huang, L.-M. Ye, Y.-F. Lan, and L. Liu, 2020, Diagenesis of tight sandstone reservoirs of Xujiahe Formation (Upper Triassic), the Xinchang Gas Field, western Sichuan Basin, China: Geological Journal, v. 55, no. 6, p. 4604–4624.

Zou, C., R. Zhu, K. Liu, L. Su, B. Bai, X. Zhang, X. Yuan, and J. Wang, 2012, Tight gas sandstone reservoirs in China: characteristics and recognition criteria: Journal of Petroleum Science and Engineering, v. 88–89, p. 82–91, doi:10.1016/j.petrol.2012.02.001.

Blank Page

Chapter 6

2D and 3D Characterisation of the pore structure in the Breagh Sandstone reservoir.

Contents

Chapter Six:

2D and 3D characterisation of the pore structure in the Breagh Sandstone reservoir.

6.1 Introduction

In chapter 5, I described and quantified the diagenetic minerals within the studied sandstone and their impact on reservoir quality. However, since tight gas reservoirs have significant primary and secondary porosity, myriads of microporosity (porosity less than 2μm) (Netto, 1993; Higgs *et al*., 2007; Nelson, 2009; Golab *et al*., 2010; Long *et al*., 2013), and pore connectivity dominated by authigenic clays and slot-like pores, adequate description of their pore systems is crucial for proper reservoir quality characterisation (Riepe *et al*., 2011).

The characteristic microporosity of tight gas reservoirs makes possible a high irreducible water saturation because water is bound to the mineral surfaces, and as such an increased rate of chemical reactions/transformations around/on the framework grains can occur. This produces diagenetic clay minerals which clog pore space, increase tortuosity of pore throats (Higgs *et al*., 2007; Desbois *et al*., 2011a; Rezaee *et al*., 2012; Zou *et al*., 2012; Gao and Li, 2016; Xi *et al*., 2016; Kadkhodaie-Ilkhchi *et al*., 2019; Wang *et al*., 2022; Lv *et al*., 2023), cause strong heterogeneities (complex pore structures) and promote even further diagenetic reactions.

The pore systems of sandstone reservoirs are thus significant as they control important parameters such as flow capacity, producible pore volumes and hydrocarbon flow rates (Golab *et al*., 2010; Lai *et al*., 2015; Schmitt *et al*., 2015; Xi *et al*., 2016; AlKharraa *et al*., 2023; Z. Wang *et al*., 2023). As a result, an understanding of the 3D pore systems, the ability to differentiate and quantify various pore types on a micron-scale and characterisation of pore interconnectivity is therefore vital in predicting tight gas reservoir productivity (Desbois *et al*., 2011a; Keller *et al*., 2011; Anovitz *et al*., 2013; Cnudde and Boone, 2013; Anovitz and Cole, 2015).

Recently, tight gas resources have become an important component of the wide hydrocarbon inventory as one of the major unconventional resources contributing significantly to the global hydrocarbon reserve (Greene *et al*., 2006; Holditch, 2006; Economides and Wood, 2009; Taylor *et al*., 2010; Dong *et al*., 2012; Zou *et al*., 2012; Stroker *et al*., 2013; Pang *et al*., 2015; Grasso, 2019) (Greene *et al*., 2006; Economides and Wood, 2009; Nehring, 2009; Taylor *et al*., 2010; Desbois *et al*., 2011a; Zou *et al*., 2012; Stroker *et al*., 2013; Pang *et al*., 2015; Grasso, 2019). A global estimate of natural gas reserves revealed approximately 70 tcm (trillion cubic meters) recoverable from tight gas and coal bed methane (McGlade *et al*., 2013). In the United Kingdom alone, an estimated 3.8 tcf of tight gas reserves are present in the Southern North Sea (OGA, 2017) (Oluwadebi *et al*., 2019). As a result, there has been an increase in research effort.

Significant research has focused on pore scale geometry in tight sandstone reservoirs (Clarkson *et al*., 2012; Loucks *et al*., 2012; Anovitz and Cole, 2015; Lai and Wang, 2015; Schmitt *et al*., 2015; Xi *et al*., 2016; Liu *et al*., 2017; Zhang *et al*., 2017; Lai *et al*., 2018; Mustafa *et al*., 2019; Qiao *et al*., 2021). The combination of traditional methods like as gas adsorption/desorption and mercury intrusion porosimetry (MIP), nuclear magnetic resonance (NMR), particle size analysis, point counting based on petrographic thin sections, environmental scanning microscopy (ESEM), X-ray fluorescence (XRF), provide a robust characterisation of the microscopic pore throat structure of tight sandstones (Desbois *et al*., 2011b; Xi *et al*., 2016) and have produced a growing body of literature on 3D analysis. For MIP methods refer to (Giesche, 2006; Comisky *et al*., 2011; Clarkson *et al*., 2012; Ziarani and Aguilera, 2012; Lai and Wang, 2015; Lai *et al*., 2015, 2016; Schmitt *et al*., 2015; Xiao *et al*., 2016; Shao *et al*., 2017; Zhang *et al*., 2017; Krakowska *et al*., 2018; Huang *et al*., 2019). For NMR refer to (Rezaee *et al*., 2012; Daigle *et al*., 2014; Tandon *et al*., 2017; Krakowska *et al*., 2018; Jin *et al*., 2020; Ge *et al*., 2023; Wang *et al*., 2023) and for XRF, refer to (Caja *et al*., 2019; Zhang *et al*., 2019; Jozanikohan and Abarghooei, 2022; Valenza *et al*., 2022).

A major contribution to the understanding of porosity evolution by compaction and diagenesis has progressed using SEM imaging technique to investigate pore microstructure (Golab *et al*., 2010; Desbois *et al*., 2011a; Zou *et al*., 2012; Sun *et al*., 2017; Wang *et al*., 2017; Oluwadebi *et al*., 2019; Bera and Shah, 2021; Wu *et al*., 2022). Although may be limited by poor quality of the investigative surface (mainly broken in the case of rock chips or embellished surface by resin colour which makes observation and interpretation difficult), SEM imaging techniques remains the most direct approach to image pore microstructure but, is inefficient as a method to analyse and quantify the 3D microstructure of a rock sample.

SEM imaging technique when coupled with a three-dimensional imaging techniques such as X-ray Computed Tomography (XCT) (Cnudde *et al*., 2006; Cnudde and Boone, 2013; Krakowska *et al*., 2018; Lai *et al*., 2018; Oluwadebi *et al*., 2019; Wang *et al*., 2022) have proven successful in studying the internal structure of many rocks at a spatial resolution better than 1μm (Golab *et al*., 2010; Riepe *et al*., 2011; Cnudde and Boone, 2013; Liu *et al*., 2017; Zhang *et al*., 2019; Lin *et al*., 2022; Su *et al*., 2022; Wang *et al*., 2022).The specimen preparation is typically minimal, and for many materials the technique is non-destructive allowing many scans to be made of the same specimen under different conditions.

In-situ mineral maps measured on the same polished plane with SEM are used to identify different pore sizes and types transforming the porosity of the rock and when combined with 3D tomographic images, the contribution of individual clay minerals to the microporosity, pore connectivity, and, the nature of the secondary porosity can be determined and quantified (Golab *et al*., 2010; Cnudde and Boone, 2013; Philipp *et al*., 2017; Kala, 2022). Petrophysical response can also be determined as well insight into the producibility may be gained (Oluwadebi *et al*., 2019).

In spite of this, research on pore system of unconventional reservoirs using 3D imaging techniques has mostly been focussed towards shale gas plays (Ross and Bustin, 2008, 2009; Clarkson *et al*., 2012; Huaqing *et al*., 2015; Ramandi *et al*., 2016; Aljamaan *et al*., 2017; Sun *et al*., 2017; Wang *et al*., 2017; Gou *et al*., 2021; Zhu *et al*., 2021; Valenza *et al*., 2022; W. Wang *et al*., 2023). The few published works on tight gas reservoirs are limited to characterization of the general pore size and pore throat distribution and their associated pore network. (Golab *et al*., 2010; Riepe *et al*., 2011; Bin *et al*., 2013; Lai *et al*., 2015, 2018; Liu *et al*., 2017; Zhang *et al*., 2019; Su *et al*., 2022).

Studies on the link between the larger scale reservoir quality prediction and microscopic pore space development of unconventional reservoirs (such as pore types, geometries, spatial distribution and their contributions to the network and gas transport) remain relatively sparse and unclear (Lai *et al*., 2018; Oluwadebi *et al*., 2019). The aim of this study therefore is to provide quantified data on pore types and pore geometry of the Breagh Sandstones. In conjunction with the XCT imaging and visualization of the sample material at the pore scale, to attempt a link between the larger scale reservoir quality and microscopic pore space development in the Breagh field for which there has been no existing study.

Pores detected in the SEM images are statistically analysed to perform porosity quantification. The SEM results allows retrieving porosity obtained and characterising them based on pore size radius which might form elementary component of porosity/permeability models based on pore structure. The results obtained have significant implications for pore connectivity, gas storage and fluid flow capacity and might also lead to the further understanding of petrophysical properties such as relative permeability and multi-phase flow simulation (Xiong *et al*., 2016).

6.2 Summary.

6.2.1 Mineralogy (detrital and authigenic).

Chapter 5 also detailed the mineralogy of the studied sandstone and thus the basis for identifying the different phases needed for this chapter. In summary, the studied sandstone is predominantly quartz arenite to sublitharenite, very fine grained to coarse grained (with granule particles at intervals) and moderately well sorted to well sorted. The detrital composition consists of monocrystalline and polycrystalline quartz, feldspars (mainly K-feldspar), lithic fragments (chert, volcanic and metamorphic), micas and trace amounts of heavy minerals.

Rock fragments are dominated by mud clast but also comprise of granite, mica schist grains, quartz-schist, and volcanic grains. They make up (trace to 2.3%, - av. 0.3%) of the grains (Table 5.1 in Chapter 5). The quartz schist grains are stable and show little deformation or alteration, whereas the mica schist and phyllite grains show varying degrees of deformation, alteration (mainly to kaolinite and illite) and in some cases dissolution.

Clay mineral (kaolinite and illite rich clay) and carbonate (mainly dolomite and calcite) cements are the most common pore-filling cements, followed by authigenic quartz cement and bituminous hydrocarbons. Haematite, pyrite, anhydrite and barite, are minor cements. See (chapter 5) for detailed mineralogy and diagenesis of the studied sandstone.

6.2.2 Permeability controls.

To link the large-scale reservoir geometry with the smaller scale pore structure, 6 samples were selected from the sandy facies. Three from delta plain environment (three from Distributary channel -FA8 and one from Braided fluvial Channel -FA9) while the last two are from the

Delta front environment (One from distributary mouth bar -FA3; and one from the proximal delta front sand- FA4).

Studies have shown that permeability-porosity trends resulting from progressive compaction or cementation in a clean sandstone, are curvilinear on the traditional log-linear plot (Shepherd, 1989; Bryant *et al*., 1993; Cade *et al*., 1994; Evans *et al*., 1997; McKinley *et al*., 2011). The onset of pore-throat blocking is marked by the steepening which defines the curve. Other cement styles, such as pore-filling carbonates or grain-coating clays, show different porosity-permeability trends thus providing the basis for predicting permeability from predictions of grain size and diagenetic style and hence identifying the important permeability controls in a set of fields data (Cade *et al*., 1994).

The cross plot of permeability against porosity for the studied samples in this research (Fig 6.1 see also chapter 5.4) shows that even though permeability generally tracks porosity, but closer look Fig 6.1 shows that the permeability- porosity trend is not completely curvilinear indicating that the factors controlling reservoir quality affect porosity and permeability differently just as have been discussed in detail in Chapter 5.7.

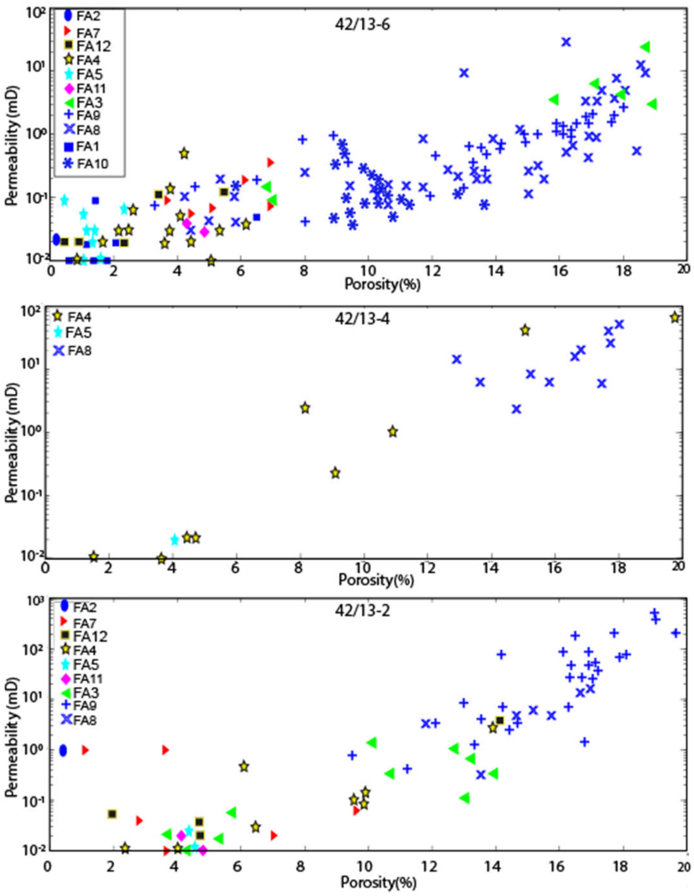

Figure 6.1: Porosity and permeability cross plot for the Breagh Field wells

The samples selected for pore size characterisation in this chapter were therefore selected to investigate how variation in the amount diagenetic cement impacts on pore size distribution but also to determine what facies are particularly affected and why.

Six samples were selected from the four sandy facies (FA3, FA4, FA8 and FA9). 3 samples have similar permeability values- less than 0.1mD and the other 3 have permeability values much higher than 0.1mD. In all cases, permeability is observed to track the amount of diagenetic cement more than it tracks porosity. (Table 6.1 and Fig 6.2).

Table 6.1: Selected samples and specific geological attributes.

Facies	Depth	Porosity (%)	Permeability (mD)	Grain size	Sorting	Diagenetic cement (% per 300 count)
FA8	7442.1	5.4	0.02	Coarse sand	Moderately Well sorted	30
FA8	7540	17.7	25	Medium sand	Moderately well sorted	20.7
FA9	7488.5	17.7	203	Coarse sand	Moderately sorted	15
FA3	7451	3.8	0.02	Medium sand	Moderately well sorted	28
FA8	7469	17.2	35	Coarse sand	Moderately well sorted	22
FA4	7497.5	6.5	0.03	Fine sand	Well sorted	34

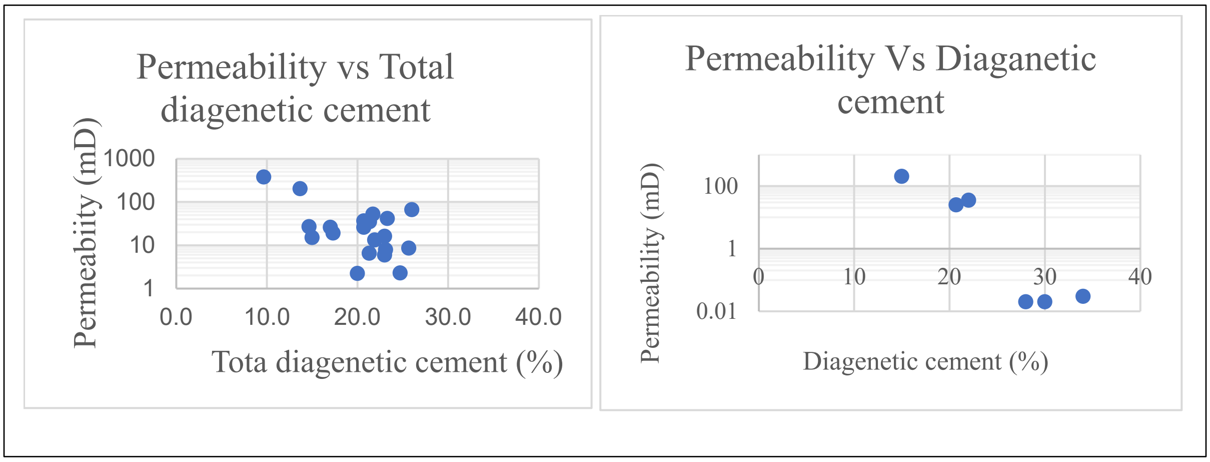

Figure 6.2: Left: Plot permeability variation with the amount of diagenetic cement for all studied samples in this research: Right: Plot permeability variation with the amount of diagenetic cement for the selected samples in this chapter.

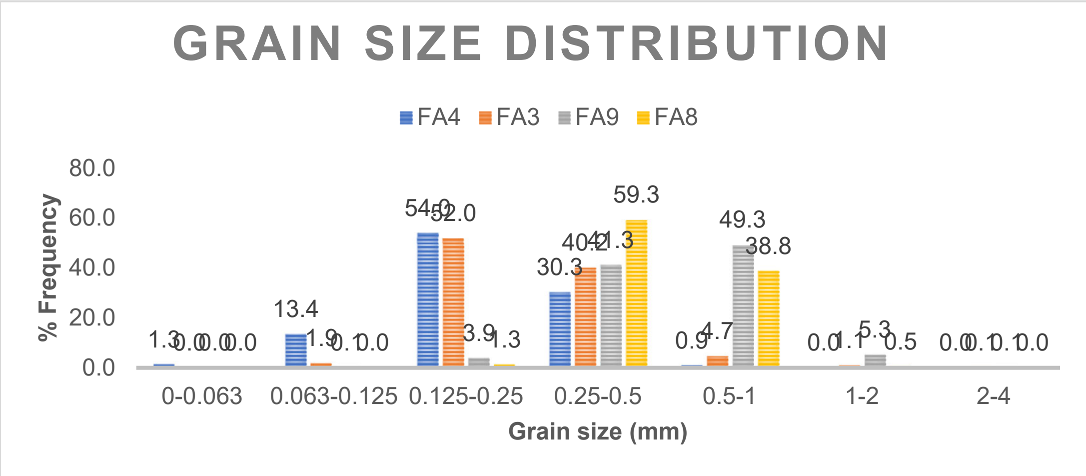

Figure 6.3: Grain size distribution for the Breagh field samples.

The grain size distribution graph (Fig 6.3) shows that the sample from 7488.5ft -FA9 facies (braided fluvial channel) which has the highest permeability out of all the studied samples not only consist of coarse sands but also has the least variation in grain size distribution when compared to the samples from the other 5 samples. Looking at the samples from FA8 facies for instance, that have more grain size and internal facies variation (see Chapter 4 for details on internal variation on the FA8 facies) with corresponding lower permeability values, it can be inferred that grain size variation is one of the controlling factors that impacts reservoir quality as some experimental studies have shown (Lawal *et al.*, 2020). Although many more data points are needed to confirm this to be the case in this study, but the direct implication of this work so far may support the conclusion in chapter 3 and 4 – that prospectivity in the Breagh area is likely to be dependent on the thick sequences of stacked braided fluvial channels.

As mentioned in chapter 3 also, thinner, and finer-grained sandstone bodies exist within delta front sands (FA4, FA5), distributary mouth bar (FA3) and abandoned channel facies (FA10) could add to the prospectivity of the Breagh field. However, understanding the pore network and distribution of these thinner, secondary reservoirs will be critical for adding pay at Breagh and other potential gas fields.

6.3 Analysis and Results.

6.3.1 Phase identification.

Two-dimensional images from SEM analysis and X-ray Computed Tomography (XCT) (Fig. 6.4 a, ai) were used to reveal the texture and the sorting of the sandstone.

The detrital grains consist of quartz, feldspar, and rock fragments, however because the feldspar and the rock fragments comprised of less (0.3%), the detrital minerals have been collectively grouped to as quartz (Fig. 6.4b). Carbonate cements (mostly dolomite) are observed filling the original intergranular pores (Fig. 6.4b–bi), authigenic clay minerals (illite and kaolinite) represents the clays and are referred to as authigenic phase. Heavy minerals including ilmenite, rutile, and haematite appear very bright in XCT due to their high attenuation coefficient (Fig. 6.4b), they constitute heavy mineral phase.

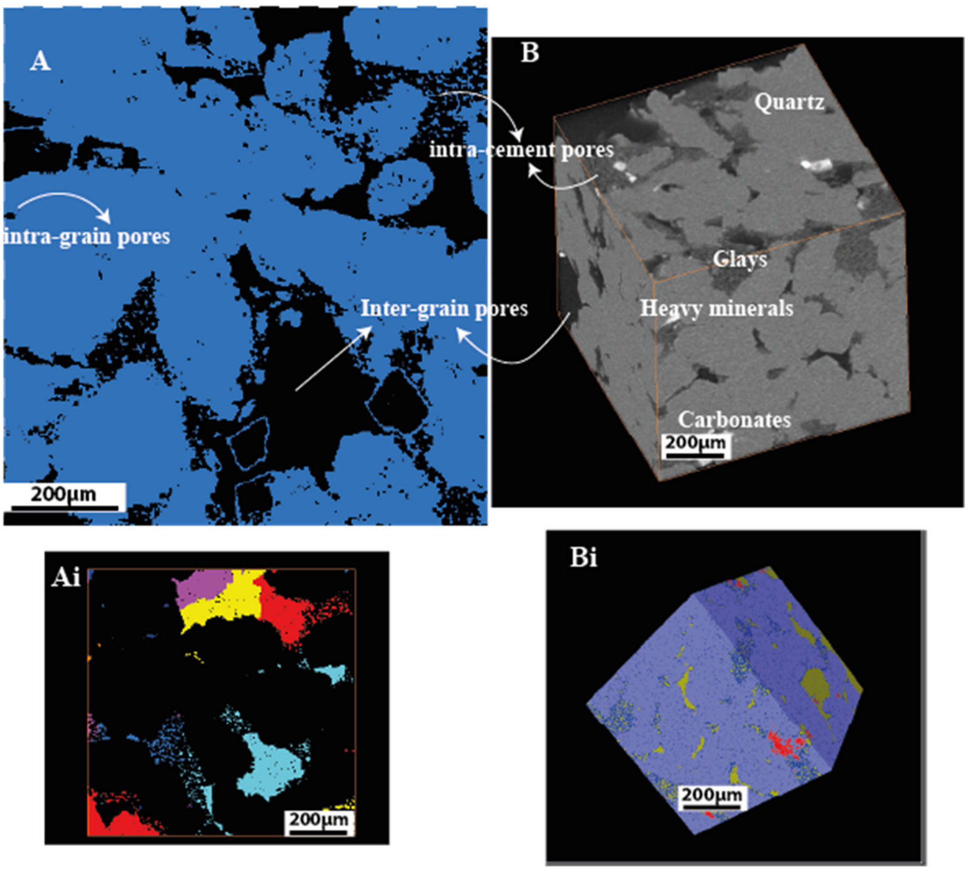

Figure 6.4: (A) 2D XCT image showing grain phase (blue) and pore space (black); (B) Greyscale image of Fig. Bi, note the very bright colour of the heavy mineral. [quartz, carbonate cements, clay cements, heavy minerals, inter-grain pores, inter-cement pores, intra-grain pores]. (Ai) Orthoslice revealing different pore dimensions; (Bi) Volume rendered image showing purple phase for the grains, the red phase represents the carbonates; the blue in between the grains are the different pore spaces, while the yellow phase represents the clays.

The 3D volume rendered image further shows the different phases of the samples, where the purple phase represents grains, the red phase represents the carbonates; the blue in-between the grains are the pore spaces, while the yellow phase represents the clays (Fig. 6.4bi). The grey scale image of the 3D volume rendered image is displayed in (Fig. 6.4b) for comparison.

6.3.2 Pore types.

Simple visual identification of different pore types was achieved with 3D XCT (Fig 6.4a, b) and 2D SEM images with the (Fig 6.5 a-d). The pores were also separated from the rest of the rock volume on 3D with the XCT by rendering an image slice into different colour phases. Both the 2D and the 3D Volume rendering of the separated pores partitioned the pore spaces into individual pores is shown in (Fig. 6a, ai, b, bi).

Three pore types were identified: inter-grain pores, intra-cement pores, and. intra-grain pores A summary of pores identified are shown in (Table 6.2)

I. Inter-grain pores occur in-between detrital grains (such as quartz and feldspar grains) or sometimes between detrital grains and authigenic minerals (carbonate and clay minerals) as well as other trace minerals. They are mostly elongated, although some are spherical and lenticular (Fig. 6.4a and b). The pore equivalent radius on XCT ranges from 8.21µm to 125.56 µm with an average of 50.56µm. Although analysis of the 2D pore size distribution reveals that the inter grain pore size radius can be as large as 200µm (Fig 6.5 a-d).

II. Intra-cement pores are bounded by cement phases, mostly within the clays and seldomly within the carbonate cement (Fig. 6.4 a and b). The pores occur as angular, polygon and spherical. The pore radius ranges from 0.8 µm to 9.8 µm with an average of 5.05 µm.

III. Intra-grain pores are bounded by (occur within) the detrital mineral grains. These pores mostly have irregular sphere geometry or elongated geometry (Fig. 6.4a and b). The pore size radius varies between 4.9 µm and 16 µm with an average of 10.65 µm.

Table 6.2: Summary of pore types.

Pore type	Location	Shape	Size (Radius- µm)
Inter- grain pore	At grain boundaries of detrital grains and authigenic minerals	Elongated, Spherical	8-125
Intra-grain pore	Present within detrital mineral grains.	Elongated, Spherical	4.9-16
Intra-cement pore	Bounded by authigenic minerals (mostly carbonate cement)	Spherical, angular, and Polygonal	0.8-9.8

6.3.3 Pore distribution on 2D.

Pore size distribution was analysed by extracting the pore space 2D SEM images using a MATLAB extract function. Six samples were selected from the sandy facies.

Analysis of the result show that pore size radius ranges from 0 – 5 µm to 100-200 µm intervals (Fig 6.5 & 6.6). In all cases the number of intra-cements an intra-grain pores (pores with pore size radius between 0.8 and 16 µm) are 3 – 4 orders of magnitude more abundant than the intergranular pores although the intergranular porosity occupies approximately 80% of the total surface area.

Further, permeability values seem to increase with pore size radius. Permeability values beyond 25 mD is observed in samples with pore size radius greater than 31µm (Fig 6.5 and table 6.1). When viewed on SEM image (Fig 6.6), these pores are oversized pores at inter-grain boundary probably created by dissolution of earlier formed minerals mostly sulphate cements (discussed in chapter 5.5.6). and have been mostly preserved by residual oil lining pores thus preventing the late stage diagenetic illite from occluding the pores.

The correlation between pore size radius and permeability is emphasized with the sample from 7488.5 ft in FA9 facies with a permeability value of 203 mD. Results of the pore extraction (Fig 6.5, 6.6c-c[1]) shows that the sample consist of two oversized pore one with a radius of 200µm and the other with a radius of 76 µm. It may be the case that the presence of these large pores has a significant impact on permeability especially when compared with the sample from 7442.1ft (FA8) with a permeability value of 0.02 mD which has a maximum pore size radius of 31µm.

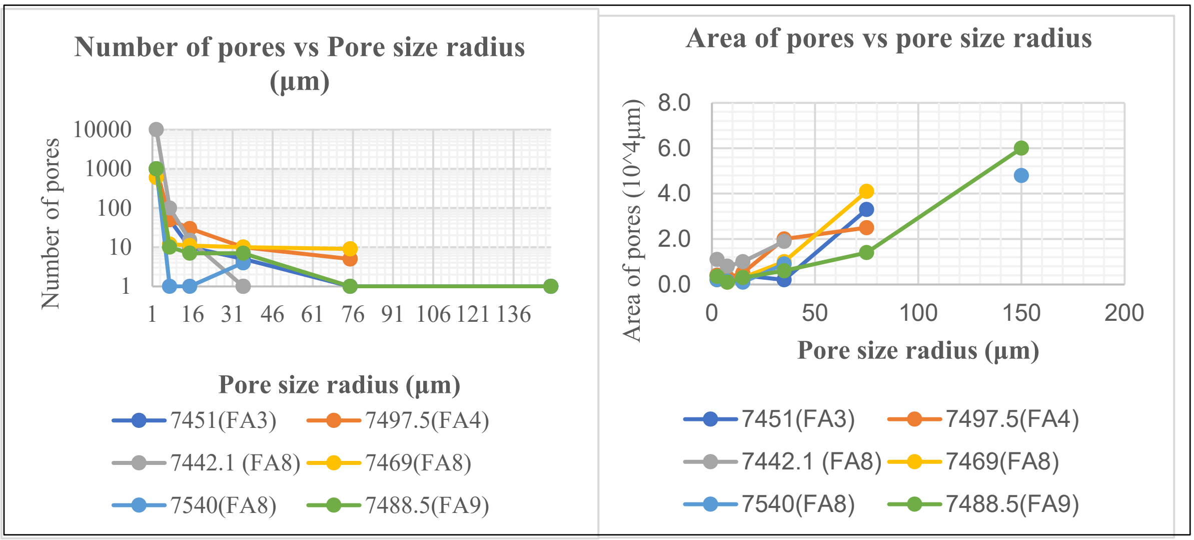

Figure 6.5: Left: Graph showing the number of pores vs pore size radius from 2D SEM image analysis; Right: Surface area of pores vs pore size radius.

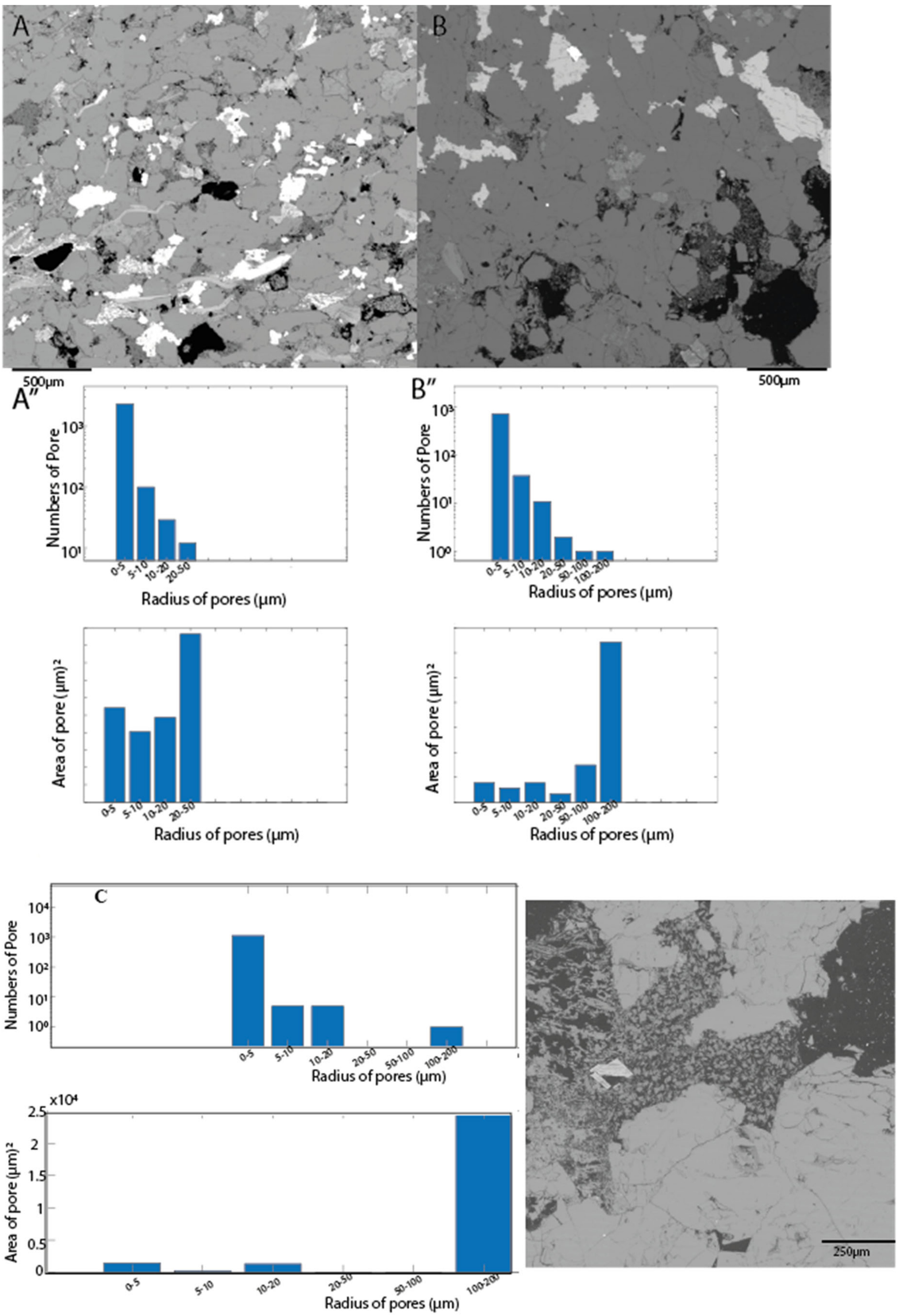
A
B
500μm
500μm
A″
B″
Numbers of Pore
Radius of pores (μm)
Area of pore (μm)²
0-5
5-10
10-20
20-50
50-100
100-200
C
x10⁴
250μm

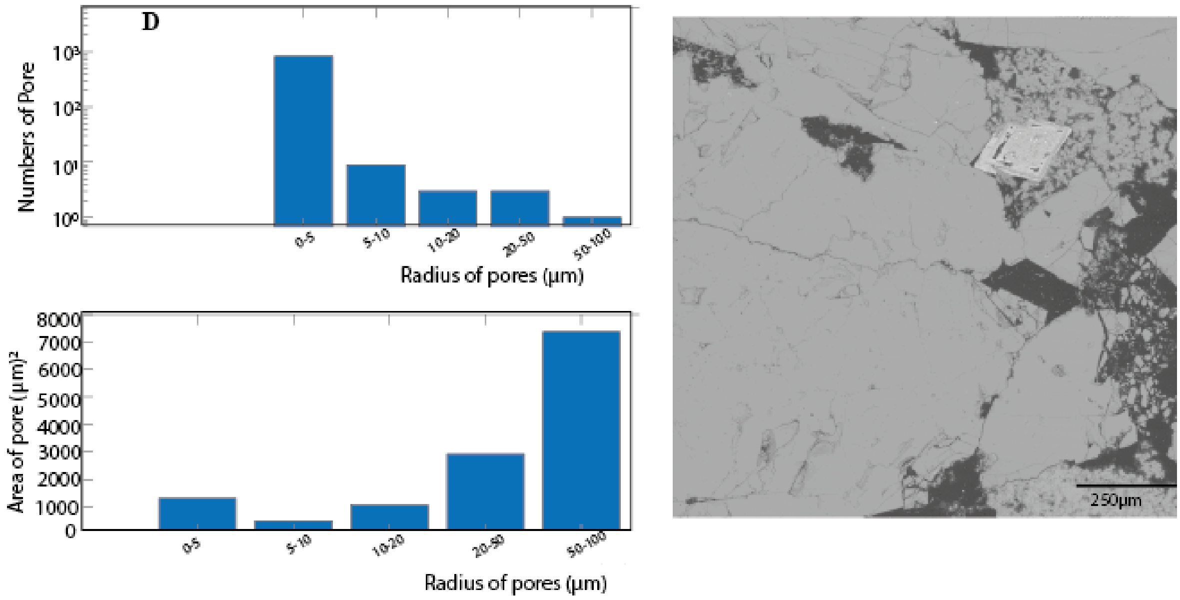

Figure 6.6: SEM image and corresponding pore size distribution for a-a¹-7442.1ft (FA8); b-b¹ -7451ft ((FA3); c-c¹ – 7488.5ft (FA9); d-d¹-7540ft (FA8).

Although the 7442.1ft sample has 9000 more pores than the 7488.5ft sample it still has a permeability value with four orders of magnitude less than the value for the 7488.ft samples despite having 10,000 pores with pore size radii of 1µm. This is consistent with literature as permeability of tight sandstone reservoirs have been noted to be mainly controlled by a size the pore radius (Xi *et al*., 2016; Xiao *et al*., 2017; Huang *et al*., 2018; Qiao *et al*., 2022; Wang *et al*., 2022).

6.3.4 Pore Network or Connectivity.

The pore network model of the studied sandstone was generated by skeletonization and pore network model (PNM) algorithms of the pore spaces in 3D, with the output image showing a skeletonized view of the pore network in the form of interconnected tubes with varying thickness, illustrated by a colour code (Fig 6.7).

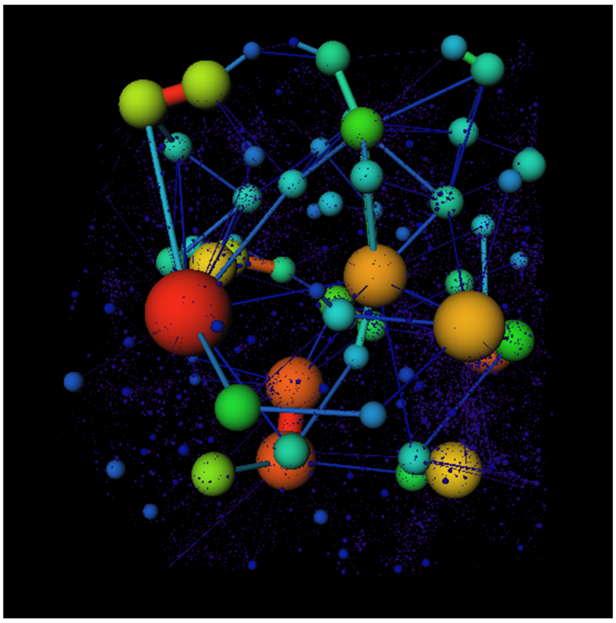

Figure 6.7: Pore network model of a sample from 7545.9ft (FA8); Balls represent the pore body, and the tubes represent the pore throat with varying length and diameters.

A 5-mm diameter core of the studied sample (7545.9 ft -FA8) was imaged using 3D X-ray micro-CT analysis yielding >4000^3 voxels (a voxel is each of an array of elements of volume that constitute a notional three dimensional space and in this case it is the smallest volume constituting the 3D image of the studied core) at 1 µm resolution, by the methodology described in (Sakellariou *et al*., 2003). Figure 6.8 shows the imaged core (6.8a) the representative elementary volume -REV (6.8b), the bounding slices for the REV (6.8c, d) and a slice each from Y-plane (6.8f), X-Plane (6.8g); and the Z-Plane (6.8h) from the tomogram. Representative elementary volume (REV) is the smallest volume over which a measurement can be made that will yield a value representative of the whole.

The working REV selected was 400 µm by 400 µm. The REV is segmented into the different component minerals and pore space- Quartz, clay carbonate and pore space (Fig 6.9). For context, Fig 6.8b is a slice of the separated shows carbonate phase in red the same process is repeated for all the component material within the rock sample.

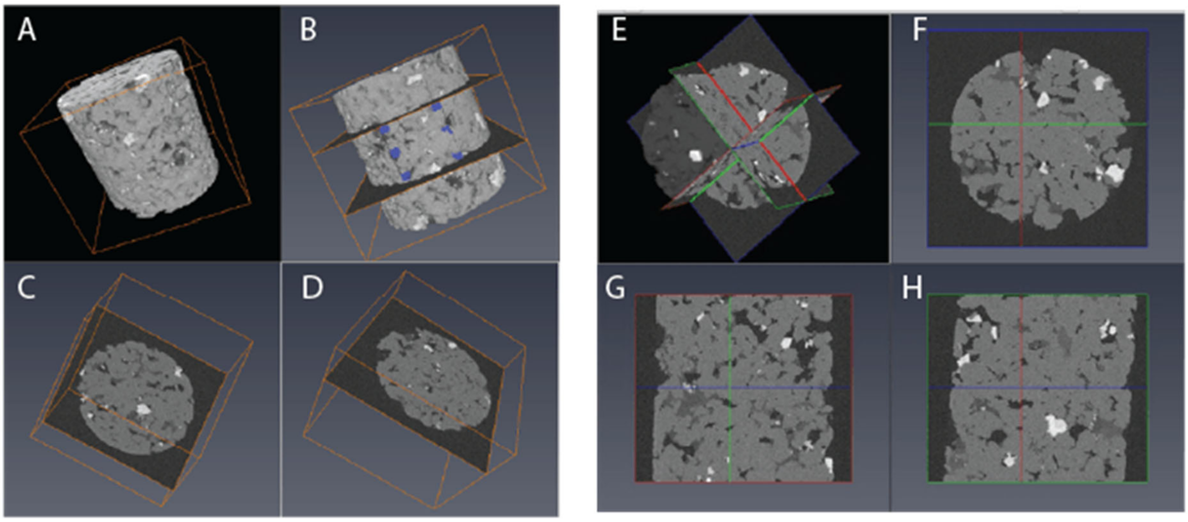

Figure 6.8: showing the imaged core (6.8a) the representative elementary volume -REV (6.8b), the bounding slices for the REV (6.8c, d) and a slice each from Y-plane (6.8f), X-Plane (6.8g); and the Z-Plane (6.8h) from the tomogram (not drawn to scale)

It should be noted that the segmentation process has no way of separating the different types of clays identified in the study area (illite and kaolinite) as the principle of micro-CT is based on the attenuation of x-rays passing through the object or sample being imaged will not be able to clearly separate between objects of similar densities. As an x-ray passes through object, the intensity of the incident x-ray beam is diminished according to the equation by (Boerckel *et al*., 2014), $I_x = I_0^{e-\mu x}$, where I_0 is the intensity of the incident beam (Chapter 1.4.6) for more details on methodology), x is the distance from the source, I_x is the intensity of the beam at distance x from the source, and μ is the linear attenuation coefficient (Stauber and Müller, 2008; Boerckel *et al*., 2014). The attenuation therefore depends on both the sample material and source energy and can be used to quantify the density of the sample being imaged. Due to the similarity in atomic mass between kaolinite and illite, it is impossible for the x-rays to discriminate between illite and kaolinite. In this chapter however, the precise discrimination between illite and kaolinite is not as important because the focus is on pore architecture which is achieved by separating the component material from the pore volume (Fig 6.9, 6.10).

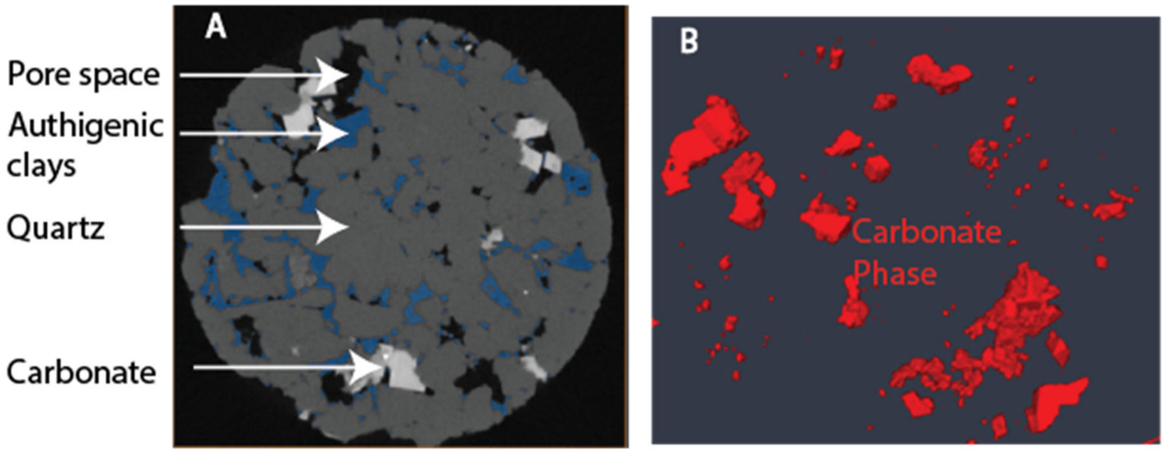

Figure 6.9: Left: A tomographic slice showing all the component materials for separation; Right: image view of a separated carbonate phase from the tomogram.

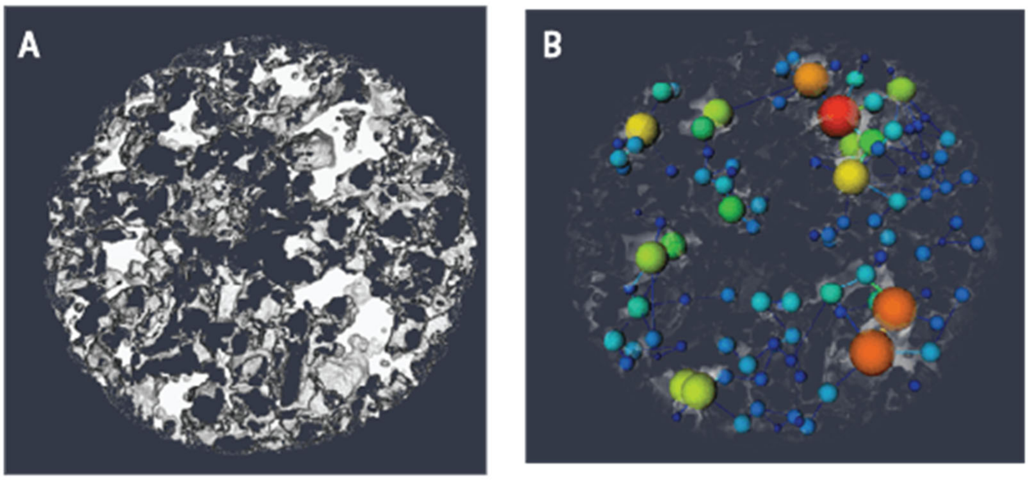

Figure 6.10: Left: Pore network model view after separation of the component material, right: skeletonized view of the pore network in the form of interconnected tubes.

Once the different materials are separated, the pore volume and pore network model can be calculated. The pore network model reveals important information about the pore architecture. Output image shows variation in the size of the pore-throat and pore body, represented as a ball and stick (Fig 6.7). Pore body sizes range from 5.25 μm to 53.65 μm in radius, whereas pore throat ranges from 0.30 μm to 35.93 μm. Pore throat channel length varies between 25. 24 to 263.8 μm and pore coordination number is from 1 to 10. Summary of pore quantification derived from the pore network model algorithms for the studied sample are shown in (see appendix 3 & 4). Isolated and connected pores can easily be distinguished visually where many pores appear as isolated pores, with some connected ones.

6.3.4.1. Significance of pore connectivity

A plot of the pore coordination number against the pore radius (Fig 6.11) shows that pore coordination number increases as the pore size radius increases. It should also be noted that the presence of many pores with similar radius does not necessarily impact pore coordination in as much as the radius is small (less than 22 μm) but a small increment in pore size radius albeit with fewer number of pores is observed to increase pore coordination number. In addition, it is not just the presence of pores with radius higher than 22 μm that increases pore coordination but also the absence of pores with pores size radius less than 22 μm. For instance, a pore coordination number of 6 and above is only achieved after pores sizes with radius less than 22 μm are absent. Table 6.2 shows that pores with pore body radius less than 22 μm are intragrain and intra-cement pores with minimal inter-grain pores.

Inter-grain pores, with radius commonly larger than 16 μm, are the dominant contributor of surface area, whereas all three pores contributed considerably to pore volume except that the intra-grain pores have minor quantity (Fig 6.12).

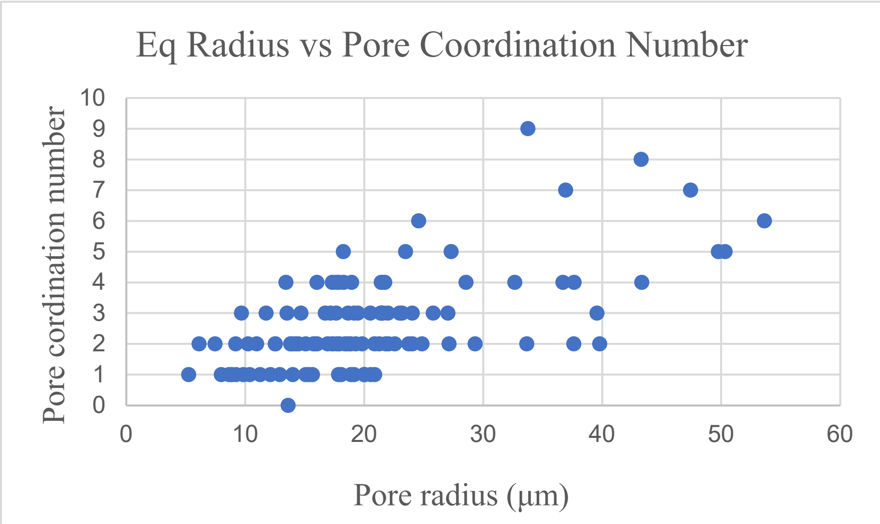

Figure 6.11: Plot of pore size radius vs pore coordination number.

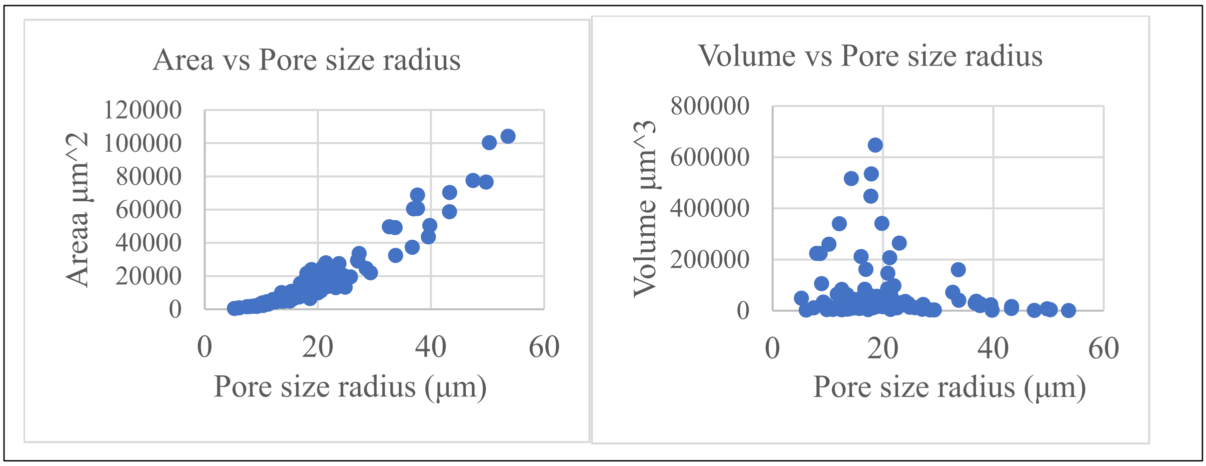

Figure 6.12: Left - surface area vs pore size radius; Right - Pore volume vs pore size radius.

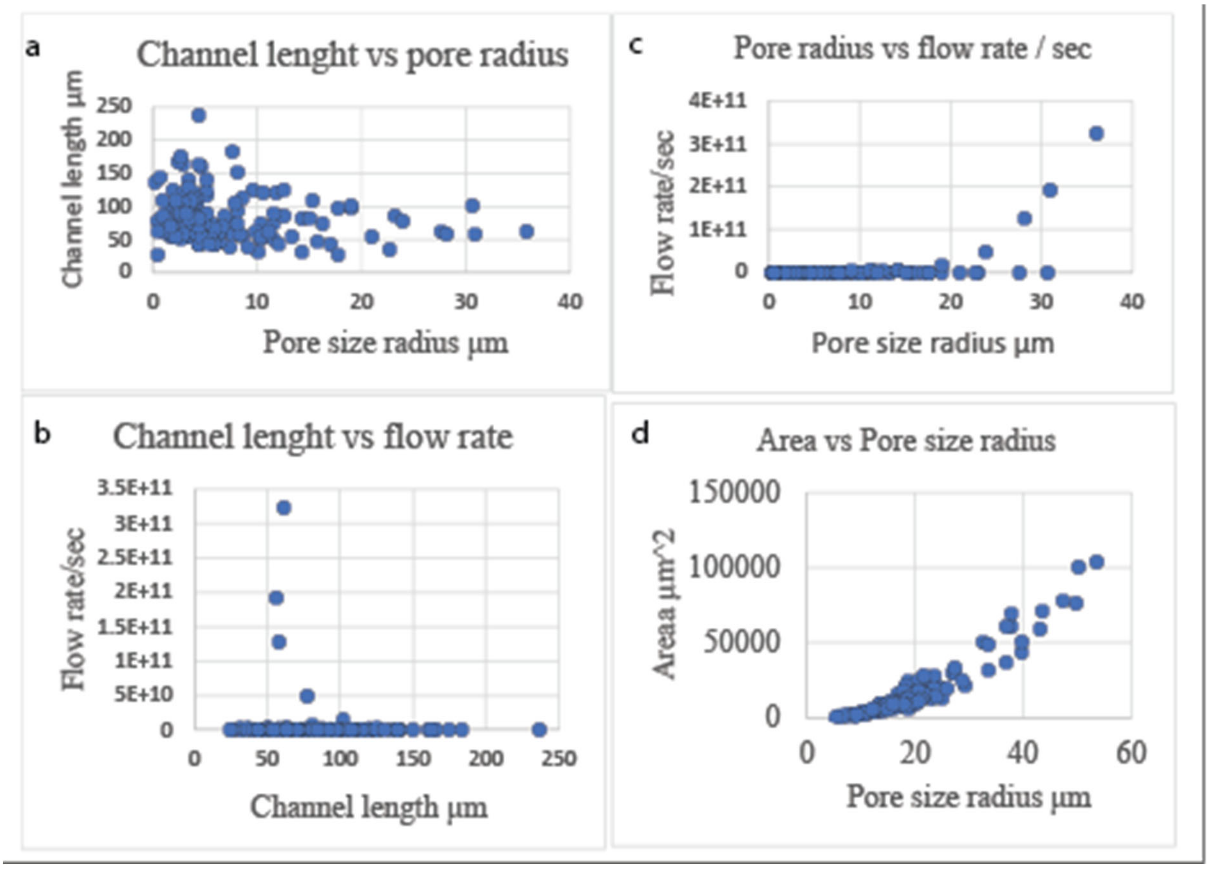

Figure 6.13 - a: Plot of channel length vs pore radius; b: Channel vs flow rate; c: pore radius vs flow rate; d: Surface area vs pore size.

The intra-grain and intra-cement have more and longer pore-throats than the pore-throats associated with inter-grain pores (Fig 6.13a), there appears to be no relationship between length of pore throat with flow rate (6.13b) as flow rate is observed to be static for all pores with pore size radius less than 22 µm (Fig 6.13c). It might be the case in fact that the intra-cement and intragrain pores throat no matter how long they are might impede flow through them when compared with the inter-grain pores since reservoirs with large pore diameter are usually associated with bulk diffusion, whereas surface diffusion often occurs with smaller pores because gas molecules tend to absorb on the pore surface than on other gas molecules (Schmitt *et al.*, 2015; Pang *et al.*, 2017; Qu *et al.*, 2020; Akilu *et al.*, 2021; Shan *et al.*, 2021). In all cases, mean surface area for inter-grain pores is about 7 times higher than intra-grain pores and 9 times than intra-cement pores (Fig 6.13a). Both intra-grain and intra-cement pores remain as part of the total pore network.

Considering the pore network in Fig 6.7, the isolated pores mostly the intra-cement and intra-grain pores have smaller sized pores, while the connected pores (mostly the inter-grain) often form a cluster, having larger open pores. The connected (clustered) pores have a significant porosity from both inter-grain and intra-grain pores. The isolated pores (Intra-grain pores and intra-cement pores) with the smaller surface area (Figs 6.5 & 6.13) and have poor spatial connectivity and would possibly act only as reservoir space without being a flow pathway. Hence, permeability is usually higher with inter-grain pore network than intra-grain or intra-cement network and so provide a possible migration pathway for gas flow. This evidence supports the hypothesis that inter-grain pores are more abundant and have a larger surface area and will therefore, provide a longer and more efficient migration pathway for gas flow (Loucks *et al*., 2012; Oluwadebi *et al*., 2019).

The study of on pore size distribution and connectivity shows that efficient pore diffusivity and tortuosity of porous media are significantly influenced by pore interconnectivity. The extracted pore networks here will be a good input in predicting multi-phase flow properties of the studied reservoir.

When combined with the SEM analysis in section 6.3.3 and table 6.1 above, it is clear the samples with the highest permeability are the samples with larger pore radius. Since the size of pore radius in this study are inextricably linked with pore types which in turn control connectivity, it can be inferred that pore size, pore types and pore connectivity are the three major controls on permeability in the studied sandstones.

6.4 Conclusion.

1. The integration of the SEM imaging technique and 3D X-ray micro-CT imaging used in this study have helped to obtain the total spectrum of pore- size distributions found within the Breagh tight sandstones reservoirs.
2. Pore types observed include inter-grain pores, intra-grain pores, and intra-cement pores within clay aggregates.
3. The pore sizes radius is significantly different for these three pore types basically varying from 0.8 µm to 200 µm.
4. Intra-cement pores have pore radius from 0.8µm to 9.6µm, intra-grain pores have pore size radius between 4.9 µm – 16 µm, and inter- grain have pores with pore size radius between 8 µm -200 µm. The wide range of size makes it difficult to understand their distribution characteristics as well as the specific controls on reservoir quality however

organizing key parameters defining permeability systematically can enhance our ability of formulating predictive models about permeability in tight sandstone reservoirs.

5. 2D SEM image analysis shows that the number of intra-cements an intra-grain pores (pores with pore size radius between 0.8 μm and 16 μm) were in all the studied sample 3 – 4 orders of magnitude more abundant than the intergranular pores although the intergranular porosity occupies approximately 80% of the total surface area. 3D XCT also validates this- Inter-grain pores, with radius commonly larger than 16μm, are the dominant contributor of surface area, whereas all three pores contributed considerably to pore volume except that the intra-grain pores have minor quantity.
6. 3D XCT also shows that pore coordination number increases as the pore size radius increases. It should also be noted that the presence of many pores with similar radius does not necessarily impact pore coordination in as much as the radius is small (less than 22μm) but a small increment in pore size radius albeit with fewer number of pores is observed to increase pore coordination number.
7. The intra-grain and intra-cement have more and longer pore-throats than the pore-throats associated with inter-grain pores (Fig 6.13a), there appears to be no relationship between length of pore throat with flow rate (6.13b) as flow rate is observed to be static for all pores with pore size radius less than 22 μm (Fig 6.13c).
8. Inter-grain pores, and those made up of relatively larger pore-throats (larger than 22μm), have the potential for continuous gas transport. Although the large number of smaller pore-throats have negligible contribution on reservoir flow potential, they are more significant for the reservoir storage capability. Reservoirs with large pore radius are usually associated with bulk diffusion (darcy flow), whereas surface diffusion often occurs with smaller pores because gas molecules tend to absorb on the pore surface than on other gas molecules (Wang *et al*., 2019; Eltahan *et al*., 2020; Sheng *et al*., 2020; Akilu *et al*., 2021; Dang *et al*., 2021, 2023; Javadpour *et al*., 2021).
9. The permeability in the studied sandstones is therefore mainly controlled by size of the pore radius, pore types and interconnectivity. These are in turn controlled by the grain size distribution (Lawal *et al*., 2020) and volume of diagenetic cement present thereby supporting the hypothesis it is the diagenetic cement that clog and transform the pore architecture as well as increase tortuosity within the pore space (Higgs *et al*., 2007; Desbois *et al*., 2011a; Rezaee *et al*., 2012; Zou *et al*., 2012; Gao and Li, 2016; Xi *et al*., 2016; Kadkhodaie-Ilkhchi *et al*., 2019; Wang *et al*., 2022; Lv *et al*., 2023). As the content of the clay minerals increases, the heterogeneity of the reservoir decreases.

10. The study on the pore size distribution and connectivity shows that efficient pore diffusivity and tortuosity of porous media are significantly influenced by pore interconnectivity. The extracted pore networks here will be a good input in predicting multi-phase flow properties of the studied reservoir.

6.5: References

Akilu, S., E. Padmanabhan, and Z. Sun, 2021, A review of transport mechanisms and models for unconventional tight shale gas reservoir systems: International Journal of Heat and Mass Transfer, v. 175, p. 121125.

Aljamaan, H., C. M. Ross, and A. R. Kovscek, 2017, Multiscale imaging of gas adsorption in shales, *in* SPE Unconventional Resources Conference: OnePetro.

AlKharraa, H. S., K.-H. A. Wolf, H. T. Kwak, I. S. Deshenenkov, M. A. AlDuhailan, M. A. Mahmoud, S. A. Arifi, N. B. AlQahtani, A. A. AlQuraishi, and P. L. Zitha, 2023, A Characterization of Tight Sandstone: Effect of Clay Mineralogy on Pore-Framework, *in* SPE Reservoir Characterisation and Simulation Conference and Exhibition: OnePetro.

Anovitz, L. M., and D. R. Cole, 2015, Characterization and analysis of porosity and pore structures: Reviews in Mineralogy and geochemistry, v. 80, no. 1, p. 61–164.

Anovitz, L. M., D. R. Cole, G. Rother, L. F. Allard, A. J. Jackson, and K. C. Littrell, 2013, Diagenetic changes in macro-to nano-scale porosity in the St. Peter Sandstone: An (ultra) small angle neutron scattering and backscattered electron imaging analysis: Geochimica et Cosmochimica Acta, v. 102, p. 280–305.

Bera, A., and S. Shah, 2021, A review on modern imaging techniques for characterization of nanoporous unconventional reservoirs: Challenges and prospects: Marine and Petroleum Geology, v. 133, p. 105287.

Bin, B., Z. Rukai, W. U. Songtao, Y. Wenjing, J. Gelb, A. Gu, X. Zhang, and S. U. Ling, 2013, Multi-scale method of Nano (Micro)-CT study on microscopic pore structure of tight sandstone of Yanchang Formation, Ordos Basin: Petroleum exploration and development, v. 40, no. 3, p. 354–358.

Boerckel, J. D., D. E. Mason, A. M. McDermott, and E. Alsberg, 2014, Microcomputed tomography: approaches and applications in bioengineering: Stem cell research & therapy, v. 5, no. 6, p. 1–12.

Bryant, S., C. Cade, and D. Mellor, 1993, Permeability prediction from geologic models: AAPG Bulletin, v. 77, no. 8, p. 1338–1350.

Cade, C. A., I. J. Evans, and S. L. Bryant, 1994, Analysis of permeability controls: a new approach: Clay Minerals, v. 29, no. 4, p. 491–502.

Caja, M. A., C. Santos, L. García, P. R. Fernández, J. L. Pérez, A. Peña, J. Canal, V. Blazquez, H. González, and V. Sánchez, 2019, Characterizing Algeria tight reservoir cutting samples with virtual microscopy, petrography, mineralogy and digital petrophysics, *in* EAGE/ALNAFT Geoscience Workshop: European Association of Geoscientists & Engineers, p. 1–5.

Clarkson, C., J. Jensen, and S. Chipperfield, 2012, Unconventional gas reservoir evaluation: what do we have to consider? Journal of Natural Gas Science and Engineering, v. 8, p. 9–33.

Cnudde, V., and M. N. Boone, 2013, High-resolution X-ray computed tomography in geosciences: A review of the current technology and applications: Earth-Science Reviews, v. 123, p. 1–17, doi:10.1016/j.earscirev.2013.04.003.

Cnudde, V., B. Masschaele, M. Dierick, J. Vlassenbroeck, L. Van Hoorebeke, and P. Jacobs, 2006, Recent progress in X-ray CT as a geosciences tool: Applied geochemistry, v. 21, no. 5, p. 826–832.

Comisky, J. T., M. Santiago, B. McCollom, A. Buddhala, and K. E. Newsham, 2011, Sample size effects on the application of mercury injection capillary pressure for determining the storage capacity of tight gas and oil shales, *in* Canadian unconventional resources conference: OnePetro.

Daigle, H., A. Johnson, and B. Thomas, 2014, Determining fractal dimension from nuclear magnetic resonance data in rocks with internal magnetic field gradients: Geophysics, v. 79, no. 6, p. D425–D431.

Dang, S., S. Mamoudou, C. Rai, and C. Sondergeld, 2023, Experimental Observation of Diffusion as the Main Drive Mechanism in Unconventional Shales, *in* SPE/AAPG/SEG Unconventional Resources Technology Conference: URTEC, p. D031S064R002.

Dang, S., S. Mukherjee, C. Sondergeld, and C. Rai, 2021, Measurement of effective tortuosity in unconventional tight rock using nuclear magnetic resonance, *in* Unconventional Resources Technology Conference, 26–28 July 2021: Unconventional Resources Technology Conference (URTeC), p. 1476–1489.

Desbois, G., J. L. Urai, P. A. Kukla, J. Konstanty, and C. Baerle, 2011a, High-resolution 3D fabric and porosity model in a tight gas sandstone reservoir: A new approach to investigate microstructures from mm-to nm-scale combining argon beam cross-sectioning and SEM imaging: Journal of Petroleum Science and Engineering, v. 78, no. 2, p. 243–257.

Desbois, G., J. L. Urai, P. A. Kukla, J. Konstanty, and C. Baerle, 2011b, High-resolution 3D fabric and porosity model in a tight gas sandstone reservoir:A new approach to investigate microstructures from mm- to nm-scale combining argon beam cross-sectioning and SEM imaging: Journal of Petroleum Science and Engineering, v. 78, no. 2, p. 243–257, doi:10.1016/j.petrol.2011.06.004.

Dong, Z., S. Holditch, D. McVay, and W. B. Ayers, 2012, Global Unconventional Gas Resource Assessment: SPE Economics & Management, v. 4, no. 04, p. 222–234, doi:10.2118/148365-PA.

Economides, M. J., and D. A. Wood, 2009, The state of natural gas: Journal of Natural Gas Science and Engineering, v. 1, no. 1–2, p. 1–13.

Eltahan, E., M. Mehrabi, K. Sepehrnoori, and F. Javadpour, 2020, On the Inference of Gas Diffusion Coefficient in Organic Matter of Shale Gas Reservoirs, *in* SPE Annual Technical Conference and Exhibition? SPE, p. D031S039R007.

Evans, J., C. Cade, and S. Bryant, 1997, A Geological Approach to Permeability Prediction in Clastic Reservoirs: p. 91–101.

Gao, H., and H. A. Li, 2016, Pore structure characterization, permeability evaluation and enhanced gas recovery techniques of tight gas sandstones: Journal of Natural Gas Science and Engineering, v. 28, p. 536–547.

Ge, X., Y. Fan, J. Liu, D. Xing, H. Xu, and F. Hu, 2023, An empirical method to correct nuclear magnetic resonance porosity of tight sandstone using low-field nuclear magnetic resonance data: AAPG Bulletin, v. 107, no. 4, p. 539–551.

Giesche, H., 2006, Mercury porosimetry: a general (practical) overview: Particle & particle systems characterization, v. 23, no. 1, p. 9–19.

Golab, A. N., M. A. Knackstedt, H. Averdunk, T. Senden, A. R. Butcher, and P. Jaime, 2010, 3D porosity and mineralogy characterization in tight gas sandstones: The Leading Edge, v. 29, no. 12, p. 1476–1483.

Gou, Q., S. Xu, F. Hao, Z. Shu, and Z. Zhang, 2021, Making sense of micro-fractures to the Longmaxi shale reservoir quality in the Jiaoshiba area, Sichuan Basin, China: Implications for the accumulation of shale gas: Journal of Natural Gas Science and Engineering, v. 94, p. 104107.

Grasso, M., 2019, Oily politics: A critical assessment of the oil and gas industry's contribution to climate change: Energy Research & Social Science, v. 50, p. 106–115.

Greene, D. L., J. L. Hopson, and J. Li, 2006, Have we run out of oil yet? Oil peaking analysis from an optimist's perspective: Energy policy, v. 34, no. 5, p. 515–531.

Higgs, K. E., H. Zwingmann, A. G. Reyes, and R. H. Funnell, 2007, Diagenesis, Porosity Evolution, and Petroleum Emplacement in Tight Gas Reservoirs, Taranaki Basin, New Zealand: Journal of Sedimentary Research, v. 77, no. 12, p. 1003–1025, doi:10.2110/jsr.2007.095.

Holditch, S. A., 2006, Tight Gas Sands: Journal of Petroleum Technology, v. 58, no. 06, p. 86–93, doi:10.2118/103356-JPT.

Huang, H., L. Chen, W. Dang, T. Luo, W. Sun, Z. Jiang, X. Tang, S. Zhang, W. Ji, and S. Shao, 2019, Discussion on the rising segment of the mercury extrusion curve in the high pressure mercury intrusion experiment on shales: Marine and Petroleum Geology, v. 102, p. 615–624.

Huang, H., W. Sun, W. Ji, R. Zhang, K. Du, S. Zhang, D. Ren, Y. Wang, L. Chen, and X. Zhang, 2018, Effects of pore-throat structure on gas permeability in the tight sandstone reservoirs of the Upper Triassic Yanchang formation in the Western Ordos Basin, China: Journal of Petroleum Science and Engineering, v. 162, p. 602–616.

Huaqing, X., X. Ruina, J. Peixue, and Z. Shangwen, 2015, Characterization of rock microstructure using 3D X-ray computed tomography: 力学学报, v. 47, no. 6, p. 1073–1078.

Javadpour, F., H. Singh, A. Rabbani, M. Babaei, and S. Enayati, 2021, Gas flow models of shale: a review: Energy & Fuels, v. 35, no. 4, p. 2999–3010.

Jin, P., Y. Hu, J. Shao, Z. Liu, G. Feng, and S. Song, 2020, Influence of temperature on the structure of pore–fracture of sandstone: Rock Mechanics and Rock Engineering, v. 53, p. 1–12.

Jozanikohan, G., and M. N. Abarghooei, 2022, The Fourier transform infrared spectroscopy (FTIR) analysis for the clay mineralogy studies in a clastic reservoir: Journal of Petroleum Exploration and Production Technology, p. 1–14.

Kadkhodaie-Ilkhchi, R., A. Kadkhodaie, R. Rezaee, and V. Mehdipour, 2019, Unraveling the reservoir heterogeneity of the tight gas sandstones using the porosity conditioned facies modeling in the Whicher Range field, Perth Basin, Western Australia: Journal of Petroleum Science and Engineering, v. 176, p. 97–115.

Kala, S., 2022, Integrated geoscientific studies on unconventional permian shale gas resources of kommugudem and mandapeta area, krishna godavari basin, India, PhD Thesis: College of Engineering, UPES, Dehradun.

Keller, L. M., L. Holzer, R. Wepf, and P. Gasser, 2011, 3D geometry and topology of pore pathways in Opalinus clay: Implications for mass transport: Applied Clay Science, v. 52, no. 1–2, p. 85–95, doi:10.1016/j.clay.2011.02.003.

Krakowska, P., E. Puskarczyk, M. Jędrychowski, M. Habrat, P. Madejski, and M. Dohnalik, 2018, Innovative characterization of tight sandstones from Paleozoic basins in Poland using X-ray computed tomography supported by nuclear magnetic resonance and mercury porosimetry: Journal of Petroleum Science and Engineering, v. 166, p. 389–405.

Lai, J., and G. Wang, 2015, Fractal analysis of tight gas sandstones using high-pressure mercury intrusion techniques: Journal of Natural Gas Science and Engineering, v. 24, p. 185–196.

Lai, J., G. Wang, Z. Fan, J. Chen, S. Wang, Z. Zhou, and X. Fan, 2016, Insight into the pore structure of tight sandstones using NMR and HPMI measurements: Energy & Fuels, v. 30, no. 12, p. 10200–10214.

Lai, J., G. Wang, Y. Ran, and Z. Zhou, 2015, Predictive distribution of high-quality reservoirs of tight gas sandstones by linking diagenesis to depositional facies: Evidence from Xu-2 sandstones in the Penglai area of the central Sichuan basin, China: Journal of Natural Gas Science and Engineering, v. 23, p. 97–111, doi:10.1016/j.jngse.2015.01.026.

Lai, J., G. Wang, Z. Wang, J. Chen, X. Pang, S. Wang, Z. Zhou, Z. He, Z. Qin, and X. Fan, 2018, A review on pore structure characterization in tight sandstones: Earth-Science Reviews, v. 177, p. 436–457.

Lawal, L. O., A. R. Adebayo, M. Mahmoud, B. M. Dia, and A. S. Sultan, 2020, A novel NMR surface relaxivity measurements on rock cuttings for conventional and unconventional reservoirs: International Journal of Coal Geology, v. 231, p. 103605.

Lin, W., Z. Wu, X. Li, Z. Yang, M. Hu, D. Han, C. Wang, and J. Zhang, 2022, Digital characterization and fractal quantification of the pore structures of tight sandstone at multiple scales: Journal of Petroleum Exploration and Production Technology, v. 12, no. 9, p. 2565–2575.

Liu, X., J. Wang, L. Ge, F. Hu, C. Li, X. Li, J. Yu, H. Xu, S. Lu, and Q. Xue, 2017, Pore-scale characterization of tight sandstone in Yanchang Formation Ordos Basin China using micro-CT and SEM imaging from nm-to cm-scale: Fuel, v. 209, p. 254–264.

Long, H., C. Nardi, N. Idowu, A. Carnerup, P. E. Øren, M. Knackstedt, T. Varslot, R. M. Sok, and A. S. Lithicon, 2013, Multi-scale imaging and modeling workflow to capture and characterize microporosity in sandstone, *in* International Symposium of the Society of Core Analysts, Napa Valley, California, USA.

Loucks, R., R. Reed, S. Ruppel, and U. Hammes, 2012, Spectrum of pore types and networks in mudrocks and a descriptive classification for matrix related pores: AAPG Bulletin, v. 96, p. 1071–1098, doi:10.1306/08171111061.

Lv, M., H. Cui, Y. Lei, K. Lei, and Y. Zhu, 2023, Study on reasonable production allocation method of tight sandstone gas reservoir—A case of XX block in ordos basin: Frontiers in Energy Research, v. 10, p. 1021989.

McGlade, C., J. Speirs, and S. Sorrell, 2013, Unconventional gas – A review of regional and global resource estimates: Energy, v. 55, p. 571–584, doi:10.1016/j.energy.2013.01.048.

McKinley, J. M., P. M. Atkinson, C. D. Lloyd, A. H. Ruffell, and R. H. Worden, 2011, How porosity and permeability vary spatially with grain size, sorting, cement volume, and mineral dissolution in fluvial Triassic sandstones: the value of geostatistics and local regression: Journal of Sedimentary Research, v. 81, no. 12, p. 844–858.

Mustafa, A., M. A. Mahmoud, and A. Abdulraheem, 2019, A review of pore structure characterization of unconventional tight reservoirs, *in* Abu Dhabi International Petroleum Exhibition and Conference: SPE, p. D031S098R001.

Nehring, R., 2009, Traversing the mountaintop: world fossil fuel production to 2050: Philosophical Transactions of the Royal Society B: Biological Sciences, v. 364, no. 1532, p. 3067–3079.

Nelson, P. H., 2009, Pore-throat sizes in sandstones, tight sandstones, and shales: AAPG Bulletin, v. 93, no. 3, p. 329–340, doi:10.1306/10240808059.

Netto, A., 1993, Pore-Size Distribution in Sandstones: GEOLOGIC NOTE: Aapg Bulletin, v. 77, no. 6, p. 1101–1104.

Oluwadebi, A. G., K. G. Taylor, and L. Ma, 2019, A case study on 3D characterisation of pore structure in a tight sandstone gas reservoir: The Collyhurst Sandstone, East Irish Sea Basin, northern England: Journal of Natural Gas Science and Engineering, v. 68, p. 102917.

Pang, X.-Q., C.-Z. Jia, and W.-Y. Wang, 2015, Petroleum geology features and research developments of hydrocarbon accumulation in deep petroliferous basins: Petroleum Science, v. 12, p. 1–53.

Pang, Y., M. Y. Soliman, H. Deng, and X. Xie, 2017, Experimental and analytical investigation of adsorption effects on shale gas transport in organic nanopores: Fuel, v. 199, p. 272–288.

Philipp, T., A. Amann-Hildenbrand, B. Laurich, G. Desbois, R. Littke, and J. L. Urai, 2017, The effect of microstructural heterogeneity on pore size distribution and permeability in Opalinus Clay (Mont Terri, Switzerland): insights from an integrated study of laboratory fluid flow and pore morphology from BIB-SEM images: Geological Society, London, Special Publications, v. 454, no. 1, p. 85–106.

Qiao, J., J. Zeng, J. Cai, S. Jiang, T. An, E. Xiao, Y. Zhang, X. Feng, and G. Yang, 2021, Pore-scale heterogeneity of tight gas sandstone: Origins and impacts: Journal of Natural Gas Science and Engineering, v. 96, p. 104248.

Qiao, J., J. Zeng, D. Chen, J. Cai, S. Jiang, E. Xiao, Y. Zhang, X. Feng, and S. Feng, 2022, Permeability estimation of tight sandstone from pore structure characterization: Marine and Petroleum Geology, v. 135, p. 105382.

Qu, Z. G., Y. Yin, H. Wang, and J. F. Zhang, 2020, Pore-scale investigation on coupled diffusion mechanisms of free and adsorbed gases in nanoporous organic matter: Fuel, v. 260, p. 116423.

Ramandi, H. L., P. Mostaghimi, R. T. Armstrong, M. Saadatfar, and W. V. Pinczewski, 2016, Porosity and permeability characterization of coal: a micro-computed tomography study: International Journal of Coal Geology, v. 154, p. 57–68.

Rezaee, R., A. Saeedi, and B. Clennell, 2012, Tight gas sands permeability estimation from mercury injection capillary pressure and nuclear magnetic resonance data: Journal of Petroleum Science and Engineering, v. 88, p. 92–99.

Riepe, L., M. H. Suhaimi, M. K. Malaysia, and M. A. Knackstedt, 2011, Application of high resolution Micro-CT imaging and pore network modeling (PNM) for the petrophysical characterization of tight gas reservoirs-a case history from a deep clastic tight gas reservoir in Oman, *in* SPE Middle East unconventional gas conference and exhibition: OnePetro.

Ross, D. J., and R. M. Bustin, 2008, Characterizing the shale gas resource potential of Devonian–Mississippian strata in the Western Canada sedimentary basin: Application of an integrated formation evaluation: AAPG bulletin, v. 92, no. 1, p. 87–125.

Ross, D. J., and R. M. Bustin, 2009, The importance of shale composition and pore structure upon gas storage potential of shale gas reservoirs: Marine and petroleum Geology, v. 26, no. 6, p. 916–927.

Sakellariou, A., T. J. Sawkins, T. J. Senden, C. H. Arns, A. Limaye, A. P. Sheppard, R. M. Sok, M. A. Knackstedt, W. V. Pinczewski, and L. I. Berge, 2003, Micro-CT facility for imaging reservoir rocks at pore scales, *in* SEG International Exposition and Annual Meeting: SEG, p. SEG-2003.

Schmitt, M., C. P. Fernandes, F. G. Wolf, J. A. B. da Cunha Neto, C. P. Rahner, and V. S. S. dos Santos, 2015, Characterization of Brazilian tight gas sandstones relating permeability and Angstrom-to micron-scale pore structures: Journal of Natural Gas Science and Engineering, v. 27, p. 785–807.

Shan, B., R. Wang, Z. Guo, and P. Wang, 2021, Contribution quantification of nanoscale gas transport in shale based on strongly inhomogeneous kinetic model: Energy, v. 228, p. 120545.

Shao, X., X. Pang, F. Jiang, L. Li, Y. Huyan, and D. Zheng, 2017, Reservoir characterization of tight sandstones using nuclear magnetic resonance and incremental pressure mercury injection experiments: implication for tight sand gas reservoir quality: Energy & Fuels, v. 31, no. 10, p. 10420–10431.

Sheng, G., Y. Su, F. Javadpour, W. Wang, S. Zhan, J. Liu, and Z. Zhong, 2020, New slip coefficient model considering adsorbed gas diffusion in shale gas reservoirs: Energy & Fuels, v. 34, no. 10, p. 12078–12087.

Shepherd, R. G., 1989, Correlations of permeability and grain size: Groundwater, v. 27, no. 5, p. 633–638.

Stauber, M., and R. Müller, 2008, Micro-Computed Tomography: A Method for the Non-Destructive Evaluation of the Three-Dimensional Structure of Biological Specimens, *in* J. J. Westendorf, ed., Osteoporosis: Methods and Protocols: Totowa, NJ, Humana Press, Methods In Molecular Biology™, p. 273–292, doi:10.1007/978-1-59745-104-8_19.

Stroker, T. M., N. B. Harris, W. C. Elliott, and J. M. Wampler, 2013, Diagenesis of a tight gas sand reservoir: upper Cretaceous Mesaverde Group, Piceance Basin, Colorado: Marine and Petroleum Geology, v. 40, p. 48–68.

Su, Y., M. Zha, L. Jiang, X. Ding, J. Qu, J. Jin, and S. Iglauer, 2022, Pore structure and fluid distribution of tight sandstone by the combined use of SEM, MICP and X-ray micro-CT: Journal of Petroleum Science and Engineering, v. 208, p. 109241.

Sun, H., J. Yao, Y. Cao, D. Fan, and L. Zhang, 2017, Characterization of gas transport behaviors in shale gas and tight gas reservoirs by digital rock analysis: International Journal of Heat and Mass Transfer, v. 104, p. 227–239.

Tandon, S., Z. Heidari, and H. Daigle, 2017, Pore-Scale Evaluation of Nuclear Magnetic Resonance Measurements in Organic-Rich Mudrocks Using Numerical Modeling, *in* SPE/AAPG/SEG Unconventional Resources Technology Conference: URTEC, p. URTEC-2674057.

Taylor, T. R., M. R. Giles, L. A. Hathon, T. N. Diggs, N. R. Braunsdorf, G. V. Birbiglia, M. G. Kittridge, C. I. Macaulay, and I. S. Espejo, 2010, Sandstone diagenesis and reservoir quality prediction: Models, myths, and reality: AAPG Bulletin, v. 94, no. 8, p. 1093–1132, doi:10.1306/04211009123.

Valenza, J. J., J. Moore, S. Sanguinito, and D. Crandall, 2022, Visualizing fracture-matrix fluid exchange in unconventional tight mudstone, *in* Unconventional Resources Technology Conference, 20–22 June 2022: Unconventional Resources Technology Conference (URTeC), p. 898–917.

Wang, G., F. Hao, W. Zhang, H. Zou, and P. Li, 2022, Characterization and origin of micropores in tight gas grainstones of the Lower Triassic Feixianguan Formation in the Jiannan gas field, Sichuan Basin: Marine and Petroleum Geology, v. 139, p. 105609.

Wang, Z., Yancheng Liu, S. Lu, L. Lin, N. Zhou, and Yang Liu, 2023, Differential development characteristics of secondary pores and effects on pore structure and movable fluid distribution in tight gas sandstones in the lower Permian, northeastern Ordos Basin, China: Geoenergy Science and Engineering, v. 224, p. 211580.

Wang, T., S. Tian, G. Li, and P. Zhang, 2019, Analytical model for real gas transport in shale reservoirs with surface diffusion of adsorbed gas: Industrial & Engineering Chemistry Research, v. 58, no. 51, p. 23481–23489.

Wang, W., R. Wang, L. Wang, Z. Qu, X. Ding, C. Gao, and W. Meng, 2023, Pore Structure and Fractal Characteristics of Tight Sandstones Based on Nuclear Magnetic Resonance: A Case Study in the Triassic Yanchang Formation of the Ordos Basin, China: ACS omega, v. 8, no. 18, p. 16284–16297.

Wang, L., S. Wang, R. Zhang, C. Wang, Y. Xiong, X. Zheng, S. Li, K. Jin, and Z. Rui, 2017, Review of multi-scale and multi-physical simulation technologies for shale and tight gas reservoirs: Journal of Natural Gas Science and Engineering, v. 37, p. 560–578.

Wu, Y., C. Liu, S. Ouyang, B. Luo, D. Zhao, W. Sun, R. S. Awan, Z. Lu, G. Li, and Q. Zang, 2022, Investigation of pore-throat structure and fractal characteristics of tight sandstones using HPMI, CRMI, and NMR methods: A case study of the lower Shihezi Formation in the Sulige area, Ordos Basin: Journal of Petroleum Science and Engineering, v. 210, p. 110053.

Xi, K., Y. Cao, B. G. Haile, R. Zhu, J. Jahren, K. Bjørlykke, X. Zhang, and H. Hellevang, 2016, How does the pore-throat size control the reservoir quality and oiliness of tight sandstones? The case of the Lower Cretaceous Quantou Formation in the southern Songliao Basin, China: Marine and Petroleum Geology, v. 76, p. 1–15, doi:10.1016/j.marpetgeo.2016.05.001.

Xiao, D., Z. Lu, S. Jiang, and S. Lu, 2016, Comparison and integration of experimental methods to characterize the full-range pore features of tight gas sandstone—A case study in Songliao Basin of China: Journal of Natural Gas Science and Engineering, v. 34, p. 1412–1421.

Xiao, D., S. Lu, J. Yang, L. Zhang, and B. Li, 2017, Classifying multiscale pores and investigating their relationship with porosity and permeability in tight sandstone gas reservoirs: Energy & Fuels, v. 31, no. 9, p. 9188–9200.

Xiong, Q., T. G. Baychev, and A. P. Jivkov, 2016, Review of pore network modelling of porous media: Experimental characterisations, network constructions and applications to reactive transport: Journal of Contaminant Hydrology, v. 192, p. 101–117, doi:10.1016/j.jconhyd.2016.07.002.

Zhang, P., Y. I. Lee, and J. Zhang, 2019, A review of high-resolution X-ray computed tomography applied to petroleum geology and a case study: Micron, v. 124, p. 102702.

Zhang, L., S. Lu, D. Xiao, and B. Li, 2017, Pore structure characteristics of tight sandstones in the northern Songliao Basin, China: Marine and Petroleum Geology, v. 88, p. 170–180, doi:10.1016/j.marpetgeo.2017.08.005.

Zhang, J., Y. Zeng, and R. Slatt, 2019, XRF (X-ray fluorescence) applied to characterization of unconventional Woodford Shale (Devonian, USA) lateral well heterogeneity: Fuel, v. 254, p. 115565.

Zhu, H., C. Huang, Y. Ju, H. Bu, X. Li, M. Yang, Q. Chu, H. Feng, P. Qiao, and Y. Qi, 2021, Multi-scale multi-dimensional characterization of clay-hosted pore networks of shale using FIBSEM, TEM, and X-ray micro-tomography: Implications for methane storage and migration: Applied Clay Science, v. 213, p. 106239.

Ziarani, A. S., and R. Aguilera, 2012, Pore-throat radius and tortuosity estimation from formation resistivity data for tight-gas sandstone reservoirs: Journal of Applied Geophysics, v. 83, p. 65–73.

Zou, C., R. Zhu, K. Liu, L. Su, B. Bai, X. Zhang, X. Yuan, and J. Wang, 2012, Tight gas sandstone reservoirs in China: characteristics and recognition criteria: Journal of Petroleum Science and Engineering, v. 88–89, p. 82–91, doi:10.1016/j.petrol.2012.02.001.

Blank Page

Chapter 7:

Synthesis, conclusion, and recommendation for future work.

Contents

Chapter Seven:

Synthesis, Conclusion, and Recommendation for future work.

7.1 Synopsis

This last chapter presents a synopsis of the main findings of this study.

This research study has analysed and characterised the Breagh Sandstone within the Lower Carboniferous, of the Southern North Sea (SNS) at a variety of scales to assess its petrography, lithofacies, and diagenetic processes (Fig 7.1), and thereby understand the diagenetic controls on reservoir quality and pore network of the studied reservoir.

This study utilized data from three offshore subsurface wells (42/13-2, 42/13-4 and 42/13a-6) from the Breagh Field as well as the interpreted Seismic lines from the PGS MegaSurvey 2015 and the INEOS Lochran 3D surveys.

This chapter integrates all the observations and assesses the results in line with the stated aims and objectives. The main objectives of the study were to: (1) determine the large-scale architecture of the sandstone and understand the facies development as well as the depositional setting; (2) assess the petrographic and mineralogical composition, of the studied sandstone towards the reconstruction of diagenetic sequence and understand the control on reservoir quality (3) model the pore system using both 2D-SEM image analysis and X-ray computed tomography (4) Link measurements of permeabilities, pore structures and digenetic minerals in order to understand and thus predict how differences in diagenesis control flow properties in low permeability sandstones. Future research work is also mentioned in this chapter.

The study provides insights into how lithofacies (primary composition, texture and sorting) and diagenesis can influence reservoir qualities of tight gas sandstones.

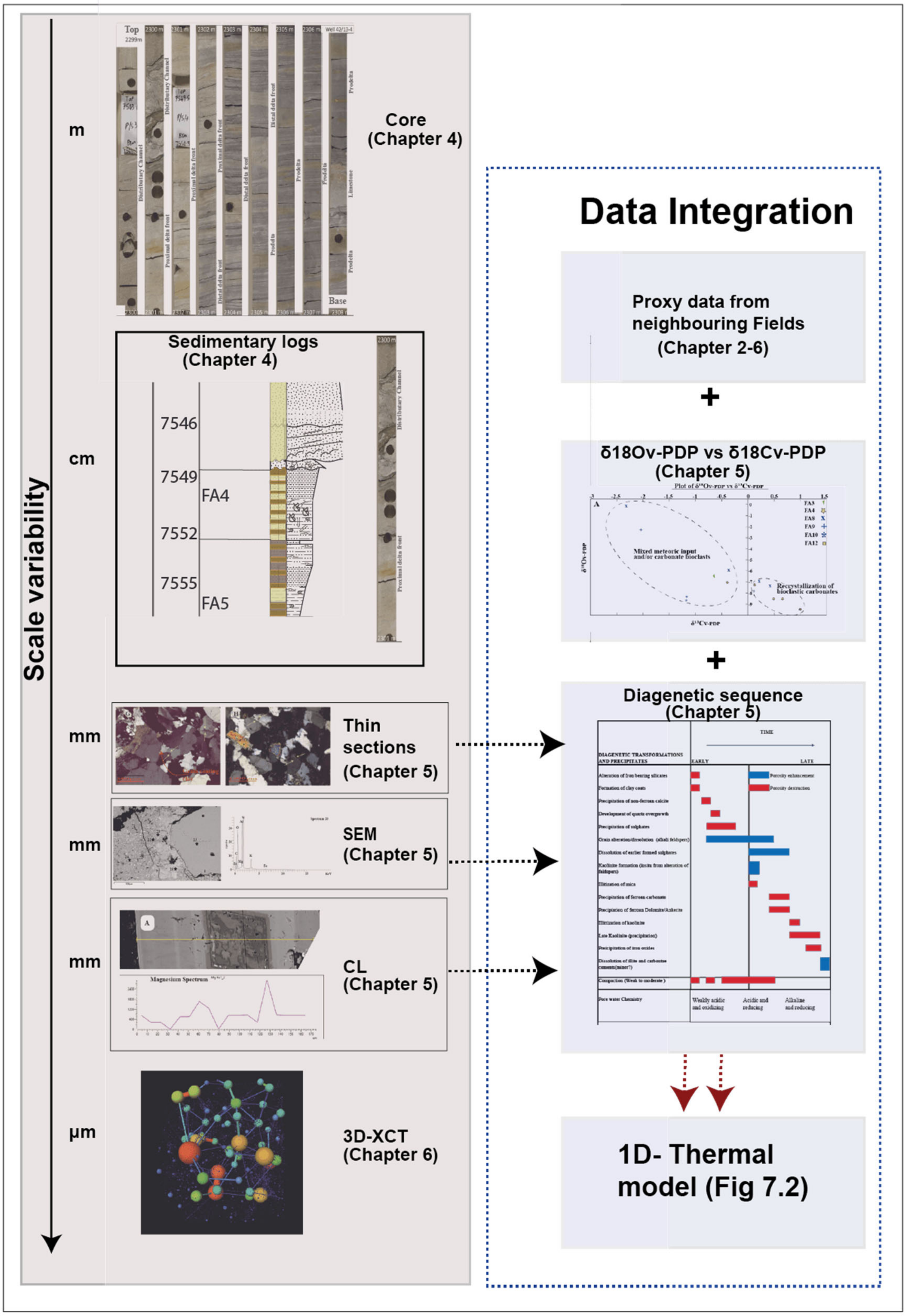

Figure 7.1: Scale of analysis (left side of Figure); and right side of Figure) Integration of petrographic, mineralogical, and stable isotope data in predicting reservoir quality of the studied sandstone.

7.2 Research summary/conclusion

Discovery of the Breagh gas field in the SNS demonstrates that the Dinantian (Visean, 346.7–330.9 Ma) reservoirs have potential to contribute to the UK's future energy mix (Booth *et al*., 2020) and provides encouragement for Lower Carboniferous clastic prospectivity in the SNS (Rodriguez *et al*., 2014; Brackenridge *et al*., 2020; Grant *et al*., 2020).

The Breagh Field (Chapter 3-Fig. 3. 2) contains a low permeability sandstone reservoir. The field lies approximately 40 miles (64 km) west of the decommissioned Esmond Field (Block 43/13a), 32 miles (51 km) NW of the Garrow Field (Block 42/25a and 43/21a), 38 miles (61 km) NE of Flamborough Head on the Yorkshire coast and 53 miles (85 km) WNW of the INEOS Oil and Gas UK-operated Cavendish Field (Block 43/19a). It lies within Quadrant 42 of the UK Southern North Sea (SNS), immediately to the north of the Sole Pit Basin. It is very close to the southern edge of the Mid North Sea High (Glennie, 1986). At this position, it forms part of the southern flank of the MNSH and is the most westerly of the fields with Carboniferous age reservoir in the SNS and northeast of the pinchout of the Lower Permian Rotliegend Group sandstones (Fig. 3. 1).

The field has an area of 94 km^2 below a four-way dip closure at the Base Permian Unconformity (BPU) (Fig. 3.3). The field has gas initially in place (GIIP) of approximately 1 tcf in the Early Carboniferous (Mississippian) Yoredale Formation, also known as the Middle Limestone Formation of the Yoredale Group onshore UK (Mclean, 2011).

The Breagh Sandstone is an important gas reservoir in the UK Southern North Sea and the Breagh Field is the first to be developed within the Early Carboniferous interval in the UK SNS. The discovery well 42/13-2 encountered a 121m of gas column within the Early Carboniferous Visean aged Yoredale Formation sandstones, and subsequent wells have indicated that the field contains a P50 reserve of 552Bcf (15.6Bcm) (Nwachukwu *et al*., 2020), with 2 MMbbl (0.32MMSm^3) recoverable condensate, making it the 60th largest gas field in the UK, in terms of ultimate recoverable reserves (Grant *et al*., 2020).

Eleven facies associations namely Limestone (FA1), prodelta (FA2), distributary mouthbar (FA3), proximal delta front sands (FA4), distal delta front sands (FA5), interdistributary bay

(FA7), distributary channel (FA8), braided fluvial channel (FA9), abandoned channel (FA10), crevasse splay (FA11) and swamp (FA12) have been identified from the studied cores. They have been grouped into marine, prodelta, delta front, and delta plain gross depositional environments as tabularized in (Table 7.1).

The facies associations are interpreted as deposited in a mixed carbonate and siliciclastic fluvio-deltaic environment and are arranged into coarsening- and cleaning-upward cycles (parasequences) bounded by flooding surfaces which is at either the base of a limestone (FA1) or a marine deposit that lies directly on top of a more proximal deposit. The facies associations record the vertical and lateral changes in delta morphology because of autocyclic and allocyclic processes within an evolving rift setting. The depositional processes that formed each cycle have important implications for the eventual reservoir quality (Symonds *et al*., 2015; Booth *et al*., 2020; Nwachukwu *et al*., 2020) and reservoir prediction away from the Breagh area into other areas of the SNS.

Table 7.2: Summary of interpreted facies associations, depositional palaeoenvironments, and study wells where facies are present. Key defining criteria- bioturbation index adapted from Taylor et al. 2003. Table format is modified after Booth et al 2020.- see also appendix 2 for lithofacies description.

ENVIRONMENT	SUBENVIRONMENT	FACIES ASSOCIATION	DESCRIPTION
Delta Plain	Swamp	FA12	Mudstones, siltstones and current-rippled and/or climbing current-rippled fine sandstones that are typically overlain by coal. Rooted horizons are observed. Weakly to highly bioturbated (0-4)
	Crevasse Splay	FA11	Erosive-based, fine to medium grained sandstone. Often upward-fining. The sandstone is moderately- to well-sorted and display cross-stratification at the base with current-ripple lamination dominating upwards. Abundant carbonaceous plant material throughout. Very weakly bioturbated (0-1)
	Abandoned Channel	FA10	Heterolithic very-fine- to fine-grained sandstones and siltstones with current ripples, occasional thin trough cross- bedding. It has deformed/slumped horizons and rooted bed tops. Includes bioturbated horizons (0-2)
	Braided fluvial channel	FA9	Erosive-based, medium to coarse grained sandstones with planar cross beds or trough cross-beds. The bases are very coarse and occasionally pebbly. The bottom horizons also contain occasional rip up clast and plant material. Bioturbation is not visible (0-1)
	Distributary Channel	FA8	Erosive-based, well-sorted, fine- to medium-grained sandstone. It consists of occasional coal clasts and plant debris.
	Interdistributary Bay	FA7	Very-fine- to fine-grained sandstones with lenticular or flaser bedding, parallel lamination, wave and current ripples. Also consist of heterolithic mudstones and siltstones. slump and water escape structures are visible. Weakly to highly bioturbated (3-5)

Delta front	Distal Delta Front sand	FA5	Alternating between muddy siltstone and silty sandstones with decemeter sized climbing ripples, wave formed ripples, horizontal planar lamination, Parallel- to ripple-laminated siltstones, and very-fine-grained sandstone. Abundant plant material are common along bedding planes. Siderite concretions are also visible. Sparsely to highly bioturbated (1-4)
	Proximal Delta Fronts Sand	FA4	Muddy, very-fine- to fine-grained sandstone with coarsening upward vertical profiles. Silt drapes are found within the sandstones. Silty mudstone and the mudstones display climbing ripples whilst the siltstones have planar parallel lamination. Abundant plant material and common coal clasts are preserved. Sparsely to weakly bioturbated (1-3)
	Distributary mouth bar	FA3	Well-sorted, medium to coarse -grained sandstones displaying trough crossbedding. Occasionally pebbly with coarse- to very- coarse-grained erosive bed bases, with rip up and coal clasts. Sparsely to moderately bioturbated (1-3)
Pro-delta	Prodelta	FA2	Dark grey massive mudstones. Sometimes laminated, with crinoid and brachiopod debris near the base. Siderite nodules are common. This FA contains rare soft-sediment deformation including convolute lamination and slump structures. Bioturbation is not common (0-1)
Carbonate Platform	Limestone	FA1	Highly bioturbated (5-6) fossiliferous limestone (corals and rugose corals), crinoid ossicles, brachiopods, bryozoa. Also, as part of this FA is muddy limestones and some mudstone partings.

Based on the classification scheme of (Pettijohn, 1957), the sandstone of the studied wells range from quartz arenite to sublitharenite. The majority of samples from both wells falls within the quartzarenite group and fewer samples are sublitharenite (Chapter 5-Table 5.; Figure 5.). Petrographic analysis of the samples indicates that the detrital grains of the Breagh Sandstone consist of very fine grained to coarse grained sandstones (with granule particles at intervals) although the medium grain ranges predominate (Chapter 5.2, Figure A- E). The grains are mostly subangular to subrounded with locally angular grains (Table 5., Figure A- E).

Compositionally, quartz is the dominant detrital mineral (25-82.3% - av. 65%) (Table 5.1 and Fig 5.1) and it is dominated by monocrystalline grains, with subordinate polycrystalline and microcrystalline grains. XRD analysis from well report corroborates the data that quartz is abundant in all samples (18-85 wt%). Feldspars are generally absent and where present is very scant (1-2counts/ per 300grains); as noted under XRD, Feldspars only make up: 0-1 wt% are composed of both potassium and plagioclase feldspar. Significant dissolution of Feldspars occurs in all samples where feldspars are seen (Figure 5.2d).

Rock fragments are dominated by mud clast but also comprise of granite, mica schist grains, quartz-schist, and volcanics. They make up (trace to 2.3%, - av. 0.3%) of the grains (Table 5.1).

The quartz schist grains are stable and show little deformation or alteration, whereas the mica schist and phyllite grains show varying degrees of deformation, alteration (mainly to kaolinite and illite) and in some cases dissolution.

Detrital micas (Trace-13.7%, av. 3%) are present in all samples in trace to minor abundances with high percentages occurring in mudrock rich sections. They also have higher abundances in the mudstones samples which are not analysed for this study. The mica minerals are predominantly muscovite with some local biotite observed under SEM. Although they appear commonly well preserved at the scale of thin section, but SEM analysis reveals that they are locally deformed **(**Figure 5.2Fi-ii). Splitting and fanning of the mica grains also occurs as observed in (Fig 5.2Fi-ii, & 5.16 k, l). Petrographic observations identify mica grain bending (Fig.5.2Fii &5.16 k, l) and the fracturing of quartz grains. Compaction thus contributed to permeability loss within the reservoir, by the deformation and bending of lithic grains, ductile grains get crushed and extruding between rigid sands grains, block pore throats and reduce the pore connectivity (Morad, 1990; Chi *et al*., 2003; Aagaard and Jahren, 2010).

Reservoirs sandstones in the Breagh Field comprises a mixture of sand sheets and channels. The Breagh sandstones have a wide range of porosity and permeability (ϕ = 0.1% - 19% and K= 0.1 mD – 379 mD) (Fig 5.5). The reservoir properties of the sandstone are relatively poor although the best reservoir intervals are found in the channel sands (FA3, FA8, FA9, and FA10) have permeability in the range 0.1 to 100 mD. (Most permeabilities are 1-10mD) and porosities in the range of 9.5–19.6% (average 11.6%). The non-channel sands (FA1, FA2, FA4, FA5, FA6, FA7 and FA11) all have porosities less than 10% and permeabilities ranges 0.1mD and 1mD (Fig 5.5).

Compaction processes rather than cementation accounts for the major destruction of the initial sandstone porosity. The COPL-CEPL results (Fig 5.4) show porosity loss for all sample sets were predominantly by mechanical compaction (Fig 5.4), with averages of 22.6% and 27.68% for the 42/13-2 and 42/13-4 sample sets, respectively. But cementation still accounts for up to 17.4% and 14.8% of porosity loss in the 42/13-2 for the 42/13-4 sample sets respectively.

The main diagenetic processes identified in the studied samples include cementation by carbonate, clay minerals and quartz cements (Fig 5.6 & 5.7). The vertical distribution of major cements in 42/13-4 and 42/13-2 well is shown in (Fig. 5.7). Clay mineral (kaolinite and illite rich clays) and carbonate (mainly dolomite and ankerite) cements are the most common pore-filling cements, followed by authigenic quartz cement and bituminous hydrocarbon. Hematite, pyrite, anhydrite and barite, are minor cements.

Contrasting characteristics between the reservoir units suggest the development of divergent diagenetic pathways. Features including at least 10 diagenetic events were observed on the studied sandstones. They are: (i) precipitation of early sulphate cements (ii) development of early quartz overgrowth (iii) initial mechanical compaction (iv) alteration and dissolution of framework grains and early diagenetic cements (v) significant secondary porosity created by cement and framework-grain dissolution (vi) precipitation of kaolinite (vii) precipitation of zoned and mottled textured iron- rich carbonate cements, (viii) at least two generations of authigenic illite, (ix) precipitation of anhydrite, halite and baryte cements and, (x) subsequent though minor dissolution of the late diagenetic illite and carbonate cement.

More than 50% of the visual porosity in the studied sandstones are noted to be secondary in origin after dissolution of sulphate cements but also to a lesser degree, dissolution of carbonate cements and unstable grains. Such secondary pore spaces have also made possible sites for significant precipitation of authigenic clay minerals, authigenic quartz, and associated intragranular and inter-crystalline microporosity that further damaged reservoir quality. Clay minerals bridge and occlude pores, resulting in further destruction of the reservoir quality.

A stacked aggregate of vermicular kaolinite is observed to occlude and fill intergranular pore, thus reducing the sandstone permeability. Kaolinite accounts for approximately 60% of the of the observed cement in the study area thereby making kaolinite the most significant diagenetic cement in the study area. Illitic clays are the second most abundant diagenetic minerals in the Breagh field samples. They account for approx. 40% of the diagenetic cements and are observed to have the most damaging effect on the permeability of the sample sets within this study. Although it was difficult discriminating detrital quartz grain from overgrowth using standard petrography, it was however observed (see Fig 5.22b) that the highest porosity ranges (samples with porosity 9%-25%) are in samples with no discernible quartz cement. Carbonate cements mostly fill intergranular pores, thus block pore throat, and prevent migration of fluid. The pattern and sequence of the diagenetic features observed in studied samples reveal that three pore-fluid regimes can be identified: (1) weakly acidic oxidizing pore waters during shallow to intermediate burial; (2) acid, reducing condition intermediate to deep burial; (3) alkaline, reducing conditions during deep burial and uplift.

The creation and destruction of secondary porosity is the result of changes in porewater chemistry during burial and subsequent uplift (Fig 7.2). Precipitation of quartz, calcite, dolomite, anhydrite, kaolinite, smectite, and illite as authigenic cements is mainly controlled by fluid flow, pore fluid chemistry and the temperature, which have all acted to reduce the reservoir quality in the studied samples.

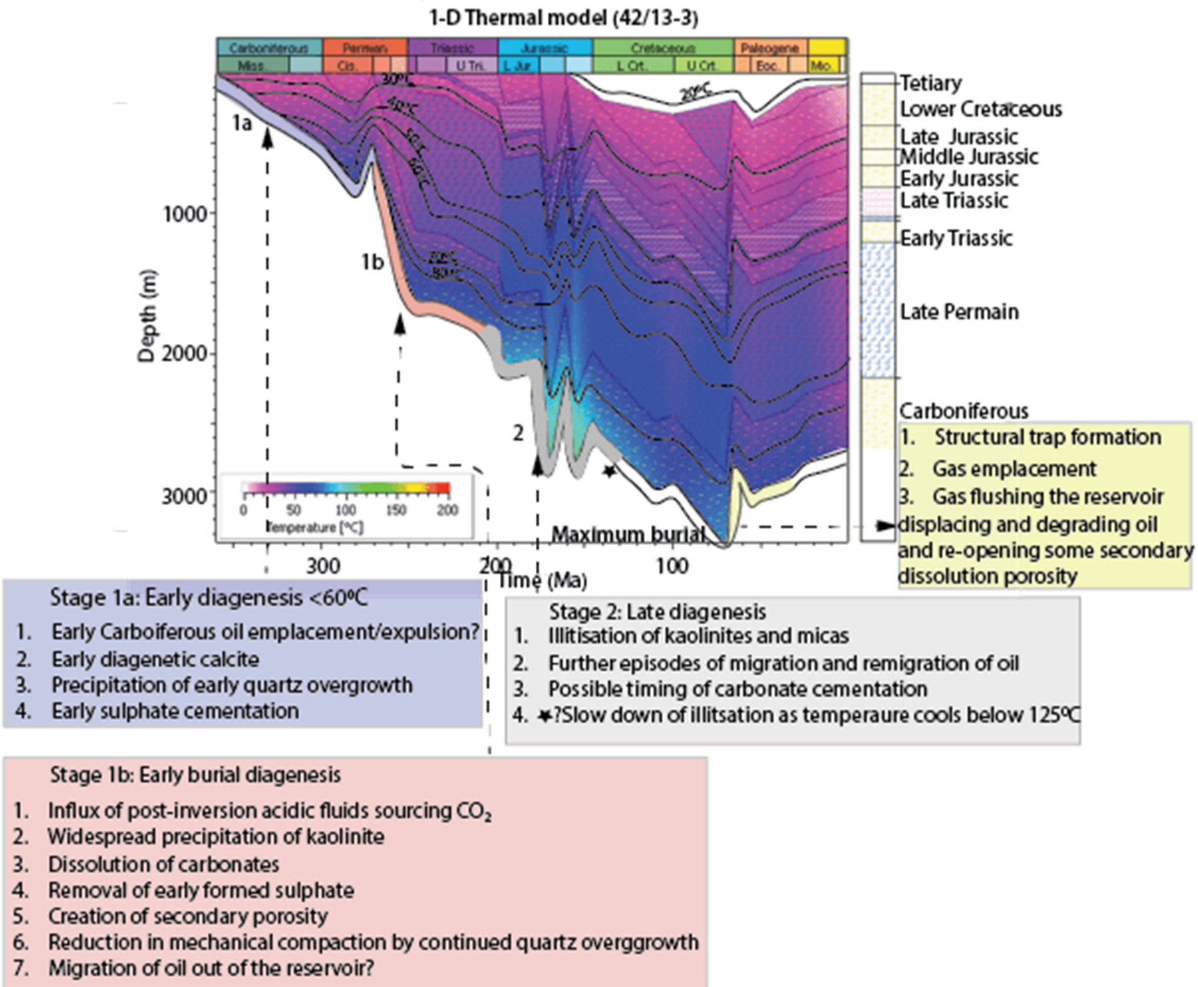

Figure 7.2: Interpreted 1D Burial thermal plot for the Breagh field using wells 42/13-3..

Further analysis of the pore microstructure using 2D SEM images and XCT allowed identification of pore types, geometry, distribution, and interconnectivity. Three types of pores were identified: inter-grain pores, intra-grains pores and intra-cement pores. Pore network system of the representative sandstone samples was also extracted. Pore size radius, pores type and interconnectivity controls permeability as well as fluid flow in a reservoir and in turn controlled by the grain size distribution (Lawal *et al.*, 2020) and volume of diagenetic cement. The approach of 3D modelling demonstrated in this study offers provision for quantification of individual pore types in terms of pore volume, area, shape as well as the pore network significant in building the spatial distribution and connectivity of the pore system. The extracted pore networks here will be a good input in predicting multi-phase flow properties of the studied reservoir.

7.3 Implication for Hydrocarbon Exploration

In the 1970's, the US government defined a tight gas reservoir as one in which the expected value of permeability to gas flow is less than 0.1mD (Holditch, 2013). It was a political definition that was used to determine which wells would receive federal and/or state tax credits for producing gas from a tight gas reservoir. In the UK, it has been defined as one with average permeability values ranging from as low as 0.01 to 1mD (OGA, 2017). Technological advances have enabled successful Southern North Sea 'tight gas' offshore field developments: Ensign, Chiswick, Babbage, Clipper South and indeed the Breagh as the first within the Lower Carboniferous stratigraphy. A combination of horizontal and hydraulic fracturing technology was applied to exploit these reservoirs (OGA, 2017).

The technical definition of a tight gas reservoir is infact a function of many physical and economic factors including flow rate, average reservoir pressure, flowing pressure, fluid properties, reservoir temperature, permeability, net pay thickness, drainage radius, well bore radius, skin factor and non-Darcy flow constant as seen equation below from (Lee, 1982).

$$P_{wf}{}^{2} = \bar{P}^{2} \text{ . } 1{,}422\frac{\mu_{\bar{p}} z_{\bar{p}g} T q_g}{kh}\left[ln\left(\frac{r_e}{r_w}\right) - 0.75 + \left(s + D\left|q_g\right|\right)\right]$$

Where the flow rate q, is a function of average reservoir pressure, flowing pressure, $p_{wf,}$ fluid properties $u_{\bar{p}}$ and$z_{\bar{p}g}$, and reservoir temperature, Permeability K, net pay thickness h, drainage radius r_e, well bore radius r_w, skin factor *s*, and a non-darcy flow constant *D*.

Hence the best definition of tight gas reservoir will be one that cannot be produced at an economic flow rate nor recover economic volumes of natural gas unless the well is stimulated by a large hydraulic fracture treatment or produce using horizontal well bore or multilateral well bores (Holditch, 2013; OGA, 2017).

The integrated approach of sedimentological, petrographic, geochemical, and pore-scale observation applied in this research has been useful to characterize how diagenesis affect important parameters of flow in a tight gas reservoir. Diagenesis has significant implications for the development and destruction of reservoir quality (porosity and permeability) of sandstones by controlling the development of pore types, pore geometry, and pore distribution.

Additionally, pore structure analysis with 2D-SEM image analysis and 3D-XCT allow identification of pore types, pore geometry, and pore distribution. These have significant implications for pore connectivity, gas storage and fluid flow capacity and could also lead to the further understanding of petrophysical properties such as relative permeability and multi-phase flow simulation (Oluwadebi *et al*., 2019). Although, porosity and permeability are the most important reservoir properties, however, pore geometry and wetting phase properties of a porous media may also influence petroleum production (Li *et al*., 2022; Qin *et al*., 2023).

The study here would also be a useful tool in understanding the control on reservoir quality in similar tight sandstone setting where the distribution of authigenic minerals, chemical reactions, and migration pathways are unclear. With further exploration into prospectivity away from the Breagh area into other areas of the SNS, integration of the diagenetic sequence (Fig 5.13) and basin models (Fig 7.1) would be useful to predict how the processes of generation, expulsion, migration, trapping, and preservation control the volumetrics, quality, and distribution of gas in the prospective reservoir.

Furthermore, the understanding of the depositional process and environment have important implications for the reservoir net/gross ratio thickness and lateral extent. In general, findings from this study provide conditioning information useful in predicting reservoir quality and may input into reservoir and hydrocarbon models to inform and guide future exploration and appraisal, as well as development and production in similar and more complex tight-gas sandstone settings.

An additional benefit for the current study may be in petroleum engineering, a thorough study of the permeability and pore network could be useful in the choice and design of drilling mud with future exploration and drilling. A careful evaluation of the Breagh Field discovery well 42/13-2 by the operator at the time the Breagh Field became commercial revealed that the previous low-rate well-test had been caused by reservoir damage prior to testing (See Chapter 3.2 for the history). The petrophysical evaluation used by the old operator relied on standard methods with no consideration given to the likelihood of deep invasion resulting from the combination of significant fluid pressure overbalance and the low permeability reservoirs (McPhee *et al*., 2008). In the integrated study that followed, the new operator used SCAL to demonstrate that the use of excess overbalance (400psi) while drilling had led to up to 60 inches of invasion of filtrate from the brine water-based mud. Well test analysis showed a skin ranging from +24 to +175. Redrilling of the well using oil-based mud with minimal overbalance led to negligible invasion and eliminated the skin. The resulting nearly six-fold increase in flow demonstrated the commercial viability of the field (Besly, 2019).

7.4 Recommendation for future work.

7.4.1 Facies analysis.

More samples should be analysed with the imaging techniques and perhaps the mudstone samples could be analysed with higher resolution facility for a wider comparison and insights into the variability of sandstones Formation. As the highly heterolithic nature of Carboniferous clastic succession in the SNS, in which thin-bedded units of mechanically strong sandstone alternate with mechanical weak and/or brittle shale and coal, could lead to extensive caving and borehole collapse unless drilling is carefully managed (Besly, 2019).

7.4.2 Mineralogy and diagenesis.

1. Application for QEMSCAN and Cathodoluminescence (CL) mapping could be useful in obtaining the distribution of the mineralogy in the studied sandstone. The CL mapping could be particularly useful for a more accurate characterization of quartz overgrowth in the studied area and so know the precise amount of quartz overgrowth necessary to reduce reservoir quality. The current study (see chapter 5. 7) already makes a link between higher porosity measurements with samples with no discernible quartz overgrowth but did not have the instrumentation for more precise measurement. However, a different methodology with a better ability to characterize

quartz cement like the CL will be useful.

2. Fluid inclusion data will be useful to calculate the homogenization temperature (th) value for the carbonate cement in the Breagh area since the studied samples contain very small inclusion (less than 20μm) and so could not be investigated for fluid inclusions. Petrographic analysis and proxy data from neighboring fields have been used to determine the timing of carbonate cement relative to the other diagenetic events in the current study (see chapter 5.6.2.5). However, because the samples used in the current study contain relatively small inclusions, samples in 42/13a-6 and the horizontal wells – 42/13-5 and 42/13-5Z might be a reasonable place to start.

3. Electron Probe Micro-Analyser (EPMA) can be used to analyze the iron content changes across the zones within the carbonate cement and so used to discriminate the fine variation in pore fluid chemistry. Both the Th value and pore fluid chemistry variation could serve as useful elemental component in hydrocarbon generation and migration model for the Early Carboniferous of the SNS.

4. Characterisation of other surrounding wells towards an understanding of their diagenetic processes and implication on reservoir quality and their comparison to those examined in this study would give insight into further exploration activities within the Lower Carboniferous Formation. Breagh Field well 42/13a-6, Crosgan well 42/15a-2 42/13a-6, 42/10b-2 and Macanta 42/14-2 will be excellent core examples.

7.4.3 Pore size architecture.

1. More sample should be analysed from each facies to properly characterise the pore size geometry distribution across the facies. This will help build a robust permeability model as well determine what zones are more productive and why. This is especially important for the thinner sands (delta front sands -FA4, FA5) and abandoned channel facies - FA10) that may have productive secondary porosity.

2. The 3D model of the pore networks generated within the sandstone units could serve as a springboard for future applications that would further the understanding of flow capacity simulations of petrophysical properties (Riepe *et al*., 2011; Zhang *et al*., 2017;

Eltom *et al*., 2019) and prediction of multiphase flow properties (Bera and Shah, 2021; Escobar *et al*., 2023).

3. Integration of 3D seismic datasets to the available datasets (core and field data) employed in this study will provide better interpretation on future hydrocarbon prospectivity on a regional context of the studied area, allowing a measure of predictability.

7.5 References

Aagaard, P., and J. Jahren, 2010, Diagenetic controls on evolution of porosity and permeability in lower Tertiary Wilcox sandstones from shallow to ultradeep (200—6700 m) burial, Gulf of Mexico Basin, USA [Marine and Petroleum Geology 27 (2010), 69—81]: Marine and petroleum geology, v. 27, no. 8.

Bera, A., and S. Shah, 2021, A review on modern imaging techniques for characterization of nanoporous unconventional reservoirs: Challenges and prospects: Marine and Petroleum Geology, v. 133, p. 105287.

Besly, B., 2019, Exploration and development in the Carboniferous of the Southern North Sea: a 30-year retrospective: Geological Society, London, Special Publications, v. 471, no. 1, p. 17–64, doi:10.1144/SP471.10.

Booth, M. G., J. R. Underhill, A. Gardiner, and D. McLean, 2020, Sedimentary and tectonic controls on Lower Carboniferous (Visean) mixed carbonate–siliciclastic deposition in NE England and the Southern North Sea: implications for reservoir architecture: Petroleum Geoscience, v. 26, no. 2, p. 204–231.

Brackenridge, R. E., J. R. Underhill, R. Jamieson, and A. Bell, 2020, Structural and stratigraphic evolution of the Mid North Sea High region of the UK Continental Shelf: Petroleum Geoscience, v. 26, no. 2, p. 154–173.

Chi, G., P. S. Giles, M. A. Williamson, D. Lavoie, and R. Bertrand, 2003, Diagenetic history and porosity evolution of Upper Carboniferous sandstones from the Spring Valley #1 well, Maritimes Basin, Canada–implications for reservoir development: Journal of Geochemical Exploration, v. 80, no. 2, p. 171–191, doi:10.1016/S0375-6742(03)00190-0.

Eltom, H. A., E. C. Rankey, S. T. Hasiotis, and R. Barati, 2019, Effect of bioturbation on petrophysical properties: Insights from geostatistical and flow simulation modeling: Marine and Petroleum Geology, v. 104, p. 259–269.

Escobar, F. H., J. D. Chamorro, and J. S. López, 2023, A New Correlation to Find the Productivity Index for Horizontal Wells in Naturally Fractured Reservoirs.: Petroleum & Coal, v. 65, no. 1.

Glennie, K. W., 1986, Development of NW Europe’s Southern Permian gas basin: Geological Society, London, Special Publications, v. 23, no. 1, p. 3–22.

Grant, R. J., M. G. Booth, J. R. Underhill, and A. Bell, 2020, Structural evolution of the Breagh area: implications for carboniferous prospectivity of the Mid North Sea High, Southern North Sea: Petroleum Geoscience, v. 26, no. 2, p. 174–203.

Holditch, S. A., 2013, Unconventional oil and gas resource development – Let’s do it right: Journal of Unconventional Oil and Gas Resources, v. 1–2, p. 2–8, doi:10.1016/j.juogr.2013.05.001.

Lawal, L. O., A. R. Adebayo, M. Mahmoud, B. M. Dia, and A. S. Sultan, 2020, A novel NMR surface relaxivity measurements on rock cuttings for conventional and unconventional reservoirs: International Journal of Coal Geology, v. 231, p. 103605.

Lee, J., 1982, Well Testing: Society of Petroleum Engineers of AIME: Dallas, TX.

Li, J., G. Fu, and Z. Liu, 2022, Quantitative characterization of the lower limit of the physical properties of tight oil reservoirs in Nano-Material porous media: Integrated Ferroelectrics, v. 227, no. 1, p. 288–303.

Mclean, D., 2011, Biostratigraphy of the Carboniferous interval in Breagh East well 42/13a-6, Southern North Sea, 68: MB Stratigraphy Ltd.

McPhee, C. A., M. R. Judt, D. McRae, and J. M. Rapach, 2008, Maximising Gas Well Potential In The Breagh Field By Mitigating Formation Damage: Society of Petroleum Engineers, doi:10.2118/115690-MS.

Morad, S., 1990, Mica alteration reactions in Jurassic reservoir sandstones from the Haltenbanken area, offshore Norway: Clays and clay minerals, v. 38, no. 6, p. 584–590.

Nwachukwu, C. M., Z. Barnett, and J. G. Gluyas, 2020, The Breagh Field, Blocks 42/12a, 42/13a and 42/8a, UK North Sea: Geological Society, London, Memoirs, v. 52, no. 1, p. 109–118.

OGA, 2017, Southern North Sea, Tight gas, Stimulation Guidance: Oil & Gas Authority.

Oluwadebi, A. G., K. G. Taylor, and L. Ma, 2019, A case study on 3D characterisation of pore structure in a tight sandstone gas reservoir: The Collyhurst Sandstone, East Irish Sea Basin, northern England: Journal of Natural Gas Science and Engineering, v. 68, p. 102917.

Pettijohn, F., 1957, Sedimentary Rocks: Harpers, New York, NY, p. 718.

Qin, X., Y. Xia, J. Qiao, J. Chen, J. Zeng, and J. Cai, 2023, Modeling of multiphase flow in low permeability porous media: Effect of wettability and pore structure properties: Journal of Rock Mechanics and Geotechnical Engineering.

Riepe, L., M. H. Suhaimi, M. K. Malaysia, and M. A. Knackstedt, 2011, Application of high resolution Micro-CT imaging and pore network modeling (PNM) for the petrophysical characterization of tight gas reservoirs-a case history from a deep clastic tight gas reservoir in Oman, *in* SPE Middle East unconventional gas conference and exhibition: OnePetro.

Rodriguez, K., R. Wrigley, N. Hodgson, and H. Nicholls, 2014, Southern North Sea: unexplored multi-level exploration potential revealed: First Break, v. 32, no. 6, p. 107–113.

Symonds, R., R. Lippmann, B. Mueller, and A. Kohok, 2015, Yoredale sandstone Architecture in Breagh Field (UK SNS). Presentation for Sedimentology of Paralic Reservoirs: Recent advances and their applications.: p. 24.

Zhang, L., S. Lu, D. Xiao, and B. Li, 2017, Pore structure characteristics of tight sandstones in the northern Songliao Basin, China: Marine and Petroleum Geology, v. 88, p. 170–180, doi:10.1016/j.marpetgeo.2017.08.005.

Blank page

Blank Page

Appendix 1

BREAGH SUMMARY TABLE		
Breagh Field	*(Data and suggested Units)*	*(Author's explanatory comments)*
Trap		
Type	Combination of tilted fault block with dip closure	
Depth to crest	8400 (ft MD) 7200 ft TVDSS	
Hydrocarbon contacts	Free Water Level at 7690 (ft TVDSS)	From 42/13a-6 Gas-Down-To (GDT) levels are established as follows 42/13-2: 7668ft TVDSS 42/13-3: 7503ft TVDSS 42/13-4: 7599ft TVDSS 42/13-5: 7347ft TVDSS
Maximum oil column thickness	NA	
Maximum gas column thickness	510 ft	
Main Pay Zone		
Formation	Middle and Lower Limestone	
Age	Visean, Early Carboniferous	
Depositional setting	Fluvial-deltaic setting	Distributary channels and sheet sands
Gross/net thickness	66 ft	
Average porosity	11.60% Zone 1B: 14% Zone 1A: 13%	Interbedded sandstones and claystones
Average net:gross ratio	Zone 1B: 0.35 Zone 1A: 0.30	:
Cutoff for net reservoir estimation	Phie 0.075 Vclay 0.4	
Permeability range Average permeability	0.1-100 mD Zone 1: 1-10 mD	
Average hydrocarbon saturation	Zone 1B: 0.65 Zone 1A: 0.7	
Productivity index range	NA	
Hydrocarbons		
Fluid type	Dry Gas	
Gas specific gravity	0.618	

Bubble point (oil)	NA	At reservoir depth (185˚F) no condensate will appear over the field life
Dew point (condensate)		
Condensate /gas ratio Water/gas ratio	3 bbl/MMscf 2 bbl/MMscf	
Formation Volume Factor (oil)	NA	
Gas Expansion Factor	0.00444	
Formation Water		
Salinity	~188,500 ppm NaCl equivalent	
Resistivity	0.056 ohm.m @ 60˚F	
Water gradient	0.49 psi/ft	From 42/13a-6
Reservoir Conditions		
Temperature @ Top reservoir	185˚F at 7200 ft TVDSS	
Pressure @ Top reservoir	3,744psia at 7200 ft TVDSS	
Gas gradient	0.088 psi/ft	From 42/13a-6
Field Size		
Area	94 km^2	
Gross Rock Volume	1220 Mm^3	
GIIP	P90: 751 bcf P50: 909 bcf P10: 1040 bcf	
Drive mechanism (primary, secondary)	Depletion	
Recovery to date - oil	NA	
Recovery to date - gas	125 bcf	
Expected ultimate recovery factor/volume - oil	NA	
Expected ultimate recovery factor/volume - gas	50% (2040)	
Production		
Start-up date	Oct-13	
Number of Exploration/Appraisal Wells	6	

Number of Production Wells	10	
Number of Injection Wells	NA	
Development scheme	Phased development	
Highest rate - gas	158 MMscf/d (November 2014)	
Planned abandonment	*Undeveloped*	

Appendix 2

Lithofacies	Sedimentary structure	Description/interpretation
massive mud	load structure, fossil fragment	Prodelta
massive, mud	parallel lamination, burrows and nodules are possible (brown patches?). some siltstones lenses are visible	Interdistributary bay
massive, mud	nodules set on load structure, horizontal planar lamination also visible	overbank or drape deposit probably floodplain or Crevasse splay
mud	Horizontal planner lamination	back swamp deposit probably interdistributary bay
Lime mud	Alternating from marl to mudstone, mudstones have brown nodules and parallel bedding	Marl
Carbonaceous mud, silt	Heterolithic deposit, carbonate concretions	Swamp deposits
Carbonate	No visible structure	Limestone
Limestone, mud	Paedogenic features	Marl
Coal, carbonaceous mud, silt	Carbonate concretions, mud films, siltstone streaks	Interdistributary bay, swamp deposits
mud silt	Heterolithic mudstones with siltstone, wave ripple and climbing ripple within the siltstone horizons	Overbank or waning flood deposit possibly indicating the end stage of a channel deposit (Braided fluvial or distributary channel)
mud silt	Lenticular lamination, large lenses of siltstone about 7.5cm across and small lenses about 1cm, silty layers are bioturbated, nodules about 4 by 2cm formed around burrow assemblage in muddy horizons	Swamp deposit probably Interdistributary bay
mud silt	Alternation between reverse grading and normal grading. rhythmic lamination to cross planar lamination. wavy lamination, climbing ripples and distorted	overbank, wanning flood deposit- Hyperpycnal flow mixed with hemipelagic deposit at background times- Distal delta front sand as in proximal or distal delta front

	climbing ripples also present, some paleosols are also visible	sand and probably some seat earth
mud, silt	Predominately muddy horizons with silt lenses; bioturbated, burrow assemblage	Crevasse splay or interdistributary bay
mud, silt	parallel lamination, load cast	Interdistributary bay
mud, silt, sand	flaser bedding with large thin drapes of mud rock, sub mm scale rhythmic lamination, sandy layer thinly laminated, parallel	overbank, wanning flood deposits
Coal	Coal	Swamp deposit
Silt, very fine sand, mud	Sandy mudstones or silty mudstones with rootlets	Palaeosol or Seat earth
silt, fine sand	multi storey fine grained sandstone to silty sandstone, low angle cross beds	Crevasse splay, scour fill, antidunes
Silt fine sand	Silty fine sandstone, with intercalated streaks of mudstone. Replete with many structures- Changes from parallel bedding to internal cross lamination to wavy bedding and some distorted climbing ripples. Normal grading to reverse bedding	Overbank or wanning flood deposit. Possibly Delta front sands or Abandoned channel fill
fine to medium sand	Internal lamination, bioturbated	Crevasse splay/ Abandoned channel
fine to medium sand	internal cross lamination with thin drapes of mudstone and or reddish-brown sandstone	Abandoned channel fill
fine to medium sand	internal flaser lamination; some disturbed bedding, no visible lamination	Crevasse splay
Fine to medium sand	submm rhythmic lamination grading, discontinuous lamination to flaser lamination, parallel wave lamination, parallel planar lamination, mud rock	scour fills, crevasse splay, dunes

	partings are also seen as well as lenticular bed parting within the siltstones	
fine to medium sand	Massive	abandoned channel fills, minor channel fills
Fine to medium sand	Distorted bedding with wet sediment deformation, fine sand sediments have intruded into the overlying. medium sands	Locally induced seismicites
Fine to medium grained sands- with silty tops	Erosive based fine to medium grained. parallel planar laminations, cross beds and current ripples are evident. The finer grained horizons at the top are more finely laminated with some mudstones at the forests of the beds.	Evidence of erosion reactivation surface, scour fills, abandoned channel.
medium to coarse sand	Dual storey silty sandstone; medium to coarse grained sandstone; ripple marks of all types, horizontal lamination	Ripple, Planar bed flow
Medium to coarse grained sandstone	Mostly massive sandstones with no internal structure, although some parallel planar laminations and current ripples are visible; Trough cross beds	Minor channel fills
Medium to coarse sand	Erosive based medium to coarse bed sandstones may be solitary or grouped, contains rip up clast with granules or pebbles at the base, crossbreds seen in medium grained horizons	Dunes, (lower flow regime)
Coarse - Very Coarse sands, pebbly and gravely	Stacks of multistorey fining upward erosive based, coarse to very coarse sandstone may be pebbly and granular at the base.	Channel fills

Appendix 3

ENVIRONMENT	SUBENVIRONMENT	FACIES ASSOCIATION	DESCRIPTION
Delta Plain	Swamp	FA12	Mudstones, siltstones and current-rippled and/or climbing current-rippled fine sandstones that are typically overlain by coal. Rooted horizons are observed. Weakly to highly bioturbated (0-4).
	Crevasse Splay	FA11	Erosive-based, fine to medium grained sandstone. Often upward-fining. The sandstone is moderately- to well-sorted and display cross-stratification at the base with current-ripple lamination dominating upwards. Abundant carbonaceous plant material throughout. Very weakly bioturbated (0-1).
	Abandoned Channel	FA10	Heterolithic very-fine- to fine-grained sandstones and siltstones with current ripples, occasional thin trough cross-bedding. It has deformed/slumped horizons and rooted bed tops. Includes bioturbated horizons (0-2).
	Braided fluvial channel	FA9	Erosive-based,medium to coarse grained sandstones with planar cross beds or trough cross-beds. The bases are very coarse and occassionaly pebbly. The bottom horizons also contain occassional rip up clast and plant material. Bioturbation is not visible (0-1)
	Distributary Channel	FA8	Erosive-based, well-sorted, fine- to medium-grained sandstone. It consist of occasional coal clasts and plant debris.
	Interdistributary Bay	FA7	Very-fine- to fine-grained sandstones with lenticular or flaser bedding, parallel lamination, wave and current ripples.Also consist of heterolithic mudstones and siltstones. slump and water escape structures is visible. Weakly to highly bioturbated (3-5).
Delta front	Distal Delta Front sand	FA5	Alternating between muddy siltstone and silty sandstones with decemeter sized climbing ripples, wave formed ripples, horizontal planar lamination, Parallel- to ripple-laminated siltstones, and, very-fine-grained sandstone.Abundant plant material are common along bedding planes. Siderite concretions are also visible. Sparsely to highly bioturbated (1-4).
	Proximal Delta Fronts Sand	FA4	Muddy, very-fine- to fine-grained sandstone with coarsening upward vertical profiles. Silt drapes are found within the sandstones. Silty mudstone and the mudstones display climbing ripples whilst the siltstones have planar parallel lamination. Abundant plant material and common coal clasts are preserved. Sparsely to weakly bioturbated (1-3).
	Distributary mouth bar	FA3	Well-sorted, medium to coarse -grained sandstones displaying trough crossbedding. Occasionally pebbly with coarse- to very-coarse-grained erosive bed bases, with rip up and coal coal clasts. Sparsely to moderately bioturbated (1-3).
Pro-delta	Prodelta	FA2	Dark grey massive mudstones. Sometines laminated, with crinoid and brachiopod debris near the base. Siderite nodules are common. This FA contains rare soft-sediment deformation including convolute lamination and slump structures. Bioturbation is not common (0-1).
Carbonate Platform	Limestone	FA1	Highly bioturbated (5-6) fossiliferous limestione (corals and rugose corals), crinoid ossicles, brachiopods, bryozoa. Also Also as part of this FA is muddy limestones and some mudstone partings.

Appendix 4

Pore ID	Volume	Area	EqRadius	LabelID	Pressure	X Coord	Y Coord	Z Coord	Pore Coordination Number
0	48207	15596	22.5773983	1	130000	1026.3	606.24	17.461	2
1	2143	1534.2	7.997935295	2	130000	916.02	701.25	3.9673	1
2	11079	4795.6	13.829422	3	130000	909.66	756.72	9.2766	2
3	223494	60614	37.64660263	4	130000	832.75	762.34	19.003	4
4	223108	68679	37.62491989	5	130000	1204.2	780.45	38.402	2
5	105635	21962	29.32511902	6	130000	1150.3	768.74	13.974	2
6	30921	19008	19.47100449	7	130000	664.84	834.52	10.537	3
7	33696	9846.9	20.03687286	8	130000	1352.1	896.56	12.222	1
8	23832	11924	17.85215569	9	130000	1259.7	918.62	10.846	1
9	4011	2293.3	9.856470108	10	130000	532.54	939.92	4.9726	1
10	259502	43516	39.56860733	11	130000	594.81	960.45	24.831	3
11	12222	5041.4	14.2895298	12	130000	1146.6	1041.5	17.859	2
12	4493	3830.4	10.23644829	13	130000	1431	1074.7	12.582	2
13	9028	4850.4	12.91717911	14	130000	980.52	1091.3	4.4623	1
14	64348	13280	24.85891724	15	130000	1328.8	1125.6	26.822	2
15	339619	58677	43.28138733	16	130000	1138.9	1127.5	28.926	8
16	3287	1679.2	9.223670006	17	130000	1412.5	1141.4	4.5753	1
17	82777	29361	27.03587341	18	130000	869.02	1163.6	11.536	3
18	27170	6387.5	18.64949417	19	130000	1213.2	1167.7	8.3417	3
19	5974	3017	11.25621128	20	130000	600.24	1178.3	10.046	1
20	62196	20240	24.57864761	21	130000	1263.6	1189.3	8.2213	6
21	52193	12980	23.18326569	22	130000	931.4	1220.7	8.7125	3
22	10129	5856.3	13.42227173	23	130000	1283	1223.3	14.463	4
23	6805	4179.3	11.75564766	24	130000	1318.6	1249.5	14.585	3
24	28254	23884	18.89428711	25	130000	1011.6	1324.7	15.303	1
25	28477	16559	18.94386482	26	130000	1242.4	1307.9	29.663	4
26	516362	76511	49.76858521	27	130000	878.83	1300.3	35.49	5
27	44596	17564	21.99897766	28	130000	810.91	1392.4	11.112	3
28	10553	9991.5	13.60700321	29	130000	741.95	1384.2	63.239	0
29	24747	21537	18.0777626	30	130000	946.27	1426.6	18.928	1
30	26099	9102.5	18.40115738	31	130000	992.48	1118.7	15.374	2
31	43484	13684	21.81458855	32	130000	1066.7	631.57	13.086	2
32	41341	18403	21.45017433	33	130000	675.28	1042	17.839	3
33	8217	4344	12.51819134	34	130000	1072.4	865	21.35	2
34	12682	6721.7	14.46659851	35	130000	732.68	1078.8	22.534	2
35	10337	8810.3	13.51352596	36	130000	710.97	1123.6	23.813	3
36	211000	60463	36.93159103	37	130000	1383.4	1176.9	35.583	7
37	83630	28966	27.12842369	38	130000	1215.8	639.1	23.31	2
38	161242	32319	33.76472855	39	130000	1233.2	1149.9	30.134	9
39	44946	23747	22.05637741	40	130000	671.84	1216.6	31.361	2
40	25594	11060	18.28170013	41	130000	1195.1	1282.8	19.088	4
41	3811	2835.1	9.689845085	42	130000	1053.4	1358.4	29.09	3

42	24061	15081	17.90915298	43	130000	1068.2	1429.9	18.243	2
43	21158	10249	17.15781784	44	130000	601.84	793.41	28.242	3
44	58217	21187	24.04291534	45	130000	636.97	744.34	42.483	3
45	23219	10611	17.69776154	46	107509	1180.7	1336.5	42.36	4
46	446966	77458	47.43097305	47	130000	1350.4	966.75	36.081	7
47	16302	6406.1	15.72959232	48	130000	984.47	1240.8	35.048	2
48	17318	7047.7	16.04980469	49	114088	753.25	734.09	42.489	2
49	534316	100298	50.3388443	50	130000	779.17	1280.2	41.197	5
50	42123	18835	21.58457947	51	100000	1022.2	944.53	51.658	3
51	20337	15492	16.9329567	52	130000	1113.5	1380.7	59.362	2
52	11530	6193.9	14.01458645	53	130000	1104	794.3	29.361	2
53	21838	9302.7	17.33969498	54	126149	1002.6	1119.7	45.553	2
54	50819	24220	22.97801781	55	100000	1123.3	1242.2	57.78	3
55	21770	11896	17.32167816	56	100000	1158	1298.9	56.041	4
56	646674	104108	53.64537811	57	130000	1283.5	1055.8	51.944	6
57	38178	25159	20.8885479	58	130000	1034.8	1243.6	52.333	1
58	54239	19551	23.4823246	59	130000	1045	851.54	49.508	5
59	33623	11068	20.02239418	60	130000	701.32	979.3	49.278	1
60	56063	27422	23.7426548	61	100000	809.43	1022.2	40.856	2
61	40999	15340	21.39086151	62	129109	1051.8	796.8	50.471	3
62	38089	18114	20.87230301	63	100000	559.38	1063.9	57.937	2
63	17278	10406	16.03743744	64	100000	1320.8	1237.2	69.562	4
64	23392	10433	17.74160767	65	102158	1222.7	1377.1	54.757	2
65	340750	70281	43.32938004	66	130000	1122.6	612.86	59.012	4
66	15178	10778	15.3594389	67	100000	1049.2	714.25	68.615	1
67	32703	10015	19.83808327	68	100000	1101	850.05	65.818	2
68	41277	27922	21.43910027	69	130000	1299.3	1311.9	52.501	4
69	29539	13197	19.17648888	70	100000	595.94	1194.3	64.765	3
70	16858	8486.4	15.90642262	71	129935	1421.3	1005	61.681	2
71	85344	33530	27.31250381	72	100000	721.89	759.35	70.79	5
72	145923	49599	32.65966797	73	130000	996.84	886.55	55.855	4
73	207167	37245	36.70658875	74	100000	1229.2	1107.8	70.812	4
74	4684	2233.9	10.37949276	75	130000	1203.8	1231.9	66.44	1
75	23737	17791	17.82840347	76	100000	883.93	1396.9	74.321	2
76	58282	14389	24.0518589	77	100000	833.53	1080.9	75.758	2
77	26672	11283	18.53484917	78	100000	999.47	1119.4	82.57	2
78	43011	16049	21.73520279	79	100000	631.22	781.03	77.066	4
79	28092	11103	18.85810471	80	100000	1072	1203.9	80.736	2
80	97587	24509	28.56063271	81	100000	891.59	1266.3	78.461	4
81	14387	7785.8	15.08784676	82	100000	1077.9	562.32	76.1	2
82	11083	8155.1	13.83108616	83	100000	769.48	850.37	82.79	2
83	264145	50350	39.80319977	84	100000	594.53	922.93	72.761	2
84	30111	13652	19.29947853	85	100000	1027.5	593.92	79.991	2
85	21937	11369	17.36585808	86	100000	735.6	1074.2	80.477	2
86	25478	12356	18.25403786	87	100000	596.63	1081.2	83.85	5
87	36192	18167	20.51987457	88	100000	765.77	1105.6	83.767	3

88	33492	10157	19.99635696	89	100000	1425.1	894.79	87.542	1
89	27906	12591	18.8163929	90	100000	978.46	941.02	80.405	2
90	13256	9593.5	14.68164349	91	100000	688.32	1147.5	81.269	3
91	11482	5719.3	13.99511147	92	100000	1237.4	1392	89.895	1
92	14407	4986	15.09483433	93	100000	825.55	1063.1	92.554	1
93	5528	4495.4	10.96881866	94	100000	1263.3	1272.3	89.802	2
94	23843	8512.7	17.85490227	95	100000	605.28	1161.3	89.041	4
95	2944	1761.8	8.890982628	96	100000	1043.8	845.41	93.007	1
96	2710	1855.8	8.648887634	97	100000	1051	944.02	94.941	1
97	71932	19385	25.7994957	98	100000	1405.8	1060.4	80.011	3
98	159924	49142	33.67247772	99	100000	882.04	777.78	80.789	2
99	40241	13290	21.25821304	100	100000	1386.7	878.96	85.673	2
100	29433	9607.1	19.1535244	101	100000	808.66	938.97	89.177	1
101	36389	11075	20.55703926	102	100000	1252.9	638.41	83.076	1
102	19629	7403.3	16.73413277	103	100000	658.77	1068.4	90.745	3
103	26306	8138.2	18.44967842	104	100000	639.36	990.03	92.684	2
104	23002	9127.3	17.64245605	105	100000	1051.3	1137	92.644	3
105	1747	1525.8	7.471391201	106	100000	634.51	831.84	95.275	2
106	8257	4967.7	12.53847122	107	100000	671.28	875.75	91.631	2
107	16052	8456.3	15.64877033	108	100000	847.94	1190.4	92.275	1
108	963	794.54	6.126031876	109	100000	977.82	1243.6	96.597	2
109	7444	5832.7	12.11265373	110	100000	943.74	1359.8	90.439	1
110	3257	1759.3	9.195522308	111	100000	571.83	1133.1	95.883	2
111	607	455.95	5.252508163	112	100000	998.7	1229.4	97.216	1

Appendix 5

Throat ID	Area	EqRadius	ChannelLength	FlowRatePerSec	Pore ID #1	Pore ID #2
0	779.513	15.752	47.8228	0	31	0
1	8.09271	1.60499	56.08	0	2	1
2	2400.79	27.6441	60.3447	0	5	4
3	166.067	7.27055	77.7249	0	3	2
4	183.291	7.63827	182.962	0	6	3
5	159.63	7.12823	68.502	0	10	9
6	0.28762	0.30257	136.734	0	46	12
7	1682.02	23.1388	86.8837	0	56	14
8	318.249	10.0649	31.8601	0	30	13
9	741.515	15.3633	108.917	0	56	38
10	983.224	17.691	96.8911	0	38	15
11	229.634	8.54955	55.3753	0	36	16
12	2.1064	0.81883	141.86	0	56	20
13	412.157	11.454	75.4198	0	36	14
14	1608.48	22.6273	34.4878	0	38	18
15	283.902	9.50626	123.503	0	36	20
16	564.678	13.4068	54.8724	0	20	18
17	505.372	12.6833	84.5912	0	21	17
18	208.295	8.14263	150.138	0	49	17
19	169.175	7.33825	39.6312	0	22	20
20	2969.09	30.7423	101.827	0	49	26
21	435.942	11.7798	120.431	0	49	27
22	341.389	10.4244	74.1599	0	46	7
23	1126.75	18.9382	99.0632	0	26	21
24	821.188	16.1676	74.7548	0	65	31
25	1393.5	21.0609	54.3715	0	38	20
26	176.28	7.49077	63.4095	584968256	72	50
27	48.9361	3.94675	105.765	0	46	8
28	36.7454	3.42001	112.645	0	36	22
29	7.95522	1.5913	77.2864	0	43	6
30	78.8997	5.01144	86.886	0	18	15
31	53.9994	4.14591	85.7783	0	72	33
32	108.352	5.87277	49.7935	0	35	34
33	44.5793	3.76697	99.5997	0	36	23
34	54.5163	4.1657	103.198	0	65	37
35	30.0583	3.0932	55.1451	0	52	5
36	85.9551	5.23071	116.403	0	40	20

37	12.3079	1.97933	55.4387	1.5821E-09	41	24
38	24.4501	2.78975	163.509	0	35	17
39	417.513	11.5282	87.5778	1260211968	48	3
40	69.0293	4.6875	68.3317	0	34	32
41	34.164	3.29769	53.3144	1.2676E-08	57	47
42	91.8792	5.40796	60.3202	125240936	45	40
43	635.703	14.225	31.8524	1944113280	53	30
44	106.461	5.8213	62.564	1.0489E-07	47	21
45	37.2544	3.44361	139.836	0	29	27
46	227.851	8.5163	112.519	0	56	46
47	29.025	3.03956	57.1703	17589622	69	19
48	113.786	6.01824	56.3168	8153990.5	61	52
49	187.657	7.72871	73.3733	572890944	97	12
50	80.7207	5.06895	125.154	0	49	39
51	102.509	5.71224	54.6611	0	40	25
52	99.9256	5.6398	73.8124	7.8326E-08	42	41
53	7.47835	1.54287	96.6765	690514	75	27
54	70.5274	4.7381	84.5548	151045.125	70	46
55	350.263	10.559	119.272	1227812224	54	15
56	57.3978	4.27438	41.4889	0	58	33
57	17.4568	2.35726	165.366	0	40	15
58	207.984	8.13655	93.3825	552938240	63	36
59	22.211	2.65894	56.374	10445744	63	23
60	18.5874	2.4324	75.5277	2.6486E-09	68	23
61	75.5596	4.90422	74.8407	0	59	32
62	1797.36	23.919	77.479	4.977E+10	73	56
63	2499.29	28.2055	58.7309	1.2695E+11	73	38
64	178.47	7.53715	58.31	652030144	78	43
65	145.906	6.81492	87.056	0	15	11
66	1132.97	18.9904	101.447	1.5104E+10	73	15
67	4057.51	35.9381	60.8661	3.2287E+11	83	10
68	16.245	2.27397	97.7969	1.5624E-09	68	22
69	131.591	6.472	46.0317	112388960	55	45
70	332.635	10.2898	49.2137	1260211968	71	48
71	301.446	9.79557	59.8977	0	72	58
72	39.9286	3.56506	66.2247	28736242	90	35
73	125.479	6.31991	61.4422	1.4837E-07	68	25
74	413.317	11.4701	50.7499	4018032128	78	44
75	85.4081	5.21404	62.0019	0	44	43
76	21.9579	2.64375	174.571	3296774.5	55	15

77	65.8773	4.57923	159.981	1.5707E-08	68	36
78	41.9785	3.65543	90.0559	0	38	22
79	636.961	14.2391	80.5327	6013605888	98	3
80	0.56562	0.42431	78.5076	0	51	42
81	58.2488	4.30595	236.8	0	46	4
82	29.0866	3.04279	70.8686	6.9121E-09	51	41
83	336.666	10.352	55.1657	72871576	61	58
84	133.549	6.51997	69.5786	305977280	81	65
85	15.8625	2.24704	63.744	4711792.5	84	0
86	53.5146	4.12725	103.504	0	87	60
87	82.5835	5.1271	59.691	24324024	64	45
88	20.1606	2.53324	90.7716	5344875.5	71	44
89	224.907	8.46109	58.3249	1035217024	67	58
90	29.7833	3.07901	69.1958	11472051	45	25
91	10.7792	1.85233	125.522	1104929.5	66	65
92	106.898	5.83325	66.5187	0	55	54
93	55.0774	4.18708	111.968	32339552	71	6
94	3014.89	30.9785	56.2763	1.928E+11	80	26
95	72.0048	4.78747	74.1109	81025568	67	61
96	48.3934	3.92481	119.257	23440634	80	49
97	83.2965	5.14918	88.9381	93120864	55	25
98	25.4461	2.846	118.369	6529583	73	11
99	22.7247	2.68952	52.4269	0	89	50
100	2.87279	0.95626	109.911	89628.8047	86	32
101	47.0821	3.87127	70.3496	37612436	101	37
102	200.652	7.99183	72.4139	0	76	60
103	263.478	9.15792	37.1517	1944113280	77	53
104	46.5443	3.84909	85.8712	30113934	69	39
105	380.823	11.01	62.5106	2769323776	89	72
106	489.114	12.4776	125.574	2274049024	97	56
107	99.1923	5.61906	48.5694	0	86	62
108	452.811	12.0056	43.6728	0	87	85
109	57.8238	4.29021	67.9855	0	79	54
110	30.5811	3.11998	94.3379	0	74	38
111	62.6681	4.46631	161.515	0	98	71
112	924.013	17.15	41.6282	0	99	88
113	83.0522	5.14163	139.397	59064976	93	38
114	29.4308	3.06074	103.822	9958604	109	26
115	113.521	6.01124	42.0334	0	94	69
116	107.626	5.85308	40.8932	24324024	91	64

117	712.411	15.0588	83.1232	0	103	83
118	34.2282	3.30078	129.786	10775097	63	38
119	47.2943	3.87998	114.243	23370630	62	10
120	34.705	3.32369	88.0759	0	90	87
121	188.793	7.75208	104.2	408306144	75	26
122	68.5588	4.6715	59.6269	0	84	81
123	43.7841	3.73322	103.867	0	106	78
124	977.369	17.6382	25.7142	0	92	76
125	45.0022	3.78479	108.807	22217412	104	15
126	22.8877	2.69914	52.0375	0	96	50
127	59.6558	4.35764	77.7278	0	102	85
128	27.0586	2.9348	103.406	0	82	71
129	20.4157	2.54922	97.0943	0	100	82
130	52.0523	4.07047	57.3915	0	106	105
131	57.9359	4.29437	43.9444	91174504	95	58
132	2.76566	0.93826	60.3167	151045.125	97	70
133	22.0287	2.64801	88.5908	0	107	80
134	66.4711	4.59983	55.6209	0	104	77
135	57.8032	4.28945	70.3075	0	93	63
136	91.0387	5.38317	44.2899	0	110	94
137	61.0846	4.40952	80.7756	0	103	102
138	34.3487	3.30659	80.6808	0	94	86
139	29.6352	3.07135	90.9901	0	108	80
140	27.2512	2.94522	58.7064	0	110	86
141	13.2681	2.05508	107.156	1961004.75	99	46
142	14.7456	2.16649	54.0682	0	105	78
143	2.32241	0.85979	84.5293	0	94	90
144	8.69496	1.66364	71.0364	0	104	79
145	0.96908	0.5554	25.2447	0	111	108
146	0.96082	0.55303	63.823	0	102	86